NNT : 0000AIXM0000

# THÈSE DE DOCTORAT

Soutenue à Aix-Marseille Université
le 11 décembre 2025 par


## Eduardo ROEMERS DE OLIVEIRA


# Détection et analyse quantitative de corps géologiques à partir de modèles numériques d'affleurements : applications à la modélisation d'analogues de gisements de pétrole et gaz

# Detection and quantitative analysis of geological bodies from Digital Outcrop Models (DOMs): applications to oil and gas reservoir analogue modelling

**Discipline**
Sciences de l'environnement

**Spécialité**
Géosciences

**École doctorale**
ED 251 – Sciences de l'environnement

**Laboratoire/Partenaires de recherche**
Petrobras - Brésil
Universidade Federal do Pampa – Brésil
Universidade Estadual de Maringá – Brésil

**Composition du jury**

**Emmanuelle VENNIN** Rapporteuse
Professeure – Université de Bourgogne
**Guillaume CAUMON** Rapporteur
Professeur – Université de Lorraine
**Sophie LELEU** Examinatrice
Docteur – Université de Bordeaux
**Jean-Luc MARI** Examinateur
Professeur – Aix-Marseille Université
**François FOURNIER** Directeur de thèse
Docteur – Aix-Marseille Université
**Sophie VISEUR** Co-directrice de thèse
Docteur – Aix-Marseille Université
**Felipe GUADAGNIN** Membre invité
Docteur – Universidade Federal do Pampa
**Samuel THIELE** Membre invité
Docteur – Helmholtz Institute Freiberg for Resource Technology, Helmholtz-Zentrum Dresden-Rossendorf
**Jean BORGOMANO** Membre invité
Professeur émérite – Aix-Marseille Université
**Guilherme GABAGLIA** Membre invité

# Affidavit

I, undersigned, Eduardo Roemers de Oliveira, hereby declare that the work presented in this manuscript is my own work, carried out under the scientific supervision of François Fournier and Sophie Viseur, in accordance with the principles of honesty, integrity and responsibility inherent to the research mission. The research work and the writing of this manuscript have been carried out in compliance with both the French national charter for Research Integrity and the Aix-Marseille University charter on the fight against plagiarism.

This work has not been submitted previously either in this country or in another country in the same or in a similar version to any other examination body.

Marseille, 13 octobre 2025

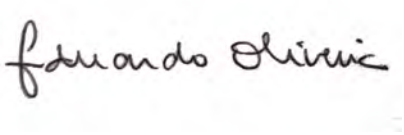

## Résumé

Les systèmes lacustres constituent des analogues de réservoir essentiels pour la province du Pré-sel brésilien, car leur hétérogénéité de faciès et leur complexité stratigraphique posent des défis persistants pour la modélisation des réservoirs. Les affleurements analogues jouent un rôle clé dans ce contexte, car ils complètent le gap de données entre l'échelle sismique régionale et l'information ponctuelle issue des forages. Les approches de terrain traditionnelles, bien qu'indispensables, restent limitées par l'accessibilité, la subjectivité dans la classification des faciès et la difficulté de transposer les observations dans des modèles tridimensionnels. Cette thèse vise à surmonter ces limites en proposant et en testant un workflow avec des méthodes multiple structurées principalement autour de la stratigraphie séquentielle à haute résolution et la modélisation numériques d'affleurement obtenus par photogrammétrie. Ce processus intègre les données de terrain et de laboratoire au sein d'outils numériques, garantissant que les observations stratigraphiques, sédimentologiques et pétrographiques restent solidement ancrées dans la pratique géoscientifique. Les méthodes numériques employées incluent les *Local Binary Patterns*, les réseaux de neurones convolutionnels et l'imagerie hyperspectrale, qui ajoutent un niveau de détail quantitatif aux approches de base.

Les recherches ont porté sur deux systèmes lacustres : la Barre du Cengle (Paléocène, France) et la Séquence Balbuena III (Maastrichtien-Danien, bassin de Salta, Argentine). Ces cas d'études contrastés ont permis d'évaluer la robustesse et la complémentarité des approches méthodologiques. L'application de la stratigraphie séquentielle à haute résolution soutenue par des modèles numériques d'affleurements de la Barre du Cengle a produit des cadres stratigraphiques détaillés, mettant en évidence le potentiel de l'analyse d'affleurements à haute résolution pour identifier les séquences de dépôt et les motifs d'empilement. L'approche a ensuite été étendue au Bassin de Salta, où la photogrammétrie a permis d'obtenir des modèles à résolution centimétrique à millimétrique, utilisés comme base pour des analyses avancées. Les classifications texturales par *Local Binary Patterns* ont révélé des motifs cohérents avec les interprétations stratigraphiques, tandis que les réseaux de neurones convolutionnels ont généré des nuages de points 3D classifiés par lithofaciès, démontrant une capacité de généralisation entre affleurements. Les données hyperspectrales permettent d'obtenir des informations sur la composition minéralogique des faciès à partir du comportement spectral. Dans l'ensemble, ces méthodes se révèlent complémentaires et leur intégration renforce le cadre géologique en fournissant une base plus solide pour l'interprétation stratigraphique, l'analyse sédimentologique, la reconnaissance des faciès et l'identification des corps géologiques.

L'apport scientifique de cette thèse réside dans son caractère intégrateur, unissant les observations traditionnelles de terrain et de laboratoire à des approches numériques afin de produire à la fois des analyses qualitatives fondées sur des preuves géologiques et des résultats quantitatifs reproductibles et transférables aux études de réservoir. Combiner les approches stratigraphiques, géométriques, texturales, spectrales et issues de l'apprentissage profond améliore l'efficacité de l'acquisition et de l'interprétation des données, tout en faisant progresser la caractérisation des affleurements analogues de réservoir. Ce travail fournit ainsi une base méthodologique solide pour de futures applications dans la province du Pré-sel brésilien, où la prise en compte de l'hétérogénéité, de la distribution des faciès et de l'architecture stratigraphique est essentielle à la modélisation réaliste des réservoirs.

**Mots-clés :** Analogues de réservoir ; Province du Pré-sel brésilien ; Stratigraphie séquentielle à haute résolution ; Modèles numériques d'affleurement ; Apprentissage profond en géosciences ; Imagerie hyperspectrale.

## Abstract

Lacustrine systems are key reservoir analogs for the Brazilian Pre-Salt Province, as their facies heterogeneity and stratigraphic complexity pose persistent challenges for reservoir modeling. Outcrop analogs are fundamental in this context because they bridge the mesoscale gap between regional seismic data and point-scale well information. Traditional field-based methods, although essential, are limited by accessibility, subjectivity in facies classification, and difficulties in scaling observations to three-dimensional reservoir models. This thesis contributes to addressing these challenges by proposing and testing a multi-method workflow structured around high-resolution sequence stratigraphy (HRSS) and photogrammetric Digital Outcrop Models (DOMs). The workflow integrates field and laboratory datasets with digital techniques, ensuring that stratigraphic, sedimentological, and petrographic observations remain firmly grounded in geoscientific practice. Methods include Local Binary Patterns (LBP), convolutional neural networks (CNNs), and hyperspectral imaging (HSI), which add quantitative detail to the core approaches.

The research focused on two lacustrine systems: the Paleocene Barre du Cengle in France and the Maastrichtian–Danian Balbuena III Sequence in the Salta Basin, Argentina. These contrasting case studies enabled the testing of methodological robustness and complementarity. The objective of this work was to evaluate whether digital and analytical methods can generate reproducible, geologically coherent, and parametrized datasets that improve facies characterization and stratigraphic interpretation, with the understanding that these outputs are expected to support future transfer to reservoir models, extending the contributions initiated in this research. The thesis first applied HRSS supported by DOMs to the Barre du Cengle, producing detailed stratigraphic frameworks that highlighted the potential of high-resolution outcrop analysis for identifying depositional sequences and stacking patterns. It was then expanded in the Salta Basin, where photogrammetry provided centimeter- to millimeter-scale DOMs, used as a platform for advanced analysis. Texture-based classification with LBP, applied in an exploratory way, revealed textural patterns consistent with stratigraphic interpretations, suggesting potential for highlighting high-resolution cyclicity and supporting the identification of stratigraphic surfaces. CNN-based classification provided robust results, successfully generating lithofacies-classified 3D point clouds and demonstrating cross-outcrop generalization capacity. Hyperspectral data added a compositional dimension, linking spectral behaviors to facies mineralogy. Overall, the results demonstrate that the different methods are complementary, and their integration strengthens the geological framework by providing a more robust basis for stratigraphic interpretation, sedimentological analysis, environmental determination, facies recognition and geobody identification.

The scientific contribution of this thesis lies in its integrative nature, uniting traditional field and laboratory observations with digital techniques to provide both qualitative insights anchored in geological evidence and quantitative outputs that extend results toward reproducible datasets with applicability to reservoir studies, while also improving efficiency in data acquisition and interpretation. By combining stratigraphic, geometric, textural, spectral, and deep learning approaches, the research advances reservoir analog outcrop characterization and provides a methodological foundation for future applications in the Brazilian Pre-Salt Province, where capturing heterogeneity, facies distribution, and stratigraphic architecture is crucial for realistic reservoir modeling.

**Keywords:** Reservoir analogs; Brazilian Pre-Salt Province; High-Resolution Sequence Stratigraphy; Digital Outcrop Models; Deep Learning in Geosciences; Hyperspectral imaging.

## Acknowledgments

Without a doubt, developing this thesis has been one of the greatest challenges I have ever faced. It was extremely demanding but also deeply rewarding, and there are many people I would like to thank.

First, I thank **Petrobras** for the opportunity and for funding this work. It is a great honor to be part of the largest Brazilian company. Many people played an essential role in this process. My sincere gratitude to **Guilherme Raja Gabaglia** for his encouragement and intellectual mentorship. Since the day I met him, he has inspired my passion for High-Resolution Stratigraphy and was the one who encouraged me to pursue this PhD in France. Among the managers who strongly supported this project, I want to thank **José Fernando Rosalba**, **Tatiane Alice Oliveira**, **Rita Parisi**, **Vinícius França**, **Igor Viegas**, and **Mariana Pinheiro**.

I also want to express my deepest gratitude to my supervisors, **François Fournier** and **Sophie Viseur**, for accepting to embark on this journey with me even before meeting me in person. Beyond the great learning experience and excellent collaboration, I truly enjoyed every moment in the lab, in the field, in Argentina, in Brazil, and in France. You gave me something priceless: your time and your patience to discuss with someone who was (and still is) learning French. I am also sincerely thankful for the time and dedication you devoted to reading this manuscript so carefully.

To my co-authors and scientific collaborators, who made me grow and mature so much during my PhD, thank you. Many of you became great friends. I am especially grateful to **Felipe Guadagnin**, **Prof. Nanni**, **Guilherme Rangel**, **Caio Almeida**, **Daniel Galvão**, **Edinho**, **Juan Hernández**, **Anderson Gonçalves**, **Ítalo Gomes**, **Ana Clara Freccia**, **Abel Guihou**, **Jules Fleury**, **Véronique Rinalducci**, **Lionel Marié**, **Pierre Deschamps**, and **Alain Tonetto**. I also thank *mes petits*, **Jérémy Marchini** and **Lorenzo D'Angelo**, the master's students who got involved in my thesis project. You are highly skilled, and it was a pleasure to be part of your academic paths.

My sincere thanks to the members of the thesis jury: **Emmanuelle Vennin**, **Guillaume Caumon**, **Sophie Leleu**, **Jean-Luc Mari**, **Samuel Thiele**, and **Jean Borgomano**, who are true scientific references for me.

Life at the lab was always pleasant. I thank all members of the CEREGE and Rhyca team for welcoming me. I also want to acknowledge my fellow PhD colleagues, who often made the lab feel like home: **Nazim**, **Paul**, **Hugo**, **Lilas**, **Stanislas**, and **Sananda** (the newest member). It was also a great pleasure to share moments with master's and PhD students such as **Anna**, **Bastien**, **Jimi**, **Morgane**, **Nathan**, and **Virgile**.

My family is my foundation. Without you, I would not have had the strength to face this challenge. **Luka**, only you can truly understand how hard it was to live in another country for several years. Thank you for all your patience and support. To my parents, **Katia** and **Paulo**, and my sisters, **Tamara** and **Flávia,** who have always been by my side, sometimes believing in me more than I did myself, this work is also for and because of you.

To my friends and colleagues from Cenpes, **Clara**, **George**, **Márcia**, and **Xingu**, thank you for your friendship and constant encouragement.

To my Brazilian friends in France, **Flavinha**, **Luíza**, **Jonathan**, **Ana, Leonardo**, and **Felipe**, thank you for your company and for the wonderful moments we shared.

And finally, *merci à la **France***. Thank you, France, for welcoming me. A country of immeasurable historical, cultural, and natural richness. I will certainly take with me many unforgettable *souvenirs* from this incredible place.

# Table of Contents

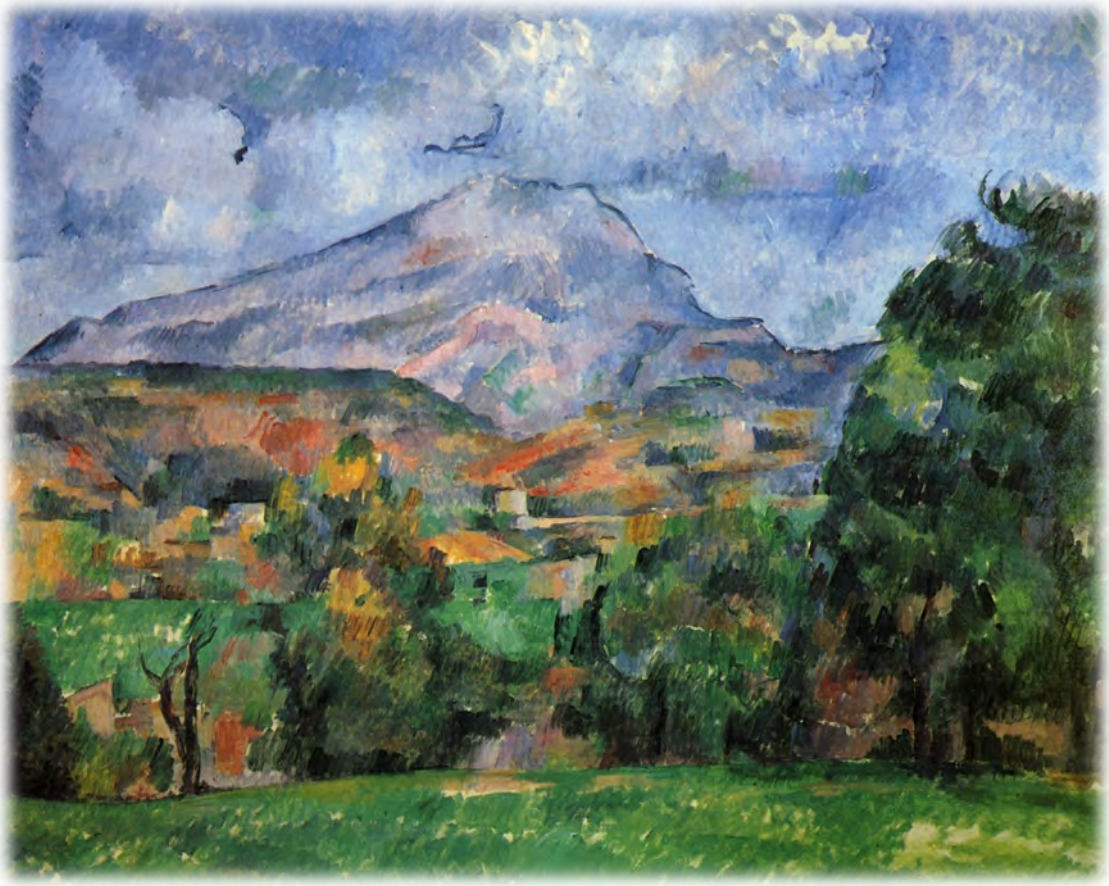

*Montagne Sainte-Victoire, Paul Cézanne, c. 1888–1890, via Wikimedia Commons.*

*« On ne connaît que les choses que l'on apprivoise... »*
*Antoine de Saint-Exupéry, Le Petit Prince (1943)*

# Chapter 1
# General Introduction

## 1.1. Scientific Context

Accurate reservoir modeling is essential for predicting hydrocarbon production performance, optimizing field development strategies, and reducing geological uncertainties. This is particularly critical in complex systems such as the Brazilian Pre-salt reservoirs of the Santos and Campos basins, which are characterized by extensive carbonate successions deposited in lacustrine environments during the rift-to-sag evolution phases of the basins (Bueno de Moraes et al., 2024). These reservoirs display layered stratigraphic architectures, marked heterogeneity caused by diagenetic processes, and complex depositional geometries (Fragoso et al., 2023; Pedrinha and Artagão, 2024). Reflecting their significance, Pre-salt fields accounted for 3.803 million barrels of oil equivalent per day (boe/d) in May 2025, representing approximately 79.8% of Brazil's total hydrocarbon output. In that month, the country produced 3.679 million barrels of oil per day, with combined oil and gas volumes totaling 4.763 million boe/d (ANP, 2025).

One of the main limitations affecting Pre-salt reservoir characterization is the restricted availability of core data, which limits the ability to define facies distributions and stratigraphic heterogeneities in detail (Guerrero et al., 2024). Seismic surveys provide large-scale structural information, but with limited vertical resolution, while well data deliver high-resolution stratigraphic records at a single location with minimal lateral continuity (Grammer et al., 2004; Howell et al., 2014). Outcrop analogs play a key role in addressing this gap by offering mesoscale geological information that effectively bridges the gap between seismic-scale and borehole-scale observations, particularly regarding sedimentary body geometries, stacking patterns, and depositional facies distribution (Borgomano et al., 2001; Howell et al., 2014).

Outcrops represent an intermediate scale between seismic and well data, allowing for the direct observation and measurement of geological features that are critical for building robust conceptual reservoir models (Grammer et al., 2004; Hodgetts, 2013). However, conventional outcrop studies rely on manual descriptions, which are time-consuming, subjective, and often lack quantitative rigor, especially when dealing with complex carbonate systems. To overcome these limitations, Digital Outcrop Models (DOMs) have been increasingly adopted as a means to systematically extract spatial parameters such as layer thicknesses, sedimentary structures, and bounding surfaces (Bellian et al., 2005; Hodgetts, 2013; Marques et al., 2020).

DOMs can be generated through various methods, including terrestrial and fixed-platform systems; however, photogrammetry or LiDAR technologies mounted on Remotely Piloted Aircraft Systems (RPAS) have become the most widely adopted approaches, enabling high-resolution 3D representations of outcrop surfaces (Marques et al., 2020; Villarreal et al., 2020). These models provide dense point clouds, 3D meshes, and textured surfaces that can be imported into reservoir modeling software, supporting both conceptual model development and geostatistical analyses (Pringle et al., 2004; Buckley et al., 2006, 2009). Despite these advantages, a significant challenge persists in the automatic identification and quantification of geological bodies within DOMs, particularly in sedimentary geology, where depositional architectures exhibit complex geometries and heterogeneous internal structures (Li et al., 2019; Roisenberg et al., 2022).

To address this challenge, this thesis proposes an innovative workflow that integrates High-Resolution Sequence Stratigraphy (HRSS) and digital methods such as Local Binary Patterns (LBP), Convolutional Neural Networks (CNNs), and hyperspectral data, aiming to automate the classification of lithofacies and stratigraphic elements in DOMs. This integration supports the extraction and parameterization of field-derived geological data, which provides valuable input for the generation of realistic reservoir models (Jones et al., 2011; Howell et al., 2014;

Fragoso et al., 2021a, 2021b; Yeste et al., 2021). Furthermore, HRSS represents not only a supporting framework for organizing digital data, but also a standalone method capable of providing critical insights for reservoir modeling. By identifying vertical and lateral facies variations, stratigraphic stacking patterns, correlation distances at different hierarchical levels, and key stratigraphic surfaces such as sealing layers or super-k intervals, HRSS contributes to defining reservoir heterogeneity and compartmentalization (Silveira, 2020; Magalhães et al., 2020; Fragoso et al., 2021a). Whereas HRSS is combined with LBP, CNN, and hyperspectral data analysis in the Salta Basin case studies, it is applied exclusively in the Cengle Plateau study, supported by photogrammetry-derived DOMs and aimed at the detailed sedimentological and stratigraphic characterization required for depositional model definition. This highlights that precise outcrop-based sedimentological and stratigraphic detailing alone can already play a central role in reservoir model development.

The present work focuses on developing conceptual depositional models in lacustrine settings, as well as generating qualitative and quantitative geological data extracted from DOMs. These contributions are framed within the “Conceptual Geological Model” step of the reservoir modeling workflow (Fig. 1.1). This step is essential for constructing more realistic geological models that better capture the heterogeneity and organization found in the subsurface.

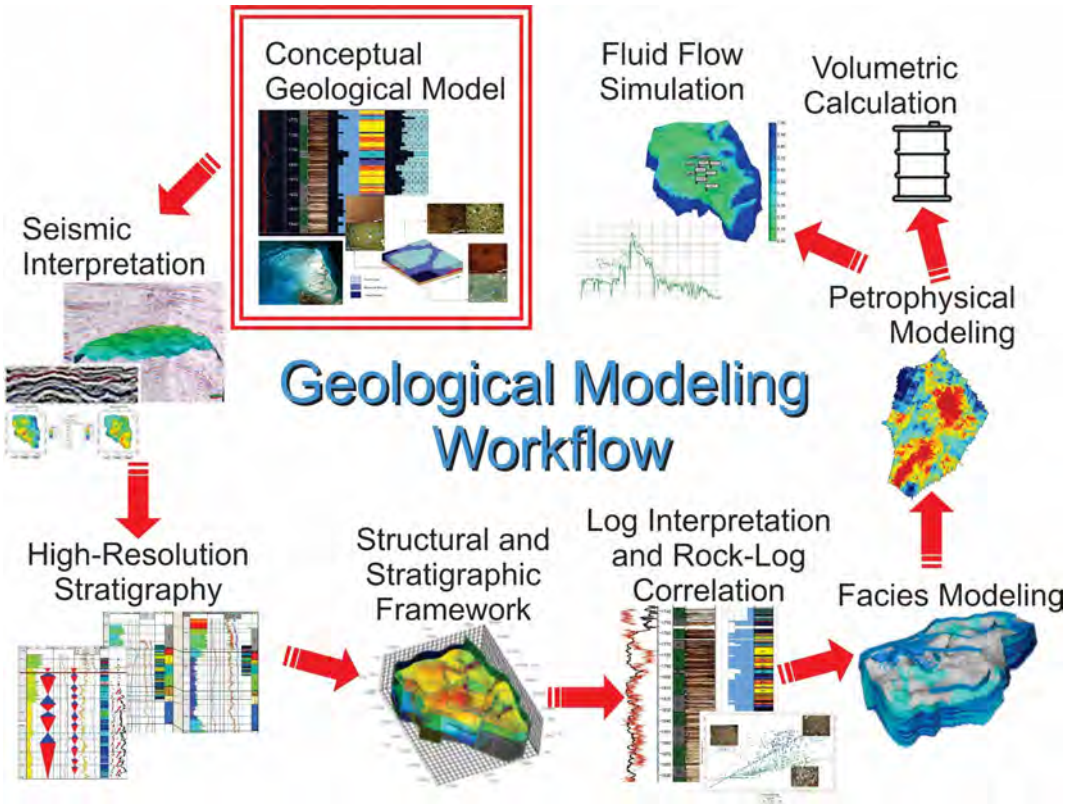


**Fig. 1.1.** General workflow for reservoir geological modeling. The highlighted step, “Conceptual Geological Model,” represents the main focus of this thesis, whose contributions are primarily situated in the integration of outcrop-derived data from DOMs, HRSS, and other advanced digital techniques. Adapted from Roemers-Oliveira et al. (2010).

The two study areas (Fig. 1.2), La Barre du Cengle in southeastern France and the Salta Basin in northwestern Argentina, were selected for the development and validation of the proposed methodologies due to their significance as analogs sharing key characteristics with Brazilian Pre-salt reservoirs, such as carbonate deposition under lacustrine conditions and stratigraphic architectures marked by high-frequency sequences. Although both settings differ from the Pre-salt in terms of lithofacies, they provide complementary and valuable contrasts for

testing digital and stratigraphic workflows. The Salta Basin exhibits more pronounced lithofacies contrasts defining elementary sequences, whereas in La Barre du Cengle these transitions are more subtle. There, color variations mainly reflect different intensities of pedogenesis, and while some features are macroscopically recognizable, detailed petrographic observations play a more central role, being required to distinguish microfacies and characterize depositional environments.

A regional geological framework for both basins is presented in Section 2.1, while more detailed information is provided in the chapters structured as scientific articles, each dedicated to the application of the proposed methods in one of the study areas.

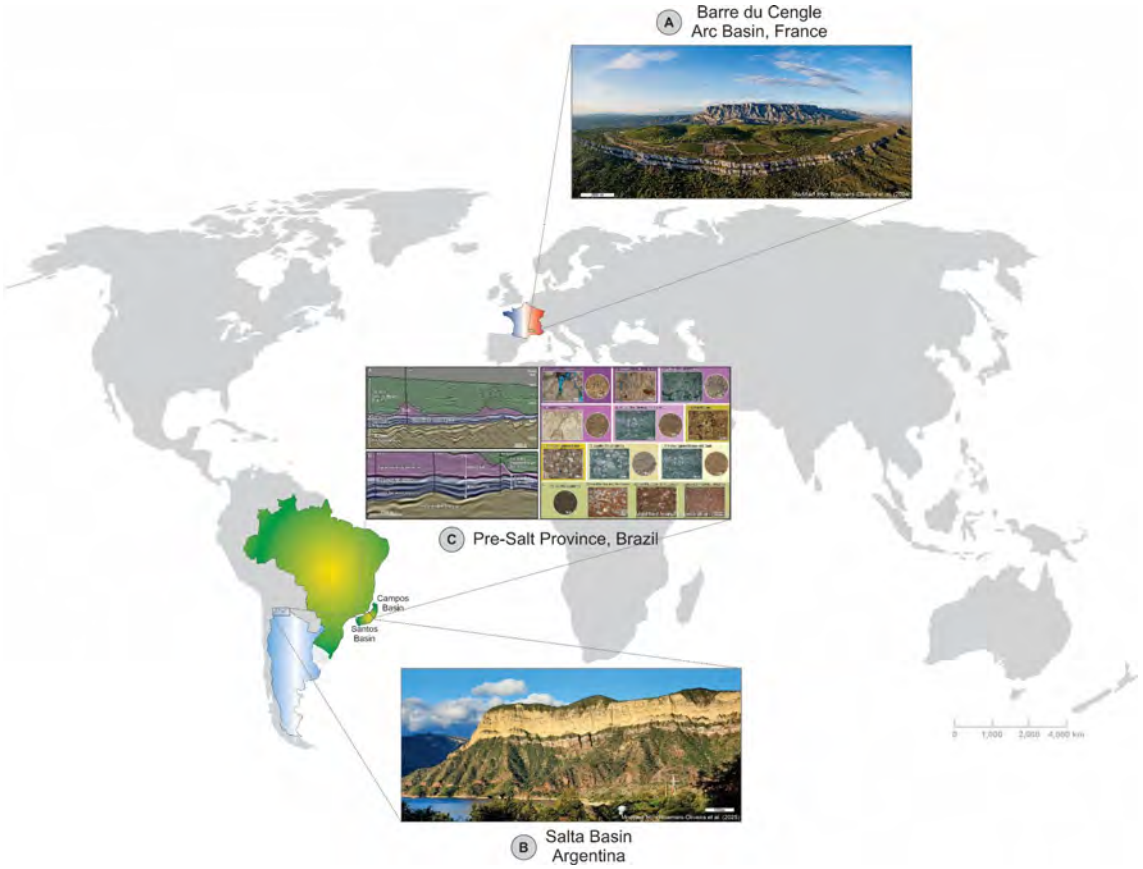


**Fig. 1.2.** Location map of the study areas and their geological context. (A) Barre du Cengle (Arc Basin, southeastern France); (B) Salta Basin (northwestern Argentina); and (C) the Brazilian Pre-salt Province, including the offshore Campos and Santos basins. Locations A and B correspond to the case studies analyzed in this work, while C represents the target reservoir systems for which the analog models are intended.

By developing and validating methodological approaches for outcrop-derived data acquisition, lithofacies classification, and stratigraphic organization, this thesis focuses on generating geological insights and parameter foundations that can support future reservoir modeling applications. The combined use of photogrammetry-based DOMs, LBP, CNN-based lithofacies classification, hyperspectral data, and HRSS provides a structured framework for extracting and organizing quantitative geological information from outcrop analogs. While direct reservoir model parameterization is beyond the scope of this work, the methods and datasets produced here are intended to contribute essential groundwork for subsequent integration into subsurface reservoir models, enhancing geological consistency and predictive capacity in carbonate-dominated lacustrine systems.

## 1.2. Objectives and Research Questions

This thesis aims to contribute to the generation and extraction of qualitative and quantitative geological data to support reservoir characterization and modeling in carbonate-dominated lacustrine settings, with particular emphasis on developing transferable approaches and insights relevant to Brazilian Pre-salt deposits. However, the methods and workflows developed throughout this research extend beyond this specific context, also contributing to the broader field of digital outcrop processing, particularly through the development and integration of advanced workflows applied to complex and diverse geological architectures. These efforts are grounded in the recognition that carbonate-dominated systems often present significant challenges for the identification and delineation of sedimentary bodies, due to their complex geometries, lateral facies transitions, diagenetic overprinting, and, in many cases, the visual similarity of facies in terms of color and texture in standard field imagery.

These aspects complicate the visual discrimination of key facies, particularly in thin or interbedded successions. In the Salta Basin (Fig. 1.3), for example, differentiating stromatolitic layers or buildups interbedded with laminite facies is often difficult, as both may present only subtle contrasts in color and texture. If this can be challenging even in accessible outcrops, as shown in Fig. 1.3, it becomes virtually impossible in steep and inaccessible cliffs (Fig. 1.4). Although cliffs offer excellent lateral continuity, the lack of physical access hinders the identification of consistent facies patterns and stratigraphic relationships.

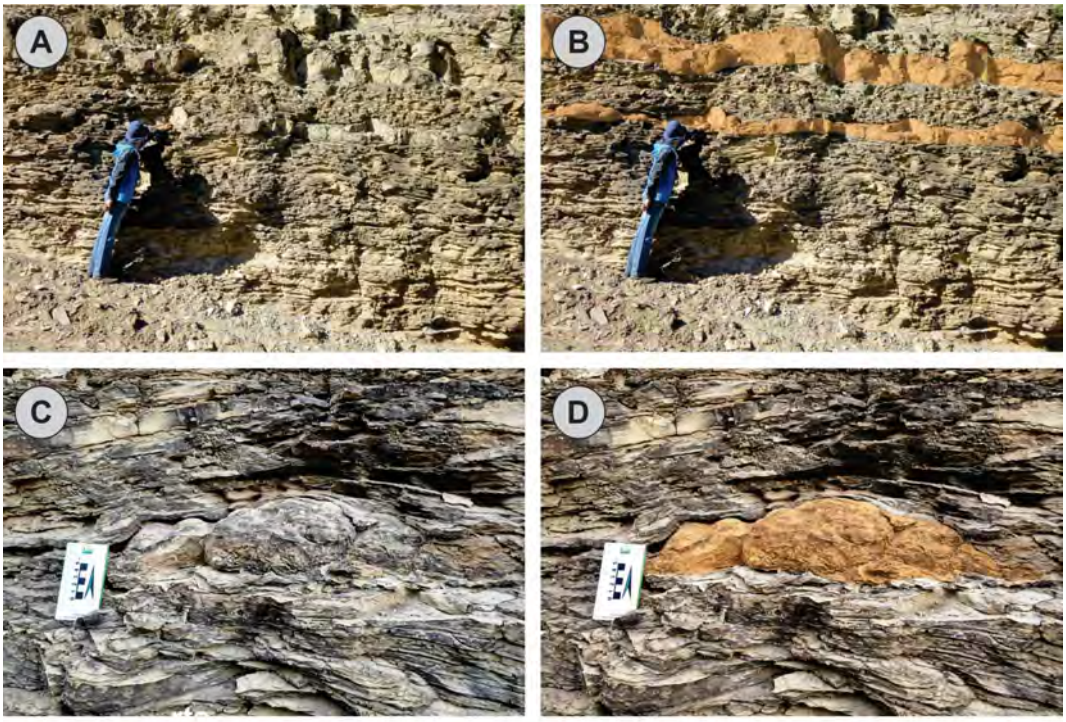


**Fig. 1.3.** Field examples from the Salta Basin illustrating the difficulty of visually distinguishing stromatolitic facies interbedded within a laminite unit. (A) Biostromes of stromatolites highlighted in orange in (B). (C) Bioherm of stromatolites highlighted in orange in (D). Visual similarities in color and texture hinder the recognition of these facies under standard field conditions. Source: Roemers-Oliveira et al. (2015).

**Fig. 1.4.** Steep cliff in the Salta Basin exposing a thick lacustrine carbonate succession on the hanging wall of a major N–S-trending fault. Despite offering excellent lateral continuity, the vertical exposure and lack of physical access prevent detailed facies characterization under standard field conditions.

The central research question that guides this work is:

**Is it possible to apply methods based on outcrop-derived data to enhance the extraction of stratigraphic elements and the detection of geological bodies in carbonate outcrop analogs?**

The underlying hypothesis is that an integrated approach, which combines field-based observations, laboratory analyses, and advanced digital tools applied to Digital Outcrop Models (DOMs), can improve the identification, organization, classification, and quantification of geological bodies in outcrop settings.

In addition, this research pursues the following specific objectives:

- To acquire high-resolution field data and generate Digital Outcrop Models (DOMs) from key lacustrine and palustrine carbonate outcrops;
- To integrate DOM-based analyses with traditional geological observations from the field and laboratory, ensuring consistent geological interpretation;
- To establish correlation patterns and distances between lacustrine and lacustrine/palustrine settings across different study areas;
- To apply and evaluate multiple methods, including High-Resolution Sequence Stratigraphy (HRSS), Local Binary Patterns (LBP), Convolutional Neural Networks (CNNs), and hyperspectral data, for the classification and extraction of lithofacies and depositional sequences within an integrated stratigraphic framework;
- To contribute to the geological knowledge of each study area by improving the understanding of their depositional architecture and stratigraphic organization;
- To contribute to the advancement of digital techniques applied to outcrop analogs, highlighting their potential for generating conceptual geological models to support reservoir characterization.

The originality of the approach lies in the integrative nature of the workflow. By combining "hard" field data with remote sensing and digital analysis, this work seeks to build a robust methodological foundation for future reservoir modeling applications based on outcrop analogs.

## 1.3. Thesis Outline

This thesis is organized into seven chapters. Following this general introduction (Chapter 1), Chapter 2 presents the Geological and Methodological Frameworks, including a review of the regional geology of the Arc and Salta Basins and an overview of the High-Resolution Sequence Stratigraphy (HRSS) and photogrammetry-based Digital Outcrop Models (DOMs), which form the methodological backbone of the thesis. Chapters 3 to 6 consist of scientific articles, each addressing specific aspects of the research. These articles are at different stages of publication and reflect the progression of the work over the course of the PhD. Chapter 7 presents a transversal discussion that integrates the insights gained from the articles, highlights overarching implications, and provides the general conclusions and perspectives for future research. A visual overview of the content of each chapter is shown in Fig. 1.5, which summarizes the thesis outline.

Each chapter reflects different challenges encountered throughout the project. Data acquisition and model processing required significant fieldwork, often carried out under challenging logistical conditions. Some parts of the work benefited from the valuable assistance of M1 and M2 students, whose support streamlined important phases of the research. In addition, the project involved extensive collaboration among institutions, including researchers from CEREGE/Aix-Marseille Université (AMU, France), Petrobras (Brazil), Geomap (Argentina), and two Brazilian universities: Universidade Federal do Pampa (Unipampa) and Universidade Estadual de Maringá (UEM).

Although grounded in formal scientific writing, this thesis also reflects the real-world constraints and iterative nature of conducting field-based research. Some aspects were developed in greater depth, while others remain open for future refinement. Overall, the manuscript seeks to balance methodological rigor with the adaptability required to deal with evolving tools, on-site constraints, analytical frameworks, and the availability of equipment and resources.

Concerning the scientific articles included in this thesis, **Chapter 3 – La Barre du Cengle** presents the results of a high-resolution stratigraphic framework developed through the application of High-Resolution Sequence Stratigraphy (HRSS) supported by Digital Outcrop Models (DOMs). The chapter corresponds to a scientific paper titled "The anatomy and stacking pattern of palustrine-dominated carbonate sequences from the Cengle Plateau, Paleocene, SE France: A multi-scalar approach" published in *Sedimentary Geology* in 2024 (Roemers-Oliveira et al., 2024a). The study provides a detailed analysis of the anatomy and internal organization of the identified sequences, including vertical stacking patterns and lateral facies variations. It also presents the first absolute age constraints for this unit, obtained via U–Pb dating on micrite, indicating that sedimentation occurred earlier than previously assumed. These findings suggest a potential revision of the Arc Basin stratigraphy. The analysis integrates petrographic, photogrammetric, geochronological, scanning electron microscopy (SEM), and geochemical data to interpret the environmental dynamics during deposition.

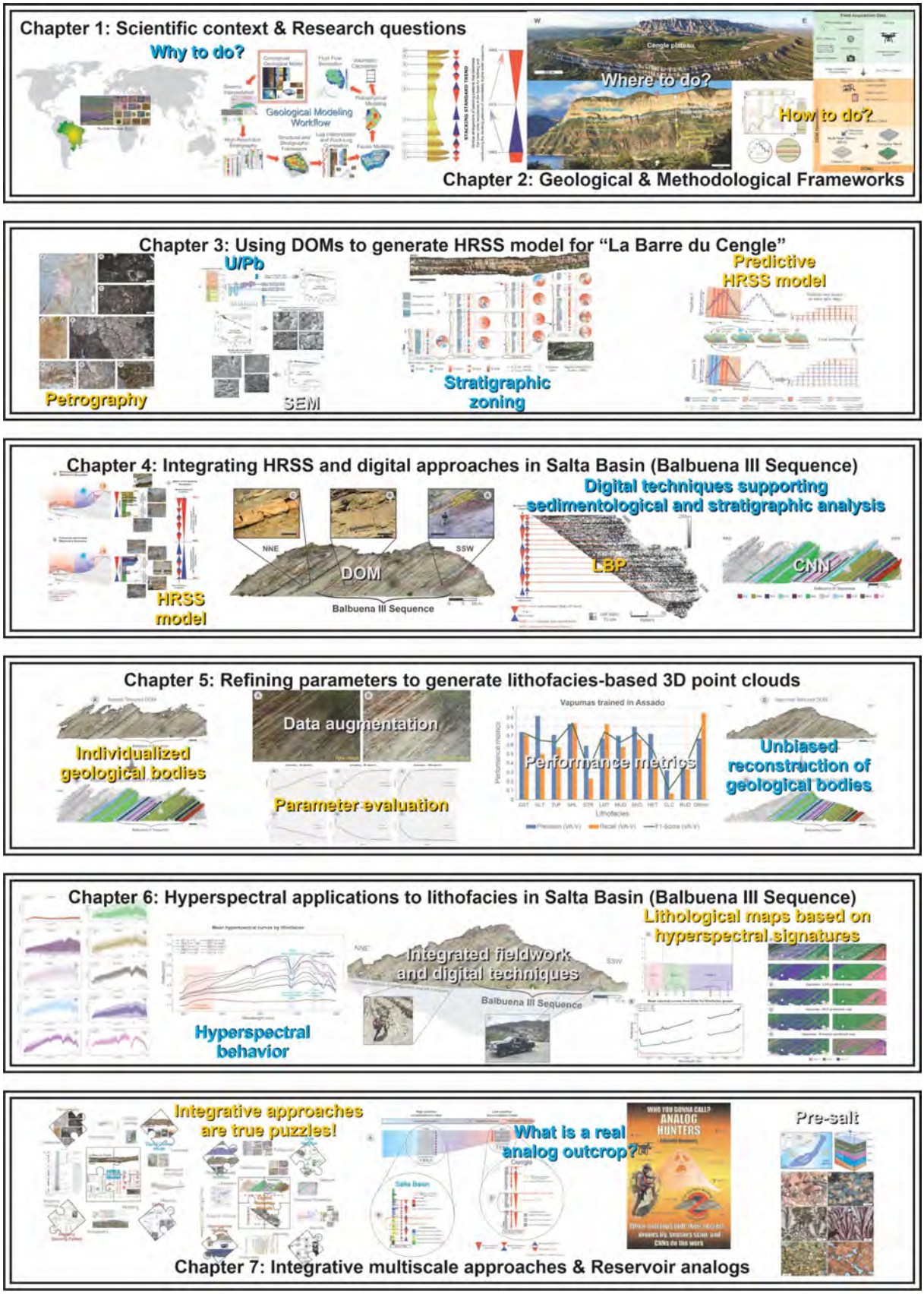


**Fig. 1.5.** Outline of the thesis chapters, providing a visual summary of their main content.

**Chapter 4 – Salta Basin** presents the high-resolution stratigraphic framework integrated with advanced digital techniques in Digital Outcrop Models (DOMs) for the Balbuena III Sequence in the Cabra Corral area, located within the Metán–Alemanía Sub-basin (Salta Basin). The study, written as a paper called "Advanced digital techniques applied to outcrop models: Integrating Local Binary Pattern (LBP) and Convolutional Neural Network (CNN) to support

stratigraphic and sedimentological interpretation of reservoir analogs in the Salta Basin, Argentina," was accepted for publication in *Marine and Petroleum Geology* on October 6, 2025 (Roemers-Oliveira et al., 2025a). The work combines High-Resolution Sequence Stratigraphy (HRSS) with digital analyses such as Local Binary Pattern (LBP) and Convolutional Neural Networks (CNNs) to investigate facies distribution and stratigraphic architecture. The HRSS provides the stratigraphic framework of the area, where elementary sequences can be traced for tens of kilometers. LBP analysis supports the identification of high-frequency cyclicity, while CNN-based segmentation enables the classification of eleven lithofacies, encompassing carbonate, siliciclastic, mixed, and volcaniclastic types. These lithofacies are associated with the scale of the elementary sequences. This classification allows the generation of lithofacies-classified 3D point clouds, enhancing the spatial visualization of facies across the outcrop. By integrating digital and traditional approaches, and by discussing the role of the Salta Basin as an analog for the Brazilian Pre-salt, the study contributes to improving the accuracy and predictive capability of reservoir analog modeling, especially in data-scarce settings such as those observed in some areas of the Pre-salt.

**Chapter 5 – CNN Optimization** was developed in collaboration with Jérémy Marchini, a master's student (M2) under my supervision, in coordination with Dr. Sophie Viseur, and further explores the application of CNNs to classify 3D point clouds by lithofacies. The manuscript "From Pixels to Point Clouds: Evaluating CNN Strategies for 3D Lithofacies Classification in Digital Outcrop Models" is planned for submission to *Geodata and AI*. The work evaluates different CNN workflow configurations using high-resolution images from two outcrops of the Balbuena III Sequence in the Salta Basin. The optimized approach allows the generation of lithofacies-classified point clouds that preserve stratigraphic coherence across these sites. In addition to refining the methodology, the work highlights key geological insights related to facies continuity, the role of lithological contrast in detecting thin beds, and the influence of geometry on classification performance. This contribution reinforces the potential of deep learning techniques to support stratigraphic and sedimentological interpretation in outcrop analog studies.

Finally, **Chapter 6 – Hyperspectral** presents the initial efforts to apply hyperspectral techniques for lithofacies classification in the Salta Basin and is structured as an article titled "Outcrop-based hyperspectral data for lithofacies discrimination in lacustrine deposits in the Salta Basin, Argentina", which is currently in preparation and will be submitted to a journal covering geosciences and remote sensing. This stage of the research posed the greatest technical challenges and represents an initial attempt to explore hyperspectral techniques within the Salta Basin, an approach that, although still emerging, is gaining increasing relevance in geosciences. Despite limitations related to the hyperspectral sensor available during fieldwork, which covered the infrared range between 900 and 1700 nm and was not optimal for differentiating carbonate facies, it was still possible to acquire non-imaging spectroscopy data that enabled the identification of spectral signatures for various facies within the Balbuena III Sequence. The study also benefited from the contribution of Lorenzo D'Angelo, a master's student (M1), who supported the development and optimization of code used to implement Linear Discriminant Analysis (LDA) as a facies classification method for the spectroscopy data. For the HSI, in addition to LDA, Multilayer Perceptron (MLP), and K-means clustering methods were also applied to generate 2D maps classified by lithofacies groups, thereby overcoming the limitations imposed by the reduced spectral range.

As complementary materials, the appendices include all abstracts submitted to conferences (Table 1.1) and a scientific article co-authored by me: Guadagnin et al. (2025), *Building of classified 3D point clouds of outcrop with automatically segmented images*. Although the study

was conducted in an area outside the scope of this thesis, its methodology played an important role in shaping the approaches developed and applied throughout the work.

**Table 1.1**. Conference contributions during the PhD period.

| Event | Date and location | Title |
|---|---|---|
| 36th International Meeting of Sedimentology | June 12-16, 2023, Dubrovnik, Croatia | Anatomy and stacking pattern of palustrine-dominated carbonate parasequence (Thanetian-Ypresian, SE France): insights from carbonate petrography associated with aerial photogrammetry |
| 17th Bathurst Meeting-International Meeting of Carbonate Sedimentologists | September 5-7, 2023, Naples, Italy | Depositional context of the Balbuena III Sequence (Maastrichtian/Danian) in the Salta Basin, Argentina: integrated approach from sedimentological, stratigraphical and digital outcrop models |
| 31e Congrès de l'ED251 2024 | May 16-17, 2024, Aix-en-Provence, France | Anatomy and stacking pattern of palustrine-dominated carbonates from "La Barre du Cengle", Paleocene, SE France |
| 6th Virtual Geoscience Conference | September 9-12, 2025, Lausanne, Switzerland | Reading Rock Record through Digital Outcrop Models: An Integrative Workflow for Decoding Stratigraphy and Facies in the Salta Basin, Argentina |
| 6th Virtual Geoscience Conference | September 9-12, 2025, Lausanne, Switzerland | Optimising Facies Interpretation Using Neural Networks on Images and Photogrammetric Data: A Case Study from Salta (Argentina) |

## 1.4. Associated Scientific Production

### 1.4.1. Peer-reviewed Publications

- Roemers-Oliveira, E., Fournier, F., Viseur, S., Raja Gabaglia, G.P., Fleury, J., Rinalducci, V., Guihou, A., Marié, L., Guadagnin, F., Deschamps, P., Tonetto, A., 2024a. The anatomy and stacking pattern of palustrine-dominated carbonate sequences from the Cengle Plateau, Paleocene, SE France: A multi-scalar approach. *Sedimentary Geology* 470, 106690. https://doi.org/10.1016/j.sedgeo.2024.106690
- Guadagnin, F., Gonçalves, Í.G., Roemers-Oliveira, E., Guedes, P.L., de Souza, E.G., Silveira, M. de M.L., Raja Gabaglia, G.P., Arienti Gonçalves, L., Oliveira, L.F.R. de, Selk, R., 2025. Building of classified 3D point clouds of outcrop with automatically segmented images. *Geodata and AI* 4, 100024. https://doi.org/10.1016/j.geoai.2025.100024
- Roemers-Oliveira, E., Viseur, S., Fournier, F., Gonçalves, Í.G., Guadagnin, F., Raja Gabaglia, G.P., Bento Freire, E., Fragoso, D.G.C., Hernández, J., Freccia, A.C., de Godoy Rangel, G., 2025. Advanced digital techniques applied to outcrop models: Integrating Local Binary Pattern (LBP) and Convolutional Neural Network (CNN) to support stratigraphic and sedimentological interpretation of reservoir analogs in the Salta Basin, Argentina. *Marine and Petroleum Geology*. https://doi.org/10.1016/

### 1.4.2. Conference Contributions

- Roemers-Oliveira, E., Fournier, F., Viseur, S., Raja Gabaglia, G.P., 2023a. Anatomy and stacking pattern of palustrine-dominated carbonate parasequences (Thanetian-Ypresian, SE France): insights from carbonate petrography associated with aerial photogrammetry, in: *36th International Meeting of Sedimentology*. IAS, Dubrovnik, p. 44.
- Roemers-Oliveira, E., Viseur, S., Fournier, F., Raja Gabaglia, G.P., Bento Freire, E., 2023b. Depositional context of the Balbuena III Sequence (Maastrichtian/Danian) in the Salta Basin, Argentina: integrated approach from sedimentological, stratigraphical and digital outcrop models, in: *17th Bathurst Meeting-International Meeting of Carbonate Sedimentologists*. Naples, p. 89.

- Roemers-Oliveira, E., Fournier, F., Viseur, S., Raja Gabaglia, G.P., Fleury, J., Rinalducci, V., Guihou, A., Marié, L., Guadagnin, F., Deschamps, P., Tonetto, A., 2024b. Anatomy and stacking pattern of palustrine-dominated carbonates from 'La Barre du Cengle", Paleocene, SE France, in: *31e Congrès de L'ED251*. Aix-en-Provence.
- Roemers-Oliveira, E., Viseur, S., Gomes-Gonçalves, Í., Guadagnin, F., Marchini, J., Rangel, G., Raja Gabaglia, G.P., Fournier, F., 2025b. Reading rock record through digital outcrop models: An integrative workflow for decoding stratigraphy and facies in the Salta Basin, Argentina, in: *6th Virtual Geoscience Conference*. Lausanne, pp. 89–90.
- Marchini, J., Roemers-Oliveira, E., Viseur, S., Gomes-Gonçalves, I., Guadagnin, F., Freccia, A.C., Rangel, G., Raja Gabaglia, G.P., Fournier, F., 2025. Optimising facies interpretation using neural networks on images and photogrammetric data: A case study from Salta (Argentina), in: *6th Virtual Geoscience Conference*. Lausanne, pp. 68–69.

### 1.4.3. Master Student Supervisions

- Master 1 – **D'ANGELO Lorenzo**, 2024. *Interprétation de faciès par analyse linéaire discriminante à partir de mesures hyperspectrales : Le cas d'étude de Salta (Argentine)*.
- Master 2 – **MARCHINI Jérémy**, 2024. *Facies Interpretation Using Neural Networks from Images and Photogrammetric Data: The Case Study of Salta (Argentina)*.

## References


ANP, B.N.A. of P.N.G. and B., 2025. Boletim Mensal da Produção de Petróleo e Gás Natural – Maio de 2025. URL https://www.gov.br/anp/pt-br/centrais-de-conteudo/publicacoes/boletins-anp/arquivos-bmppgn/2025/maio.pdf (accessed 7.11.25).

Bellian, J.A., Kerans, C., Jennette, D.C., 2005. Digital outcrop models: Applications of terrestrial scanning lidar technology in stratigraphic modeling. Journal of Sedimentary Research 75, 166–176. https://doi.org/10.2110/jsr.2005.013

Borgomano, J., Van Konijnenburg, J.-H., Jauffred, J.-C., 2001. Anatomy of carbonate bodies For hydrocarbon reservoir modeling: Applications, limitations and Future developments. Géologie Méditerranéenne 28, 23–26. https://doi.org/https://doi.org/10.3406/geolm.2001.1682

Buckley, S.J., Howell, J.A., Enge, H.D., Leren, B.L.S., Kurz, T.H., 2006. Integration of terrestrial laser scanning, digital photogrammetry and geostatistical methods for high-resolution modelling of geological outcrops, in: International Archives of the Photogrammetry, Remote Sensing and Spatial Information Sciences. ISPRS.

Buckley, S.J., Schwarz, E., Terlaky, V., Howell, J.A., Arnott, R.W.C., 2009. Terrestrial Laser Scanning Combined with Photogrammetry for Digital Outcrop Modelling, in: Bretar, F., Pierrot-Deseilligny, M., Vosselman, G. (Eds.), Laser Scanning 2009. IAPRS, Paris.

Bueno de Moraes, M.F., Viana, A.R., Jahnert, R.J., Machado, M.A.P., Chagas, A.A.P., 2024. O Pré-sal nas Bacias de Campos e Santos: como tudo começou, in: Chagas, A.A.P., Araújo, C.C. de, Santos, L.A. (Eds.), As grandes descobertas do pré-sal no Atlântico Sul. Rio de Janeiro, pp. 21–69.

D'Angelo, L., 2025. Interprétation de faciès par analyse linéaire discriminante à partir de mesures hyperspectrales : Le cas d'étude de Salta (Argentine) (MSc thesis). Aix-Marseille Université, Marseille.

Fragoso, D.G.C., Gabaglia, G.P.R., Magalhães, A.J.C., Scherer, C.M.D.S., 2021a. Cyclicity and hierarchy in sequence stratigraphy: An integrated approach. Brazilian Journal of Geology 51, e20200106. https://doi.org/10.1590/2317-4889202120200106

Fragoso, D.G.C., Melo, A.H. de, Gonçalves, L.A., Bunevich, R.B., Araujo, J. de A.M., Costa, T.C. da, Pedrosa, C.A., Scherer, C.M.D.S., 2023. High-resolution sequence stratigraphy applied to reservoir characterization of the Brazilian Cretaceous pre-salt section, Campos Basin: Guidelines for geological modeling and reservoir management. Marine and Petroleum Geology 151, 106203. https://doi.org/10.1016/j.marpetgeo.2023.106203

Fragoso, D.G.C., Raja Gabaglia, G.P., Magalhães, A.J.C., 2021b. Estratigrafia de Alta Resolução Aplicada ao Zoneamento e à Caracterização de Reservatórios: Uma Abordagem Conceitual e Metodológica, in: 50 Congresso Brasileiro de Geologia. Brasília.

Grammer, G.M., Harris, P.M., Eberli, G.P., 2004. Integration of Outcrop and Modern Analogs in Reservoir Modeling: Overview with Examples from the Bahamas, in: Grammer, G.M., Harris, P.M., Eberli, G.P. (Eds.), Integration of Outcrop and Modern Analogs in Reservoir Modeling: AAPG Memoir 80. pp. 1–22.

Guadagnin, F., Gonçalves, Í.G., Roemers-Oliveira, E., Guedes, P.L., de Souza, E.G., Silveira, M. de M.L., Raja Gabaglia, G.P., Arienti Gonçalves, L., Oliveira, L.F.R. de, Selk, R., 2025. Building of classified 3D point clouds of outcrop with automatically segmented images. Geodata and AI 4, 100024. https://doi.org/10.1016/j.geoai.2025.100024

Guerrero, J.C., Brazil, F.A. de F., Carvalho, R.K., Silva, C.M. de A., Moliterno, A.M.C., Araújo, C.H.V., Barbosa, G.F., Yamato, A.A., Cacela, A.S.M., Leite, C. de O.N., Rocha, N.P., Oliveira, V.C.B. de, Campos, M.T.R., Silva, V.G.M. da R. e, Natori, H.O.H., Lima, F.P., Oliveira, D.L. de, Queiroz, L.E.S., Souza, L.B. de, Cruz, E.M.A., 2024. Campo de Búzios: a jornada desde a caracterização dos reservatórios ao início do desenvolvimento da produção AUTORES, in: Chagas, A.A.P., Araújo, C.C. de, Santos, L.A. (Eds.), As grandes descobertas do Pré-sal no Atlântico Sul. Rio de Janeiro, pp. 946–1037.

Hodgetts, D., 2013. Laser scanning and digital outcrop geology in the petroleum industry: A review. Marine and Petroleum Geology. https://doi.org/10.1016/j.marpetgeo.2013.02.014

Howell, J.A., Martinius, A.W., Good, T.R., 2014. The application of outcrop analogues in geological modelling: a review, present status and future outlook. Geological Society, London, Special Publications 387, 1–25. https://doi.org/10.1144/sp387.12

Jones, R.R., Pringle, J.K., McCaffrey, K.J.W., Imber, J., Wightman, R.H., Guo, J., Long, J.J., 2011. Extending Digital Outcrop Geology into the Subsurface, in: Outcrops Revitalized. SEPM (Society for Sedimentary Geology), pp. 31–50. https://doi.org/10.2110/sepmcsp.10.031

Li, L., Wang, R., Lin, J., Xiao, Z., Hui, Y., 2019. A novel approach for extraction of ripple mark parameters based on SfM. Sedimentary Geology 392. https://doi.org/10.1016/j.sedgeo.2019.105523

Magalhães, A.J.C., Raja Gabaglia, G.P., Fragoso, D.G.C., Bento Freire, E., Lykawka, R., Arregui, C.D., Silveira, M.M.L., Carpio, K.M.T., De Gasperi, A., Pedrinha, S., Artagão, V.M., Terra, G.J.S., Bunevich, R.B., Roemers-Oliveira, E., Gomes, J.P., Hernández, J.I., Hernández, R.M., Bruhn, C.H.L., 2020. High-resolution sequence stratigraphy applied to reservoir zonation and characterisation, and its impact on production performance - shallow marine, fluvial downstream, and lacustrine carbonate settings. Earth-Science Reviews 210, 103325. https://doi.org/10.1016/j.earscirev.2020.103325

Marchini, J., 2025. Facies Interpretation Using Neural Networks from Images and Photogrammetric Data: The Case Study of Salta (Argentina) (MSc thesis). Aix-Marseille Université, Marseille.

Marchini, J., Roemers-Oliveira, E., Viseur, S., Gomes-Gonçalves, I., Guadagnin, F., Freccia, A.C., Rangel, G., Raja Gabaglia, G.P., Fournier, F., 2025. Optimising Facies Interpretation Using Neural Networks on Images and Photogrammetric Data: A Case Study from Salta (Argentina), in: 6th Virtual Geoscience Conference. Lausanne, pp. 68–69.

Marques, A., Horota, R.K., de Souza, E.M., Kupssinskü, L., Rossa, P., Aires, A.S., Bachi, L., Veronez, M.R., Gonzaga, L., Cazarin, C.L., 2020. Virtual and digital outcrops in the petroleum industry: A systematic review. Earth-Science Reviews. https://doi.org/10.1016/j.earscirev.2020.103260

Pedrinha, S., Artagão, V. de M., 2024. High-resolution stratigraphy and characterization of reservoir-critical heterogeneities in the giant Tupi Field, pre-salt Santos Basin, Brazil. Geological Society, London, Special Publications 548. https://doi.org/10.1144/SP548-2023-91

Pringle, J.K., Westerman, A.R., Clark, J.D., Drinkwater, N.J., Gardiner, A.R., 2004. 3D high-resolution digital models of outcrop analogue study sites to constrain reservoir model uncertainty: an example from Alport Castles, Derbyshire, UK. Petroleum Geoscience 10, 343–352.

Roemers-Oliveira, E., Casagrande, J., Furuie, R., Mendes, M., Pedrinha, S., Ramos-Pinto, M.G.F.D., 2010. Geological 3D modeling of carbonate reservoirs. Petrobras. Internal Report.

Roemers-Oliveira, E., Fernandes, L.A., Bento Freire, E., Amarante Simões, L.S., 2015. Microbial filaments in stromatolites and laminites of Balbuena III Sequence (Maastrichtian/Danian) of Yacoraite Formation in Metán-Alemania Sub-basin, Salta region, Argentina, and its palaeoenvironmental significance. Brazilian Journal of Geology 45, 399–413. https://doi.org/10.1590/2317-488920150030255

Roemers-Oliveira, E., Fournier, F., Viseur, S., Raja Gabaglia, G.P., 2023a. Anatomy and stacking pattern of palustrine-dominated carbonate parasequences (Thanetian-Ypresian, SE France): insights from carbonate petrography associated with aerial photogrammetry, in: 36th International Meeting of Sedimentology. IAS, Dubrovnik, pp. 44–44.

Roemers-Oliveira, E., Fournier, F., Viseur, S., Raja Gabaglia, G.P., Fleury, J., Rinalducci, V., Guihou, A., Marié, L., Guadagnin, F., Deschamps, P., Tonetto, A., 2024a. The anatomy and stacking pattern of palustrine-dominated carbonate sequences from the Cengle Plateau, Paleocene, SE France: A multi-scalar approach. Sedimentary Geology 470, 106690. https://doi.org/10.1016/j.sedgeo.2024.106690

Roemers-Oliveira, E., Fournier, F., Viseur, S., Raja Gabaglia, G.P., Fleury, J., Rinalducci, V., Guihou, A., Marié, L., Guadagnin, F., Deschamps, P., Tonetto, A., 2024b. Anatomy and stacking pattern of palustrine-dominated carbonates from 'La Barre du Cengle", Paleocene, SE France, in: 31e Congrès de L`ED251. Aix-en-Provence.

Roemers-Oliveira, E., Viseur, S., Fournier, F., Gonçalves, Í.G., Guadagnin, F., Raja Gabaglia, G.P., Bento Freire, E., Fragoso, D.G.C., Hernández, J., Freccia, A.C., de Godoy Rangel, G., 2025a. Advanced digital techniques applied to outcrop models: Integrating Local Binary Pattern (LBP) and Convolutional Neural Network (CNN) to support stratigraphic

and sedimentological interpretation of reservoir analogs in the Salta Basin, Argentina. Marine and Petroleum Geology. https://doi.org/10.1016/

Roemers-Oliveira, E., Viseur, S., Fournier, F., Raja Gabaglia, G.P., Bento Freire, E., 2023b. Depositional context of the Balbuena III Sequence (Maastrichtian/Danian) in the Salta Basin, Argentina: integrated approach from sedimentological, stratigraphical and digital outcrop models, in: 17th Bathurst Meeting-International Meeting of Carbonate Sedimentologists. Naples, pp. 89–89.

Roemers-Oliveira, E., Viseur, S., Gomes-Gonçalves, Í., Guadagnin, F., Marchini, J., Rangel, G., Raja Gabaglia, G.P., Fournier, F., 2025b. Reading Rock Record through Digital Outcrop Models: An Integrative Workflow for Decoding Stratigraphy and Facies in the Salta Basin, Argentina, in: 6th Virtual Geoscience Conference. Lausanne, pp. 89–90.

Roisenberg, H.B., Bállico, M.B., Guadagnin, F., Manna, M.O., de Souza, E.G., 2022. Digital Outcrop Models applied to high-resolution stratigraphy in braided fluvial systems: A study case at Jaicós formation in Parnaíba Basin, NE Brazil. Journal of South American Earth Sciences 119, 104006. https://doi.org/10.1016/j.jsames.2022.104006

Silveira, M. de M.L., 2020. Análisis estratigráfico secuencial de alta resolución y modelado geológico 3D en secciones sedimentarias transicionales y continentales del Jurásico Inferior a Medio del sector sur de la Cuenca Neuquina como análogo en la caracterización de reservorios de hidrocarburos (PhD thesis). Universidad Nacional de La Plata, La Plata.

Villarreal, C.A.J., Rojas, J.D.D., Ríos, C.A.R., 2020. 3D digital outcrop modelling of the Lower Cretaceous Los Santos formation sandstones, Mesa de Los Santos region (Colombia): Implications for structural analysis. Journal of Structural Geology 141. https://doi.org/10.1016/j.jsg.2020.104214

Yeste, L.M., Palomino, R., Varela, A.N., McDougall, N.D., Viseras, C., 2021. Integrating outcrop and subsurface data to improve the predictability of geobodies distribution using a 3D training image: A case study of a Triassic Channel – Crevasse-splay complex. Marine and Petroleum Geology 129, 105081. https://doi.org/10.1016/j.marpetgeo.2021.105081

*Montagne Sainte-Victoire, Paul Cézanne, 1904, via Wikimedia Commons.*

*« La géologie est le chevalet du paysage »*

*Sylvain Tesson, Aphorismes sous la lune et autres pensées sauvages (2008)*

# Chapter 2
# Geological and Methodological Frameworks

## 2.1. Geological Setting

This section summarizes the main geological features and provides the regional geological context of the two study areas addressed in this thesis: the Arc Basin in southeastern France, where the Cengle Plateau outcrop is located, and the Salta Basin in northwestern Argentina, which includes outcrops of the Balbuena III Sequence.

### 2.1.1. Arc Basin (SE France)

The Arc Basin (Fig. 2.1), covering approximately 1,600 km², constitutes the largest syncline in the Provence region (Westphal and Durand, 1990). It preserves a continental sedimentary record spanning from the Upper Cretaceous (Late Santonian) to the Middle Eocene (Lutetian) (Durand and Tempier, 1968). Geographically, the basin forms an east–west elongated depression bounded by well-defined Provençal massifs and structural highs. The north includes Saint-Chamas and La Fare, the Eguilles hills, and Montagne Sainte-Victoire; the south, La Nerthe and L'Étoile with Regagnas, Olympe, and Aurélien. The Plateau d'Ollière marks the east, and the Étang de Berre the western outlet, where the Arc River drains into the lagoon (Durand and Guieu, 1980). The hydrographic network is organized around the Arc River, which flows westward, while the Durance River captures part of the northern hinterland. This physiography shows the control of surrounding uplifts on basin confinement and sediment distribution (Leleu et al., 2009).

Based on the geographical and structural characteristics of the region, the Arc Basin can be subdivided into two sectors (Leleu, 2005): (i) the Gardanne Basin to the east, bounded to the north by Montagne Sainte-Victoire and to the south by Mont Aurélien, the Étoile Massif, and the Regagnas Dome, with the Plateau d'Ollières marking its eastern limit; and (ii) the Aix-en-Provence Basin to the west, opening toward the Étang de Berre, bounded to the south by the Nerthe Massif and to the north by the Saint-Chamas chain. Although this study refers to the Arc Basin without distinction between its internal subdivisions, it is worth noting that the study area, the Cengle Plateau, is located within the sector commonly referred to as the Aix-en-Provence Basin. This nomenclature appears in the literature (e.g., Durand, 1963; Cojan et al., 2000; Cojan and Moreau, 2006), where the term Aix-en-Provence Basin is used to refer to the areas that include the studied site.

The Cengle Plateau (Fig. 2.2) lies within this regional framework in the Provence region of southeastern France, immediately south of Montagne Sainte-Victoire and approximately 15 km east of Aix-en-Provence. The plateau has an elliptical shape, measuring about 7 km in length (east–west) and 2 km across, with an average altitude of 500 m. In its central portion, an elongated elevation reaches ~600 m. The cliff exposes 20–35 m of lacustrine–palustrine limestones belonging to the "Calcaire de Saint-Marc" Formation, part of the Arc Basin stratigraphy, which will be detailed later.

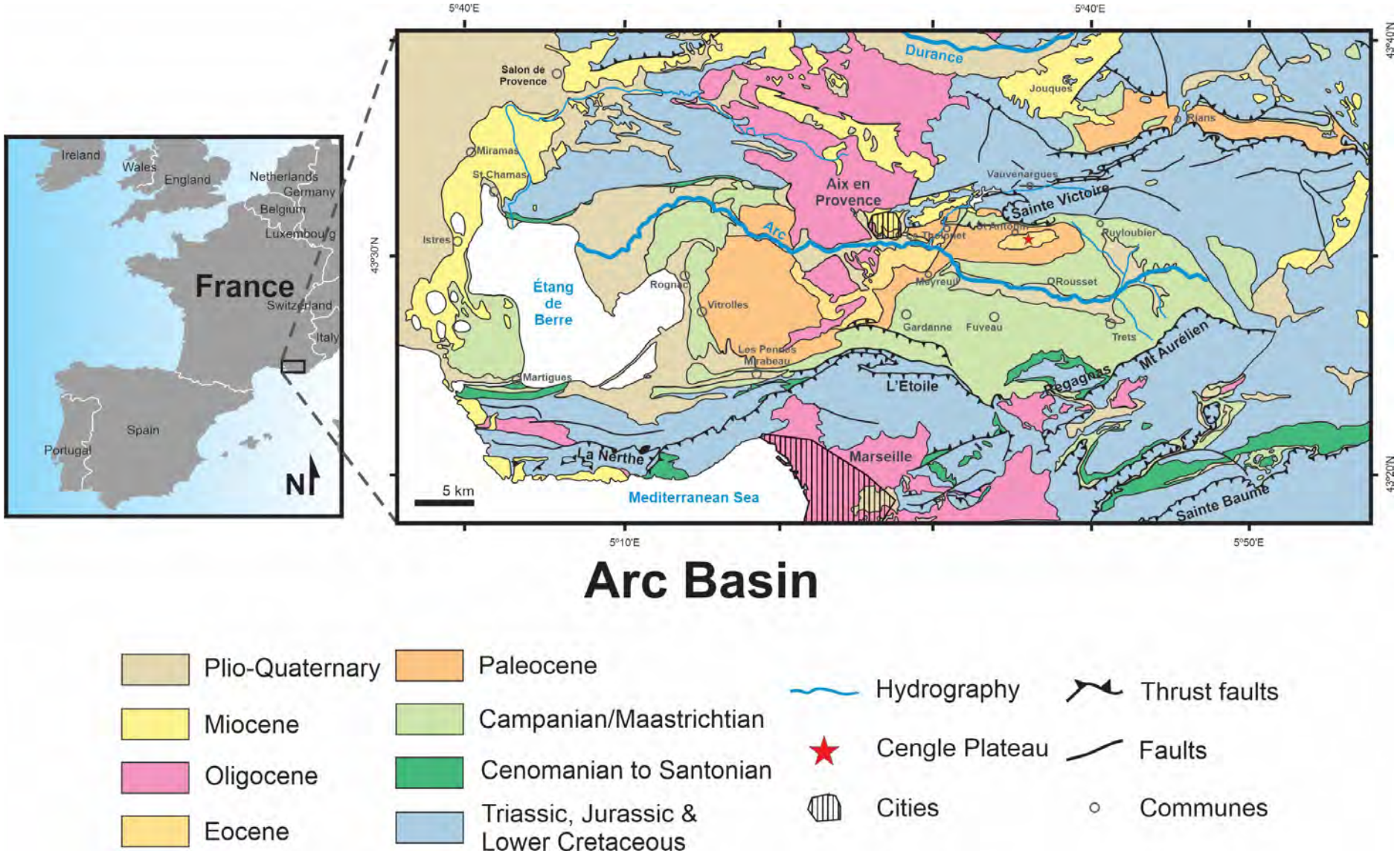


**Fig. 2.1.** Simplified geological map of the Arc Basin (1:250,000), modified from Rouire (1979) after Leleu (2005). The red star indicates the location of the Cengle Plateau.


**Fig. 2.2**. Panoramic view of the Cengle Plateau taken from the south, looking northward, with Montagne Sainte-Victoire in the background. Photograph by Georges Flayols (courtesy).

### 2.1.1.1. Structural Geology and Geotectonic Evolution

The onset of deposition in the Arc Basin took place during the Late Santonian, a time when sedimentary environments in Provence were undergoing a major transition. Until then, the southern part of the region had been dominated by marine sedimentation linked to the South-Provence Basin (Tortosa and Leleu, 2020 and references therein). A long-lasting marine transgression, active from the Early to Middle Cenomanian, continued to influence the area until the Late Santonian (Floquet, 2020). It was during this interval that compressional Pyrenean-Provençal tectonics induced uplift of the South-Provence Basin, leading to the development of lagoonal deposits that represent the final phase of its marine record (Tortosa and Leleu, 2020). Following the latest Santonian, the development of the Arc Basin syncline generated accommodation space that facilitated subsequent continental sedimentation (Cojan and Moreau, 2006).

Throughout the Upper Cretaceous to the Middle Eocene, the Arc Basin underwent continuous subsidence that allowed the accumulation of more than 2,000 m of continental deposits (Cojan, 1993), beginning in the Campanian (Durand, 1984). Despite the long duration of this interval, the basin paleogeography remained relatively stable (Cojan and Moreau, 2006). The sedimentary record consists of successions ranging from braided fluvial systems on silty floodplains to shallow lacustrine carbonates (Durand, 1984; Cojan, 1993).

Structural reorganizations in the Arc Basin are recorded by discontinuities and hiatuses within the sedimentary succession that can be directly attributed to synsedimentary tectonics. Cojan et al. (2000) emphasized that accommodation was not created uniformly but reflected periodic tectonic readjustments, leading to the local preservation of thicker successions in depocenters while uplifted zones record stratigraphic gaps or condensed sections. This pattern illustrates the alternation between phases of tectonic activity, which generated depocenters and uplifted source areas, and intervals of relative quiescence, when relief was subdued and sediment supply diminished (Cojan, 1993).

Within this framework, synsedimentary faulting played a central role in shaping both accommodation space and drainage organization. East–west faults defined the main depositional axes, whereas NNE–SSW faults controlled lateral facies variability and localized subsidence (Cojan, 1993; Cojan and Moreau, 2006). Regionally, this structural framework was reinforced by thrust contacts that marked the transition between the Mesozoic substratum and the Cretaceous–Paleogene cover (Leleu et al., 2009). These tectonic controls promoted a heterogeneous distribution of depositional environments, with coarse-grained alluvial fans developing along uplifted margins and interfingering with finer-grained floodplain and lacustrine–palustrine facies in central depressions. In stratigraphic terms, this interplay is expressed by lateral transitions from conglomeratic belts of Campanian–Maastrichtian and Paleocene age at the basin margins to lacustrine successions in the depocenters, reflecting the

diachronous nature of facies boundaries (Leleu et al., 2009). Although not the focus of this study, alluvial fans are important geomorphic markers of tectonic pulses and highlight the connectivity between proximal and distal depositional systems.

As highlighted by Tortosa and Leleu (2020) and Leleu and Tortosa (2020), the Pyrenean-Provençal orogeny was the main factor influencing tectonic and sedimentary evolution throughout the history of the Arc Basin. First, the deep reactivation of Triassic evaporite detachments triggered thrusting and deformation of the post-Triassic succession, producing the first reliefs in the region. This tectonic framework established the conditions for a continental marshy basin during the Late Santonian to Early Campanian, bounded by uplifted margins with only moderate relief (Tortosa and Leleu, 2020). These early deformations strongly conditioned sedimentation by creating depocenters where accommodation was concentrated and by supplying detrital material from uplifted source areas.

From the Middle Campanian onward, tectonic activity intensified, marking an important pulse of the Pyrenean-Provençal orogeny (Tortosa and Leleu, 2020). The main depocenter progressively shifted westward toward the Vitrolles area, while sedimentation decreased along the basin margins. At the same time, localized thrusting and folding produced tectonically active paleoreliefs, such as the so-called paleo-Regagnas, paleo-Étoile, and paleo-Sainte-Victoire. These structures, although not directly equivalent to the modern mountain ranges, occupied the same geographic sectors and were subject to intense erosion. Their dismantling generated coarse breccia deposits during the Late Campanian, which accumulated at the foot of these reliefs (Tortosa and Leleu, 2020). This period of tectonic activity was followed, in the latest Campanian to earliest Maastrichtian, by a phase of quiescence. Widespread lacustrine sedimentation sealed the Sainte-Victoire breccias, marking a phase of tectonic tranquility that interrupted sediment supply from the previously uplifted reliefs. Subsequent Maastrichtian sedimentation, represented by the Upper Rognacian facies (dominated by lacustrine and palustrine carbonates), continued without breccia deposition, reflecting this more stable tectonic context.

During the Paleogene and Eocene, the basin continued to record exclusively continental environments, including terrestrial, fluvial, lacustrine, and palustrine facies (Leleu and Tortosa, 2020). The main deformation of Provence, corresponding to the emplacement of the Sainte-Baume nappe and major thrust sheets, is conventionally attributed to the Bartonian, representing the peak of Pyrenean-Provençal tectonics. Between the Late Cretaceous breccia events and this principal deformation, another tectonic phase is recorded along the northern margin of the Arc Basin. The Dano–Selandian breccias of Montagne Sainte-Victoire, associated with renewed erosion and the development of alluvial fans at the mountain front (Leleu, 2005), testify to this intermediate deformation and further highlight the alternation between tectonic activity and quiescence that characterizes the basin’s evolution.

#### 2.1.1.2. Stratigraphy

Stratigraphically, the successions of the Arc Basin were first classified into a series of local stages (e.g., Valdonnian, Fuvelian, Bégudian, Rognacian, and Vitrollian) defined from stratotypes at their respective type localities (Matheron, 1878; Villot, 1883; Babinot and Durand, 1980). Each stage was characterized by facies composed of alternating limestones, sandstones, and claystones, identified on the basis of their lithological attributes and fossil content. However, these local stages are no longer formally employed in stratigraphy, except occasionally by paleontologists working on highly localized studies (Tortosa and Leleu, 2020). In practice, they essentially represent facies units whose lithological similarity may mask chronological differences: depositional environments of different ages can appear

contemporaneous, while comparable facies may in fact be diachronous. The associated fossil assemblages help refine paleoenvironmental interpretations but do not resolve these uncertainties. Despite these limitations, the local stages laid the foundation for the present chrono-lithostratigraphic framework of the basin. Later studies (Durand, 1984; Cojan et al., 2000; Cojan and Moreau, 2006) correlated them with international marine stages, relying on biostratigraphic evidence, carbon-isotope stratigraphy, and paleomagnetic data. In the current framework (Fig. 2.3), as summarized by Cojan et al. (2000) and Tortosa and Leleu (2020), the principal limestone intervals are regarded as the main lithostratigraphic units of the basin.

The stratigraphic succession is therefore presented below through a synthesis of the main units, from the Valdonnian to the Lutetian, with age correlations to the international time scale shown in Fig. 2.3. The descriptions are primarily based on Tortosa and Leleu (2020) for the Upper Cretaceous succession, and on Leleu and Tortosa (2020) for the Paleogene units, while other references are cited where appropriate to provide further detail and context.

## Valdonnian–Fuvelian

From a biostratigraphic perspective, Babinot and Durand (1980) demonstrated that the Valdonnian and Fuvelian cannot be clearly differentiated, as they share broadly similar faunal assemblages. For this reason, the two are often grouped into a Valdo–Fuvelian unit, although they are still presented separately for clarity.

The **Valdonnian** deposits display significant lateral and vertical variability across the Arc Basin. In the central part of the basin, thicknesses may reach 70 m, with basal reddish clays containing sandstone lenses overlain by white to gray marls and lacustrine limestones rich in charophytes and locally with pisoids. Toward the upper part of the succession, floodplain and palustrine deposits become dominant, recording swampy environments rich in mollusks and freshwater vertebrates such as turtles and crocodiles. In the southern and western margins, the unit may exceed 100 m, including alternations of marls, marly limestones, lignitic layers, and occasional sandstones or microconglomerates.

The **Fuvelian** succession is equally heterogeneous. North of the Étang de Berre, the facies are mainly fluvial, characterized by sandstones and clays, while near the foothills of Sainte-Victoire lacustrine and delta-lacustrine deposits dominate. Toward the eastern sector, near Trets, the deposits return to more fluvial settings. Thicknesses range from 120 to more than 250 m depending on location. In several areas, lignite horizons and highly fossiliferous marls are preserved, yielding abundant gastropods, bivalves, charophytes, pollen, and vertebrate remains, including crocodiles, turtles, and dinosaurs. The lignites of the Fuvelian were mined in underground galleries until 2003, making the Arc Basin the seventh most important coalfield in France in terms of production.

These successions record the establishment of a vast marshy system with interconnected lakes that expanded and contracted through time. The absence of mature paleosols and pedogenic features suggests relatively persistent water levels, limiting vegetation to lake margins but favoring the accumulation of organic matter in basin interiors. The abundant macro- and microflora, including ferns, conifers, palms, and angiosperms, indicate a warm and humid tropical climate. Taken together, the Valdonnian and Fuvelian illustrate the interplay between fluvial input and lacustrine development, reinforcing their interpretation as closely related depositional stages best understood within a unified Valdo–Fuvelian framework.

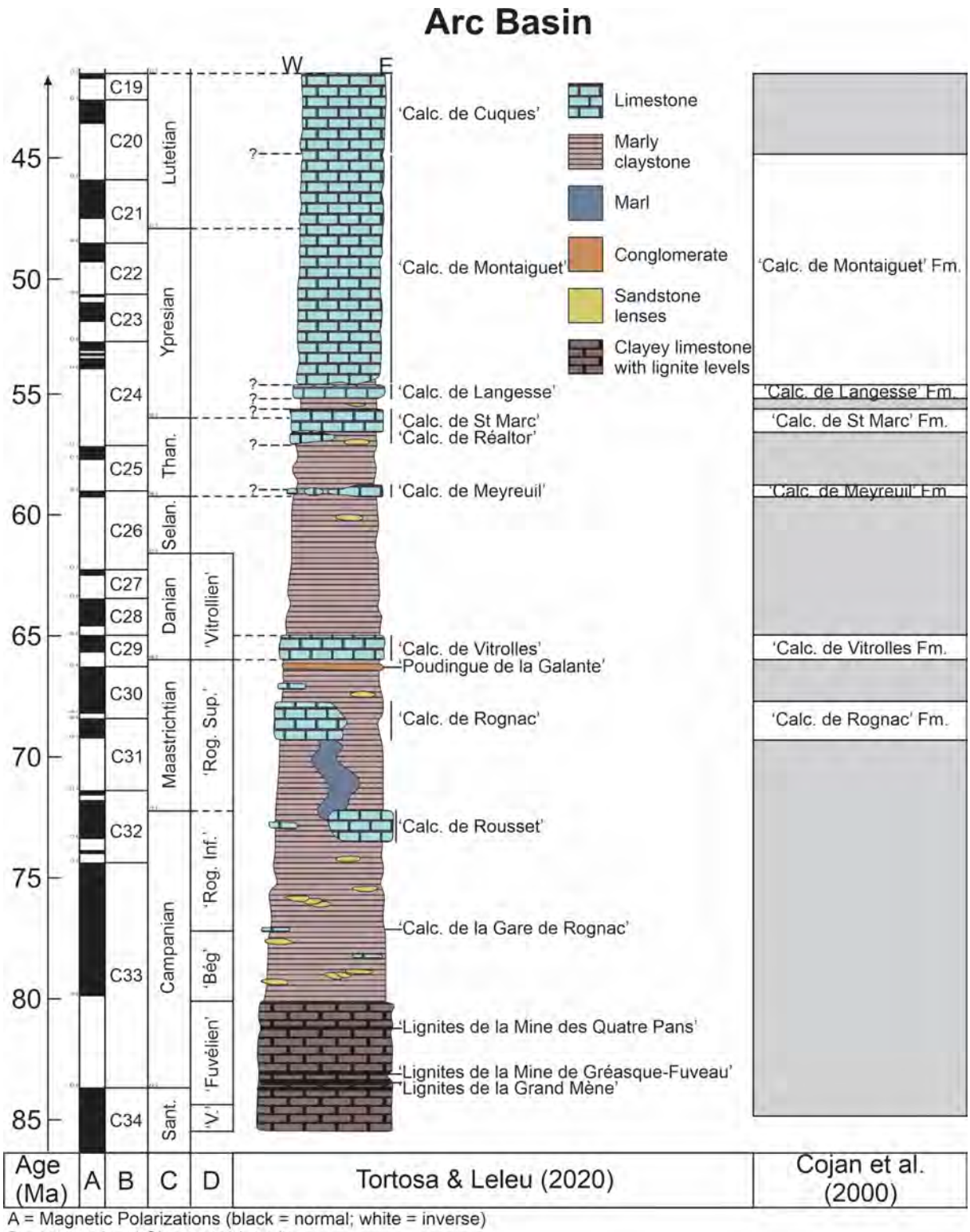


**Fig. 2.3.** Chronostratigraphic chart of the Arc Basin after Cojan et al. (2000) and Tortosa and Leleu (2020).

## Bégudian and Rognacian

In the same way as the preceding stages, the Bégudian and Rognacian are closely related and often difficult to separate. From a biostratigraphic standpoint, Babinot and Durand (1980) demonstrated that they cannot be clearly differentiated, as they share broadly similar molluscan

assemblages with only minor floristic differences. For this reason, they are sometimes grouped into a single Bégudo–Rognacian unit, although they are presented separately here for clarity. The distinction is further supported by tectonic evidence, since a regional phase of deformation in the eastern Arc Basin produced a stratigraphic unconformity between the Fuvelian and the overlying Bégudian deposits.

The **Bégudian** succession is typically composed of alternating marls, sandstones, and lacustrine carbonates, which display significant lateral variability across the basin. In the Fuveau area, the unit includes marls and limestones with charophytes, pisolitic horizons with unionid bivalves, and interbedded sandstones and reddish clays. To the east and southwest, conglomerates and breccias testify to syntectonic alluvial fan systems, whereas in the western sectors the succession thickens to several hundred meters and becomes dominated by fluvio–deltaic deposits with local lacustrine intervals. This variability reflects contrasting sediment sources and subsidence regimes throughout the basin.

The **Rognacian** is generally characterized by alternations of red and variegated clays, sandstones, and lacustrine limestones. In its type area around Rognac and Vitrolles, the succession begins with red clays overlain by lacustrine carbonates known as the “Calcaire de Rognac” (‘Calcaire de Rognac’ Formation, Cojan et al., 2000). These carbonates, up to 30 m thick, are rich in charophytes and display nodular and palustrine features. Biostratigraphic studies have shown that these limestones are diachronous: the carbonates of Rognac and Vitrolles are Maastrichtian in age, whereas equivalent deposits at Rousset belong to the late Campanian (Garcia and Vianey-Liaud, 2001). The upper part of the Rognacian is marked by the conglomeratic “Poudingue de la Galante”, a 2–4 m thick unit composed of polymictic lithic clasts. Well exposed in the Vitrolles area and at the base of Montagne Sainte-Victoire, it has been interpreted as the lateral equivalent of sandstone lenses at the same stratigraphic level in the Rognac sector. Stratigraphically, it occupies the uppermost Maastrichtian and directly underlies the Calcaire de Vitrolles, providing a reliable regional marker horizon. Its significance is further emphasized by the fact that the Cretaceous/Paleogene (K/Pg) boundary is positioned immediately above this unit, identified in the Arc Basin by a pronounced negative $\delta^{13}C$ excursion (Cojan et al., 2000).

Paleoenvironmental reconstructions indicate that the Bégudian and lower Rognacian correspond to the development of the “Paleo-Arc River”, a major fluvial system that drained adjacent reliefs and terminated in shallow lakes (Cojan et al., 2003). Floodplain deposits and abundant fossil eggs document the coexistence of soils, seasonal overbank sedimentation, and dinosaur nesting grounds. From the Late Campanian to Early Maastrichtian, these fluvial systems gave way to more extensive lacustrine environments, represented by carbonate successions such as the Calcaire de Rognac. Toward the end of the Maastrichtian, increasing aridity led to a contraction of lake areas and culminated in the deposition of the Poudingue de la Galante, immediately below the K/Pg boundary, marking the transition to the Paleogene succession (Cojan and Moreau, 2006).

## Vitrollian (Calcaire de Vitrolles)

The Paleocene succession in Provence is dominated by red siltstones, occasionally interbedded with continental carbonates expressed as paleosols or lacustrine–palustrine limestone beds, and locally by thick breccia lobes. Within this context, the palustrine “Calcaire de Vitrolles” (‘Calcaire de Vitrolles’ Formation, Cojan et al., 2000), originally defined as the Vitrollian Stage (Matheron, 1878), constitutes the most characteristic unit of the interval. These limestones are typically mottled and multicolored (pink, red, yellow, gray, or whitish), displaying abundant root traces and burrows, and were historically exploited as decorative

“false marble”. The formation is particularly prominent between Ventabren and Pennes-Mirabeau, where it reaches ~50 m in thickness, and extends more discontinuously toward Meyreuil and the northeastern margin of the Cengle Plateau. This distribution provides insight into the paleogeography of the so-called “Vitrolles paleolake”.

At the base of Montagne Sainte-Victoire, the unit is overlain by thick breccias enriched in microcodium, which rest unconformably on Upper Jurassic strata. Above, the succession consists of up to 100 m of red marls interbedded with conglomerates and breccias, sometimes steeply tilted or overturned, as observed between Beaurecueil and Saint-Antonin-sur-Bayon. Fossil content is sparse and uncertain: the gastropods *Physa montensis* and *Physa prisca* have been reported, but their stratigraphic significance remains questionable.

Regionally, facies variations are observed. In the Coudoux area, Vitrollian deposits locally include siliceous travertines, whereas in the Rians Basin, the interval is represented by ~50 m of wine-colored mudstones with lenses of mottled breccias. In the Alpilles sector, limestones with microcodium crusts overlie red continental mudstones, which themselves rest on the Calcaire de Rognac. These red mudstones are sometimes mapped as Vitrollian, although their exact age (Maastrichtian or Paleocene) remains unresolved.

Paleoenvironmental reconstructions indicate alternating palustrine–lacustrine limestones and fluvial argillaceous–arenaceous deposits, similar to those of the Upper Cretaceous. Fossil assemblages, mainly charophytes and mollusks, provide the main criteria for distinguishing these environments, although the record remains relatively sparse.

## Thanetian (Calcaires de Meyreuil)

The Thanetian succession in Provence is primarily represented by the “Calcaires de Meyreuil” (‘Calcaire de Meyreuil’ Formation, Cojan et al., 2000), which have yielded a diverse molluscan fauna including *Physa prisca* and *Limnaeact rollandi*. The overlying clays, locally reaching up to 100 m in thickness, contain charophytes and thin eggshell fragments attributed to *Ornitholithus biroi*, possibly belonging to gastornithids or ratites (Feist-Castel, 1975; Dughi and Sirugue, 1968; Buffetaut and Angst, 2014). These records document the early Paleocene reappearance of large terrestrial vertebrates in the fossil record, following the extinction of non-avian dinosaurs at the K/Pg boundary.

Regionally, facies expressions vary. Around the Étang de Berre, lenticular lacustrine limestones of probable Thanetian age are locally silicified and associated with smectite- and attapulgite-bearing marls. South of Ventabren, similar red clays overlie silicified limestones and may contain thin breccia lenses. In the Réaltor sector, between Vitrolles and Aix-en-Provence, the upper part of the succession comprises alternating limestones and marls known as the “Calcaires et Marnes du Réaltor et du Grand Arbois”. This interval is fossiliferous, with *Physa prisca*, charophytes, and microcodium. Thickness varies significantly: while limestones measure ~10 m in the southern cliffs, they expand considerably in the gorges of the Arc River at Roquefavour and across the central Arbois Plateau, thinning laterally into wedges toward the basin margins.

Other occurrences are more fragmentary. In the Saint-Rémy-de-Provence area, ~10 m of gravels and red marls are tentatively assigned to the Thanetian, though lacking diagnostic fossils. In the Rians Basin, the unit is represented by ~110 m of bright red clays with quartz grains, interbedded with multicolored breccia lenses containing Jurassic limestone clasts. Its basal part comprises a silicified lacustrine limestone bed up to 3 m thick.

Paleoenvironmental reconstructions indicate that Thanetian environments alternated between lacustrine and fluvial episodes, continuing the patterns already established in earlier Paleocene successions.

## Lower Ypresian (Calcaires de Saint-Marc)

Overlying the Thanetian red clays, the “Calcaires de Saint-Marc” (‘Calcaire de Saint-Marc’ Formation, Cojan et al., 2000), formerly referred to the Sparnacian (Lower Ypresian), are now assigned to the upper Thanetian–Ypresian transition. This lacustrine formation is particularly rich in charophytes, microcodium debris, and gastropods such as *Limnaea longissima*, *Physa draparnaudi*, *Physa columnaris*, and *Planorbis sparnensis*. Thick avian eggshells (*Ornitholithus arcuatus*), probably belonging to large gastornithids such as *Gastornis (=Diatryma)*, have also been documented based on theoretical egg volume estimations (Dughi and Sirugue, 1968; Buffetaut and Angst, 2014). The limestones are overlain by 20–60 m of red marls containing lenses of fluvial conglomerates, which have also yielded fragments of thick avian eggshells. Together, these limestones and marls form the Petit Arbois Plateau (eastern Réaltor Basin) and the hills south of Calas.

Paleoenvironmental interpretations indicate the persistence of lacustrine settings at the transition between the Paleocene and Eocene, with adjacent floodplain systems contributing terrigenous sediments. The association of charophytes, gastropods, and avian eggshells reflects the ecological diversity of these shallow-water and marginal environments, while the occurrence of fluvial conglomerates records episodic high-energy influxes into the basin. Magnetostratigraphic and chemostratigraphic analyses (Cojan et al., 2000) identified the Paleocene–Eocene Thermal Maximum (PETM) within the Saint-Marc Limestone – the most rapid and intense warming event of the Cenozoic – characterized by a temperature increase exceeding 6 °C over approximately 20 kyr (e.g., Kirtland Turner et al., 2017).

## Note on the Barre du Cengle

The “Calcaire du Cengle” is considered part of the same lithostratigraphic unit as the “Calcaire de Saint-Marc”. This correlation, already recognized by Matheron (1868, cited in Dughi and Sirugue, 1968), based on the consistency of the limestone–marl alternations overlying the “Calcaire de Vitrolles”. On the left bank of the Arc River, the succession from base to top comprises: “Calcaire de Vitrolles”, red marls, “Calcaire de Meyreuil”, red marls, and “Calcaire de Saint-Marc”, overlain by red marls. On the western slope of the Cengle Plateau, the equivalent succession is: “Calcaire de Vitrolles”, red marls, “Calcaire de Beaurecueil”, red marls, and “Calcaire du Cengle”, overlain by red marls. In this study, the expression “Calcaire du Cengle” (or Cengle limestone) is used with a geographical connotation, while the corresponding lithostratigraphic unit is referred to as the “Calcaire de Saint-Marc” Formation, following Corroy and Touraine (1961) and Cojan et al. (2000).

In the Cengle Plateau region (Fig. 2.4), lacustrine limestones are interbedded with reddish marls and mudstones deposited in floodplain environments. The main limestone intervals are represented by the “Calcaire de Rognac”, “Calcaire de Vitrolles”, and “Calcaires de Saint-Marc” (Durand and Tempier, 1968). Above the Cengle cliff, reddish marls from floodplain deposits form the plateau top (Durand, 1963).

The Cengle limestones have yielded a variety of fossils, including charophyte fragments, bivalve and gastropod mollusks, ostracods, and microcodium debris (Durand, 1963). Bivalves (Durand, 1963) and gastropods such as *Physa prisca*, *Physa columnaris*, *Succinea sparnacensis*, and *Planorbis sparnacensis* have been identified (Feist-Castel, 1975; Durand, 1984). Charophytes such as *Sphaerochara edda* were described in the lower part of the Calcaire de Saint-Marc Formation (Arc Valley region; Feist-Castel, 1975), leading to the assignment of an Upper Thanetian age to the base of the unit.

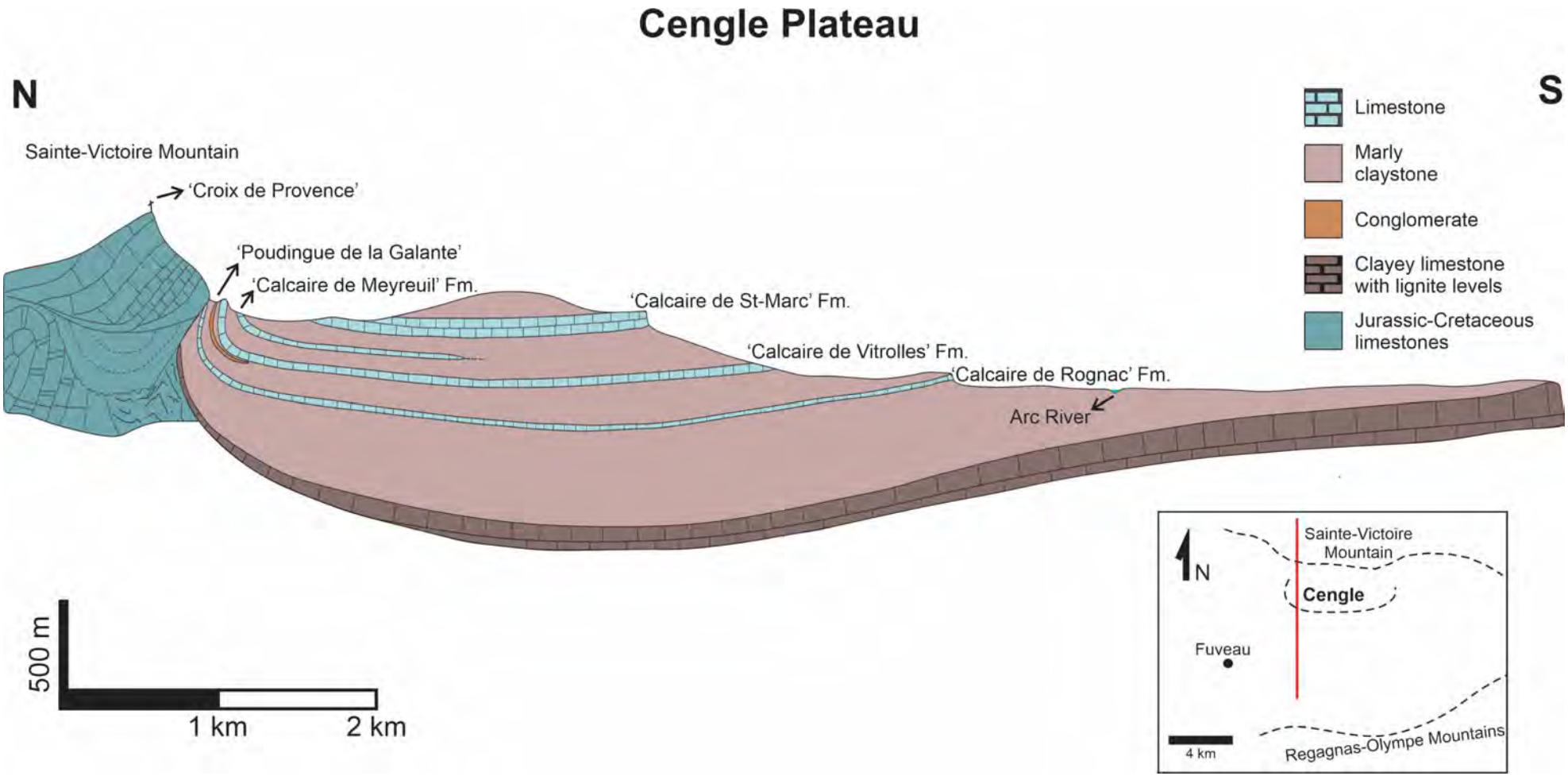


**Fig. 2.4.** Simplified N–S stratigraphic section of formations and facies in the Cengle Plateau region (modified after Durand and Tempier, 1968).

Provence is internationally renowned for its fossil eggshells, ranging from dinosaur remains in the Campanian and Maastrichtian successions to giant bird eggshells in Paleocene and Eocene deposits, also recorded in the Cengle Plateau. Below the Cengle limestones, thin eggshells of *Ornitholithus biroi* have been documented, while the marly intervals at the top of the plateau contain thick eggshells of *Ornitholithus arcuatus* (Durand, 1984; Angst et al., 2015).

## Lower Ypresian (Calcaires de Langesse)

The “Calcaires de Langesse” (‘Calcaire de Langesse’ Formation, Cojan et al., 2000), formerly dated to the Lower Lutetian, are now placed within the Lower Ypresian. This lacustrine limestone unit, 30–40 m thick in the Arc Basin, has yielded abundant charophytes, Microcodium debris, and gastropods such as Physa columnaris. Near the locality of Palette, a clay–lignite horizon within the unit has provided numerous vertebrate remains, including mammals, turtles, crocodilians, and birds, making it one of the most fossiliferous levels of the Lower Eocene succession in Provence. In the Rians syncline, the Ypresian interval is represented by micaceous sands and limestones with Bithynia, ranging from 50 to 350 m in thickness. To the northwest, in the Orgon sector, the Eocene succession is composed of ~30 m of reddish sands and clays.

Paleoenvironmental interpretations indicate that the “Calcaire de Langesse” formed within shallow lacustrine systems developed during a humid climatic phase of the early Eocene. Lignitic horizons record floodplain environments, while associated vertebrate faunas, including the Palette locality (~56 Ma), document the onset of mammalian diversification in Provence. The distinct composition of these faunas compared to northern France and Britain highlights a paleobiogeographic differentiation, likely linked to the climatic perturbations of the PETM (Leleu and Tortosa, 2020).

## Upper Ypresian to Lower Lutetian (Calcaires du Montaiguet)

Following a thin marl interval, the “Calcaires du Montaiguet” (‘Calcaire du Montaiguet’ Formation, Cojan et al., 2000) mark a major lacustrine limestone development assigned to the Upper Ypresian–Lower Lutetian. These white to light-gray limestones are rich in charophytes, stromatolites, microcodium, and gastropods such as *Planorbis pseudoammonius*, *Limnaea aquensis*, and *Bulimus hopei*. In the Milles area, the unit reaches up to 50 m in thickness. Comparable lacustrine deposits occur in the northwestern part of the département: compact white limestones with flint, up to 25 m thick, exposed at Mallemort, Eygalières, and Orgon, have yielded *Amphidromus hopei* and *Rillya matheroni* and are also assigned to the Lutetian.

Regionally, other lithostratigraphic equivalents include the “Calcaires de Cuques”, ~60 m thick, composed of whitish to gray limestones rich in gastropods such as *Planorbis pseudoammonius*, *Limnaea sp.*, and *Strophosoma golfieri*. Their base is obscured by Quaternary alluvium of the Arc Valley, preventing direct correlation with the Calcaires du Montaiguet. In the Orgon sector, the “Calcaires d’Eygalières” form a continuous cuesta, consisting of up to 30 m of palustrine–lacustrine facies. These include nodular limestones with root traces and burrows, clayey limestones with strong nodular features, and flint-bearing lacustrine intervals. The molluscan fauna is diverse, including species typically Lutetian such as *Helix eygalierensis*, *Romanella hopei*, *Rillya matheroni*, *Filholia subcylindrica*, *Rillya gibba*, and *Galba michelini*.

In the Maussane syncline, the Lutetian is represented by white tufaceous limestones, often fetid and locally silicified, as well as reddish breccias cemented by calcareous–siliceous matrices. Collectively, these formations illustrate a widespread lacustrine expansion during the Upper Ypresian–Lower Lutetian, alternating with floodplain and palustrine environments.

### 2.1.2. Salta Basin (NW Argentina)

The Salta Group Basin (Turner, 1958), more commonly referred to as the Salta Basin (Marquillas et al., 2005), occupies a broad area of northwestern Argentina, where nearly 70% of its extent lies, as well as parts of southern Bolivia and western Paraguay, covering ~150,000 km² (Del Papa and Salfity, 1999). Its sedimentary fill, up to 5,000 m thick (Marquillas et al., 2005), records the development of an intracontinental rift within the South American plate, initiated during the breakup of Gondwana in the Patagonian orogenic cycle (Keidel, 1921; Bianucci and Homovc, 1982). Rifting began in the Cretaceous and persisted until the late Eocene, when the onset of Andean orogenesis replaced extensional tectonics by compressional regimes (Hernández and Echavarria, 2009). Structurally, the basin is subdivided into seven sub-basins (Marquillas et al., 2005): Tres Cruces, Lomas de Olmedo, Metán, Alemanía (Reyes, 1972; Salfity, 1982), El Rey (Salfity, 1980), Sey (Schwab, 1984), and Brealito (Sabino, 2002). For simplification, the basin is grouped into four broader sub-units: Lomas de Olmedo in the east, Sey in the west, Tres Cruces in the north, and Metán–Alemanía in the south (Fig. 2.5). The southernmost sub-basin, Metán–Alemanía, constitutes the focus of the present study.

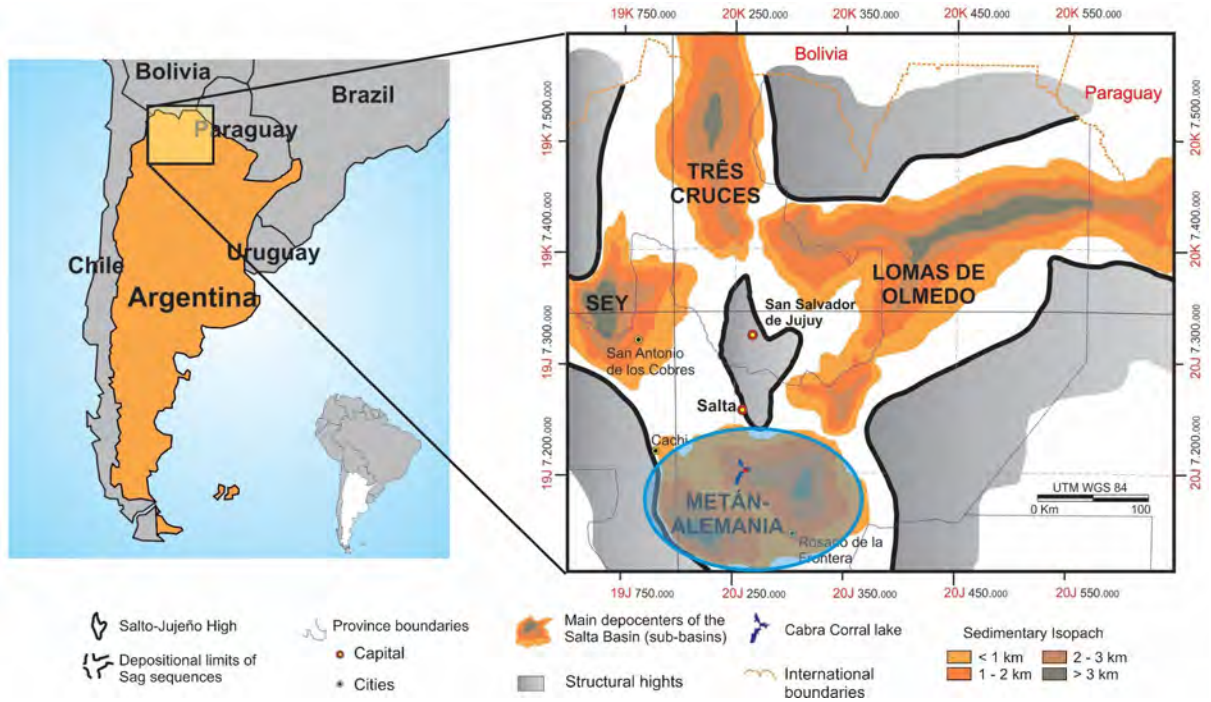


**Fig. 2.5.** Location map of the Salta Basin and its sub-basins, showing isopach contours of the Yacoraite Formation (modified from Roemers-Oliveira et al., 2015 after Bento Freire, 2012). The blue circle marks the studied sub-basin.

The history of geological knowledge in the region is closely tied to hydrocarbon exploration. The earliest written accounts of oil seeps date back to the mid-17th century, reported by Franciscan missionaries in Tarija (Dorfman, 1942). Systematic exploration began in the early 20th century, led by the state company YPF, which identified minor non-commercial oil accumulations (Disalvo, 2002). The first commercial discovery was made in the Lomas de Olmedo Sub-basin in the late 1940s, targeting fractured and karstified carbonates of the Yacoraite Formation (Maastrichtian–Danian). Production peaked at ~50,000 barrels per day during the 1970s (Disalvo, 2002), and wells drilled exceeded 5,000 m in measured depth.

This breakthrough highlighted the petroleum potential of the Yacoraite reservoirs and directed subsequent studies toward the Metán–Alemanía Sub-basin, where continuous and well-exposed outcrops provided an exceptional opportunity for detailed stratigraphic and paleoenvironmental analyses. Seminal contributions include Hernández et al. (1999), Sial et al.

(2001), Disalvo et al. (2002), Marquillas et al. (2003, 2005, 2007), and Hernández et al. (2008). More recent high-resolution stratigraphic studies expanded this framework, including those of Bento Freire (2012), Gomes (2013), Pedrinha (2014), Roemers-Oliveira (2014), Pedrinha et al. (2015), Roemers-Oliveira et al. (2015), Bunevich (2016), Bunevich et al. (2017), Deschamps et al. (2020), Gomes et al. (2020), Villafañe et al. (2022), Ceolin et al. (2022), Oliveira Santos et al. (2023), and Fragoso (2023). Complementary detailed analyses have also been conducted in the Tres Cruces Sub-basin (e.g., Mutti et al., 2023; Vallati et al., 2023).

#### 2.1.2.1. Structural Geology and Geotectonic Evolution

The geotectonic evolution of the Salta Basin is complex, reflecting the influence of several orogenic cycles from the Cretaceous to the compressional regime of the Andean orogeny in the Eocene (Hernández and Echavarria, 2009). The basin originated as an intracontinental rift during the Cretaceous (Bianucci and Homovc, 1982), linked to the breakup of Gondwana and the opening of the South Atlantic, a process related to the Patagonian orogenic cycle. Its evolution was marked by two main stages, rift and post-rift (sag), each associated with distinct subsidence mechanisms and depositional architectures.

The rift stage was characterized by crustal extension during the Cretaceous, producing sedimentary fills exceeding 4,000 m in thickness Marquillas et al. (2005). According to Hernández et al. (1999), these deposits rest unconformably on the basin basement. Ramos (1988) argued that rifting was controlled by inherited structural lineaments from Permian to Triassic/Jurassic paleo-rifts related to the Gondwanan orogenic cycle. These lineaments generated differential subsidence, producing internal highs locally referred to as “umbrais” (Comínguez and Ramos, 1995; Cristallini et al., 1997), generating sub-basins (Fig. 2.5). Among these, the Salta–Jujuy High acted as a central uplift, imparting a radial geometry to the basin, which was bounded externally by structural arches (Sabino, 2004). The Metán–Alemanía Sub-basin, studied in this work, is confined by the Transpampeano–Púnico and Pampeano arches to the west/southwest and east/southeast, respectively. Within this framework, the Guachipas High separates the Metán and Alemanía depocenters. The wedge-shaped geometry of syn-rift successions further highlights the strong tectonic control on accommodation (Hernández et al., 1999).

The post-rift (sag) stage began in the Maastrichtian with a significant decrease in subsidence rates and reduced sediment supply from the basin margins. This stage was dominated by thermal subsidence (Del Papa and Salfity, 1999; Salfity and Marquillas, 1999), with sedimentation progressively covering structural highs and merging the sub-basins generated during the rift stage into a broad, shallow depression with tabular geometries. In the Metán–Alemanía Sub-basin, for instance, north–south cross-sections illustrate the contrast between the thick rift infill and the thinner, more uniform sag deposits (Fig. 2.6A). East–west cross-sections further highlight the tabular, unfaulted geometry characteristic of the sag stage (Fig. 2.6B). Although the sag phase began in the Maastrichtian, the Salta–Jujuy High persisted as a positive feature until the late Danian, when it was finally onlapped (Gómez Omil and Boll, 1999, 2005).

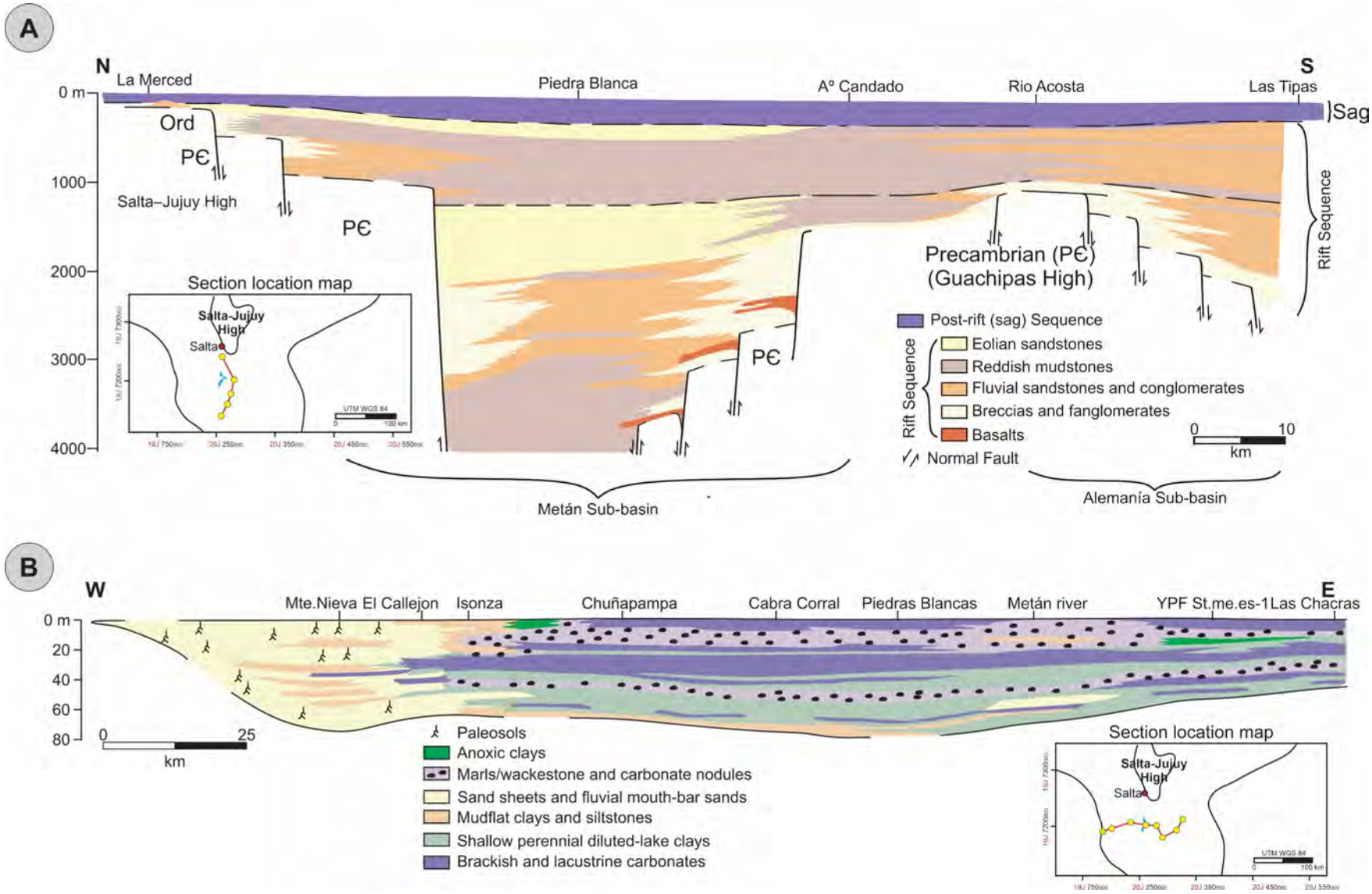


**Fig. 2.6.** Stratigraphic sections of the Metán–Alemanía Sub-basin. (A) North–south section showing rift deposits significantly thicker than those of the sag stage. (B) East–west section illustrating the tabular and unfaulted geometry of the sag stage. Modified from Hernández et al. (1999) after Bento Freire (2012).

While several studies interpret this sag stage as a continuous evolution into the Eocene (e.g., Reyes and Salfity, 1973; Cristallini et al., 1997; Marquillas et al., 2005), others (e.g., Bianucci et al., 1981; Gómez Omil et al., 1989; Gómez Omil and Boll, 1999; Hernández et al., 1999) have documented a significant change in subsidence patterns during the Paleocene. This tectonic renewal, referred to as the Pre-Olmedo phase, represents a second rifting episode marked by a regional erosional unconformity and rejuvenated fluvial drainage, particularly along the margins of the Lomas de Olmedo Sub-basin. However, this phase did not generate depocenters comparable in thickness to those of the first rift stage, and its deposits were soon overlain by regionally extensive tabular strata, initiating a renewed sag stage that persisted into the Eocene.

The final stage corresponds to the Andean orogeny or Andean cycle (Ramos, 1988). During this compressional phase, the basin evolved into a foreland system, undergoing deformation, inversion, folding, and fault reactivation (Hernández and Echavarria, 2009). According to Gómez Omil and Boll (1999), these structures generated hydrocarbon traps that remain important exploration targets.

#### 2.1.2.2. Stratigraphy

The stratigraphy of the Salta Basin has been systematically studied since the late nineteenth century. The first comprehensive classification was proposed by Brackebusch (1891), who referred to the Cretaceous succession of the region as the *Salta System*. With the subsequent development of geological methods and concepts, Turner (1958) redefined this succession as the Salta Group, encompassing strata from the Cretaceous to the Paleogene in northwestern Argentina.

In its traditional lithostratigraphic framework, the Salta Group is subdivided into three main subgroups (e.g., Gómez Omil and Boll, 2005; Marquillas et al., 2005):

- the Pirgua Subgroup (Reyes and Salfity, 1973), composed of the La Yesera, Las Curtiembres, and Los Blanquitos formations;
- the Balbuena Subgroup (Moreno, 1970), including the Lecho, Yacoraite, and Olmedo/Tunal formations. The Tunal Formation is regarded as a lateral equivalent of the Olmedo Formation in the Metán–Alemanía Sub-basin. These units are absent in the Tres Cruces and Sey sub-basins; and
- the Santa Bárbara Subgroup (Moreno, 1970), which comprises the Mealla, Maíz Gordo, and Lumbrera formations.

This lithostratigraphic arrangement has provided the basic nomenclatural framework that has guided regional studies for decades. However, with the development of sequence stratigraphy, alternative schemes emphasized the recognition of supersequences and sequences, bounded by unconformities and stratigraphic surfaces of regional significance (e.g., Bianucci et al., 1981; Gómez Omil and Boll, 1999; Hernández et al., 1999). In this approach, the Pirgua, Balbuena, Santa Bárbara, and Lumbrera units are treated as supersequences, each internally subdivided into sequences that reflect changes in accommodation and sediment supply.

The comparison between the lithostratigraphic and sequence stratigraphic frameworks is shown in Fig. 2.7, which highlights their temporal correspondence. Fig. 2.8 further illustrates this duality in the Metán–Alemanía Sub-basin, showing a fault block in the Cabra Corral area with the formations identified according to the lithostratigraphic nomenclature on the left, and the equivalent sequence stratigraphic terminology on the right.

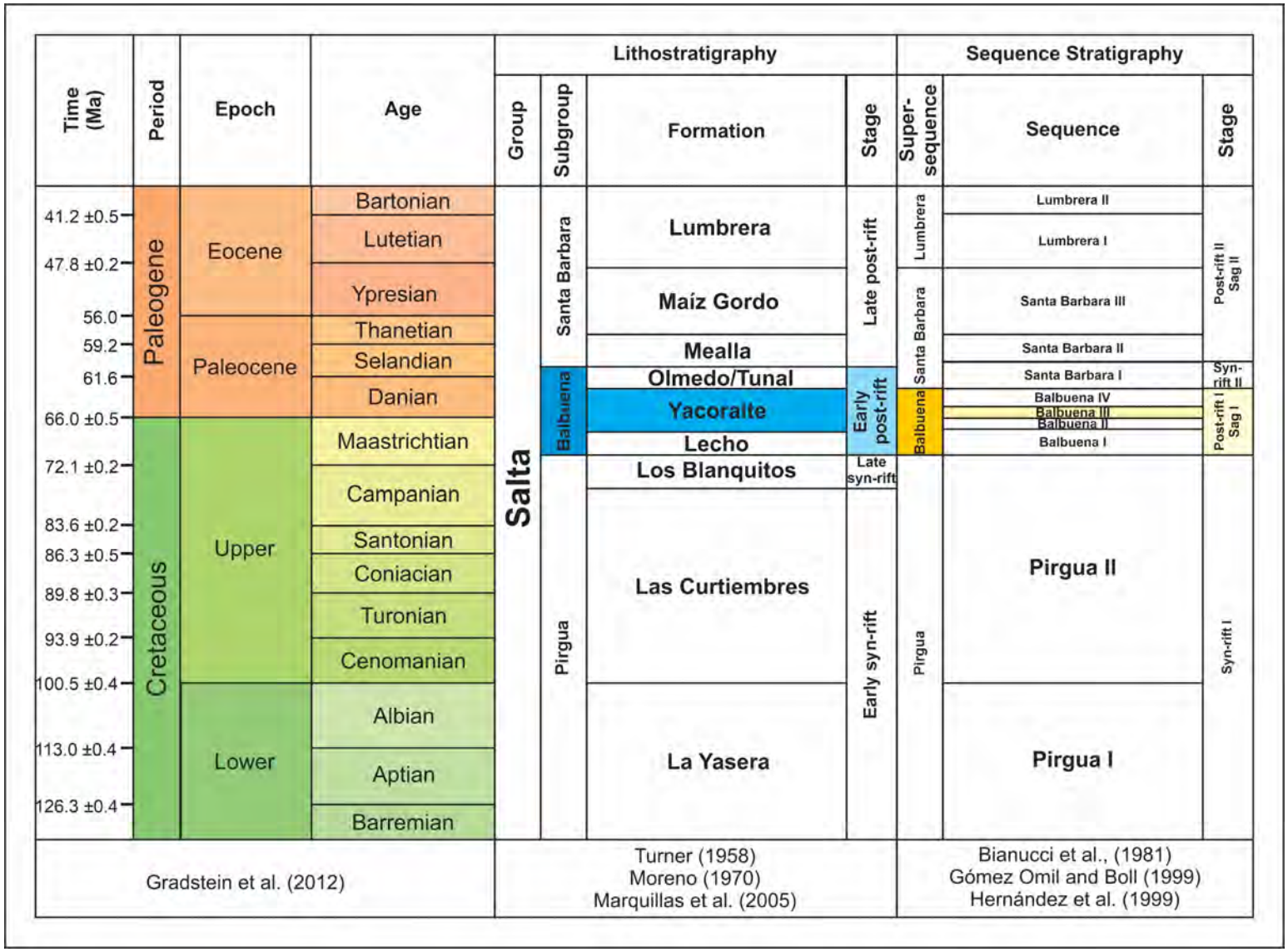


**Fig. 2.7.** Stratigraphic framework of the Salta Basin, illustrating the correspondence between lithostratigraphic and sequence stratigraphic classifications. In both, the unit analysed in this study is highlighted.

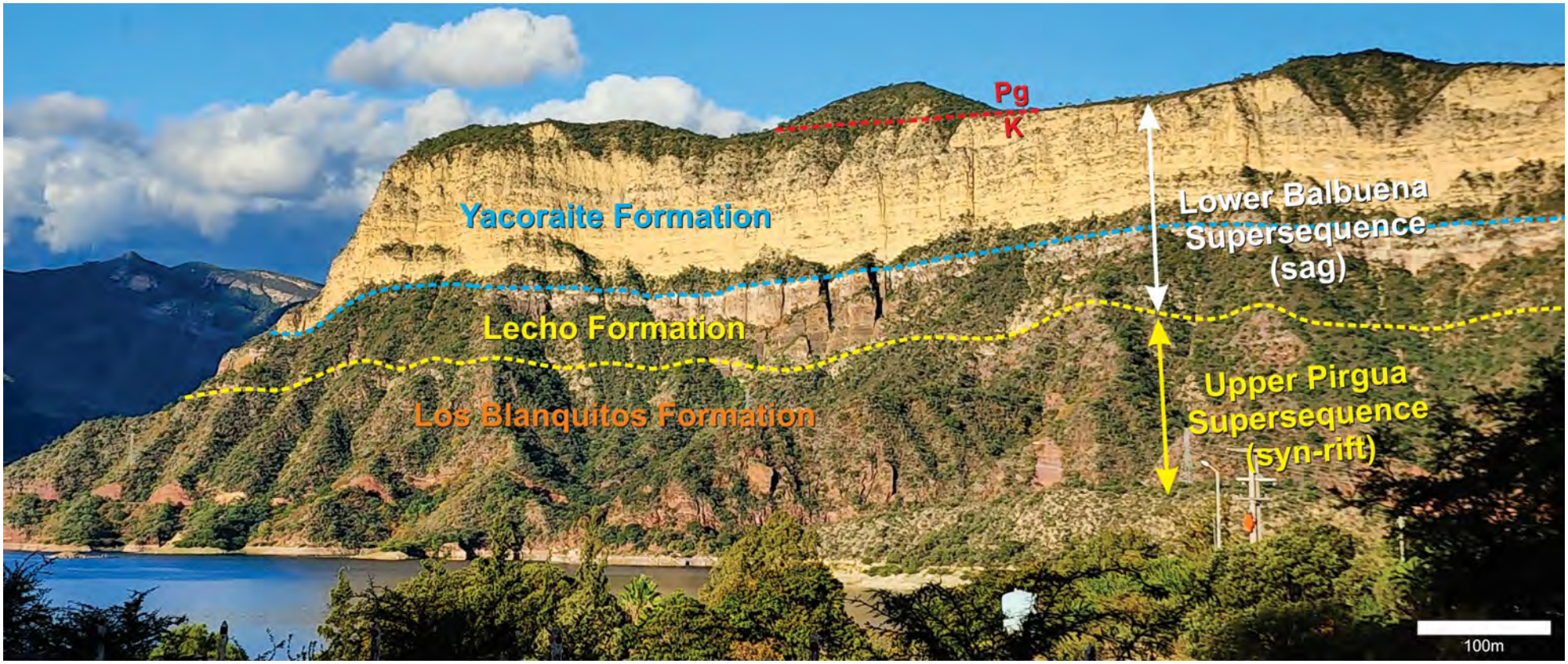


**Fig. 2.8.** Outcrop view of a fault block in the Metán–Alemanía Sub-basin, near the Cabra Corral reservoir (adapted from Bento Freire, 2012). The lithostratigraphic nomenclature is shown on the left, and the sequence stratigraphic nomenclature on the right. The red line on the top indicates the Cretaceous–Paleogene (K/Pg) boundary.

The descriptions that follow are primarily based on Hernández et al. (1999), while additional references are incorporated where necessary to provide further detail and context. The chronostratigraphic nomenclature is consistent with the Geologic Time Scale of Gradstein et al. (2012).

## Pirgua Supersequence (Barremian to Campanian)

The Pirgua Supersequence comprises predominantly continental clastic successions, ranging from proximal alluvial fan deposits to mudflat facies, with subordinate volcanic rocks occurring locally. Its basal boundary is defined by the regional unconformity that marks the onset of Salta Group deposition, whereas its top is delineated by an abrupt shift from alluvial fan systems to fluvial floodplain green shales. This unit displays the most restricted distribution within the Salta Group, being confined to sub-basins and small half-grabens controlled by rift-related faults (Gómez Omil et al., 1989). Internally, it is subdivided into two sequences, Pirgua I and Pirgua II.

The Pirgua I Sequence, corresponding to the La Yesera Formation, records the progressive distalization of facies induced by tectonic reactivation, with transitions from coarse-grained alluvial fan deposits to fine-grained mudflat facies. Rapid tectonically driven subsidence created substantial accommodation, but sediment supply was insufficient to fully infill the available space.

The Pirgua II Sequence, which includes the Las Curtiembres and Los Blanquitos formations, comprises successions grading from mudflats to distal alluvial fans, braided river systems, and terminal fans. Compared with the Pirgua I Sequence, it is more widely distributed, reflecting reduced structural compartmentalization and an increase in sediment transport efficiency.

### Balbuena Supersequence (Campanian to Danian)

The Balbuena Supersequence corresponds to the post-rift (sag) phase of the Salta Basin and is typified by laterally extensive, tabular successions that may locally acquire wedge-shaped geometries. Its strata are laterally continuous and display well-developed cyclicity, interpreted as the combined result of eustatic fluctuations and climatic forcing (Boll and Hernández, 1985; Hernández et al., 1999). Correlations can be traced for tens of kilometers, underscoring the regional persistence of these deposits (e.g. Bento Freire, 2012; Pedrinha et al., 2015).

This supersequence includes the clastic facies of the Lecho Formation and the lacustrine carbonates of the Yacoraite Formation. Marine influence has been reported in the Tres Cruces, Sey, and Lomas de Olmedo sub-basins, whereas in the Metán–Alemanía Sub-basin deposition remained essentially lacustrine (Bento Freire, 2012; Pedrinha, 2014; Roemers-Oliveira, 2014). Paleogeographic reconstructions at the K/Pg boundary (Fig. 2.9) indicate that northern sub-basins were directly connected to a marine corridor from the north, while the Metán–Alemanía Sub-basin was only sporadically influenced during episodes of maximum lake expansion, when spillovers enabled temporary connections (Bento Freire, 2012).

Its basal contact is defined by onlap relationships with the Pirgua Supersequence or older units, and its upper boundary is a regional unconformity related to the “Pre-Olmec tectonic phase.” The Yacoraite Formation is especially significant: fractured carbonates within this unit host the main hydrocarbon reservoirs of the basin and also contain uranium mineralization. Facies distribution across sub-basins is strongly controlled by structural highs and differential subsidence. In the Metán–Alemanía Sub-basin, these factors condition the siliciclastic–carbonate transition. Facies distribution across sub-basins is strongly controlled by structural highs. In the Metán–Alemanía Sub-basin, siliciclastic input derived predominantly from the

west, while the Guachipas High acted as a physical barrier, trapping coarse siliciclastic deposits in the Alemanía sector. Consequently, carbonate sedimentation became more prominent in the Metán depocenter, as illustrated in Fig. 2.6B.

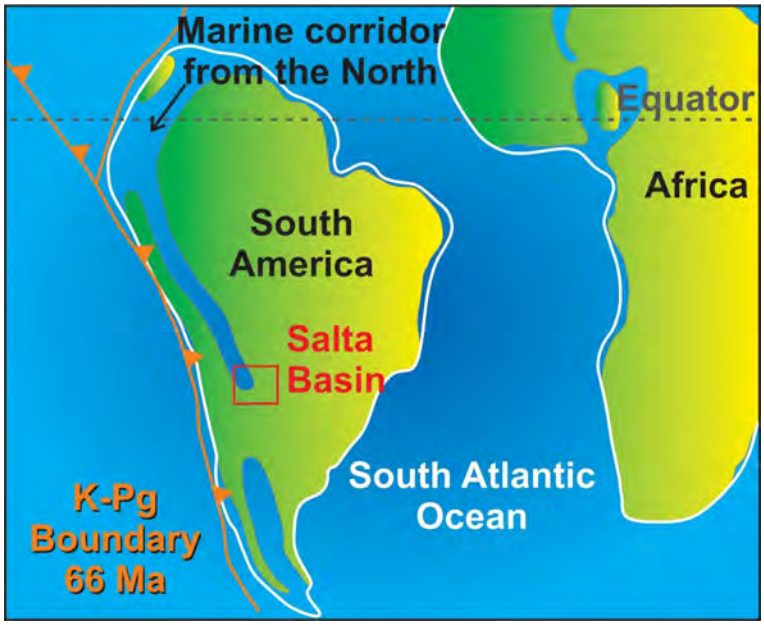


**Fig. 2.9.** Paleogeographic reconstruction at the K/Pg boundary. A northern marine corridor influenced the Salta Basin, while the southern Metán–Alemanía Sub-basin remained mostly lacustrine. Adapted from Scotese (2001) after Roemers-Oliveira (2014).

Internally, the Balbuena Supersequence is subdivided into four sequences (Balbuena I to IV). These were originally classified as third-order sequences (Boll, 1991; Hernández et al., 1999, 2008). A similar third-order subdivision was later proposed by Deschamps et al. (2020), who recognized four medium-duration sequences within the Yacoraite Formation in the Metán–Alemanía Sub-basin. More recently, Fragoso (2023), drawing on modern concepts and terminological refinements in sequence stratigraphy, reinterpreted the Balbuena Supersequence as a first-order cycle, with its internal subdivisions corresponding to second-order sequences. This reinterpretation stems from the recognition that the Balbuena records a complete basin-filling cycle developed under a consistent tectonic regime (sag phase).

Balbuena I Sequence, dominated by the Lecho Formation, records a transition from fluvial and eolian deposits to lacustrine carbonates and pelitic facies of the Yacoraite Formation. Its high-frequency cyclicity and correlation potential were highlighted by Boll and Hernández (1985).

Balbuena II Sequence, corresponding to the Amblayo Member of the Yacoraite Formation, comprises shallow lacustrine carbonates, clastic deposits, and paleosols indicative of alternating arid and humid phases. Progradational stacking patterns and oolitic grainstones document episodes of high-energy deposition. Facies architecture and depositional dynamics were described in detail by Pedrinha et al. (2015) and later reinterpreted within a cyclostratigraphic framework by Fragoso (2023).

Balbuena III Sequence, with its base associated with the Güemes Member, differs from the others due to the predominance of pelitic facies interbedded with fine sandstones and lacustrine carbonates. This interval, commonly referred to as the “Limoarcillosa,” has been extensively studied by Roemers-Oliveira (2014) and Roemers-Oliveira et al. (2015). These studies demonstrated that the upward transition from siliciclastic facies at the base to carbonate facies at the top reflects a shift from open- to closed-lake depositional conditions. Importantly, the

base of this sequence coincides with the K/Pg boundary, defined by $\delta^{13}C$ and $\delta^{18}O$ isotopic anomalies (Marquillas et al., 2003).

Balbuena IV Sequence, equivalent to the Alemanía Member, is the most laterally extensive unit, reflecting the peak of thermal subsidence. Deposits display tabular to wedge-shaped geometries and encompass widespread carbonate and siliciclastic successions. Detailed facies descriptions and depositional interpretations have been provided by Bento Freire (2012), Gomes (2013), Bunevich et al. (2017), and Gomes et al. (2020).

## Santa Bárbara Supersequence (Danian to Ypresian)

The Santa Bárbara Supersequence is composed of thick continental clastic successions bounded by regional unconformities (Hernández et al., 1999). Its external geometry evolves from wedge-shaped at the base to more tabular forms at the top. Deposits consist mainly of red beds, fluvial systems, and shallow lacustrine facies. The supersequence is subdivided into three sequences, from base to top, Santa Bárbara I to III.

The Santa Bárbara I Sequence is regarded by some authors as evidence of a second syn-rift phase (Bianucci et al., 1981; Gómez Omil et al., 1989; Gómez Omil and Boll, 1999). It is composed predominantly of clastic facies, including braided river systems, distal alluvial fans, and mudflats, which grade into shallow lacustrine deposits in central sectors. This sequence is absent in the Sey and Tres Cruces sub-basins, but is represented by the Olmedo Formation in the Lomas de Olmedo Sub-basin and the Tunal Formation in the Metán–Alemanía Sub-basin. In Lomas de Olmedo, it includes the Salino Member, which comprises evaporitic deposits reaching up to 900 m in thickness (Moreno, 1970).

The Santa Bárbara II Sequence is dominated by mudstones and marls, with a distinctive lacustrine interval at the top known as the "Faja Gris," which serves as an important stratigraphic marker across the basin. This sequence corresponds to the Mella Formation and marks the onset of the second post-rift phase, which continued until the deposition of the Lumbrera Supersequence.

The Santa Bárbara III Sequence, equivalent to the Maíz Gordo Formation, consists of green and gray mudstones interbedded with sandstones and conglomerates. These deposits reflect humid climatic conditions and the widespread expansion of lacustrine environments.

## Lumbrera Supersequence (Ypresian to Priabonian?)

The Lumbrera Supersequence, subdivided into Lumbrera I and Lumbrera II, corresponds to the Lumbrera Formation. It consists of continental deposits primarily linked to fluvial and lacustrine systems. Its base is marked by a regional unconformity, representing the last extensional response of the post-rift phase in the basin, whereas its top records the onset of compressional tectonics associated with foreland basin development (Hernández et al., 1999).

The Lumbrera I Sequence is characterized by fluvial systems that evolve into ephemeral channels and saline mudflats, indicative of semi-arid conditions. It culminates in a lacustrine expansion under more humid climates, producing carbonate-rich deposits interbedded with paleosols. Within this sequence, the "Faja Verde I" forms a key stratigraphic marker that supports regional correlations.

The Lumbrera II Sequence reflects the progressive influence of compressional tectonics, with deposition marked by lacustrine retraction and the development of red beds and fluvial systems. The "Faja Verde II," located at the base of this sequence, constitutes another important stratigraphic marker, allowing refined regional stratigraphic interpretations.

## 2.2. Methodological Framework: An Integrated Stratigraphic and Digital Approach

This thesis adopts a multimethodological approach, combining fieldwork data acquisition, laboratory analyses, and digital techniques to generate qualitative, interpretative, and quantitative geological data from outcrop analogs. The methods employed across the different case studies include detailed vertical stratigraphic logging, sample collection, spectral gamma-ray logging, RPAS-based image surveys, field and image-based hyperspectral data, petrographic thin sections, stable C–O isotope analysis, U/Pb dating of carbonates, scanning electron microscopy (SEM), X-ray fluorescence (XRF), High-Resolution Sequence Stratigraphy (HRSS), photogrammetry for the generation of Digital Outcrop Models (DOMs), Local Binary Patterns (LBP), Convolutional Neural Networks (CNN), Linear Discriminant Analysis (LDA), Multilayer Perceptron (MLP), k-means clustering (k-means), and statistical tools such as Principal Component Analysis (PCA) and Hierarchical Agglomerative Clusters (HAC). As this thesis follows an article-based structure, these methods are presented in detail within the corresponding chapters (Chapters 3–6). Among them, two stand out as the methodological backbone of this research and are therefore described in detail here: HRSS and photogrammetry-based DOMs.

HRSS provides the stratigraphic framework necessary to anchor the data in both time and space, allowing the identification of key surfaces, correlation distances, and vertical and lateral facies variations. This stratigraphic control is essential for interpreting architectural patterns and supporting predictive applications in reservoir characterization. Photogrammetry, in turn, enables the digitization of outcrops into high-resolution, georeferenced 3D models, allowing the extraction of a significantly larger volume of data compared to conventional fieldwork. The resulting DOMs serve as a digital platform for the application of advanced techniques, such as LBP, CNN, and hyperspectral data analysis. Together, HRSS and DOMs form the foundation for integrating traditional stratigraphic concepts with emerging digital techniques, providing both context and structure to the analytical workflow developed in this thesis.

### 2.2.1. High-Resolution Sequence Stratigraphy (HRSS)

High-Resolution Sequence Stratigraphy (HRSS) is a methodology for stratigraphic analysis designed to organize and interpret sedimentary successions by identifying depositional units and key bounding surfaces at a meter to decimeter scale. This approach integrates sedimentological and stratigraphic observations within a temporal and spatial framework, allowing for the reconstruction of depositional dynamics and the prediction of facies architecture in both vertical and lateral dimensions. Its application is particularly relevant in carbonate and continental systems, where high-frequency variations in base level and sediment supply can generate well-defined stratigraphic cycles (Vail et al., 1977; Catuneanu et al., 2009).

At its core, HRSS is based on the recognition that sedimentary deposits are structured by relative base-level fluctuations, which control the availability of accommodation space and, consequently, the patterns of sediment accumulation and preservation (Posamentier and Allen, 1999; Catuneanu, 2006). These base-level changes can be driven by a combination of allocyclic controls, such as tectonics, climate, and eustasy, and autocyclic processes, including internal dynamics like progradation–retrogradation cycles, delta lobe switching, or carbonate productivity fluctuations (Galloway, 1989; Einsele, 1992; Schlager, 2005). In this sense, HRSS aims to differentiate these signals and provide a genetically coherent organization of the stratigraphic record.

A foundational concept in HRSS, already anticipated by Barrell (1917), is that most of geological time is not recorded in continuous sedimentation but rather marked by gaps due to non-deposition or erosion. According to this author, the recurrent pattern of stratigraphic organization, including both the rock record and the gaps, is a product of base-level rise and fall occurring in multiple amplitudes and frequencies. In this sense, the preserved sedimentary record corresponds to a tiny fraction of the geological time, and its completeness is a function of the observation scale, with higher-resolution timescales typically revealing greater discontinuities (Sadler, 1999). This idea is graphically represented in the harmonic view proposed by Fragoso et al. (2021), adapted from Barrell (1917), which depicts sedimentary stacking as the product of multiple-frequency base-level oscillations, with preserved strata occupying only a small fraction of total time (Fig. 2.10). In this model, many intervals are expressed solely by surfaces (disconformities), not strata. The implication is that HRSS relies heavily on the recognition and correlation of these surfaces to reconstruct the depositional history of a basin.

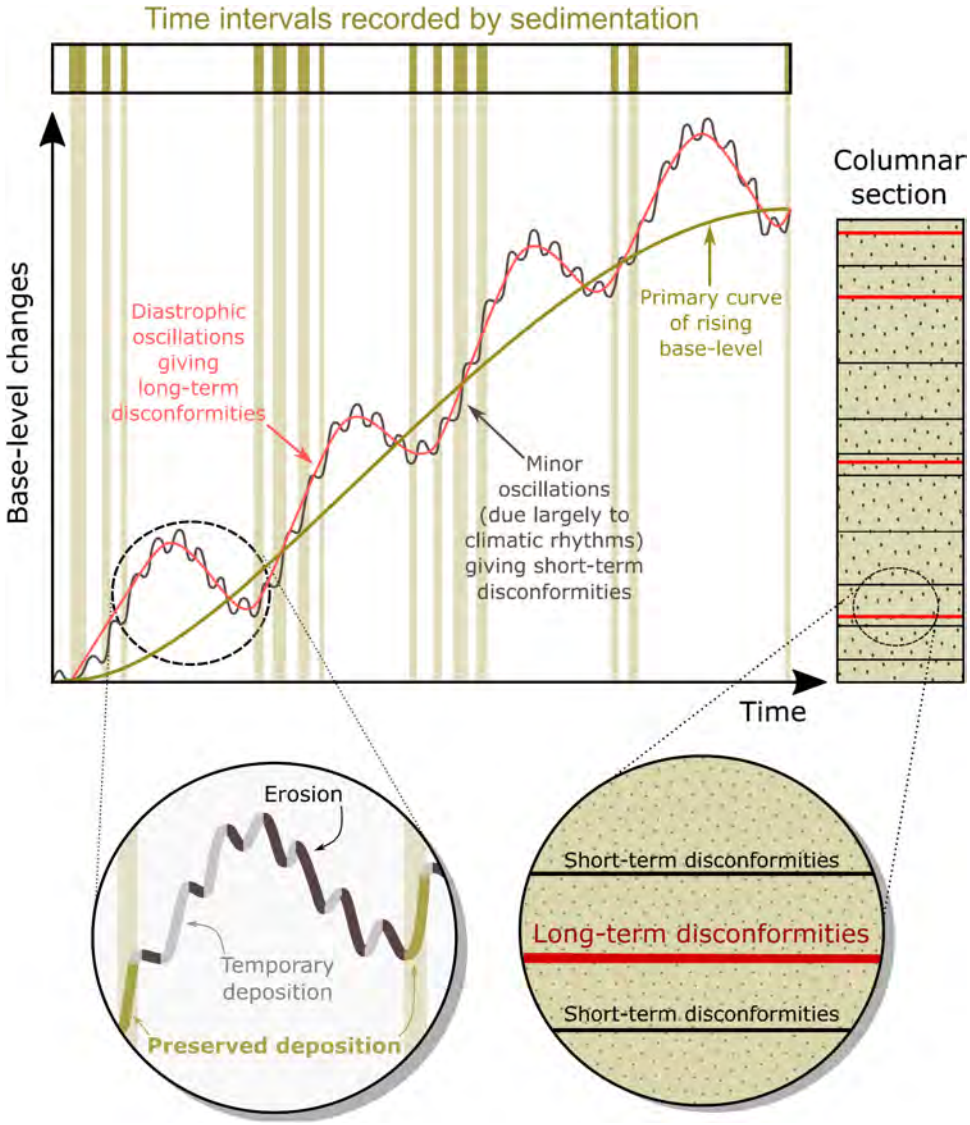


**Fig. 2.10.** Conceptual model representing sedimentary stacking as a product of multi-frequency base-level fluctuations. The preserved strata correspond to short periods of deposition, while most of the geological time is represented by gaps highlighted in the upper portion of the graph. These intervals are often materialized in the rock record as surfaces (disconformities), not strata. Source: Fragoso et al. (2021), modified from (Barrell, 1917).

The term “sequence” first appeared in the literature in the work of Sloss et al. (1949), who characterized it as a succession of strata in a cratonic setting, bounded at the top and base by

unconformities that can be traced and correlated over great distances. However, it was only in the 1970s that Sequence Stratigraphy became consolidated as a robust method for stratigraphic analysis of sedimentary units, following the advent of Seismic Stratigraphy and advances in petroleum exploration. In this context, the works of Mitchum (1977) and Vail et al. (1977), published in the book Seismic Stratigraphy – Applications to Hydrocarbon Exploration (Payton, 1977), are of particular relevance. Mitchum (1977) laid the foundations of modern Sequence Stratigraphy, defining a depositional sequence as a stratigraphic unit composed of a relatively conformable succession of genetically related strata, bounded at the top and base by unconformities or their correlative conformities. Vail et al. (1977) presented the concepts of seismic stratigraphy and proposed a global eustatic cycle chart. Subsequently, several authors (e.g., Van Wagoner et al., 1988; Posamentier et al., 1988; Galloway, 1989; Embry and Johannessen, 1992) adopted Sequence Stratigraphy as a working method to explain their observations. However, at that time there was no standardization of concepts and terminology, which meant that each study applied it according to local observations and needs.

To understand how sequence stratigraphy evolved as a discipline and how its definitions have changed over time, a conceptual synthesis diagram based on (Catuneanu, 2006) is presented in Fig. 2.11. This figure shows the historical progression from the initial definition by Sloss of large-scale sequences to more recent interpretations that incorporate seismic, genetic, and transgressive-regressive models (e.g., Sloss, 1963; Mitchum, 1977; Galloway, 1989; Hunt and Tucker, 1992; Embry, 1993). The diversity of approaches illustrated underscores the complexity of bounding surface identification and the differing roles of base-level changes in defining stratigraphic packages.

According to the standardized definition proposed by Catuneanu et al. (2009, 2011), a sequence corresponds to “a succession of strata deposited during a full cycle of change in accommodation or sediment supply,” regardless of time or spatial scale, or the controlling mechanisms. This research adopts the concepts presented in these works, which allow: (a) defining a depositional sequence as being bounded by any two stratigraphic surfaces of the same genesis, thus enclosing a complete sedimentary cycle; and (b) applying consistent nomenclature across all frequencies, regardless of order.

In practical terms, HRSS organizes the sedimentary record into sequences—genetically related strata bounded by key stratigraphic surfaces. These sequences are commonly structured into multiple hierarchical levels (Catuneanu et al., 2009). Higher-order sequences reflect long-term tectonic or eustatic trends, while lower-order sequences, such as meter-scale sequences, are often the result of high-frequency climatic or orbitally forced variations (Strasser et al., 1999). In this context, the term "sequence" refers to the mappable package observed in the outcrop, while "cycle" denotes the external or internal process responsible for its formation. This distinction is essential in studies of stratigraphic architecture and in predictive applications such as reservoir modeling.

In modern Sequence Stratigraphy concepts, sequences can be generated at different frequencies, in line with the definition by Catuneanu and Zecchin (2013), in which they are described as cycles of changes in stratal stacking patterns, categorized into system tracts and delineated by sequence stratigraphic surfaces. In HRSS applications, medium- and high-frequency sequences are often the most relevant. Petroleum field studies have shown that medium-frequency sequences commonly correlate with production data (e.g., Fragoso et al., 2023; Pedrinha and Artagão, 2024). High-frequency sequences may become more significant in mature fields, where high-resolution studies can identify bypassed oil volumes and, through HRSS-based reinterpretation, lead to increased production, as demonstrated for the Fazenda Santa Luzia onshore field (Magalhães et al., 2020).

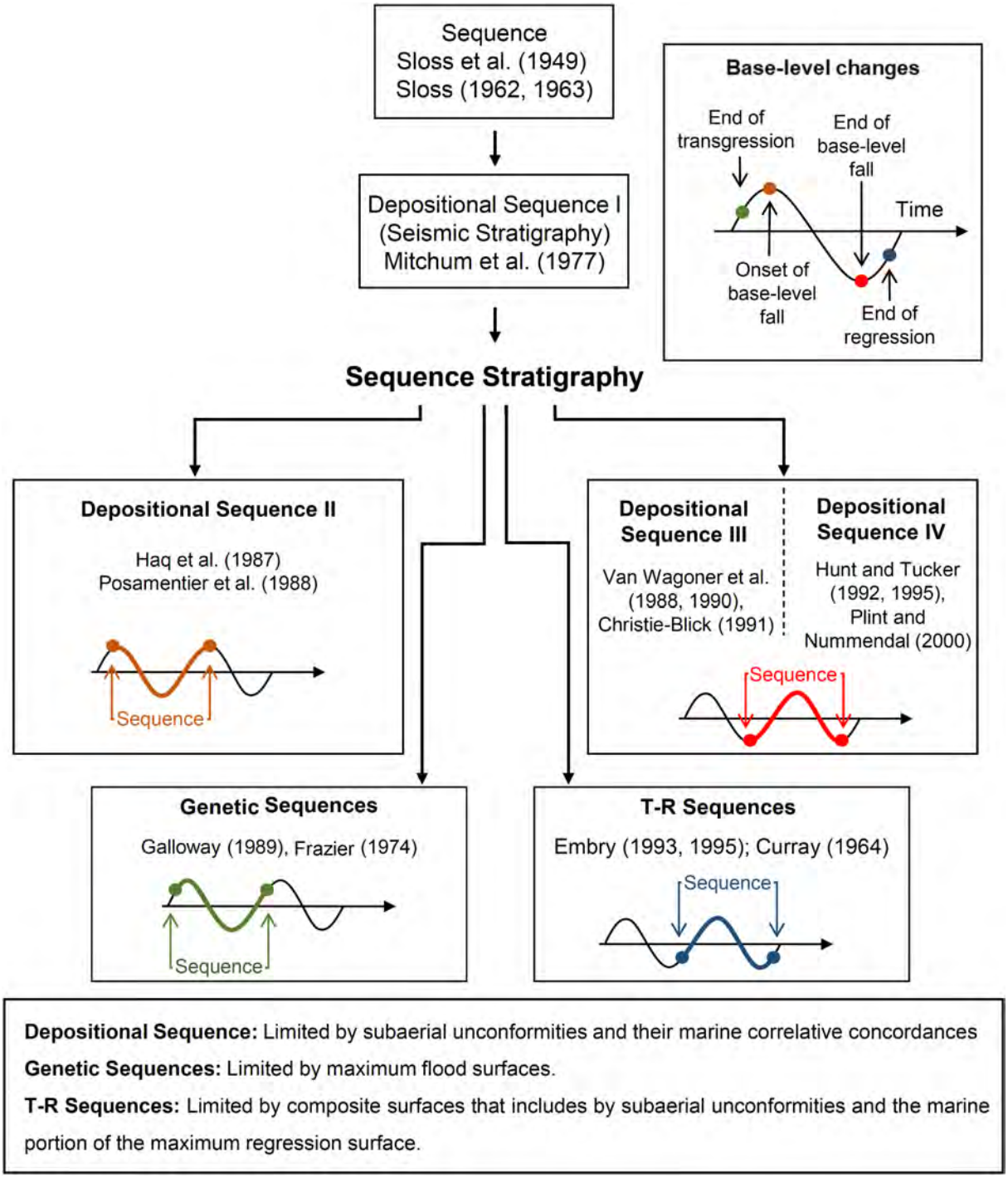


**Fig. 2.11.** Conceptual diagram illustrating the evolution of sequence stratigraphy models, from large-scale unconformity-bounded sequences to more refined stratigraphic units controlled by base-level fluctuations. Source: Fragoso et al. (2021), modified from Catuneanu (2006).

To support the consistent application of HRSS, a set of observable criteria has been established to guide the identification and hierarchical organization of stratigraphic sequences. These include: (1) the recognition of sequence anatomies as vertical stacking patterns, as defined by Zecchin (2007) and Catuneanu and Zecchin (2013); (2) the recurrence of stacking patterns in vertical successions; (3) the analysis of trends in higher-frequency sequences to define lower-frequency packages; and (4) the mappability of stacking patterns and their bounding surfaces across laterally continuous sections, whether in outcrops, seismic profiles, or subsurface datasets. The last three criteria follow the framework proposed by Silveira (2020), Magalhães et al. (2020), and Fragoso et al. (2021, 2022).

These criteria are not rigid rules, but context-sensitive guidelines that must be adapted based on the resolution of the available data, the spatial scale of observation, and the dominant control mechanisms of the depositional system. In general, higher-frequency sequences exhibit more detailed internal architecture but reduced lateral continuity, whereas lower-frequency sequences tend to be more mappable and regionally extensive. Fig. 2.12 summarizes these observable criteria and illustrates how stratigraphic organization evolves from facies trends to stacking patterns and bounding surfaces.

One of the strengths of HRSS lies precisely in its predictive capability. By identifying vertical and lateral facies trends and understanding their cyclicity, HRSS enables the inference of reservoir properties in areas with limited data. For instance, a progradational stacking pattern may indicate coarsening-upward units with good reservoir potential, whereas retrogradational trends might point to finer-grained facies with sealing capacity. Additionally, the recognition of sequence boundaries and condensed sections supports the subdivision of the stratigraphic record into genetically coherent compartments, which is essential for understanding reservoir heterogeneity and compartmentalization (Magalhães et al., 2020).

In the context of this thesis, HRSS is systematically applied across all case studies. It serves both as a structural framework for integrating digital data and as an independent analytical tool for interpreting facies distributions, identifying features such as sealing or high-permeability layers, and evaluating the correlation potential of stratigraphic surfaces across different hierarchical levels. The two main outcrop analogs analyzed in this work demonstrate the complementary roles of HRSS in different geological contexts. In both cases, the identification of vertical stacking pattern sequences is supported by consistent stratigraphic criteria, including the use of two key bounding surfaces: the Maximum Retraction Surface (MRS) and the Maximum Expansion Surface (MES). These surfaces correspond, respectively, to the surfaces of maximum regression and maximum flooding in marine settings, adapted here to lacustrine environments following Fragoso et al. (2023). The MRS, frequently associated with subaerial exposure, is adopted in this thesis as the sequence boundary, ensuring consistency in the hierarchical organization of the stratigraphic framework.

In the Barre du Cengle study, HRSS is used as the primary methodological axis. The presence of well-exposed, palustrine-dominated carbonates allowed for its application with high spatial precision. Photogrammetry-derived Digital Outcrop Models (DOMs) enabled the detailed tracing and correlation of stratigraphic surfaces that would have been difficult to follow using traditional field methods alone. The ability to identify such sequences, even in complex lacustrine settings, was instrumental in defining depositional models and interpreting the temporal evolution of the system. The correlation of medium-frequency sequences, a key element in understanding stratigraphic architecture, would not have been feasible without the support of DOMs, confirming their synergistic role in enhancing HRSS applications in analog-based studies.

In the Salta Basin case studies, HRSS is systematically applied in combination with digital techniques such as LBP, CNN-based image classification, and hyperspectral analysis. It provides the essential stratigraphic framework within which these digital classifications are interpreted and integrated. By enabling the identification of key bounding surfaces, HRSS supports the assessment of lateral facies variability and depositional architecture. HRSS is particularly critical for interpreting the distribution of heterogeneities in the Balbuena III Sequence, supporting the identification of reservoir-prone intervals and sealing units, and aiding in the understanding of depositional geometries.

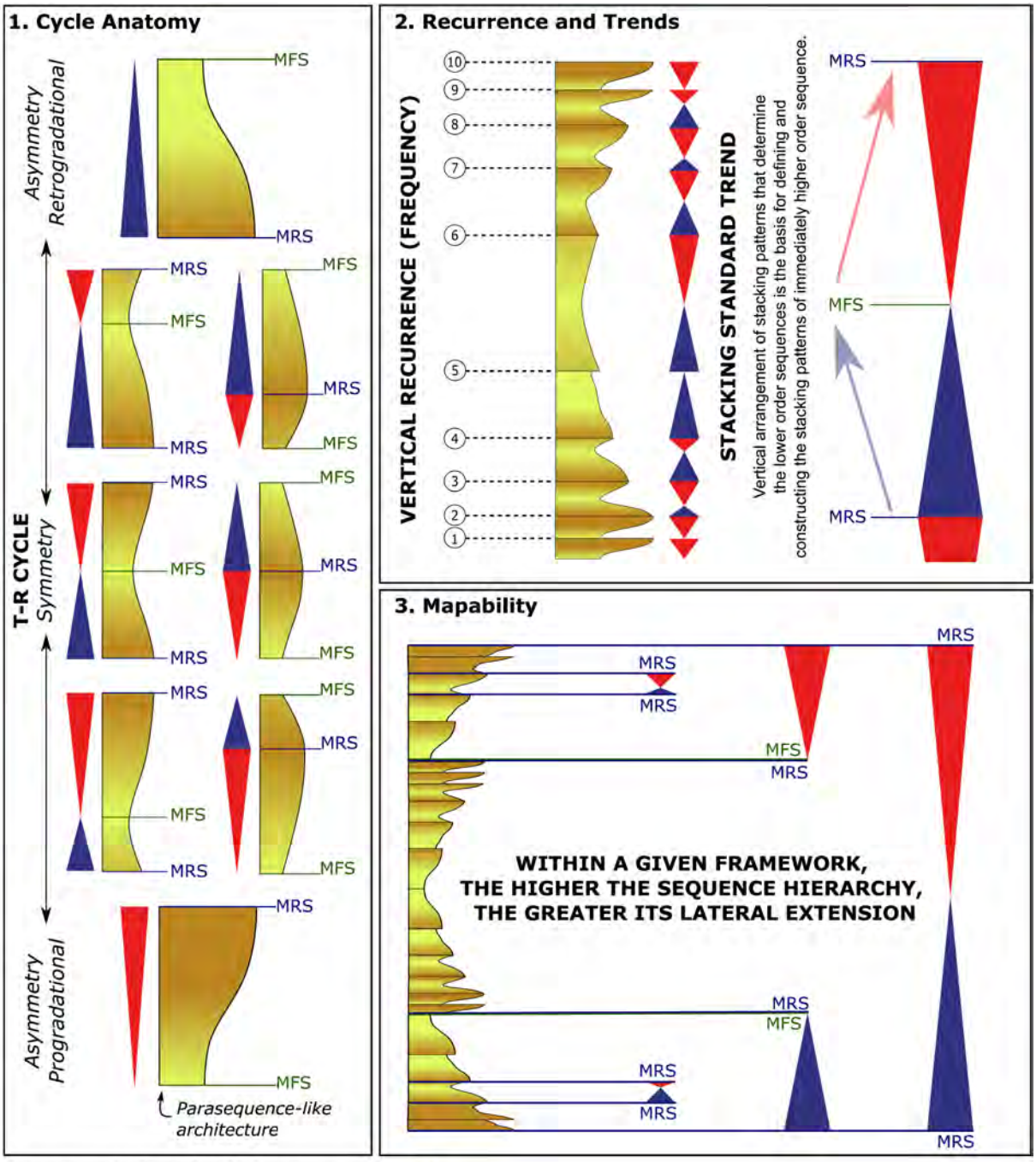


MFS: maximum flooding surface; MRS: maximum regressive surface.

**Fig. 2.12.** Criteria for applying High-Resolution Sequence Stratigraphy (HRSS). Source: Fragoso et al. (2021), integrating stacking pattern anatomies (Zecchin, 2007; Catuneanu and Zecchin, 2013) with recurrence, trend, and mappability criteria used as hierarchical organization guidelines (Silveira, 2020; Magalhães et al., 2020).

It is worth emphasizing that HRSS is not limited to static facies interpretation but also serves as a crucial tool in dynamic reservoir characterization. When integrated with petrophysical and geochemical datasets, HRSS helps clarify the stratigraphic controls on porosity and permeability distribution. This is particularly relevant in carbonate systems, where diagenetic overprinting can obscure original depositional features (Lucia, 2007; Ahr, 2008; Kargarpour, 2020). In such cases, the reconstruction of stacking patterns and accommodation trends is key to assessing whether reservoir quality is primarily controlled by primary or secondary porosity (Magalhães et al., 2020).

The systematic application of HRSS throughout this thesis highlights its central role in bridging traditional stratigraphic analysis with advanced digital methods. By establishing a

stratigraphic framework that is both temporally and spatially coherent, HRSS not only contextualizes digital data but also enhances their geological relevance. This integrative approach reinforces the interpretation of heterogeneities and supplies robust input for the development of geologically consistent reservoir models. In this sense, HRSS stands not merely as a methodological foundation but as a critical interface between observation, interpretation, and modeling.

### 2.2.2. Photogrammetry-based Digital Outcrop Models (DOMs)

Photogrammetry is a remote sensing technique that reconstructs three-dimensional (3D) geometries from overlapping two-dimensional (2D) images, allowing the generation of Digital Outcrop Models (DOMs), also referred to as Virtual Outcrop Models (VOMs), which accurately represent geological surfaces (Westoby et al., 2012; Bistacchi et al., 2022; Tavani et al., 2024). In geosciences, photogrammetry-derived DOMs have become fundamental tools for outcrop-based investigations, with numerous applications in structural geology and karst systems (e.g., Corradetti et al., 2018; Larssen et al., 2020; Villarreal et al., 2020; Janocha et al., 2021; Panara et al., 2023; Pereira et al., 2024), as well as in stratigraphy and sedimentary geology (e.g., Javernick et al., 2014; Bilmes et al., 2019; Li et al., 2019; Rohmana et al., 2019; Ramdani et al., 2022; Roisenberg et al., 2022), and other related applications.

The photogrammetric workflow generally begins with image acquisition, which requires careful planning to ensure adequate coverage and optimal overlap (typically greater than 65%) from multiple perspectives. Since photogrammetry is based on the principle of parallax—the apparent displacement of objects at different distances when viewed from at least two different viewpoints—images must be captured from varied angles to enable precise 3D reconstruction (James and Robson, 2012; Westoby et al., 2012; Bistacchi et al., 2022; Tavani et al., 2024).

While DOMs can be generated from terrestrial cameras, the widespread adoption of Remotely Piloted Aircraft System (RPAS) has significantly enhanced and popularized photogrammetric data acquisition in the field. Since the 2010s, drone-based photogrammetry has become increasingly prevalent, favored for its operational simplicity, portability, and relatively low cost (Bemis et al., 2014; Eltner et al., 2016; Bistacchi et al., 2022). As a result, this technique has gained prominence over LiDAR (Light Detection and Ranging)-based methods, even though the term "DOM" was originally introduced to describe LiDAR-derived datasets (Bellian et al., 2005).

After image acquisition, 3D reconstruction is performed through Structure-from-Motion (SfM) algorithms (Lowe, 2004; Snavely et al., 2006; Westoby et al., 2012), which simultaneously estimate camera positions and generate sparse point clouds based on matched features across images. These sparse clouds are then densified using Multi-View Stereo (MVS) algorithms (Furukawa and Hernández, 2015). In some cases, pre-processing steps may be applied to correct exposure-related issues and ensure consistent lighting across the image set, thereby improving the quality of feature matching during reconstruction (Bistacchi et al., 2022). The result is a point-cloud DOM, which represents the outcrop surface as a dense set of points with X, Y, Z coordinates and additional attributes such as RGB values. These RGB properties are derived by projecting the color information from the original photographs onto the corresponding points in the cloud. This native colorization is inherent to photogrammetric workflows (Bistacchi et al., 2022). The dense point cloud can be further interpolated into a triangular mesh using surface reconstruction algorithms such as Poisson surface reconstruction (Kazhdan and Hoppe, 2013). This mesh can then be textured with the original images (Hanusch, 2008), resulting in a textured-surface DOM that preserves the photorealistic appearance of the

outcrop. Fig. 2.13 summarizes the photogrammetric workflow using RPAS, from field data acquisition to the generation of high-resolution DOMs.

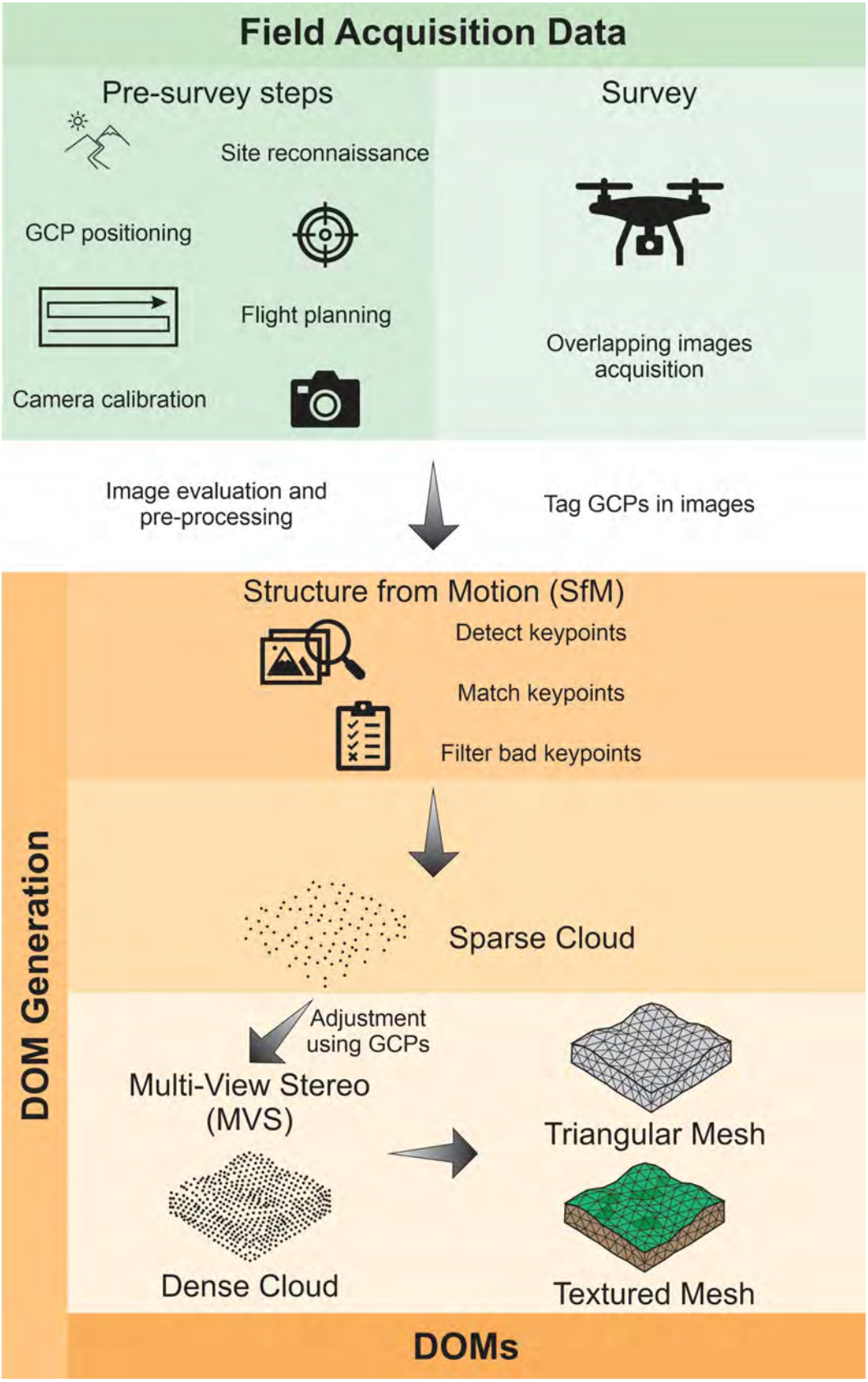


**Fig. 2.13.** Illustrative workflow for the generation of Digital Outcrop Models (DOMs) from photogrammetric data acquired using Remotely Piloted Aircraft Systems (RPAS). The flowchart outlines the key stages, from field planning and image acquisition to point cloud densification and mesh generation. Adapted from Viana et al. (2018).

In general, point-cloud DOMs offer higher geometric accuracy and are ideal for analyzing discontinuities such as fractures, joints, foliations, or bedding planes. In contrast, textured mesh models represent smoothed versions of the original point cloud, often resulting in slightly blurred edges at transitions between facets. These models are preferable when visual image information is more critical than precise 3D geometry and are commonly used for mapping linear features (e.g., polylines) or areal features (e.g., polygons) (Bistacchi et al., 2022).

The entire SfM-MVS workflow is available in various software packages, including free tools (e.g., Meshroom) and commercial solutions. Among the latter, Metashape is widely used due to its intuitive and user-friendly interface.

Regarding model resolution, Bistacchi et al. (2022) emphasized that an appropriate ground resolution (e.g., pixels per meter) is essential when planning photogrammetric surveys, as it determines the level of detail that can be extracted from the resulting DOM. The resolution must be sufficient to capture the smallest features of interest, while avoiding unnecessarily long acquisition and processing times.

Typically, camera parameters such as pixel size and focal length remain fixed during acquisition, making the camera-to-target distance the main factor controlling ground resolution. Assuming a simple pinhole camera model (Tsai, 1987), ground resolution (GR) can be calculated using the following formula:

$$GR = p\frac{d-f}{f}$$

Where $d$ is the distance from the camera to the outcrop, $f$ is the focal length, $p$ is the sensor pixel size (sensor width divided by the number of pixels along the width).

In this equation, units are considered homogeneous. Therefore, if all linear units are expressed in meters, GR will be expressed in meters per pixel.

Then, knowing the image dimensions in pixels ($wp$ for width and $hp$ for height), it is possible to calculate the corresponding real-world dimensions ($W$ and $H$) of the area covered by the image using the following equations:

$$W = \frac{wp}{GR}$$

$$H = \frac{hp}{GR}$$

To improve positional accuracy, Ground Control Points (GCPs) measured via differential Global Navigation Satellite System (GNSS) are often integrated into the model optimization step (e.g., Turner et al., 2012; Duelis Viana et al., 2016; Riquelme et al., 2017). These help reduce geometric distortions and ensure spatial consistency across datasets (James and Robson, 2012). However, in studies where local relative accuracy is more important than absolute geolocation, such as detailed facies analysis, reliable stratigraphic interpretations can still be achieved without GCPs, as long as acquisition geometry is robust and internal consistency is maintained (Eltner et al., 2016).

Once DOMs are generated, they can be interpreted using a wide range of software solutions that support either dense point clouds or textured meshes. Examples include CloudCompare, Lime (Buckley et al., 2019), Skua/Gocad, and Move. Additionally, an increasing number of custom applications are being developed or enhanced in Python, enabling flexible workflows for data processing, feature extraction, and geological interpretation (e.g., Borghini et al., 2024; Namongo Soro et al., 2024; Guadagnin et al., 2025). Moreover, DOMs are increasingly being

adopted in virtual reality environments, further expanding their utility in geological analysis and education (e.g., Seers et al., 2022; Pugsley et al., 2022).

In this thesis, photogrammetry-based Digital Outcrop Models (DOMs) were employed in both study areas: the Barre du Cengle in southern France and the Salta Basin in northwestern Argentina. In each case, the models were processed using the commercial software Metashape (Agisoft, 2023), which enabled efficient image alignment, 3D reconstruction, and texturing.

At the Barre du Cengle, data acquisition was performed using a DJI Phantom 4 RTK, a RPAS equipped with a 20-megapixel 1-inch CMOS sensor and a mechanical shutter, allowing high-quality image capture during flight (Fig. 2.14). The onboard RTK module, combined with a GNSS receiver, provided centimeter-level positioning accuracy. Additionally, twenty GCPs were distributed across the site and measured using Trimble R8 RTK GNSS receivers to enhance model accuracy. The GCPs were marked on the outcrop surface with cross-shaped symbols using water-washable, environmentally friendly spray paint. All positioning was referenced to the French RGF93 geodetic system. The survey resulted in over 10,000 images captured with varied tilt angles (0°–45°) and sufficient overlap (≥80% forward, ≥65% lateral). Four models were generated: one lower-resolution model (2.4 cm/pixel) encompassing the entire cliff, and three high-resolution models (ranging from 6.1 to 7.8 mm/pixel), each focused on areas where detailed sedimentological logs were measured.

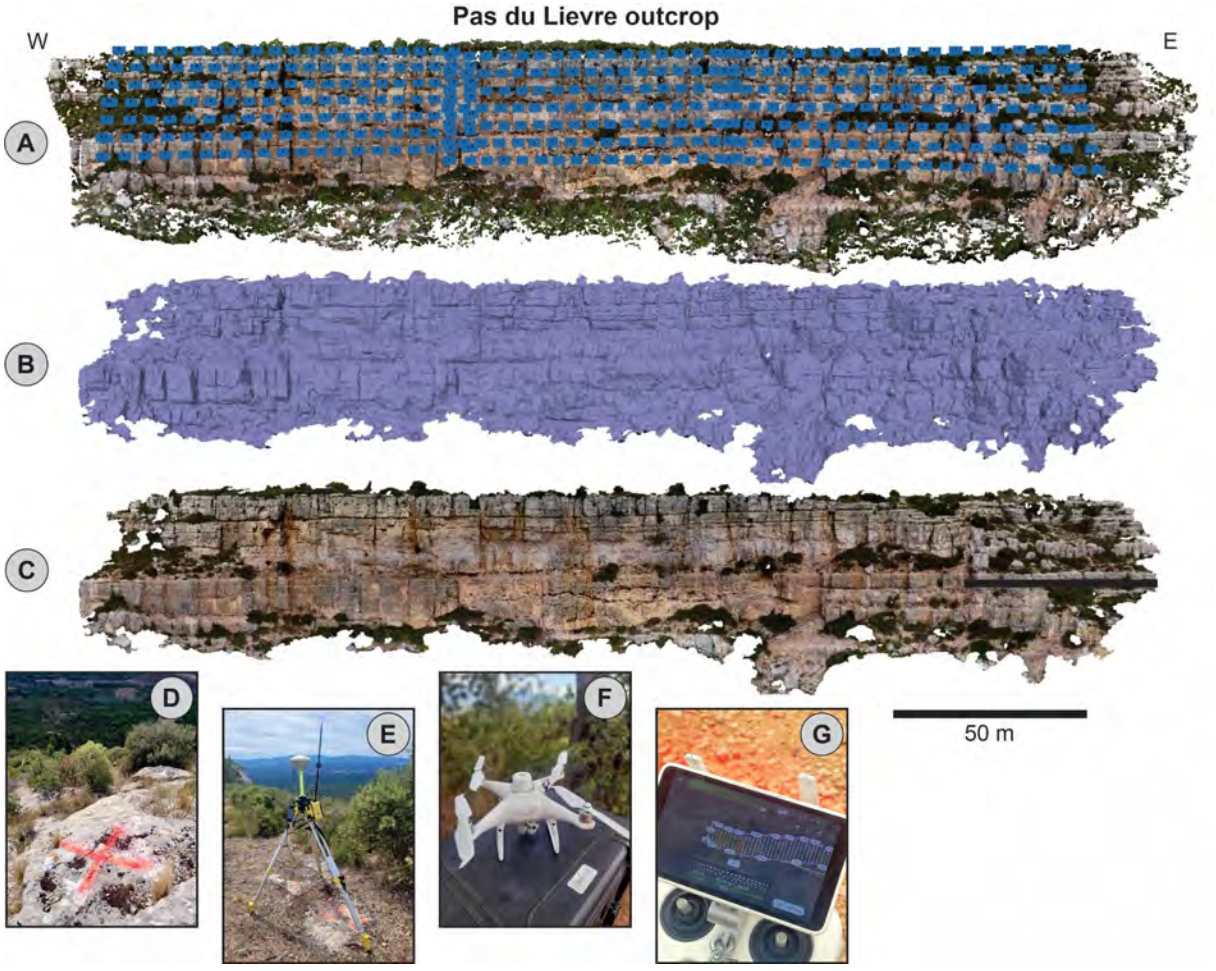


**Fig. 2.14**. Photogrammetric survey at the Pas du Lièvre outcrop, La Barre du Cengle. (A) Dense point cloud with photograph positions and orientations (blue rectangles). (B) Triangulated mesh. (C) Textured DOM. (D) GCP marked on the outcrop surface. (E) GNSS RTK base station. (F) DJI Phantom 4 RTK RPAS. (G) Flight plan displayed on the control screen.

In the Salta Basin (Fig. 2.15), DOMs were produced for selected outcrops using a DJI Matrice 300 RTK RPAS mounted with a DJI Zenmuse P1 full-frame camera and a 35 mm lens. The flights were supported by a DJI D-RTK 2 base station, enabling real-time RTK correction with high spatial accuracy. Unlike the approach in France, no GCPs were used, as the RTK system alone ensured sufficient geolocation precision for the intended analyses. Thanks to favorable terrain conditions, the RPAS was able to operate at close range, at least 8 meters from the outcrop, with the camera facing the outcrop surface. Images were acquired while the RPAS hovered steadily, ensuring evenly spaced and sharply focused photographs. A total of 947 images were collected across two outcrops (Assado and Vapumas), which are part of this study, achieving a ground resolution of approximately 2 mm per pixel. This extremely high-resolution dataset was essential for the detailed facies characterization and stratigraphic interpretation conducted in this work. All positioning was referenced to the WGS 84 geodetic system (EPSG: 32720).

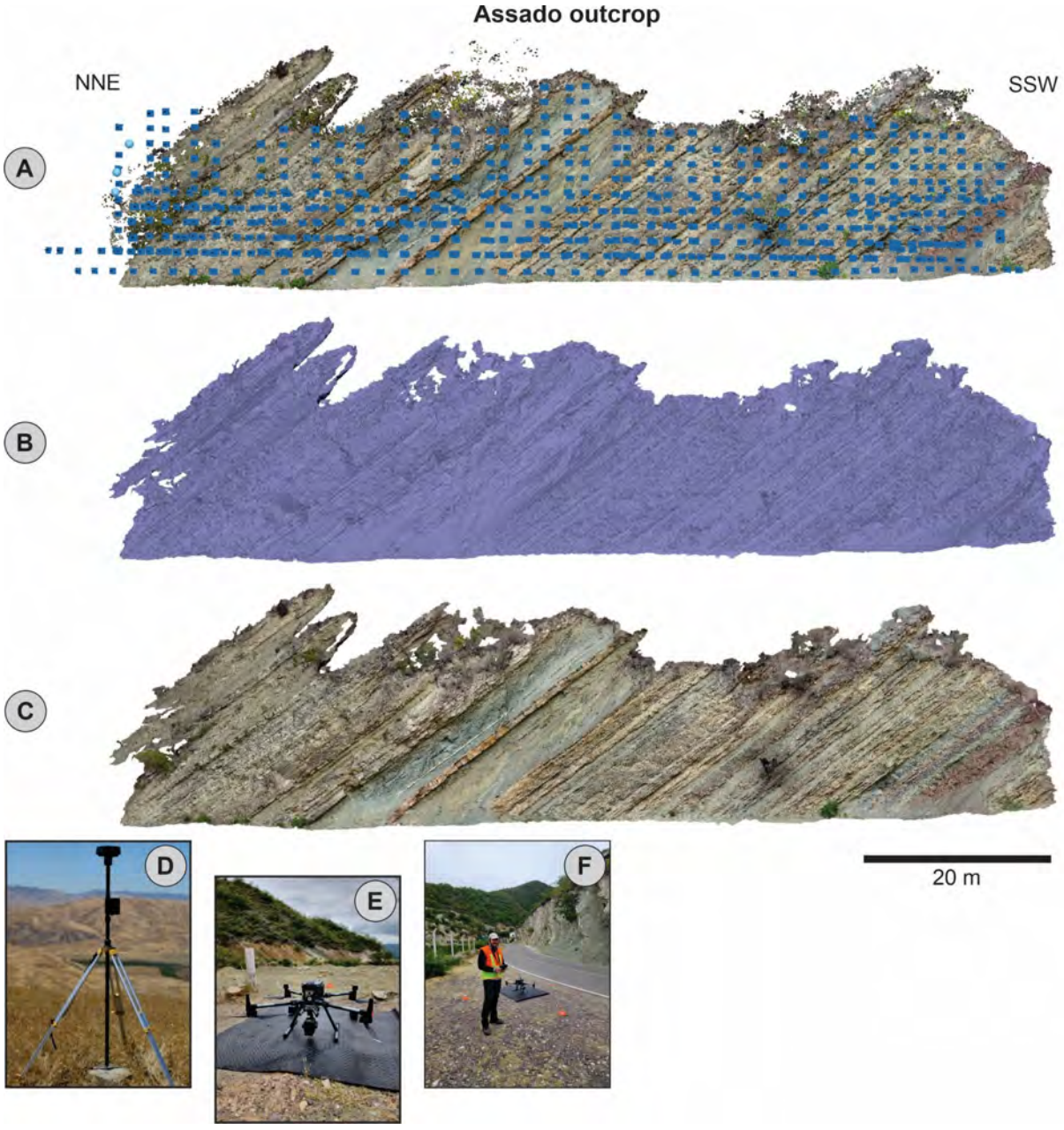


**Fig. 2.15.** Photogrammetric survey at the Assado outcrop in the Salta Basin. (A) Dense point cloud with photograph positions and orientations (blue rectangles). (B) Triangulated mesh. (C) Textured DOM. (D) GNSS RTK base station. (E) DJI Matrice 300 RTK RPAS. (F) Field acquisition activity.

## References


Agisoft, 2023. Agisoft Metashape Professional v2.0.1 (Version 2.0.1) [software]. https://www.agisoft.com

Ahr, W.M., 2008. Geology of Carbonate Reservoirs: The Identification, Description, and Characterization of Hydrocarbon Reservoirs in Carbonate Rocks. Wiley. https://doi.org/10.1002/9780470370650

Angst, D., Amiot, R., Buffetaut, E., Fourel, F., Martineau, F., Lazzerini, N., Lécuyer, C., 2015. Diet and climatic context of giant birds inferred from δ13Cc and δ18Oc values of Late Palaeocene and Early Eocene eggshells from southern France. Palaeogeography, Palaeoclimatology, Palaeoecology 435, 210–221. https://doi.org/10.1016/j.palaeo.2015.06.011

Babinot, J.-F., Durand, J.-P., 1980. Les étages continentaux du Crétacé supérieur et du Paléocène en Provence. Mémoire du Bureau de Recherches Géologiques et Minières 109, 171–192.

Barrell, J., 1917. Rhythms and the measurements of geologic time. Geological Society of America Bulletin 28, 745–904. https://doi.org/10.1130/GSAB-28-745

Bellian, J.A., Kerans, C., Jennette, D.C., 2005. Digital outcrop models: Applications of terrestrial scanning lidar technology in stratigraphic modeling. Journal of Sedimentary Research 75, 166–176. https://doi.org/10.2110/jsr.2005.013

Bemis, S.P., Micklethwaite, S., Turner, D., James, M.R., Akciz, S., T. Thiele, S., Bangash, H.A., 2014. Ground-based and UAV-Based photogrammetry: A multi-scale, high-resolution mapping tool for structural geology and paleoseismology. Journal of Structural Geology. https://doi.org/10.1016/j.jsg.2014.10.007

Bento Freire, E., 2012. Caracterização Estratigráfica em Alta Resolução das Sequências Calcárias de Origem Microbiana do Intervalo Paleocênico da Formação Yacoraite (Sequência Balbuena IV) Na Região de Salta-Argentina (MSc thesis). Universidade Federal do Rio de Janeiro, Rio de Janeiro.

Bianucci, H., Acevedo, O., Cerdán, J., 1981. Evolución tectono-sedimentaria del Grupo Salta en la subcuenca de Lomas de Olmedo (Provincias de Salta y Formosa), in: VIII Congreso Geológico Argentino. Servicio Geológico Nacional, San Luis, pp. 159–172.

Bianucci, H., Homovc, J.F., 1982. Tectonogenesis de un sector de la Cuenca del Subgrupo Pirgua, noroeste argentino, in: Congreso Latinoamericano de Geologia. Servicio Geologico Nacional, Buenos Aires, pp. 539–546.

Bilmes, A., D'Elia, L., Lopez, L., Richiano, S., Varela, A., Alvarez, M. del P., Bucher, J., Eymard, I., Muravchik, M., Franzese, J., Ariztegui, D., 2019. Digital outcrop modelling using "structure-from- motion" photogrammetry: Acquisition strategies, validation and interpretations to different sedimentary environments. Journal of South American Earth Sciences 96, 102325. https://doi.org/10.1016/j.jsames.2019.102325

Bistacchi, A., Mittempergher, S., Martinelli, M., 2022. Digital Outcrop Model Reconstruction and Interpretation, in: Bistacchi, A., Massironi, M., Viseur, S. (Eds.), 3D Digital Geological Models: From Terrestrial Outcrops to Planetary Surfaces. Wiley, pp. 11–32. https://doi.org/https://doi.org/10.1002/9781119313922.ch2

Boll, A., 1991. Identificación y correlación de secuencias somerizantes del Miembro Las Avispas (Formación Yacoraite). Noroeste Argentino., in: X Congreso Geológico Argentino. Asociación Geológica Argentina, San Miguel de Tucumán, pp. 153–156.

Boll, A., Hernández, R.M., 1985. Área Tres Cruces. Provincia de Jujuy. Análisis estratigráfico-estructural. Evaluación como objetivo exploratorio.

Borghini, L., Striglio, G., Bacchiani, G., La Bruna, V., Balsamo, F., Bonini, L., Bezerra, F.H.R., 2024. Fracture analyser: a Python toolbox for the 2D analysis of fracture patterns. Italian Journal of Geosciences 143, 1–15. https://doi.org/10.3301/IJG.2024.16

Brackebusch, L., 1891. Mapa geológico del interior de la República Argentina. 1 mapa, a color. Escala 1:1 000 000.

Buckley, S.J., Ringdal, K., Naumann, N., Dolva, B., Kurz, T.H., Howell, J.A., Dewez, T.J.B., 2019. LIME: Software for 3-D visualization, interpretation, and communication of virtual geoscience models. Geosphere 15, 222–235. https://doi.org/10.1130/GES02002.1

Buffetaut, E., Angst, D., 2014. Stratigraphic distribution of large flightless birds in the Palaeogene of Europe and its palaeobiological and palaeogeographical implications. Earth-Science Reviews. https://doi.org/10.1016/j.earscirev.2014.07.001

Bunevich, R.B., 2016. Caracterização e interpretação bioarquitetural de microbialitos lacustres da sequência Balbuena IV (Daniano), bacia de Salta-Argentina (MSc thesis). Universidade Federal do Rio de Janeiro, Rio de Janeiro.

Bunevich, R.B., Borghi, L., Gabaglia, G.P.R., Terra, G.J.S., Bento Freire, E., Lykawka, R., Fragoso, D.G.C., 2017. Microbialitos da Sequência Balbuena IV (Daniano), Bacia de Salta, Argentina: caracterização de intrabioarquiteturas e de microciclos. Pesquisas em Geociências 44, 177–202.

Catuneanu, O., 2006. Principles of Sequence Stratigraphy. Elsevier.

Catuneanu, O., Abreu, V., Bhattacharya, J.P., Blum, M.D., Dalrymple, R.W., Eriksson, P.G., Fielding, C.R., Fisher, W.L., Galloway, W.E., Gibling, M.R., Giles, K.A., Holbrook, J.M., Jordan, R., Kendall, C.G.S.C., Macurda, B., Martinsen, O.J., Miall, A.D., Neal, J.E., Nummedal, D., Pomar, L., Posamentier, H.W., Pratt, B.R., Sarg, J.F., Shanley, K.W., Steel, R.J., Strasser, A., Tucker, M.E., Winker, C., 2009. Towards the standardization of sequence stratigraphy. Earth-Science Reviews 92, 1–33. https://doi.org/10.1016/j.earscirev.2008.10.003

Catuneanu, O., Galloway, W.E., Kendall, C.G.S.C., Miall, A.D., Posamentier, H.W., Strasser, A., Tucker, M.E., 2011. Sequence Stratigraphy: methodology and nomenclature. Newsletters on Stratigraphy 44, 173–245. https://doi.org/10.1127/0078-0421/2011/0011

Catuneanu, O., Zecchin, M., 2013. High-resolution sequence stratigraphy of clastic shelves II: Controls on sequence development. Marine and Petroleum Geology 39, 26–38. https://doi.org/10.1016/j.marpetgeo.2012.08.010

Ceolin, D., dos Santos Filho, M.A.B., Salamoni Terra, G.J., Fragoso, D.G.C., Bunevich, R.B., Fauth, G., Hernández, J.I., Hernández, R.M., 2022. Ostracods from upper Yacoraite Formation (Danian), Salta Basin, Western Argentina: Taxonomy and paleoenvironmental indicators of climatic signals in lacustrine deposits. Journal of South American Earth Sciences 116. https://doi.org/10.1016/j.jsames.2022.103836

Cojan, I., 1993. Alternating Fluvial and Lacustrine Sedimentation: Tectonic and Climatic Controls (Provence Basin, S. France, Upper Cretaceous/Palaeocene), in: Alluvial Sedimentation. pp. 425–438. https://doi.org/https://doi.org/10.1002/9781444303995.ch27

Cojan, I., Moreau, M.-G., 2006. Correlation of Terrestrial Climatic Fluctuations with Global Signals During the Upper Cretaceous–Danian in a Compressive Setting (Provence, France). Journal of Sedimentary Research 76, 589–604. https://doi.org/10.2110/jsr.2006.045

Cojan, I., Moreau, M.-G., Stott, L.E., 2000. Stable carbon isotope stratigraphy of the Paleogene pedogenic series of southern France as a basis for continental-marine correlation. Geology 28, 259–262. https://doi.org/10.1130/0091-7613(2000)28<259:SCISOT>2.0.CO;2

Cojan, I., Renard, M., Emmanuel, L., 2003. Palaeoenvironmental reconstruction of dinosaur nesting sites based on a geochemical approach to eggshells and associated palaeosols (Maastrichtian, Provence Basin, France). Palaeogeography, Palaeoclimatology, Palaeoecology 191, 111–138. https://doi.org/10.1016/S0031-0182(02)00655-7

Comínguez, A.H., Ramos, V.A., 1995. Geometry and Seismic Expression of the Cretaceous Salta Rift System, Northwestern Argentina, in: Tankard, A.J., Suárez, R., Welsink, H.J. (Eds.), Petroleum Basins of South America: AAPG Memoir 62. pp. 325–340.

Corradetti, A., Tavani, S., Parente, M., Iannace, A., Vinci, F., Pirmez, C., Torrieri, S., Giorgioni, M., Pignalosa, A., Mazzoli, S., 2018. Distribution and arrest of vertical through-going joints in a seismic-scale carbonate platform exposure (Sorrento peninsula, Italy): insights from integrating field survey and digital outcrop model. Journal of Structural Geology 108, 121–136. https://doi.org/10.1016/j.jsg.2017.09.009

Corroy, G., Touraine, F., 1961. Données nouvelles sur la stratigraphie du Grand-Cabri et du Cengle (Bouches-du-Rhone). Bulletin de la Société Géologique de France S7-III, 77–81. https://doi.org/10.2113/gssgfbull.S7-III.1.77

Cristallini, E., Cominguez, A.H., Ramos, V.A., 1997. Deep structure of the Metan-Guachipas region: tectonic inversion in Northwestern Argentina. Journal of South American Earth Sciences 10, 403–421. https://doi.org/https://doi.org/10.1016/S0895-9811(97)00026-6

Del Papa, C.E., Salfity, J.A., 1999. View of Non-marine Paleogene sequences, Salta Group, Northwest Argentina. Acta Geologica Hispanica 34, 105–121.

Deschamps, R., Rohais, S., Hamon, Y., Gasparrini, M., 2020. Dynamic of a lacustrine sedimentary system during late rifting at the Cretaceous-Palaeocene transition: Example of the Yacoraite Formation, Salta Basin, Argentina. The Depositional Record 2020, 490–523. https://doi.org/10.1002/dep2.116

Disalvo, A., 2002. Cuenca del noroeste: marco geológico y reseña histórica de la actividad petrolera. En Rocas reservorio de las cuencas productivas de la Argentina, in: Shiuma, M., Hinterwimmer, G., Vergani, G. (Eds.), V Congreso de Exploración y Desarrollo de Hidrocarburos. Instituto Argentino del Petróleo y del Gas (IAPG), Mar del Plata, pp. 663–677.

Disalvo, A., Schelotto, M.L.R., Omil, R.G., Hoffman, C., Benítez, J., Hurtado, S., 2002. Los reservorios de la Formación Yacoraite, in: Schiuma, M., Hinterwimmer, G., Vergani, G. (Eds.), Rocas reservorios de las cuencas productivas de la Argentina: V Congreso de Exploración y Desarrollo de Hidrocarburos. Instituto Argentino del Petróleo y del Gas (IAPG), Mar del Plata, pp. 717–738.

Dorfman, A., 1942. Historia de la evolución industrial argentina: continuación. Servir 6, 4095–4124.

Duelis Viana, C., Endlein, A., Ademar da Cruz Campanha, G., Henrique Grohmann, C., 2016. Algorithms for extraction of structural attitudes from 3D outcrop models. Computers & Geosciences 90, 112–122. https://doi.org/10.1016/j.cageo.2016.02.017

Dughi, R., Sirugue, F., 1968. Marnes a œufs d'oiseaux du Paléocène de Basse-Provence. Bulletin de la Société Géologique de France S7-X, 542–548. https://doi.org/10.2113/gssgfbull.S7-X.5.542

Durand, J.-P., 1984. Paléocène et Éocène, in: Debrand-Passard, S. (Ed.), Synthèse Géologique Du Sud-Est de La France. Mémoire Du Bureau de Recherches Géologiques et Minières. BRGM, pp. 426–429.

Durand, J.-P., 1963. Les formations fluvio-lacustres éocènes du plateau du Cengle près d'Aix-en-Provence. Annales de la faculté des sciences de Marseille 34, 83–105.

Durand, J.-P., Guieu, G., 1980. Cadre structural du bassin de l'Arc. Le gisement de charbon du bassin de l'Arc, Houillères de Provence. Industrie minérale 69, 3–12.

Durand, J.P., Tempier, C., 1968. Le bassin de l'Arc, in: Excursion Géologique En Basse-Provence Occidentale. Marseille, pp. 25–33.

Einsele, G., 1992. Sedimentary Basins: Evolution, Facies, and Sediment Budget. Springer-Verlag.

Eltner, A., Kaiser, A., Castillo, C., Rock, G., Neugirg, F., Abellán, A., 2016. Image-based surface reconstruction in geomorphometry – merits, limits and developments. Earth Surface Dynamics 4, 359–389. https://doi.org/10.5194/esurf-4-359-2016

Embry, A.F., 1993. Transgressive–regressive (T–R) sequence analysis of the Jurassic succession of the Sverdrup Basin, Canadian Arctic Archipelago. Canadian Journal of Earth Sciences 30, 301–320. https://doi.org/10.1139/e93-024

Embry, A.F., Johannessen, E.P., 1992. T–R sequence stratigraphy, facies analysis and reservoir distribution in the uppermost Triassic–Lower Jurassic succession, western Sverdrup Basin, Arctic Canada, in: Vorren. T. O., Bergsager, E., Dahl-Stamnes, Ø.A., Holter, E., Johansen, B., Lie, E., Lund, T.B. (Eds.), Norwegian Petroleum Society Special Publications. Elsevier, pp. 121–146. https://doi.org/10.1016/B978-0-444-88943-0.50013-7

Feist-Castel, M., 1975. Répartition des Charophytes dans le Paléocène et l'Éocène du bassin d'Aix-en-Provence. Bulletin de la Société Géologique de France S7-XVII, 88–97. https://doi.org/10.2113/gssgfbull.S7-XVII.1.88

Floquet, M., 2020. Le Bassin marin Sud-Provençal : de son extension à partir du Cénomanien (vers -100 Ma) jusqu'à sa fermeture au Santonien supérieur (vers -84 Ma), in: La Géologie Des Bouches-Du-Rhône, Roches et Paysages Remarquables. BRGM Editions, pp. 69–86.

Fragoso, D.G.C., 2023. Princípios e Práticas da Ciclicidade e da Hierarquização na Estratigrafia de Alta Resolução: Uma Abordagem Metodológica e Aplicada à Caracterização de Reservatórios (PhD thesis). Universidade Federal do Rio Grande do Sul, Porto Alegre.

Fragoso, D.G.C., Gabaglia, G.P.R., Magalhães, A.J.C., Scherer, C.M.D.S., 2021. Cyclicity and hierarchy in sequence stratigraphy: An integrated approach. Brazilian Journal of Geology 51, e20200106. https://doi.org/10.1590/2317-4889202120200106

Fragoso, D.G.C., Kuchenbecker, M., Magalhães, A.J.C., Scherer, C.M.D.S., Gabaglia, G.P.R., Strasser, A., 2022. Cyclicity in Earth sciences, quo vadis? Essay on cycle concepts in geological thinking and their historical influence on stratigraphic practices. History of Geo- and Space Sciences 13, 39–69. https://doi.org/10.5194/hgss-13-39-2022

Fragoso, D.G.C., Melo, A.H. de, Gonçalves, L.A., Bunevich, R.B., Araujo, J. de A.M., Costa, T.C. da, Pedrosa, C.A., Scherer, C.M.D.S., 2023. High-resolution sequence stratigraphy applied to reservoir characterization of the Brazilian Cretaceous pre-salt section, Campos Basin: Guidelines for geological modeling and reservoir management. Marine and Petroleum Geology 151, 106203. https://doi.org/10.1016/j.marpetgeo.2023.106203

Furukawa, Y., Hernández, C., 2015. Multi-View Stereo: A Tutorial. Foundations and Trends® in Computer Graphics and Vision 9, 1–148. https://doi.org/10.1561/0600000052

Galloway, W.E., 1989. Genetic Stratigraphic Sequences in Basin Analysis I: Architecture and Genesis of Flooding-Surface Bounded Depositional Units. AAPG Bulletin 73, 125–142. https://doi.org/10.1306/703C9AF5-1707-11D7-8645000102C1865D

Garcia, G., Vianey-Liaud, M., 2001. Dinosaur eggshells as biochronological markers in Upper Cretaceous continental deposits. Palaeogeography, Palaeoclimatology, Palaeoecology 169, 153–164. https://doi.org/10.1016/S0031-0182(01)00215-2

Gomes, J.P.B., 2013. Simulação de processos deposicionais: caracterização de dois ciclos de alta frequência da Sequência Balbuena IV, Bacia do noroeste argentino (MSc thesis). Universidade Federal do Rio Grande do Sul, Porto Alegre.

Gomes, J.P.B., Bunevich, R.B., Tonietto, S.N., Alves, D.B., Santos, J.F., Whitaker, F.F., 2020. Climatic signals in lacustrine deposits of the Upper Yacoraite Formation, Western Argentina: Evidence from clay minerals, analcime, dolomite and fibrous calcite. Sedimentology 67, 2282–2309. https://doi.org/10.1111/sed.12700

Gómez Omil, R.J., Boll, A., 2005. Cuenca Cretácica del Noroeste Argentino, in: VI Congreso de Exploración y Desarrollo de Hidrocarburos: Ampliando las Fronteras. IAPG, Mar del Plata, pp. 63–73.

Gómez Omil, R.J., Boll, A., 1999. Sistema petrolero de la cuenca cretácica del noroeste argentino, in: IV Congreso de Exploración y desarrollo de hidrocarburos. IAPG, Mar del Plata, pp. 101–112.

Gómez Omil, R.J., Boll, A., Hernández, R.M., 1989. Cuenca cretácico-terciaria del Noroeste argentino (Grupo Salta), in: Chebli, G.A., Spalletti, L.A. (Eds.), Cuencas Sedimentarias Argentinas. Tucumán, pp. 43–64.

Gradstein, F.M., Ogg, J.G., Schmitz, M.D., Ogg, G.M., 2012. The Geologic Time Scale 2012. Elsevier.

Guadagnin, F., Gonçalves, Í.G., Roemers-Oliveira, E., Guedes, P.L., de Souza, E.G., Silveira, M. de M.L., Raja Gabaglia, G.P., Arienti Gonçalves, L., Oliveira, L.F.R. de, Selk, R., 2025. Building of classified 3D point clouds of outcrop with automatically segmented images. Geodata and AI 4, 100024. https://doi.org/10.1016/j.geoai.2025.100024

Hanusch, T., 2008. A new texture mapping algorithm for photorealistic reconstruction of 3D objects, in: The International Archives of the Photogrammetry, Remote Sensing and Spatial Information Sciences. Beijing, pp. 699–706. https://doi.org/https://doi.org/10.3929/ethz-b-000011977

Hernández, R., Echavarria, L., 2009. Faja Plegada y Corrida Subandina del Noroeste Argentino: Estratigrafía, Geometría y Cronología de la Deformación. Revista de la Asociación Geológica Argentina 65, 68–80.

Hernández, R.M., Disalvo, A., Boll, A., Gómez Omil, R., Gallli, C., 1999. Estratigrafia secuencial del Grupo Salta, con enfasis en las subcuencas de Metan-Alemania, noroeste Argentino, in: Bonorino, G.G., Omarini, R., Viramonte, J. (Eds.), Geología del Noroeste Argentino, Relatorio del XIV Congreso Geológico Argentino. pp. 263–283.

Hernández, R.M., Omil, G.R., Boll, A., 2008. Estratigrafía, Tectónica y Potencial petrolero del rift cretácico em la Provincia de Jujuy, in: XVII Congreso Geológico Argentino. Asociación Geológica Argentina, Jujuy, pp. 207–232.

Hunt, D., Tucker, M.E., 1992. Stranded parasequences and the forced regressive wedge systems tract: deposition during base-level'fall. Sedimentary Geology 81, 1–9. https://doi.org/10.1016/0037-0738(92)90052-S

James, M.R., Robson, S., 2012. Straightforward reconstruction of 3D surfaces and topography with a camera: Accuracy and geoscience application. Journal of Geophysical Research: Earth Surface 117. https://doi.org/10.1029/2011JF002289

Janocha, J., Smyrak-Sikora, A., Senger, K., Birchall, T., 2021. Seeing beyond the outcrop: Integration of ground-penetrating radar with digital outcrop models of a paleokarst system. Marine and Petroleum Geology 125. https://doi.org/10.1016/j.marpetgeo.2020.104833

Javernick, L., Brasington, J., Caruso, B., 2014. Modeling the topography of shallow braided rivers using Structure-from-Motion photogrammetry. Geomorphology 213, 166–182. https://doi.org/10.1016/j.geomorph.2014.01.006

Kargarpour, M.A., 2020. Carbonate reservoir characterization: an integrated approach. Journal of Petroleum Exploration and Production Technology 10, 2655–2667. https://doi.org/10.1007/s13202-020-00946-w

Kazhdan, M., Hoppe, H., 2013. Screened poisson surface reconstruction. ACM Transactions on Graphics 32, 1–13. https://doi.org/10.1145/2487228.2487237

Keidel, J., 1921. Sobre la distribución de los depósitos glaciares del Permico conocidos en la Argentina y su significación para la estratigrafia de la serie del Gondwana y la paleogeografia del Hemisferio Austral. Boletim da Academia Nacional de Ciencias 25, 239–368.

Kirtland Turner, S., Hull, P.M., Kump, L.R., Ridgwell, A., 2017. A probabilistic assessment of the rapidity of PETM onset. Nature Communications 8, 353. https://doi.org/10.1038/s41467-017-00292-2

Larssen, K., Senger, K., Grundvåg, S.A., 2020. Fracture characterization in Upper Permian carbonates in Spitsbergen: A workflow from digital outcrop to geo-model. Marine and Petroleum Geology 122. https://doi.org/10.1016/j.marpetgeo.2020.104703

Leleu, S., 2005. Les cônes alluviaux Crétacé Supérieur/Paléocène en Provence : traceurs de l'évolution morpho-tectonique des stades précoces de collision. Université Louis Pasteur, Strasbourg.

Leleu, S., Ghienne, J.-F., Manatschal, G., 2009. Alluvial fan development and morpho-tectonic evolution in response to contractional fault reactivation (Late Cretaceous–Palaeocene), Provence, France. Basin Research 21, 157–187. https://doi.org/https://doi.org/10.1111/j.1365-2117.2008.00378.x

Leleu, S., Tortosa, T., 2020. Les ultimes formations continentales du Paléogène : du Danien au Lutétien (de -66 Ma à -43 Ma environ), in: La Géologie Des Bouches-Du-Rhône. Roches et Paysages Remarquables. BRGM Editions, pp. 104–116.

Li, L., Wang, R., Lin, J., Xiao, Z., Hui, Y., 2019. A novel approach for extraction of ripple mark parameters based on SfM. Sedimentary Geology 392. https://doi.org/10.1016/j.sedgeo.2019.105523

Lowe, D.G., 2004. Distinctive Image Features from Scale-Invariant Keypoints. International Journal of Computer Vision 60, 91–110. https://doi.org/https://doi.org/10.1023/B:VISI.0000029664.99615.94

Lucia, F.J., 2007. Carbonate Reservoir Characterization: An Integrated Approach, Second Edition. ed. Springer, New York.

Magalhães, A.J.C., Raja Gabaglia, G.P., Fragoso, D.G.C., Bento Freire, E., Lykawka, R., Arregui, C.D., Silveira, M.M.L., Carpio, K.M.T., De Gasperi, A., Pedrinha, S., Artagão, V.M., Terra, G.J.S., Bunevich, R.B., Roemers-Oliveira, E., Gomes, J.P., Hernández, J.I., Hernández, R.M., Bruhn, C.H.L., 2020. High-resolution sequence stratigraphy applied to reservoir zonation and characterisation, and its impact on production performance - shallow marine, fluvial downstream, and lacustrine carbonate settings. Earth-Science Reviews 210. https://doi.org/10.1016/j.earscirev.2020.103325

Marquillas, R., Del Papa, C., Sabino, I., Heredia, J., 2003. Prospección del límite K/T en la cuenca del Noroeste, Argentina. Revista de la Asociación Geológica Argentina 58, 271–274.

Marquillas, R., Sabino, I., Sial, A.N., Del Papa, C., Ferreira, V., Matthews, S., 2007. Carbon and oxygen isotopes of Maastrichtian-Danian shallow marine carbonates: Yacoraite Formation, northwestern Argentina. Journal of South American Earth Sciences 23, 304–320. https://doi.org/10.1016/j.jsames.2007.02.009

Marquillas, R.A., Del Papa, C., Sabino, I.F., 2005. Sedimentary aspects and paleoenvironmental evolution of a rift basin: Salta Group (Cretaceous-Paleogene), northwestern Argentina. International Journal of Earth Sciences 94, 94–113. https://doi.org/10.1007/s00531-004-0443-2

Matheron, P., 1878. Recherches paléontologiques dans le Midi de la France. Quinzième partie. Terrain Tertiaire. Marseille.

Mitchum, R.M., 1977. Seismic Stratigraphy and Global Changes of Sea Level, Part 11: Glossary of Terms used in Seismic Stratigraphy, in: Seismic Stratigraphy — Applications to Hydrocarbon Exploration. American Association of Petroleum Geologists, pp. 205–212. https://doi.org/10.1306/M26490C13

Moreno, J.A., 1970. Estratigrafía y paleogeografía del Cretácico Superior en la Cuenca del Noroeste Argentino, con especial mención de los Subgrupos Balbuena y Santa Bárbara. Revista de la Asociación Geológica Argentina 25, 9–44.

Mutti, M., Vallati, M., Tomás, S., Galli, C., Bahniuk Rumbelsperger, A.M., Maerz, S., Coira, B., 2023. Constraining depositional evolution and reservoir compartmentalization in a mixed carbonate-siliciclastic lacustrine system: The Yacoraite formation, Salta Group, NW Argentina. Marine and Petroleum Geology 149. https://doi.org/10.1016/j.marpetgeo.2022.106049

Namongo Soro, P.J., Lamarche, J., Viseur, S., Richard, P., Messaadi, F., 2024. FracAbut: A python toolbox for computing fracture stratigraphy using interface impedance. Computers & Geosciences 190, 105656. https://doi.org/10.1016/j.cageo.2024.105656

Oliveira Santos, J.A., Uhlein, A., Dantas, M., de Morais Coutinho, G., Spier, T.J., Masse Vieira, K.H., Trindade Prado, A.C., Macharet, D., Uhlein, G.J., Novo, T., Reis, H., Farias, F.A., Freire, E.B., Carnier Fragoso, D.G., 2023. Constructing high-resolution stratigraphic frameworks by the application of signal analysis techniques: Example of Balbuena IV sequence, Yacoraite formation, Salta Basin. Marine and Petroleum Geology 157. https://doi.org/10.1016/j.marpetgeo.2023.106470

Panara, Y., Chandra, V., Finkbeiner, T., Petrovic, A., Zühlke, R., Khanna, P., Vahrenkamp, V., 2023. Fracture intensity and associated variability: A new methodology for 3D digital outcrop model analysis of carbonate reservoirs. Marine and Petroleum Geology 158. https://doi.org/10.1016/j.marpetgeo.2023.106532

Payton, C.E., 1977. Seismic Stratigraphy — Applications to Hydrocarbon Exploration. American Association of Petroleum Geologists. https://doi.org/10.1306/M26490

Pedrinha, S., 2014. Análise estratigráfica em depósitos lacustres maastrichtianos da Formação Yacoraite (Bacia de Salta - Argentina): definição e rastreabilidade de sequências de alta resolução (MSc thesis). Unesp Rio Claro, Rio Claro.

Pedrinha, S., Artagão, V. de M., 2024. High-resolution stratigraphy and characterization of reservoir-critical heterogeneities in the giant Tupi Field, pre-salt Santos Basin, Brazil. Geological Society, London, Special Publications 548. https://doi.org/10.1144/SP548-2023-91

Pedrinha, S., Raja Gabaglia, G.P., Lykawka, R., Dias-Brito, D., 2015. High-resolution sequence tracking in Metán-Alemania Sub-basin (Salta Basin Maastrichtian – Argentina): detailed stratigraphic anatomy of a lacustrine system under the influence of microbial processes. Boletim de Geociências da Petrobras 23.

Pereira, J.V.F., Medeiros, W.E., Dantas, R.R.S., Bezerra, F.H.R., La Bruna, V., Xavier, M.M., Maia, R.P., Gomes, D.D.M., Silva, D.C.C., Maciel, I.B., 2024. An integrated 3D digital model of stratigraphy, petrophysics and karstified fracture network for the Cristal Cave, NE-Brazil. Journal of Structural Geology 178. https://doi.org/10.1016/j.jsg.2023.105013

Posamentier, H.W., Jervey, M.T., Vail, P.R., 1988. Eustatic Controls on Clastic Deposition I—Conceptual Framework, in: Wilgus, Cheryl.K., Hastings, B.S., Posamentier, H., Van Wagoner, J., Ross, C.A., Kendall, C.G.St.C. (Eds.), Sea-Level Changes: An Integrated Approach. SEPM (Society for Sedimentary Geology), pp. 109–124. https://doi.org/10.2110/pec.88.01.0109

Posamentier, H.W., Allen, G.P., 1999. Siliciclastic Sequence Stratigraphy-Concepts and Applications. SEPM (Society for Sedimentary Geology), Tulsa. https://doi.org/10.2110/csp.99.07

Pugsley, J.H., Howell, J.A., Hartley, A., Buckley, S.J., Brackenridge, R., Schofield, N., Maxwell, G., Chmielewska, M., Ringdal, K., Naumann, N., Vanbiervliet, J., 2022. Virtual field trips utilizing virtual outcrop: construction, delivery and implications for the future. Geoscience Communication 5, 227–249. https://doi.org/10.5194/gc-5-227-2022

Ramdani, A., Khanna, P., Gairola, G.S., Hanafy, S., Vahrenkamp, V., 2022. Assessing and processing three-dimensional photogrammetry, sedimentology, and geophysical data to

build high-fidelity reservoir models based on carbonate outcrop analogues. AAPG Bulletin 106, 1975–2011. https://doi.org/10.1306/05152221092

Ramos, V.A., 1988. The tectonics of the Central Andes: 30o to 33o latitude, in: Clark, S., Burchfiel, D. (Eds.), Processes In Continental Litospheric Deformation. The Geological Society of America, pp. 31–54.

Reyes, F.C., 1972. Correlaciones en el Cretácico de la cuenca Andina de Bolivia, Perú y Chile. Revista Técnica de Yacimientos Petrolíferos Fiscales Bolivianos 1, 101–144.

Reyes, F.C., Salfity, J.A., 1973. Consideraciones sobre la estratigrafia del Cretacico (Subgrupo Pirgua) del noroeste argentino, in: V Congreso Geológico Argentino. Asociación Geológica Argentina, Córdoba, pp. 335–385.

Riquelme, A., Cano, M., Tomás, R., Abellán, A., 2017. Identification of Rock Slope Discontinuity Sets from Laser Scanner and Photogrammetric Point Clouds: A Comparative Analysis. Procedia Engineering 191, 838–845. https://doi.org/10.1016/j.proeng.2017.05.251

Roemers-Oliveira, E., 2014. Contexto deposicional da Sequência Balbuena III (Maastrichtiano/Daniano) da Formação Yacoraite na sub-bacia de Metán-Alemania, na região de Salta, Argentina (MSc thesis). Unesp Rio Claro, Rio Claro.

Roemers-Oliveira, E., Fernandes, L.A., Bento Freire, E., Amarante Simões, L.S., 2015. Microbial filaments in stromatolites and laminites of Balbuena III Sequence (Maastrichtian/Danian) of Yacoraite Formation in Metán-Alemania Sub-basin, Salta region, Argentina, and its palaeoenvironmental significance. Brazilian Journal of Geology 45, 399–413. https://doi.org/10.1590/2317-488920150030255

Rohmana, R.C., Fardiansyah, I., Taufani, L., Harishidayat, D., 2019. Depositional processes and facies architecture of Balikpapan Sandstone Formation, application of 3D Digital Outcrop Model (DOM) to identify reservoir geometry and distribution in deltaic system. Scientific Contributions Oil and Gas 42, 35–42. https://doi.org/DOI:10.29017/SCOG.41.1.35-42

Roisenberg, H.B., Bállico, M.B., Guadagnin, F., Manna, M.O., de Souza, E.G., 2022. Digital Outcrop Models applied to high-resolution stratigraphy in braided fluvial systems: A study case at Jaicós formation in Parnaíba Basin, NE Brazil. Journal of South American Earth Sciences 119, 104006. https://doi.org/10.1016/j.jsames.2022.104006

Rouire, J., 1979. Notice explicative de la carte géologique de Marseille 1/250 000. Orléans.

Sabino, I.F., 2004. Estratigrafía de la Formación La Yesera (Cretácico): Base del relleno sinrift del Grupo Salta, noroeste argentino. Revista de la Asociación Geológica Argentina 59, 341–359.

Sabino, I.F., 2002. Geología del Subgrupo Pirgua (Cretácico) del noroeste argentino (PhD Thesis). Universidad Nacional de Salta, Salta.

Sadler, P.M., 1999. The influence of hiatuses on sediment accumulation rates, in: Bruns, P., Hass, H.C. (Eds.), On the Determination of Sediment Accumulation Rates, GeoResearch Forum. Trans Tech Publications, Zurich, Switzerland, pp. 15–40.

Salfity, J.A., 1982. Evolución paleogeográfica del Grupo Salta (Cretácico-Eogénico), Argentina, in: V Congreso Latinoamericano de Geología. Buenos Aires, pp. 11–26.

Salfity, J.A., 1980. Estratigrafía de la Formación Lecho (Cretácico) en la Cuenca Andina del Norte Argentino (Publicación Especial). Universidad Nacional de Salta, Salta.

Salfity, J.A., Marquillas, R.A., 1999. La cuenca cretácico-terciaria del norte argentino, in: Caminos, R. (Ed.), Geología Argentina. Instituto de Geología y Recursos Minerales, Buenos Aires, pp. 613–626.

Schlager, W., 2005. Carbonate Sedimentology and Sequence Stratigraphy. SEPM (Society for Sedimentary Geology). https://doi.org/10.2110/csp.05.08

Schwab, K., 1984. Contribución al conocimiento del sector occidental de la cuenca sedimentaria del Grupo Salta (Cretácico-Eogénico) en noroeste argentino, in: IX Congreso Geológico Argentino. San Carlos de Bariloche, pp. 586–604.

Scotese, C.R., 2001. Paleomap Project [WWW Document]. Drexel University. URL http://www.scotese.com (accessed 9.3.25).

Seers, T.D., Sheharyar, A., Tavani, S., Corradetti, A., 2022. Virtual outcrop geology comes of age: The application of consumer-grade virtual reality hardware and software to digital outcrop data analysis. Computers and Geosciences 159. https://doi.org/10.1016/j.cageo.2021.105006

Sial, A.N., Ferreira, V.P., Toselli, A.J., Parada, M.A., Acenolaza, F.G., Pimentel, M.M., Alonso, R.N., 2001. Carbon and Oxygen Isotope Compositions of Some Upper Cretaceous-Paleocene Sequences in Argentina and Chile. International Geology Review 43.

Silveira, M. de M.L., 2020. Análisis estratigráfico secuencial de alta resolución y modelado geológico 3D en secciones sedimentarias transicionales y continentales del Jurásico Inferior a Medio del sector sur de la Cuenca Neuquina como análogo en la caracterización de reservorios de hidrocarburos (PhD thesis). Universidad Nacional de La Plata, La Plata.

Sloss, L.L., 1963. Sequences in the Cratonic Interior of North America. Geological Society of America Bulletin 2, 93–114. https://doi.org/doi:10.1130/0016-7606(1963)74[93:SITCIO]2.0.CO;2

Sloss, L.L., Krumbein, W.C., Dapples, E.C., 1949. Integrated Facies Analysis, in: Longwell, C.R., Moore, R.C., McKee, E.D., Müller, S.W., Spieker, E.M., Wood, H.E., Sloss, L.L., Krumbein, W.C., Dapples, E.C. (Eds.), Sedimentary Facies in Geologic History. The Geological Society of America, pp. 91–124. https://doi.org/10.1130/MEM39-p91

Snavely, N., Seitz, S.M., Szeliski, R., 2006. Photo tourism: Exploring photo collections in 3D. ACM Transactions on Graphics 25, 835–846. https://doi.org/10.1145/1141911.1141964

Strasser, A., Pittet, B., Hillgärtner, H., Pasquier, J.-B., 1999. Depositional sequences in shallow carbonate-dominated sedimentary systems: concepts for a high-resolution analysis. Sedimentary Geology 128, 201–221. https://doi.org/10.1016/S0037-0738(99)00070-6

Tavani, S., Corradetti, A., Marcuri, M., Seers, T., 2024. Virtual outcrop models of geological structures: From the construction of photogrammetric 3D models to their application towards the analysis of geological structures. Società Geologica Italiana.

Tortosa, T., Leleu, S., 2020. Les bassins continentaux et la première orogenèse provençale au Crétacé final : du Santonien terminal au Maastrichtien (-85 Ma à -66 Ma), in: La Géologie Des Bouches-Du-Rhône. Roches et Paysages Remarquables. BRGM Editions, pp. 87–103.

Tsai, R., 1987. A versatile camera calibration technique for high-accuracy 3D machine vision metrology using off-the-shelf TV cameras and lenses. IEEE Journal on Robotics and Automation 3, 323–344. https://doi.org/10.1109/JRA.1987.1087109

Turner, D., Lucieer, A., Watson, C., 2012. An Automated Technique for Generating Georectified Mosaics from Ultra-High Resolution Unmanned Aerial Vehicle (UAV) Imagery, Based on Structure from Motion (SfM) Point Clouds. Remote Sensing 4, 1392–1410. https://doi.org/10.3390/rs4051392

Turner, J.C.M., 1958. Estratigrafía del Cordón de Escaya y de la Sierra de Rinconada (Jujuy). Revista De La Asociación Geológica Argentina 13, 15–41.

Vail, P.R., Mitchum, R.M., Thompson, S., 1977. Seismic Stratigraphy and Global Changes of Sea Level, Part 4: Global Cycles of Relative Changes of Sea Level, in: Payton, C.E. (Ed.), Seismic Stratigraphy — Applications to Hydrocarbon Exploration. AAPG, pp. 83–97. https://doi.org/10.1306/M26490C6

Vallati, M., Tomás, S., Galli, C., Winterleitner, G., Mutti, M., 2023. Depositional controls in an ancient, closed lake system: A high-resolution and multi-scalar case study from the Yacoraite Formation (Salta Basin, Argentina). Sedimentary Geology 454. https://doi.org/10.1016/j.sedgeo.2023.106456

Van Wagoner, J.C., Posamentier, H.W., Mitchum, R.M., Vail, P.R., Sarg, J.F., Loutit, T.S., Hardenbol, J., 1988. An overview of the fundamentals of sequence stratigraphy and key definitions, in: Wilgus, Cheryl.K., Hastings, B.S., Posamentier, H., Van Wagoner, J., Ross, C.A., Kendall, C.G.St.C. (Eds.), Sea-Level Changes: An Integrated Approach. SEPM (Society for Sedimentary Geology), pp. 39–45. https://doi.org/10.2110/pec.88.01.0039

Viana, C.D., Grohmann, C.H., Busarello, M. dos S.T., Garcia, G.P.B., 2018. Structural analysis of clastic dikes using Structure from Motion - Multi-View Stereo: a case-study in the Paraná Basin, southeastern Brazil. Brazilian Journal of Geology 48, 839–852. https://doi.org/10.1590/2317-4889201800201898

Villafañe, P.G., Frías-Saba, R. del C., Della-Vedova, M., Citton, P., Díaz-Martínez, I., de Valais, S., Aceñolaza, F.G., Marquillas, R.A., Cónsole-Gonella, C., 2022. Microbialitic deposits of the Yacoraite Formation, NW Argentina: distribution, environments, paleoecology, and economic implications. Brazilian Journal of Geology 52. https://doi.org/10.1590/2317-4889202220210088

Villarreal, C.A.J., Rojas, J.D.D., Ríos, C.A.R., 2020. 3D digital outcrop modelling of the Lower Cretaceous Los Santos formation sandstones, Mesa de Los Santos region (Colombia): Implications for structural analysis. Journal of Structural Geology 141. https://doi.org/10.1016/j.jsg.2020.104214

Villot, M., 1883. Étude sur le bassin de Fuveau et sur un grand travail à y exécuter. Annales des Mines 8, 5–66.

Westoby, M.J., Brasington, J., Glasser, N.F., Hambrey, M.J., Reynolds, J.M., 2012. “Structure-from-Motion” photogrammetry: A low-cost, effective tool for geoscience applications. Geomorphology 179, 300–314. https://doi.org/10.1016/j.geomorph.2012.08.021

Westphal, M., Durand, J.-P., 1990. Magnetostratigraphie des séries continentales fluvio-lacustres du Crétacé supérieur dans le synclinal de l’Arc (région d’Aix-en-Provence, France). Bulletin de la Société Géologique de France VI, 609–620. https://doi.org/10.2113/gssgfbull.VI.4.609

Zecchin, M., 2007. The architectural variability of small-scale cycles in shelf and ramp clastic systems: The controlling factors. Earth-Science Reviews 84, 21–55. https://doi.org/10.1016/j.earscirev.2007.05.003

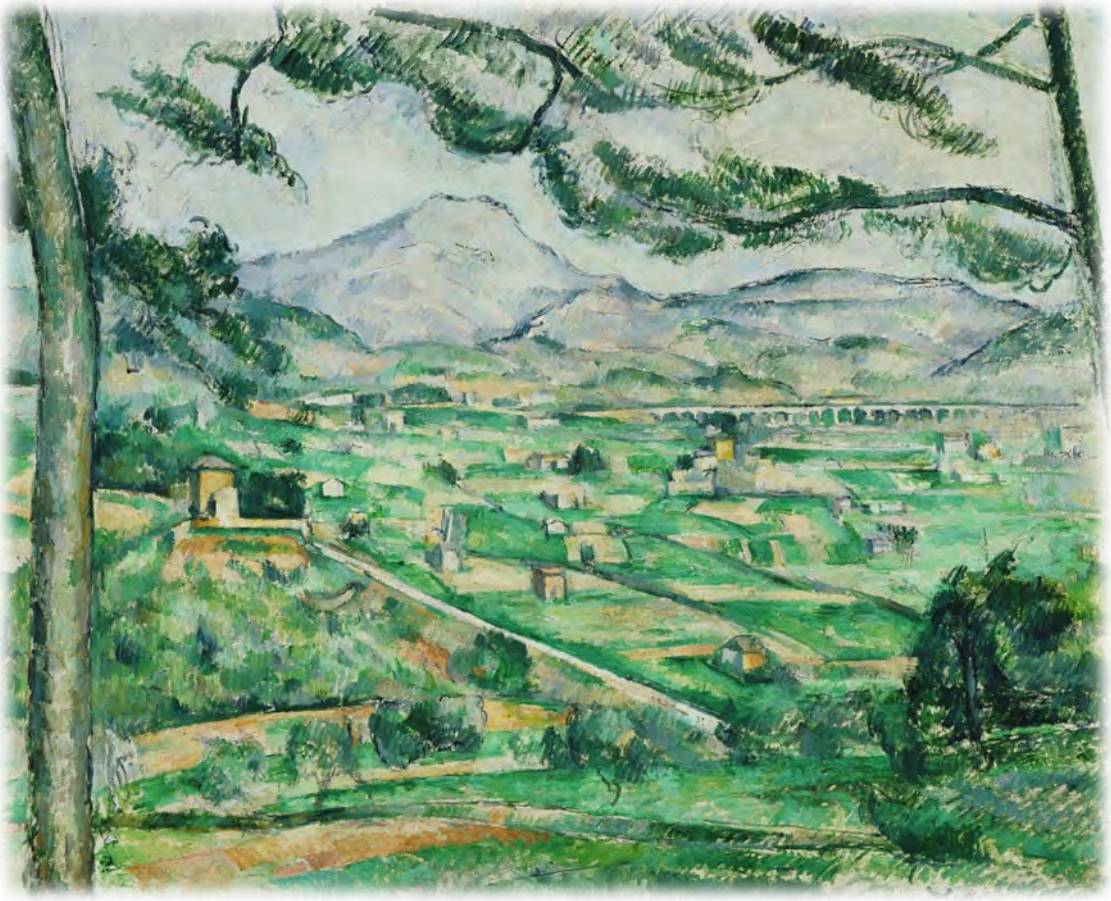

*Mont Sainte-Victoire, Paul Cézanne, c. 1886–1887, via Wikimedia Commons.*

*« Pour bien peindre un paysage, je dois découvrir d'abord les assises géologiques. »*

*Paul Cézanne, Conversations avec Cézanne (M. Doran, 1978)*

## Chapter 3
## La Barre du Cengle

This chapter is based on the article published in *Sedimentary Geology* (470, 106690, 2024). The original publication can be accessed at: https://doi.org/10.1016/j.sedgeo.2024.106690.

# The anatomy and stacking pattern of palustrine-dominated carbonate sequences from the Cengle Plateau, Paleocene, SE France: A multi-scalar approach

Eduardo Roemers-Oliveira[1,2], François Fournier[1], Sophie Viseur[1], Guilherme Pederneiras Raja Gabaglia[2], Jules Fleury[1], Véronique Rinalducci[1], Abel Guihou[1], Lionel Marié[1], Felipe Guadagnin[3], Pierre Deschamps[1], Alain Tonetto[4]

[1]Aix Marseille Université, CNRS, IRD, INRAE, CEREGE, Aix-en-Provence, France
[2]Petrobras – Petróleo Brasileiro S.A, Rio de Janeiro, Brazil
[3]Universidade Federal do PAMPA, Caçapava do Sul, Brazil
[4]Aix Marseille Université, CNRS, FSCM, UAR 1739, PRATIM, Marseille, France

## Abstract

An integrated approach combining petrography, photogrammetry, geochronology, SEM, and geochemical data was utilized to analyze lithofacies, stacking patterns, and lateral facies variations, and to interpret environmental dynamics during the deposition of carbonates from 'La Barre du Cengle' in the Early Paleogene. Located in the SE of France, the elliptical Cengle Plateau stretches 7 km from east to west and is 2 km wide, featuring cliffs ranging in thickness from 20 to 35 m. These cliffs showcase grayish, beige, and pinkish limestones dominated by palustrine facies, forming part of the 'Calcaire de Saint Marc' Formation of the Arc Basin. Sedimentary deposits within this interval were repeatedly subjected to subaerial exposure due to fluctuations in lake levels driven by climate, resulting in the organization of elementary sequences at decimetric to metric scales, which stack up into small-scale sequences at the decametric order. Deposition occurred under mainly subarid climatic conditions, with paleogeographic variations in the basin corresponding to changes in lake base levels over time and space. At least four frequencies of base level variation are present: very high and seasonal frequency, responsible for the formation of palustrine facies; high frequency, which generates the elementary sequences; medium frequency, which leads to the formation of the small-scale sequences; and low frequency which corresponds to the deposition of the entire set of limestones that form the Cengle cliff. The transition between lacustrine, palustrine, and pedogenic environments consistently occurs from west to east over time. In the more distal regions, the proportion of lacustrine facies tends to increase, and the thicknesses of the preserved sedimentary record tend to be greater. Conversely, palustrine and pedogenic facies predominate in the more proximal areas, typically resulting in decreased thickness.

**Keywords:** Continental carbonates; Limestones; Pedogenesis; Cyclicity; Arc Basin; Digital outcrop models

## 3.1. Introduction

Continental carbonate sediments encompass a wide variety of deposits, including lacustrine facies, which may undergo pedogenesis, giving rise to palustrine (Freytet and Verrecchia, 2002; Alonso-Zarza and Wright, 2010a) and pedogenic facies (if the subaerial exposure is longer – Alonso-Zarza and Wright, 2010a) caused by the drop in the lake's water level. This exposure induces varying degrees of modification in the primary sediments (Freytet and Plaziat, 1982; Wright and Platt, 1995; Freytet and Verrecchia, 2002; Alonso-Zarza, 2003; Alonso-Zarza and Wright, 2010a), thus making challenging the differentiation between palustrine and pedogenic

carbonates. The cyclic nature of many carbonate deposits (Wright and Platt, 1995) results in a polyphasic development of pedogenic figures, sometimes causing a telescoping of sedimentary cycles, making them difficult to individualize. Additionally, groundwater calcrete development during prolonged subaerial exposures complicates the interpretation of palustrine cyclothems (Alonso-Zarza, 2003; Wanas and Soliman, 2014).

Numerous studies have been previously conducted regarding the cyclic stacking pattern of lacustrine–palustrine deposits (e.g., Platt and Wright, 1992; Wright and Platt, 1995; Armenteros et al., 1997; Alonso-Zarza et al., 2011; Méndez-Bedia et al., 2020). The introduction of the 'exposure index' concept (Platt and Wright, 1992) gives rise to implementing a semi-quantitative method for defining and characterizing palustrine carbonate sequences in one dimension. On the other hand, the published literature lacks examples of 2D or 3D characterization of these sequences, making it possible to highlight lateral variations in vertical stacking pattern and exposure index, and finally to define detailed architectures in lake margin and palustrine settings.

This research focuses on conducting a detailed analysis of palustrine-dominated limestone sequences outcropping on the cliffs of the Cengle Plateau in southeastern France. This provides the unique opportunity to study the development and lateral evolution of palustrine-dominated sequences over a distance of up to 7 km, analyze their vertical stacking pattern in 2D, and highlight different orders of cyclicity.

The Cengle Plateau cliff, locally known as 'La Barre du Cengle' or 'Calcaire du Cengle', is part of the 'Calcaire de Saint-Marc' Formation within the Arc Basin (Durand, 1984; Cojan et al., 2000). The age of deposition of this carbonate formation was assigned to the Thanetian–Ypresian, including, therefore, the Paleocene–Eocene boundary (Feist-Castel, 1975; Durand, 1984; Cojan et al., 2000; Tortosa and Leleu, 2020). Despite extensive exposure, access to the Cengle Plateau is limited due to geomorphological constraints, potentially contributing to the scarcity of complete sedimentological studies of this formation. The sole comprehensive study providing detailed descriptions of some stratigraphic profiles in the area dates back to the sixties, when Durand (1963) offered a thorough description of lithotypes and interpretations based on petrographic data.

This paper not only aims to provide a detailed description of the facies found in the palustrine-dominated environment within a high-resolution stratigraphic framework but also: i) to investigate the processes responsible for their formation; ii) to develop an exposure index as a relative indicator of subaerial exposure time; iii) to create a predictive model for the spatial distributions of the facies, anatomies, and stacking patterns; and iv) to provide insights into the paleogeography, tectonic evolution and paleoclimate of southeastern France during the Early Paleogene.

An integrated approach was employed to accomplish this study, combining traditional and digital geological methods. Field data collected from vertical stratigraphic profiles and results from petrographic, sedimentological, geochemical, geochronological, and stratigraphic analyses were integrated into a Digital Outcrop Model (DOM) generated through aerial photogrammetry acquired by a Remotely Piloted Aerial System (RPAS).

## 3.2. Geological setting

The Cengle Plateau is in the Provence region of southeastern France (Fig. 3.1), south of Montagne Sainte-Victoire, around 15 km east of Aix-en-Provence. The plateau has an elliptical shape, measuring about 7 km in length from east to west and 2 km across, with an average altitude of 500 m. The cliff thickness, which exposes the lacustrine–palustrine limestones of the

Cengle (‘Calcaire de Saint-Marc’ Formation), part of the Arc Basin, varies from 35 m in the West to just under 20 m in the East. Talus deposits of rock debris from the same formation are found at its base.

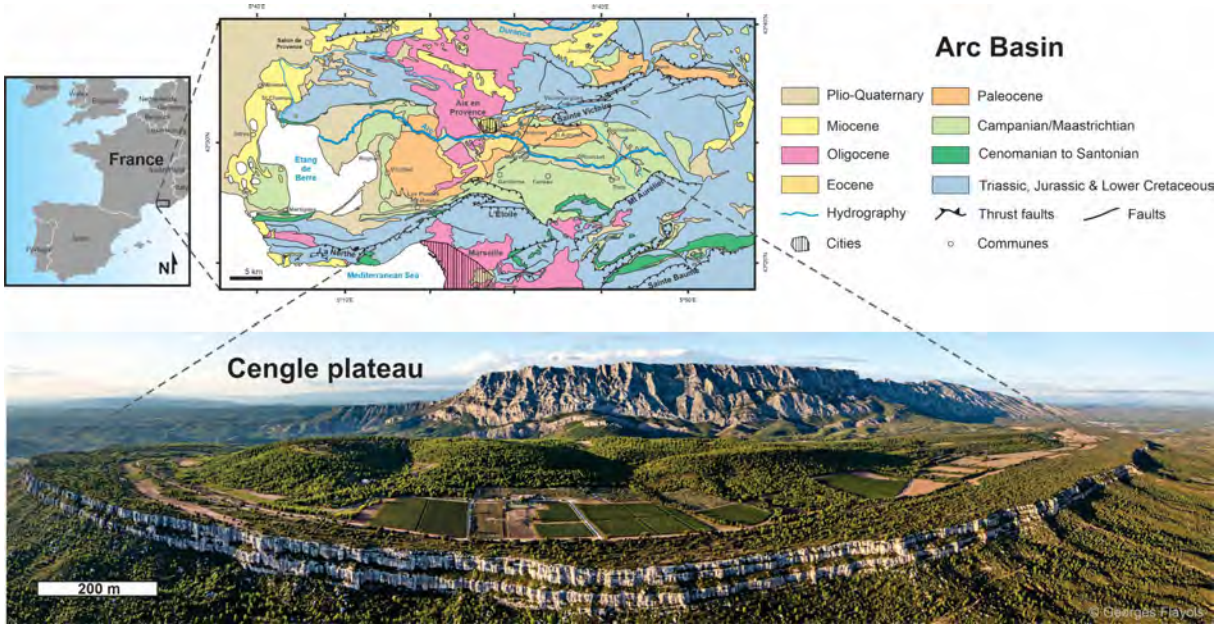


**Fig. 3.1.** Location of the Cengle Plateau. Simplified geological map of the Arc Basin (1:250,000), modified from Rouire (1979) after Leleu (2005). Panoramic photograph (© Georges Flayols) of the Cengle plateau and Sainte-Victoire Mountain in the background.

Covering an approximate area of 1600 km$^2$, the Arc Basin is the largest syncline in the Provence region (Westphal and Durand, 1990). Its geological orientation is from east to west and preserves a continental sedimentary record from the Upper Cretaceous (Santonian) to the Middle Eocene (Lutetian) (Durand and Tempier, 1968). The deposition of the Arc Basin during the late Santonian marks a transition from predominantly marine sedimentation of the South-Provence Basin (Tortosa and Leleu, 2020 and references therein), which prevailed in the southern region of Provence until that time, to primarily continental sedimentation. The progressive marine transgression that inundated the Provence region from the early to middle Cenomanian persisted until the late Santonian (Floquet, 2020). At this time, the subsidence rate of the South-Provence Basin decreased due to compressional Pyreneo-Provençal deformation, while subsidence in the Arc Basin intensified (Cojan and Moreau, 2006).

From the Late Cretaceous to the Middle Eocene, continuous subsidence in the Arc Basin led to the gradual accumulation of thicknesses exceeding 2000 m (Cojan, 1993) of continental sediments, commencing in the Campanian (Durand, 1984; Leleu, 2005). During this interval, the basin paleogeography displayed minimal variation (Cojan and Moreau, 2006; Tortosa and Leleu, 2020), with intercalated sequences evolving from braided fluvial deposits across silty floodplains to shallow lacustrine carbonate deposits (Durand, 1984; Cojan, 1993). As discussed by Cojan (1993), the basin paleogeography is governed by two fault systems: one oriented E-W, which defines the drainage pattern, and another NNE–SSW, controlling lateral facies variations. In this context, deposition is influenced by both tectonic and climatic factors.

Stratigraphically, the various sequences deposited in the Arc Basin were initially designated by local stages (Valdonian, Fuvelian, Bégudian, Rognacian, and Vitrollian), named after type localities situated in the Aix-en-Provence region (Matheron, 1878; Villot, 1883). These local stages correspond to facies characterized by alternations of limestones, sandstones, and claystones, defined by their lithological nature and fossil content. These local stages formed the basis for the current chrono-lithostratigraphic framework of the basin. Studies (Durand, 1984;

Cojan et al., 2000; Cojan and Moreau, 2006) have sought to correlate the local stages with international marine stages, primarily relying on biostratigraphic, carbon isotopic, and paleomagnetic data. The current lithostratigraphic section of the Arc Basin (Fig. 3.2A), as outlined by Cojan et al. (2000) and Tortosa and Leleu (2020), regards the principal limestone intervals as the main lithostratigraphic units of the Basin.

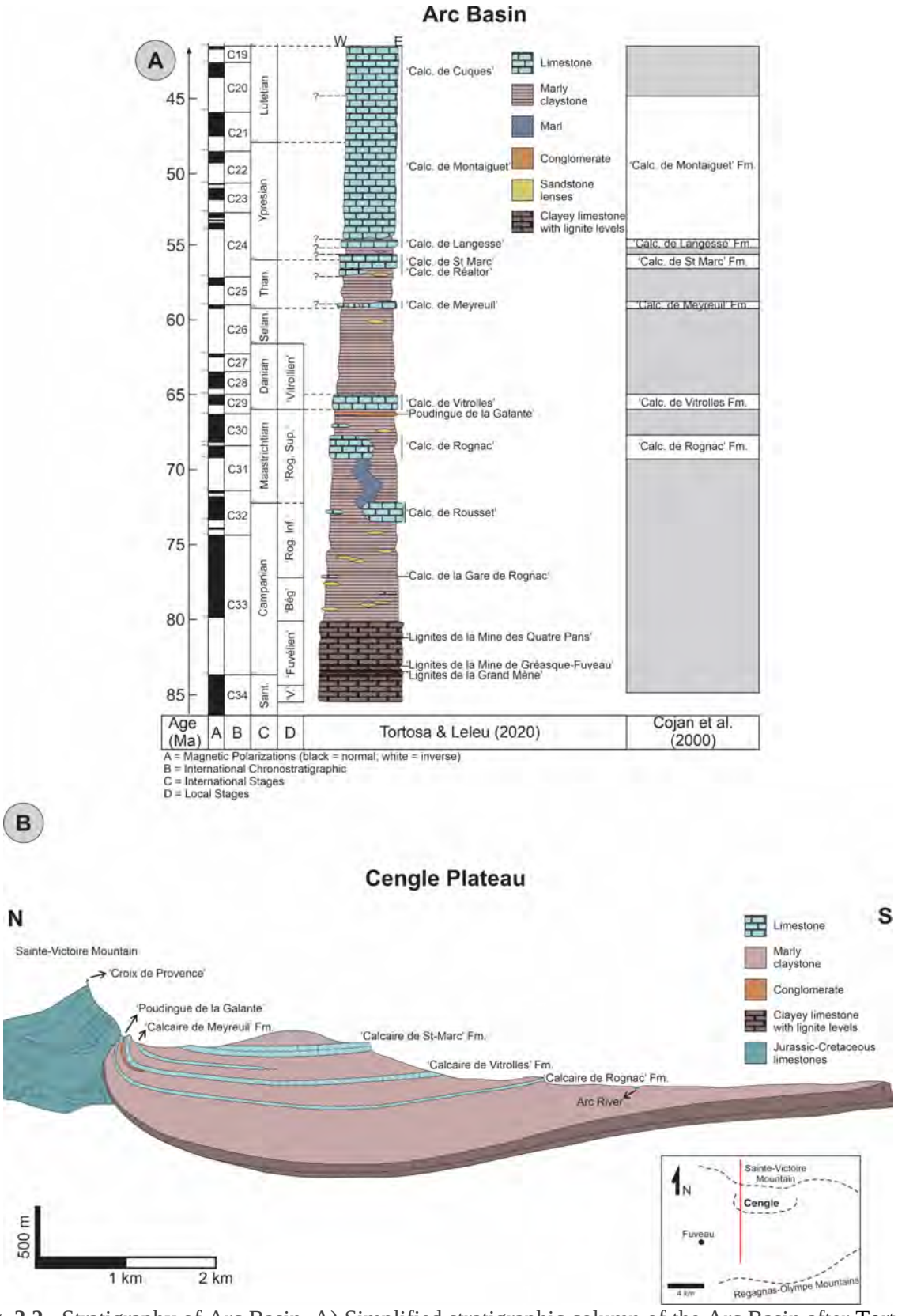


**Fig. 3.2.** Stratigraphy of Arc Basin. A) Simplified stratigraphic column of the Arc Basin after Tortosa and Leleu (2020). B) Simplified N–S stratigraphic section of formations and facies occurring in the Cengle plateau region after Durand and Tempier (1968).

In the eastern part of the Arc Basin, a significant marker bed, known as the 'Poudingue de la Galante', occurs a few meters below the 'Calcaire de Vitrolles' Formation. This lithological unit consists of a conglomerate composed of lithic fragments of various compositions. It represents an upper Maastrichtian deposit, with a thickness ranging from 2 to 4 m, located in the Vitrolles region and at the base of Sainte-Victoire Mountain. It likely correlates with scattered sandstone lenses found in the same position in the Rognac area (Tortosa and Leleu, 2020). Besides serving as an excellent correlation horizon, the K/Pg (Cretaceous/Paleogene) boundary is just above this stratum. This interpretation aligns with the findings by Cojan et al. (2000), who linked the K/Pg boundary to a pronounced negative $\delta^{13}C$ signal.

In this study, when referring to the 'Calcaire du Cengle' or Cengle limestone among other variations, it implies a geographical connotation. When discussing the lithostratigraphic unit to which the Cengle limestones belong, it will be referred to as the 'Calcaire Saint-Marc' Formation, as suggested by Corroy and Touraine (1961), Cojan et al. (2000) and Tortosa and Leleu (2020). In the Cengle Plateau region (Fig. 3.2B), lacustrine limestone deposits are interbedded with reddish marl and claystone deposits formed in river floodplain environments. Regarding fossils in the Cengle limestones, the literature records fragments of charophytes, bivalve and gastropod mollusks, ostracods, and *Microcodium* debris (Durand, 1963). Bivalve mollusks (Durand, 1963) and gastropods such as *Physa prisca, Physa columnaris, Succinea sparnacensis,* and *Planorbis sparnacensis,* have been identified (Feist-Castel, 1975; Durand, 1984). The Provence region is internationally recognized for its dinosaur eggshells (Campanian and Maastrichtian intervals) and giant bird eggshells in the Paleocene and Eocene units, including the Cengle region. Below the Cengle limestones, thin eggshells of *Ornitholithus biroi* are found, while in the marly intervals at the summit of the Cengle Plateau, thick eggshells of *Ornitholithus arcuatus* occur (Durand, 1984; Angst et al., 2015).

## 3.3. Database and methods

### 3.3.1. Field data acquisition

The escarpment of the Cengle Plateau is quite steep, but access via the D56C road cuts through the structure, and some trails that ascend the plateau are mainly used for hiking activities.

Four vertical stratigraphic profiles (Pas de la Vache, Pas de Monsieur, Pas du Lièvre, and La Route) were surveyed at a detailed scale (1:40), following the method described in Miall (2000), totaling 110 m of vertical sections. In these profiles, macroscopic identification of facies, textures, and sedimentary structures was carried out. In the field, the lacustrine–palustrine facies were described following the terminology available in Alonso-Zarza and Wright (2010a) in conjunction with Dunham's classification for carbonates (Dunham, 1962), which is based on recognizable depositional textures of limestones. Photographic documentation of macrofacies was also conducted, and samples were collected for petrography, stable isotope analysis, and U–Pb dating. Throughout the vertical stratigraphic profiles, 262 samples were taken, resulting in 262 data points with stable carbon and oxygen isotope data, 140 petrographic thin sections, and 6 samples suitable for U–Pb radiometric dating of carbonates.

In subsequent field stages, aerial photography was carried out using a RPAS, as detailed in the Photogrammetry section.

### 3.3.2. Photogrammetry

To generate DOMs, aerial photogrammetric surveys were conducted using a RPAS. The equipment employed was the DJI Phantom 4 RTK. This device is outfitted with a 20-megapixel

1-inch CMOS sensor camera, a Global Navigation Satellite System (GNSS), and a Real-Time Kinematic (RTK) module. The sensor's mechanical shutter facilitates image capture while the equipment is in motion, expediting the process of photographic acquisition. The RTK module provides positioning information with centimeter-level accuracy in real time. To mitigate distortions and enhance the precision and accuracy of geopositioning in the generated models, coordinates for twenty Ground Control Points (GCPs) were acquired during fieldwork. These points were marked with crosses, serving as markers for indicating the GCPs on the individual images. A pair of Trimble GNSS RTK R8 receivers was employed with the base receiver remaining stationary at a point with known coordinates. The entire acquisition process was georeferenced in accordance with the French geodetic network, RGF93 (EPSG: 4171).

More than 10,000 aerial photographs were acquired with the camera tilt ranging from 0 to 45º, utilizing semi-automatic and manual flight plans. These images were captured with a minimum of 80% forward and 65% side overlap. The survey resulted in four models: one covering the entire cliff at a lower resolution of 2.4 cm per pixel, and three higher-resolution models at Pas de Monsieur (7.8 mm per pixel), Pas du Lièvre (6.1 mm per pixel), and La Route (1.2 cm per pixel), where sedimentological logs were acquired.

The DOMs were processed using the Agisoft® Metashape Professional Edition software (v.2.0.1) through the Structure from Motion and Multi-View Stereo (SfM-MVS) workflow. This workflow is well-established and widely employed for generating virtual models of outcrops (Lowe, 2004; Brunier et al., 2016; Marques et al., 2020; Bistacchi et al., 2022). As a result, dense point clouds were obtained, and triangulated meshes were generated by interpolation and textured with outcrop images to produce the photorealistic models. Afterward, geological interpretations of the DOMs were carried out using the Petex® Move software (v.2022).

### 3.3.3. Petrographic characterization

A total of 140 thin sections, prepared from field-collected samples, were analyzed using a petrographic transmitted polarized light microscope. Microscopic petrography was of paramount importance for facies characterization, as it enabled a detailed analysis of their constituents (grains, matrix, and cements). Furthermore, it allowed the identification of textures and microstructures, from which information on depositional and diagenetic contexts was obtained. Microscopic descriptions followed the carbonate classification by Dunham (1962), and the proportions of rock constituents in the thin sections were estimated visually by comparing them with specific tables (Baccelle and Bosellini, 1965; Matthew et al., 1991, cited in Flügel, 2010).

The petrographic thin section descriptions were combined with field observations, resulting in the characterization of the carbonate lithofacies and the exposure index presented in this study. The exposure index is a semiquantitative method designed to identify features of subaerial exposures and assign a relative temporal evolution to the observed pedogenic transformations. This approach is akin to methodologies employed by other researchers focusing on palustrine-dominated environments (e.g., Platt and Wright, 1992; Armenteros et al., 1997; Alonso-Zarza and Wright, 2010a).

### 3.3.4. U–Pb dating

U–Pb analyses were carried out at CEREGE, Aix-en-Provence, France, using an ESI 193nm excimer laser ablation system coupled to an Element XR SF-ICP-MS (more details of the parameters used can be found in Table S3.1). Calcitic components such as limestone micrite,

early diagenetic features, and late cements identified after petrographic characterization from six samples of the Pas de la Vache, Pas du Lièvre, and La Route profiles were analyzed distinctly on 30 and 100 µm-thick thin sections using a laser ablation spot size of 150 µm in diameter. After data processing, ages for each selected calcitic component were derived from Tera–Wasserburg diagrams obtained using the IsoplotR software (Vermeesch, 2018), and plotted in the Tera–Wasserburg space. WC1 was used as a primary standard to correct $^{238}U/^{206}Pb$ fractionation (Roberts et al., 2017) and AUG-B6 as a secondary standard (Pagel et al., 2018) to check for accuracy. Ages are quoted at a 95% confidence interval, including the propagation of systematic uncertainty of the standards per Horstwood et al. (2016).

Thirteen samples were selected for radiometric U–Pb dating based on the constituents observed in thin sections. Among these, only six samples (V-40, L-4, L-6, R-3, R-7, and R-55) exhibited adequate uranium and lead proportions for dating. Initial analyses were conducted directly on 30 µm-thick thin sections. Following these analyses, three samples (R-3, R-7, and R-55) were chosen for the preparation of thicker thin sections (100 µm-thickness). The obtained data underwent dendrogram analysis using Hierarchical Cluster Analysis (HCA) to group them based on similarities, considering both the determined ages and associated errors (utilizing standard correction error). Subsequently, the IsoplotR software was employed to calculate the weighted average (Vermeesch, 2018) for the groups determined by HCA.

### 3.3.5. SEM analysis

The scanning electron microscope (SEM) was used to comprehend the results obtained from carbonate dating using the U–Pb method. This instrument, known for its ability to generate highly magnified images with a good depth of field, can be used, among other applications, to analyze microtextural features of the matrix and cements in sedimentary rock samples (Welton, 1984). SEM analyses were conducted at the PRATIM Research Platform, Aix-Marseille University, using the Zeiss EVO 15 scanning electron microscope. The analyses were performed directly on the same three 100 µm-thick thin sections that were used for U–Pb dating. The thin sections, covered with gold, underwent analysis under high vacuum. Observations were conducted at an acceleration voltage of 15 kV, with a working distance of approximately 10 mm. SEM images were captured using the Secondary Electrons (SE1) imaging mode, generated by electron beams emitted from a heated LAB6 filament.

### 3.3.6. C and O stable isotopes

To obtain insights into lake base level variations and its paleohydrology, 262 powdered samples of the Cengle limestones were collected using a Dremel micro-drill. Subsequently, stable isotope analyses of carbon and oxygen in bulk rock were conducted at the GeoZentrum Nordbayern department, Friedrich-Alexander-Universität Erlangen-Nürnberg (Germany). This analytical approach involved reacting the powders with 100% phosphoric acid at 70°C using a Gasbench II connected to a ThermoFisher DELTA V Plus mass spectrometer. All values are reported per mil (‰) relative to the standard sample of belemnites known as VPDB (Vienna Pee Dee Belemnite) (Sharp, 2017; Hoefs, 2015). To ensure reproducibility and accuracy, replicate analyses of laboratory standards were conducted, calibrated by assigning $\delta^{13}C$ values of +1.95‰ to NBS19 and −47.3‰ to IAEA-CO9, and $\delta^{18}O$ values of −2.20‰ to NBS19 and −23.2‰ to NBS18. Reproducibility for $\delta^{13}C$ and $\delta^{18}O$ was ±0.04 and ±0.06 (1 standard deviation), respectively. Standard NBS 19 was additionally analyzed as a quality control sample.

## 3.4. Results and interpretations

### 3.4.1. Carbonate lithofacies

Eight distinct lithofacies were identified and grouped into three facies associations: lacustrine (Fig. 3.3), palustrine (Fig. 3.4 and Fig. 3.6), and pedogenic (Fig. 3.7). These lithofacies are described below (and summarized in Table 3.1).

#### 3.4.1.1. Lacustrine facies association (LC)

##### 3.4.1.1.1. *Microcodium*-bioclastic wackestone and packstone (LC-1)

Macroscopically, bioclastic wackestones and packstones are tight limestones exhibiting gray and beige hues (Fig. 3.3A). They are made of a densely packed dark micrite matrix encasing allochems whose proportions range from 15 to 65%. These rocks predominantly display a massive bedding structure, characterized by homogeneous layers (>10 cm thick) that lack internal sedimentary structures. In the thin section, the micrite presents a clotted appearance. Key allochems consist of *Microcodium* crystal fragments, with their proportion defining the microfacies as either wackestone or packstone. These fragments appear as disaggregated and reworked prismatic crystals, occasionally showing internal dissolution, measuring 45 to 100 µm in length, with a modal concentration between 60 and 70 µm. Up to 20% of additional grains comprise ostracod shells, both articulated and disarticulated, fragmented or intact; gastropod (Fig. 3.3B) and bivalve shell fragments; occasional clasts from longitudinal and cross sections of charophyte thalli (Fig. 3.3B) and gyrogonites (Fig. 3.3C). Scarce submillimeter-thick rootlet marks (Fig. 3.3D), filled with mosaic calcite cement occur.

*Interpretation:* The substantial micrite content suggests the formation of lithofacies LC-1 in a low-energy setting (Flügel, 2010). The fossil assemblage indicates typical lacustrine sedimentation (Gierlowski-Kordesch, 2010). *Microcodium* crystals originate within a pedogenic setting (Alonso-Zarza, 2003; Alonso-Zarza and Wright, 2010b; Flügel, 2010) and are transported to the lake as debris. *Microcodium* fragments originating from the coastal area exhibit abundance variations, reflecting various positions relative to the lake's shoreline. A higher content in *Microcodium* suggests deposition closer to the lake margins, while a lower proportion indicates sedimentation in a more distal area. The presence of charophytes points to deposition in an oligotrophic lacustrine environment with shallow, fresh to brackish waters (Flügel, 2010), especially in alkaline/calcium-rich lakes with clear waters (Scholle and Ulmer-Scholle, 2003). Subaquatic plants could be responsible for the observed rootlet marks.

##### 3.4.1.1.2. Intraclastic wackestone–packstone (LC-2)

The LC-2 facies corresponds to gray and beige intraclastic bioclastic wackestones and packstones. Descriptively, it closely resembles the LC-1 lithofacies, primarily differing in the presence of mud intraclasts. The mud intraclasts range from 10 to 60%, with sizes spanning from 100 µm to 2 mm. They display morphologies ranging from spherical to elongated, with angular to rounded contours. These intraclasts possess a clotted internal structure and, in some instances, exhibit irregular microbial coatings (Fig. 3.3E) resembling oncoids. Rare tubes of calcimicrobial filaments (measuring up to 100 µm in length and possessing submicrometric thickness, with dense micritic carbonate precipitation around their sheaths) were also observed. The most prevalent grains consist of fragmented and reworked prismatic crystals of

*Microcodium*, ranging from 10 to 45%. Fragments of charophyte stems, gyrogonites, ostracods, gastropods, and bivalves complete the fossil assemblage.

*Interpretation:* The lithofacies LC-2 signifies deposition in coastal lacustrine regions. Intraclasts are weakly consolidated fragments of penecontemporaneous carbonate sediments eroded by action of waves or currents in the coastal regions of the lake, often redeposited within the same depositional sequence (Scholle and Ulmer-Scholle, 2003). The presence of micrite, along with heterogeneity in intraclast sizes, and the occurrence of microbial coatings on some of them, suggests deposition in a low to moderate energy environment. The presence of coated grains and calcimicrobial filaments suggests microbial influence, likely originating from cyanobacteria (Scholle and Ulmer-Scholle, 2003; Flügel, 2010).

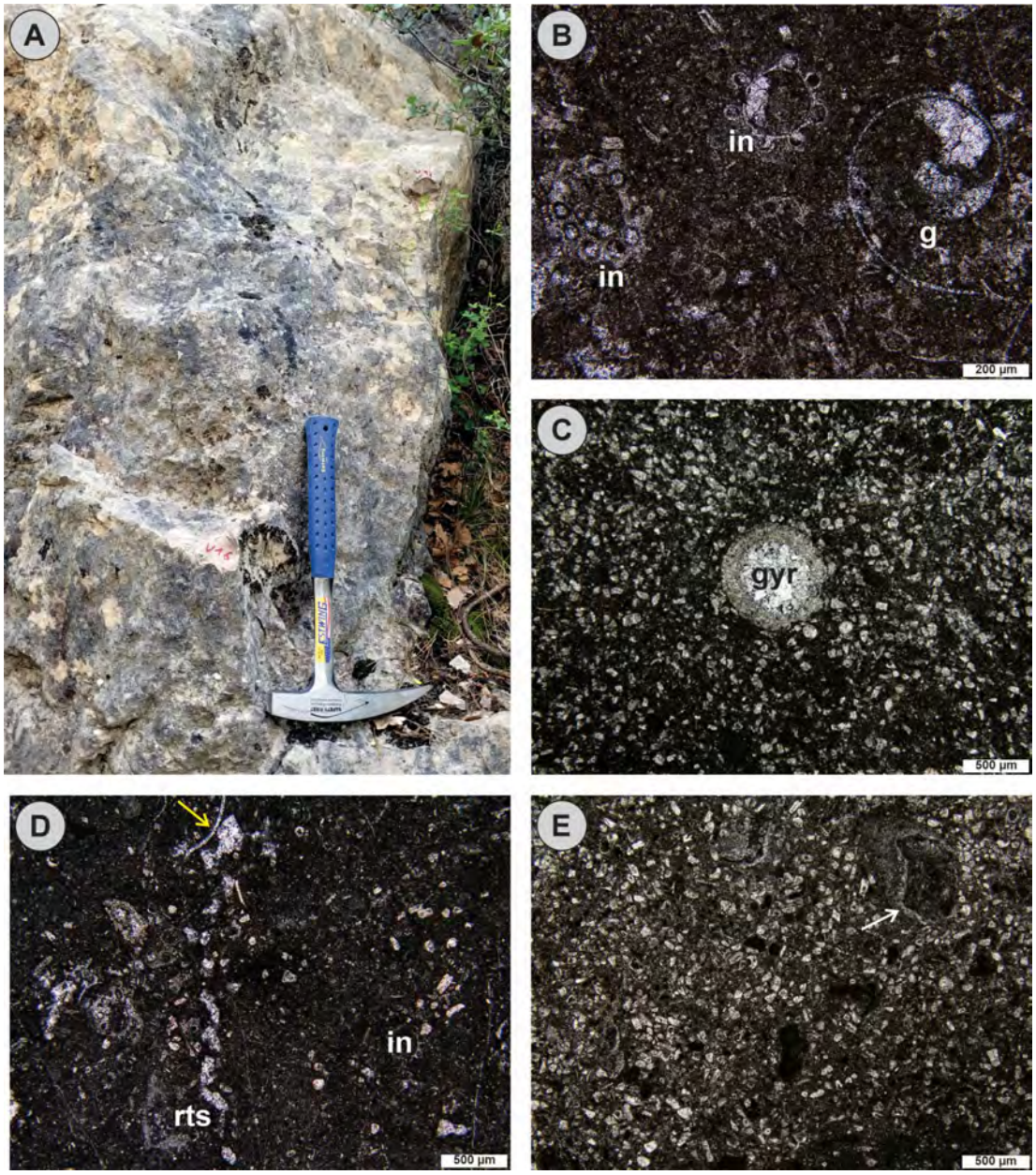


**Fig. 3.3**. Lacustrine facies association. A) Field view of facies LC-1 at Pas de la Vache outcrop. Hammer length measures 28 cm. B) Fossil assemblage commonly found in the lacustrine facies: Cross-section of an internode (in) of charophyte thallus revealing central and cortical cell cavities, along with a gastropod shell (g). C) Charophyte gyrogonite (gyr) embedded in bioclastic wackestone with *Microcodium* debris. D) Rootlet traces (rts) filled with calcite cement within facies LC-1. The yellow arrow indicates an ostracod carapace fragment. E) Intraclastic limestone (lithofacies LC-2) showcasing a wide range of intraclast sizes, including those with microbial coatings (white arrow). All photomicrographs were captured using parallel polarizers.

### 3.4.1.2. Palustrine facies association (PL)

#### 3.4.1.2.1. Cracked mottled limestones (PL-1)

The cracked mottled limestones (Fig. 3.4A) correspond to a palustrine lithofacies, exhibiting constant interfingering with lacustrine lithofacies. In the field, PL-1 is characterized by gray–beige–pink mottling, displaying indications of incipient subaerial exposure. In thin sections, this lithofacies appears as a bioclastic wackestone (occasionally packstone) with a densely compacted dark micritic matrix. Within this lithofacies, the same set of allochems observed in lacustrine lithofacies is identified. However, there is a noticeable reduction in *Microcodium* debris, rarely exceeding 40%, and an increase in the presence of charophyte fragments. In certain instances, these fragments can become the dominant bioclasts, reaching percentages of up to 20%. Better-preserved rosettes of *Microcodium* aggregates can be observed. The distinctive feature of this lithofacies is the presence of planar to irregular desiccation cracks (Fig. 3.4B), occasionally circumgranular, with submicrometric-thick filled by both mosaic calcite cement and microsparitic silt. Geopetal structures, such as cavities filled with vadose silt and sealed by blocky sparry calcite, are common, as well irregular cavities (dissolution vugs) of various sizes infilled with mosaic calcite spar. At the top of the section exposed in the Pas du Lièvre outcrop, benthic foraminifers of the genus *Rosalina* (Fig. 3.5) associated with these facies were identified in three samples. The foraminifers measure between 100 and 400 µm in length, featuring a hyaline test with a micritic coating.

*Interpretation:* Lithofacies PL-1 marks transitioning from a lacustrine to a palustrine environment. Alternating exposure and submergence give rise to features mirroring lake-level fluctuations and water table changes. Cracks result from desiccation processes caused by intermittent subaerial exposures (Armenteros et al., 1997; Alonso-Zarza and Wright, 2010a; Flügel, 2010). The mottled pattern indicates iron remobilization owing to changes in groundwater redox potential during water table oscillations (Freytet, 1973; Freytet and Plaziat, 1982), evident through globular halos in thin sections (Alonso-Zarza, 2003; Alonso-Zarza and Wright, 2010a). The presence of cavities with vadose silt characterizes the vadose diagenetic environment. Situated above the water table, between the land surface and the meteoric phreatic zone, this setting results in pores filled with fresh water and/or air (Flügel, 2010). In general, all diagenetic features are early and typical of the vadose environment, practically penecontemporaneous to deposition. Only calcite blocky cement might postdate slightly, forming in vadose or phreatic conditions (Flügel, 2010). Root and rootlet marks, highlight the impact of vegetation cover (Platt and Wright, 1992; Armenteros et al., 1997; Alonso-Zarza, 2003). The occurrence of benthic foraminifera likely indicates an increase in lake salinity during the late phase of Cengle limestone deposition. The genus *Rosalina* is a shallow-water benthic foraminifer, which is typically found in brackish water deposits (e.g., Le Calvez, 1970), either in marginal areas or in saline lakes.

#### 3.4.1.2.2. Nodular-brecciated limestones (PL-2)

The limestones of lithofacies PL-2 exhibit a macroscopic color range from beige to pink, occasionally displaying mottled patterns. These limestones are characterized by brecciated and nodular textures (Fig. 3.4C, E). The presence of centimetric angular fragments of the host rock identifies the brecciated texture. Conversely, in the nodular texture, the centimetric fragments assume rounded shapes. This lithofacies is commonly crosscut by columnar structures, which consist in vertical, massive, elongated and irregularly shaped carbonate tubes, that reach ≥50 cm in length. Under microscopic analysis, bioclastic wackestones with brecciated and nodular features can be identified. Submicrometric cracks filled with mosaic calcite cement and/or

microsparitic silt enclose millimeter to centimeter-sized clasts. Cracks in brecciated areas are irregular (Fig. 3.4D), while in nodular areas, they tend to be predominantly circumgranular (Fig. 3.4F). Importantly, no indications of clast displacement or rotation are observed. A transition from brecciated microfacies to nodular microfacies (often multiphasic – Fig. 3.4G) is evident. Globular halos (Fig. 3.4H) can also be seen in some thin sections. Despite a general trend toward a reduced proportion of bioclasts (<40%, commonly below 20%), it is still possible to identify the same fossils found within lacustrine facies, with *Microcodium* fragments being the most abundant. Additionally, lithofacies PL-2 exhibits irregular cavities of varying sizes, filled with mosaic sparry calcite, sometimes with silt at the bottom.

*Interpretation*: Nodulation initiates as a brecciated texture and evolves into a nodular texture, and results from repeated exposures induced by episodic fluctuations in the water levels of lakes undergoing intermittent desiccation (Armenteros et al., 1997; Flügel, 2010). The processes of shrinkage and expansion, driven by sediment desiccation and rewetting, typical of palustrine environments, generate cracks subsequently infilled under vadose and phreatic oxidizing conditions (Freytet, 1973; Armenteros et al., 1997; Alonso-Zarza and Wright, 2010a). According to Alonso-Zarza and Wright (2010a), these limestones may develop distinctive beds of metric thickness, indicating that the entire lacustrine succession experienced subaerial exposure during a single or multiple events. In other scenarios, only the upper or lower portion of the lacustrine deposit displays nodulation or brecciation, suggesting a shorter duration of subaerial exposure.

#### 3.4.1.2.3. Intraclastic packstone-grainstone (PL-3)

Lithofacies PL-3 comprises grainy limestones. This facies has been identified in only four samples. Macroscopically, it exhibits a color range from gray to beige, displaying a pseudo-oolitic texture (Fig. 3.6A). Microscopically, it is classified as intraclastic packstone and grainstone. Clasts are predominantly rounded (rarely elongated), resulting in a grainy texture to the facies, with sizes varying from very fine sand to very coarse sand, indicating poor sorting. The ‘grains’ possess well-defined micritized edges, and infrequently display microbial coatings. In certain situations, intraclasts are exclusively represented by a *Microcodium* crystal surrounded by a micritic coating (Fig. 3.6B). This characteristic highlights that this component has persisted as a resistant entity during the process of grainification. While most grains exhibit a clotted internal structure (descriptively considered as peloids), in larger grains, it becomes possible to discern that they originate from bioclastic wackestone, with discernible fragments of *Microcodium* crystals and charophytes. No other fossils were observed. Mosaic calcite cement occurs between the grains (Fig. 3.6B, C). Additionally, irregular cavities resembling fenestral pores are observed and filled with mosaic sparry calcite.

*Interpretation:* The presence of rounded intraclasts, micritized edges, grains with microbial coatings, poor sorting, fenestral structures, and desiccation cracks suggests the ‘grainification’ process as the origin of lithofacies PL-3. The term ‘grainification’ refers to the *in situ* formation of grainstones (Freytet and Plaziat, 1982; Mazzullo and Birdwell, 1989; Wright, 1990). This process resembles the one responsible for forming lithofacies PL-1 and PL-2, but is more advanced, transforming the entire lacustrine mud into ‘grains’. As discussed by Wright (1990) and illustrated by Freytet and Plaziat (1982), this process is characteristic of palustrine limestones, where cycles of wetting and drying, expansion and contraction, as well as bioturbation, generate clasts from lacustrine mud that gradually detach as they undergo rotation. Additionally, Mazzullo and Birdwell (1989) demonstrated that the development of fenestral fabric in micritic sediments, coupled with root and fungal activity, plays a significant role in ‘grainification’, with the resulting product being termed ‘diagenetic grainstones’ by them.

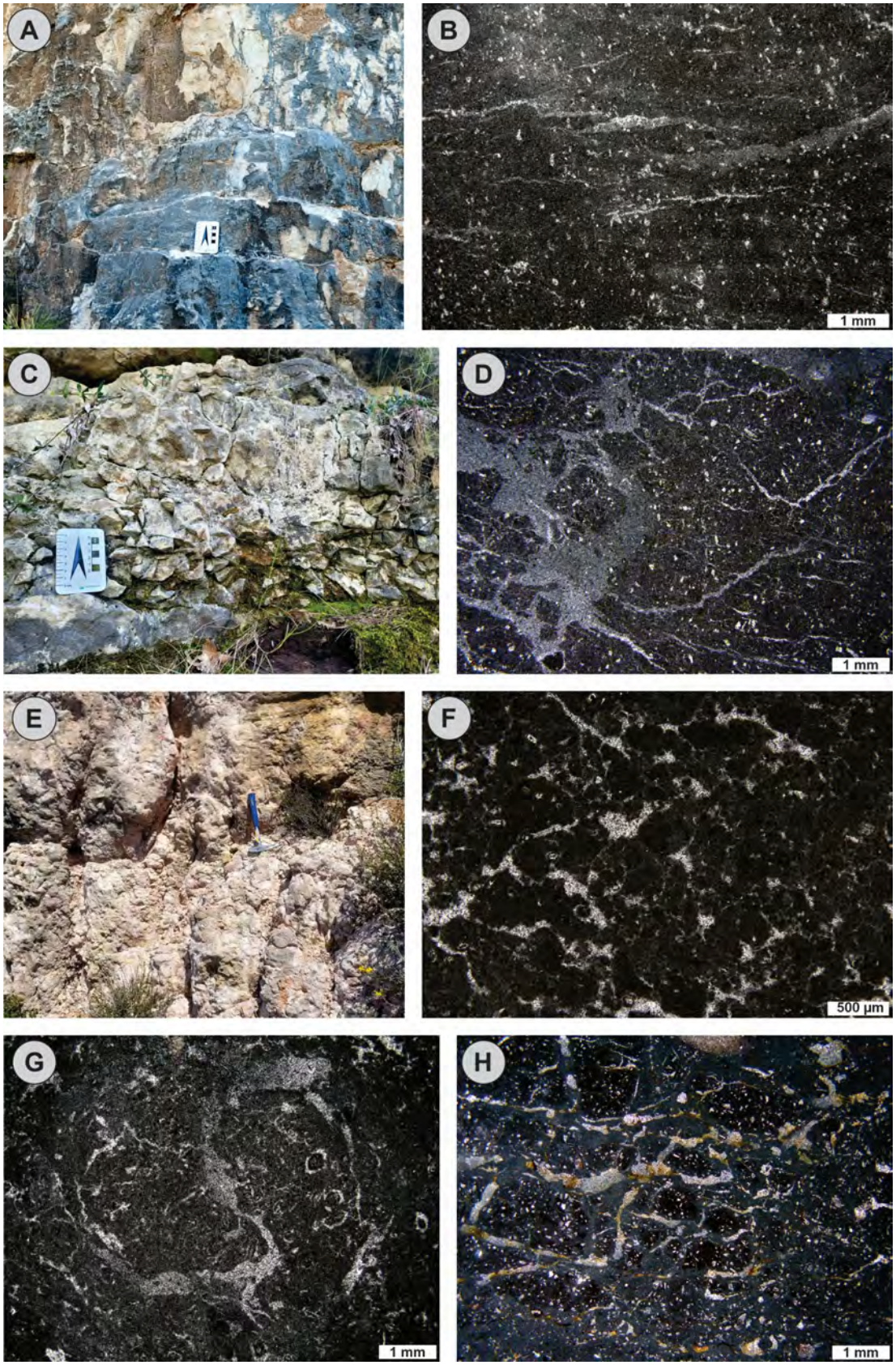


**Fig. 3.4.** Photographs illustrating palustrine facies PL-1 and PL-2. A) Lithofacies PL-1 at the Pas du Lièvre outcrop. B) Planar cracks within bioclastic wackestone, Facies PL-1. C) Brecciated PL-2 facies at the Pas de la Vache outcrop. D) Detailed view of the brecciated PL-2 facies, highlighting the contrast in angular clast size and silty material filling cracks. E) Nodular PL-2 facies observed at the Pas du Lièvre outcrop. Hammer length measures 28 cm. F) Circumgranular cracks within the nodular PL-2 facies. G) Multiphase nature of nodulation in lithofacies PL-2. H) Circumgranular cracks within lithofacies PL-2 showing globular halos and the presence of silty material in addition to cement filling the cracks. All photomicrographs were taken using parallel polarizers.

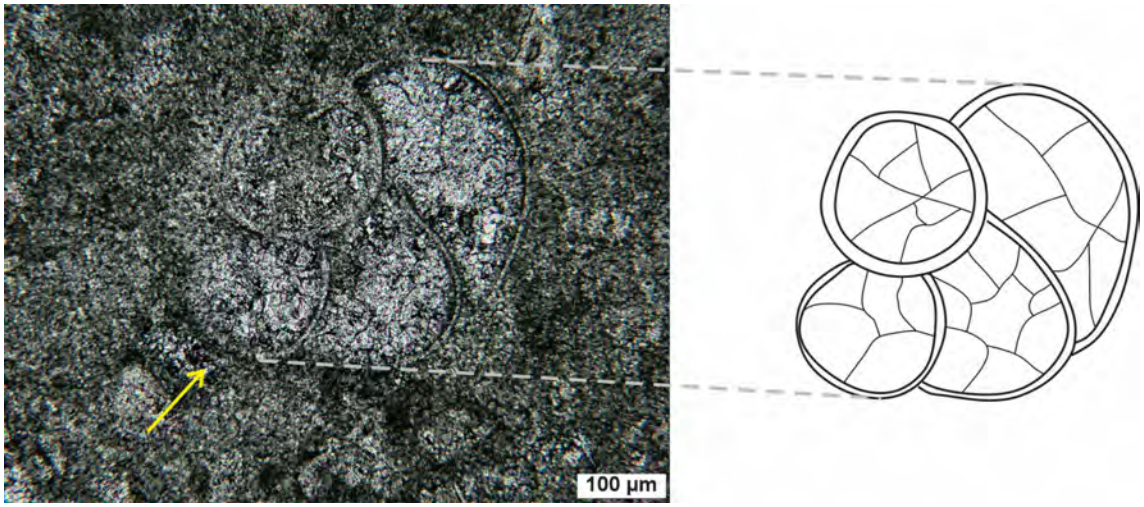


**Fig. 3.5.** Photomicrograph of benthic foraminifera (cf. *Rosalina*) (yellow arrow) in PL-1 lithofacies under parallel polarizers. This figure was originally published as supplementary material.

#### 3.4.1.2.4. Pseudomicrokarstic limestones (PL-4)

Pseudomicrokarstic limestones correspond to lithofacies PL-4. Macroscopically, these limestones exhibit a mottled gray-reddish tonality, reminiscent of breccias (Fig. 3.6D), albeit with restricted spatial distribution. This lithofacies is commonly associated with surfaces with more prominent subaerial exposure. When observed in thin sections, such materials reveal themselves as brecciated intraclastic bioclastic wackestones, featuring cavities visible to the naked eye (with dimensions of up to 10 mm in width), which are filled with diverse materials (Fig. 3.6D, E). Aside from micrite, the predominant constituent within the host rock comprises disintegrated prism-shaped crystals of *Microcodium*, the proportion of which may vary between 5% and 50%. Some better-preserved *Microcodium* rosettes are present. In certain thin sections, fragments of charophytes, ostracods, and mollusks (both bivalves and gastropods) have also been identified. The intraclasts, composed of mudstone fragments and bioclastic wackestone, can constitute up to 20% of the thin sections. They possess subangular to subrounded contours, with lengths of up to 3 mm, with some displaying microbial or micritic coating. This phenomenon imparts a granular aspect to the rock in specific regions. Concerning the cavities, these are distributed throughout the matrix and may contain rounded intraclasts and silty material (Fig. 3.6F) and are also cemented by coarse mosaic calcite crystals, reaching lengths of up to 500 µm.

*Interpretation:* The origin of pseudomicrokarst is related to the colonization of mud by long-rooted grass, which was recently exposed, and its subsequent evolution into a complex facies resulting from various stages of dissolution and void infillings (Freytet and Verrecchia, 2002). This facies has been recognized in palustrine and pedogenic profiles since the work of Plaziat and Freytet (1978), who employed this term to describe limestones with irregular and complex cavities resembling a karstic system, in which the cavities are predominantly small, mostly cylindrical, and vertically elongated. As Alonso-Zarza and Wright (2010a) discussed, the prefix ‘pseudo’ is used because cavity enlargement primarily occurs through mechanical processes resulting from root action and desiccation; dissolution is a secondary factor. The cavities exhibit sharp boundaries and generally display highly irregular forms, although rounded edges indicating some dissolution contribution may also be observed. According to the observations of Freytet and Plaziat (1982), cavity infillings are complex and include peloids, coated grains, and intraclasts, as well as various types of cement, ranging from vadose to coarser blocky forms.

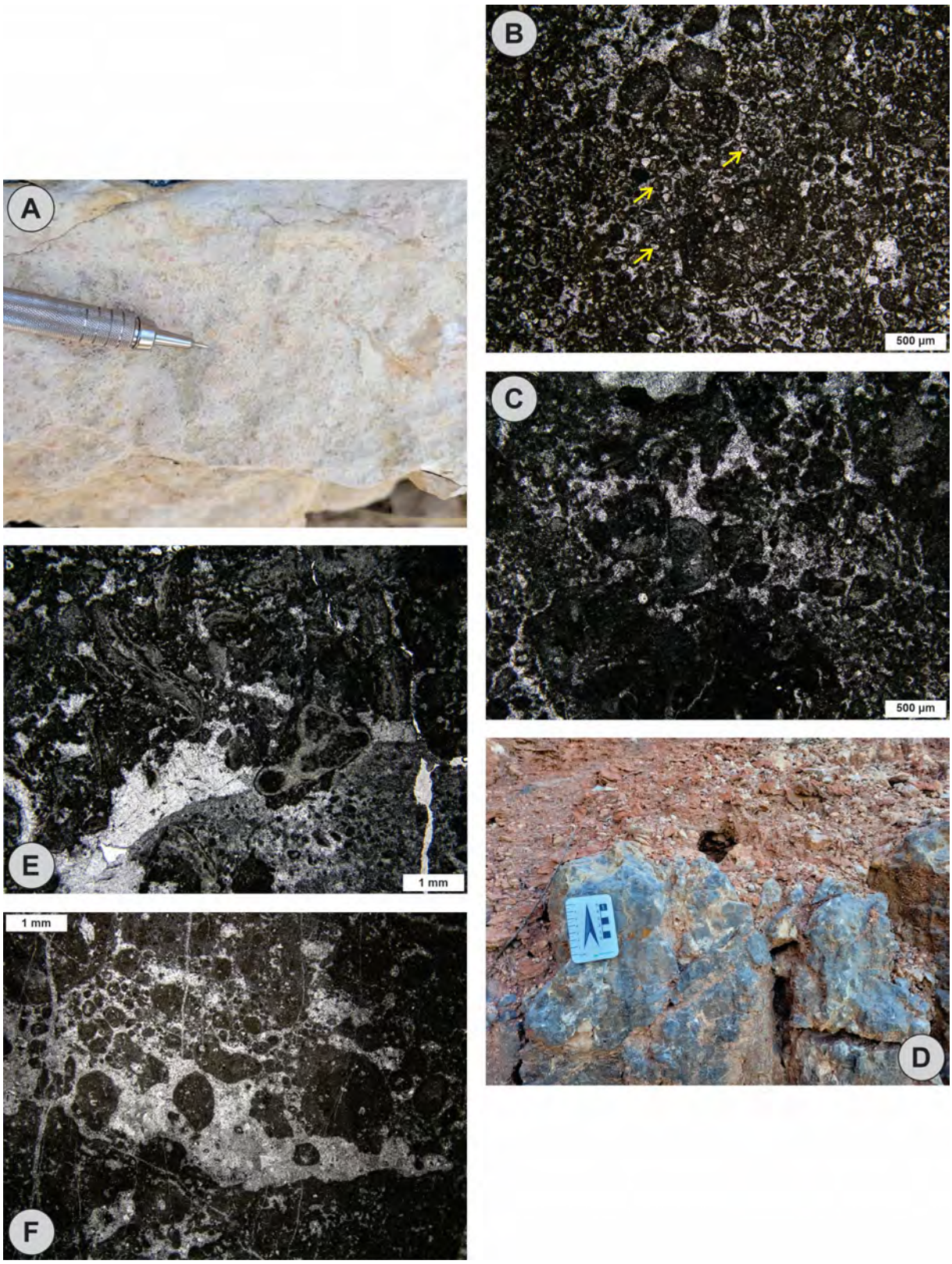


**Fig. 3.6.** Palustrine facies PL-3 and PL-4. A) Lithofacies PL-3 at the Pas de Monsieur outcrop. The pencil tip is 5 mm for scale. B) Thin section of intraclastic packstone-grainstone (PL-3). Note the wide range of grain sizes and the calcite cement filling all interparticle spaces. Yellow arrows indicate intraclasts composed of isolated single-crystal of *Microcodium* with micritic coating. C) Detail of lithofacies PL-3, intraclastic packstone–grainstone. D) Lithofacies PL-4 at the Pas du Lièvre outcrop, showing the contact between carbonate and a thin soil cover. The irregular contact is due to pseudomicrokarst features. E) Facies PL-4. Diverse components, including cements, peloids, intraclasts, and enveloped grains, with cavity-filling. F) Pseudomicrokarst filled with mud intraclasts, silty material, and coarse mosaic calcite cement. All photomicrographs were captured using parallel polarizers.

### 3.4.1.3. Pedogenic facies association (PD)

#### 3.4.1.3.1. Pisolithic mottled intraclastic limestones (PD-1)

Lithofacies PD-1 (Fig. 3.7A-C) is characterized by pisoliths within gray–red–pink mottled intraclastic limestones. The rock displays an overall nodular texture, with occurrences of intraclasts of varying sizes embedded in a matrix ranging from bioclastic wackestone to packstone, occasionally brecciated. The intraclasts display sizes that range from very fine sand to very coarse sand, with a preference for a spherical shape (sometimes elongated) and feature a clotted internal structure. A significant aspect of this facies is the individualization and rotation of specific intraclasts, irregularly coated with microbial material, larger than 1 mm, resulting in the formation of pisoids. In portions dominated by pisoids, mosaic calcite cement filling interparticle spaces is conceivable. Alongside circumgranular cracks, irregular cavities are frequently encountered and filled with vadose silt, and the prevalence of sparry calcite in mosaic patterns and pseudomicrokarst is notable. Within the host rock matrix, disintegrated prismatic *Microcodium* crystals are identified, varying in abundance from 15% to 40%, along with fragments of charophytes that can constitute up to 10%, and traces (<1%) of gyrogonites, ostracods (including intact specimens), gastropods, and bivalves.

*Interpretation:* The mottled appearance, combined with a matrix containing materials of varying dimensions and compositions, along with the presence of pisoids, indicates that facies PD-1 typically results from pedogenic processes, displaying inherent similarities with the alpha (non-biogenic influence) and beta (biogenic influence) caliche fabrics, as documented by Alonso-Zarza and Wright (2010b). The pisoids identified within lithofacies PD-1 align with the description of ‘caliche pisoids’ presented by Flügel (2010). According to Flügel (2010), ‘caliche pisoids’ originate in situ, exhibiting dimensions ranging from approximately 2 mm to several centimeters. They often exhibit weak or faint laminae with varying thickness and alternating light and dark layers. These pisoids are frequently observed to possess a clotted peloidal texture and a mud-supported fabric.

#### 3.4.1.3.2. Microcodium mottled limestones (PD-2)

The PD-2 facies (Fig. 3.7D, E) is characterized by a bioclastic wackestone, notably featuring well-preserved *Microcodium* aggregates. In the field, they are represented by their mottled gray–red–pink appearance. The distinctive hallmark of this facies is the presence of these *Microcodium* aggregates, which appear to be either *in situ* or in immediate proximity to their site of formation. The host rock is identified as a bioclastic *Microcodium* wackestone or packstone, exhibiting a clotted matrix appearance. Within this matrix, disintegrated prismatic *Microcodium* crystals constitute 15% to 40% of its composition, as in other lacustrine and palustrine facies associations. Some samples display fragments of charophytes, ostracods, gastropods, and bivalves. Irregular cavities filled with vadose silt and mosaic calcite cement are present. The well-preserved *Microcodium* aggregates exhibit lamellar or rosette forms, resembling types I (‘corn-cob’) and II (‘lamellar’) as defined by Bodergat (1974). The prismatic calcite crystals are elongated in these cases, with dimensions ranging from 0.2 to 1 mm in length and 0.03 to 0.1 mm in width. The cutting orientation influences the morphology of the aggregates. Type I aggregates, known as ‘corn-cob’, can adopt a rosette configuration when cross-sectioned or a lamellar form when longitudinally sectioned. Well-preserved aggregates may occupy fractures or cavities (in these instances, the host rock generally exhibits breccias, pseudokarsts and occasionally a granular texture due to ‘grainification’) associated with exposure surfaces or embedded within the host rock matrix (see Fig. 3.8 for a comparative

analysis of the various *Microcodium* morphologies identified in the carbonates of the study area).

At the La Route outcrop associated with this facies, a discontinuous layer (Fig. 3.7F) approximately 30 cm thick is present, showcasing two distinct features. The first corresponds to a crust (Fig. 3.7G) of crystalline limestone. Petrographic analysis reveals the presence of rhombic (which predominate) and lamellar crystals, exhibiting diverse granulation patterns of calcite. The rhombic crystals range in size from 0.2 to 1.3 mm in length and 0.2 to 0.4 mm in width. The lamellar crystals have dimensions ranging from 0.7 to 2 mm in length and 0.05 to 0.15 mm in width. The porosity within this lithology is notably high, of the intercrystalline type, at approximately 30%. The second feature also pertains to a crystalline limestone; however, this one is a product of intense substitution by granular calcite crystals, measuring around 0.05 mm in diameter. Small areas with preserved original protolith display a mudstone containing calcitic pseudomorphs after gypsum (Fig. 3.7H). These pseudomorphs adopt diamond-shaped forms and have a length of approximately 0.2 mm.

*Interpretation:* In lithofacies PD-2, the well-preserved *Microcodium* crystals predominate. According to Flügel (2010), the morphology of calcite crystals within the *Microcodium*, characterized by elongated, radiating, petal-like elements clustered in ring-like structures, suggests the influence of a meteorically influenced environment, such as that found in paleosols. This feature serves as an indicator for identifying continental conditions and subaerial exposure. Despite being a common element in caliches and having been studied since the early 20$^{th}$ century, the origin of *Microcodium* remains controversial. Its origin has been correlated with algae, roots, fungi, microbes, and even diagenesis (inorganic origin), as presented by Esteban (1974). Flügel (2010) presents a comprehensive interpretation of *Microcodium*, considering it as '*calcified mycorrhizae, a symbiotic association between soil fungi and cortical cells of plant roots, or as bacteria or algae'*.

Regarding the crystalline limestone crust, due to its association with a subaerial exposure surface and pedogenic processes, it is plausible that it represents crusts that were originally composed of *Microcodium* crystals (Type II, according to Bodergat, 1974), which were subsequently dissolved and replaced by rhombohedral and lamellar calcite crystals. This mineralogical substitution may be a contributing factor to the observed high porosity. Furthermore, calcitic pseudomorphs after gypsum indicate that pedogenesis occurred in an arid to semi-arid, evaporitic setting.

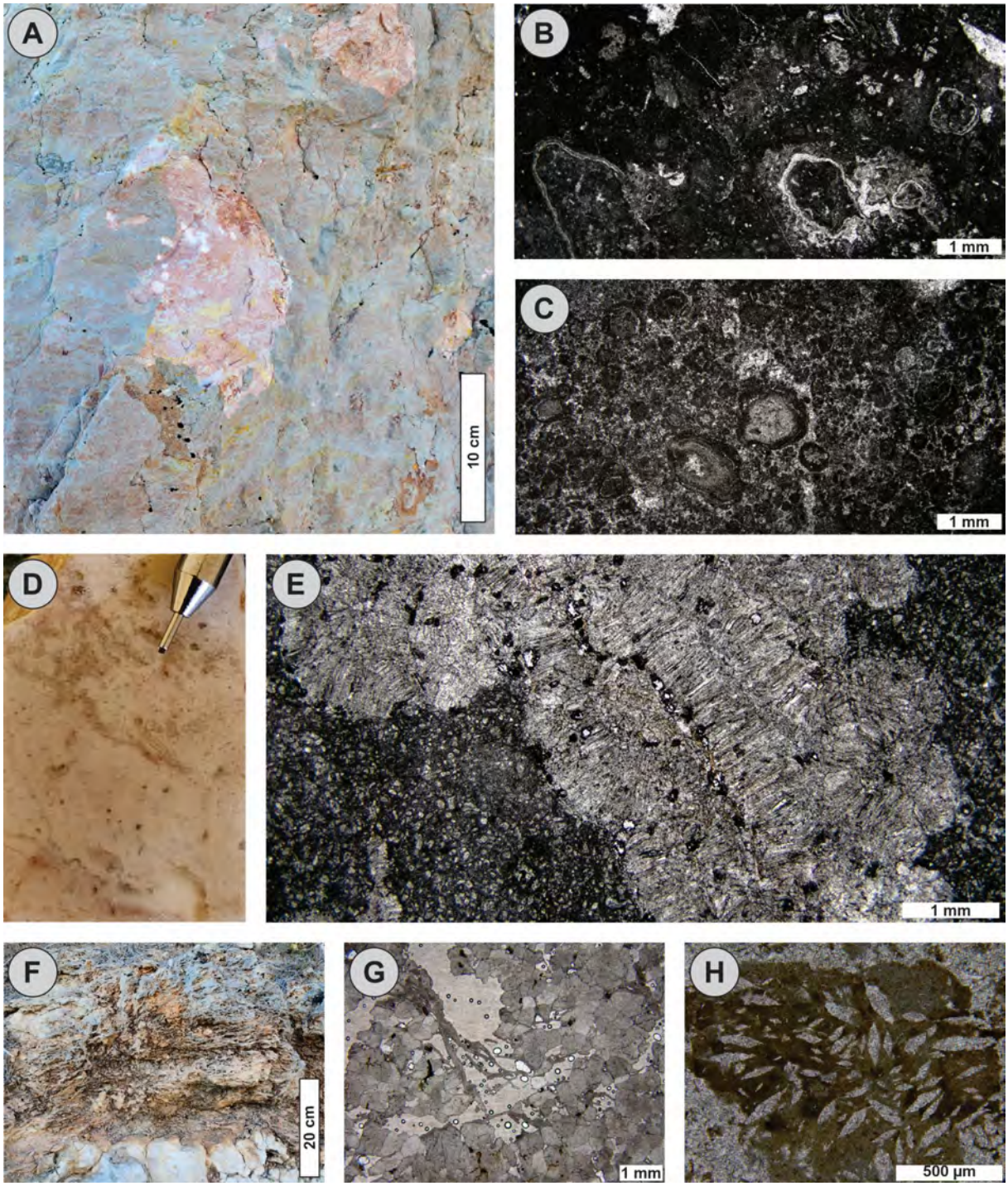


**Fig. 3.7.** Pedogenic facies association. A) Macroscopic photograph of lithofacies PD-1 at La Route outcrop. B–C) Photomicrographs of facies PD-1. Note the presence of materials of various sizes and pisoids with microbial coatings. D) Macroscopic sample of facies PD-2. The darker material indicated by the pencil corresponds to *Microcodium* aggregates. The pencil tip provides a scale reference of 0.5 mm. E) Detail of a *Microcodium* aggregate from facies PD-2. Observe how crystals develop within the mud matrix. F) Crystalline limestone crust containing rhombohedral and lamellar calcite crystals (G), as well as calcite pseudomorphs after gypsum (H). All thin-section photographs were captured using parallel polarizers.

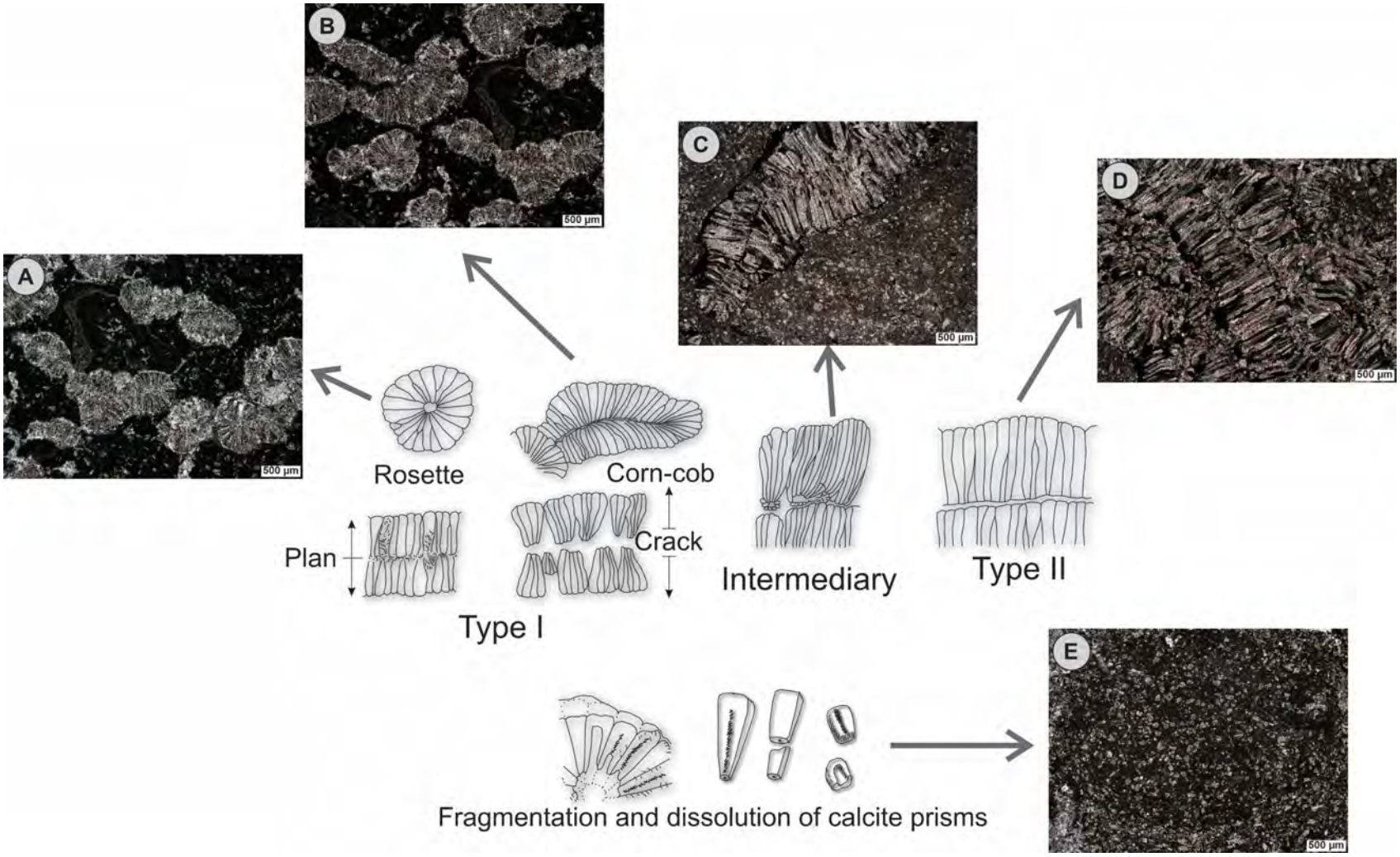


**Fig. 3.8.** *Microcodium* morphologies found in Cengle limestones. Sketch after Plaziat (1984) with examples from the study area. The photomicrographs depict the prevalence of rosette-like aggregates (A); transverse and longitudinal sections (B) showcasing type I, commonly referred to as "corn-cob" morphology; an intermediate morphology bridging between types I and II (C); and type II morphology, often described as "lamellar" (D). E) Remnants of *Microcodium* crystals displaying fragmentation and partial dissolution within calcite prisms in mud-supported facies. Photomicrographs in A, B, and E were captured using parallel polarizers, while those in C and D were taken using crossed polarizers. This figure was originally published as supplementary material.

**Table 3.1.** Lithofacies summary for Cengle Plateau cliff limestones. This table was originally published as supplementary material.

| Facies Association | Lithofacies | Fossils and dominant components | Dominant features | Subordinate features | Process and paleoenviromental interpretation |
|---|---|---|---|---|---|
| Lacustrine (LC) | LC-1: *Microcodium*-bioclastic wackestone and packstone | Density packed dark micrite matrix; *Microcodium* crystal debris; ostracod, gastropod, bivalve and charophyte fragments | Massive bedding structure | Rootlets marks; stylolites; submillimeter fractures enveloped by brown material (iron oxides) | Shallow low-energy lake deposition; abundance of *microcodium* fragments reflects distance from the lake's shoreline |
| | LC-2: Intraclastic wackestone–packstone | Density packed dark micrite matrix; Mud intraclasts; *Microcodium* crystal debris; charophyte, ostracod, gastropod and bivalve fragments; calcimicrobial filaments | Massive bedding structure | Partially recrystallized matrix | Low to moderate-energy lake shore deposition with microbial influence |
| Palustrine (PL) | PL-1: Cracked mottled limestones | Density packed dark micrite matrix; *Microcodium* crystal and charophyte debris; ostracod, gastropod and bivalve fragments; benthic foraminifers | Mottling; planar to irregular desiccation cracks; vadose silt; fenestral/vugular porosity filled with mosaic sparry calcite; rootlets and root marks | Globular halos; rootlets and root marks | Alternating conditions of exposure and lacustrine submersion in a vadose diagenetic environment |
| | PL-2: Nodular-brecciated limestones | Angular to rounded fragments of the host rock; *Microcodium* crystal, charophyte, ostracod, gastropod and bivalve fragments | Brecciated and nodular textures; circumgranular cracks, globular halos; irregular cavities filled with mosaic sparry calcite | Small brown/red amorphous spots (iron oxide); traces (<1%) of very fine sand-sized angular quartz grains | Sediment shrinkage and expansion processes induced by episodic fluctuations in the water levels of lakes in a palustrine environment |

**Table 3.1.** Lithofacies summary for Cengle Plateau cliff limestones (continuation). This table was originally published as supplementary material.

| Facies Association | Lithofacies | Fossils and dominant components | Dominant features | Subordinate features | Process and paleoenviromental interpretation |
|---|---|---|---|---|---|
| Palustrine (PL) | PL-3: Intraclastic packstone–grainstone | Rounded mud clasts, sometimes with micritized edges and microbial coatings; rare fragments of *Microcodium* and charophytes | Granular texture; irregular cavities filled with mosaic sparry calcite; planar, irregular and circumgranular cracks | Brown/red material (small spots and around the grains); planar, irregular, and circumgranular cracks filled with mosaic calcite cement | Grainification process (*in situ* formation of grainstones by cycles of wetting and drying) in a palustrine environment |
| | PL-4: Pseudomicrokarstic limestones | Subangular to subrounded intraclasts; M*icrocodium* fragments; well-preserved *Microcodium* rosettes; rare fragments of charophytes, ostracods, bilvalves and gastropods | Abundant cavities filled with different materials (mud intraclasts, silt and coarse cements) | Irregular to circumgranular submicrometric fractures; root marks filled with fine-grained mosaic calcite cement; partially recrystallized/neomorphized matrix | Cavity enlargement due to mechanical processes resulting from root action and desiccation in a palustrine environment |
| Pedogenic (PD) | PD-1: Pisolithic mottled intraclastic limestones | Pisoliths with microbial coating; intraclasts; rare fragments of *Microcodium* crystals, charophytes, ostracods, gastropods and bilvalves | Mottling; nodular texture; interparticle porosity filled by mosaic calcite cement; circumgranular cracks; irregular cavities filled with vadose silt and mosaic sparry calcite; pseudomicrokarst | Root marks filled with fine-grained mosaic calcite cement; recrystallized/neomorphized matrix | In situ origin 'caliche pisoids' with microbial influence. Advanced stage of pedogenesis in a pedogenic environment (paleosol) |
| | PD-2: *Microcodium* mottled limestones | Well-preserved *Microcodium* aggregates (rosette, 'corn-cob' and lammelar configurations); microcodium crystal debris, rare fragments of charophytes, ostracods, gastropods, and bivalves | Mottling; irregular cavities filled with vadose silt and mosaic sparry calcite; pseudokarst | irregular to circumgranular cracks; clotted, brecciated and granular textures | In situ origin of *Microcodium* by symbiotic association between soil fungi and cortical cells of plant roots, or as bacteria or algae. Advanced stage of pedogenesis in a pedogenic environment (paleosol) |

### 3.4.2. Exposure index and vertical stacking pattern of sequences

#### 3.4.2.1. Exposure index

Based on a thorough analysis of facies, an Exposure Index (EI) for the carbonates found within the Cengle Plateau cliff was introduced in order to identify and characterize various types and orders of vertical stacking patterns. Fig. 3.9 presents a schematic and idealized vertical facies profile, highlighting the facies and microstructures representative of the developed Exposure Index. This index ranges from zero to five, with higher values signifying a more pronounced intensity of pedogenesis. The profile is schematic in nature, representing a trend in pedogenesis evolution.

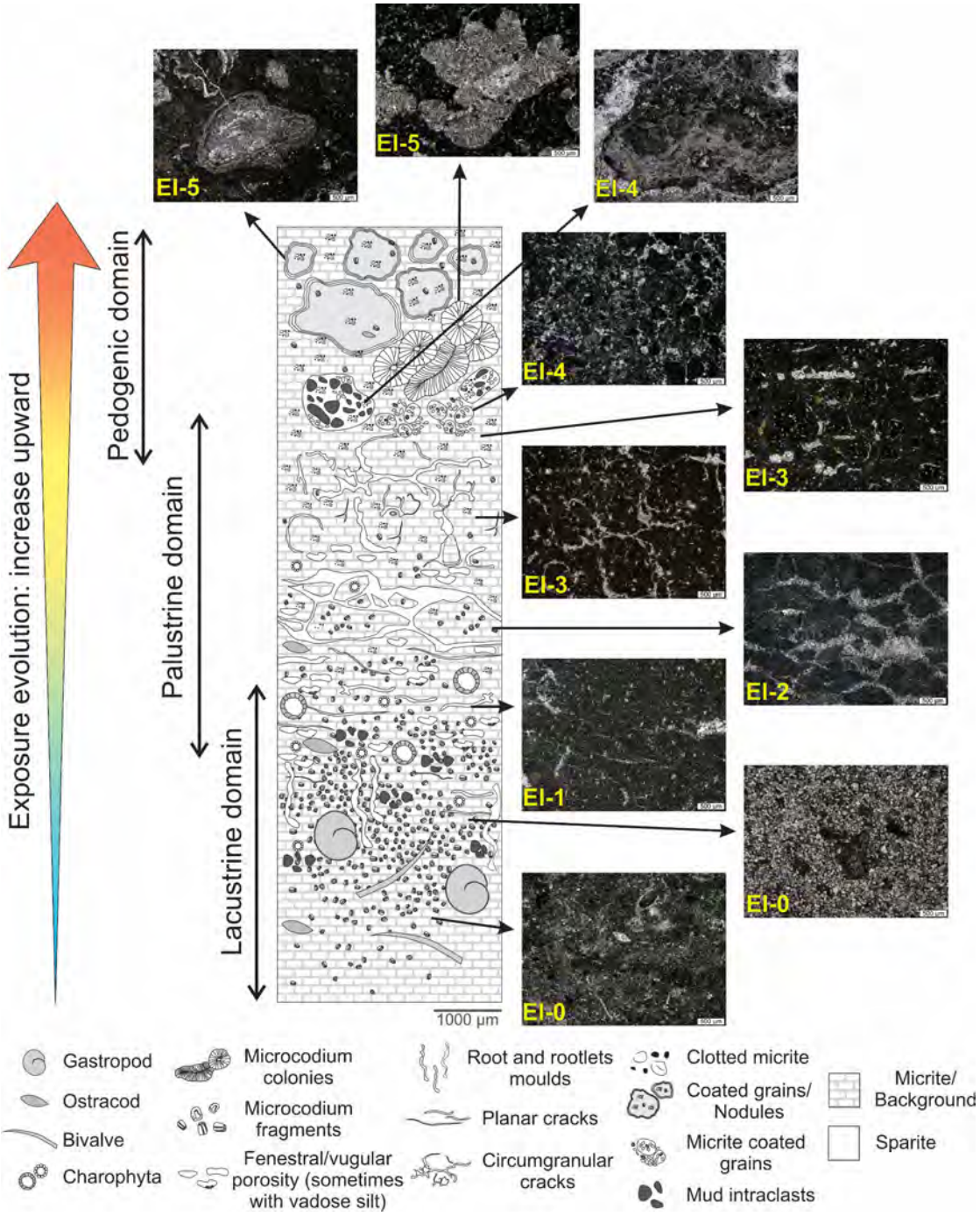


**Fig. 3.9.** Schematic vertical facies profile with Exposure Index (EI) for pedogenesis in the study area. EI-0: no exposure, lacustrine facies (LC-1 and LC-2). EI-1: Initial exposure, PL-1 facies. EI-2: Brecciated PL-2 facies. EI-3: Nodular PL-2 facies. EI-4: Further evolved palustrine facies, PL-3 and PL-4. EI-5: Pedogenic facies (PD-1 and PD-2).

The Exposure Index values are associated with the following meaning:

**EI-0:** The zero index indicates the absence of exposure features and is typified by facies LC-1 and LC-2, characteristic of the lacustrine environment. The more distal lacustrine facies are encountered at the base of the profile, represented by bioclastic wackstones with a lower proportion of bioclasts from the lake's border. Progressing upward, the more proximal lacustrine facies are primarily denoted by bioclastic packstones, featuring a considerably higher percentage of *Microcodium* crystal debris.

**EI-1:** Index one is distinguished by incipient exposure features and is embodied by the PL-1 facies, marked by horizontal cracks, often exhibiting a mottled pattern.

**EI-2 and EI-3:** Indices two and three are characterized by palustrine facies PL-2. Brecciated textures denote index two, while the nodular texture hallmarks index three. Both features are generated by the drying and wetting process experienced by sediments under subaerial exposure.

**EI-4:** Index four is typified by facies PL-3 and PL-4. Within palustrine facies, these indices encompass the more advanced facies transitioning into the pedogenic domain.

**EI-5:** Finally, exposure index five includes pedogenic facies, either PD-1 or PD-2. These facies exhibit characteristics akin to those observed in paleosols and signify the most advanced stages of pedogenesis in the study area.

#### 3.4.2.2. Vertical stacking pattern of sequences

Vertical stacking patterns ultimately result from repetitive base level changes operating on different frequencies (Barrell, 1917; Magalhães et al., 2020; Fragoso et al., 2021), with lower hierarchies imposing constraints on the higher ones. At least four frequencies of cyclicity that leave distinct marks on the rocks of the study area were identified:

i) Very high-frequency cyclicity: refers to seasonal cyclicity, responsible for the transition from lacustrine to palustrine facies on the lake margins due to very short-term subaerial exposures. As this is a continuous process, it does not result in easily discernible surfaces;

ii) High-frequency cyclicity: corresponds to cyclicity responsible for the vertical organization into sequences on a decimeter-to-meter scale (see Fig. 3.10). These sequences are marked by horizontal discontinuities representing stratigraphic surfaces formed during short-term subaerial exposures;

iii) Medium-frequency cyclicity: this cyclicity is responsible for the formation of sequences that are correlatable over the entire extent of the studied cliff (numbers 1, 2, and 3 in Fig. 3.10). These sequences have an average thickness of 10 m and are bounded by exposure surfaces generated due to long-term subaerial exposures; and

iv) Low-frequency cyclicity: corresponds to the deposition of the entire set of palustrine-dominated carbonates composing the cliff of the Cengle Plateau. This cyclicity is responsible for maintaining favorable environmental conditions for carbonate deposition.

In the context of Sequence Stratigraphy, high- and medium-frequency cyclicities are responsible for generating sequences, in line with the Catuneanu and Zecchin (2013) concept, in which sequences are defined as cycles of changes in stratal stacking patterns, categorized into system tracts and delineated by sequence stratigraphic surfaces. Therefore, the following sections will detail the different vertical stacking pattern sequences associated with these two frequencies.

Within these vertical stacking pattern sequences, two critical surfaces, namely, the Maximum Retraction Surface (MRS) and the Maximum Expansion Surface (MES), as used by Fragoso et al. (2023), have been observed. These surfaces correspond to surfaces of maximum regression and maximum flooding in the marine realm, adapted to the lacustrine environment. The MRS, often associated with subaerial exposure, has been utilized as the sequence boundary.

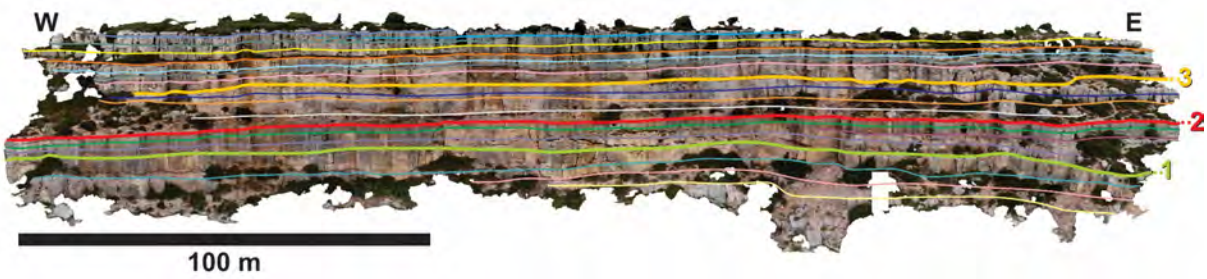


**Fig. 3.10.** Pas du Lièvre DOM illustrates the organization of cyclicity in the study area. The colored lines correspond to the sequence boundaries of the sequences. The numbers 1, 2 and 3 correspond to the surfaces that could be traced along the entire cliff of the Cengle Plateau. The other surfaces have variable mappability, ranging from tens of meters to a kilometer. This figure was originally published as supplementary material.

#### 3.4.2.2.1. High-frequency vertical stacking patterns

The products generated by very high-frequency cyclicity are stacked in high-frequency sequences, which correspond to 'elementary sequences' in line with Strasser et al. (1999) and Strasser (2018). These authors define elementary sequences as the shortest units wherein facies evolution indicates environmental change. This study identified five distinct patterns of elementary sequences (Fig. 3.11), listed below. These patterns encompass two distinct anatomies: i) transgressive–regressive (T–R) sequences, which consist of symmetrical sequences; and ii) regressive (R) sequences, corresponding to asymmetrical sequences (Zecchin, 2007; Catuneanu and Zecchin, 2013; Fragoso et al., 2021).

##### 3.4.2.2.1.1. Lacustrine *T-R* sequences

The first elementary sequence identified within the study area is the lacustrine *T–R* sequence (Fig. 3.11A). This sequence is notable for its exclusive lacustrine deposits (LC facies association), comprising both more distal facies, indicative of the transgressive hemi-cycle, and shallowing upward, proximal facies, representing the regressive hemi-cycle. This vertical stacking pattern is observed in only 7% of the sequences within the Cengle plateau cliff and was specifically identified in the Pas de la Vache (22% of the sequences) and Pas de Monsieur (14% of the sequences) outcrops. Within this configuration, it is possible to discern both the MES, demarcating the transition from a retrogradational stacking pattern to a progradational pattern, and the MRS, signifying the shift from a progradational stacking pattern to a retrogradational one.

*Interpretation:* The lacustrine *T–R* sequence originates in a lacustrine environment, with the stacking pattern reflecting a complete cycle of lake level variation without subaerial exposure. This stacking pattern suggests formation in a region located relatively far from the lake edge, which experiences reduced susceptibility to very high-frequency lake level fluctuations in comparison to the coastal regions of the lacustrine system. Consequently, as a result of greater available space for sedimentation, enhanced potential for preservation and hierarchical stratigraphic control, the rocks formed and preserved in this environmental position tend to exhibit greater thickness.

#### 3.4.2.2.1.2. Lacustrine–palustrine *R* sequences

The lacustrine–palustrine *R* sequences, as illustrated in Fig. 3.11B, are characterized by the coexistence of both lacustrine and palustrine facies. Within this framework, proximal lacustrine facies (LC-1 and LC-2) are overlain by palustrine facies, primarily PL-1. The tops of the sequences are limited by the MRS, marked by subaerial exposure features corresponding to EI 2 or 3. This variant accounts for 13% of the identified sequences in the study area, constituting 45% of the sequences observed in the Pas de la Vache outcrop, 7% in the Pas de Monsieur, and 10% in the Pas du Lièvre. This configuration was not observed in the La Route outcrop.

*Interpretation:* The lacustrine–palustrine *R* sequences represent upward-shoaling cycles (progradational stacking pattern), composed of lacustrine and palustrine facies. The effect of very high-frequency drops in the lake level affecting the sediment surface in the upper part of the sequence by very short-term subaerial exposure leads to the development of palustrine facies. This characteristic allows for the interpretation of sedimentation in a shallow proximal environment. The high-frequency lake level drop generates the MRS, delineating the elementary sequence boundary and leading to the development of more evolved exposure features compared to those present in the palustrine facies at the top of the sequence.

#### 3.4.2.2.1.3. Palustrine *R* sequences

The palustrine *R* sequences (Fig. 3.11C) consist of vertical stacks composed exclusively of palustrine facies (PL-1 to PL-4). This stacking pattern predominates (55% of the total number of interpreted sequences) in the study area and has been identified in all four analyzed outcrops (33% in the Pas de la Vache, 57% in the Pas de Monsieur, 75% in the Pas du Lièvre, and 33% in La Route). Sometimes, a sequence may consist of a single palustrine lithofacies, such as PL-2. These sequences are bounded by the MRS, associated with subaerial exposure features corresponding to EI 3 or 4.

*Interpretation:* Palustrine *R* sequences also represent upward-shoaling cycles composed solely of palustrine facies. The MRS that delimits the sequences is generated by high-frequency base level drops, resulting in short-term subaerial exposures. At this point, the subaerial exposure develops nodular, grainy, and pseudomicrokarst features. When two such sequences overlap, the MES is not distinguishable, but it is adjacent to the MRS. In order to form subaqueous facies over subaerial exposure features, it is necessary to have created space for deposition. Thus, the MES indicates the rise in the lake level and marks a shift in the shoreline of the lake.

#### 3.4.2.2.1.4. Palustrine–pedogenic sequences

Palustrine–pedogenic sequences (Fig. 3.11D) can be identified by the presence of palustrine facies (PL-2 to PL-4) overlain by pedogenic facies (PD-1 and/or PD-2). This stacking pattern corresponds to an evolution of the palustrine *R* sequence type. In the studied profiles, these sequences account for approximately 20% of the sections, with the exception of the Pas de la Vache outcrop, where they were absent. In the Pas de Monsieur outcrop, they represent 22%, while in the Pas du Lièvre, they account for 10%, and in La Route, 50%. The MRSs are on the tops of these sequences and are typically well-defined due to the development of pedogenic features corresponding to index 5 of the EI.

*Interpretation:* The rocks comprising the palustrine–pedogenic sequences are associated with long-term subaerial exposures, during which pedogenic processes intensify. In such contexts, when the lake has completely desiccated, leaving no space for sediment accumulation, high-frequency base level fluctuations influence only the position of the groundwater table and the vertical extent of pedogenic transformations.

#### 3.4.2.2.1.5. Amalgamated pedogenic sequences

The amalgamated pedogenic sequences, as illustrated in Fig. 3.11E, correspond to intervals composed exclusively of pedogenic facies (PD-1 and/or PD-2) as an evolution of the palustrine–pedogenic sequence type. This stacking pattern accounts for 5% of the interpreted sequences in the area, occurring only at the Pas du Lièvre outcrop, where they represent 5%, and at the La Route site, where they comprise 17% of the sequences. In these cases, due to the more pervasive pedogenesis, primary features are intensely overprinted. This makes the identification of sequence boundaries challenging and leads to the overlap of pedogenic intervals within several amalgamated sequences. Only when overlapped by other types of sequences present in the Cengle cliff, showing an abrupt change in facies, it becomes possible to identify the MRS at the top of the sequences.

*Interpretation:* The presence of exclusively pedogenic facies suggests pervasive pedogenesis associated with prolonged subaerial exposures (even more extended than those interpreted for palustrine–pedogenic sequences), resulting in substantial modification of lacustrine and palustrine sedimentary deposits. These modifications give these deposits remarkable similarities to paleosols. Furthermore, within these intervals, it is possible to observe root concretions (represented by columnar structures – Fig. 3.11L) ranging from decimetric to metric dimensions and pseudomicrokarst features, indicating the establishment of dense vegetation in areas near the lake margins.

### 3.4.2.2.2. Small-scale vertical stacking patterns

Small-scale vertical stacking patterns, or small-scale sequences, correspond to the stacking of elementary sequences (Strasser et al., 1999; Strasser, 2018), which, in the study area, have an average thickness of 10 m. Small-scale sequences delineate the stratigraphic intervals, as described in the following section, and are bounded by maximum retraction surfaces, which are mapped throughout the Cengle Plateau cliff. The anatomy of the small-scale sequences varies depending on their position within the lake, with a general trend for the thickness of the elementary sequences to decrease toward the mid-frequency MRS. Fig. 3.11F–I presents examples of small-scale sequences formed in more distal and proximal areas. Fig. 3.11J–K illustrates the result of these sequences after being subjected to long-term subaerial exposure events.

The small-scale sequence in the distal area exhibits an upward shallowing trend. This results from the evolution of distal and proximal lacustrine facies (lacustrine *T–R* sequence-type) into palustrine facies (lacustrine–palustrine *R* and palustrine *R* sequences), demonstrating a trend of decreasing accommodation rate conditioned by medium-frequency base level variations (Fig. 3.11F). In the study area, these sequences are mainly present in the Pas de la Vache (Fig. 3.11G) and Pas de Monsieur outcrops. In the more proximal region, a small-scale sequence is represented by the superposition of several *R*-type palustrine sequences (Fig. 3.11H). This anatomy is typical of extremely shallow environments, which are constantly subjected to short-term subaerial exposures, resulting from high-frequency base level variations. Small-scale sequences with these characteristics are observed in the Pas de Monsieur, Pas du Lièvre (Fig. 3.11I), and La Route profiles.

In both cases, during long-term subaerial exposure periods, conditioned by the medium-frequency base level drop, pedogenic facies may form. As a result, the sequences will be represented mainly at the top by palustrine–pedogenic (Fig. 3.11J) and/or pedogenic amalgamated elementary sequences (Fig. 3.11K). The evolution of pedogenic features will be proportional to the duration of subaerial exposure. With pedogenetic evolution, it is possible

that columnar features generated by root concretions will form, as well as pseudomicrokarst features, which could make it difficult to identify high-frequency sequences.

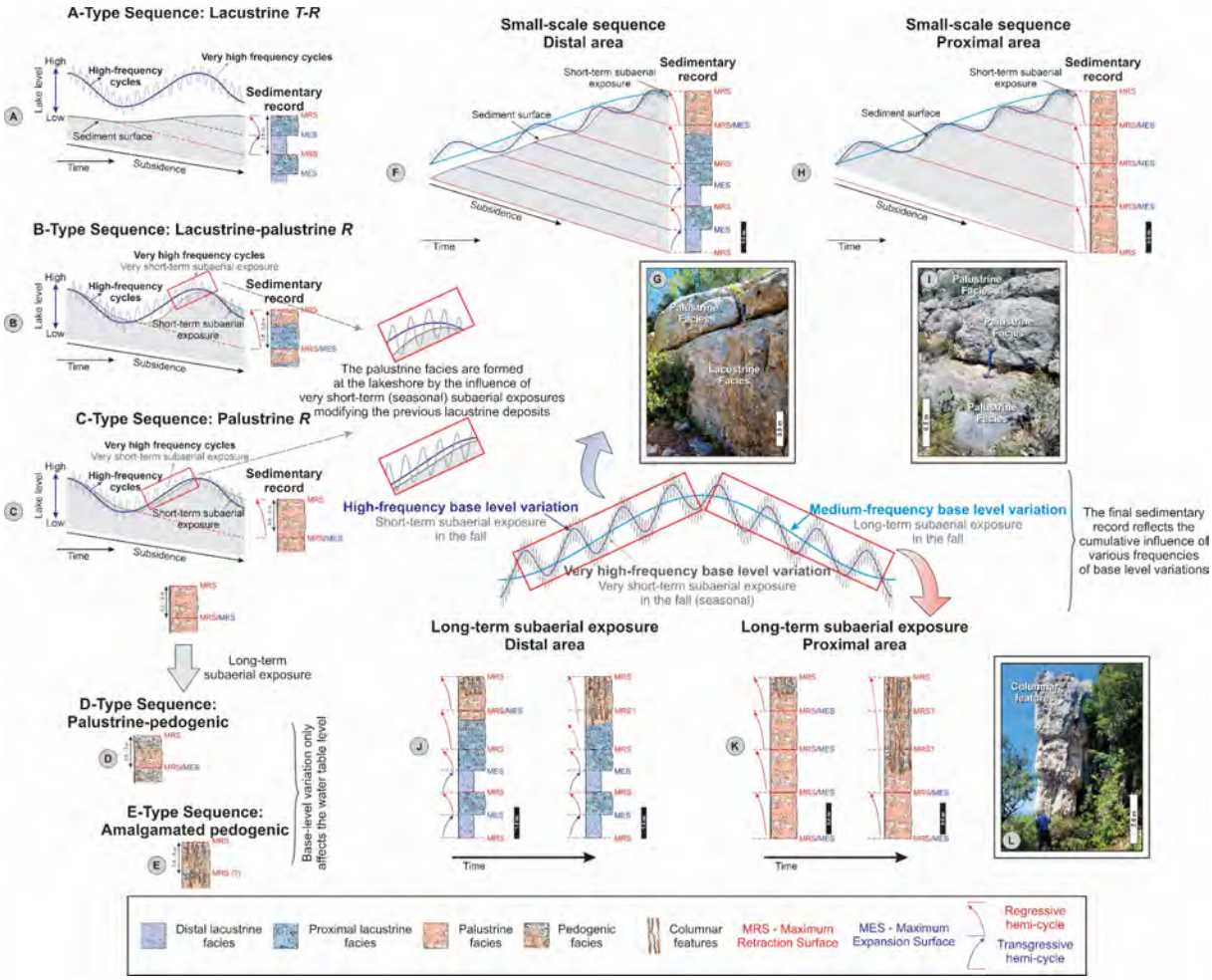


**Fig. 3.11.** Vertical stacking pattern anatomies at different scales identified in the carbonate rocks of the Cengle Cliffs. Letters A to E correspond to elementary sequences or high-frequency sequences: A) Lacustrine *T*–*R* sequence. B) Lacustrine–palustrine *R* sequence. C) Palustrine *R* sequence. D) Palustrine–pedogenic sequence. E) Amalgamated pedogenic sequence. F to I correspond to small-scale sequences: F) Small-scale sequence formed in more distal areas. G) Small-scale sequence found in the Pas de la Vache outcrop. H) Small-scale sequence formed in more proximal areas. I) Small-scale sequence found in the Pas du Lièvre outcrop. J and K represent the effects of long-term subaerial exposure on the sequences represented by the letters F and H, respectively. L) Columnar features formed by root concretions. Schematics of lake level variation curves and the resulting sedimentary records were adapted from the work of Strasser et al. (1999) and Strasser (2018) in shallow marine carbonates for the lacustrine–palustrine context.

### 3.4.3. Lateral variation in vertical stacking patterns

Using low-resolution DOM covering the entire extent of the Cengle Plateau cliff, three significant MESs of medium frequency were identified. These surfaces were mappable across the study area; however, in certain areas, correlations were inferred due to the presence of vegetation cover or fallen blocks. These three surfaces were used to divide the study area into four stratigraphic intervals, from the base to the top, referred to as Cengle-I, Cengle-II, Cengle-III, and Cengle-IV. This facilitated a comparison of the vertical evolution and lateral variation of stacking pattern sequences within each of these intervals, as illustrated in Fig. 3.12. The percentage shown in the text refers to the frequency of occurrence of each type of high-frequency sequence (elementary sequences) within each stratigraphic interval.

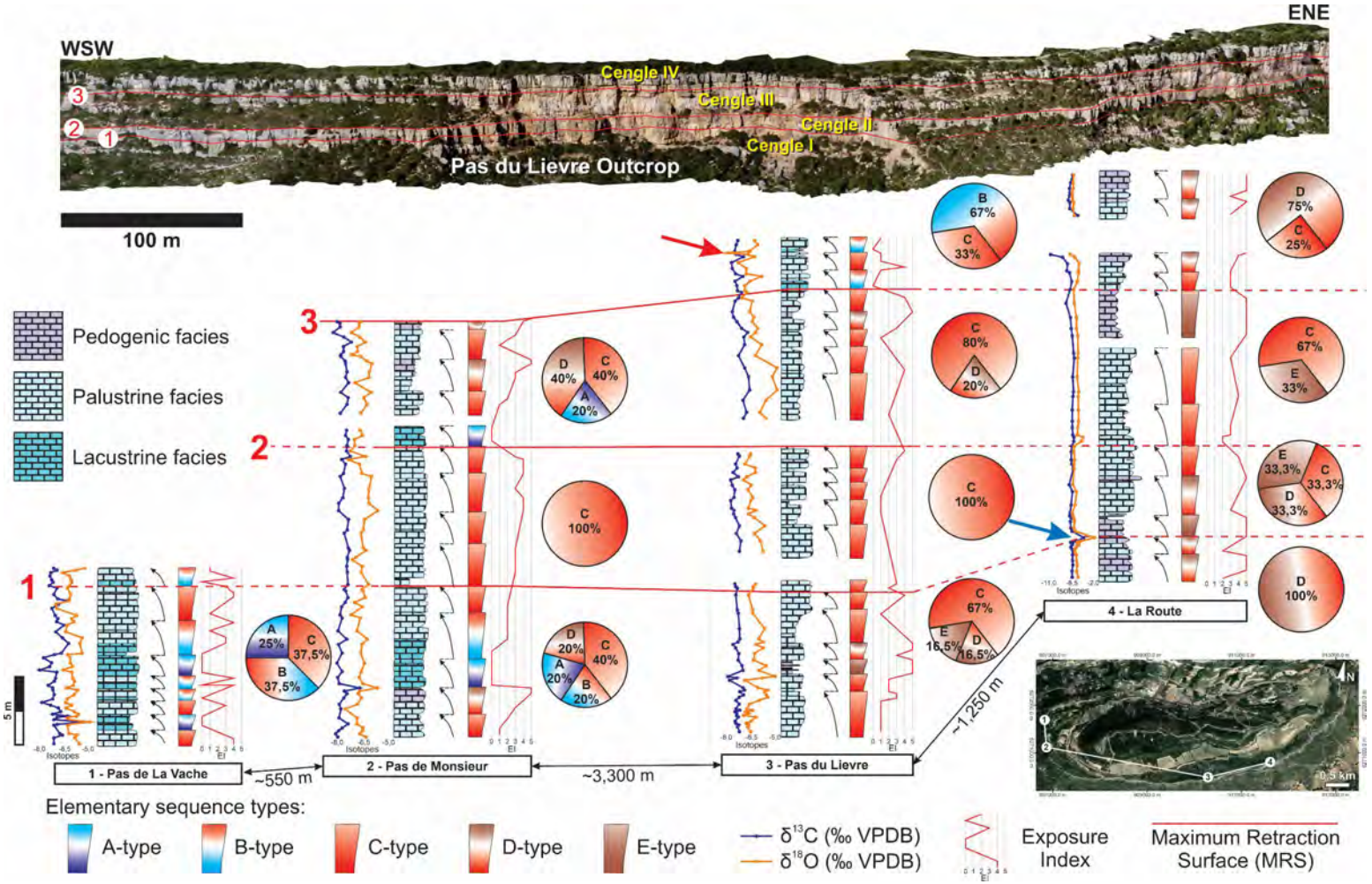


**Fig. 3.12.** Correlation and lateral variations (indicated by pie charts) of the types of vertical stacking patterns for the four stratigraphic sections surveyed in the study area. The positions of the profiles are shown in the plan view of the Cengle Plateau at the bottom right. Each sedimentary profile is depicted with facies associations and sequence types, alongside C and O stable isotope logs and exposure index logs. For details of the sequence types, refer to Fig. 3.11. At the top, Pas du Lièvre DOM illustrates the main surfaces (numbers 1, 2 and 3 – red lines) that can be traced along the entire cliff. These surfaces subdivide the cliff of the Cengle Plateau into four stratigraphic intervals: Cengle-I to Cengle-IV, from the base to the top. The blue arrow at the bottom of La Route profile indicates a peak of more positive isotopes, corresponds to the sample in which calcite pseudomorphs after gypsum were identified. The red arrow indicates the position of the samples with foraminifera.

The basal interval, Cengle-I, is the best-preserved, as it was observed at all four survey points for stratigraphic sections. However, at the La Route outcrop, only the top of this interval is exposed. While sequences with palustrine and pedogenic characteristics (sequences of types C, D, and E) predominate in Cengle-I, there is preservation of sequences with lacustrine facies (sequences of types A and B) in the Pas de la Vache and Pas de Monsieur outcrops located to the west. In the Pas de Vache profile, sequences of types B and C account for 37.5%, while sequences of type A constitute 25%. In Pas de Monsieur, sequences of type C amount to 40%, while those of types A, B, and D correspond to 20%. At Pas du Lièvre, 67% of the sequences are of type C, with 16.5% for each of types D and E. In the La Route outcrop, all sequences belong to type D. In the Cengle-I interval, a progressive transition from lacustrine to palustrine environments is evident, which, in turn, gradually transitions to the pedogenic environment from west to east.

The Cengle-II interval is characterized by intense pedogenesis. Lacustrine facies are only found in the Pas de la Vache section, which records exclusively the base of the Cengle-II interval. In the Pas de Monsieur and Pas du Lièvre outcrops, 100% of the sequences are of type C, while in the La Route outcrop, sequences of types C, D, and E are equally distributed, with each type representing 33.3%. Although this stratigraphic interval still exhibits occurrences of lacustrine facies in the Pas de la Vache section, the exclusive presence of palustrine facies in the Pas de Monsieur and Pas du Lièvre locations indicates that the lake during deposition of the Cengle-II stratigraphic interval was shallow and flat. Minor fluctuations in the lake level were sufficient to expand the area dominated by palustrine facies. Furthermore, the identification of sequences displaying pedogenic facies associated with palustrine facies in the La Route section highlights proximal conditions for this profile.

In the Cengle-III stratigraphic interval, a prevalence of sequences exhibiting palustrine and pedogenic characteristics is observed. Lacustrine facies are exclusively encountered in the Pas de Monsieur outcrop, where 40% of the sequences are of type C, 20% of type A, and 40% of type D. In Pas du Lièvre, 80% of the sequences correspond to type C, with 20% falling into type D. In the La Route profile, 67% of the sequences are classified as type C, and 33% as type E. This pattern suggests a return to a depositional configuration akin to that of the Cengle-I interval, marked by the presence of lacustrine facies in the Pas de Monsieur section. Notably, pedogenic sequences are distinctly present in all three profiles documenting this interval (Pas de Monsieur, Pas du Lièvre, and La Route). This evidence indicates prolonged periods of exposure, during which pedogenic features, including the common occurrence of root traces, developed. It is interesting to observe that, like the Cengle-II interval, the La Route section exhibits a reduced number of sequences compared to the other profiles. This suggests that pedogenesis played a significant role in obscuring the primary features, making it challenging to discern the original sequences. Given the increased sequence thickness, it is plausible that these sequences represent an amalgamation of two or more of them.

The upper interval, Cengle-IV, is preserved only in the Pas du Lièvre and La Route outcrops. Lacustrine facies, in the Pas du Lièvre profile, were observed exclusively in this interval, where 67% of the sequences are type B and 33% type C. Notably, foraminifera of the genus *Rosalina* were identified in thin sections of the Pas du Lièvre profile within this interval. In the La Route profile, sequences of type D predominate, accounting for 75%, while the remaining 25% correspond to sequences of type C. The occurrence of lacustrine facies and the presence of foraminiferal fossils within this interval of the Pas du Lièvre profile are atypical and unexpected. These characteristics indicate saline lake water during that period. The predominance of pedogenic sequences in the La Route profile reinforces the association of this profile, across all stratigraphic intervals, with more proximal conditions compared to the other

profiles studied. This suggests a zonation within the depositional profile, with a transition from lacustrine to palustrine, and ultimately to pedogenic environments from west to east.

### 3.4.4. U–Pb dating and SEM observation of micrites

Ten ages from U–Pb analyses performed on various carbonate phases from 6 samples were obtained and are presented in Fig. 3.13 and summarized in Table 3.2. All ages were obtained using the isochron defined in the Tera–Wasserburg diagram (examples in Fig. 3.13B, C, H). It is noteworthy that the samples which yielded TW isochrons do not show very radiogenic $^{238}U/^{206}Pb$, the maximum value is between 50 and 60 in sample R-55 while most of the values are <30 (see Fig. 3.13). However, the relatively small analytical uncertainties on $^{207}Pb/^{206}Pb$ due to [Pb] of up to 2.7 µg/g and on $^{238}U/^{206}Pb$ due to in-depth homogeneity of the samples define isochrons that are robust and provide geological meaning to the U–Pb ages.

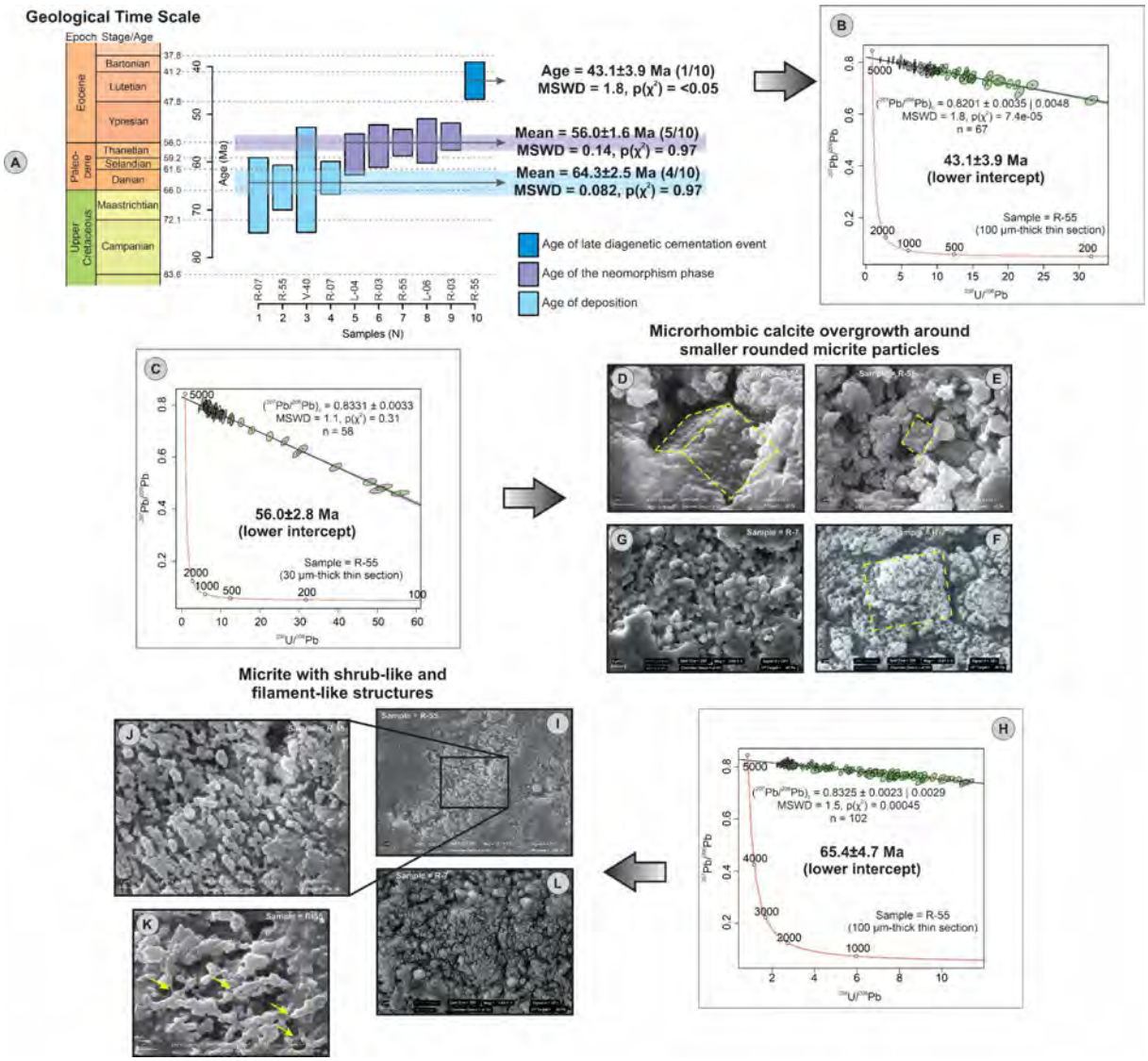


**Fig. 3.13.** Isochrons and SEM images for 'La Barre du Cengle' limestones. A) Age groups of the study area. Geological Time Scale based on Gradstein et al. (2012). B) Isochron representing the late cementation event. C) Isochron representing the age calculated for the neomorphism phase. D to G) Representative SEM images of the neomorphism event. Yellow lines represent the interpretation of the overgrowth of calcite rhombs encompassing small and rounded micrite particles. H) Isochron representing the age calculated for the primary micrite. I to L) SEM images representing primary microbial micrite. Images in I, J, and L depict shrub-like structures, whereas image K shows filament-like structures (denoted by the yellow arrows).

**Table 3.2.** Results of U–Pb dating on carbonates from "La Barre du Cengle". N = sample ID; Ma = millions of years; MSWD = mean square weighted deviation; p($\chi^2$) = chi-square test probability; n = number of spots for isochron determination.

| N | Sample (facies) | Stratigraphic interval | Analyzed element(s) | U-Pb age (Ma) | Confidence interval 95% (Ma) | 2s (including syst uncertainty) (Ma) | MSWD | p($\chi^2$) | n spots |
|---|---|---|---|---|---|---|---|---|---|
| 1 | R-07 (PL-1) | Cengle-I | Micrite | 66.9 | ±4.6 | ±7.9 | 2.5 | <0.05 | 150 |
| 2 | R-55 (PD-1) | Cengle-IV | Micrite | 65.4 | ±3.0 | ±4.7 | 1.5 | <0.05 | 102 |
| 3 | V-40 (PL-4) | Cengle-I | Micrite + *Microcodium* crystals | 63.8 | ±7.3 | ±10.9 | 2 | <0.05 | 75 |
| 4 | R-07 (PL-1) | Cengle-I | Micrite + early sparite | 63.3 | ±1.2 | ±3.4 | 2.7 | <0.05 | 118 |
| 5 | L-04 (PL-1) | Cengle-I | Micrite + early sparite | 58.4 | ±2.1 | ±4.3 | 2.8 | <0.05 | 124 |
| 6 | R-03 (PD-1) | Cengle-I | Micrite + *Microcodium* crystals | 56.7 | ±2.1 | ±4.4 | 3.1 | <0.05 | 117 |
| 7 | R-55 (PD-1) | Cengle-IV | Micrite + grain coating | 56.0 | ±1.4 | ±2.8 | 1.1 | 0.31 | 58 |
| 8 | L-06 (PL-1) | Cengle-I | Micrite | 55.6 | ±3.2 | ±4.6 | 1.5 | <0.05 | 71 |
| 9 | R-03 (PD-1) | Cengle-I | Micrite + *Microcodium* crystals | 54.8 | ±1.2 | ±2.8 | 1.5 | <0.05 | 187 |
| 10 | R-55 (PD-1) | Cengle-IV | Late sparite | 43.1 | ±2.5 | ±3.9 | 1.8 | <0.05 | 67 |

U–Pb analyses, followed by HCA and weighted average calculation (not applicable to the third group, represented by a single age), resulted in three distinct age groups (Fig. 3.13A): i) 64.3±2.5 Ma, derived from measurements conducted on micrite, sparry calcite cements and *Microcodium* crystals; ii) 56.1±1.6 Ma, also obtained from analyses on micrite, sparry calcite cements and *Microcodium* crystals; and iii) 43.1±3.9 Ma, resulting from a single sample, where the points generating the isochron were obtained from sparry calcite cement, composed of coarse mosaic crystals.

In order to interpret the dating results, the 100 µm-thick thin sections were analyzed using SEM. The analysis focused on the micrite to try to understand the two oldest ages obtained, as the most recent age is clearly a diagenetic phase of late cementation in the meteoric realm. After thorough investigation, two distinct groups of micrite with characteristics that could elucidate the obtained results were identified.

The first group consists of shrub-like structures, composed of small rounded micrite particles (around 0.05 and 0.1 µm) (Fig. 3.13I, J, L). Within these shrub-like structures, microbial filament-like structures were identified (Fig. 3.13K). The presence of filaments in SEM images of carbonate rocks is often associated with interpreting the influence of microbial activity in the formation of the hosting deposits (e.g., Folk, 1993; Bahniuk et al., 2015; Roemers-Oliveira et al., 2015). Thus, it is plausible to relate this microbial-origin micrite as primary and associate it with the oldest mean age (64.3±2.5 Ma). In addition, calcite spars yielding a similar age (sample R-07) likely represent an early stage of meteoric cementation during a subaerial exposure associated with high-frequency cyclicity.

The second group, corresponding to the overgrowth of microrhombic calcite (Fig. 3.13D–G), encompasses the smaller, rounded micrite particles, interpreted as primary. This phenomenon is identified as a phase of neomorphism, which refers to the development of new crystals in a rock through recrystallization under temperature and pressure conditions different from those under which the rock was originally lithified. As indicated by Boggs (2011), neomorphism can affect both carbonate grains and micrite, generally resulting in the enlargement of calcite crystal size. Therefore, due to its more recent diagenetic nature, neomorphism has been associated with a mean maximum age of 56.0±1.6 Ma. Such microcalcite overgrowths likely also developed within *Microcodium* aggregates as suggested by similar ages obtained in sample R-03. In addition, the same range of ages has been obtained

for sparry cement (L-04 sample) thus suggesting that a later stage of sparry calcite cementation occurred coevally with the formation of microrhombic calcite overgrowths.

In the context of the obtained ages, sample R-55 is noteworthy, located at the top of the La Route profile within the uppermost interval (Cengle IV), recording all three identified age events (see Table 3.2). This observation underscores the coexistence of these events within the study area. The oldest age obtained in micrite is 65.4±4.7 Ma, thus suggesting a depositional age no younger than 60.7 Ma for the Cengle IV interval.

Regarding sample R-07, positioned in the basal portion of the La Route profile (Cengle-I interval), it exhibits the deposition age with the least error. The results from this sample indicate a deposition age ranging from 66.7 to 59.9 Ma. Given the well-constrained K/Pg boundary in the Arc Basin (below the 'Calcaire de Vitrolles' formation, Fig. 3.2), notably evidenced by magnetostratigraphic studies (Westphal and Durand, 1990; Cojan et al., 2000), and by the distribution of dinosaur eggshells in its continental deposits (Garcia and Vianey-Liaud, 2001), it is inferred that the limestone of the Cengle formed after the K/Pg boundary. By calibrating the obtained ages with the Geological Time Scale (Gradstein et al., 2012), a Danian to early Selandian deposition age can be assigned to the carbonates of 'La Barre du Cengle'.

Applying the same rationale to determine the age of neomorphism, sample R-55 stands out, displaying the least uncertainty for this event. It indicates an age for neomorphism ranging from 58.8 to 53.2 Ma, placing it between the Thanetian and Ypresian Stages.

### 3.4.5. C and O stable isotopes

The isotopic composition of whole-rock bulk samples from the Cengle Plateau cliff reveals negative $\delta^{13}C$ and $\delta^{18}O$ values (Fig. 3.14), ranging from −10.85 to −4.76‰ and −7.57 to −2.71‰, respectively, relative to the VPDB standard. Despite this wide range, the distribution histograms (Fig. 3.14A, B) show that 88% of $\delta^{13}C$ data falls within the range of −7.55 to −6.67‰, with a mode representing 38% of the data between −7.33 and −7.11‰. Similarly, for $\delta^{18}O$, 82% of the values range from −6.82 to −5.82‰, with a mode comprising 31% of the data between −6.57 and −6.32‰. In Fig. 3.12, vertical and lateral trends of the $\delta^{18}O$ and $\delta^{13}C$ isotopic signatures for the four profiles and four stratigraphic intervals are also displayed.

Fig. 3.14C–F depicts the cross-plot of $\delta^{18}O$ versus $\delta^{13}C$ for 260 of the 262 samples analyzed for stable isotopes. Outliers with anomalous data (sample R-13: $\delta^{13}C$ = −4.76‰, $\delta^{18}O$ = −2.71‰; and sample R-49: $\delta^{13}C$ = −10.85‰, $\delta^{18}O$ = −7.29‰) were excluded from the dataset, as they probably represent specific events. A factor potentially contributing to some very negative $\delta^{13}C$ values is the presence of *Microcodium* content within these samples, either in the form of well-preserved aggregates or as debris. *Microcodium* crystals are known to exhibit markedly negative $\delta^{13}C$ values, as evidenced by previous studies (e.g., $\delta^{13}C$ −20.7‰ in lamellar aggregates reported by Kabanov et al., 2008, and $\delta^{13}C$ ranging from −8 to −12.8‰ for 'corn-cob' aggregates in Pujalte et al., 2019).

A low covariance is observed, with a coefficient of determination ($R^2$) of only 0.2003 (Fig. 3.14C). Geographical positioning of data (Fig. 3.14D), stratigraphic intervals (Fig. 3.14E), or sequence types (Fig. 3.14F) does not reveal clear vertical or lateral trends. As discussed by Alonso-Zarza (2003), deciphering isotope data in palustrine-dominated environments is challenging due to the influence of meteoric diagenetic processes common in these carbonates, which result in the loss of primary markers and data homogenization.

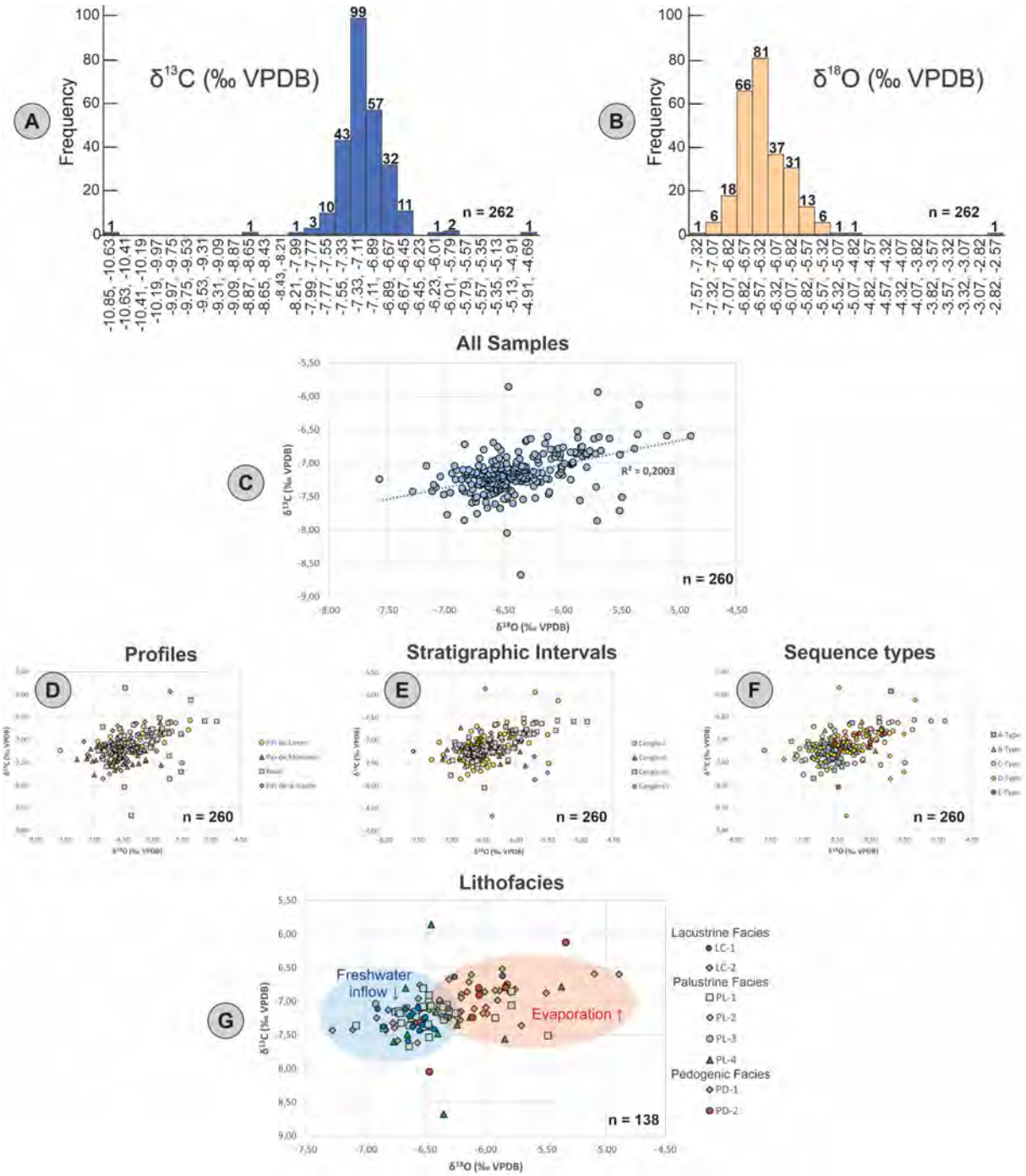


**Fig. 3.14.** Results of $\delta^{13}C$ and $\delta^{18}O$ isotopic data from the carbonates of the Cengle Plateau cliff. A) Histogram of the distribution of $\delta^{13}C$. B) Histogram of the distribution of $\delta^{18}O$. C) Cross plot of $\delta^{18}O$ versus $\delta^{13}C$ for all the samples analyzed. D) Cross plot of $\delta^{18}O$ versus $\delta^{13}C$ for all the samples labeled by profiles. E) Cross plot of $\delta^{18}O$ versus $\delta^{13}C$ for all the samples labeled by stratigraphic intervals. F) Cross plot of $\delta^{18}O$ versus $\delta^{13}C$ for all the samples labeled by sequence types. The sequence types are labeled according to Fig. 3.11. G) Cross plot of $\delta^{18}O$ versus $\delta^{13}C$ for all the samples with thin sections labeled by lithofacies.

In Fig. 3.14G, stable isotope data were plotted by facies, using only the samples with thin sections (n = 138). This selection was made to mitigate errors associated with facies definition without proper petrographic control. Table 3.3 presents the variation and averages of stable isotope values for each of the interpreted lithofacies for the 'La Barre du Cengle'. An important result is that lacustrine facies are significantly depleted in $\delta^{13}C$ and $\delta^{18}O$ compared to palustrine and pedogenic facies, leading to apparent covariance between $\delta^{13}C$ and $\delta^{18}O$ (Fig. 3.14G). This relationship between depositional facies and isotopic signature suggests that a primary signal,

linked to depositional or early diagenetic conditions, has been preserved despite the development of late-stage neomorphic features revealed by SEM analyses and U/Pb ages (Fig. 3.13). As commonly evidenced in many modern and ancient lakes (e.g., Leng and Marshall, 2004; Horton et al., 2016), the distinct isotopic composition between lacustrine (LC-1 and LC-2)/distal palustrine (PL-1) facies and more proximal palustrine (PL-2 to PL-4)/pedogenic (PD-1 and PD-2) facies may result from distinct freshwater inflow–evaporation balance, the lacustrine/distal palustrine facies being associated with more freshwater inflow and the proximal palustrine/pedogenic facies being related to more evaporated water. Such an interpretation is strongly supported by results from the Road profile where a significantly $\delta^{18}O$ and $\delta^{13}C$-enriched composition occurs at the base of the section (indicated by the blue arrow in Fig. 3.12). This peak corresponds to the sample in which calcite pseudomorphs after gypsum were identified, indicating a period of increased aridity and the development of evaporites in proximal areas. This interpretation implies, therefore, that lake level variations are forced by changes in water inflow–evaporation balance in the lake and supports the interpretation of allocyclicity for elementary and small-scale sequences.

**Table 3.3.** Variation and averages of $\delta^{13}C$ and $\delta^{18}O$ stable isotope values by lithofacies for samples with thin sections in the study area. Values in ‰, relative to the VPDB standard.

| Facies association | Lithofacies | Number of samples | $\delta^{13}C$ variation (‰ VPDB) | $\delta^{13}C$ average (‰ VPDB) | $\delta^{18}O$ variation (‰ VPDB) | $\delta^{18}O$ average (‰ VPDB) |
|---|---|---|---|---|---|---|
| Lacustrine (LC) | LC-1: *Microcodium*-bioclastic wackestone and packstone | 16 | −7,59 to −6.62 | −7.19 | −6,90 to −5.86 | −6.52 |
| | LC-2: Intraclastic wackestone–packstone | 4 | −7.23 to −7.13 | −7.19 | −6.81 to −6.23 | −6.51 |
| Palustrine (PL) | PL-1: Cracked mottled limestones | 31 | −7.67 to −6.81 | −7.20 | −7.08 to −5.48 | −6.46 |
| | PL-2: Nodular-brecciated limestones | 40 | −7.58 to −6.52 | −7.06 | −7.28 to −4.89 | −6.26 |
| | PL-3: Intraclastic packstone–grainstone | 4 | −7.32 to −6.75 | −7.11 | −6.92 to −5.82 | −6.50 |
| | PL-4: Pseudomicrokarstic limestones | 16 | −8,68 to −5.86 | −7.25 | −6.77 to −5.37 | −6.36 |
| Pedogenic (PD) | PD-1: Pisolithic mottled intraclastic limestones | 19 | −7.61 to −6.76 | −7.16 | −6.91 to −5.50 | −6.37 |
| | PD-2: *Microcodium* mottled limestones | 8 | −8.05 to −6.13 | −7.06 | −6.55 to −5.33 | −6.09 |

## 3.5. Discussion

### 3.5.1. Depositional model of a palustrine-dominated lake margin

As properly discussed by Alonso-Zarza and Wright (2010a), palustrine carbonates can occur in depositional settings characterized by very low gradients of the lake margin and low energy. Fine-grained carbonates, primarily muds, formed in freshwater, are subjected to subaerial exposure related to fluctuations in the water level. Pedogenic processes modify the carbonate substrates, giving rise to a variety of palustrine facies and microfabrics, as reviewed by Freytet and Verrecchia (2002). Since the studies by Freytet (1965, 1971), palustrine carbonates have been conceptualized as products of pedogenic modification of non-marine carbonates.

Based on investigations of recent palustrine carbonates in the Florida Everglades, United States (Platt and Wright, 1992), it has been observed that desiccation cracks result from subaerial exposure lasting approximately 4.5 months annually. Consequently, these subaerial exposures, responsible for the formation of palustrine features, are regarded as seasonal and occur at very high frequency. Prolonged subaerial exposure, which occurs less frequently, is responsible for the transformation of lacustrine or palustrine facies into pedogenic ones. This

occurs under two conditions: first, during prolonged lake level drops that expose significant areas of the sedimentary environment, and second, in the shoreline area. The latter is more likely to remain under subaerial exposure for an extended period as it is the first to emerge and the last to be submerged. Thus, the higher proportion of pedogenic facies in the La Route profile indicates a more proximal condition compared to the other profiles studied.

An overview of the depositional environment dominated by palustrine conditions is presented in Fig. 3.15. Lacustrine facies are formed in submerged conditions. Palustrine environments, however, occupy the zone between the minimum and maximum lake levels. In the emergent portion, always under subaerial exposure, pedogenic facies are developed and exhibit intrinsic soil and calcrete characteristics. Changes in the lake shoreline over time altered its paleogeography, resulting in the overlapping of different subenvironments (lacustrine, palustrine, and pedogenic) at the same geographical location. Vertical facies successions reflect lateral changes in the depositional environment due to variations in the base level. Due to the flat surfaces, even minor lake level drops are sufficient to expose and pedogenize a significant portion of the area. These factors have contributed to palustrine conditions predominating over lacustrine ones in the investigated area.

The predominant component in the rocks of the studied area is micrite, corresponding to primary lacustrine mud (sometimes with pedogenesis features overprinted), typical of low-energy and low-gradient lakes. SEM analysis revealed shrub-like and filament-like structures, suggesting that this micrite was generated by microbial activity. *Microcodium* debris plays a significant role in the carbonates of ‘La Barre du Cengle’. In situ aggregates of rosettes and lamellar *Microcodium* occur in association with pedogenic facies, while dissociated prism debris is abundant in both palustrine and lacustrine facies. Freytet and Plaziat (1982) noted that *Microcodium* prisms can be dissociated and corroded due to water circulation, reflecting the cyclic nature of lake level fluctuations. These crystals, formed in emergent areas, were reworked and transported to submerged zones after base level rise.

Analyzing the stratigraphic intervals (Cengle I to Cengle IV), a consistent pattern emerges: lacustrine facies predominate to the west (e.g., Pas de la Vache and Pas de Monsieur outcrops), while pedogenic facies are more abundant to the east (e.g., Pas du Lièvre and La Route profiles). The transitions between lacustrine, palustrine, and pedogenic environments consistently occur from west to east over time. Based on observed facies transitions along the section depicted in Fig. 3.12, the complete transition of lacustrine > palustrine > pedogenic settings within the same stratigraphic interval (e.g., Cengle I and II) occurs within approximately 4 to 5 km. This pattern parallels the model proposed by Armenteros et al. (1997) for the transition from lacustrine to palustrine facies in the Bembridge Limestone (Late Eocene, England).

Identifying contemporary environments that closely resemble ancient settings is challenging, but certain regions have been suggested as modern analogs for palustrine deposits. Examples include the wetlands of ‘Las Tablas de Daimiel’ in Spain (Alonso-Zarza et al., 2006), the Florida Everglades in the United States (Platt and Wright, 1992), and more recently, the Sian Ka'an area in the Yucatán Peninsula, Mexico (Platt and Wright, 2023). The Florida Everglades and Sian Ka'an represent extensive, shallow carbonate marshes with diverse subenvironments, including freshwater lakes and brackish lagoons with a clear marine influence. Therefore, the ‘Las Tablas de Daimiel’ wetlands in Spain serve as the most suitable analog for the palustrine deposits of the ‘Calcaire de St Marc’ Formation, particularly in the region of the Cengle Plateau. These wetlands exhibit a sedimentary record similar to ancient palustrine carbonates, with palustrine limestone formation primarily occurring along the margins of shallow lakes.

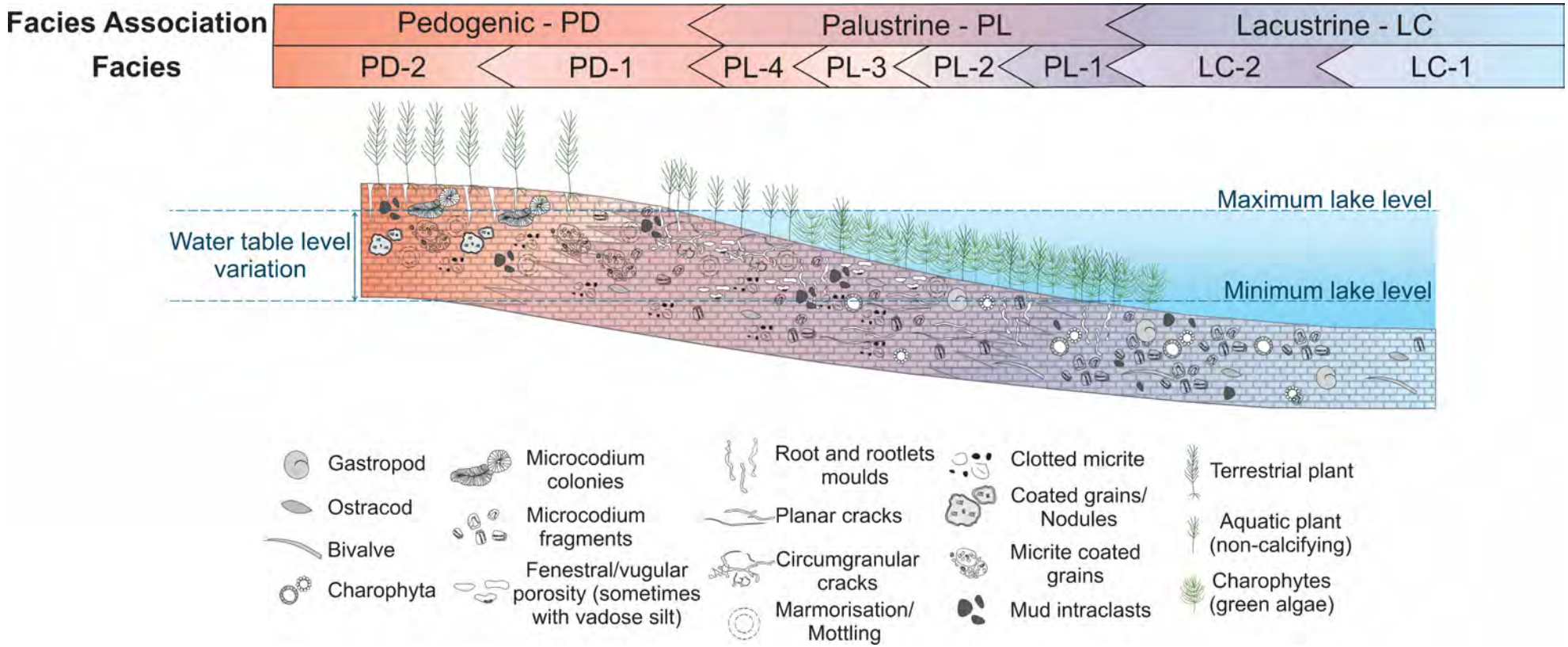


**Fig. 3.15.** Depositional profile for palustrine-dominated lake margin. The profile is derived from the model proposed by Alonso-Zarza (2003) and adapted to the lithofacies and components identified in the carbonates of the Cengle Plateau cliff. While the model is not to scale, the transition between lacustrine, palustrine and pedogenic environments in the studied area is estimated to be on the order of 5 km.

### 3.5.2. Depositional sequence development

The mechanisms driving the formation of high-frequency depositional sequences, associated with fluctuations in the base level, have been detailed in section 3.4.2.2.1 and illustrated in Fig. 3.11. During periods of high-frequency oscillations in lake levels, the sedimentary record undergoes construction and modification, resulting in facies preservation over geological time. While direct evidence of lake level drops is evident primarily in elementary sequences of types D and E, where thick pedogenetic profiles are identified, correlations between the sections (Fig. 3.12) reveal lateral transitions to sequences of types A, B, or C, indicating that these also result from lake level fluctuations.

The high-frequency depositional sequences present challenges in correlation. Nevertheless, these high-frequency sequences collectively give rise to medium-scale sequences, delineated by the stratigraphic intervals Cengle-I to Cengle-IV, which are traceable along the entire Cengle Plateau cliff. As evidenced by Magalhães et al. (2020) and Fragoso et al. (2021), mappability decreases with increasing frequency. High-frequency allocyclic sequences in outcrops tend to exhibit smaller lateral extents compared to medium and low-frequency sequences.

Hence, repeated vertical stacking patterns, clearly cyclical in nature, along with frequent exposure features marking base level falls (also denoted by isotopic signatures), which organize into mappable medium-scale sequences, evidenced by a general trend of decreasing thicknesses of the elementary sequences toward the medium-frequency MRS indicate allocyclic control over the sedimentation of the carbonates of ‘La Barre du Cengle’.

Cojan (1993), in her study of other intervals from Late Cretaceous and Paleogene in the Arc Basin, had already suggested that the deposition of carbonate formations was controlled by the climate. This observation is in line with the interpretation of this study, which places climate as the main responsible for the cyclical high and low frequency variations in the lake level. Wetter periods lead to lake level rises, increasing the area covered by water. Conversely, drier periods expose a substantial portion of the lake subaerially, giving rise to extensive pedogenic facies.

Due to the complex sedimentary dynamics in palustrine-dominated environments, the outcomes generated and preserved depend on the specific basin position under analysis. Following an examination of various vertical stacking patterns observed in the study area and prior discussions, a conceptual model is proposed (Fig. 3.16) for the deposition of outcropping limestones in ‘La Barre du Cengle’. The model simulates the sedimentary record's outcome based on lake level curves at two different frequencies and positions over time. The two presented frequencies correspond to the long-term lake water level control (medium-frequency cycles) and short-term variations (high-frequency cycles). The longer wavelength, lower frequency curve governs the long-term lake water level, while the higher frequency curves control short-term lake level fluctuations.

After a medium-frequency base level fall, the entire sequence may experience subaerial exposure, resulting in pedogenic facies that may obscure and complicate the identification of high-frequency sequences due to advanced pedogenesis stages. During periods of subaerial exposure, deposition halts, leading to condensed time intervals on maximum retraction surfaces, with durations depending on the associated order. Although estimating this time precisely is challenging, the exposure index serves as a relative time indicator, distinguishing between very short, short and long-term subaerial exposures.

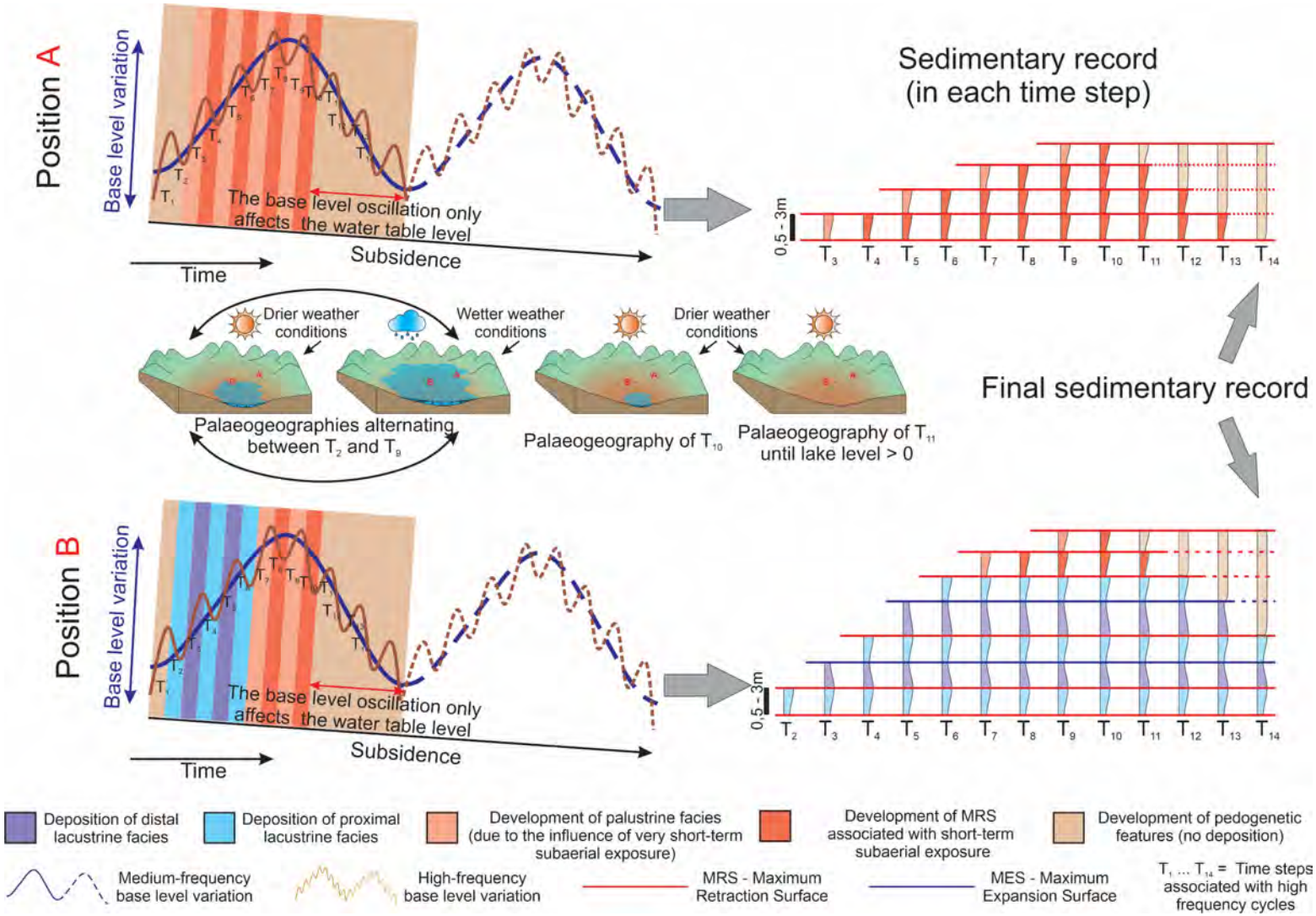


**Fig. 3.16.** Conceptual model of deposition and stacking patterns for the carbonates of the Cengle Plateau cliff for the proximal (A) and distal (B) regions over $T_1$ to $T_{14}$. Each time step represents a high-frequency cycle. During $T_1$ and $T_2$ in position A, and $T_1$ in position B, there is no deposition due to the rise in the base level will first restore the water table level.

Due to differences in accommodation space, potential of preservation and sediment supply, distinct stacking patterns and preserved sedimentary records characterize areas A (proximal area) and B (lake center area) differently. In position A, with a low positive accommodation rate and lower sediment preservation due to repeated subaerial exposures thicknesses tend to be smaller, featuring vertical stacking patterns of palustrine *R* sequences, palustrine–pedogenic sequences, and amalgamated pedogenic sequences. Conversely, in position B, characterized by a high positive accommodation rate, and higher sediment preservation due to scarcer subaerial exposures, thicknesses tend to be larger, with predominating stacking patterns of lacustrine *T*−*R* sequences, lacustrine–palustrine *R* sequences, and palustrine *R* sequences. This variation justifies the observed thickness disparity in the deposits of the Cengle Plateau cliff toward the east, decreasing from 35 m to about 20 m in thickness, where the proportions of pedogenic facies gradually increase. In addition, such a difference in accommodation space between A and B was probably triggered and maintained over time by a difference in the rate of tectonic subsidence between the margins and the axial zone of the Arc syncline. It is crucial for preserving generated palustrine and pedogenic features that the lake base level rises anew, preserving the preceding sedimentary deposit and initiating a new low-frequency deposition sequence, perpetuating the process.

Identifying the time associated with the cyclic climate-controlled character in the study area poses a significant challenge, primarily due to the lack of age data with adequate resolution. U−Pb dating measurements obtained for the Cengle Plateau limestones feature an average error margin of 4 million years, exceeding the expected deposition time for the observed sequences, whether at high or medium frequencies. Studies combining magnetostratigraphy with U−Pb dating data could help constrain the timescale and establish a suitable temporal framework to address the issue of dating depositional sequences. Given the wide influence of astronomical cycles on climate, these mechanisms are presumed to be responsible for the cyclic patterns observed in the studied area. These astronomical cycles control insolation on Earth (Jouzel et al., 2007; Hinnov, 2013; Oliveira et al., 2017; Fragoso et al., 2021), thereby influencing climate dynamics. It is hypothesized that high-frequency cycles may be linked to suborbital cycles (<10 thousand years), reflecting the expected sedimentary dynamics in palustrine environments and the limited correlation potential of high-frequency sequences. Conversely, lower-frequency cycles, with their greater mappability, could be associated with shorter-duration orbital cycles, such as precession (~20-ky), as linked by Kruiver et al. (2002) to each 6-meter-thick late Miocene palustrine–alluvial continental sequences of Librilla (SW Spain).

### 3.5.3. Later diagenetic evolution and burial history

Based on petrographic and SEM analyses, two late diagenetic events have been identified and dated. The first corresponds to neomorphism, characterized by the calcite overgrowth phase on micrite particles, dated to the Thanetian–Ypresian. Given that the rocks outcropping in the Cengle cliff were deposited during the Danian–Selandian, it is reasonable to infer that ‘La Barre du Cengle’ was already sufficiently buried in a meteoric phreatic environment conducive to the development of calcite overgrowths by around 56 Ma ago. This burial must have reached its peak when the overlain ‘Calcaire de Langesse’ and ‘Calcaire de Montaiguet’ formations were deposited. The Palette mammal deposit (Savage et al., 1965; Godinot, 1984; Godinot et al., 1987), located at the top of the ‘Calcaire de Langesse’ Formation (Durand, 1984), is well dated to the Early Ypresian (Godinot, 1984; Godinot et al., 1987). Lastly, a late meteoric cementation phase during the Lutetian–Bartonian (43.1±3.9 Ma) was identified.

### 3.5.4. Paleoclimatic and paleogeographic implications

Currently, the deposits of the 'Calcaire de St Marc' Formation, including the Cengle limestones, are interpreted as Thanetian–Ypresian in age (Cojan et al., 2000; Angst et al., 2015; Tortosa and Leleu, 2020). This formation encompasses the globally recognized Paleocene−Eocene Thermal Maximum (PETM), an episode of extreme global warming lasting 150 to 200 thousand years, occurring from the late Paleocene to the early Eocene (e.g., Zachos et al., 1993, 2005). In the Arc Basin, a negative $\delta^{13}C$ anomaly, associated with paleomagnetic data, led Cojan et al. (2000) to place the PETM within the 'Calcaire de St Marc' Formation. However, the results of this study, based on U–Pb dating on carbonates from the Cengle Plateau cliff, indicate a Danian to early Selandian age, meaning 5 million years before the PETM.

Tanrattana et al. (2020) conducted a study on climatic evolution in Western Europe based on leaf physiognomy. The analysis of data from three Paleocene localities, two in France (Sézanne and Menat) and one in Belgium (Gelinden), led to the conclusion that the Paleocene began with relatively warmer and moister conditions, with a cooling observed during the Selandian. Subsequently, a gradual increase in temperature and precipitation amplitude was observed during the Selandian until the PETM. In general, the climate in Europe was warmer and drier in the Early Eocene (e.g., deposits generated during the PETM in the Tremp-Graus Basin, Spain – Payros et al., 2022, and in Sardinia – Murru et al., 2003).

The Cengle cliff carbonates were deposited at latitudes like the present-day, between 40 and 45°N. According to Arostegi et al. (2011), who used clay mineralogies from continental–coastal sequences of the Pyrenean Basin, adjacent to the Arc Basin, for paleoclimatic interpretations, the Paleocene climate was warm, with variations between aridity and humidity, with periods of more pronounced aridity during the late Danian and early Selandian.

Palustrine carbonates, sensitive to climate, do not form in extremely arid or humid conditions, but are favorable in subarid and subhumid climates (Alonso-Zarza, 2003). In subhumid climates, these deposits tend to show a higher organic matter content, while in semi-arid climates, they exhibit prominent pseudomicrokarst development at the top of sequences, where organic matter is scarcely preserved. Regarding the predominance of *Microcodium*, its presence may indicate an arid/semi-arid climate context, often associated with calcretes whose formation requires pronounced dry seasons (Wright and Tucker, 1991).

Based on the above, in the paleoclimatic context, the deposition of the Cengle Cliff carbonates in the study area occurred within a warm subarid climatic setting, characterized by intercalations between drier and wetter conditions, which resulted in fluctuations in the lake level. At orbitally controlled frequencies (high and medium frequencies), lacustrine facies formation predominates during wetter periods (accompanied by the generation and transport of *Microcodium*-debris into the lake), while pedogenic transformations (and the generation of in situ *Microcodium* aggregates in subaerially exposed areas) predominate during drier periods. Obviously, even drier climates with intense evaporation must have occurred at specific times and could, for example, have been responsible for the formation of gypsum deposits observed at the base of La Route section at the top of the Cengle-I stratigraphic interval (blue arrow in Fig. 3.12). On the other hand, the very high frequency (seasonal, annual) lake level fluctuations were responsible for the development of palustrine facies in the wetland belts along the shoreline of Cengle Lake.

In the paleogeographic context, the analyzed rocks originated in a lacustrine system, where fluctuations in the lake base level, controlled by climatic variations, constantly modified the paleogeography resulting in shifts of the lake shoreline.

The presence of benthic foraminifera at the top of the Pas du Lièvre section (red arrow in Fig. 3.12), within the Cengle-IV stratigraphic interval, was noted. Although foraminifera can occur in lacustrine environments (Flügel, 2010), their presence often indicates an increase in salinity, but not necessarily a direct connection to the sea. As highlighted by Lettéron et al. (2017, 2018), benthic foraminifera can inhabit saline lakes not connected to the sea, as evidenced by the studies conducted by Cann and De Deckker (1981) in Australia and Plaziat (1991) in Egypt. Long-distance transport by birds may explain the colonization of foraminifera in isolated lakes, as documented by Patterson et al. (1997) in Holocene lakes. Lettéron et al. (2017) describe various ways in which lakes can become more saline over time, including leaching of salt formations and subsequent salt concentration through evaporation, mixing with hydrothermal fluids, connection to the sea through structural corridors or groundwater inflows, exhumation of salt diapirs, and accumulation of marine aerosols over an exposed continent. In the Arc Basin, the leaching of Triassic evaporites outcropping in the drainage area, such as in surrounding massifs (Etoile and Sainte-Baume) resulting from Pyreneo-Provençal structuration, may have significantly enriched the lake water in sulfate.

The age of the Cengle limestones being Dano–early Selandian, as indicated by U–Pb dating, may suggest a potential relationship between increased salinity and marine transgression events recorded in Bas-Languedoc during the late Danian and early Selandian (Combes et al., 2007, 2008; Peybernès et al., 2014) as presented in paleogeographic reconstructions in Fig. 3.17. Combes et al. (2007) identified three marine transgression events dated at 62.5 Ma, ~61 Ma, and ≥59.2 Ma, based on microfauna in marine deposits filling paleokarsts. Although such marine channels and gulfs did not reach the studied region near Aix-en-Provence, they may have influenced lake salinity through underground hydrodynamics, with salt concentration possibly intensified by evaporation.

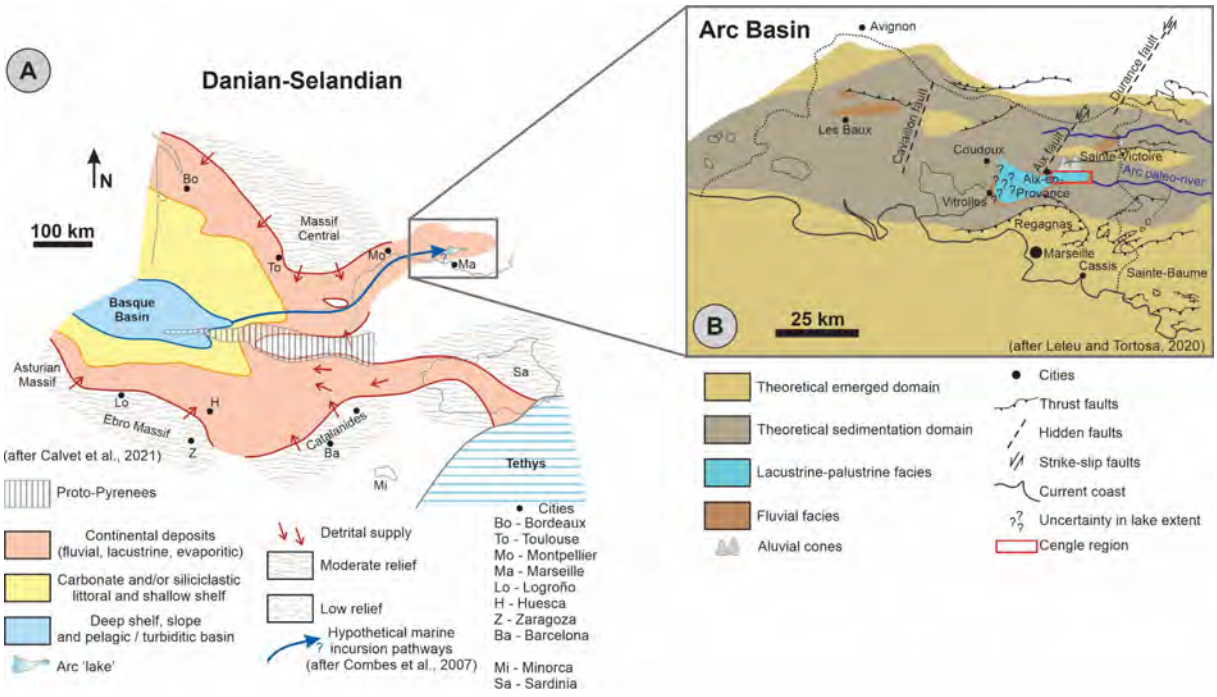


**Fig. 3.17.** Paleogeographic reconstructions maps. A) Paleogeography of the Pyrenees from early Paleocene (Danian–Selandian) after Calvet et al. (2021), showing hypothetical marine pathways (after Combes et al., 2007) to Arc Basin. B) Paleogeography of the Arc Basin from the same period after Leleu and Tortosa (2020).

## 3.6. Conclusion

The detailed analysis of lithofacies, vertical stacking patterns, and lateral facies variations, combined with the investigation of carbon and oxygen isotopic data, along with U–Pb dating on carbonates in the limestone outcrops of the Cengle Plateau cliff, has provided relevant insights into the interaction of lacustrine, palustrine, and pedogenic environments. This integrated approach not only enhances the understanding of sedimentary processes but also contributes to a more comprehensive view of environmental dynamics in palustrine-dominated depositional sequences:

- In this depositional context, the proposed conceptual model and exposure index underscore the importance of facies analysis, their anatomies, stacking patterns, and hierarchies. These aspects reflect climate and paleogeographic changes in the basin, controlling not only sedimentary dynamics but also influencing the preservation process in the geological record. These findings are not only applicable in other areas with similar sedimentary contexts but also possess predictive value, anticipating the types of facies, their extensions, and thicknesses based on the position of the basin (proximal or distal).
- In the studied area, the recurrence of depositional sequences, influenced by high-frequency fluctuations in lake level, highlights the importance of pedogenesis in the formation of these deposits, with palustrine conditions prevailing over lacustrine ones. Long-term subaerial exposures, controlled by low-frequency fluctuations in the base level, form pedogenic facies, mainly at the top of lower-order stratigraphic sequences and in coastal regions of the lake.
- The allocyclic nature of the deposition of the limestones of ‘La Barre du Cengle’ is indicated by the recurrence of elementary sequences, organized into small-scale sequences, which are mappable throughout the area, combined with hierarchical stratigraphic control, wherein lower hierarchies impose restrictions on higher hierarchies. Despite the challenge in dating different frequencies controlling lake level variation, cyclic climatic variations, potentially linked to orbital and suborbital cycles, appear to shape the observed sedimentary record.
- The deposition age of the carbonates of the Cengle Plateau cliff has been assigned to the Danian to early Selandian.
- In the paleoclimatic scenario of the deposition of the studied carbonates, subarid climatic conditions predominated. *Microcodium in situ* aggregates formed under the influence of drier climates and were reworked and transported as debris to the lake during wetter periods.
- In paleogeographic terms, cyclic high and medium-frequency fluctuations in the base level modified the paleogeography of the lake over time and space. The presence of benthic foraminifera at the top of the section indicates salinity variations, possibly influenced by marine transgressions.

## Acknowledgments

The authors would like to thank the *Domaine des Masques* and the other landowners along the Cengle Plateau who graciously granted access to their areas, facilitating fieldwork and data collection. Special thanks to Mr. Georges Flayols for providing a panoramic photograph of the Cengle Plateau. We are also grateful to Mr. Louis Godaert for his assistance with operating the SEM and to Mr. Jean-Pierre Margerel for identifying the genus of foraminifera present in the study area. We extend our appreciation to Petrobras for funding and supporting this work. Additionally, we would like to acknowledge Dr. André Strasser and an anonymous reviewer

for their insightful comments and thorough reviews, as well as to the Editor-in-Chief, Dr. Catherine Chagué, for her valuable suggestions. Their feedback was instrumental in significantly improving this manuscript.

## References

Alonso-Zarza, A.M., 2003. Palaeoenvironmental significance of palustrine carbonates and calcretes in the geological record. Earth-Science Reviews 60, 261–298. https://doi.org/10.1016/S0012-8252(02)00106-X

Alonso-Zarza, A.M., Dorado-Valiño, M., Valdeolmillos-Rodríguez, A., Ruiz-Zapata, M.B., 2006. A recent analogue for palustrine carbonate environments: The Quaternary deposits of Las Tablas de Daimiel wetlands, Ciudad Real, Spain. Special Paper of the Geological Society of America 416, 153–168. https://doi.org/10.1130/2006.2416(10)

Alonso-Zarza, A.M., Genise, J.F., Verde, M., 2011. Sedimentology, diagenesis and ichnology of Cretaceous and Palaeogene calcretes and palustrine carbonates from Uruguay. Sedimentary Geology 236, 45–61. https://doi.org/10.1016/j.sedgeo.2010.12.003

Alonso-Zarza, A.M., Wright, V.P., 2010a. Palustrine Carbonates, in: Alonso-Zarza, A.M., Tanner, L.H. (Eds.), Carbonates in Continental Settings Facies, Environments, and Processes, Developments in Sedimentology. Elsevier, Amsterdam, pp. 103–131. https://doi.org/10.1016/S0070-4571(09)06102-0

Alonso-Zarza, A.M., Wright, V.P., 2010b. Calcretes, in: Alonso-Zarza, A.M., Tanner, L.H. (Eds.), Carbonates in Continental Settings Facies, Environments, and Processes, Developments in Sedimentology. Elsevier, Amsterdam, pp. 225–267. https://doi.org/10.1016/S0070-4571(09)06105-6

Angst, D., Buffetaut, E., Lécuyer, C., Amiot, R., Smektala, F., Giner, S., Méchin, A., Méchin, P., Amoros, A., Leroy, L., Guiomar, M., Tong, H., Martinez, A., 2015. Fossil avian eggs from the Palaeogene of southern France: new size estimates and a possible taxonomic identification of the egg-layer. Geological Magazine 152, 70–79. https://doi.org/DOI: 10.1017/S0016756814000077

Armenteros, I., Daley, B., García, E., 1997. Lacustrine and palustrine facies in the Bembridge Limestone (late Eocene, Hampshire Basin) of the Isle of Wight, southern England. Palaeogeography, Palaeoclimatology, Palaeoecology 128, 111–132. https://doi.org/https://doi.org/10.1016/S0031-0182(96)00108-3

Arostegi, J., Baceta, J.I., Pujalte, V., Carracedo, M., 2011. Late Cretaceous—Palaeocene mid-latitude climates: inferences from clay mineralogy of continental-coastal sequences (Tremp-Graus area, southern Pyrenees, N Spain). Clay Minerals 46, 105–126. https://doi.org/10.1180/claymin.2011.046.1.105

Baccelle, L., Bosellini, A., 1965. Diagrammi per la stima visiva della composizione percentuale nelle roccē sedimentarie. Annali della Università di Ferrara, Sezione IX. Scienze Geologiche e Paleontologiche 1 4, 59–62.

Bahniuk, A.M., Anjos, S., França, A.B., Matsuda, N., Eiler, J., Mckenzie, J.A., Vasconcelos, C., 2015. Development of microbial carbonates in the Lower Cretaceous Codó Formation (north-east Brazil): Implications for interpretation of microbialite facies associations and palaeoenvironmental conditions. Sedimentology 62, 155–181. https://doi.org/10.1111/sed.12144

Barrell, J., 1917. Rhythms and the measurements of geologic time. Geological Society of America Bulletin 28, 745–904. https://doi.org/10.1130/GSAB-28-745

Bistacchi, A., Mittempergher, S., Martinelli, M., 2022. Digital Outcrop Model Reconstruction and Interpretation, in: Bistacchi, A., Massironi, M., Viseur, S. (Eds.), 3D Digital Geological Models: From Terrestrial Outcrops to Planetary Surfaces. Wiley, pp. 11–32. https://doi.org/https://doi.org/10.1002/9781119313922.ch2

Bodergat, A.-M., 1974. Les microcodiums. Milieux et modes de développement. Documents des Laboratoires de Géologie de la Faculté des Sciences de Lyon 62, 137–255.

Boggs, S., 2011. Principles of Sedimentology and Stratigraphy, 5th ed. Pearson.

Brunier, G., Fleury, J., Anthony, E.J., Gardel, A., Dussouillez, P., 2016. Close-range airborne Structure-from-Motion Photogrammetry for high-resolution beach morphometric surveys: Examples from an embayed rotating beach. Geomorphology 261, 76–88. https://doi.org/10.1016/j.geomorph.2016.02.025

Calvet, M., Gunnell, Y., Laumonier, B., 2021. Denudation history and palaeogeography of the Pyrenees and their peripheral basins: an 84-million-year geomorphological perspective. Earth-Science Reviews 215, 103436. https://doi.org/10.1016/J.EARSCIREV.2020.103436

Cann, J.H., De Deckker, P., 1981. Fossil Quaternary and Living Foraminifera from Athalassic (Non-Marine) Saline Lakes, Southern Australia. Journal of Paleontology 55, 660–670.

Catuneanu, O., Zecchin, M., 2013. High-resolution sequence stratigraphy of clastic shelves II: Controls on sequence development. Marine and Petroleum Geology 39, 26–38. https://doi.org/10.1016/j.marpetgeo.2012.08.010

Cojan, I., 1993. Alternating Fluvial and Lacustrine Sedimentation: Tectonic and Climatic Controls (Provence Basin, S. France, Upper Cretaceous/Palaeocene), in: Alluvial Sedimentation. pp. 425–438. https://doi.org/https://doi.org/10.1002/9781444303995.ch27

Cojan, I., Moreau, M.-G., 2006. Correlation of Terrestrial Climatic Fluctuations with Global Signals During the Upper Cretaceous–Danian in a Compressive Setting (Provence, France). Journal of Sedimentary Research 76, 589–604. https://doi.org/10.2110/jsr.2006.045

Cojan, I., Moreau, M.-G., Stott, L.E., 2000. Stable carbon isotope stratigraphy of the Paleogene pedogenic series of southern France as a basis for continental-marine correlation. Geology 28, 259–262. https://doi.org/10.1130/0091-7613(2000)28<259:SCISOT>2.0.CO;2

Combes, P.J., Peybernès, B., Fondecave-Wallez, M.J., Séranne, M., Lesage, J.L., Camus, H., 2008. Reply to comment on Latest-Cretaceous/Paleocene karsts with marine infillings from Languedoc (South of France); paleogeographic, hydrogeologic and geodynamic implications. Geodinamica Acta. https://doi.org/10.3166/ga.21.139-143

Combes, P.J., Peybernès, B., Fondecave-Wallez, M.J., Séranne, M., Lesage, J.L., Camus, H., 2007. Latest-Cretaceous/Paleocene karsts with marine infillings from Languedoc (South of France); paleogeographic, hydrogeologic and geodynamic implications. Geodinamica Acta 20, 301–326. https://doi.org/10.3166/ga.20.301-326

Corroy, G., Touraine, F., 1961. Données nouvelles sur la stratigraphie du Grand-Cabri et du Cengle (Bouches-du-Rhone). Bulletin de la Société Géologique de France S7-III, 77–81. https://doi.org/10.2113/gssgfbull.S7-III.1.77

Dunham, R.J., 1962. Classification of Carbonate Rocks According to Depositional Texture, in: Ham, W.E. (Ed.), Classification of Carbonate Rocks - A Symposium. American Association of Petroleum Geologists, Tulsa, pp. 108–121.

Durand, J.-P., 1984. Paléocène et Éocène, in: Debrand-Passard, S. (Ed.), Synthèse Géologique Du Sud-Est de La France. Mémoire Du Bureau de Recherches Géologiques et Minières. BRGM, pp. 426–429.

Durand, J.-P., 1963. Les formations fluvio-lacustres éocènes du plateau du Cengle près d'Aix-en-Provence. Annales de la faculté des sciences de Marseille 34, 83–105.

Durand, J.P., Tempier, C., 1968. Le bassin de l'Arc, in: Excursion Géologique En Basse-Provence Occidentale. Marseille, pp. 25–33.

Esteban, M., 1974. Caliche textures and Microcodium. Bollettino della Società Geologica Italiana 92, 105–125.

Feist-Castel, M., 1975. Répartition des Charophytes dans le Paléocène et l'Éocène du bassin d'Aix-en-Provence. Bulletin de la Société Géologique de France S7-XVII, 88–97. https://doi.org/10.2113/gssgfbull.S7-XVII.1.88

Floquet, M., 2020. Le Bassin marin Sud-Provençal : de son extension à partir du Cénomanien (vers -100 Ma) jusqu'à sa fermeture au Santonien supérieur (vers -84 Ma), in: La Géologie Des Bouches-Du-Rhône, Roches et Paysages Remarquables. BRGM Editions, pp. 69–86.

Flügel, E., 2010. Microfacies of Carbonate Rocks: Analysis, Interpretation and Application, 2nd ed. Springer Berlin Heidelberg, Berlin, Heidelberg. https://doi.org/10.1007/978-3-642-03796-2

Folk, R.L., 1993. SEM imaging of bacteria and nannobacteria in carbonate sediments and rocks. Journal of Sedimentary Petrology 63, 990–999. https://doi.org/10.1306/D4267C67-2B26-11D7-8648000102C1865D

Fragoso, D.G.C., Gabaglia, G.P.R., Magalhães, A.J.C., Scherer, C.M.D.S., 2021. Cyclicity and hierarchy in sequence stratigraphy: An integrated approach. Brazilian Journal of Geology 51, e20200106. https://doi.org/10.1590/2317-4889202120200106

Fragoso, D.G.C., Melo, A.H. de, Gonçalves, L.A., Bunevich, R.B., Araujo, J. de A.M., Costa, T.C. da, Pedrosa, C.A., Scherer, C.M.D.S., 2023. High-resolution sequence stratigraphy applied to reservoir characterization of the Brazilian Cretaceous pre-salt section, Campos Basin: Guidelines for geological modeling and reservoir management. Marine and Petroleum Geology 151, 106203. https://doi.org/10.1016/j.marpetgeo.2023.106203

Freytet, P., 1973. Petrography and paleo-environment of continental carbonate deposits with particular reference to the upper cretaceous and lower eocene of languedoc (Southern France). Sedimentary Geology 10, 25–60. https://doi.org/10.1016/0037-0738(73)90009-2

Freytet, P., 1971. Paléosols résiduels et paléosols alluviaux hydromorphes dans le Crétacé Supérieur et l'Eocene basal en Languedoc. Revue de Géographie Physique et de Géologie Dynamique 2, 245–268.

Freytet, P., 1965. Sédimentation microcyclothématique avec croûte zonaire à algues dans le Calcaire de Veauce de Chauffour-Ethrechy (S.-et-O.). Bulletin de la Societé Géologique de France 7, 309–313.

Freytet, P., Plaziat, J.-C., 1982. Continental Carbonate Sedimentation and Pedogenesis - Late Cretaceous and Early Tertiary of Southern France, Contributions to Sedimentology. E. Schweizerbart, Stuttgart.

Freytet, P., Verrecchia, E.P., 2002. Lacustrine and palustrine carbonate petrography: an overview. Journal of Paleolimnology 27, 221–237. https://doi.org/10.1023/A:1014263722766

Garcia, G., Vianey-Liaud, M., 2001. Dinosaur eggshells as biochronological markers in Upper Cretaceous continental deposits. Palaeogeography, Palaeoclimatology, Palaeoecology 169, 153–164. https://doi.org/10.1016/S0031-0182(01)00215-2

Gierlowski-Kordesch, E.H., 2010. Lacustrine Carbonates, in: Alonso-Zarza, A.M., Tanner, L.H. (Eds.), Carbonates in Continental Settings Facies, Environments, and Processes, Developments in Sedimentology. Elsevier, Amsterdam, pp. 1–101. https://doi.org/10.1016/S0070-4571(09)06101-9

Godinot, M., 1984. Un nouveau genre de Paromomyidae (Primates) de l'Eocène Inférieur d'Europe: A New Genus of Paromomyidae (Primates) from the Lower Eocene of Europe. Folia Primatologica 43, 84–96. https://doi.org/10.1159/000156174

Godinot, M., Crochet, J.-Y., Hartenberger, J.-L., Lange-Badré, B., Russell, D.E., Sigé, B., 1987. Nouvelles données sur les mammifères de Palette (Éocène inferieur, Provence). Münchner geowiss, Abh. 10, 273–288.

Gradstein, F.M., Ogg, J.G., Schmitz, M.D., Ogg, G.M., 2012. The Geologic Time Scale 2012. Elsevier.

Hinnov, L.A., 2013. Cyclostratigraphy and its revolutionizing applications in the earth and planetary sciences. Geological Society of America Bulletin 125, 1703–1734. https://doi.org/10.1130/B30934.1

Hoefs, J., 2015. Stable Isotope Geochemistry, 7th ed. Springer International Publishing, Cham. https://doi.org/10.1007/978-3-319-19716-6

Horstwood, M.S.A., Košler, J., Gehrels, G., Jackson, S.E., McLean, N.M., Paton, C., Pearson, N.J., Sircombe, K., Sylvester, P., Vermeesch, P., Bowring, J.F., Condon, D.J., Schoene, B., 2016. Community-Derived Standards for LA-ICP-MS U-(Th-)Pb Geochronology – Uncertainty Propagation, Age Interpretation and Data Reporting. Geostandards and Geoanalytical Research 40, 311–332. https://doi.org/10.1111/j.1751-908X.2016.00379.x

Horton, T.W., Defliese, W.F., Tripati, A.K., Oze, C., 2016. Evaporation induced 18O and 13C enrichment in lake systems: A global perspective on hydrologic balance effects. Quaternary Science Reviews 131, 365–379. https://doi.org/10.1016/j.quascirev.2015.06.030

Jouzel, J., Masson-Delmotte, V., Cattani, O., Dreyfus, G., Falourd, S., Hoffmann, G., Minster, B., Nouet, J., Barnola, J.M., Chappellaz, J., Fischer, H., Gallet, J.C., Johnsen, S., Leuenberger, M., Loulergue, L., Luethi, D., Oerter, H., Parrenin, F., Raisbeck, G., Raynaud, D., Schilt, A., Schwander, J., Selmo, E., Souchez, R., Spahni, R., Stauffer, B., Steffensen, J.P., Stenni, B., Stocker, T.F., Tison, J.L., Werner, M., Wolff, E.W., 2007. Orbital and Millennial Antarctic Climate Variability over the Past 800,000 Years. Science 317, 793–796. https://doi.org/10.1126/science.1141038

Kabanov, P., Anadón, P., Krumbein, W.E., 2008. Microcodium: An extensive review and a proposed non-rhizogenic biologically induced origin for its formation. Sedimentary Geology 205, 79–99. https://doi.org/10.1016/j.sedgeo.2008.02.003

Kruiver, P.P., Krijgsman, W., Langereis, C.G., Dekkers, M.J., 2002. Cyclostratigraphy and rock-magnetic investigation of the NRM signal in late Miocene palustrine-alluvial

deposits of the Librilla section (SE Spain). Journal of Geophysical Research: Solid Earth 107. https://doi.org/10.1029/2001jb000945

Le Calvez, Y., 1970. Contribution à l'étude des foraminifères paléogènes du Bassin de Paris. Cahiers de Paléontologie, CNRS, Paris.

Leleu, S., 2005. Les cônes alluviaux Crétacé Supérieur/Paléocène en Provence : traceurs de l'évolution morpho-tectonique des stades précoces de collision. Université Louis Pasteur, Strasbourg.

Leleu, S., Tortosa, T., 2020. Les ultimes formations continentales du Paléogène : du Danien au Lutétien (de -66 Ma à -43 Ma environ), in: La Géologie Des Bouches-Du-Rhône. Roches et Paysages Remarquables. BRGM Editions, pp. 104–116.

Leng, M.J., Marshall, J.D., 2004. Palaeoclimate interpretation of stable isotope data from lake sediment archives. Quaternary Science Reviews 23, 811–831. https://doi.org/10.1016/j.quascirev.2003.06.012

Lettéron, A., Fournier, F., Hamon, Y., Villier, L., Margerel, J.P., Bouche, A., Feist, M., Joseph, P., 2017. Multi-proxy paleoenvironmental reconstruction of saline lake carbonates: Paleoclimatic and paleogeographic implications (Priabonian-Rupelian, Issirac Basin, SE France). Sedimentary Geology 358, 97–120. https://doi.org/10.1016/j.sedgeo.2017.07.006

Lettéron, A., Hamon, Y., Founier, F., Séranne, M., Pellenard, P., Joseph, P., 2018. Reconstruction of a saline, lacustrine carbonate system (Priabonian, St-Chaptes Basin, SE France): depositional models, paleogeographic and paleoclimatic implications. Sedimentary Geology 367, 20–47. https://doi.org/10.1016/j.sedgeo.2017.12.023

Lowe, D.G., 2004. Distinctive Image Features from Scale-Invariant Keypoints. International Journal of Computer Vision 60, 91–110. https://doi.org/https://doi.org/10.1023/B:VISI.0000029664.99615.94

Magalhães, A.J.C., Raja Gabaglia, G.P., Fragoso, D.G.C., Bento Freire, E., Lykawka, R., Arregui, C.D., Silveira, M.M.L., Carpio, K.M.T., De Gasperi, A., Pedrinha, S., Artagão, V.M., Terra, G.J.S., Bunevich, R.B., Roemers-Oliveira, E., Gomes, J.P., Hernández, J.I., Hernández, R.M., Bruhn, C.H.L., 2020. High-resolution sequence stratigraphy applied to reservoir zonation and characterisation, and its impact on production performance - shallow marine, fluvial downstream, and lacustrine carbonate settings. Earth-Science Reviews 210, 103325. https://doi.org/10.1016/j.earscirev.2020.103325

Marques, A., Horota, R.K., de Souza, E.M., Kupssinskü, L., Rossa, P., Aires, A.S., Bachi, L., Veronez, M.R., Gonzaga, L., Cazarin, C.L., 2020. Virtual and digital outcrops in the petroleum industry: A systematic review. Earth-Science Reviews. https://doi.org/10.1016/j.earscirev.2020.103260

Matheron, P., 1878. Recherches paléontologiques dans le Midi de la France. Quinzième partie. Terrain Tertiaire. Marseille.

Matthew, A.J., Woods, A.J., Oliver, C., 1991. Spots before the eyes: new comparison charts for visual percentage estimation in archaeological material, in: Middleton, A.P., Freestone, I.C. (Eds.), Recent Developments in Ceramic Petrology. British Museum Occasional Paper, London, pp. 211–263.

Mazzullo, S.J., Birdwell, B.A., 1989. Syngenetic formation of grainstones and pisolites from fenestral carbonates in peritidal settings. Journal of Sedimentary Petrology 59, 605–611. https://doi.org/10.1306/212F9002-2B24-11D7-8648000102C1865D

Méndez-Bedia, I., Gallastegui, G., Busquets, P., Césari, S.N., Limarino, C.O., Prats, E., Cardó, R., Colombo, F., 2020. Pedogenic and subaerial exposure microfabrics in a late Carboniferous-early Permian carbonate-volcanic lacustrine-palustrine system (San Ignacio Formation, Frontal Cordillera, Argentina). Andean Geology 47, 275–294. https://doi.org/10.5027/andgeov47n2-3214

Miall, A.D., 2000. Principles of Sedimentary Basin Analysis, 3rd ed. Springer, Berlin. https://doi.org/10.1007/978-3-662-03999-1

Murru, M., Ferrara, C., Da Pelo, S., Ibba, A., 2003. The Palaeocene–Middle Eocene deposits of Sardinia (Italy) and their palaeoclimatic significance. Comptes Rendus - Geoscience 335, 227–238. https://doi.org/10.1016/S1631-0713(03)00029-4

Oliveira, M.J. de, Carneiro, C.D.R., Vecchia, F.A. da S., Baptista, G.M. de M., 2017. Ciclos climáticos e causas naturais das mudanças do clima. Terrae Didatica 13, 149–184. https://doi.org/10.20396/td.v13i3.8650958

Pagel, M., Bonifacie, M., Schneider, D.A., Gautheron, C., Brigaud, B., Calmels, D., Cros, A., Saint-Bezar, B., Landrein, P., Sutcliffe, C., Davis, D., Chaduteau, C., 2018. Improving paleohydrological and diagenetic reconstructions in calcite veins and breccia of a sedimentary basin by combining Δ47 temperature, δ18Owater and U-Pb age. Chemical Geology 481, 1–17. https://doi.org/10.1016/J.CHEMGEO.2017.12.026

Patterson, R.T., Mckillop, W.B., Kroker, S., Nielsen, E., Reinhardt, E.G., 1997. Evidence for rapid avian-mediated foraminiferal colonization of Lake Winnipegosis, Manitoba, during the Holocene Hypsithermal. Journal of Paleolimnology 18, 131–143. https://doi.org/10.1023/A:1007927622654

Payros, A., Pujalte, V. no, Schmitz, B., 2022. Mid- latitude alluvial and hydroclimatic changes during the Paleocene–Eocene Thermal Maximum as recorded in the Tremp- Graus Basin, Spain. Sedimentary Geology 435. https://doi.org/10.1016/j.sedgeo.2022.106155

Peybernès, B., Melinte-Dobrinescu, M., Fondecave-Wallez, M.-J., 2014. Découverte de nannofossiles calcaires paléocènes dans les brèches marines remplissant les paléokarsts du synclinal d'Amélie-les-Bains (couverture de la Haute-Chaîne Primaire, Pyrénées Orientales, France). Revue de Paléobiologie 33, 455–462.

Platt, N.H., Wright, V.P., 2023. Flooding of a carbonate platform: The Sian Ka'an Wetlands, Yucatán, Mexico—A model for the formation and evolution of palustrine carbonate factories around the modern Caribbean Sea and in the depositional record. Depositional Record 9, 99–151. https://doi.org/10.1002/dep2.217

Platt, N.H., Wright, V.P., 1992. Palustrine carbonates and the Florida Everglades; towards an exposure index for the fresh-water environment? Journal of Sedimentary Petrology 62, 1058–1071. https://doi.org/https://doi.org/10.1306/D4267A4B-2B26-11D7-8648000102C1865D

Plaziat, J.-C., 1991. Paleogeographic significance of the Cardium, Potamids and Foraminifera living in intra-continental salt lakes of North Africa (Sahara Quaternary, Egypt Present lakes). Journal of African Earth Sciences 12, 383–389. https://doi.org/10.1016/0899-5362(91)90087-F

Plaziat, J.-C., 1984. Le domaine pyrénéen de la fin du Crétacé à la fin de l'Éocène. Stratigraphie, paléoenvironnements et évolution paléogéographique (3 vol.). Université Paris-Sud, Orsay.

Plaziat, J.C., Freytet, P., 1978. Le pseudo-microkarst pédologique: un aspect particulier des paléo-pédogenèses développées sur les dépôts calcaires lacustres dans le Tertiaire du Languedoc. Compte Rendus Academie des Sciences de Paris 286, 1661–1664.

Pujalte, V., Monechi, S., Ortíz, S., Orue-Etxebarria, X., Rodríguez-Tovar, F., Schmitz, B., 2019. Microcodium-rich turbidites in hemipelagic sediments during the Paleocene–Eocene Thermal Maximum: Evidence for extreme precipitation events in a Mediterranean climate (Río Gor section, southern Spain). Global and Planetary Change 178, 153–167. https://doi.org/10.1016/j.gloplacha.2019.04.018

Roberts, N.M.W., Rasbury, E.T., Parrish, R.R., Smith, C.J., Horstwood, M.S.A., Condon, D.J., 2017. A calcite reference material for LA-ICP-MS U-Pb geochronology. Geochemistry, Geophysics, Geosystems 18, 2807–2814. https://doi.org/10.1002/2016GC006784

Roemers-Oliveira, E., Fernandes, L.A., Bento Freire, E., Amarante Simões, L.S., 2015. Microbial filaments in stromatolites and laminites of Balbuena III Sequence (Maastrichtian/Danian) of Yacoraite Formation in Metán-Alemania Sub-basin, Salta region, Argentina, and its palaeoenvironmental significance. Brazilian Journal of Geology 45, 399–413. https://doi.org/10.1590/2317-488920150030255

Roemers-Oliveira, E., Fournier, F., Viseur, S., Raja Gabaglia, G.P., Fleury, J., Rinalducci, V., Guihou, A., Marié, L., Guadagnin, F., Deschamps, P., Tonetto, A., 2024. The anatomy and stacking pattern of palustrine-dominated carbonate sequences from the Cengle Plateau, Paleocene, SE France: A multi-scalar approach. Sedimentary Geology 470, 106690. https://doi.org/10.1016/j.sedgeo.2024.106690

Rouire, J., 1979. Notice explicative de la carte géologique de Marseille 1/250 000. Orléans.

Savage, D.E., Russell, D.E., Louis, P., 1965. European Eocene Equidae (Perissodactyla). Berkeley: University of California Press.

Scholle, P.A., Ulmer-Scholle, D.S., 2003. A Color Guide to the Petrography of Carbonate Rocks: Grains, textures, porosity, diagenesis. American Association of Petroleum Geologists, Tulsa. https://doi.org/10.1306/M77973

Sharp, Z., 2017. Principles of Stable Isotope Geochemistry, 2nd ed.

Strasser, A., 2018. Cyclostratigraphy of Shallow-Marine Carbonates – Limitations and Opportunities, in: Montenari, M. (Ed.), Stratigraphy & Timescales. Academic Press, pp. 151–187. https://doi.org/10.1016/bs.sats.2018.07.001

Strasser, A., Pittet, B., Hillgärtner, H., Pasquier, J.-B., 1999. Depositional sequences in shallow carbonate-dominated sedimentary systems: concepts for a high-resolution analysis. Sedimentary Geology 128, 201–221. https://doi.org/10.1016/S0037-0738(99)00070-6

Tanrattana, M., Boura, A., Jacques, F.M.B., Villier, L., Fournier, F., Enguehard, A., Cardonnet, S., Voland, G., Garcia, A., Chaouch, S., De Franceschi, D., 2020. Climatic evolution in western europe during the cenozoic: Insights from historical collections using leaf physiognomy. Geodiversitas 42, 151–174. https://doi.org/10.5252/geodiversitas2020v42a11

Tortosa, T., Leleu, S., 2020. Les bassins continentaux et la première orogenèse provençale au Crétacé final : du Santonien terminal au Maastrichtien (-85 Ma à -66 Ma), in: La Géologie Des Bouches-Du-Rhône. Roches et Paysages Remarquables. BRGM Editions, pp. 87–103.

Vermeesch, P., 2018. IsoplotR: A free and open toolbox for geochronology. Geoscience Frontiers 9, 1479–1493. https://doi.org/10.1016/j.gsf.2018.04.001

Villot, M., 1883. Étude sur le bassin de Fuveau et sur un grand travail à y exécuter. Annales des Mines 8, 5–66.

Wanas, H.A., Soliman, H.E., 2014. Calcretes and palustrine carbonates in the Oligo-Miocene clastic-carbonate unit of the Farafra Oasis, Western Desert, Egypt: Their origin and paleoenvironmental significance. Journal of African Earth Sciences 95, 145–154. https://doi.org/10.1016/j.jafrearsci.2014.03.012

Welton, J.E., 1984. SEM Petrology Atlas. American Association of Petroleum Geologists. https://doi.org/10.1306/Mth4442

Westphal, M., Durand, J.-P., 1990. Magnetostratigraphie des séries continentales fluvio-lacustres du Crétacé supérieur dans le synclinal de l'Arc (région d'Aix-en-Provence, France). Bulletin de la Société Géologique de France VI, 609–620. https://doi.org/10.2113/gssgfbull.VI.4.609

Wright, V.P., 1990. Syngenetic formation of grainstones and pisolites from fenestral carbonates in peritidal settings; discussion and reply. Journal of Sedimentary Petrology 60, 309–310. https://doi.org/https://doi.org/10.1306/212F9188-2B24-11D7-8648000102C1865D

Wright, V.P., Platt, N.H., 1995. Seasonal wetland carbonate sequences and dynamic catenas: a re-appraisal of palustrine limestones. Sedimentary Geology 99, 65–71. https://doi.org/10.1016/0037-0738(95)00080-R

Wright, V.P., Tucker, M.E., 1991. Calcretes. Wiley. https://doi.org/10.1002/9781444304497

Zachos, J.C., Lohmann, K.C., Walker, J.C.G., Wise, S.W., 1993. Abrupt climate change and transient climates during the Paleogene: a marine perspective. The Journal of Geology 101, 191–213. https://doi.org/10.1086/648216

Zachos, J.C., Röhl, U., Schellenberg, S.A., Sluijs, A., Hodell, D.A., Kelly, D.C., Thomas, E., Nicolo, M., Raffi, I., Lourens, L.J., McCarren, H., Kroon, D., 2005. Rapid Acidification of the Ocean During the Paleocene-Eocene Thermal Maximum. Science 308, 1611–1615. https://doi.org/10.1126/science.1109004

Zecchin, M., 2007. The architectural variability of small-scale cycles in shelf and ramp clastic systems: The controlling factors. Earth-Science Reviews 84, 21–55. https://doi.org/10.1016/j.earscirev.2007.05.003

# Supplementary table

**Table S3.1**. Laser ablation ICP-MS parameters used for dating.

| | |
|---|---|
| **Sample preparation** | |
| Sample preparation | ~30 or ~100 µm slices |
| Imaging | Optical |
| **LASER ablation system U-Pb dating** | |
| Make, Model & Type | ESI, NWR193 |
| Ablation cell & size | TV2 150mmx150mm |
| LASER wavelength (nm) | 193 |
| Pulse duration (ns) | 4 |
| Fluence ($J.cm^{-2}$) | 0.9 - 1.4 |
| Repetition rate (Hz) | 15 |
| Spot size (µm) | 150 |
| Sampling | Spot |
| Carrier gas | He 5.0 ~0.9 $l.min^{-1}$, Ar make-up gas ~1 $l.min^{-1}$ combined using a Y-piece ~50cm before the connection to the injector |
| Ablation duration (s) | 3s warmup - 4 s preablation - 15 s washout - 3s warmup - 20 s ablation - 15 s washout |
| **ICP-MS system U-Pb dating** | |
| Make, Model & Type | Thermo Fisher Scientific, Element XR |
| RF Power (W) | 1200 - 1300 |
| Make-up gas flow ($l.min^{-1}$) | ~1 |
| Detection System | SEM forced in counting mode |
| Masses measured | 206Pb, 207Pb, 208Pb, 232Th, 238U |
| Integration time per peak (s) | 0.04, 0.04, 0.02, 0.012, 0.012 |
| Total integration time per cycle (s) | 0.129 // Mass accuracy option |
| Sensitivity | ~100 kcps for 823 ng/g U |
| IC dead time (s) | 26 |
| **Data processing U-Pb dating** | |
| Gas blank | on-peak zero substraction, ~7s signal intensity integration during the washout between each preablation and ablation |
| Calibration | Daily tuning with NIST-612 then during sequence analyses use of NIST-614 glass standard as primary reference material for drift (Woodhead and Hergt, 2001); WC-1 carbonate reference material for matrix matching of $^{206}Pb/^{238}U$; AUG-B6 as secondary material; JCP1-np from myStandards GmbH for [U], [Pb], [Th] calibration |
| Reference material info | WC1 (Roberts et al. 2017) and AUG-B6 (Pagel et al. 2018) |
| Data processing | Raw intensities, baseline subtraction, calulation of log-ratios with Iolite 3.65 (Paton et al, 2011)<br>Instrumental drift check, geometric averages of the ratios and $^{206}Pb/^{238}U$ ratios corrections using a fractionation factor calculated from WC1 radiogenic intercept with the concordia, exclusion of spots with mean $^{207}Pb$ intensities using a cutoff value calculated by adding ten times the standard deviation to the average baseline intensity on $^{207}Pb$ for each session using an in-house Excel spreadsheet<br>IsoplotR (Vermeesch, 2018) for T-W isochrons (model-1), 2s as input, 95% confidence interval as output, intercept ages and initial Pb compositions |
| Mass discrimination | 1 set of standards every ~75 spots |
| Common-Pb correction, composition and uncertainty | None applied. Ages calculated from regressions used in Tera Wasserburg plots |
| Uncertainty level & propagation | Ages are quoted at 95% confidence interval including the propagation of systematic uncertainty by quadratic addition of 2.5% on WC1 age and an extra 3.5% to account for the uncertainty on AUG-B6 secondary standard which is still under evaluation through an inter laboratory comparison |
| Quality control / Validation | AUG-B6 - mean age: 42Ma±2Ma (2SD, n=3) in agreement with the age published by Pagel et al (2018): 43Ma±1.5Ma |

*Le Barrage de François Zola, Paul Cézanne, 1879, via Wikimedia Commons.*

*« Que ta vision soit à chaque instant nouvelle. Le sage est celui qui s'étonne de tout. »*

*André Gide, Les nourritures terrestres (1897)*

## Chapter 4
## Salta Basin

This chapter is based on the article accepted for publication in *Marine and Petroleum Geology* on October 6, 2025.

# Advanced digital techniques applied to outcrop models: Integrating Local Binary Pattern (LBP) and Convolutional Neural Network (CNN) to support stratigraphic and sedimentological interpretation of reservoir analogs in the Salta Basin, Argentina

Eduardo Roemers-Oliveira[1,2], Sophie Viseur[1], François Fournier[1], Ítalo Gomes Gonçalves[3], Felipe Guadagnin[3], Guilherme Pederneiras Raja Gabaglia[2], Ednilson Bento Freire[2], Daniel Galvão Carnier Fragoso[2,4,5], Juan Hernández[6], Ana Clara Freccia[3], Guilherme de Godoy Rangel[3]

[1]Aix Marseille Université, CNRS, IRD, INRAE, CEREGE, Aix-en-Provence, France
[2]Petrobras – Petróleo Brasileiro S.A, Rio de Janeiro, Brazil
[3]Universidade Federal do PAMPA, Caçapava do Sul, Brazil
[4]Programa de Pós-graduação em Geologia UFMG, Belo Horizonte, Brazil
[5]Laboratório de Estudos Tectônicos (LESTE/UFVJM), Diamantina, Brazil
[6]Geomap, Salta, Argentina

## Abstract

Digital Outcrop Models (DOMs), empowered by advanced digital techniques, have revolutionized the study of outcrop analogs for petroleum reservoir characterization by enabling the extraction of key quantitative parameters for modeling. The limited availability of subsurface data often constrains reservoir characterization, making outcrop analogs essential tools for improving geological models. The analogs bridge the gap between borehole-derived information and regional-scale seismic data, providing crucial mesoscale insights. In this context, this study proposes an integrative workflow combining high-resolution sequence stratigraphy (HRSS) with digital techniques to enhance the understanding of depositional settings and extract data from the Balbuena III Sequence of the Salta Basin, Argentina, a well-established stratigraphic basin analog for Brazilian pre-salt carbonate reservoirs. The workflow combines traditional field-based methods with advanced digital techniques applied to photogrammetric data, including Local Binary Pattern (LBP) analysis and Convolutional Neural Networks (CNNs). LBP analysis correlated with stratigraphic interpretation demonstrated promising potential for characterizing the high-frequency cyclicity observed in the study area. CNN-based segmentation classified and delineated eleven lithofacies, including carbonate, siliciclastic, mixed, and volcanic facies. This segmentation allows for the generation of lithofacies-classified 3D point clouds and a detailed spatial representation of facies distribution across the outcrop. Digital approaches enable more in-depth analysis by increasing efficiency, accuracy, and the capacity to analyze large datasets. By combining digital and traditional methods, this work improves the analysis of outcrop analogs, which contributes to more accurate geological modeling and enhances the predictive capability of petroleum fields and hydrocarbon recovery.

**Keywords:** Digital Outcrop Models (DOMs); High-resolution sequence stratigraphy (HRSS); Lacustrine carbonates; Photogrammetry; Lithofacies classification; 3D point clouds;

## 4.1. Introduction

Effective reservoir management depends on accurate characterization, which can establish critical parameters such as the dimensions of sedimentary bodies, their connectivity, the vertical

and lateral organization of intervals with good porosity and permeability, and the identification of key sealing intervals. These elements directly improve hydrocarbon recovery forecasts (Kenter et al., 2010; Marques et al., 2020; Magalhães et al., 2020). However, such characterization is challenging due to inherent limitations in subsurface data acquisition. While seismic data provides a broad regional structural view, their vertical resolution is limited. Conversely, well data offer high-resolution vertical details but lack lateral continuity.

Outcrop analogs have been extensively used to improve the geological characterization of reservoirs and address these constraints (Grammer et al., 2004; Hodgetts, 2013). These studies offer mesoscale continuity, generally absent in subsurface datasets, and provide valuable insights into facies distribution, depositional architectures, stacking patterns, and internal heterogeneity of reservoirs. Thus, outcrops bridge regional-scale seismic interpretations and localized borehole observations (Pringle et al., 2004; Jones et al., 2011; Howell et al., 2014; Yeste et al., 2021). Integrating outcrop-derived data with numerical models has proven effective in refining reservoir simulations and reducing geological interpretation uncertainties (da Silva Bomfim et al., 2025).

In recent years, Digital Outcrop Models (DOMs) have significantly advanced the quantification of geological data in the field by enabling the systematic extraction of essential parameters for reservoir modeling (Hodgetts, 2013). The widespread use of high-resolution digital cameras and LiDAR (Light Detection and Ranging) sensors, often mounted on Remotely Piloted Aircraft Systems (RPAS), has greatly boosted the generation of these models (Marques et al., 2020; Villarreal et al., 2020; da Silva Bomfim et al., 2025). DOMs have become fundamental tools in outcrop-based studies, allowing for virtual revisits, improving the interpretation of structures and stratigraphy in digital environments, and supporting more robust quantitative analyses (Bellian et al., 2005; Jones et al., 2011; Burnham and Hodgetts, 2019). Furthermore, they enable imaging of outcrops in remote or hard-to-access areas, aligning with innovative workflows such as those proposed by Villarreal et al. (2022).

The application of DOMs spans multiple geoscience disciplines, including reservoir modeling (e.g., Pringle et al., 2004; Buckley et al., 2006; 2009; Zhanfeng et al., 2015; Cabello et al., 2018; Siddiqui et al., 2019), structural geology and karst systems (e.g., Corradetti et al., 2018; Larssen et al., 2020; Villarreal J et al., 2020; Janocha et al., 2021; Panara et al., 2023; Pereira et al., 2024), as well as stratigraphy and sedimentary geology (e.g., Bellian et al., 2005; Fabuel-Perez et al., 2010; Javernick et al., 2014; Bilmes et al., 2019; Li et al., 2019; Priddy et al., 2019; Freitas et al., 2021; Roisenberg et al., 2022).

In general, the outputs generated during the construction of DOMs, such as dense point clouds, 3D meshes, and textured models, can be integrated into three-dimensional modeling software or virtual reality environments. These products enable geological interpretation, data extraction, and multiscale analysis. Tools described in the literature allow for automatic (e.g., Kudelski et al., 2010; Vöge et al., 2013; Zhang et al., 2018) or semi-automatic (e.g., Kudelski et al., 2009; Gigli and Casagli, 2011; Riquelme et al., 2014) mapping of discontinuities based on point clouds and meshes. The automated or semi-automated detection of such features has significantly improved discontinuity identification, expanding its application in structural geology, particularly in the fracture mapping.

In sedimentary geology, however, the identification of geological bodies from DOMs presents additional challenges, including (1) the complex geometries of sedimentary bodies, (2) the variability of their internal structures, and (3) the need for prior stratigraphic framework knowledge to accurately interpret the extracted information. Such interpretations are typically performed manually and demand significant expertise and time (e.g., Khanna et al., 2020;

Ramdani et al., 2022a, 2022b). These approaches often integrate valuable field observations, which is crucial for acquiring key quantitative parameters for reservoir modeling. However, they still rely on labor-intensive workflows.

Recent advances in computer vision and machine learning have enabled new strategies for extracting geological information from DOMs. For example, Local Binary Pattern (LBP) analysis has been successfully applied to structural and stratigraphic interpretation tasks, such as detecting paleoseismic events from fault scarps (Viseur et al., 2022). Convolutional Neural Networks (CNNs) have been used for lithofacies classification across various types of geological data, including outcrop images (e.g., Malik et al., 2022), 3D models (e.g., Sato et al., 2025), hand samples (e.g., Fan et al., 2020; Jeong et al., 2020; Liu et al., 2020), cores and well logs (e.g., Pires de Lima et al., 2019; Shehata et al., 2021; Zhang et al., 2021; Falivene et al., 2022), and petrographic thin sections (e.g., Cheng and Guo, 2017; Koeshidayatullah et al., 2020; Liu and Song, 2020; Xu et al., 2022; Genesis et al., 2024).

This study proposes an integrative workflow to improve the understanding of depositional environments, facies architecture, and cyclic stacking patterns within the Balbuena III Sequence, located in the southern part of the Salta Basin, within the Metán-Alemanía Sub-basin. Most of the studied outcrops are located near the Cabra Corral reservoir, where well-exposed carbonate and mixed deposits occur (Fig. 4.1). These outcrops are considered stratigraphic analogs for the Brazilian pre-salt carbonate reservoirs (e.g., Bento Freire et al., 2011; Raja Gabaglia et al., 2011; Lykawka et al., 2012; Terra et al., 2015; Magalhães et al., 2020; Fragoso et al., 2024), whose commercial discovery occurred in 2006 (Bueno de Moraes et al., 2024; Pedrinha and Artagão, 2024). The workflow integrates traditional field methods, such as stratigraphic descriptions, gamma-ray profiling, and thin-section analyses, with advanced digital techniques, including LBP and CNNs integrated with photogrammetry, to enable quantitative data extraction and automated lithofacies classification. While a similar CNN-photogrammetry approach has been previously applied (Guadagnin et al., 2025), the present study builds upon it by targeting a broader range of lithofacies in a more geologically complex setting.

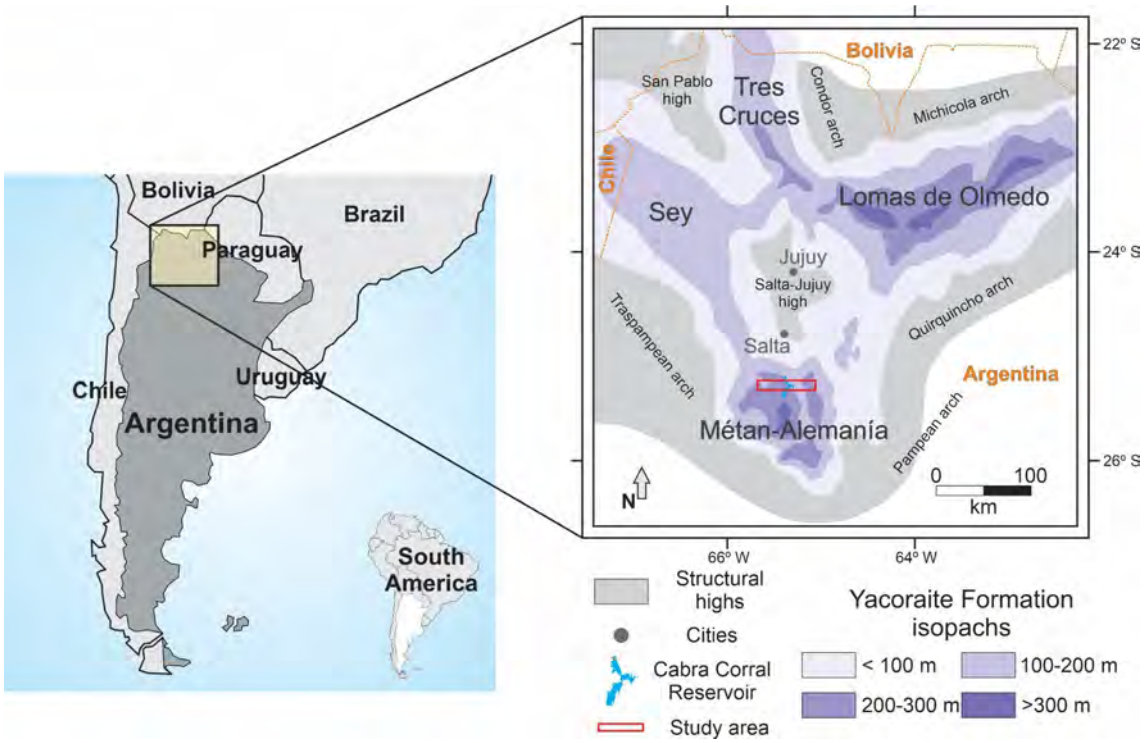


**Fig. 4.1.** Location map of the Salta Basin and its sub-basins, including isopachs of the Yacoraite Formation (modified from Marquillas et al., 2011), with a red rectangle highlighting the study area.

## 4.2. Geological setting

The Salta Group Basin (Turner, 1958), also referred to as the Salta Basin (Marquillas et al., 2005), extends across northwestern Argentina, where approximately 70% of its area is located, as well as southern Bolivia and western Paraguay, encompassing around 150,000 km² (Del Papa and Salfity, 1999). Characterized by an extensive sedimentary record with thicknesses reaching up to 5,000 meters (Marquillas et al., 2005), this intracontinental rift within the South American plate originated during the breakup of Gondwana in the Patagonian orogenic cycle (Keidel, 1921; Bianucci and Homovc, 1982). Rifting commenced in the Cretaceous and continued until the end of the Eocene, when the Andean orogeny started, replacing the extensional regime with a contractional one (Hernández and Echavarria, 2009). Although the literature describes the Salta Basin as composed of seven sub-basins defined by structural highs (Marquillas et al., 2005), this study adopts a simplified grouping into four main sectors: Lomas de Olmedo (east), Sey (west), Tres Cruces (north), and Metán-Alemanía (south) (Fig. 4.1).

The discovery of commercial oil in fractured and karstified carbonate reservoirs of the Yacoraite Formation within the Lomas de Olmedo Sub-basin in the late 1940s, whose daily production reached 50,000 barrels in the 1970s (Disalvo, 2002), spurred further studies in other parts of the Salta Basin, especially in the continuous and readily accessible outcrops of the Metán–Alemania Sub-basin. Since then, the basin has been the focus of intensive research in sedimentology, paleontology, and stratigraphy (e.g., Salfity, 1979; Salfity and Marquillas, 1981; Marquillas, 1985; Del Papa, 1994; Marquillas et al., 1997, 2003, 2005, 2007; Hernández et al., 1999, 2008; Sial et al., 2001; Disalvo et al., 2002).

From the 2010s onward, high-resolution stratigraphic studies gained prominence in the Metán–Alemanía Sub-basin (e.g., Bento Freire, 2012; Gomes, 2013; Pedrinha, 2014; Roemers-Oliveira, 2014; Pedrinha et al., 2015; Roemers-Oliveira et al., 2015; Bunevich, 2016; Bunevich et al., 2017; Deschamps et al., 2020; Gomes et al., 2020; Villafañe et al., 2022; Ceolin et al., 2022; Oliveira Santos et al., 2023; Fragoso, 2023). Similar studies have recently been conducted in the Tres Cruces Sub-basin (e.g., Mutti et al., 2023; Vallati et al., 2023).

### 4.2.1. Tectonic evolution

The geotectonic evolution of the Salta Basin is marked by a series of complex tectonic episodes from the Cretaceous through the compressive processes of the Andean Orogeny in the Eocene (Hernández and Echavarria, 2009). The sedimentary fill of the basin is traditionally divided into two major phases: syn-rift and post-rift (sag).

The syn-rift phase, which developed during the Cretaceous, was characterized by crustal extension that generated depocenters up to 4,000 meters thick (Marquillas et al., 2005). Rift phase deposits exhibit a basal unconformity with the underlying basement (Hernández et al., 1999). The opening of the basin was influenced by inherited Permian and Triassic/Jurassic structural lineaments related to the Gondwanan orogenic cycle (Ramos, 1988). Reactivation of these faults caused spatial variations in subsidence, leading to the development of internal highs, including a prominent central structure known as the Salta–Jujuy Arch, which imparted a radial geometry to the basin (Sabino, 2004).

The post-rift (sag) phase, primarily governed by thermal subsidence (Del Papa and Salfity, 1999; Salfity and Marquillas, 1999), began in the Maastrichtian. Sediment supply from the basin margins progressively buried structural highs, resulting in the unification of sub-basins formed during the rifting phase. Consequently, the sedimentary architecture became broader, shallower, and more tabular in geometry (Hernández et al., 1999). The Salta–Jujuy Arch

remained exposed as a central high until the late Danian, when it was finally covered by post-rift deposits (Gómez Omil and Boll, 1999, 2005).

There is no consensus regarding whether the sag phase continued uninterrupted into the Eocene. While some authors argue for a single, uninterrupted phase (e.g., Reyes and Salfity, 1973; Cristallini et al., 1997; Marquillas et al., 2005), others suggest a shift in tectonic regime during the Paleocene. These studies propose a second rifting episode known as the Pre-Olmec Phase (e.g., Bianucci et al., 1981; Gómez Omil et al., 1989; Gómez Omil and Boll, 1999), marked by regional erosional unconformities and drainage rejuvenation, especially along the margins of the Lomas de Olmedo Sub-basin. However, this event did not generate substantial depocenters, and its deposits were quickly covered by regionally tabular layers, interpreted by some as a second sag stage extending into the Eocene.

The final tectonic phase of the Salta Basin is associated with the Andean Orogeny (Ramos, 1988), marked by the subduction of the Nazca Plate beneath the South American. This phase, developing mainly from the Oligocene onwards, imposed a typical foreland basin regime with structural inversions, folding (anticlines and synclines), and fault reactivation. These processes generated significant structural traps, which have become regional exploration targets (Gómez Omil and Boll, 1999; Hernández and Echavarria, 2009).

### 4.2.2. Stratigraphic framework of the Salta Basin

The study of sedimentary units in the Salta Basin began in 1891 with Brackebusch, who initially referred to the Cretaceous succession as the ‘Salta System’. In 1958, Turner revised this classification, redefining it as the ‘Salta Group’, encompassing Cretaceous to Paleogene strata. Today, the Salta Group is divided into three main subgroups: Pirgua (Reyes and Salfity, 1973), Balbuena, and Santa Bárbara (both defined by Moreno, 1970). From a sequence stratigraphy perspective (Bianucci et al., 1981; Gómez Omil and Boll, 1999; Hernández et al., 1999), four supersequences are considered: Pirgua, Balbuena, Santa Bárbara, and Lumbrera. Their relationship with the lithostratigraphic classification is illustrated in Fig. 4.2. These supersequences are described as follows: 1) the Pirgua Supersequence (Barremian–Campanian) consists of continental clastic deposits formed in a syn-rift setting, restricted to half-grabens, and is subdivided into Pirgua I and Pirgua II; 2) the Balbuena Supersequence (Campanian–Danian) was deposited during the post-rift sag phase and contains four sequences (I–IV) characterized by alternations of clastic sediments, lacustrine carbonates, and local marine facies; 3) the Santa Bárbara Supersequence (Danian–Ypresian) is composed of red continental clastic deposits whose geometry evolves from wedge-shaped at the base to tabular at the top. It comprises three sequences (I–III) that record transitions to lacustrine environments and increasingly humid climatic conditions; and 4) the Lumbrera Supersequence (Ypresian–Priabonian?) includes fluvial and lacustrine deposits divided into two sequences, marking the transition from the post-rift stage to a compressional regime associated with foreland basin development. The top of the Lumbrera Supersequence marks the transition to compressional regimes associated with the onset of foreland basin development (Hernández et al., 1999).

### 4.2.3. The Balbuena Supersequence (Campanian to Danian)

The Balbuena Supersequence, deposited during the post-rift (sag) phase, is characterized by tabular to slightly wedge-shaped geometries and sub-horizontal, laterally continuous bedding (Hernández et al., 1999). Its strata exhibit well-developed cyclicity, driven by eustatic and climatic fluctuations (Boll and Hernández, 1985; Hernández et al., 1999). This supersequence comprises four sequences, from base to top: Balbuena I through IV (Boll, 1991; Hernández et al., 1999, 2008).

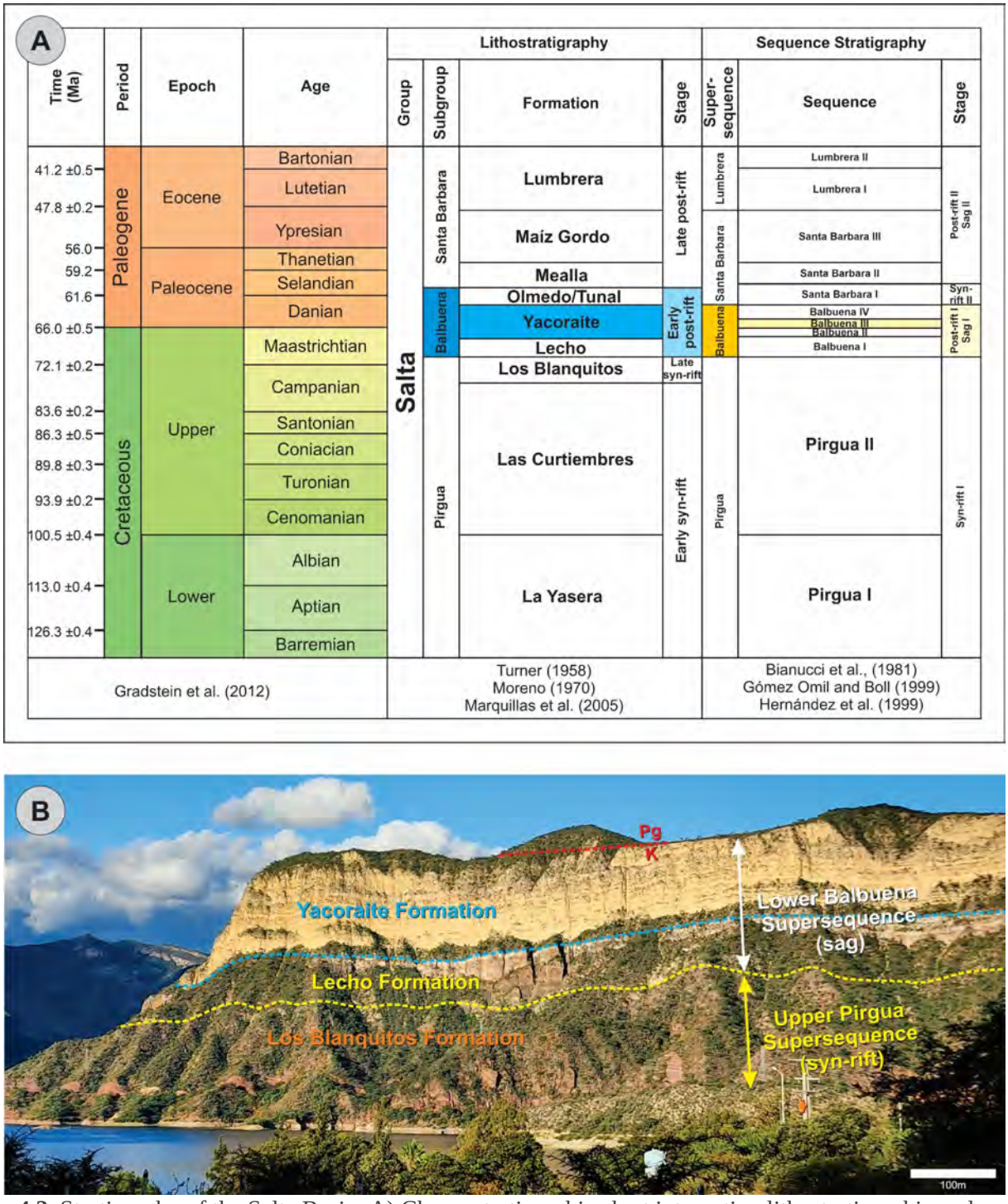


**Fig. 4.2.** Stratigraphy of the Salta Basin. A) Chronostratigraphic chart integrating lithostratigraphic and sequence stratigraphic classifications. Colored markers indicate the unit analyzed in this study. B) Footwall block of a fault exposed in an outcrop near the Cabra Corral reservoir (image adapted from Bento Freire, 2012). The stratigraphic nomenclature displays lithostratigraphic terms on the left and sequence stratigraphic terms on the right. The red line marks the K/Pg boundary.

It begins with clastic eolian facies of the Lecho Formation, which leveled the basin floor, and is overlain by lacustrine carbonates of the Yacoraite Formation. Evidence of marine influence has been reported in the Tres Cruces, Sey, and Lomas del Olmedo sub-basins. The base of the unit displays onlap relationships with the underlying Pirgua Supersequence or older strata (Hernández et al., 1999), while the top is bounded by a regional unconformity related to the 'Pre-Olmec tectonic phase' (Bianucci et al., 1981). Notably, the Yacoraite Formation, rich in carbonates, functions both as a hydrocarbon reservoir and a source rock (Gómez Omil and Boll, 1999; Salfity and Marquillas, 1999), and also hosts uranium mineralization (Salfity and

Marquillas, 1999). The lateral distribution of lacustrine facies varies among sub-basins, primarily governed by synsedimentary subsidence and sediment supply modulated by orbital and climatic forcing. In the Metán–Alemanía Sub-basin, a structural high separating the two sub-basins strongly influences the transition between siliciclastic and carbonate facies. Acting as a physical barrier, this structure traps coarser siliciclastic sediments in the more proximal zones of the basin. Deposits within the Metán–Alemanía Sub-basin can be laterally correlated over tens of kilometers (e.g., Bento Freire, 2012; Roemers-Oliveira, 2014; Pedrinha et al., 2015; Magalhães et al., 2020;), providing excellent exposures for high-resolution stratigraphic studies, as conducted in this work focusing on the Balbuena III Sequence.

The Balbuena I Sequence represents the lower part of the supersequence and is dominated by clastic deposits (Lecho Formation). It comprises fluvial and eolian facies that transition progressively into lacustrine carbonate and pelitic intervals at the base of the Yacoraite Formation. These deposits exhibit high-frequency cyclicity and moderate correlation potential (Boll and Hernández, 1985).

The Balbuena II Sequence, corresponding to the Amblayo Member of the Yacoraite Formation, includes shallow lacustrine carbonates, clastic layers, and paleosols indicative of arid periods, followed by a shift to more humid conditions with enhanced sediment input (Hernández et al., 1999). Progradational patterns are evident, along with high-energy facies such as oolitic grainstones. Its correlation potential, facies architecture, and depositional dynamics have been detailed by Pedrinha et al. (2015) and later reinterpreted using a cyclostratigraphic approach by Fragoso (2023).

The Balbuena III Sequence, whose basal part corresponds to the Güemes Member (Reyes, 1972; Marquillas et al., 2007), differs from the others due to the dominance of pelitic facies, interbedded with fine sandstones and lacustrine carbonates (Hernández et al., 1999). Commonly referred to as the 'Limoarcillosa' section, this interval has been extensively described, and its high-resolution correlation was established by Roemers-Oliveira (2014), providing further insight into its depositional character. A detailed sedimentological and stratigraphic analysis for this unit is presented in Section 4.4.

The Balbuena IV Sequence, equivalent to the Alemanía Member of the Yacoraite Formation, is the most extensive. It exhibits a tabular to wedge-shaped geometry and records the peak of thermal subsidence, with widespread deposition of carbonate and clastic sediments (Hernández et al., 1999). High-resolution correlations, facies descriptions, and interpretations of depositional processes have been presented by Bento Freire (2012), Bunevich et al. (2017), Gomes et al. (2020), and Magalhães et al. (2020).

Hernández et al. (1999) originally classified these units as third-order sequences, following the sequence stratigraphy concept proposed by Vail et al. (1977). Deschamps et al. (2020) focusing on the Yacoraite Formation in the Metán–Alemanía Sub-basin, also proposed a fourfold subdivision based on third-order trends. Although they do not explicitly refer to the Balbuena I–IV Sequences, the defined units closely correspond to them. More recently, Fragoso (2023), drawing on the conceptual and terminological standards of sequence stratigraphy sensu Catuneanu et al. (2011), reinterpreted the Balbuena Supersequence as a first-order sequence, as it records a complete basin-filling cycle under a consistent tectonic regime (sag phase). Accordingly, each of the Balbuena Sequences (I to IV) was reclassified as second-order.

## 4.3. Database and methods

### 4.3.1. Field data acquisition

This study incorporates data from 14 outcrops of the Balbuena III Sequence in the Salta Basin (Table 4.1). Most of these outcrops are located near the Cabra Corral reservoir, with two additional sites situated farther afield: Chuñapampa to the west and Piedras Blancas to the east.

**Table 4.1.** Outcrop names, UTM coordinates, and measured thicknesses of the Balbuena III Sequence in the Salta Basin.

| | Outcrop | UTM coordinates (Datum WGS84) | Measured thickness of the Balbuena III Sequence |
|---|---|---|---|
| 1 | Chunãpampa | 20J 0233454 E / 7204354 N | 29.4 m |
| 2 | Viñuales | 20J 0256764 E / 7201335 N | 16.0 m |
| 3 | Ponte | 20J 0259345 E / 7201873 N | 33.2 m |
| 4 | Cedamavi | 20J 0259884 E / 7202140 N | 32.2 m |
| 5 | Finca el Retiro | 20J 0260135 E / 7202159 N | 31.2 m |
| 6 | Vapumas | 20J 0260670 E / 7202127 N | 32.0 m |
| 7 | Assado | 20J 0260922 E / 7202232 N | 31.6 m |
| 8 | Enseada | 20J 0261590 E / 7202266 N | 32.2 m |
| 9 | Lomito | 20J 0262343 E / 7201424 N | 33.4 m |
| 10 | Ravina | 20J 0268101 E / 7200325 N | 25.1 m |
| 11 | Dique Compensador | 20J 0269935 E / 7200476 N | 34.6 m |
| 12 | Piedras Blancas | 20J 0279229 E / 7200347 N | 32.0 m |
| 13 | Astronauta | 20J 0258453 E / 7204027 N | 30.0 m |
| 14 | Tartaruga | 20J 0256158 E / 7195458 N | 33.0 m |

Vertical stratigraphic sections were measured at a 1:40 scale, following the methodology outlined by Miall (2000), resulting in 425.9 meters of cumulative logged sections. During fieldwork, facies were macroscopically identified and photographed. Additional data collection included spectral gamma-ray profiling and sampling for petrographic thin section preparation. The identified facies encompass carbonates, siliciclastics, mixed facies, and volcaniclastic rocks.

Carbonate rocks were classified according to Grabau (1904), Dunham (1962), Embry and Klovan (1971), and Terra et al. (2010). Siliciclastic rocks were categorized following Picard (1971), while volcaniclastic rocks were classified using Schmid (1981). Mixed facies were classified based on the methodology of Zuffa (1980).

Gamma-ray logs, totaling 350 meters of cumulative length across all outcrop sections, were acquired using a portable gamma spectrometer, model RS-230BGO Super-Spec® (Radiation Solutions Inc.). Measurements were taken at 20 cm intervals, with a 60-second acquisition time, as recommended for spectral measurements (K, U, and Th) to improve reliability and reduce noise, following the protocol presented by Sêco et al. (2021). The recorded data include total gamma-ray emissions (nGv/h), potassium (K %), uranium (U %), and thorium (Th ppm) concentrations. These gamma-ray values supported correlations among the different outcrops and provided insights into the stratigraphic sequences.

### 4.3.2. Petrographic characterization

Petrographic analysis was conducted on 109 thin sections prepared from field samples and examined under a transmitted polarized light microscope. This analysis enabled detailed

observation of rock constituents, such as grains, matrix, and cements, as well as the identification of textures and microstructures, providing insights into depositional and diagenetic environments. Carbonate rocks were described in thin section and classified following Dunham (1962), Embry and Klovan (1971), and Terra et al. (2010). Siliciclastic rocks were classified according to Picard (1971), mixed facies according to Zuffa (1980), and volcaniclastic rocks following Schmid (1981). The proportions of rock constituents in the thin sections were visually estimated by comparison with standard reference charts (e.g., Baccelle and Bosellini, 1965; Matthew et al., 1991). Thin sections of limestone samples were stained with a combined solution of alizarin red-S and potassium ferricyanide, primarily to distinguish calcite from dolomite. In this staining method, calcite and its polymorphs acquire a reddish hue, while non-ferroan dolomite remains unstained (Dickson, 1965,1966). No ferroan dolomite was observed.

### 4.3.3. Photogrammetry

To generate high-resolution Digital Outcrop Model (DOM) for the Assado outcrop, an aerial photogrammetric survey was conducted using a DJI Matrice 300 RTK RPAS mounted with a DJI Zenmuse P1 full-frame camera with a 35mm lens. The RPAS position was corrected in real time using a DJI D-RTK 2 Global Navigation Satellite System base station, ensuring high accuracy in data collection with a geopositioning error of just a few centimeters in X, Y, and Z. The aerial photographs were captured with the camera oriented at a 90° angle to the target, and due to accessibility constraints, the RPAS maintained a minimum distance of 8 meters from the outcrop (with an average of 12.9 m), ensuring high-detail image acquisition. A total of 497 images were collected, resulting in a remarkably high resolution for the model, approximately 2 mm per texture element.

Images were acquired with the RPAS hovering at stationary positions, achieving consistent image spacing and meeting minimum overlaps of 80% forward and 70% side. However, the stationary acquisition process was time-consuming, resulting in significant variations in lighting throughout the acquisition campaign. To mitigate lighting variations, a Python-based workflow (Python, 2023) performed histogram matching of all images to a reference image, followed by histogram equalization. This process minimized shadow effects and lighting differences, ensuring consistent illumination across the outcrop. Following this, the images were processed using a well-established photogrammetric workflow based on Structure-from-Motion and Multi-View Stereo (SfM-MVS) techniques (e.g., Lowe, 2004; Westoby et al., 2012; Bistacchi et al., 2022), effectively generating digital outcrop models. The processing was conducted using Agisoft Metashape (Agisoft Metashape, 2023), producing dense point clouds and triangulated meshes, which were textured with the original outcrop images to create a photorealistic model. Additionally, the photogrammetry workflow was employed to construct the classified 3D point cloud, utilizing masks generated by the CNN method, as described in the CNN methodology section (Section 4.3.5).

### 4.3.4. LBP analysis

The Local Binary Pattern (LBP) technique (Ojala et al., 1994; Ojala et al., 1996; Ojala et al., 2002) is a widely used texture descriptor that encodes local spatial patterns by generating a binary code for each pixel based on the differences between its intensity value and those of neighboring pixels. This method evaluates the grayscale intensity values within a circular neighborhood around a central pixel ($I_P$). For each of the eight neighboring pixels ($I_n$) n $\in$ [1;8], a binary value is assigned based on the comparison with the central pixel as follows: if $I_n \geq I_P$, the result is encoded as 1; otherwise, it is 0. These binary values are then weighted by

powers of two, aggregated, and summed to generate a unique descriptor for each grid cell, $c_i, i \in [1, N]$ with $N$ the total number of grid cells, as defined in Eq. (1):

$$P = LBP\,(c_i) = \sum_{n=0}^{7} s\,(I_n - I_P) \cdot 2^n \quad (1)$$

The function $s(x)$, which determines the binary output, is defined in Eq. (2):

$$s(x) = \begin{cases} 1, & if\ x \geq 0 \\ 0, & if\ x < 0 \end{cases} \quad (2)$$

In this work, the LBP method was applied to process outcrop data and support the interpretation of high-frequency stratigraphic cyclicity. The objective was to compare the LBP-derived textural patterns with stratigraphic stacking trends interpreted as regressive and transgressive hemicycles at high resolution. This analysis was implemented as a plugin within the open-source software CloudCompare (CloudCompare, 2024), using point cloud data as the primary input (sensu Viseur et al., 2022). As illustrated in Fig. 4.3, a grid is first generated over the outcrop surface. The grid resolution is user-defined, allowing flexibility to adjust the resolution according to the desired scale of analysis. To obtain a single gray level per grid cell, the gray values of the points contained within each grid cell were averaged. Then, the classical LBP algorithm is applied. Finally, the computed LBP values are averaged across horizontal bands of the grid to generate a profile of mean values (Fig. 4.3).

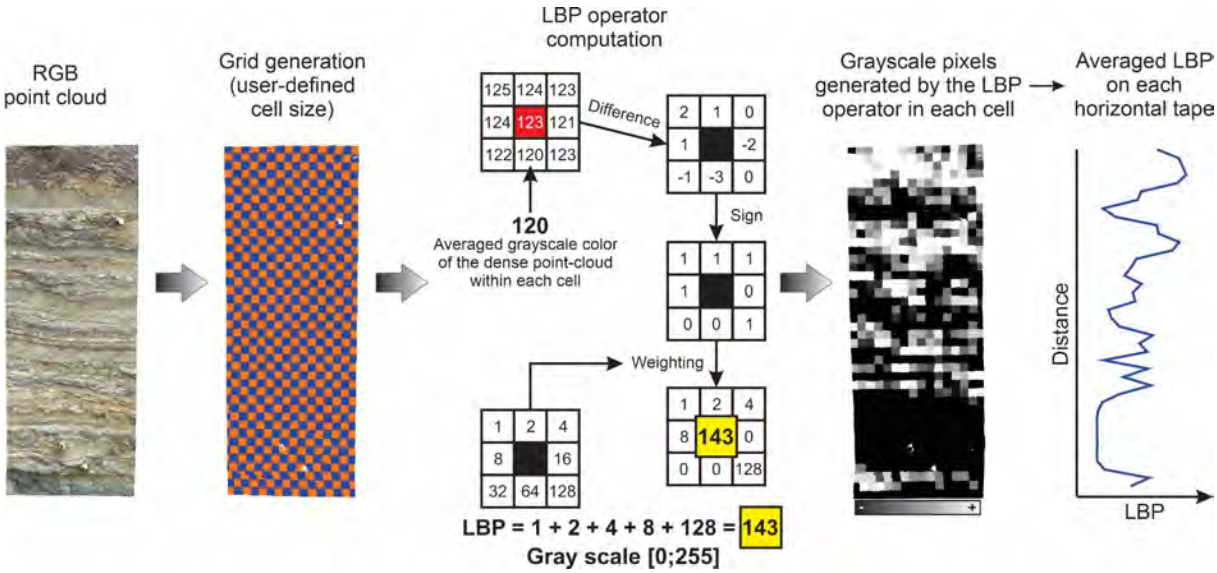


**Fig. 4.3.** Workflow illustrating the application of LBP analysis to outcrop data, focusing on texture characterization based on grayscale values.

### 4.3.5. Lithofacies-classified 3D point cloud

This methodology, previously applied by Guadagnin et al. (2025), integrates CNN-based segmentation of outcrop images with a photogrammetry workflow to build a classified 3D point cloud for rock facies analysis (Fig. 4.4). This combined approach enables precise facies classification and spatial reconstruction.

CNN is a supervised deep-learning technique that requires expert-labeled data for training. In this study, 49 outcrop images were labeled by an interpreter to distinguish rock facies, excluding irrelevant features such as vegetation and sky, which were grouped into an ‘others’ category. This subset represents approximately 10% of the full dataset, composed of 497 images, and was used to train the CNN model.

The lithofacies segmentation was performed using a U-Net convolutional neural network (Ronneberger et al., 2015) implemented in Python (Python, 2023) using the TensorFlow (TensorFlow, 2024) deep learning library. The model consists of an encoder-decoder structure with skip connections, four convolutional blocks in the encoder, and a symmetrical decoder that progressively restores spatial resolution through upsampling. Each convolutional layer uses ReLU activation, HeNormal initialization, and a 3 × 3 kernel, with the number of filters doubling at each depth level. A dropout rate between 0.1 and 0.3 was applied to reduce overfitting, and optional residual connections were tested. The final output is obtained through a 1 × 1 convolution followed by a softmax activation. Training was performed with the Adam optimizer (learning rate of $1 \times 10^{-4}$), using a validation split of 10% to monitor performance. The model was trained with a batch size of 10 for 100 epochs.

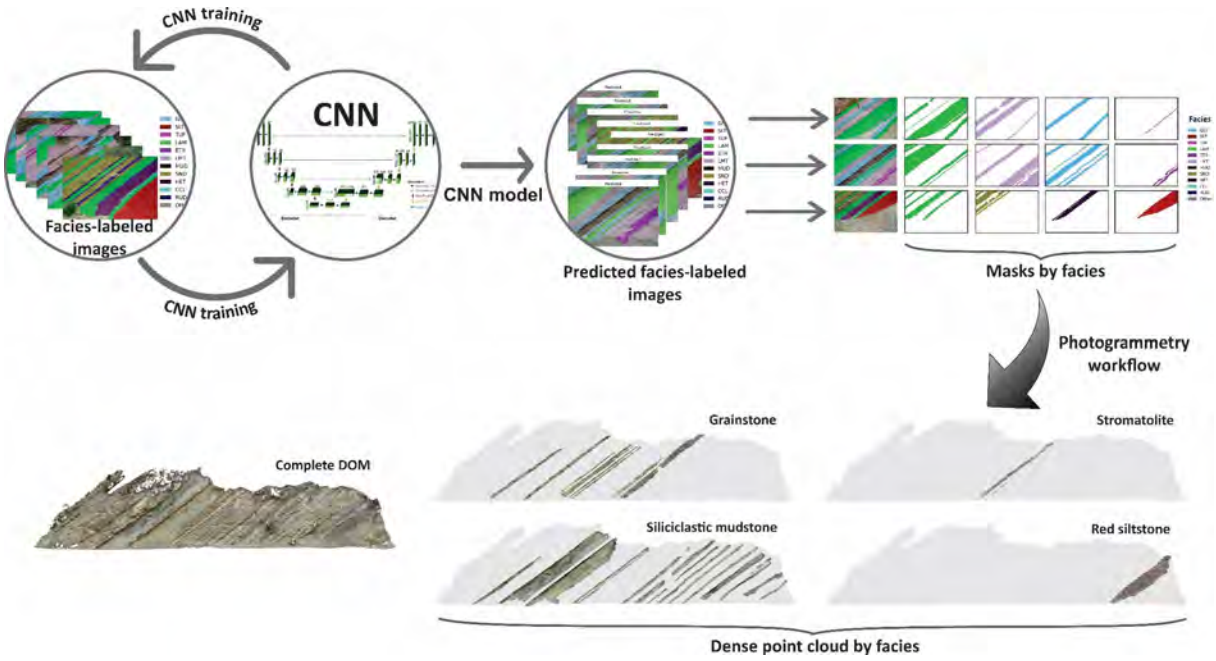


**Fig. 4.4.** Workflow illustrating the generation of a lithofacies-classified 3D dense point cloud, using facies-labeled images processed with a CNN model.

The labeled images were used to train the CNN model by minimizing the differences between the model predictions and the true labels in the dataset. The training process employed a pixel-wise cross-entropy loss function, commonly used in segmentation tasks, to optimize model performance. After achieving an accuracy above 80%, the CNN model was retrained with all available labeled images to further enhance its performance and then applied to segment all remaining non-labeled images in the dataset. Pre-processing steps included downscaling the image resolution from 8,192 × 5,460 pixels to 384 × 256 pixels, following the approach of Guadagnin et al. (2025), and applying data augmentation techniques (Shorten and Khoshgoftaar, 2019) to improve the model's robustness. Entropy maps, which quantify the uncertainty in lithofacies predictions based on pixel-wise probability distributions, were used for qualitative assessment of model confidence. This approach highlights areas of high or low uncertainty in the classification results, as also described by Guadagnin et al. (2025).

In the photogrammetry phase, the 3D point cloud construction followed a standard workflow. After creating a sparse point cloud, segmentation results from the CNN model were imported as masks into separate data 'chunks' within the software, each chunk representing a distinct lithofacies. This segmented approach enabled classification during the dense cloud generation process, ensuring facies-specific point clouds. Unlike the 2D masks, the 3D classified model provides a continuous spatial representation of facies across the outcrop, supporting more integrated geological interpretation. After manual refinement to remove

misclassified points, points corresponding to each lithofacies were assigned specific colors in CloudCompare (CloudCompare, 2024) to facilitate visualization of the high-resolution classified 3D models.

## 4.4. Sedimentological and stratigraphic framework of the Balbuena III Sequence

This section will present an overview of the main characteristics of the sedimentary-stratigraphic framework, highlighting the key elements that supported the implementation of the digital approaches used in this study.

### 4.4.1. General characteristics

The thickness of the SBIII varies between 30 and 35 meters, and this entire interval is typically exposed within each of the studied outcrops. The strata are tilted at an average angle of 30° to 40° relative to their original horizontal deposition (Fig. 4.5), a feature commonly observed in the Subandean fold and thrust belt of Northwest Argentina due to Andean tectonics (Hernández and Echavarria, 2009).

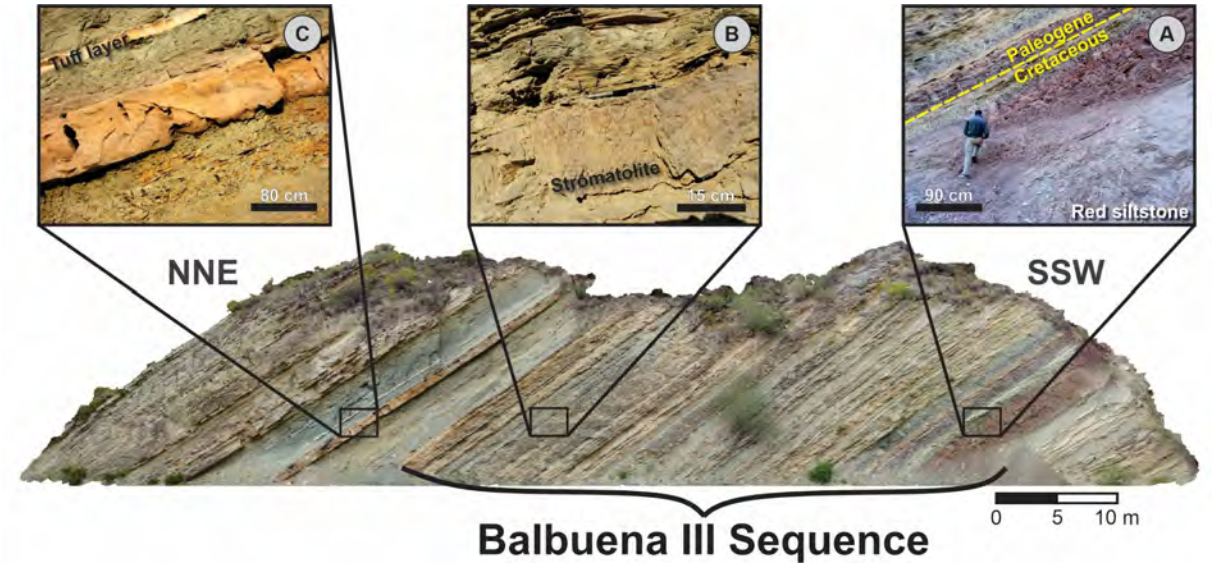


**Fig. 4.5.** Assado DOM showing the Balbuena III Sequence and its key stratigraphic markers, presented in stratigraphic order: A) basal red siltstone unit; B) cerebroid columnar stromatolite layer; C) volcanic tuff layer. Figure layout inspired by Roemers-Oliveira et al. (2015), now applied to the new digital outcrop model.

In the central part of the studied area, where the main outcrops are concentrated, the SBIII is relatively easy to identify in the field due to the presence of key stratigraphic markers. Its basal portion is characterized by a red siltstone unit up to 3 meters thick (Fig. 4.5A). Just above this layer lies the Paleogene–Cretaceous boundary, identified by Marquillas et al. (2007) based on carbon and oxygen isotope anomalies. Approximately two-thirds up from the base, a cerebroid columnar stromatolite layer (Fig. 4.5B) provides another distinct marker. Above the SBIII, within the overlying Balbuena IV Sequence, a 15-20 cm thick volcanic tuff layer (Fig. 4.5C) occurs just above a limestone bed isolated between two pelitic layers.

The base of SBIII is composed of fine-grained quartz arenites interbedded with pelites (shales and siltstones). Toward the top, carbonate facies such as calcarenites, laminites, and stromatolites become more prominent, intercalated with pelites and carbonate mudstones, as illustrated in the columnar section (Fig. 4.6). These compositional variations reflect a shift in the hydrological regime controlling sedimentation across the sequence. At the basal portion,

the interpreted lacustrine deposition operated under a hydrologically open system, allowing substantial external sediment influx into the basin. In contrast, the upper portion of the sequence records a transition to a hydrologically closed lake system, characterized by reduced external sediment supply, increased evaporation, and conditions favorable for carbonate production.

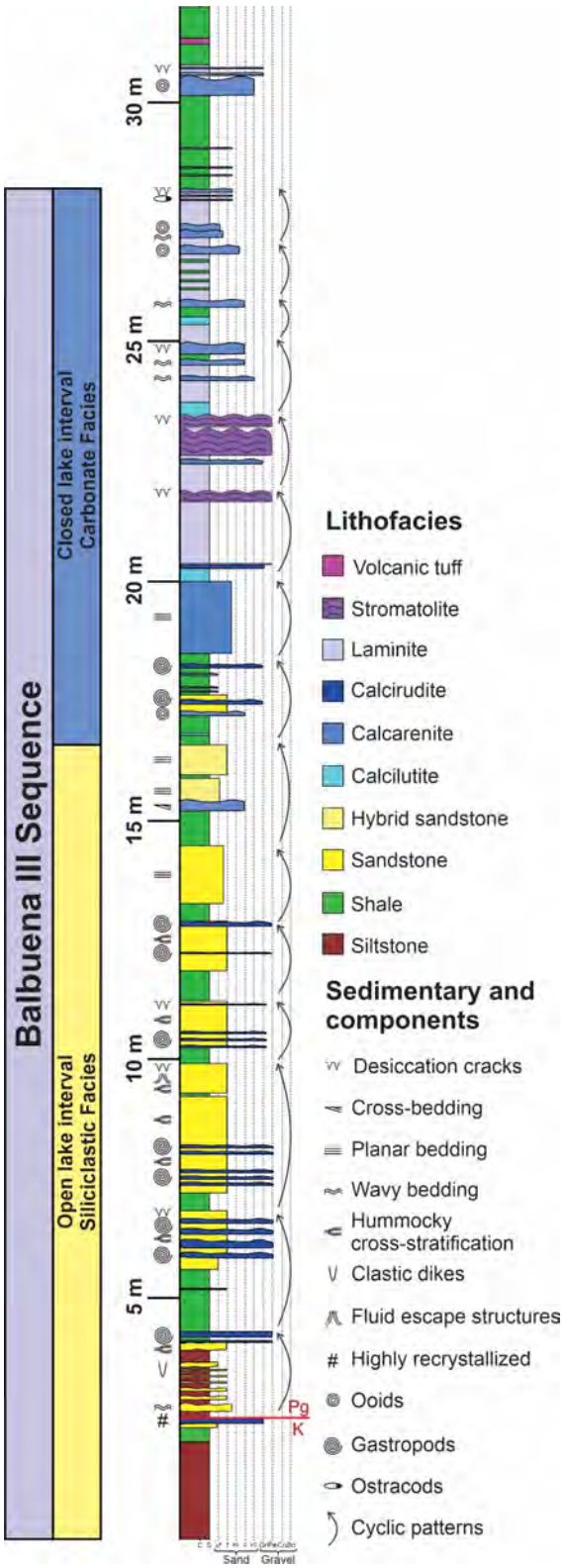


**Fig. 4.6.** Vertical stratigraphic section of the Balbuena III Sequence at the Vapumas outcrop, near the Cabra Corral reservoir, showing lithofacies, sedimentary structures, and components (adapted from Roemers-Oliveira et al., 2015). The Cretaceous (K)/Paleogene (Pg) boundary is marked by a red line at the base of the section. Curved arrows highlight cyclicity. Grain size classification follows Wentworth (1922); for visualization purposes, laminite and stromatolite facies are standardized as silt and pebble, respectively.

### 4.4.2. Lithofacies Associations

The facies of SBIII are grouped into four distinct facies associations (FA), each reflecting genetic relationships and depositional environments. These associations capture the variability in hydrological regimes and sediment supply, driven primarily by climatic conditions, transitioning between open and closed lacustrine systems. The alternation between open and closed lake conditions represents a shift in hydrologic and sedimentary dynamics, providing insights into past climatic fluctuations and basin evolution. Below, each FA is described, highlighting its characteristic facies, sedimentary structures, and depositional processes. Further details about the facies are summarized in Table 4.2, while Fig. 4.7 and Fig. 4.8 present a compilation of representative macro- and microphotographs illustrating some of the facies identified within the Balbuena III Sequence. Additionally, Fig. 4.9 shows the schematic distribution of facies along a depositional profile for the open- and closed-lake intervals (Fig. 4.9A and Fig. 4.9B, respectively). The mnemonics used are **S** for siliciclastic facies, **C** for carbonate, **M** for mixed, and **V** for volcanic.

Open lake conditions during a humid phase were characterized by significant siliciclastic input, driven by river inflows, and were conducive to the deposition of coarse-grained littoral facies and fine-grained pelagic facies. In contrast, closed lake conditions during an arid phase were marked by limited siliciclastic input, increased evaporation, and enhanced carbonate production, reflecting a transition to hydrologically restricted settings.

#### 4.4.2.1. FA1 – Littoral Open Lake Association (LOLA): Siliciclastic-dominated facies representing marginal and shallow environments in open lacustrine systems

The LOLA encompasses deposits formed in shallow, coastal zones of an open lacustrine system, which may be wave-dominated. This association is primarily characterized by siliciclastic facies, such as siltstones with incipient lamination (S1 – Fig. Fig. 4.7A–B) and heterolites composed of shale and fine-grained sandstones exhibiting hummocky cross-stratification (S4 – Fig. 4.7D, F) or low-angle cross-stratification (S5 – Fig. 4.7G). Desiccation cracks are frequently observed (Fig. 4.7I). Additionally, some layers include carbonate-rich facies, such as rudstones (C7 – Fig. 4.7E) or floatstones (C8) dominated by gastropod shells. Occasionally, siliciclastic sandstones incorporate carbonate components, including bioclasts, peloids, and ooids, forming hybrid sandstones (M2).

This association reflects a high-energy depositional environment influenced by fluvial and shoreline processes, with significant siliciclastic sediment input. Periodic stabilization of substrates, evidenced by gastropods and bioturbation, suggests alternating high- and low-energy conditions. Wave reworking, current activity, and combined flow regimes, along with episodes of subaerial exposure, as indicated by desiccation cracks, are consistent with a hydrologically open lake system. Siliciclastic sedimentation predominates, but carbonate production occurred during calmer and/or chemically stressed intervals, which are frequently associated with gastropod mortality accumulations. The presence of S1 at the base of the section marks a mudflat plain indicative of maximum lake retraction and low accommodation conditions.

**Table 4.2.** Description and interpretation of lithofacies from the Balbuena III Sequence, Salta Basin, highlighting sedimentological characteristics and depositional environments.

| Lithofacies | | Brief description | Interpretation |
|---|---|---|---|
| Siliciclastic | S1 | Siltstone with micaceous clay and incipient planar-parallel lamination | Deposition in muddy plains in a supralittoral subenvironment |
| | S2 | Heterolithic facies with shale and very fine sandstone showing wavy lamination | Mud decantation (predominant) and sand deposition by oscillatory flows in littoral to sublittoral subenvironment |
| | S3 | Claystone with planar-parallel lamination | Decantation in profundal subenvironment |
| | S4 | Heterolithic facies composed of very fine sandstone with hummocky cross-stratification and shale | Mud decantation and sand deposition (predominant) by oscillatory flows in littoral to sublittoral subenvironment |
| | S5 | Very fine sandstone with low-angle cross-stratification | Sand deposition in a high-energy littoral subenvironment |
| Carbonate | C1 | Laminated mudstone | Micrite deposition in low-energy profundal subenvironment |
| | C2 | Massive mudstone | Micrite deposition in low-energy profundal subenvironment |
| | C3 | Oolitic packstone with low-angle to wavy cross-stratification | Deposition near oolitic sand banks in littoral to sublittoral subenvironment |
| | C4 | Ostracodal packstone | Deposition in a moderate-energy littoral subenvironment influenced by waves |
| | C5 | Peloidal wavy packstone | Deposition in moderate-energy littoral subenvironment influenced by waves |
| | C6 | Massive oolitic wavy grainstone | Deposition in oolitic sand banks in high-energy littoral subenvironment |
| | C7 | Peloidal grainstone with cross-stratification | Deposition in high-energy oolitic banks within a littoral subenvironment influenced by oscillatory or combined flows |
| | C8 | Gastropod bioclastic rudstone | Deposition in a moderate-energy supralittoral subenvironment |
| | C9 | Gastropod bioclastic floatstone | Deposition in a moderate/low-energy supralittoral subenvironment |
| | C10 | Columnar domal cerebroid stromatolite | Cyanobacteria bioinduction in the photic zone of a littoral subenvironment |
| | C11 | Crenulated laminite | Cyanobacteria bioinduction of a supralittoral subenvironment |
| Mixed | M1 | Marl with planar-parallel lamination | Decantation in profundal subenvironment |
| | M2 | Hybrid arenite | Deposition of hybrid sands in a moderate to high-energy littoral subenvironment with variable siliciclastic influx |
| Volcanic | V1 | Volcanic vitreous tuff | Sedimentation of material from volcanic eruptions |

#### 4.4.2.2. FA2 – Profundal Open Lake Association (POLA): Mixed siliciclastic-carbonate facies representing deep environments in open lacustrine systems

The POLA encompasses facies deposited in the deeper, low-energy zones of an open lacustrine system. Fine-grained siliciclastic deposits predominate, including siltstones with lenses of fine sandstone (S2 – Fig. 4.7C) and claystone (S3 – Fig. 4.7H), accompanied by minor marl facies exhibiting alternating thin carbonate and siliciclastic laminae (M1).

This association reflects sedimentation primarily by suspension fallout in distal, low-energy areas of the lake under an open hydrological regime. The lack of wave or current influence and the dominance of mud-rich, silty sediments point to deposition in the pelagic zone. Sedimentary processes were driven by hypopycnal plumes from fluvial inputs, with suspended sediment settling to the lake floor. The finer grain sizes and the absence of high-energy sedimentary structures indicate calm depositional conditions in these profundal settings.

#### 4.4.2.3. FA3 – Littoral Closed Lake Association (LCLA): Carbonate-dominated facies representing marginal and shallow environments in closed lacustrine systems

The LCLA is characterized by carbonate-dominated facies deposited in shallow waters of a hydrologically closed lake system. These facies include low-angle to wavy cross-stratified oolitic packstones (C3), bioclastic packstones to ostracode (C4 – Fig. 4.8E), peloidal wavy packstones (C5), massive oolitic grainstones (C6 – Fig. 4.8A–B, D), cross-stratified peloidal grainstones (C7 – Fig. 4.8G), cerebroid columnar stromatolites (C10 – Fig. 4.8H, J–M), and crenulated laminites (C11 – Fig. 4.8C, F). Occasional mixed facies (M2) are also interbedded within this association. Desiccation cracks (Fig. 4.8M) are frequently observed beneath stromatolite and laminite layers.

This facies association reflects a hydrologically closed lacustrine environment, where reduced sediment input and elevated evaporation rates favored carbonate sedimentation. The dominance of micritic mud, ooid and skeletal grains, along with features such as stromatolites and microbial mats (crenulated laminites), indicates depositional processes dominated by chemical and biological activity. Wave and current activity contributed to the formation of granular facies such as grainstones and packstones, highlighting moderate to high-energy conditions in shallow lake margins. Fluctuating water levels led to subaerial exposure, denoted by the desiccation cracks.

#### 4.4.2.4. FA4 – Profundal Closed Lake Association (PCLA): Carbonate and siliciclastic mudstones representing deep environments in closed lacustrine systems

The PCLA is characterized by low-energy deposits in the deeper, pelagic zones of a hydrologically closed lacustrine system. The facies are dominated by laminated (C1) and massive carbonate mudstones (C2 – Fig. 4.8I), with minor occurrences of plane-parallel laminated claystones (S3) and marls (M1).

This association reflects sedimentation under calm, restricted conditions in the profundal regions of a closed lake system. The predominance of fine-grained carbonate mudstones and the minimal siliciclastic input indicate limited external sediment supply. Sedimentation

primarily occurred through suspension fallout, with carbonate precipitation influenced by microbial activity. During slightly more humid periods, hyperpycnal plumes could have sporadically delivered siliciclastic material to these deeper lake zones.

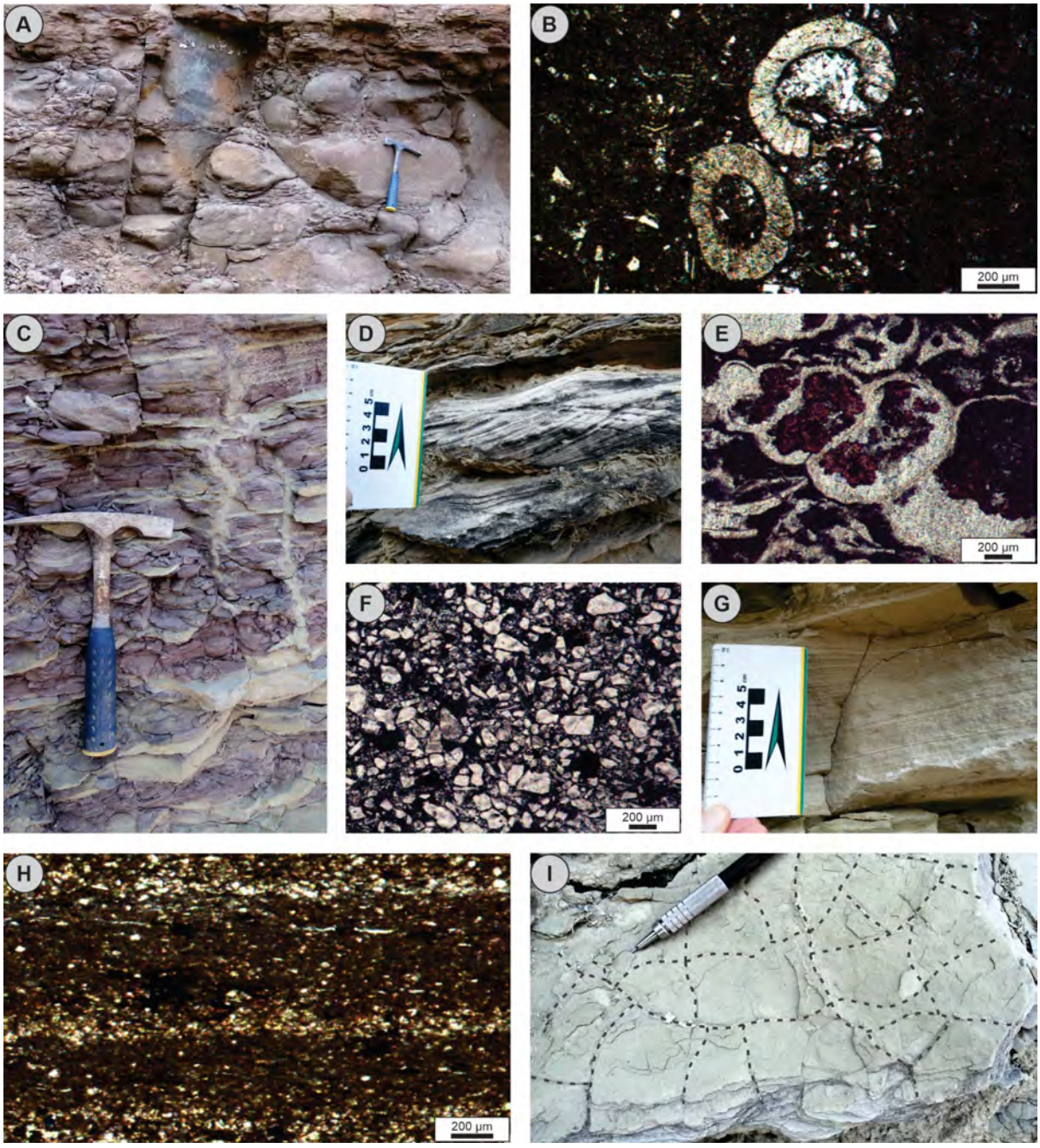


**Fig. 4.7.** Representative lithofacies from the open lake interval of the Balbuena III Sequence in the Metán-Alemanía Sub-basin. The name at the end of each description corresponds to the respective outcrop: A) Red siltstone (S1), Finca el Retiro; B) Charophyte gyrogonites within facies S1, parallel-polarized light, Enseada; C) Clastic dykes in facies S2 (siltstones with lenses of fine sandstone), Assado; D) Hummocky cross-stratified sandstone surrounded by siliciclastic mudstone (S4), Vapumas; E) Photomicrograph of gastropod bioclastic rudstone (C7), parallel-polarized light, thin section stained with alizarin, Vapumas; F) Photomicrograph of facies S4, parallel-polarized light, Enseada; G) Low-angle cross-stratified sandstone (S5), Cedamavi; H) Photomicrograph of siliciclastic mudstone with plane-parallel lamination (S3), cross-polarized light, Vapumas; I) Desiccation cracks (outlined by dashed lines) on top of the S4 facies, Vapumas.


**Fig. 4.8.** Representative lithofacies from the closed lake interval of the Balbuena III Sequence in the Metán-Alemanía Sub-basin. The name at the end of each description corresponds to the respective outcrop: A) Massive grainstone (C6) with wavy bedforms, Vapumas; B) Photomicrograph of oolitic grainstone, parallel-polarized light, Enseada; C) Crenulated laminate (C11), Finca el Retiro; D) Photomicrograph of massive oolitic grainstone, parallel-polarized light, Vapumas; E) Photomicrograph of bioclastic packstone to ostracode, parallel-polarized light, Ponte; F) Photomicrograph of crenulated laminite, parallel-polarized light, thin section stained with alizarin, Vapumas; G) Photomicrograph of peloidal grainstone (C7), cross-polarized light, Enseada; H) Domical stromatolite (C10), Lomito; I) Photomicrograph of massive carbonate mudstone (C2), parallel-polarized light, thin section stained with alizarin, Lomito; J) Detail of the cerebroid texture of stromatolite (C10), Assado; K) Photomicrograph of columnar domical stromatolite, parallel-polarized light, Tartaruga; L) Detail of fascicular crystal occurrence within columnar domical stromatolite, parallel-polarized light, Enseada; M) Desiccation cracks observed on top of the cerebroid stromatolite facies, Astronauta.

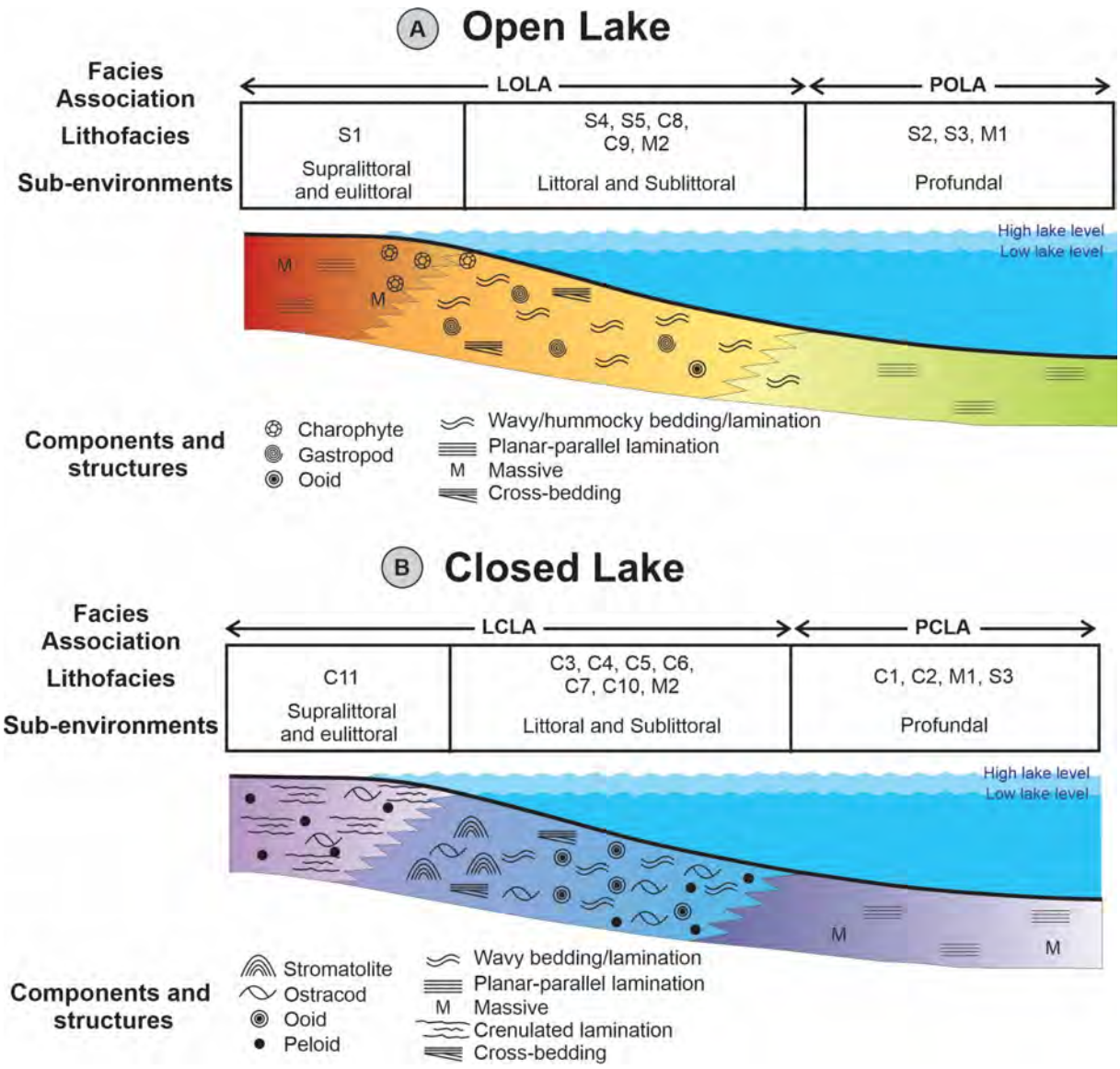


**Fig. 4.9.** Schematic distribution of lithofacies along depositional profiles for the lower Open Lake (A) and upper Closed Lake (B) intervals. Lithofacies mnemonics correspond to those listed in Table 4.2.

### 4.4.3. High-resolution Sequence Stratigraphy

The SBIII displays well-defined depositional patterns that reflect climate-driven hydrological and sedimentological dynamics. These patterns are expressed through a hierarchy of stratigraphic sequences corresponding to different frequencies of base-level changes. At least three scales of depositional sequences are identified within the SBIII: low, medium, and high-frequency sequences.

Low-frequency sequences encompass the entirety of the SBIII and have traditionally been interpreted as third-order cycles (Hernández et al., 1999), although more recent studies suggest a second-order interpretation as an alternative (Fragoso, 2023; Fragoso et al., 2024). These sequences reflect long-term climatic oscillations, transitioning between open lake systems during humid phases, dominated by siliciclastic facies, and closed lake systems during arid phases, characterized by carbonate-dominated facies (Roemers-Oliveira, 2014).

Medium-frequency sequences correspond to stratigraphic intervals that exhibit consistent thickening and thinning trends of high-frequency sequences. These sequences are delineated by key stratigraphic surfaces: the Maximum Retraction Surface (MRS), marking maximum lake

contraction, and the Maximum Expansion Surface (MES), representing maximum lake flooding (e.g., Fragoso et al., 2023; Roemers-Oliveira et al., 2024). The MES is associated with retrogradational stacking patterns, while the MRS marks a transition to progradational stacking. These medium-frequency sequences are highly correlatable and provide a framework for regional stratigraphic correlation.

High-frequency sequences (elementary sequences) are the primary units in this study. These sequences are characterized by vertical stacking patterns of facies associations, reflecting base-level fluctuations. High-frequency sequences are traceable across distances of tens of kilometers, as demonstrated in the stratigraphic correlation section.

#### 4.4.3.1. Elementary Sequences in SBIII

Within SBIII, two main types of elementary sequences (Fig. 4.10) are identified: siliciclastic-dominated and carbonate-dominated sequences. Each sequence represents a complete cycle of transgressive-regressive (T–R) deposition, reflecting short-term and multiple-event base-level variations. These sequences are characterized by distinct facies associations and stacking patterns, with thicknesses ranging from 1 to 2 meters. In both sequence types, the MES corresponds to maximum lake expansion, while the MRS marks maximum lake contraction.

##### 4.4.3.1.1. Siliciclastic-dominated sequences

These sequences (Fig. 4.10A) are typical of the lower interval of the SBIII, where profundal pelagic facies (POLA) are overlain by littoral facies (LOLA). The sequences exhibit upward-shallowing trends, with fine-grained siliciclastic facies at the base transitioning to coarser-grained sandstones and hybrid facies toward the top. Desiccation cracks, though not deeply penetrating, are common in the uppermost layers. These patterns reflect a lake expansion phase followed by contraction, possibly driven by multiple-event shifts from humid to arid climatic conditions.

##### 4.4.3.1.2. Carbonate-dominated sequences

These sequences (Fig. 4.10B) dominate the upper SBIII and comprise pelagic facies (PCLA) overlain by littoral carbonate facies (LCLA). They also exhibit upward-shallowing trends but are characterized by carbonate facies indicative of high carbonate productivity during lake contraction phases. In arid conditions, bioinduced facies, such as stromatolites and laminites, become prominent. Desiccation cracks are often observed at the top of these sequences, marking subaerial exposure during multiple-event lake contraction.

#### 4.4.3.2. Medium-Frequency Sequences

Medium-frequency sequences correspond to the stacking of high-frequency sequences and are conceptually aligned with the small-scale sequences defined by Strasser et al. (1999) and Strasser (2018). These sequences are characterized by thickening or thinning upward trends in the hemicycles of high-frequency sequences (Fig. 4.10C).

For the SBIII, considering the MRS as the sequence boundary, four medium-frequency sequences, with thicknesses between 6 and 9 meters, were interpreted. These sequences provide a critical framework for understanding the interplay of sediment supply and accommodation space in the context of medium-term base-level changes. A hierarchical organization is recognized: the lower two medium-frequency sequences, corresponding to the open-lake interval, contain three and four siliciclastic-dominated elementary sequences, respectively,

while the upper two sequences, within the closed-lake interval, each contain four carbonate-dominated elementary sequences.

### 4.4.4. Stratigraphic Correlation

A defining feature of the Balbuena Supersequence is the correlatability of its depositional sequences across multiple frequency scales—low, medium, and high—since they represent the SAG deposits of the basin. All high-frequency sequences within the SBIII were successfully correlated across the studied outcrops, covering distances of up to 45 km. Although no detailed structural data exist for the study area, a regional estimate indicates ~36% shortening in the Subandean fold-and-thrust belt at this latitude (Hernández and Echavarria, 2009). This suggests that, before deformation, the lateral extent of these sequences may have reached ~70 km, further emphasizing their stratigraphic continuity.

This extensive lateral continuity, together with the recurrence of stacking pattern signatures, vertical trends in their arrangement, the internal Transgressive-Regressive (T-R) structure, and the mappability of sequences and their stratigraphic surfaces, collectively underscores the allocyclic nature of these depositional sequences, as proposed by Bento Freire (2012), Pedrinha (2014), and Roemers-Oliveira (2014), and highlighted by Magalhães et al. (2020).

To illustrate these correlations, an east-west stratigraphic cross-section was constructed (Fig. 4.11), using the K/Pg boundary as a datum. This chronostratigraphic marker, at 66 Ma, is located immediately above the red siltstones of facies S1. This facies, deposited in the shallowest (supralittoral) environment of the open lake interval, represents the stage of maximum lake retraction. The low-frequency MRS, which marks the onset of a transgressive trend in SBIII, lies immediately above this unit. The upper boundary of the low-frequency sequence is also marked by an MRS, coinciding with an abrupt facies change in which siliciclastic pelagic facies overlie carbonate rocks from the closed lake interval of the SBIII.

The stratigraphic correlation highlights the consistent recurrence of elementary sequences, with 15 identified across the study area: seven siliciclastic-dominated and eight carbonate-dominated, grouped into four small-scale sequences. Medium-frequency MRS surfaces are represented by red lines in the cross-section (Fig. 4.11), while high-frequency MRS surfaces are depicted in other colors. Correlations were based on facies associations, with elementary sequences consistently showing littoral facies overlying pelagic ones, characterizing transgressive–regressive (T–R) cycles. Gamma ray profiles provided additional support for correlations, particularly in carbonate intervals with subtle facies contrasts.

This high-resolution stratigraphic framework reinforces the utility of the SBIII as a model for understanding depositional processes in lacustrine basins. The integration of stratigraphic surfaces and facies stacking patterns reveals the underlying controls of sedimentation and accommodation space within the Metán-Alemanía Sub-basin, offering a valuable analog for similar lacustrine systems in the geological record.

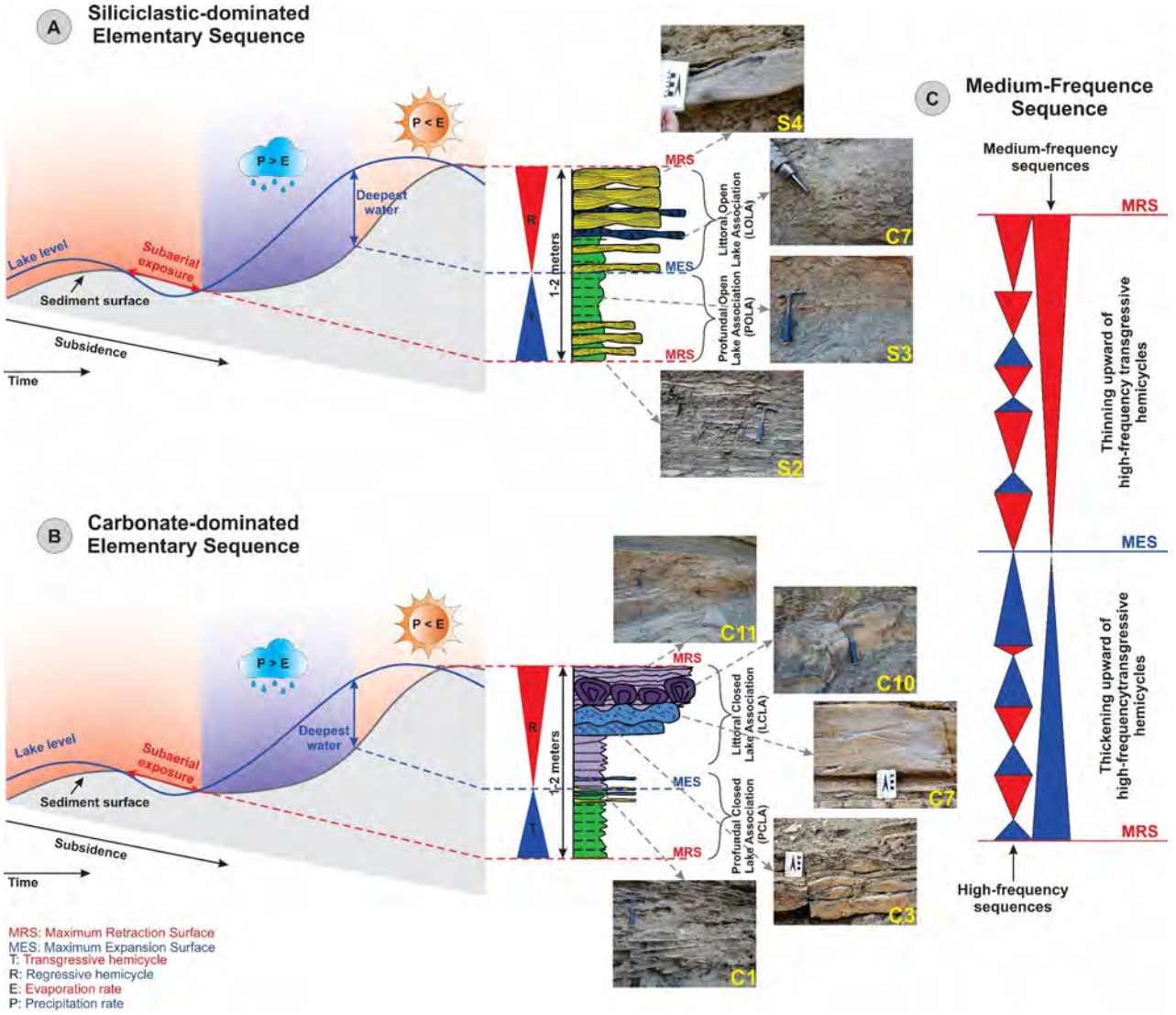


**Fig. 4.10.** Stratigraphic model illustrating climate-controlled transgressive-regressive cycles in carbonate lacustrine settings, with idealized elementary and medium-frequency sequences of SBIII. A) Siliciclastic-dominated sequence. B) Carbonate-dominated sequence. C) Medium-frequency sequence based on stacking trend analysis of elementary sequences. For scale, the hammer is 28 cm long and the pencil tip is 5 mm wide. For the facies legend, refer to the main text or Table 4.2.

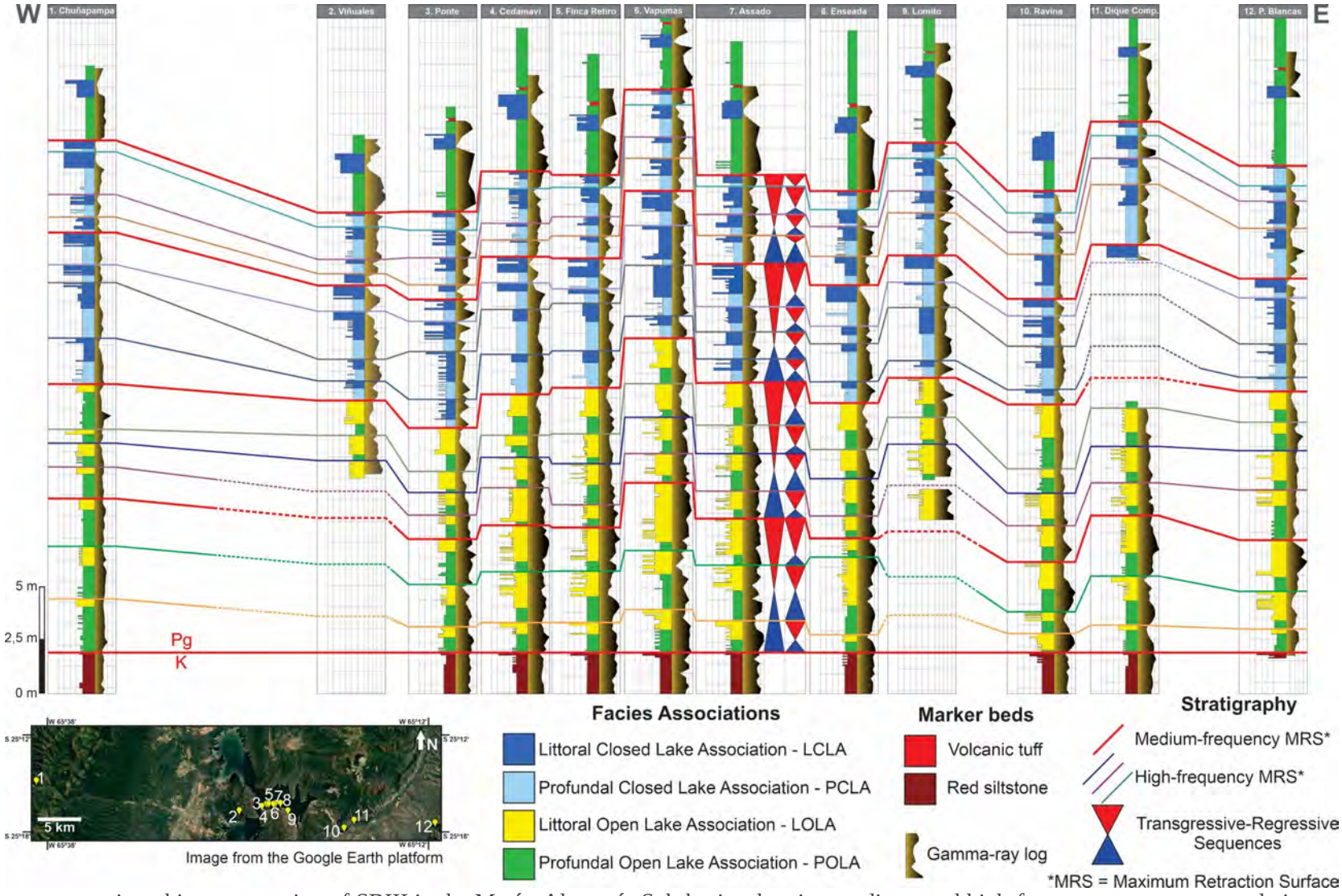


**Fig. 4.11.** East–west stratigraphic cross-section of SBIII in the Metán-Alemanía Sub-basin, showing medium- and high-frequency sequence correlations using the K/Pg boundary as a datum. Facies are color-coded by lithofacies associations, highlighting a transition from open- to closed-lake conditions from base to top. Stratigraphic profiles were mirrored to align with gamma-ray data, thereby facilitating section correlation.

## 4.5. LBP and stratigraphic cyclicity

The LBP analysis was performed from a stratigraphic perspective, aiming to evaluate its correspondence with the stacking trends identified within the SBIII. As the Assado outcrop exhibits tilted strata due to Andean tectonic deformation (Fig. 4.5), a flattening procedure was applied to align the layers horizontally, minimizing grid distortions (Fig. 4.12C). Two representative sections were selected for testing: section 1, corresponding to the basal open-lake interval dominated by siliciclastic facies (Fig. 4.12A), and section 2, representing the upper closed-lake interval characterized by carbonate-dominated facies (Fig. 4.12B).

For each section, LBP analyses used grids with square cells of 5, 10, 20, and 30 cm per side. These tests aimed to assess how grid resolution influences the detection of textural patterns and their correspondence with stratigraphic cyclicity, with the aim of identifying the scale that best captures high-frequency cyclicity. Finer grids enhanced sensitivity to subtle variations by better capturing local grayscale contrasts, whereas coarser grids averaged these differences, reducing the preserved textural detail.

In section 1 (Fig. 4.12A), which corresponds to the open-lake interval dominated by siliciclastic lithofacies, the LBP analysis applied with different grid resolutions reveals significant variation in the detection of high-frequency stratigraphic cyclicity. At finer resolution (5 cm per side), the LBP profile captures a high density of local textural variations. However, this level of detail tends to reflect the internal heterogeneity of individual hemicycles—highlighting interbedded facies within regressive intervals—rather than broader cyclic patterns. In contrast, the 10 cm per side grid provides a more regular LBP profile, closely aligned with the interpreted stacking trends. The transitions between lighter and darker trend LBP values correspond to the alternation between transgressive and regressive hemicycles, reflecting systematic differences in local contrast patterns at this scale. Grid resolutions of 20 and 30 cm per side result in progressively smoothed profiles, with a noticeable loss of stratigraphic resolution and a reduction in the number of cycles identified, particularly in thinner sequences. These observations suggest that finer grids enhance lithofacies contrast, whereas intermediate resolutions, such as 10 cm per side, better capture the signal associated with elementary stratigraphic sequences, typically expressed at 1–2 meters in thickness.

Section 2 (Fig. 4.12B), representing the closed-lake interval with predominantly carbonate lithofacies, exhibits more subtle textural contrasts between transgressive and regressive hemicycles. Despite this, the LBP method remains effective at identifying cyclicity, especially when using intermediate resolution grids. At 5 cm per side, the profile becomes irregular and overly sensitive to centimeter-scale variations, often reflecting internal lamination or small-scale heterogeneity within facies such as stromatolites and laminites. The 10 cm per side grid resolution appears to provide the most suitable match for this scale of high-frequency sequences, with LBP peaks aligning more closely with the interpreted cycles, including portions of the succession where transgressive hemicycles are partially preserved or visually less distinguishable. Grid resolutions of 20 and 30 cm per side significantly reduce the number of observable cycles, with broader, less distinct variations in the LBP profile that fail to correspond to the stratigraphic framework. As in section 1, the 10 cm per side resolution represents a good compromise between textural sensitivity and stratigraphic significance, allowing for the recognition of stacking patterns associated with short-term lake-level fluctuations.

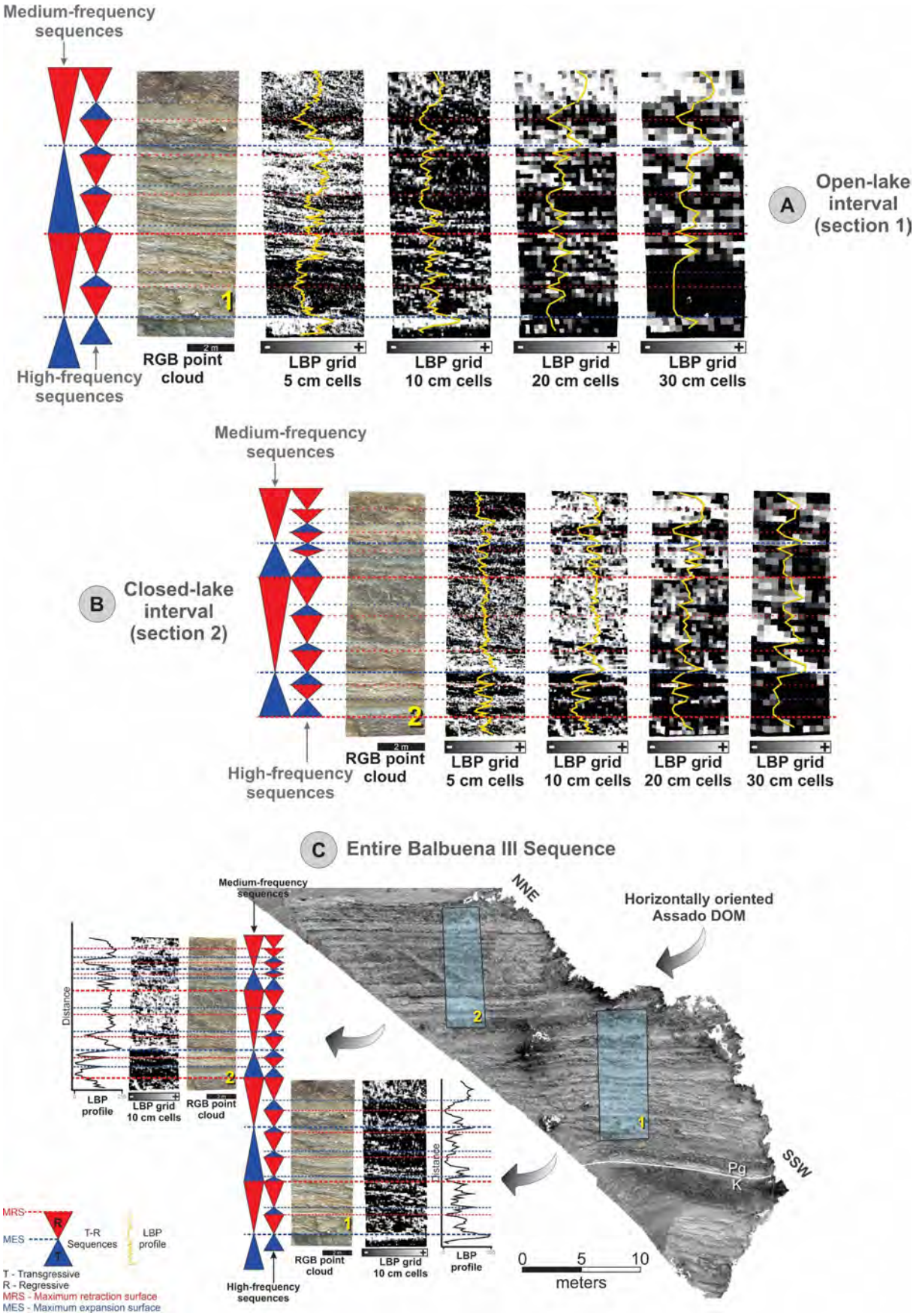


**Fig. 4.12.** High- and medium-frequency sequences of SBIII in the Assado DOM correlated with LBP analysis. A) Open-lake interval. B) Closed-lake interval. C) Entire Balbuena III Sequence. The white line marks the K/Pg boundary as identified on the DOM.

Across both sections, the LBP profiles exhibit a general trend that reflects the stratigraphic stacking patterns interpreted in the field. In most transgressive hemicycles, the profile tends to show a progressive increase in LBP values upward, while regressive hemicycles are typically marked by a decrease. This pattern is particularly clear in section 1 (open-lake interval), where fine-grained and homogeneous transgressive deposits are overlain by more heterolithic regressive facies, resulting in regular and alternating LBP profiles that align closely with interpreted cycles. In section 2 (closed-lake interval), the same trend is observed, although it is less distinct. This reduced clarity is attributed to the more limited development of facies associated with transgressive hemicycles, leading to lower textural contrast between cycles.

In both intervals, the LBP profiles at 10 cm per side resolution exhibit notable overall correspondence with the interpreted stratigraphic boundaries. However, a few minor deviations are observed, where isolated peaks do not fully align with the previously defined cycle limits. These deviations may reflect internal facies heterogeneity within hemicycles, particularly in intervals with interbedded lithotypes, or may indicate areas where the stratigraphic interpretation could be further refined. Nonetheless, the general agreement between LBP-derived patterns and field-based interpretations highlights the potential of this method for detecting high-frequency stratigraphic sequences.

Based on the results obtained in sections 1 and 2, the 10 cm per side grid resolution was selected for application across the entire Assado outcrop. This resolution provided the best balance between capturing local textural variation and preserving the signal associated with elementary stratigraphic sequences. The resulting LBP DOM (Fig. 4.13) reveals a well-organized pattern of alternating light and dark horizontal bands that correspond to the overall stacking architecture of SBIII. The basal portion of the outcrop (SSW), which encompasses the open-lake interval, shows distinct banding with regular alternations, consistent with the high-frequency cycles interpreted in section 1. The upper portion (NNE), representing the closed-lake interval, exhibits a somewhat more irregular pattern, reflecting the lower contrast between facies observed in section 2. Several laterally continuous bright bands in the LBP image correspond to major peaks previously identified in the section-based LBP profiles, illustrating the sensitivity of the method to pronounced textural transitions at outcrop scale.

Fig. 4.13 also presents a correlation between high-frequency Maximum Retraction Surfaces (MRS) and the LBP results mapped across the entire Assado outcrop. Continuous lines indicate surfaces with clearer correspondence to well-defined dark bands—zones of lower LBP values—whereas dashed lines represent less evident or more laterally discontinuous features. The focus on MRS stems from the observation that the end of regressive hemicycles tends to yield lower LBP values, which appear as darker bands in the LBP-rendered DOM. This makes them more easily identifiable and traceable across the outcrop using grid-based analysis. Although preliminary and based on visual inspection, this correlation highlights the potential of LBP-based mapping to support the identification and lateral continuity of high-frequency stratigraphic surfaces when integrated with architectural and facies-based interpretations. This approach remains exploratory, and further studies are needed to quantitatively validate the method for use in stratigraphic frameworks. It is important to note, however, that the correlation of these surfaces must also consider outcrop geometry and potential lithological contrasts unrelated to stratigraphic stacking, since textural variation may also result from lateral facies changes or, when present, from structural deformation. The latter can be mitigated through preprocessing.

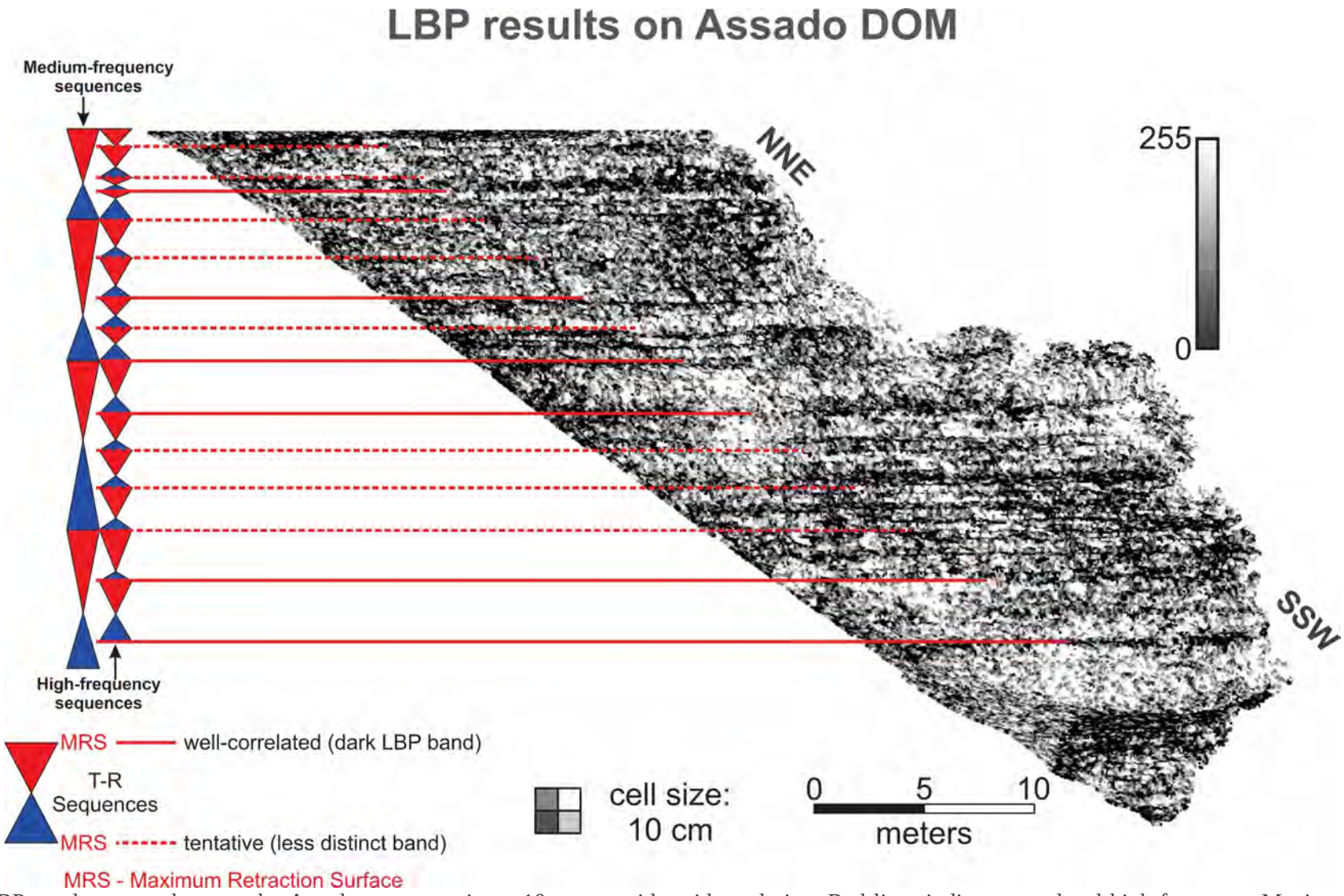


**Fig. 4.13.** LBP results mapped across the Assado outcrop using a 10 cm per side grid resolution. Red lines indicate correlated high-frequency Maximum Retraction Surfaces (MRS), identified based on stacking patterns and dark LBP bands. Continuous lines represent well-correlated surfaces, whereas dashed lines indicate surfaces with less well-defined correlations.

## 4.6. CNN and lithofacies-classified 3D point cloud

### 4.6.1. Labeled images

The first step required to implement the workflow of the CNN and lithofacies-classified 3D point cloud is the labeling of lithofacies in the photographs acquired in the field using an RPAS. This is the most time-consuming stage and requires an expert with thorough knowledge of the stratigraphy and sedimentology of the study area to accurately label the facies. Achieving good results with the fewest possible labeled images used for training is the key objective. Initially, 5% of the dataset from the Assado outcrop (25 out of 497 images) was labeled, yielding an accuracy below 60%. This proportion was later increased to 10% (49 images), improving accuracy to over 80%.

In practice, the labeling of lithofacies in the SBIII is not a straightforward process; it is inherently interpretative. This complexity arises because lithofacies often cannot be easily distinguished due to their similar colors or their intercalation with other facies. The reduced resolution (384 × 256 pixels) used during CNN model training decreases processing time but inevitably causes a loss of fine detail. The objective of the classification, however, is not to detect all centimeter-scale variations, but to recognize facies at the scale of the hemicycles of the elementary sequences, which are also relevant to the reservoir scale. Consequently, some lithofacies were grouped into broader classes (Fig. 4.14). Heterolithic facies, for example, composed of intercalations up to 10 cm thick, may not be discernible at the reduced resolution and were therefore treated as a single type.

| Name | Label | Grouped lithofacies codes | Brief description | Lithofacies Association |
|---|---|---|---|---|
| Siltstone | **SLT** | S1 | Red siltstone (base of SBIII) | FA1 - Littoral Open Lake Association **LOLA** |
| Sandstone | **SND** | S4, S5, M2 | Fine/very fine sandstones (possibly hybrid) with truncated, wavy, or low-angle cross-laminations interbedded with shale | |
| Rudstone | **RUD** | C8, C9 | Bioclastic rudstone and floatstone composed of gastropod shells | |
| Crystalline carbonate | **CLC** | S1 | Crystalline carbonate with charophyte fragments occurring as lenses within facies S1 | |
| Heterolith | **HET** | S2 | Heterolith of shale with very fine sandstone lenses (linsen) | FA2 - Profundal Open Lake Association **POLA** |
| Shale | **SHL** | S3, M1 | Shale (F3) and laminated marl (M1). Note: this FA can occur in both the open-lake and closed-lake intervals | |
| Laminite | **LMT** | C11 | Crenulated laminite | FA3 - Littoral Closed Lake Association **LCLA** |
| Grainstone | **GST** | C3, C4, C5, C6, C7, M2 | Grainstones and packstones with cross-bedding, wavy, or trough stratifications. Hybrid sandstone may occur | |
| Stromatolite | **STR** | C10 | Columnar domal cerebroid stromatolite | |
| Mudstone | **MUD** | C1, C2, M1 | Laminated or massive mudstone | FA4 - Profundal Closed Lake Association - **PCLA** |
| Tuff | **TUF** | V1 | Volcanic tuff | – |
| Others | **Others** | – | Vegetation, sky, clouds, road | – |

**Fig. 4.14.** Summary of labels used in the CNN-based classification, including lithofacies and non-geological classes.

For instance, the 'sandstone' facies represents heterolithic deposits composed of siliciclastic mudstones and fine-grained sandstones, exhibiting hummocky or low-angle cross-stratification. Similarly, granular carbonate facies such as grainstone and packstone could not be distinguished from field-acquired photographs and were all assigned to the general class of 'grainstone.' Although this approach simplifies the classification, it ensures that the CNN model is trained with consistent and interpretable data, which is critical for predictive performance. Of the 11 lithofacies used, only two markedly thin layers (~15 cm thick) were retained as individual classes due to their specific stratigraphic importance in the study area: crystalline limestone, which marks the K–Pg boundary, and volcanic tuff, which is datable and may be relevant in geochronological studies. Fig. 4.15 presents examples of labeled photographs.

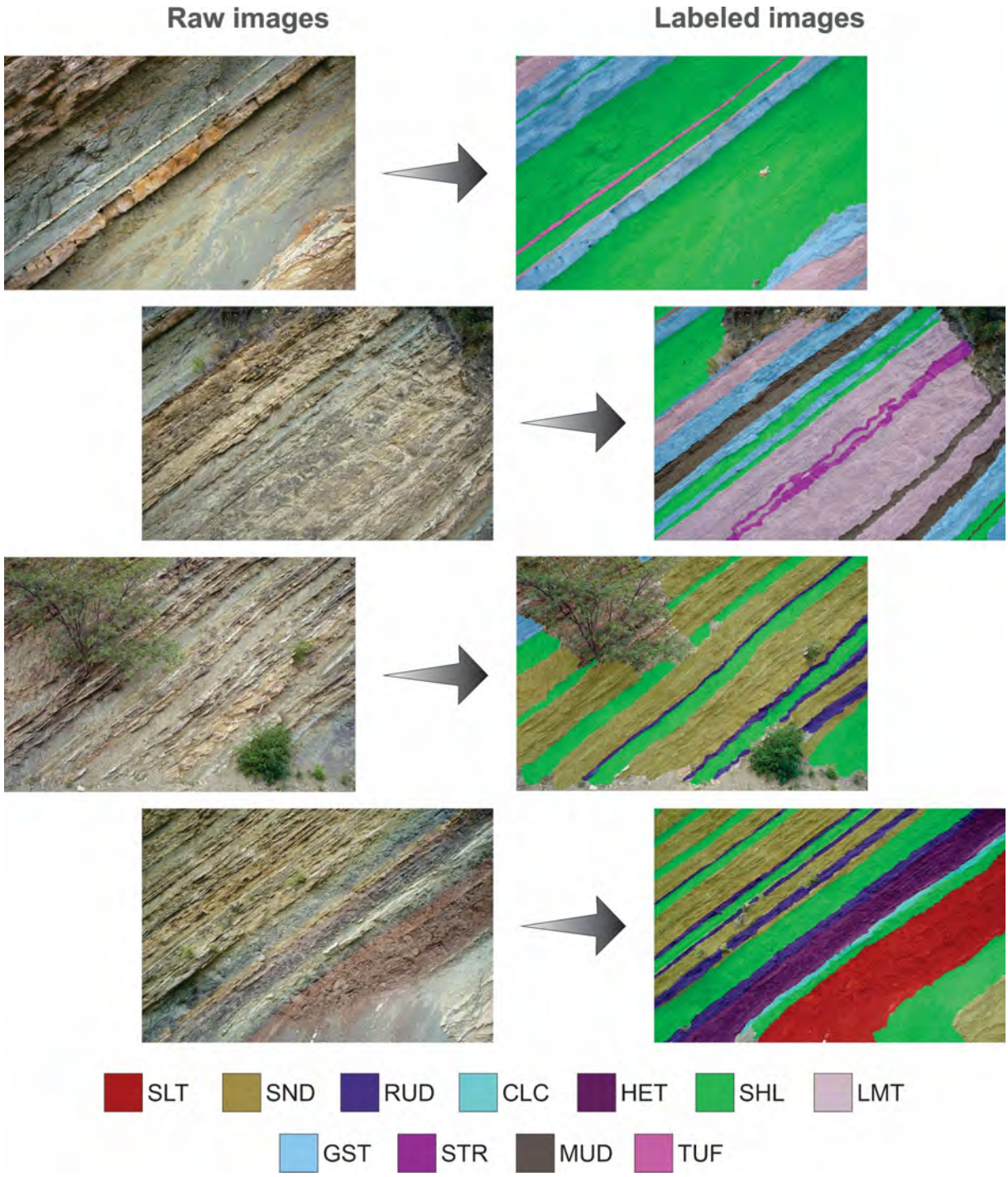


**Fig. 4.15.** Comparison of raw and labeled images. The left image shows the original, non-interpreted photo, while the right image presents the same photo with lithofacies labels used in the CNN approach, as defined in Fig. 4.14.

### 4.6.2. CNN model

The labeled images were divided into two groups: the first was used to train the CNN model, and the second was reserved for evaluating model accuracy. For the Assado outcrop, 497 photos were used to generate the virtual outcrop model. Of these, 49 images (10%) were labeled, with 50% allocated for training and 50% for model validation. Image selection was random, but it was monitored to ensure that all lithofacies and the entire stratigraphic sequence were represented in both the training and validation subsets. After training, a global accuracy of 84% was obtained. Table 4.3 presents the precision, recall, and F1 score parameters obtained for the CNN model applied to the Assado outcrop. Precision measures the proportion, for each category, of correct predictions compared to all predicted. Recall evaluates the ability to detect

all actual positives, and F1 Score is the harmonic mean between Precision and Recall ratios, providing an overall balanced measure of model performance. Fig. 4.16 illustrates some examples of validation results, showing the correspondence between predicted classes and the labeled images considered as true for the validation metrics.

**Table 4.3.** Performance metrics (Precision, Recall, and F1 Score) for the CNN model applied to the Assado outcrop, showing the global accuracy and results by individual classes.

| | Lithofacies | Precision | Recall | F1 Score |
|---|---|---|---|---|
| 1 | GST | 0.79 | 0.83 | 0.81 |
| 2 | STR | 0.55 | 0.51 | 0.53 |
| 3 | LMT | 0.84 | 0.80 | 0.82 |
| 4 | MUD | 0.83 | 0.87 | 0.85 |
| 5 | SND | 0.72 | 0.81 | 0.76 |
| 6 | HET | 0.96 | 0.79 | 0.86 |
| 7 | RUD | 0.80 | 0.63 | 0.71 |
| 8 | CLC | 0.76 | 0.32 | 0.45 |
| 9 | SHL | 0.90 | 0.93 | 0.91 |
| 10 | SLT | 0.96 | 0.83 | 0.89 |
| 11 | TUF | 0.66 | 0.43 | 0.52 |
| 12 | Others | 0.84 | 0.82 | 0.83 |
| | **Global accuracy** | | | **84%** |

The model achieved global accuracy of 84%, but this figure alone does not provide a complete assessment of performance for each class, particularly in cases of imbalanced datasets. In such scenarios, metrics such as Precision, Recall, and F1 Score provide a more detailed perspective. Some classes achieved the highest scores among the dataset, such as HET (96% Precision, 79% Recall, 86% F1 Score) and SLT (96%, 83%, 89%), demonstrating the model's ability to consistently identify these lithofacies. The SHL class also yielded similarly high values, with 90%, 93%, and 91% for Precision, Recall, and F1 Score, respectively. Furthermore, the MUD class exhibited a balanced performance across metrics, with 83% Precision, 87% Recall, and 85% F1 Score.

Other classes showed moderate performance, such as GST (79%, 83%, 81%), LMT (84%, 80%, 82%), and SND (72%, 81%, 76%), indicating that the model performed adequately but with potential for improvement. The moderate performance observed for the SND lithofacies can be attributed to the confusion the model had between SND and GST lithofacies within the same layer, as indicated by the white arrows in Fig. 4.16C. The 'Others' class also displayed consistent results, with 84% Precision, 82% Recall, and 83% F1 Score, as it represents all non-rock features in the photographs, such as roads, sky, and vegetation.

On the other hand, some classes exhibited lower performance, such as STR (55%, 51%, 53%), CLC (76%, 32%, 45%), and TUF (66%, 43%, 52%). These results are mainly associated with the limitation imposed by the downscaling of the original images. Using the actual downscaled resolution (384 × 256) and the acquisition geometry (DJI P1 with 35 mm lens at ~12.9 m camera-to-target distance), the effective pixel size in the reduced images is about 3.4 cm/pixel. For thin layers such as CLC and TUF, whose thickness is represented by only a few pixels at this resolution, accurate segmentation becomes intrinsically difficult. For the CLC class (yellow arrow in Fig. 4.16D), the high Precision (76%) suggests that when the model predicts this lithofacies, it is generally correct, but the very low Recall (32%) indicates that many true instances are missed. This behavior may be because CLC corresponds to a single layer within the stratigraphic sequence. The TUF class (red arrow in Fig. 4.16A) exhibits both

low Precision (66%) and low Recall (43%), reflecting the same scale-driven constraint. The STR class (55% Precision, 51% Recall, 53% F1-score) presents a more balanced performance compared to CLC and TUF but still falls within the low-performance category. Although STR is more abundant, it typically occurs interbedded with the LMT facies, often sharing similar color patterns, and the reduced resolution also hindered the model's ability to distinguish the textural details separating STR from LMT. Another noteworthy observation is that the CNN model often merges the two thinner stromatolite (STR) layers present within the middle portion of SBIII into a single layer (as indicated by the blue arrow in Fig. 4.16B), a behavior consistent with the resolution limitation.

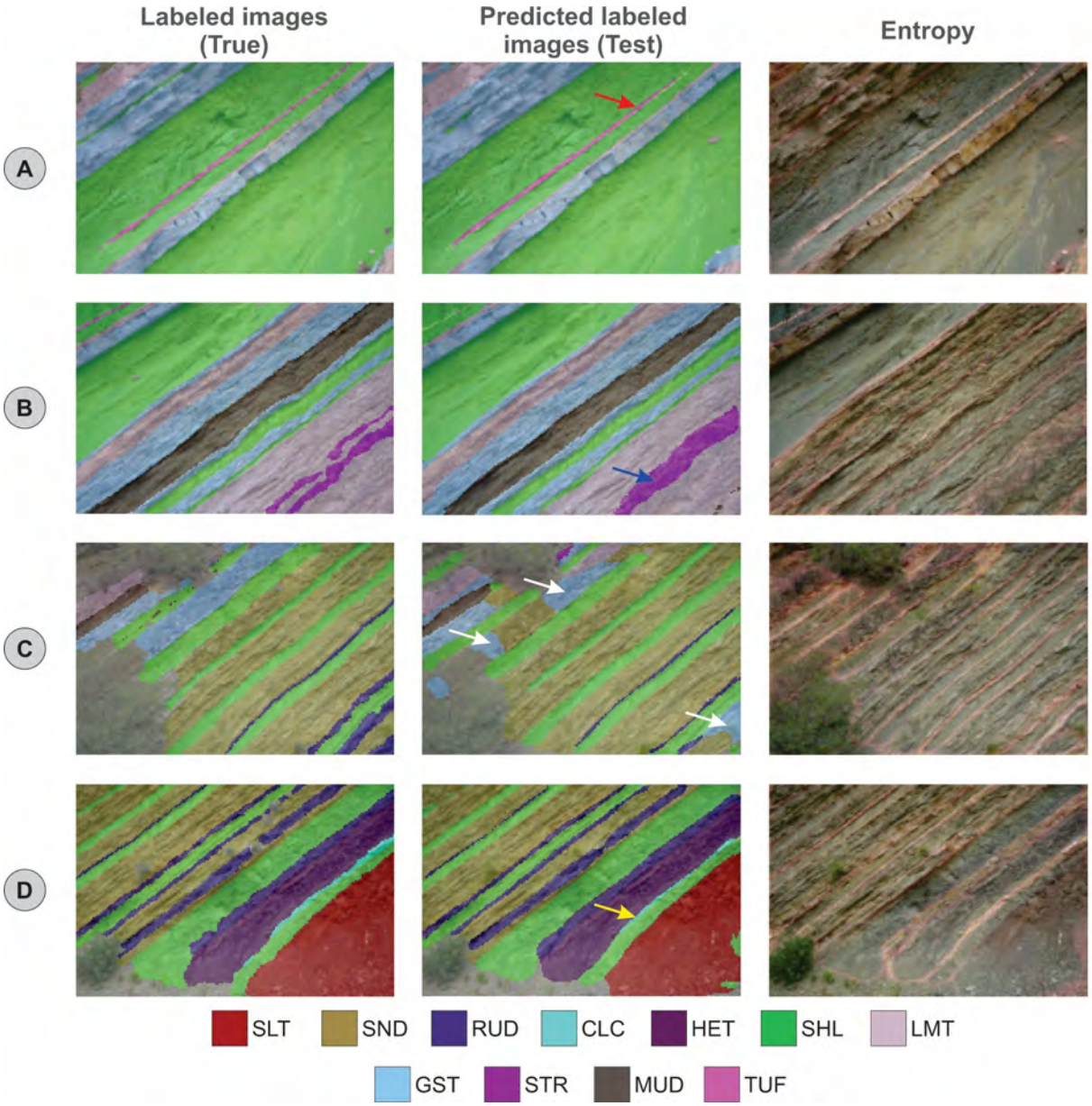


**Fig. 4.16.** Examples of validation results comparing predicted classes and labeled images used as ground truth. Arrows highlight key features: red (A) – tuff layer; blue (B) – stromatolite beds predicted as a single one by the model; white (C) – areas of confusion between sandstone and grainstone; yellow (D) – thin crystalline carbonate layer.

### 4.6.3. Lithofacies-classified 3D point cloud

As an output of the Python (2023) CNN code, in addition to lithofacies predictions on the images, masks are generated for each lithofacies (Fig. 4.17A). This protocol enables the masks to be imported into Metashape (Agisoft Metashape, 2023) and used to generate lithofacies-

based 3D point clouds. This approach is particularly advantageous not only because it allows for the generation of lithofacies-based 3D point clouds but also because it ensures that only the most robust predictions, identified in more than one photograph, are considered. Through the photogrammetry workflow combining Structure-from-Motion and Multi-View Stereo (SfM-MVS), matching points between multiple photographs are required (Fig. 4.17B). This process inherently filters out isolated predictions that may have been incorrectly interpreted by the CNN model in individual images and ensures consistency by integrating only the facies predictions that appear in multiple images.

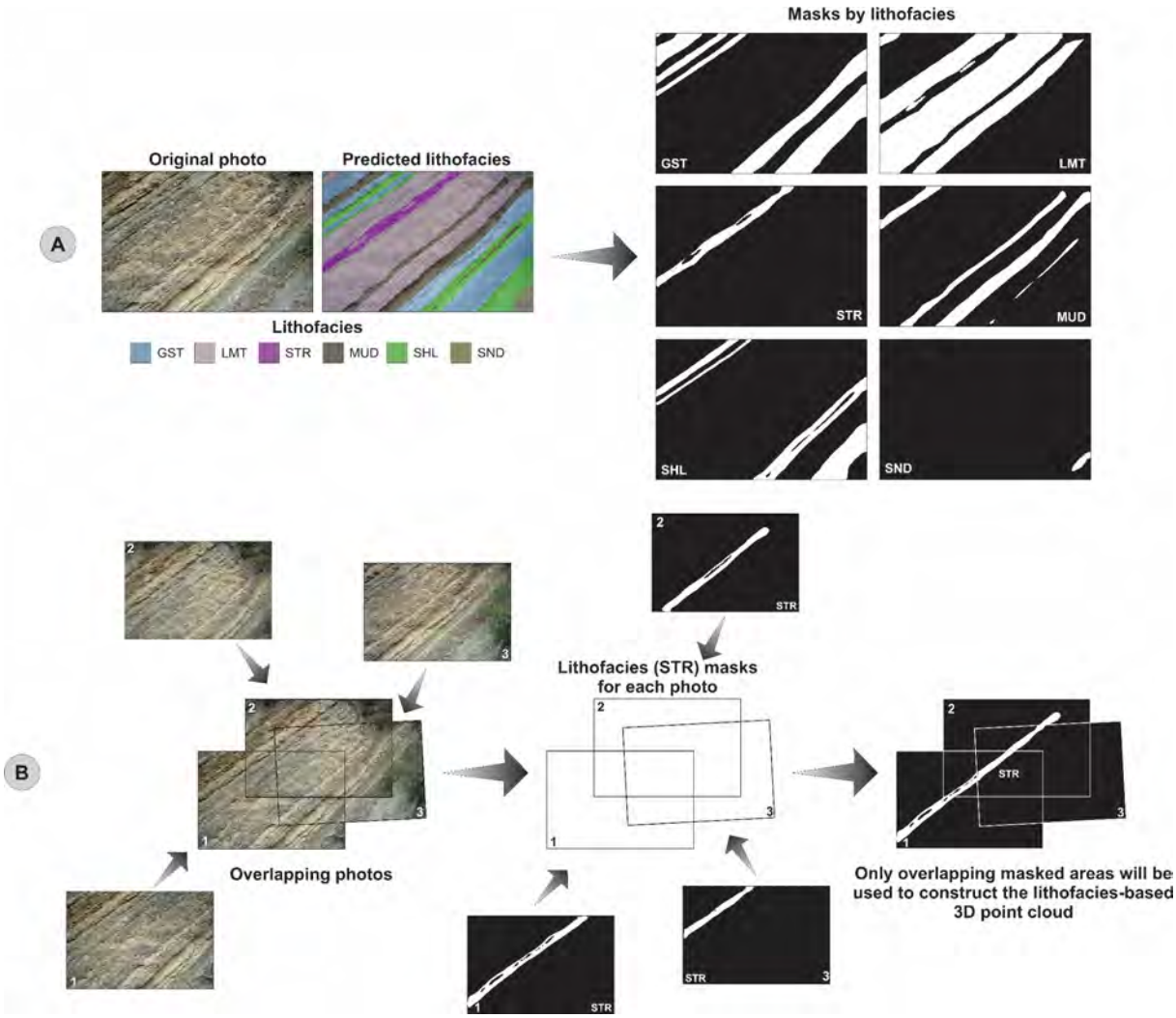


**Fig. 4.17.** Illustration of the process for generating lithofacies masks, a key step in constructing lithofacies-based 3D point clouds. A) Example of mask generation for multiple lithofacies from a single photograph using CNN; white areas correspond to regions included in the photogrammetry workflow. B) Overlapping photographs showing only the mask for a single lithofacies (STR). These masks are combined across images to identify consistent predictions, which are then used to construct the lithofacies-based 3D point cloud. Final classified point clouds are presented in Fig. 4.18. Lithofacies labels follow Fig. 4.14.

In the Metashape software (Agisoft Metashape, 2023), all the original-resolution images (8192 × 5660 pixels) used to generate the DOM are utilized to create a sparse point cloud of the outcrop. Subsequently, this cloud is duplicated across multiple chunks, each representing a specific lithofacies. For each chunk, the masks corresponding to that lithofacies, generated in .jpg format for all images, are imported. This enables the generation of a dense point cloud for each chunk, resulting in lithofacies-based dense point clouds that are qualitatively evaluated to allow manual removal of mismatched points. Consequently, the final 3D point cloud reveals

the spatial distribution of specific lithofacies as distinct geological bodies (Fig. 4.18 and Fig. 4.19). These bodies represent the preserved architectural elements within the outcrop studied.

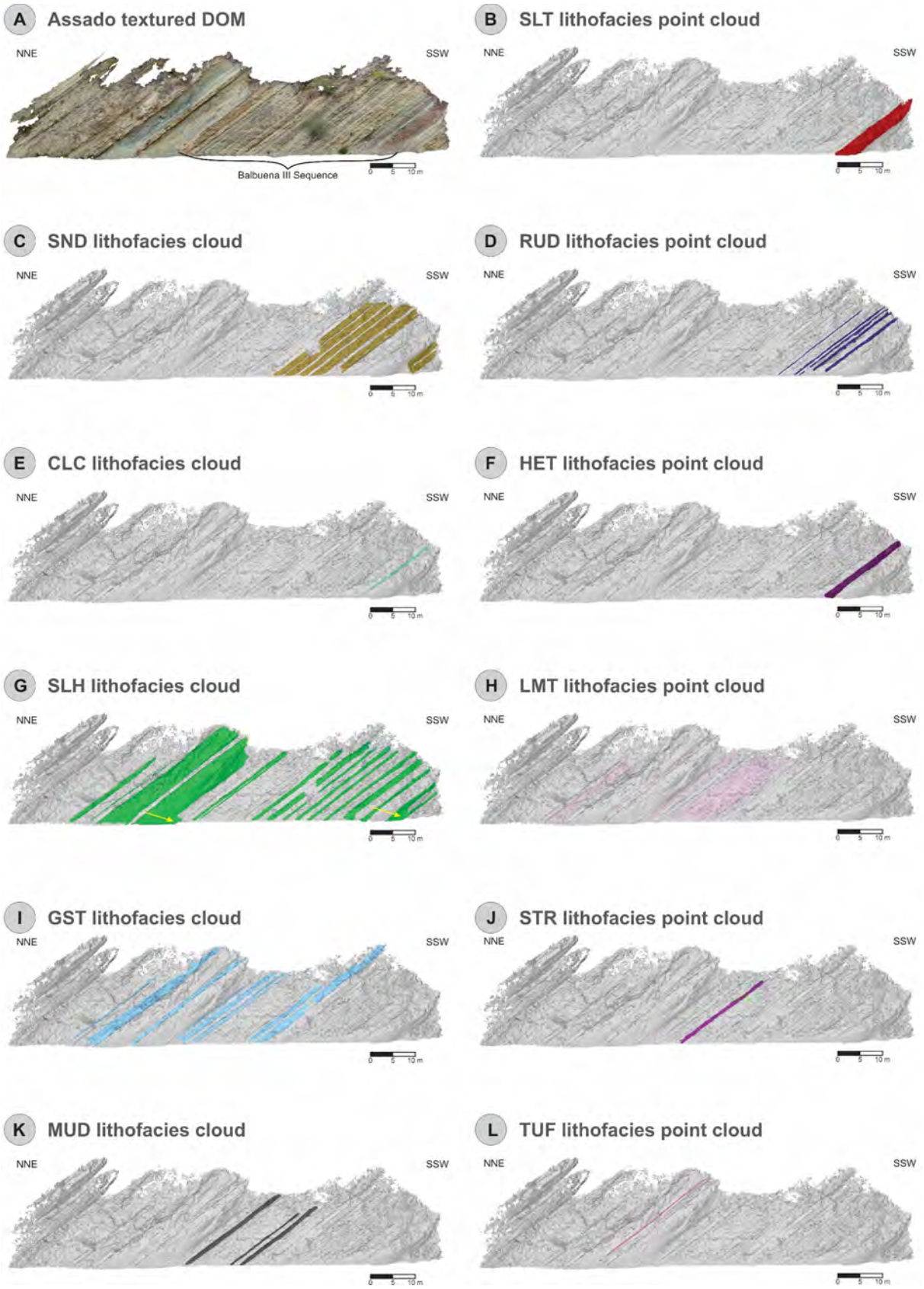


**Fig. 4.18.** 3D point cloud classified by facies (B–L) from the Assado DOM (A) of the Balbuena III Sequence, located in the Metán-Alemanía Sub-basin within the Cabra Corral reservoir region. The gray point cloud represents the dense point cloud of the studied outcrop. Lithofacies labels are detailed in Fig. 4.14.

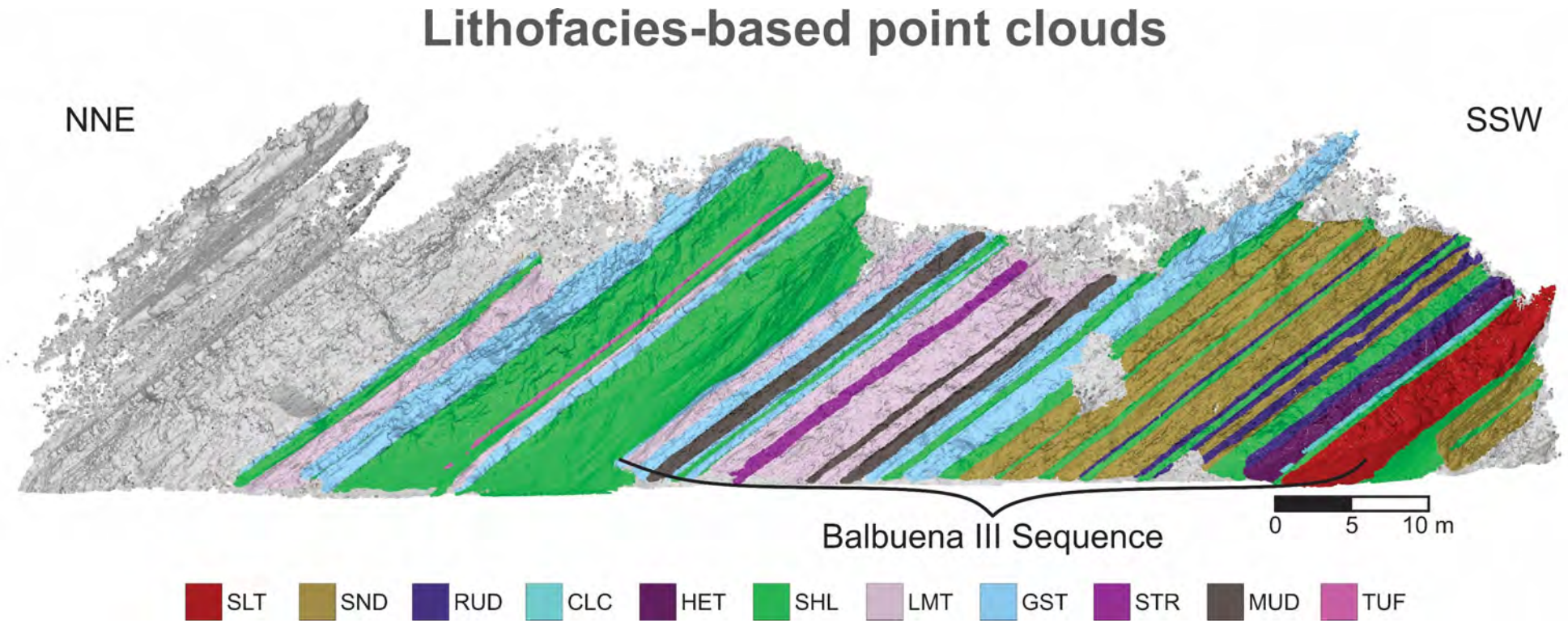


**Fig. 4.19.** Lithofacies-classified 3D point cloud of the Assado outcrop. Complementary to **Fig. 4.18**, this figure shows the fully classified 3D point cloud, integrating all lithofacies into a single visualization. The gray points represent the dense point cloud of the studied outcrop. Labels follow the classification in Fig. 4.14.

## 4.7. Discussion

### 4.7.1. Integrating digital and traditional methods for analog outcrop analysis in the Salta Basin

The integration of digital techniques with traditional field-based methods, as implemented in this study, represents a key aspect demonstrating the significant advantages of this hybrid approach. While conventional techniques—such as field data acquisition and laboratory analyses—have proven highly effective for generating knowledge and defining the depositional and stratigraphic models of the study area, digital approaches have enabled the extraction of stratigraphic and sedimentological information in an automated or semi-automated manner. This has facilitated the processing of large datasets and led to considerable time savings. Moreover, digital outcrop models obtained via RPAS allow data extraction in areas with restricted access, thereby expanding their potential for analysis and application.

High-resolution digital outcrop models played a crucial role in the analysis conducted here, enabling the production of photorealistic models that, in addition to serving as the basis for all subsequent digital analyses, preserve geological information with high fidelity. For example, the DOM of the Assado outcrop (Fig. 4.18A) exhibits a textural resolution of approximately 1.6 mm, and the point cloud density is about 208,000 pts/m². This high resolution permits the identification of different lithofacies by visual inspection, including the recognition of millimetric laminations in facies such as stromatolites and laminites. This level of detail allows for a qualitative evaluation of the dense, lithofacies-classified point clouds generated by the integrated CNN and photogrammetry workflow. However, although these models are extremely data-intensive and require high-performance computing for processing, it is possible to reduce the resolution when necessary to facilitate information extraction. It should be noted, however, that the reverse is not possible: if the models are initially acquired at low resolution, even artificial enhancement techniques cannot compensate for the loss of detail, precluding the generation of high-resolution models faithful to reality.

Field observations and petrographic thin section analysis supported the grouping of lithofacies (Fig. 4.14) used in the application of CNN techniques to outcrop photographs. This synergy improved both the accuracy of the classifications and the geological relevance of the digital outputs. Similarly, the results obtained from LBP analysis were qualitatively consistent with the stacking patterns described in the field and with the high-frequency stratigraphic framework observed in the study area, although further quantitative validation would be advisable to confirm this agreement.

Nevertheless, the accuracy of digital analyses is heavily dependent on the quality and resolution of the input data, as well as the prior geological knowledge required for result evaluation. For instance, during the training of the CNN model, the resolution of the labeled images was significantly reduced to decrease training time, which resulted in the loss of some details. The CLC and TUF lithofacies, corresponding to thin layers, performed less satisfactorily compared to other lithofacies (see Table 4.3). Entropy maps (Fig. 4.16) demonstrate that the highest uncertainties—represented by reddish tones—are concentrated in the thinner layers and at the contacts between different facies, since, at reduced scale, a single pixel may contain information from more than one lithological type, thereby hindering prediction. However, the relevance of these limitations depends on the purpose of the interpretative analysis. For example, in the context of the present study area, if the objective is to evaluate reservoir quality characteristics, the model's difficulty in predicting a 10-cm-thick layer of volcanic tuff may not pose a significant problem. This lithofacies is characterized by

fine particles, extremely low permeability, and occurs within a shale unit with similar petrophysical characteristics. In other geological contexts, even thin or discontinuous layers could significantly influence reservoir performance; for instance, a tuff layer within a permeable geological body could act as a barrier to fluid flow. Additionally, in stratigraphic studies where volcanic tuffs are targeted as potential datable horizons, their accurate recognition becomes essential to support reliable geochronological frameworks.

Furthermore, as illustrated by the white arrows in Fig. 4.16C, the CNN model frequently confuses the SND and GST lithofacies, placing them in the same layer. Although both facies are granular in nature, they differ in composition, with SND being siliciclastic and GST carbonate. This outcome was anticipated given the gradational transition between predominantly siliciclastic and carbonate facies, where hybrid sandstones occur. Since this transitional facies was not explicitly defined as a separate class during training—because distinguishing it by the naked eye is challenging and requires petrographic microscopy—such confusion in the predictions is to be expected. Therefore, it is incumbent upon the interpreter to verify whether the SND or GST facies should be preserved for a given interval, with the possibility of manually excluding or modifying classifications that do not align with the expected geological interpretation. Another aspect requiring improvement in the CNN model is the prediction of rock fragments, particularly within muddy facies that tend to fragment and remain on the outcrop. To prevent the model from misclassifying these fragments as part of the 'others' class when a photo contains many fragments, they are currently interpreted as part of the lithofacies from which they originated. However, when the facies-classified point cloud is generated, an artifact is introduced that does not accurately represent the true geometry of the geological body, as indicated by the yellow arrows in Fig. 4.18G. Although not implemented in this work, it is recommended that a new class be introduced to represent rock fragments, enabling them to be classified and isolated more directly, thereby reducing the need for extensive manual editing.

Transforming the DOM into an LBP-rendered surface provides a computationally lightweight and efficient way to highlight textural variation using grayscale values alone, but its effectiveness can be affected by variations in lighting, surface geometry, and facies contrast. Unlike RGB imagery, which requires processing across three color channels, LBP encodes local differences using a single grayscale channel, making it especially suitable for large-scale applications where data volume and processing time are limiting factors. The application of the LBP method to digital outcrop models demonstrated its potential as a complementary tool for stratigraphic interpretation, particularly in identifying high-frequency cyclicity. By encoding local grayscale variations, LBP values reflected systematic trends along stacking patterns, allowing correlation with transgressive–regressive hemicycles described in the field. Lower LBP values at the ends of regressive hemicycles—represented by darker bands in the LBP-rendered DOM—could be associated with the identification of Maximum Retraction Surfaces (MRS). Although the 10 cm per side grid resolution proved to be the most suitable for this study, the optimal cell size may vary depending on the objectives, the characteristics of the outcrop, and the thickness of the elementary stratigraphic sequences under investigation. Therefore, determining the appropriate resolution requires testing and calibration based on the scale of stratigraphic features of interest. Despite the promising results, the method remains sensitive to variations in facies architecture and outcrop geometry, and its effectiveness depends on the depositional context. Future applications that integrate LBP with surface roughness analysis may offer additional insights not only for refining the interpretation of stratigraphic cyclicity, but also for supporting the recognition of facies based on their combined textural and morphological characteristics.

An additional observation from the multi-resolution analysis was the recurrence of certain LBP peaks across all tested grid sizes. These persistent responses are primarily associated with strong textural contrasts within the outcrop and are more evident in coarser grids, where stacking patterns tend to be oversmoothed. Rather than capturing the organization of elementary sequences, these signals reflect broader variations in texture, which may correspond to specific facies with distinct depositional or diagenetic signatures. In some cases, such peaks could represent features of interest for petrophysical evaluation or act as mappable horizons within the DOM. While not necessarily tied to stratigraphic boundaries, their consistency across scales suggests that LBP can assist in highlighting textural anomalies that merit further geological investigation.

The integration of CNN-based lithofacies classification and LBP analysis provided valuable support for the stratigraphic and lithofacies interpretations of analog outcrops in this study. CNN allowed for the automated generation of classified point clouds from large image datasets. LBP offered a simple and efficient way to detect systematic textural variations across the outcrop. Although promising, digital methods should not replace field and laboratory analyses. Their role is to complement traditional approaches and increase the efficiency and consistency of geological interpretations.

### 4.7.2. The Salta Basin as an analog for Pre-Salt reservoirs

The Pre-Salt reservoirs consist of rock formations located beneath a thick salt layer, extending for more than 800 km along the Brazilian offshore margin, from Espírito Santo to Santa Catarina states. These reservoirs are buried between 3,000 and 4,000 meters below the seafloor and are in water depths ranging from 1,500 to 3,000 meters. The Pre-Salt reservoirs exhibit challenging characteristics, including layered stratigraphic architectures, shrubstone-rich carbonate successions, and significant heterogeneity driven by diagenetic processes and structural compartmentalization (Bueno de Moraes et al., 2024).

One of the main challenges in Pre-Salt reservoir characterization is the limited availability of core data, which hampers the detailed interpretation of facies distributions and stratigraphic heterogeneities. Even 19 years after the first commercial Pre-Salt well was drilled, core availability remains limited compared to the vast extent of these reservoirs, as coring operations are highly costly. In this context, the Salta Basin in Argentina is a suitable analog due to its similar geotectonic evolution and stratigraphic architecture, a rift-to-sag basin with lacustrine carbonates (Bento Freire et al., 2011; Terra et al., 2012).

A key factor supporting the use of Salta as an analog is the presence of carbonate deposition associated with high-frequency base-level fluctuations, enabling the correlation of stratigraphic sequences, including high-frequency ones, across tens of kilometers. This depositional model and its correlatable potential align with those presented in Fragoso et al. (2023) and Pedrinha and Artagão (2024), who quantified multiple sequence hierarchies, found that medium-frequency sequences with thicknesses ranging from ~5 to a few tens of meters are the most relevant for reservoir modeling, as they can be correlated over ~15–20 km and match the scale of production data. Although both studies describe higher-frequency sequences, the scarcity and heterogeneity of core data in producing fields limit the correlation of metric-scale units. The contrast between the well-documented Tupi Field (Santos Basin), with over 100 wells and extensive core coverage enabling a finer characterization, and the Brava Reservoir (Campos Basin), where only one of the three wells contained 42 m of core, highlights the impact of data availability on reservoir interpretation. This scarcity underscores the value of well-exposed outcrop analogs such as those in the Salta Basin, where detailed facies analysis supports the

definition and correlation of key stratigraphic surfaces, improving the robustness of production-scale interpretations.

As discussed in Section 4.7.3, HRSS further supports delineation of stratigraphic surfaces and the recognition of transgressive-regressive cycles that control compartmentalization and fluid pathways. Establishing a detailed stratigraphic framework is crucial for delineating production zones and optimizing reservoir development strategies in Pre-Salt reservoirs (Guerrero et al., 2024). The Salta Basin, with its well-preserved depositional record and correlatable high-frequency sequences (Bento Freire, 2012; Pedrinha, 2014; Roemers-Oliveira, 2014; Fragoso et al., 2024; this work), provides a practical framework to quantify sedimentary body geometry and spatial distribution, supporting improved reservoir characterization and predictive simulations.

### 4.7.3. The use of outcrop analogs for reservoir modeling

Outcrop analogs provide both conceptual frameworks validated by real-world observations and quantitative data that support parameterization in numerical models, including sedimentary body dimensions, facies stacking patterns, and geostatistical parameters (Howell et al., 2014). These elements are especially critical in carbonate reservoirs, where depositional complexity and diagenetic modifications strongly influence reservoir quality (Grammer et al., 2004; Lucia, 2007; Ahr, 2008).

Within this scope, HRSS offers a structured approach to mapping stratigraphic units below seismic resolution, often linked to allogenic controls such as base-level variations (Silveira, 2020; Magalhães et al., 2020; Fragoso et al., 2021a, 2021b; Fragoso et al., 2022). Criteria for identifying these sequences include: (I) a transgressive-regressive (T-R) stacking pattern, (II) vertical recurrence of these patterns, (III) trend analysis to define lower-frequency sequences, and (IV) mappability of stacking patterns and their bounding stratigraphic surfaces (Silveira, 2020; Magalhães et al., 2020; Fragoso et al., 2021a, 2021b). Such criteria are relevant in a variety of environments, influencing both heterogeneity and depositional architecture.

HRSS allows stratigraphic zonation, improving correlation potential and supporting predictions of high-permeability zones, sealing intervals, and heterogeneity distribution at the metric scale (Grammer et al., 2004; Magalhães et al., 2020; Fragoso et al., 2021a).

The quantitative characterization of carbonate geobodies is also essential for reservoir modeling approaches, whether in stochastic geostatistical simulation, object-based modeling (e.g., Adams et al., 2005), or process-based forward modeling. In carbonates, body geometry, internal heterogeneity, and diagenetic overprints can generate complex relationships between sequence stratigraphy and reservoir architecture, where depositional and diagenetic processes do not conform to timelines (Borgomano et al., 2001; Fournier and Borgomano, 2007). Outcrop-based observations help define fluid pathways, structural planes, and heterogeneity patterns, thereby reducing uncertainties in hydrocarbon exploration and development.

In recent years, process-based modeling has gained relevance as a predictive tool, enabling the testing of depositional scenarios and their impact on reservoir heterogeneity and connectivity (Granjeon, 1996). For carbonate-related deposits, forward modeling can reproduce spatial facies distribution and stacking patterns, increasing the predictive capacity of reservoir models (e.g., Warrlich et al., 2008; Hawie et al., 2015, 2017; Liechoscki de Paula Faria et al., 2017; Borgomano et al., 2020a, 2020b). Comparing such simulations to real-world exposures allows parameter refinement and improves the accuracy and reliability of depositional models.

## 4.8. Conclusions

This study applied an integrated approach combining High-Resolution Sequence Stratigraphy (HRSS) and digital techniques, including Local Binary Pattern (LBP) analysis and Convolutional Neural Networks (CNNs), to outcrop data from the Balbuena III Sequence (SBIII) in the Salta Basin. The objective was to explore methods capable of extracting and interpreting geological parameters from Digital Outcrop Models (DOMs) in a way that supports reservoir analog studies.

Results indicate that the transition from an open-lake to a closed-lake hydrological system exerted a major influence on sedimentary architecture and lithotype distribution in SBIII. Facies stacking patterns reveal climate-driven base-level fluctuations controlling sedimentation, preservation, and stratigraphic heterogeneity. The application of HRSS enabled the identification of elementary, medium, and low-frequency sequences, demonstrating that lacustrine deposits can present a high degree of stratigraphic organization and correlation potential across extensive distances. This metric scale is often the most difficult to resolve using subsurface datasets; in such cases, outcrop observations provide essential constraints.

The LBP method represents a first, still preliminary and exploratory approach. Qualitative assessment of the results revealed patterns that align with stratigraphic interpretations, suggesting potential for highlighting cyclicity and stratigraphic surfaces. Further studies should explore different processing configurations and develop quantitative validation metrics to strengthen its applicability within stratigraphic frameworks.

The CNN models met the intended objective of identifying facies at the scale of hemicycles within elementary sequences, which is directly relevant to stratigraphic framework construction and reservoir-scale interpretation. Among the 11 facies considered, the finer ones such as crystalline limestone and volcanic tuff (thickness < 20 cm) showed lower classification performance, mainly due to the downscaling adopted in this study. Future tests should evaluate other downscaling configurations, considering the specific goals of each application.

From an applied perspective, the integration of HRSS, LBP, and CNN-based classification offers a complementary framework to traditional geological methods, contributing to the efficiency of outcrop interpretation and generating quantitative inputs for reservoir modeling. Although each component has limitations, the workflow demonstrates how digital techniques can reduce the manual workload associated with DOM analysis while providing reproducible, structured outputs. Continued refinement and validation will expand their applicability, contributing to the advancement of digital approaches in geosciences and to more robust reservoir analog studies.

## Acknowledgements

The authors would like to thank Petrobras (Brazil) for funding and supporting this research. Imagery acquisition was funded through a Petrobras–Unipampa cooperation agreement supported by the Brazilian National Agency of Petroleum, Natural Gas and Biofuels (ANP), No. 0050.0121770.22.9 (SIGITEC 2022/00056–5). We are also grateful to Geomap (Argentina) and its CEO, Roberto Hernández, for their kind assistance and invaluable logistical support during the fieldwork. Special thanks are extended to Brenda Schreiner, Ezequiel Galvão, Gerson Terra, João Paulo Borges Gomes, Ricardo Lykawka, Ronaldo Selk, and Saulo Pedrinha for their contributions to data acquisition, insightful discussions, and collaborative efforts. We also thank Dr. Gaurav Gairola and an anonymous reviewer for their constructive feedback, and

Luca Colombera (Associate Editor) and Tim Horscroft (Managing Editor) for their editorial handling and valuable comments on the manuscript.

## References

Adams, E.W., Grotzinger, J.P., Watters, W.A., Schröder, S., McCormick, D.S., Al-Siyabi, H.A., 2005. Digital characterization of thrombolite-stromatolite reef distribution in a carbonate ramp system (terminal proterozoic, Nama Group, Namibia). American Association of Petroleum Geologists Bulletin 89, 1293–1318. https://doi.org/10.1306/06160505005

Agisoft Metashape, 2023. Agisoft Metashape Professional v2.0.1 (Version 2.0.1) [software]. https://www.agisoft.com

Ahr, W.M., 2008. Geology of Carbonate Reservoirs: The Identification, Description, and Characterization of Hydrocarbon Reservoirs in Carbonate Rocks. Wiley. https://doi.org/10.1002/9780470370650

Baccelle, L., Bosellini, A., 1965. Diagrammi per la stima visiva della composizione percentuale nelle roccē sedimentarie. Annali della Università di Ferrara, Sezione IX. Scienze Geologiche e Paleontologiche 1 4, 59–62 (in Italian).

Bellian, J.A., Kerans, C., Jennette, D.C., 2005. Digital outcrop models: Applications of terrestrial scanning lidar technology in stratigraphic modeling. Journal of Sedimentary Research 75, 166–176. https://doi.org/10.2110/jsr.2005.013

Bento Freire, E., 2012. Caracterização Estratigráfica em Alta Resolução das Sequências Calcárias de Origem Microbiana do Intervalo Paleocênico da Formação Yacoraite (Sequência Balbuena IV) Na Região de Salta-Argentina (MSc thesis). Universidade Federal do Rio de Janeiro, Rio de Janeiro (in Portuguese).

Bento Freire, E., Lykawka, R., Raja Gabaglia, G.P., Rodrigues, E.B., Terra, G.J.S., 2011. Searching for Potential Analogues for the Pre-Salt Santos Basin, Brazil: High-Resolution Stratigraphic Studies of Microbialite-Bearing Successions from Salta Basin, Argentina, in: AAPG International Conference and Exhibition. Milan.

Bianucci, H., Acevedo, O., Cerdán, J., 1981. Evolución tectono-sedimentaria del Grupo Salta en la subcuenca de Lomas de Olmedo (Provincias de Salta y Formosa), in: VIII Congreso Geológico Argentino. Servicio Geológico Nacional, San Luis, pp. 159–172 (in Spanish).

Bianucci, H., Homovc, J.F., 1982. Tectonogenesis de un sector de la Cuenca del Subgrupo Pirgua, noroeste argentino, in: Congreso Latinoamericano de Geologia. Servicio Geologico Nacional, Buenos Aires, pp. 539–546 (in Spanish).

Bilmes, A., D'Elia, L., Lopez, L., Richiano, S., Varela, A., Alvarez, M. del P., Bucher, J., Eymard, I., Muravchik, M., Franzese, J., Ariztegui, D., 2019. Digital outcrop modelling using "structure-from- motion" photogrammetry: Acquisition strategies, validation and interpretations to different sedimentary environments. Journal of South American Earth Sciences 96, 102325. https://doi.org/10.1016/j.jsames.2019.102325

Bistacchi, A., Mittempergher, S., Martinelli, M., 2022. Digital Outcrop Model Reconstruction and Interpretation, in: Bistacchi, A., Massironi, M., Viseur, S. (Eds.), 3D Digital Geological Models: From Terrestrial Outcrops to Planetary Surfaces. Wiley, pp. 11–32. https://doi.org/https://doi.org/10.1002/9781119313922.ch2

Boll, A., 1991. Identificación y correlación de secuencias somerizantes del Miembro Las Avispas (Formación Yacoraite). Noroeste Argentino., in: X Congreso Geológico Argentino. Asociación Geológica Argentina, San Miguel de Tucumán, pp. 153–156 (in Spanish).

Boll, A., Hernández, R.M., 1985. Área Tres Cruces. Provincia de Jujuy. Análisis estratigráfico-estructural. Evaluación como objetivo exploratorio (in Spanish).

Borgomano, J., Lanteaume, C., Léonide, P., Fournier, F., Montaggioni, L.F., Masse, J.P., 2020a. Quantitative carbonate sequence stratigraphy: Insights from stratigraphic forward models. AAPG Bulletin 104, 1115–1142. https://doi.org/10.1306/11111917396

Borgomano, J., Massonnat, G., Lanteaume, C., Danquigny, C., Samson, P., Rolando, J.-P., Rebelle, M., 2020b. Application of Stratigraphic Forward Modelling to Carbonate Reservoir Characterization – A New Paradigm from the Albion R&D Project, in: Abu Dhabi International Petroleum Exhibition & Conference. SPE. https://doi.org/10.2118/202775-MS

Borgomano, J., Van Konijnenburg, J.-H., Jauffred, J.-C., 2001. Anatomy of carbonate bodies For hydrocarbon reservoir modeling: Applications, limitations and Future developments. Géologie Méditerranéenne 28, 23–26. https://doi.org/https://doi.org/10.3406/geolm.2001.1682

Brackebusch, L., 1891. Mapa geológico del interior de la República Argentina. 1 mapa, a color. Escala 1:1 000 000 (in Spanish).

Buckley, S.J., Howell, J.A., Enge, H.D., Leren, B.L.S., Kurz, T.H., 2006. Integration of terrestrial laser scanning, digital photogrammetry and geostatistical methods for high-resolution modelling of geological outcrops, in: International Archives of the Photogrammetry, Remote Sensing and Spatial Information Sciences. ISPRS.

Buckley, S.J., Schwarz, E., Terlaky, V., Howell, J.A., Arnott, R.W.C., 2009. Terrestrial Laser Scanning Combined with Photogrammetry for Digital Outcrop Modelling, in: Bretar, F., Pierrot-Deseilligny, M., Vosselman, G. (Eds.), Laser Scanning 2009. IAPRS, Paris.

Bueno de Moraes, M.F., Viana, A.R., Jahnert, R.J., Machado, M.A.P., Chagas, A.A.P., 2024. O Pré-sal nas Bacias de Campos e Santos: como tudo começou, in: Chagas, A.A.P., Araújo, C.C. de, Santos, L.A. (Eds.), As grandes descobertas do pré-sal no Atlântico Sul. Rio de Janeiro, pp. 21–69 (in Portuguese).

Bunevich, R.B., 2016. Caracterização e interpretação bioarquitetural de microbialitos lacustres da sequência Balbuena IV (Daniano), bacia de Salta-Argentina (MSc thesis). Universidade Federal do Rio de Janeiro, Rio de Janeiro (in Portuguese).

Bunevich, R.B., Borghi, L., Gabaglia, G.P.R., Terra, G.J.S., Bento Freire, E., Lykawka, R., Fragoso, D.G.C., 2017. Microbialitos da Sequência Balbuena IV (Daniano), Bacia de Salta, Argentina: caracterização de intrabioarquiteturas e de microciclos. Pesquisas em Geociências 44, 177–202 (in Portuguese).

Burnham, B.S., Hodgetts, D., 2019. Quantifying spatial and architectural relationships from fluvial outcrops. Geosphere 15, 236–253. https://doi.org/10.1130/GES01574.1

Cabello, P., Domínguez, D., Murillo-López, M.H., López-Blanco, M., García-Sellés, D., Cuevas, J.L., Marzo, M., Arbués, P., 2018. From conventional outcrop datasets and digital outcrop models to flow simulation in the Pont de Montanyana point-bar deposits

(Ypresian, Southern Pyrenees). Marine and Petroleum Geology 94, 19–42. https://doi.org/10.1016/j.marpetgeo.2018.03.040

Catuneanu, O., Galloway, W.E., Kendall, C.G.S.C., Miall, A.D., Posamentier, H.W., Strasser, A., Tucker, M.E., 2011. Sequence Stratigraphy: methodology and nomenclature. Newsletters on Stratigraphy 44, 173–245. https://doi.org/10.1127/0078-0421/2011/0011

Ceolin, D., dos Santos Filho, M.A.B., Salamoni Terra, G.J., Fragoso, D.G.C., Bunevich, R.B., Fauth, G., Hernández, J.I., Hernández, R.M., 2022. Ostracods from upper Yacoraite Formation (Danian), Salta Basin, Western Argentina: Taxonomy and paleoenvironmental indicators of climatic signals in lacustrine deposits. Journal of South American Earth Sciences 116. https://doi.org/10.1016/j.jsames.2022.103836

Cheng, G., Guo, W., 2017. Rock images classification by using deep convolution neural network, in: Journal of Physics: Conference Series. Institute of Physics Publishing, p. 012089. https://doi.org/10.1088/1742-6596/887/1/012089

CloudCompare, 2024. CloudCompare v2.13.2 (Version 2.13.2) [software]. https://www.cloudcompare.org/

Corradetti, A., Tavani, S., Parente, M., Iannace, A., Vinci, F., Pirmez, C., Torrieri, S., Giorgioni, M., Pignalosa, A., Mazzoli, S., 2018. Distribution and arrest of vertical through-going joints in a seismic-scale carbonate platform exposure (Sorrento peninsula, Italy): insights from integrating field survey and digital outcrop model. Journal of Structural Geology 108, 121–136. https://doi.org/10.1016/j.jsg.2017.09.009

Cristallini, E., Cominguez, A.H., Ramos, V.A., 1997. Deep structure of the Metan-Guachipas region: tectonic inversion in Northwestern Argentina. Journal of South American Earth Sciences 10, 403–421. https://doi.org/https://doi.org/10.1016/S0895-9811(97)00026-6

da Silva Bomfim, L., Soares, M.V.T., Vidal, A.C., Pedrini, H., 2025. Geological reservoir characterization tasks based on computer vision techniques. Marine and Petroleum Geology. https://doi.org/10.1016/j.marpetgeo.2024.107231

Del Papa, C., 1994. Estratigrafía y Sedimentología de la Formación Maíz Gordo (Paleoceno) en el sur de la cuenca del Grupo Salta (PhD thesis). Universidad Nacional de Salta, Salta (in Spanish).

Del Papa, C.E., Salfity, J.A., 1999. View of Non-marine Paleogene sequences, Salta Group, Northwest Argentina. Acta Geologica Hispanica 34, 105–121.

Deschamps, R., Rohais, S., Hamon, Y., Gasparrini, M., 2020. Dynamic of a lacustrine sedimentary system during late rifting at the Cretaceous-Palaeocene transition: Example of the Yacoraite Formation, Salta Basin, Argentina. The Depositional Record 2020, 490–523. https://doi.org/10.1002/dep2.116

Dickson, J.A.D., 1966. Carbonate Identification and Genesis as Revealed by Staining. SEPM Journal of Sedimentary Research 36, 491–505. https://doi.org/10.1306/74D714F6-2B21-11D7-8648000102C1865D

Dickson, J.A.D., 1965. A Modified Staining Technique for Carbonates in Thin Section. Nature 205, 587. https://doi.org/https://doi.org/10.1038/205587a0

Disalvo, A., 2002. Cuenca del noroeste: marco geológico y reseña histórica de la actividad petrolera. En Rocas reservorio de las cuencas productivas de la Argentina, in: Shiuma, M., Hinterwimmer, G., Vergani, G. (Eds.), V Congreso de Exploración y Desarrollo de

Hidrocarburos. Instituto Argentino del Petróleo y del Gas (IAPG), Mar del Plata, pp. 663–677 (in Spanish).

Disalvo, A., Schelotto, M.L.R., Omil, R.G., Hoffman, C., Benítez, J., Hurtado, S., 2002. Los reservorios de la Formación Yacoraite, in: Schiuma, M., Hinterwimmer, G., Vergani, G. (Eds.), Rocas reservorios de las cuencas productivas de la Argentina: V Congreso de Exploración y Desarrollo de Hidrocarburos. Instituto Argentino del Petróleo y del Gas (IAPG), Mar del Plata, pp. 717–738 (in Spanish).

Dunham, R.J., 1962. Classification of Carbonate Rocks According to Depositional Texture, in: Ham, W.E. (Ed.), Classification of Carbonate Rocks - A Symposium. American Association of Petroleum Geologists, Tulsa, pp. 108–121.

Embry, A.F., Klovan, J.E., 1971. A Late Devonian reef tract on northeastern banks island, N.W.T. Bulletin of Canadian Petroleum Geology 19, 730–781. https://doi.org/https://doi.org/10.35767/gscpgbull.19.4.730

Fabuel-Perez, I., Hodgetts, D., Redfern, J., 2010. Integration of digital outcrop models (DOMs) and high resolution sedimentology - workflow and implications for geological modelling: Oukaimeden Sandstone Formation, High Atlas (Morocco). Petroleum Geoscience 16, 133–154. https://doi.org/10.1144/1354-079309-820

Falivene, O., Auchter, N.C., de Lima, R.P., Kleipool, L., Solum, J.G., Zarian, P., Clark, R.W., Espejo, I., 2022. Lithofacies identification in cores using deep learning segmentation and the role of geoscientists: Turbidite deposits (Gulf of Mexico and North Sea). AAPG Bulletin 106, 1357–1372. https://doi.org/10.1306/03112221015

Fan, G., Chen, F., Chen, D., Dong, Y., 2020. Recognizing multiple types of rocks quickly and accurately based on lightweight CNNs model. IEEE Access 8, 55269–55278. https://doi.org/10.1109/ACCESS.2020.2982017

Fournier, F., Borgomano, J., 2007. Geological significance of seismic reflections and imaging of the reservoir architecture in the Malampaya gas field (Philippines). American Association of Petroleum Geologists Bulletin 91, 235–258. https://doi.org/10.1306/10160606043

Fragoso, D.G.C., 2023. Princípios e Práticas da Ciclicidade e da Hierarquização na Estratigrafia de Alta Resolução: Uma Abordagem Metodológica e Aplicada à Caracterização de Reservatórios (PhD thesis). Universidade Federal do Rio Grande do Sul, Porto Alegre (in Portuguese).

Fragoso, D.G.C., Gabaglia, G.P.R., Magalhães, A.J.C., Scherer, C.M.D.S., 2021a. Cyclicity and hierarchy in sequence stratigraphy: An integrated approach. Brazilian Journal of Geology 51, e20200106. https://doi.org/10.1590/2317-4889202120200106

Fragoso, D.G.C., Kuchenbecker, M., Magalhães, A.J.C., Scherer, C.M.D.S., Gabaglia, G.P.R., Strasser, A., 2022. Cyclicity in Earth sciences, quo vadis? Essay on cycle concepts in geological thinking and their historical influence on stratigraphic practices. History of Geo- and Space Sciences 13, 39–69. https://doi.org/10.5194/hgss-13-39-2022

Fragoso, D.G.C., Melo, A.H. de, Gonçalves, L.A., Bunevich, R.B., Araujo, J. de A.M., Costa, T.C. da, Pedrosa, C.A., Scherer, C.M.D.S., 2023. High-resolution sequence stratigraphy applied to reservoir characterization of the Brazilian Cretaceous pre-salt section, Campos Basin: Guidelines for geological modeling and reservoir management. Marine and Petroleum Geology 151, 106203. https://doi.org/10.1016/j.marpetgeo.2023.106203

Fragoso, D.G.C., Raja Gabaglia, G.P., Magalhães, A.J.C., 2021b. Estratigrafia de Alta Resolução Aplicada ao Zoneamento e à Caracterização de Reservatórios: Uma Abordagem Conceitual e Metodológica, in: 50 Congresso Brasileiro de Geologia. Brasília (in Portuguese).

Fragoso, D.G.C., Roemers-Oliveira, E., Raja Gabaglia, G.P., Pedrinha, S., Faresin, A.C., Sabaraense, L.D., Scherer, C.M.S., 2024. Unveiling Sequence-Generating Mechanisms in a Carbonate Lacustrine System: An Integrated Stratigraphic Investigation in the Yacoraite Formation (Salta Group – Argentina), in: 51 Congresso Brasileiro de Geologia. Belo Horizonte.

Freitas, B.T., Silva, L.H.G., Almeida, R.P., Galeazzi, C.P., Figueiredo, H.G., Tamura, L.N., Janikian, L., Figueiredo, F.T., Assine, M.L., 2021. Cross-strata palaeocurrent analysis using virtual outcrops. Sedimentology 68, 2397–2421. https://doi.org/10.1111/sed.12855

Genesis, G., Gomes, I.F., Barbosa, J.A., DE ARAÚJO, A.F.L., Ramos, G.M.S., 2024. Machine learning-based classification of petrofacies in fine laminated limestones. Anais da Academia Brasileira de Ciencias 96. https://doi.org/10.1590/0001-3765202420230041

Gigli, G., Casagli, N., 2011. Semi-automatic extraction of rock mass structural data from high resolution LIDAR point clouds. International Journal of Rock Mechanics and Mining Sciences 48, 187–198. https://doi.org/10.1016/j.ijrmms.2010.11.009

Gomes, J.P.B., 2013. Simulação de processos deposicionais: caracterização de dois ciclos de alta frequência da Sequência Balbuena IV, Bacia do noroeste argentino (MSc thesis). Universidade Federal do Rio Grande do Sul, Porto Alegre (in Portuguese).

Gomes, J.P.B., Bunevich, R.B., Tonietto, S.N., Alves, D.B., Santos, J.F., Whitaker, F.F., 2020. Climatic signals in lacustrine deposits of the Upper Yacoraite Formation, Western Argentina: Evidence from clay minerals, analcime, dolomite and fibrous calcite. Sedimentology 67, 2282–2309. https://doi.org/10.1111/sed.12700

Gómez Omil, R.J., Boll, A., 2005. Cuenca Cretácica del Noroeste Argentino, in: VI Congreso de Exploración y Desarrollo de Hidrocarburos: Ampliando las Fronteras. IAPG, Mar del Plata, pp. 63–73 (in Spanish).

Gómez Omil, R.J., Boll, A., 1999. Sistema petrolero de la cuenca cretácica del noroeste argentino, in: IV Congreso de Exploración y desarrollo de hidrocarburos. IAPG, Mar del Plata, pp. 101–112 (in Spanish).

Gómez Omil, R.J., Boll, A., Hernández, R.M., 1989. Cuenca cretácico-terciaria del Noroeste argentino (Grupo Salta), in: Chebli, G.A., Spalletti, L.A. (Eds.), Cuencas Sedimentarias Argentinas. Tucumán, pp. 43–64 (in Spanish).

Grabau, A.W., 1904. On the classification of sedimentary rocks. The American Geologist 33, 228–247.

Grammer, G.M., Harris, P.M., Eberli, G.P., 2004. Integration of Outcrop and Modern Analogs in Reservoir Modeling: Overview with Examples from the Bahamas, in: Grammer, G.M., Harris, P.M., Eberli, G.P. (Eds.), Integration of Outcrop and Modern Analogs in Reservoir Modeling: AAPG Memoir 80. pp. 1–22.

Granjeon, D., 1996. Modélisation stratigraphique déterministe: Conception et applications d'un modèle diffusif 3D multilithologique (PhD thesis). Université de Rennes 1 (in French).

Guadagnin, F., Gonçalves, Í.G., Roemers-Oliveira, E., Guedes, P.L., de Souza, E.G., Silveira, M. de M.L., Raja Gabaglia, G.P., Arienti Gonçalves, L., Oliveira, L.F.R. de, Selk, R.,

2025. Building of classified 3D point clouds of outcrop with automatically segmented images. Geodata and AI 4, 100024. https://doi.org/10.1016/j.geoai.2025.100024

Guerrero, J.C., Brazil, F.A. de F., Carvalho, R.K., Silva, C.M. de A., Moliterno, A.M.C., Araújo, C.H.V., Barbosa, G.F., Yamato, A.A., Cacela, A.S.M., Leite, C. de O.N., Rocha, N.P., Oliveira, V.C.B. de, Campos, M.T.R., Silva, V.G.M. da R. e, Natori, H.O.H., Lima, F.P., Oliveira, D.L. de, Queiroz, L.E.S., Souza, L.B. de, Cruz, E.M.A., 2024. Campo de Búzios: a jornada desde a caracterização dos reservatórios ao início do desenvolvimento da produção AUTORES, in: Chagas, A.A.P., Araújo, C.C. de, Santos, L.A. (Eds.), As grandes descobertas do Pré-sal no Atlântico Sul. Rio de Janeiro, pp. 946–1037 (in Portuguese).

Hawie, N., Barrois, A., Marfisi, E., Murat, B., Hall, J., El-Wazir, Z., Al-Madani, N., Aillud, G., 2015. Forward stratigraphic modelling, deterministic approach to improve carbonate heterogeneity prediction; Lower cretaceous, Abu Dhabi, in: Society of Petroleum Engineers - Abu Dhabi International Petroleum Exhibition and Conference, ADIPEC 2015. Society of Petroleum Engineers. https://doi.org/10.2118/177519-ms

Hawie, N., Deschamps, R., Granjeon, D., Nader, F.H., Gorini, C., Müller, C., Montadert, L., Baudin, F., 2017. Multi-scale constraints of sediment source to sink systems in frontier basins: a forward stratigraphic modelling case study of the Levant region. Basin Research 29, 418–445. https://doi.org/10.1111/bre.12156

Hernández, R., Echavarria, L., 2009. Faja Plegada y Corrida Subandina del Noroeste Argentino: Estratigrafía, Geometría y Cronología de la Deformación. Revista de la Asociación Geológica Argentina 65, 68–80 (in Spanish).

Hernández, R.M., Disalvo, A., Boll, A., Gómez Omil, R., Gallli, C., 1999. Estratigrafia secuencial del Grupo Salta, con enfasis en las subcuencas de Metan-Alemania, noroeste Argentino, in: Bonorino, G.G., Omarini, R., Viramonte, J. (Eds.), Geología del Noroeste Argentino, Relatorio del XIV Congreso Geológico Argentino. pp. 263–283 (in Spanish).

Hernández, R.M., Omil, G.R., Boll, A., 2008. Estratigrafía, Tectónica y Potencial petrolero del rift cretácico em la Provincia de Jujuy, in: XVII Congreso Geológico Argentino. Asociación Geológica Argentina, Jujuy, pp. 207–232 (in Spanish).

Hodgetts, D., 2013. Laser scanning and digital outcrop geology in the petroleum industry: A review. Marine and Petroleum Geology. https://doi.org/10.1016/j.marpetgeo.2013.02.014

Howell, J.A., Martinius, A.W., Good, T.R., 2014. The application of outcrop analogues in geological modelling: a review, present status and future outlook. Geological Society, London, Special Publications 387, 1–25. https://doi.org/10.1144/sp387.12

Janocha, J., Smyrak-Sikora, A., Senger, K., Birchall, T., 2021. Seeing beyond the outcrop: Integration of ground-penetrating radar with digital outcrop models of a paleokarst system. Marine and Petroleum Geology 125. https://doi.org/10.1016/j.marpetgeo.2020.104833

Javernick, L., Brasington, J., Caruso, B., 2014. Modeling the topography of shallow braided rivers using Structure-from-Motion photogrammetry. Geomorphology 213, 166–182. https://doi.org/10.1016/j.geomorph.2014.01.006

Jeong, J., Park, E., Emelyanova, I., Pervukhina, M., Esteban, L., Yun, S.T., 2020. Interpreting the Subsurface Lithofacies at High Lithological Resolution by Integrating Information From Well-Log Data and Rock-Core Digital Images. Journal of Geophysical Research: Solid Earth 125. https://doi.org/10.1029/2019JB018204

Jones, R.R., Pringle, J.K., McCaffrey, K.J.W., Imber, J., Wightman, R.H., Guo, J., Long, J.J., 2011. Extending Digital Outcrop Geology into the Subsurface, in: Outcrops Revitalized. SEPM (Society for Sedimentary Geology), pp. 31–50. https://doi.org/10.2110/sepmcsp.10.031

Keidel, J., 1921. Sobre la distribución de los depósitos glaciares del Permico conocidos en la Argentina y su significación para la estratigrafia de la serie del Gondwana y la paleogeografia del Hemisferio Austral. Boletim da Academia Nacional de Ciencias 25, 239–368 (in Spanish).

Kenter, J.A., Playton, T., Harries, P. (Mitch), Katz, D., Bellian, J., 2010. Application of Outcrop Analogs to Characterize Carbonate Reservoirs in the Pricaspian Basin, in: All Days - SPE Caspian Carbonates Technology Conference. Society of Petroleum Engineers. https://doi.org/10.2118/139934-MS

Khanna, P., Hopson, H.H., Droxler, A.W., Droxler, D.A., Lehrmann, D., Kubik, B., Proctor, J., Singh, P., (Mitch) Harris, P.M., 2020. Late Cambrian microbial build-ups, Llano Area, Central Texas: A three-phase morphological evolution. Sedimentology 67, 1135–1160. https://doi.org/10.1111/sed.12679

Koeshidayatullah, A., Morsilli, M., Lehrmann, D.J., Al-Ramadan, K., Payne, J.L., 2020. Fully automated carbonate petrography using deep convolutional neural networks. Marine and Petroleum Geology 122, 104687. https://doi.org/10.1016/j.marpetgeo.2020.104687

Kudelski, D., Mari, J.-L., Viseur, S., 2010. 3D Feature Line Detection Based on Vertex Labeling and 2D Skeletonization, in: 2010 Shape Modeling International Conference. IEEE, Aix-en-Provence, pp. 246–250. https://doi.org/10.1109/SMI.2010.35

Kudelski, D., Viseur, S., Mari, J.-L., 2009. Revue Électronique Francophone d'Informatique Graphique. Revue Électronique Francophone d'Informatique Graphique 3, 1–9.

Larssen, K., Senger, K., Grundvåg, S.A., 2020. Fracture characterization in Upper Permian carbonates in Spitsbergen: A workflow from digital outcrop to geo-model. Marine and Petroleum Geology 122. https://doi.org/10.1016/j.marpetgeo.2020.104703

Li, L., Wang, R., Lin, J., Xiao, Z., Hui, Y., 2019. A novel approach for extraction of ripple mark parameters based on SfM. Sedimentary Geology 392. https://doi.org/10.1016/j.sedgeo.2019.105523

Liechoscki de Paula Faria, D., Tadeu dos Reis, A., Gomes de Souza, O., 2017. Three-dimensional stratigraphic-sedimentological forward modeling of an Aptian carbonate reservoir deposited during the sag stage in the Santos basin, Brazil. Marine and Petroleum Geology 88, 676–695. https://doi.org/10.1016/j.marpetgeo.2017.09.013

Liu, X., Song, H., 2020. Automatic identification of fossils and abiotic grains during carbonate microfacies analysis using deep convolutional neural networks. Sedimentary Geology 410, 105790. https://doi.org/10.1016/j.sedgeo.2020.105790

Liu, X., Wang, H., Jing, H., Shao, A., Wang, L., 2020. Research on intelligent identification of rock types based on faster R-CNN method. IEEE Access 8, 21804–21812. https://doi.org/10.1109/ACCESS.2020.2968515

Lowe, D.G., 2004. Distinctive Image Features from Scale-Invariant Keypoints. International Journal of Computer Vision 60, 91–110. https://doi.org/https://doi.org/10.1023/B:VISI.0000029664.99615.94

Lucia, F.J., 2007. Carbonate Reservoir Characterization: An Integrated Approach, Second Edition. ed. Springer, New York.

Lykawka, R., Bento Freire, E., Rodrigues, E.B., Terra, G.J.S., Raja Gabaglia, G.P., Hernández, R.M., Hernández, J.I., 2012. Multiple-scale stratigraphic analysis of stromatolite-rich deposits from the Maastrichtian/Paleocene Salta Basin, Argentina: characterization of outcropping analogues to support the reservoir modelling of giant Pre-Salt oil fields from offshore Brazil, in: 34th International Geological Congress, Unearthing Our Past and Future–Resourcing Tomorrow. Brisbane.

Magalhães, A.J.C., Raja Gabaglia, G.P., Fragoso, D.G.C., Bento Freire, E., Lykawka, R., Arregui, C.D., Silveira, M.M.L., Carpio, K.M.T., De Gasperi, A., Pedrinha, S., Artagão, V.M., Terra, G.J.S., Bunevich, R.B., Roemers-Oliveira, E., Gomes, J.P., Hernández, J.I., Hernández, R.M., Bruhn, C.H.L., 2020. High-resolution sequence stratigraphy applied to reservoir zonation and characterisation, and its impact on production performance - shallow marine, fluvial downstream, and lacustrine carbonate settings. Earth-Science Reviews 210. https://doi.org/10.1016/j.earscirev.2020.103325

Malik, O.A., Puasa, I., Lai, D.T.C., 2022. Segmentation for Multi-Rock Types on Digital Outcrop Photographs Using Deep Learning Techniques. Sensors 22, 8086. https://doi.org/10.3390/s22218086

Marques, A., Horota, R.K., de Souza, E.M., Kupssinskü, L., Rossa, P., Aires, A.S., Bachi, L., Veronez, M.R., Gonzaga, L., Cazarin, C.L., 2020. Virtual and digital outcrops in the petroleum industry: A systematic review. Earth-Science Reviews. https://doi.org/10.1016/j.earscirev.2020.103260

Marquillas, R., Del Papa, C., Sabino, I., Heredia, J., 2003. Prospección del límite K/T en la cuenca del Noroeste, Argentina. Revista de la Asociación Geológica Argentina 58, 271–274 (in Spanish).

Marquillas, R., Sabino, I., Sial, A.N., Del Papa, C., Ferreira, V., Matthews, S., 2007. Carbon and oxygen isotopes of Maastrichtian-Danian shallow marine carbonates: Yacoraite Formation, northwestern Argentina. Journal of South American Earth Sciences 23, 304–320. https://doi.org/10.1016/j.jsames.2007.02.009

Marquillas, R.A., 1985. Estratigrafía, sedimentología y paleoambientes de la Formación Yacoraite (Cretáceo Superior) en el tramo austral de la cuenca, norte argentino. Universidad Nacional de Salta, Salta (in Spanish).

Marquillas, R.A., Del Papa, C., Sabino, I.F., 2005. Sedimentary aspects and paleoenvironmental evolution of a rift basin: Salta Group (Cretaceous-Paleogene), northwestern Argentina. International Journal of Earth Sciences 94, 94–113. https://doi.org/10.1007/s00531-004-0443-2

Marquillas, R.A., Salfity, J.A., González, R., Matthews, S., Battaglia, R., 1997. Geología del Grupo Salta (Cretácico-Eoceno) en la comarca de Huaytiquina, Puna argentina, in: VIII Congreso Geológico Chileno. pp. 139–143 (in Spanish).

Marquillas, R.A., Salfity, J.A., Matthews, S.J., Matteini, M., Dantas, E., 2011. U-Pb zircon age of the Yacoraite Formation and its significance to the Cretaceous-Tertiary boundary in the Salta Basin, Argentina. Cenozoic Geology of the Central Andes of Argentina 227–246.

Matthew, A.J., Woods, A.J., Oliver, C., 1991. Spots before the eyes: new comparison charts for visual percentage estimation in archaeological material, in: Middleton, A.P., Freestone,

I.C. (Eds.), Recent Developments in Ceramic Petrology. British Museum Occasional Paper, London, pp. 211–263.

Miall, A.D., 2000. Principles of Sedimentary Basin Analysis, 3rd ed. Springer, Berlin. https://doi.org/10.1007/978-3-662-03999-1

Moreno, J.A., 1970. Estratigrafía y paleogeografía del Cretácico Superior en la Cuenca del Noroeste Argentino, con especial mención de los Subgrupos Balbuena y Santa Bárbara. Revista de la Asociación Geológica Argentina 25, 9–44 (in Spanish).

Mutti, M., Vallati, M., Tomás, S., Galli, C., Bahniuk Rumbelsperger, A.M., Maerz, S., Coira, B., 2023. Constraining depositional evolution and reservoir compartmentalization in a mixed carbonate-siliciclastic lacustrine system: The Yacoraite formation, Salta Group, NW Argentina. Marine and Petroleum Geology 149. https://doi.org/10.1016/j.marpetgeo.2022.106049

Ojala, T., Pietika, M., Mäenpää, T., 2002. Multiresolution Gray-Scale and Rotation Invariant Texture Classification with Local Binary Patterns. IEEE Transactions on Pattern Analysis and Machine Intelligence 24, 971–987. https://doi.org/DOI:10.1109/TPAMI.2002.1017623

Ojala, T., Pietikäinen, M., Harwood, D., 1996. A Comparative Study of Texture Measures with Classification Based on Feature Distributions. Pattern Recognition 29, 51–59. https://doi.org/https://doi.org/10.1016/0031-3203(95)00067-4

Ojala, T., Pietikäinen, M., Harwood, D., 1994. Performance Evaluation of Texture Measures with Classification Based on Kullback Discrimination of Distributions, in: 12th International Conference on Pattern Recognition. IEEE, Jerusalem, pp. 582–585. https://doi.org/10.1109/ICPR.1994.576366

Oliveira Santos, J.A., Uhlein, A., Dantas, M., de Morais Coutinho, G., Spier, T.J., Masse Vieira, K.H., Trindade Prado, A.C., Macharet, D., Uhlein, G.J., Novo, T., Reis, H., Farias, F.A., Freire, E.B., Carnier Fragoso, D.G., 2023. Constructing high-resolution stratigraphic frameworks by the application of signal analysis techniques: Example of Balbuena IV sequence, Yacoraite formation, Salta Basin. Marine and Petroleum Geology 157. https://doi.org/10.1016/j.marpetgeo.2023.106470

Panara, Y., Chandra, V., Finkbeiner, T., Petrovic, A., Zühlke, R., Khanna, P., Vahrenkamp, V., 2023. Fracture intensity and associated variability: A new methodology for 3D digital outcrop model analysis of carbonate reservoirs. Marine and Petroleum Geology 158. https://doi.org/10.1016/j.marpetgeo.2023.106532

Pedrinha, S., 2014. Análise estratigráfica em depósitos lacustres maastrichtianos da Formação Yacoraite (Bacia de Salta - Argentina): definição e rastreabilidade de sequências de alta resolução (MSc thesis). Unesp Rio Claro, Rio Claro (in Portuguese).

Pedrinha, S., Artagão, V. de M., 2024. High-resolution stratigraphy and characterization of reservoir-critical heterogeneities in the giant Tupi Field, pre-salt Santos Basin, Brazil. Geological Society, London, Special Publications 548. https://doi.org/10.1144/SP548-2023-91

Pedrinha, S., Raja Gabaglia, G.P., Lykawka, R., Dias-Brito, D., 2015. High-resolution sequence tracking in Metán-Alemania Sub-basin (Salta Basin Maastrichtian – Argentina): detailed stratigraphic anatomy of a lacustrine system under the influence of microbial processes. Boletim de Geociências da Petrobras 23.

Pereira, J.V.F., Medeiros, W.E., Dantas, R.R.S., Bezerra, F.H.R., La Bruna, V., Xavier, M.M., Maia, R.P., Gomes, D.D.M., Silva, D.C.C., Maciel, I.B., 2024. An integrated 3D digital model of stratigraphy, petrophysics and karstified fracture network for the Cristal Cave, NE-Brazil. Journal of Structural Geology 178. https://doi.org/10.1016/j.jsg.2023.105013

Picard, M.D., 1971. Classification of Fine-grained Sedimentary Rocks. SEPM Journal of Sedimentary Research Vol. 41, 179–195. https://doi.org/10.1306/74D7221B-2B21-11D7-8648000102C1865D

Pires de Lima, R., Suriamin, F., Marfurt, K.J., Pranter, M.J., 2019. Convolutional neural networks as aid in core lithofacies classification. Interpretation 7, SF27–SF40. https://doi.org/10.1190/INT-2018-0245.1

Priddy, C.L., Pringle, J.K., Clarke, S.M., Pettigrew, R.P., 2019. Application of photogrammetry to generate quantitative geobody data in ephemeral fluvial systems. Photogrammetric Record 34, 428–444. https://doi.org/10.1111/phor.12299

Pringle, J.K., Westerman, A.R., Clark, J.D., Drinkwater, N.J., Gardiner, A.R., 2004. 3D high-resolution digital models of outcrop analogue study sites to constrain reservoir model uncertainty: an example from Alport Castles, Derbyshire, UK. Petroleum Geoscience 10, 343–352.

Python, 2023. Python v3.11.4 (Version 3.11.4) [software]. https://www.python.org/

Raja Gabaglia, G.P., Bento Freire, E., Terra, G.J.S., Rodrigues, E.B., Lykawka, R., Hernández, R.M., 2011. Cyclostratigraphy and climatic control on microbiol influenced sedimentation (Balbuena Supersequence, Yacoraite Formation, Paleocene, Salta–Argentina, in: 28th Internatinal Association of Sedimentology Meeting. Zaragosa.

Ramdani, A., Khanna, P., De Jong, S., Gairola, G.S., Hanafy, S., Vahrenkamp, V., 2022a. Three-dimensional morphometric analysis and statistical distribution of the Early Kimmeridgian Hanifa Formation stromatoporoid/coral buildups, central Saudi Arabia. Marine and Petroleum Geology 146, 105934. https://doi.org/10.1016/j.marpetgeo.2022.105934

Ramdani, A., Khanna, P., Gairola, G.S., Hanafy, S., Vahrenkamp, V., 2022b. Assessing and processing three-dimensional photogrammetry, sedimentology, and geophysical data to build high-fidelity reservoir models based on carbonate outcrop analogues. AAPG Bulletin 106, 1975–2011. https://doi.org/10.1306/05152221092

Ramos, V.A., 1988. The tectonics of the Central Andes: 30o to 33o latitude, in: Clark, S., Burchfiel, D. (Eds.), Processes In Continental Litospheric Deformation. The Geological Society of America, pp. 31–54.

Reyes, F.C., 1972. Correlaciones en el Cretácico de la cuenca Andina de Bolivia, Perú y Chile. Revista Técnica de Yacimientos Petrolíferos Fiscales Bolivianos 1, 101–144 (in Spanish).

Reyes, F.C., Salfity, J.A., 1973. Consideraciones sobre la estratigrafia del Cretacico (Subgrupo Pirgua) del noroeste argentino, in: V Congreso Geológico Argentino. Asociación Geológica Argentina, Córdoba, pp. 335–385 (in Spanish).

Riquelme, A.J., Abellán, A., Tomás, R., Jaboyedoff, M., 2014. A new approach for semi-automatic rock mass joints recognition from 3D point clouds. Computers and Geosciences 68, 38–52. https://doi.org/10.1016/j.cageo.2014.03.014

Roemers-Oliveira, E., 2014. Contexto deposicional da Sequência Balbuena III (Maastrichtiano/Daniano) da Formação Yacoraite na sub-bacia de Metán-Alemania, na região de Salta, Argentina (MSc thesis). Unesp Rio Claro, Rio Claro (in Portuguese).

Roemers-Oliveira, E., Fernandes, L.A., Bento Freire, E., Amarante Simões, L.S., 2015. Microbial filaments in stromatolites and laminites of Balbuena III Sequence (Maastrichtian/Danian) of Yacoraite Formation in Metán-Alemania Sub-basin, Salta region, Argentina, and its palaeoenvironmental significance. Brazilian Journal of Geology 45, 399–413. https://doi.org/10.1590/2317-488920150030255

Roemers-Oliveira, E., Fournier, F., Viseur, S., Raja Gabaglia, G.P., Fleury, J., Rinalducci, V., Guihou, A., Marié, L., Guadagnin, F., Deschamps, P., Tonetto, A., 2024. The anatomy and stacking pattern of palustrine-dominated carbonate sequences from the Cengle Plateau, Paleocene, SE France: A multi-scalar approach. Sedimentary Geology 470, 106690. https://doi.org/10.1016/j.sedgeo.2024.106690

Roemers-Oliveira, E., Viseur, S., Fournier, F., Gonçalves, Í.G., Guadagnin, F., Raja Gabaglia, G.P., Bento Freire, E., Fragoso, D.G.C., Hernández, J., Freccia, A.C., de Godoy Rangel, G., 2025a. Advanced digital techniques applied to outcrop models: Integrating Local Binary Pattern (LBP) and Convolutional Neural Network (CNN) to support stratigraphic and sedimentological interpretation of reservoir analogs in the Salta Basin, Argentina. Marine and Petroleum Geology. https://doi.org/10.1016/

Roisenberg, H.B., Bállico, M.B., Guadagnin, F., Manna, M.O., de Souza, E.G., 2022. Digital Outcrop Models applied to high-resolution stratigraphy in braided fluvial systems: A study case at Jaicós formation in Parnaíba Basin, NE Brazil. Journal of South American Earth Sciences 119, 104006. https://doi.org/10.1016/j.jsames.2022.104006

Ronneberger, O., Fischer, P., Brox, T., 2015. U-Net: Convolutional Networks for Biomedical Image Segmentation, in: Navab, N., Hornegger, J., Wells, W.M., Frangi, A.F. (Eds.), 18th International Conference on Medical Image Computing and Computer-Assisted Intervenction - MICCAI. Springer International Publishing, Switzerland, pp. 234–241. https://doi.org/10.1007/978-3-319-24574-4_28

Sabino, I.F., 2004. Estratigrafía de la Formación La Yesera (Cretácico): Base del relleno sinrift del Grupo Salta, noroeste argentino. Revista de la Asociación Geológica Argentina 59, 341–359.

Salfity, J.A., 1979. Paleogeología de la cuenca del Grupo Salta (Cretácico-Eogénico) del norte de Argentina, in: VII Congreso Geológico Argentino. Asociación Geológica Argentina, Neuquén, pp. 505–515 (in Spanish).

Salfity, J.A., Marquillas, R.A., 1999. La cuenca cretácico-terciaria del norte argentino, in: Caminos, R. (Ed.), Geología Argentina. Instituto de Geología y Recursos Minerales, Buenos Aires, pp. 613–626 (in Spanish).

Salfity, J.A., Marquillas, R.A., 1981. Las unidades estratigráficas cretácicas del norte de la Argentina, in: Volkheimer, W., Musacchio, E.A. (Eds.), Cuencas Sedimentarias Del Jurásico y Cretácico de América Del Sur. Buenos Aires, pp. 303–317 (in Spanish).

Sato, R., Kikuchi, K., Naruse, H., 2025. Automatic facies classification using convolutional neural network for three-dimensional outcrop data: Application to the outcrop of the mass-transport deposit. AAPG Bulletin 109, 271–286. https://doi.org/10.1306/12162423082

Schmid, R., 1981. Descriptive nomenclature and classification of pyroclastic deposits and fragments: Recommendations of the IUGS Subcommission on the Systematics of Igneous

Rocks. Geology 9, 41–43. https://doi.org/10.1130/0091-7613(1981)9<41:DNACOP>2.0.CO;2

Sêco, S.L.R., Pereira, A.J.S.C., Duarte, L. V., Domingos, F.P., 2021. Sources of uncertainty in field gamma-ray spectrometry: Implications for exploration in the Lower-Middle Jurassic sedimentary succession of the Lusitanian Basin (Portugal). Journal of Geochemical Exploration 227, 106799. https://doi.org/10.1016/j.gexplo.2021.106799

Shehata, A.A., Osman, O.A., Nabawy, B.S., 2021. Neural network application to petrophysical and lithofacies analysis based on multi-scale data: An integrated study using conventional well log, core and borehole image data. Journal of Natural Gas Science and Engineering 93, 104015. https://doi.org/10.1016/j.jngse.2021.104015

Shorten, C., Khoshgoftaar, T.M., 2019. A survey on Image Data Augmentation for Deep Learning. Journal of Big Data 6, 60. https://doi.org/10.1186/s40537-019-0197-0

Sial, A.N., Ferreira, V.P., Toselli, A.J., Parada, M.A., Acenolaza, F.G., Pimentel, M.M., Alonso, R.N., 2001. Carbon and Oxygen Isotope Compositions of Some Upper Cretaceous-Paleocene Sequences in Argentina and Chile. International Geology Review 43.

Siddiqui, N.A., Ramkumar, M., Rahman, A.H.A., Mathew, M.J., Santosh, M., Sum, C.W., Menier, D., 2019. High resolution facies architecture and digital outcrop modeling of the Sandakan formation sandstone reservoir, Borneo: Implications for reservoir characterization and flow simulation. Geoscience Frontiers 10, 957–971. https://doi.org/10.1016/j.gsf.2018.04.008

Silveira, M. de M.L., 2020. Análisis estratigráfico secuencial de alta resolución y modelado geológico 3D en secciones sedimentarias transicionales y continentales del Jurásico Inferior a Medio del sector sur de la Cuenca Neuquina como análogo en la caracterización de reservorios de hidrocarburos (PhD thesis). Universidad Nacional de La Plata, La Plata.

Strasser, A., 2018. Cyclostratigraphy of Shallow-Marine Carbonates – Limitations and Opportunities, in: Montenari, M. (Ed.), Stratigraphy & Timescales. Academic Press, pp. 151–187. https://doi.org/10.1016/bs.sats.2018.07.001

Strasser, A., Pittet, B., Hillgärtner, H., Pasquier, J.-B., 1999. Depositional sequences in shallow carbonate-dominated sedimentary systems: concepts for a high-resolution analysis. Sedimentary Geology 128, 201–221. https://doi.org/10.1016/S0037-0738(99)00070-6

TensorFlow, 2024. TensorFlow v2.18.0 (Version 2.18.0) [software]. https://www.tensorflow.org

Terra, G.J.S., Raja Gabaglia, G.P., Bento Freire, E., Lykawka, R., Bunevich, R.B., Hernández, R.B., Hernández, J.I., 2015. Balbuena Supersequence, Salta Basin, Argentina: a good analog for Phanerozoic lacustrine microbialite-bearing reservoirs, in: Geoscience Technology Workshops (GTW): Carbonate Plays around the World- Analogues to Support Exploration and Development. AAPG, New Orleans.

Terra, G.J.S., Rodrigues, E.B., Bento Freire, E., Lykawka, R., Raja Gabaglia, G.P., Hernández, R.M., Hernández, J.I., 2012. Salta Basin, Argentina: A Good Analog for Phanerozoic Lacustrine Microbialite-Bearing Reservoirs, in: AAPG Hedberg Conference "Microbial Carbonate Reservoir Characterization". AAPG, Houston.

Terra, G.J.S., Spadini, A.R., França, A.B., Sombra, C.L., Zambonato, E.E., Juschaks, L.C. da S., Arienti, L.M., Erthal, M.M., Blauth, M., Franco, M.P., Matsuda, N.S., Silva, N.G.C.

da, Moretti Jr, P.A., D'Avila, R.S.F., Souza, R.S. de, Tonietto, S.N., Anjos, S.M.C. dos, Campinho, V.S., Winter, W.R., 2010. Classificação de rochas carbonáticas aplicável às bacias sedimentares brasileiras. Boletim de Geociências da Petrobras 18, 9–29 (in Portuguese).

Turner, J.C.M., 1958. Estratigrafía del Cordón de Escaya y de la Sierra de Rinconada (Jujuy). Revista De La Asociación Geológica Argentina 13, 15–41 (in Spanish).

Vail, P.R., Mitchum, R.M., Thompson, S., 1977. Seismic Stratigraphy and Global Changes of Sea Level, Part 4: Global Cycles of Relative Changes of Sea Level, in: Payton, C.E. (Ed.), Seismic Stratigraphy — Applications to Hydrocarbon Exploration. AAPG, pp. 83–97. https://doi.org/10.1306/M26490C6

Vallati, M., Tomás, S., Galli, C., Winterleitner, G., Mutti, M., 2023. Depositional controls in an ancient, closed lake system: A high-resolution and multi-scalar case study from the Yacoraite Formation (Salta Basin, Argentina). Sedimentary Geology 454. https://doi.org/10.1016/j.sedgeo.2023.106456

Villafañe, P.G., Frías-Saba, R. del C., Della-Vedova, M., Citton, P., Díaz-Martínez, I., de Valais, S., Aceñolaza, F.G., Marquillas, R.A., Cónsole-Gonella, C., 2022. Microbialitic deposits of the Yacoraite Formation, NW Argentina: distribution, environments, paleoecology, and economic implications. Brazilian Journal of Geology 52. https://doi.org/10.1590/2317-4889202220210088

Villarreal, C.A., Garzón, C.G., Mora, J.P., Rojas, J.D., Ríos, C.A., 2022. Workflow for capturing information and characterizing difficult-to-access geological outcrops using unmanned aerial vehicle-based digital photogrammetric data. Journal of Industrial Information Integration 26. https://doi.org/10.1016/j.jii.2021.100292

Villarreal J, C.A., Rojas D, J.D., Ríos R, C.A., 2020. 3D digital outcrop modelling of the Lower Cretaceous Los Santos formation sandstones, Mesa de Los Santos region (Colombia): Implications for structural analysis. Journal of Structural Geology 141. https://doi.org/10.1016/j.jsg.2020.104214

Viseur, S., Lamara, T., Parel, G., Benedetti, L., 2022. Automatic tools for quantitative analysis of multi-scale spatial slip variabilities from DEM and DOM, in: 21 Anual Conferebce of the International Association for Mathematical Geosciences. IAMG.

Vöge, M., Lato, M.J., Diederichs, M.S., 2013. Automated rockmass discontinuity mapping from 3-dimensional surface data. Engineering Geology 164, 155–162. https://doi.org/10.1016/j.enggeo.2013.07.008

Warrlich, G., Bosence, D., Waltham, D., Wood, C., Boylan, A., Badenas, B., 2008. 3D stratigraphic forward modelling for analysis and prediction of carbonate platform stratigraphies in exploration and production. Marine and Petroleum Geology 25, 35–58. https://doi.org/10.1016/j.marpetgeo.2007.04.005

Wentworth, C.K., 1922. A Scale of Grade and Class Terms for Clastic Sediments. The Journal of Geology 30, 377–392. https://doi.org/DOI:10.1086/622910

Westoby, M.J., Brasington, J., Glasser, N.F., Hambrey, M.J., Reynolds, J.M., 2012. "Structure-from-Motion" photogrammetry: A low-cost, effective tool for geoscience applications. Geomorphology 179, 300–314. https://doi.org/10.1016/j.geomorph.2012.08.021

Xu, Z., Ma, W., Lin, P., Hua, Y., 2022. Deep learning of rock microscopic images for intelligent lithology identification: Neural network comparison and selection. Journal of Rock

Mechanics and Geotechnical Engineering 14, 1140–1152. https://doi.org/10.1016/j.jrmge.2022.05.009

Yeste, L.M., Palomino, R., Varela, A.N., McDougall, N.D., Viseras, C., 2021. Integrating outcrop and subsurface data to improve the predictability of geobodies distribution using a 3D training image: A case study of a Triassic Channel – Crevasse-splay complex. Marine and Petroleum Geology 129, 105081. https://doi.org/10.1016/j.marpetgeo.2021.105081

Zhanfeng, Q., Anjiang, S., Jianfeng, Z., Chang, S., Yana, C., 2015. Three-dimensional carbonate reservoir geomodeling based on the digital outcrop model. Petroleum Exploration and Development 42, 358–368.

Zhang, J., Ambrose, W., Xie, W., 2021. Applying convolutional neural networks to identify lithofacies of large-n cores from the Permian Basin and Gulf of Mexico: The importance of the quantity and quality of training data. Marine and Petroleum Geology 133, 105307. https://doi.org/10.1016/j.marpetgeo.2021.105307

Zhang, P., Du, K., Tannant, D.D., Zhu, H., Zheng, W., 2018. Automated method for extracting and analysing the rock discontinuities from point clouds based on digital surface model of rock mass. Engineering Geology 239, 109–118. https://doi.org/10.1016/j.enggeo.2018.03.020

Zuffa, G.G., 1980. Hybrid Arenites: Their Composition and Classification. SEPM Journal of Sedimentary Research 50, 21–29. https://doi.org/10.1306/212F7950-2B24-11D7-8648000102C1865D

*Hameau à Payennet près de Gardanne, Paul Cézanne, c. 1886-1890, via Wikimedia Commons.*

*« Nous comprenons de manière de plus en plus précise, que tout peut arriver dans ce monde et singulièrement ce que nous n'avons pas prévu. »*
*Boris Vian, L'Écume des jours (1947)*

# Chapter 5
# CNN Optimization

This chapter is based on an article in preparation for submission to *Geodata and AI*.

# From Pixels to Point Clouds: Evaluating CNN Strategies for 3D Lithofacies Classification in Digital Outcrop Models

Eduardo Roemers-Oliveira[1,2*], Jérémy Marchini[1], Sophie Viseur[1], Ítalo Gomes Gonçalves[3], Felipe Guadagnin[3], François Fournier[1], Ana Clara Freccia[3], Guilherme de Godoy Rangel[3], Guilherme Pederneiras Raja Gabaglia[2]

[1]Aix Marseille Université, CNRS, IRD, INRAE, CEREGE, Aix-en-Provence, France
[2]Petrobras – Petróleo Brasileiro S.A, Rio de Janeiro, Brazil
[3]Universidade Federal do PAMPA, Caçapava do Sul, Brazil

## Abstract

Convolutional neural networks (CNNs) have increasingly been applied in geosciences for automated lithofacies classification. However, defining optimal methodological configurations that balance classification accuracy and operational efficiency, especially for 3D lithofacies modeling from outcrop imagery, remains underexplored. This study systematically evaluates supervised CNN strategies for lithofacies classification using high-resolution images from two outcrops of the Balbuena III Sequence in the Salta Basin, Argentina. Eleven lithofacies classes were manually labeled on 2D photographs based on expert interpretation, and the CNN was trained on this labeled dataset. Parameters such as image resolution, training duration, labeling proportions, geological interpretation strategies, and data augmentation were tested. Results demonstrate that a configuration combining double-resolution images, 100 training epochs, labeled data covering approximately half of the outcrop area, and the use of both raw and histogram-equalized images achieves robust classification performance while reducing manual annotation effort. The optimized CNN workflow successfully generated geologically coherent 3D lithofacies-classified point clouds, validated by cross-outcrop tests. Beyond methodological insights, the study highlights key geological observations, including the lateral continuity of major lithofacies, the importance of lithological contrast in detecting thin layers, and the influence of facies geometry on classification accuracy. While findings are specific to the Balbuena III Sequence, this work can, however, be considered a guideline for applying such an approach to similar sedimentological and stratigraphic contexts. This work advances the integration of deep learning techniques within geosciences, providing a practical contribution toward developing automated tools that complement traditional field-based stratigraphic and sedimentological analysis.

**Keywords:** Deep learning in geosciences; Facies classification; RPAS imagery; Facies mapping; Lithofacies 3D point cloud; Salta Basin.

## 5.1. Introduction

Convolutional neural networks (CNNs), first introduced as “convolutional networks” by LeCun et al. (1989), are a class of deep learning algorithms inspired by the hierarchical organization of the visual cortex as described by Hubel and Wiesel (1968). Practical applications of CNNs in image classification began in the 1990s, including their successful use for handwritten digit recognition, notably with the MNIST dataset (LeCun et al., 1998). A decade later, the breakthrough performance of the AlexNet architecture in the 2012 ImageNet Large Scale Visual Recognition Challenge (ILSVRC) marked a turning point, demonstrating that deep CNNs could outperform traditional machine learning techniques in complex visual tasks (Krizhevsky et al., 2012). This capability is fundamentally linked to the hierarchical

structure of deep learning architectures, where complex features are progressively built from simpler patterns across multiple hidden layers (Goodfellow et al., 2016; Karpatne et al., 2019).

Since then, CNNs have become a core component of image-based classification and segmentation workflows across multiple scientific domains, and geosciences have been no exception. Their applications have expanded rapidly, encompassing seismic interpretation (e.g., Souza et al., 2020), rock sample imaging (e.g., Fan et al., 2020; Falivene et al., 2022), and thin-section imagery (e.g., Cheng and Guo, 2017; Koeshidayatullah et al., 2020), enabling the automation of tasks traditionally reliant on manual expert interpretation. In sedimentology and stratigraphy, CNNs have shown promise in outcrop analysis, supporting the recognition of facies in photographic surveys (e.g., Malik et al., 2022) and 3D surface models (e.g., Sato et al., 2025).

However, lithofacies classification poses distinct challenges compared to conventional computer vision tasks. Unlike standard image datasets, the interpretation of geological imagery often requires specialized domain knowledge, as the visual similarity between classes can be substantial. As a result, labeling datasets for CNN training typically demands both sedimentological and stratigraphic expertise, supported by field and laboratory data. This grounding is essential to ensure that facies assignments are not only visually coherent, but also geologically meaningful, factors that significantly influence model performance and reproducibility.

In addition, the impact of methodological choices, such as image resolution, input preprocessing (e.g., histogram equalization), training duration, and facies labeling strategies, on classification accuracy and generalization remains underexplored. These factors are especially critical when CNN outputs are integrated into Digital Outcrop Models (DOMs) for sedimentological and stratigraphic analysis, where classification reliability directly affects spatial interpretation in three dimensions. This raises the central research question: Which CNN methodological configurations optimize the trade-off between classification accuracy and operational efficiency in 3D lithofacies modeling from outcrop imagery?

This study addresses these gaps by systematically evaluating supervised CNN strategies for lithofacies classification based on high-resolution imagery acquired using Remotely Piloted Aircraft Systems (RPAS) from two outcrops of the Balbuena III Sequence in the Salta Basin, Argentina (Fig. 5.1). An eleven-class lithofacies scheme was used to label the images, and several training configurations were tested, including different image inputs and data augmentation approaches. Performance was assessed using standard classification metrics, and the best-performing models were used to construct lithofacies-classified 3D DOMs from photogrammetric point clouds. Additionally, a cross-outcrop generalization test was conducted, applying a CNN trained on one outcrop to a distinct exposure. This approach enables a robust validation of parameter choices and contributes to advancing reproducible and transferable workflows for stratigraphic interpretation using CNNs.

The methodological pipeline applied in this study builds upon the CNN-to-point cloud workflow originally proposed by Guadagnin et al. (2025) and adapted for the Salta Basin by Roemers-Oliveira et al. (2025). By systematically evaluating alternative methodological configurations, this work aims to optimize classification performance and efficiency, establishing a guideline for 3D lithofacies classification in DOMs using CNNs.

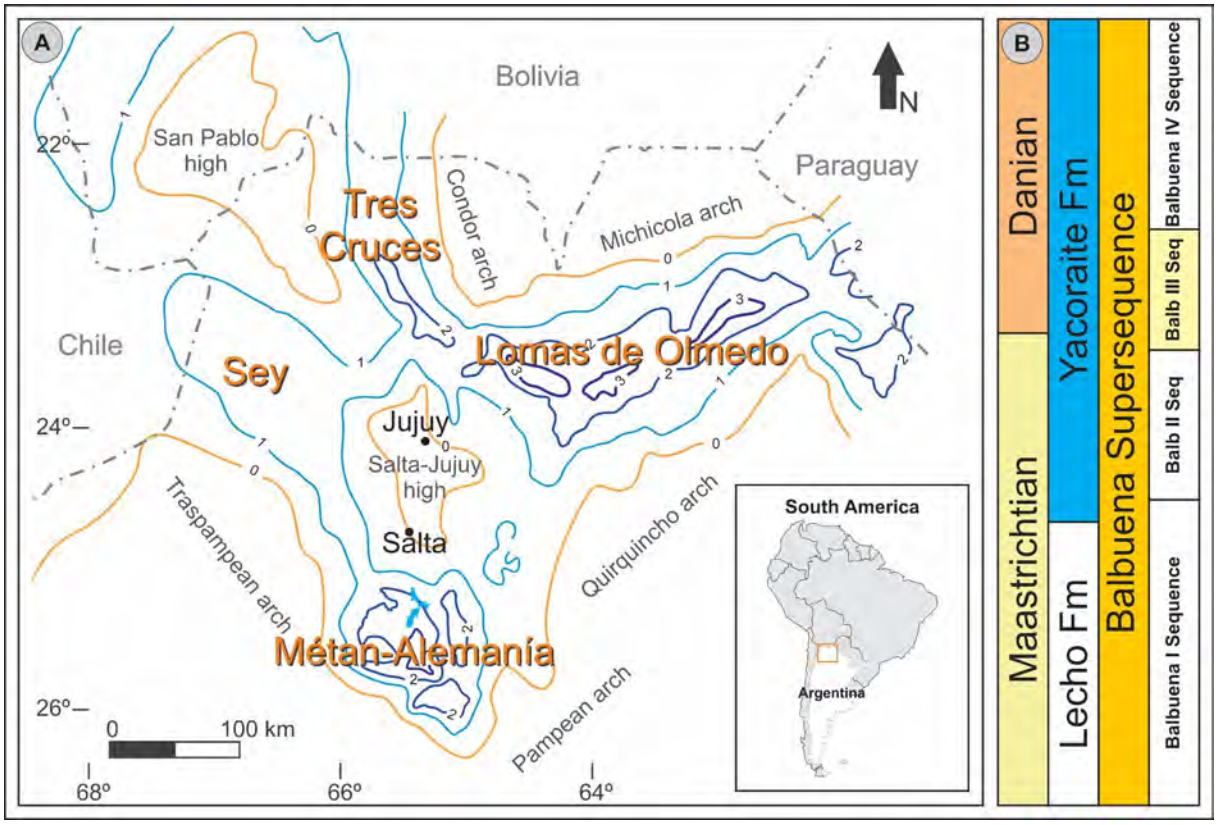


**Fig. 5.1.** Location of the Salta Basin in northwest Argentina, South America. A) Isopach map showing thickness variations of the Yacoraite Formation (values in hundreds of meters). The map also highlights the main sub-basins, delineated by structural highs and arcs. B) Simplified stratigraphic column of the Balbuena Supersequence, showing the four internal sequences (Balbuena I to IV), with emphasis on the Balbuena III Sequence, the focus of this study, and its correlation with formations. Modified from Marquillas et al. (2011) and Villafañe et al. (2022).

## 5.2. Geological context

### 5.2.1. Salta Basin overview

The stratigraphy of the Salta Basin has been interpreted through two main approaches: lithostratigraphy, which emphasizes lithological facies and unit boundaries (Turner, 1958; Marquillas et al., 2005), and sequence stratigraphy, which focuses on depositional sequences and their temporal relationships (Bianucci et al., 1981; Gómez Omil and Boll, 1999; Hernández et al., 1999, 2008). This study adopts the sequence stratigraphy framework, focusing on the Balbuena Supersequence, particularly the Balbuena III Sequence, which corresponds to the Yacoraite Formation of the Salta Group. This approach allows a detailed temporal and depositional characterization of the studied unit.

The Salta Basin (Fig. 5.1A), located in northwest Argentina, experienced alternating extensional and compressional tectonic phases. The initial extensional phase, linked to the breakup of Gondwana and the opening of the South Atlantic Ocean during the Early Cretaceous (Keidel, 1921; Ramos, 1988), led to syn-rift sedimentation starting in the Barremian stage (Marquillas et al., 2005). Subsequent compressional phases are associated with the Andean orogeny (Hernández and Echavarria, 2009).

The basin can be subdivided into four sub-basins: Lomas de Olmedo (east), Sey (west), Tres Cruces (north), and Metán-Alemania (south). The sedimentary fill is mainly divided into syn-rift (Pirgua Supersequence) and post-rift (Balbuena Supersequence) phases, the latter further

subdivided into four depositional sequences (Balbuena I to IV) spanning from Maastrichtian to Danian (Hernández et al., 1999), as illustrated in Fig. 5.1B.

### 5.2.2. Balbuena III Sequence

This study concentrates on the Balbuena III Sequence within the Metán-Alemania sub-basin, which records the transition from the Maastrichtian to Danian stages (Marquillas et al., 2003). The sequence is composed of lacustrine carbonate, siliciclastic, and mixed facies deposited under primary climatic control, which regulates the lake base level and drives the development of a cyclic pattern formed by repetitive elementary sequences (Roemers-Oliveira et al., 2025). The cyclic pattern consists of elementary sequences, each representing depositional cycles controlled by fluctuations in lake level driven by climatic variations.

The Balbuena III Sequence exhibits an evolution from an open lake system at its base to a closed lake system towards the top, which controls the main rock types present in each interval. Based on this evolution, four facies associations can be distinguished (Roemers-Oliveira et al., 2025):

- **Littoral Open Lake Association (LOLA)**: siliciclastic-dominated sandstones and siltstones deposited in shallow, wave-influenced settings.

- **Profundal Open Lake Association (POLA)**: fine-grained siliciclastic and mixed facies deposited in deeper, low-energy environments.

- **Littoral Closed Lake Association (LCLA)**: carbonate-rich grainstones, packstones, and stromatolites in shallow, evaporitic settings.

- **Profundal Closed Lake Association (PCLA)**: laminated carbonate mudstones and marls in deep, restricted lacustrine environments.

Stratigraphic cyclicity is observed at multiple scales, with sequences representing transgressive-regressive cycles marked by Maximum Retraction Surfaces (MRS) and Maximum Expansion Surfaces (MES). These cycles are traceable across numerous outcrops and can be correlated laterally over distances of tens of kilometers, reflecting climatic and hydrological variations controlling sedimentation (Roemers-Oliveira et al., 2025).

The present study focuses on two well-exposed outcrops of the Balbuena III Sequence: Assado and Vapumas, located on the shore of Cabra Corral Lake. These outcrops exhibit well-preserved lithofacies associations representative of the lacustrine depositional environments described above. A detailed stratigraphic correlation between these outcrops, based on the elementary transgressive-regressive (T-R) sequences and sedimentological characteristics, is presented in Fig. 5.2, illustrating the depositional patterns within the sequence.

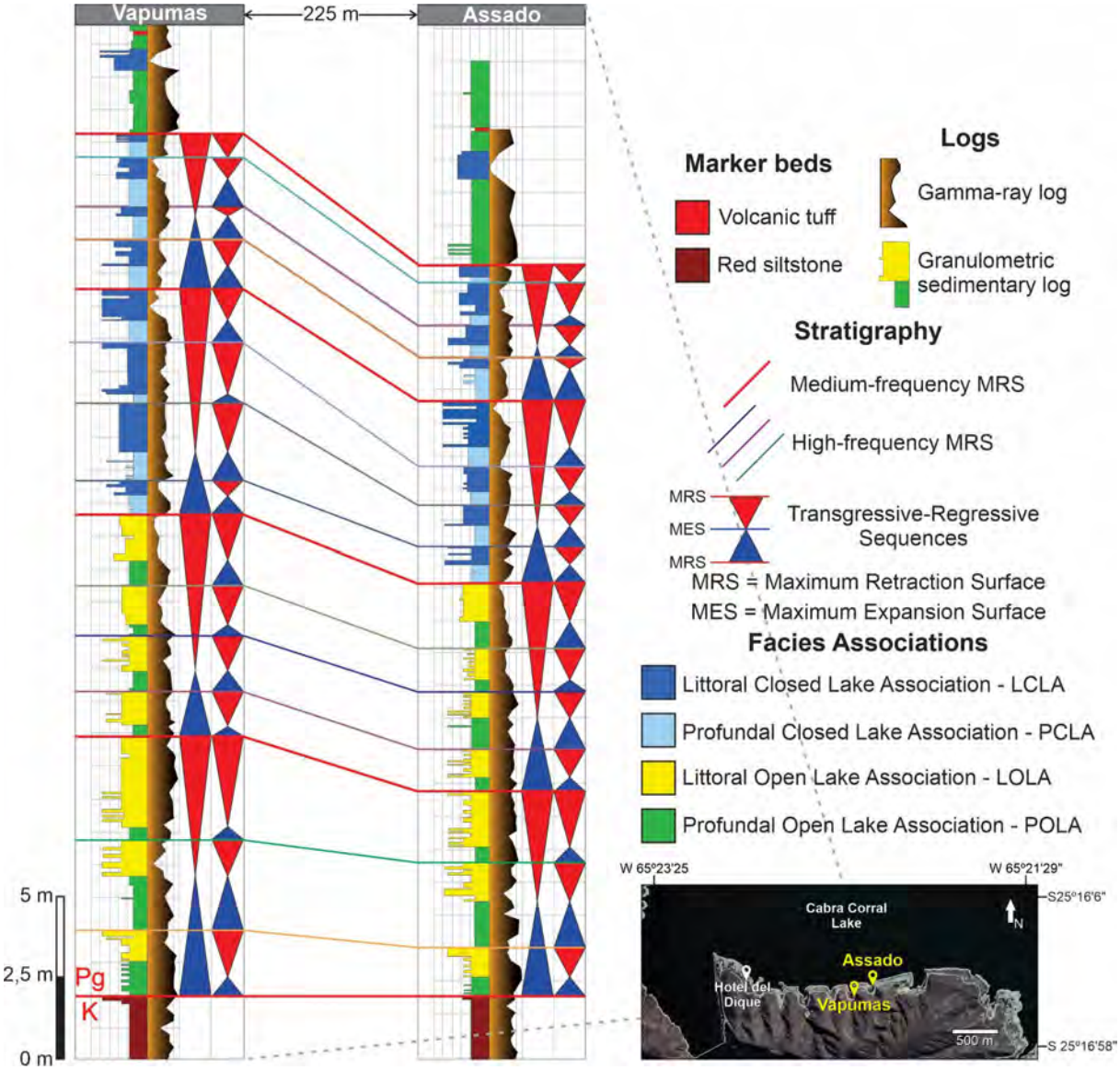


**Fig. 5.2.** Stratigraphic correlation between the Vapumas and Assado outcrops of the Balbuena III Sequence (Metán-Alemania sub-basin, Salta Basin, Argentina). The correlation is based on elementary transgressive-regressive (T-R) sequences and sedimentological characteristics. Granulometric sedimentary logs were mirrored to align with gamma-ray logs. Modified from Roemers-Oliveira et al. (2025). Map data from Google Earth.

## 5.3. Materials and methods

### 5.3.1. Workflow overview

The proposed workflow for lithofacies classification and 3D point cloud generation is based on the integration of supervised convolutional neural networks (CNN) and photogrammetric modeling, as presented in Fig. 5.3. The pipeline begins with high-resolution image acquisition using RPAS, followed by expert-based manual labeling of lithofacies. These labeled images are used to train a CNN model, which predicts facies classes on photographs downscaled in spatial resolution for computational efficiency. Model performance is quantitatively assessed through standard classification metrics (described in Section 5.3.2), allowing for the comparison of different training strategies and the selection of the most effective configuration — which constitutes the core objective of this study. For each predicted image, binary masks are then generated per lithofacies and applied to the equalized photos at their original spatial resolution. Photogrammetric reconstruction is performed with point matching restricted to the

masked regions, resulting in lithofacies-classified 3D point clouds. The main steps of this workflow are detailed in the following subsections.

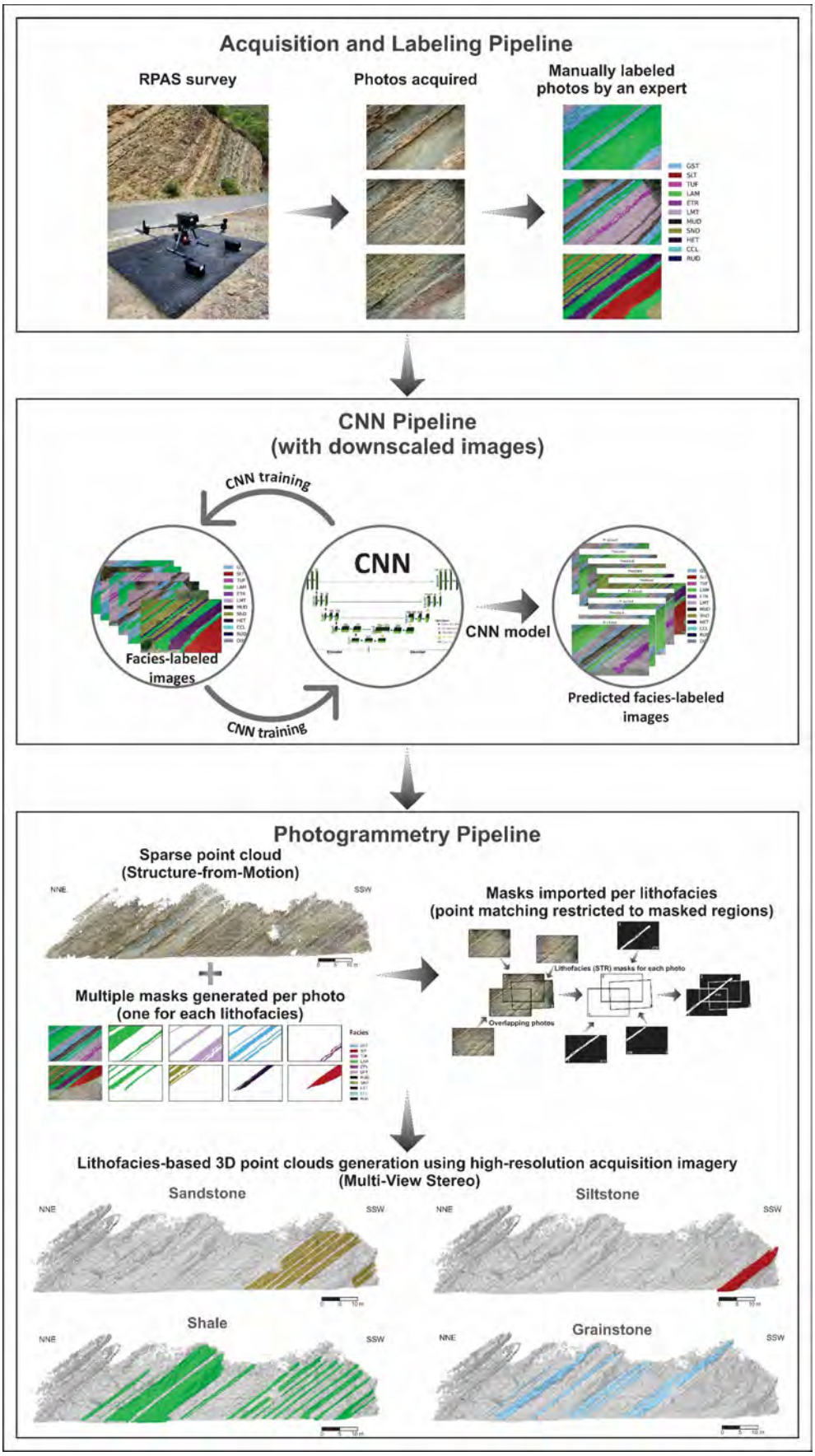


**Fig. 5.3.** Overview of the methodological workflow, from RPAS imagery acquisition to 3D point cloud generation through masked photogrammetric reconstruction. The masks are produced by a CNN model trained using expert-labeled data. Modified from Roemers-Oliveira et al. (2025).

### 5.3.1.1. Data acquisition and available datasets

This study utilizes high-resolution image datasets from two closely spaced outcrops of the Balbuena III Sequence, Assado and Vapumas, located within the Metán-Alemania sub-basin along the shore of Cabra Corral Lake (see Fig. 5.2). Both outcrops have a similar stratigraphic thickness of approximately 32 meters.

Image acquisition was conducted using a DJI Matrice 300 RTK RPAS equipped with a DJI Zenmuse P1 full-frame camera (35 mm lens, 8192 × 5460-pixel resolution). Geolocation accuracy was ensured by real-time correction from a DJI D-RTK 2 GNSS base station, providing positioning within a few centimeters. During the survey, a minimum distance of 8 meters from the outcrop surfaces was maintained to optimize image resolution and coverage, with an average distance of 12.9 meters.

The images were captured while the RPAS remained stationary in the air, ensuring consistent spacing and overlap between consecutive shots, with a minimum forward overlap of 80% and side overlap of 70%. Although this stationary method enhanced image consistency, it prolonged the data collection time, resulting in significant variations in lighting conditions throughout the survey. To mitigate these effects, histogram matching equalization was applied using a Python-based algorithm (Python, 2023). A single image was first manually corrected in Adobe Photoshop (Adobe Inc, 2024) to serve as the reference, and this correction was then used to homogenize lighting and contrast across the entire dataset. A comparison between a raw image and its histogram-equalized counterpart is presented in Fig. 5.4. Consequently, two image sets were generated for each outcrop: 497 raw images for Assado and 450 raw images for Vapumas, along with corresponding histogram-equalized versions.

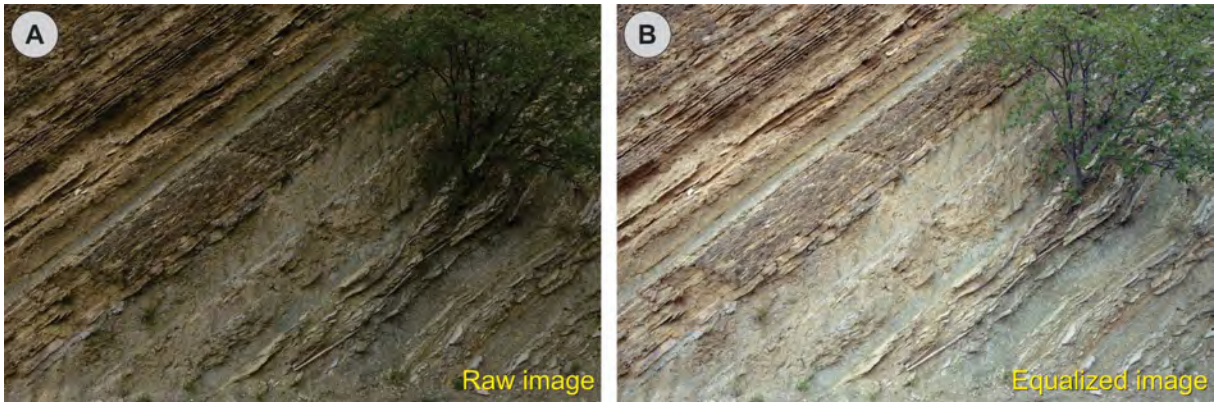


**Fig. 5.4**. Comparison between a raw image (A) and its corresponding histogram-equalized counterpart (B) from the Assado outcrop dataset. Histogram equalization was applied to reduce lighting and contrast variations, enhancing image consistency for further processing.

### 5.3.1.2. Lithofacies labeling

Accurate lithofacies labeling of outcrop images is a critical step in the proposed workflow, enabling detailed pixel-wise classification necessary for subsequent 3D modeling. The labeling process involves assigning a lithofacies class to each pixel in the images, which supports precise spatial mapping of geological units and enhances the interpretability of the resulting models.

Due to the complexity of the images and the need for interpretative consistency, manual annotation was restricted to a subset of images, consisting of 49 images from the Assado outcrop and 31 from Vapumas. These images were chosen to cover the entire spatial extent of the outcrops, ensuring that all lithofacies, including those with lower occurrence proportion, were adequately represented. This manual labeling was performed by experts using Adobe Photoshop (Adobe Inc, 2024), where each lithofacies was assigned a specific binary mask

forming the ground truth required for supervised CNN training. Each mask represents a lithofacies class, creating individual class layers used during the training process. Fig. 5.5 illustrates the eleven lithofacies classes employed for labeling, with representative photographs of each lithofacies, as well as examples of labeled images from the Vapumas outcrop. An additional class, “others” (Fig. 5.5), was defined to include image portions not corresponding to lithofacies (e.g., vegetation, sky, road).

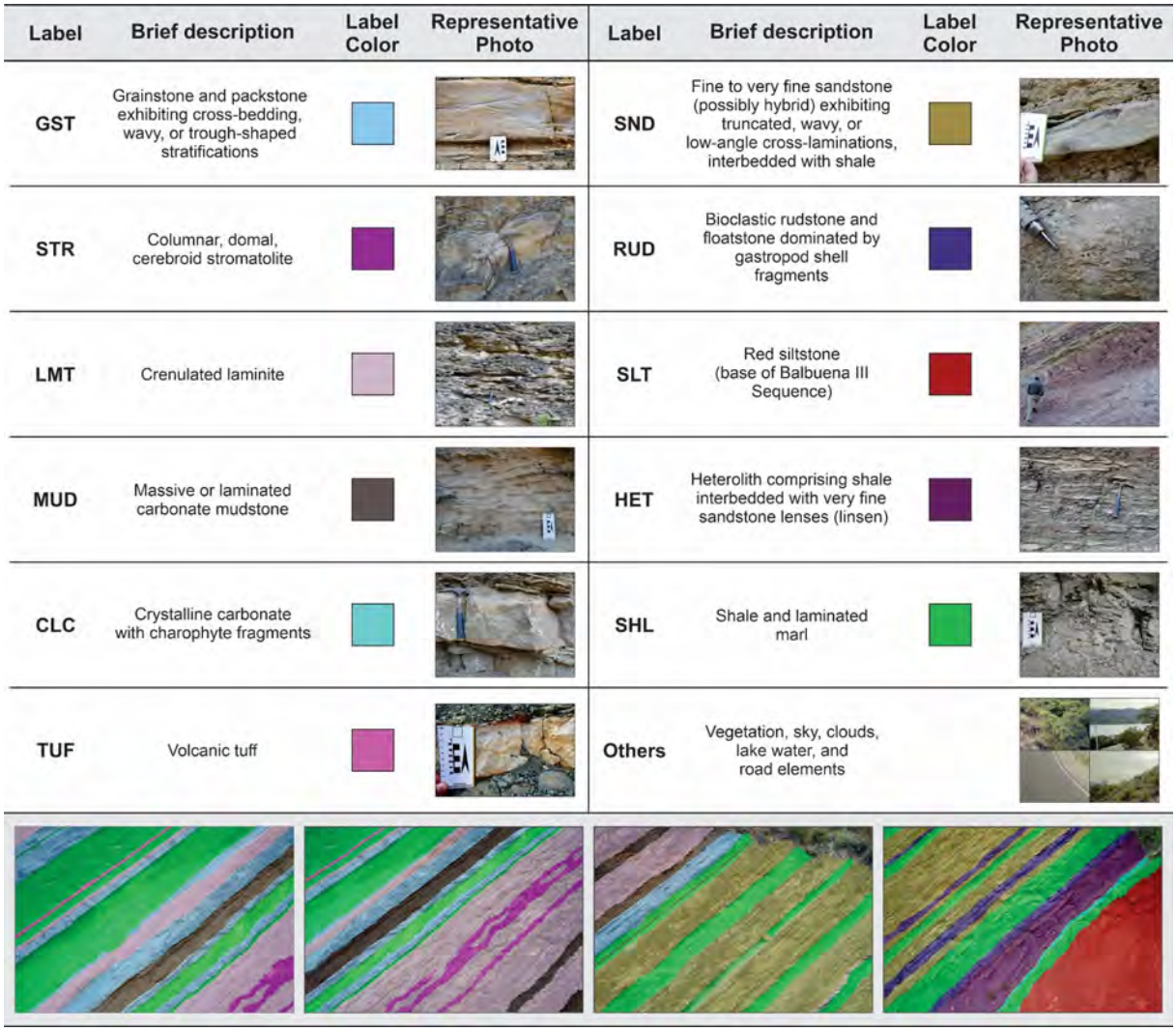


**Fig. 5.5.** Summary of lithofacies classes used for image labeling. The table lists the class labels, brief geological descriptions, corresponding mask colors, and representative field photographs illustrating each lithofacies. Colors were consistently applied throughout the study for lithofacies identification in image segmentation and 3D modeling. At the bottom, examples of labeled outcrop images illustrating the spatial distribution of lithofacies at the Vapumas outcrop. Labeling followed the established protocol described in (Roemers-Oliveira et al., 2025), ensuring methodological consistency across studies.

By limiting manual labeling to a subset of images used for CNN training, this workflow enables consistent and scalable facies classification across the dataset, transferring expert knowledge with reproducible performance while handling large-scale data processing.

#### 5.3.1.3. CNN architecture and training

In supervised approaches, CNN models are trained exclusively on labeled data, relying entirely on expert-provided annotations to learn the association between input images and predefined class labels. Lithofacies segmentation was performed using a U-Net architecture

(Ronneberger et al., 2015), implemented in Python (Python, 2023) with the TensorFlow deep learning library (TensorFlow, 2024), widely used for semantic segmentation tasks.

The model follows a standard encoder–decoder design, with four downsampling blocks, each applying max pooling and connected through skip connections. Each block consists of two 3 x 3 convolutional layers with ReLU activation, and the number of filters doubles with depth (32, 64, 128, 256), followed by a bottleneck with 512 filters. The decoder mirrors the encoder to restore spatial resolution, also using ReLU activation in its convolutional layers. The final output is produced by a 1 × 1 convolution with softmax activation. The model was trained using the Adam optimizer, with 10% of the data reserved for validation to monitor performance. Data augmentation was incorporated into the training pipeline using geometric transformations such as flipping, cropping, rotation, and translation (Shorten and Khoshgoftaar, 2019), increasing dataset diversity and helping the model generalize better.

The manually labeled subset of images was split equally into training and validation sets (50%/50%). To ensure reproducibility and comparability across multiple training runs, a fixed random seed (101) was set, guaranteeing consistent selection between training and validation images for meaningful comparisons. All CNN training and inference tests were performed on a laptop equipped with a 12th-generation Intel Core i9 processor, an Nvidia 3080 Ti graphics card, and 64 GB of RAM.

After initial model training and validation, once satisfactory performance metrics were obtained, the CNN was retrained using the full set of manually labeled images to maximize the training dataset. This expanded training improved model robustness and generalization. The refined model was subsequently applied to classify all remaining unlabeled images in the dataset, ensuring comprehensive lithofacies segmentation across the entire image collection.

### 5.3.2. Performance evaluation

Model performance was evaluated using a holdout set comprising 50% of the manually labeled images not included in the training subset, providing an independent assessment of the model's generalization capabilities. The evaluation metrics were derived from the confusion matrix components defined as:

- **True Positive (TP):** Number of pixels correctly predicted as belonging to a given lithofacies class.

- **False Positive (FP):** Number of pixels incorrectly predicted as belonging to a given class.

- **True Negative (TN):** Number of pixels correctly predicted as not belonging to a given class.

- **False Negative (FN):** Number of pixels incorrectly predicted as not belonging to a given class.

From these components, the following standard classification metrics (Manning et al., 2009; Powers, 2011; Goodfellow et al., 2016) were calculated:

- **Accuracy:** The overall correctness of the predictions, calculated as

$$Accuracy = \frac{\mathrm{TP} + \mathrm{TN}}{TP + TN + FP + FN}$$

• **Precision:** The proportion of predicted positive pixels that are correctly identified, defined as

$$Precision = \frac{\mathrm{TP}}{TP + FP}$$

• **Recall:** The proportion of actual positive pixels that are correctly identified by the model, also called sensitivity, given by

$$Recall = \frac{\mathrm{TP}}{TP + FN}$$

• **F1-Score:** The harmonic mean of precision and recall, which balances the two metrics to provide a single performance score

$$F1 = 2 \times \frac{\mathrm{Precision} \times \mathrm{Recall}}{Precision + Recall}$$

Accuracy was computed as a global metric reflecting the overall correctness of the model's predictions across all classes, while precision, recall, and F1-score were calculated for each individual lithofacies class to assess the model's discriminatory performance at the class level.

Additionally, the loss function was monitored during training to quantify the discrepancy between predicted outputs and ground truth labels. Lower loss values indicate better model performance and convergence, as the model parameters are optimized iteratively to minimize this loss. Together, these metrics provide a comprehensive and robust framework to assess CNN model performance, enabling objective comparison between different training strategies presented in this work.

### 5.3.3. Lithofacies-based point cloud generation

Lithofacies-specific 3D point clouds were generated using Agisoft Metashape (Agisoft Metashape, 2023). This process requires a fully labeled image dataset, obtained by applying the trained CNN to classify all images from the two outcrops analyzed in this study. Processing begins with the generation of a sparse point cloud during the image alignment stage using the Structure-from-Motion (SfM) technique (Westoby et al., 2012), employing all photos from each outcrop. This sparse cloud represents the initial 3D reconstruction, created from tie points detected across overlapping images. Subsequently, dense point clouds are generated through Multi-View Stereo (MVS) algorithms, following the widely adopted SfM-MVS workflow for 3D photogrammetric reconstruction from overlapping images (e.g., Lowe, 2004; Furukawa and Hernández, 2015; Bistacchi et al., 2022).

Conventional photogrammetric reconstruction methods utilize the entire image dataset indiscriminately. In contrast, the present workflow employs only the segmented portions of each image, corresponding to specific lithofacies masks (as illustrated in Fig. 5.3), to reconstruct facies-specific 3D models. To achieve this, the sparse point cloud is duplicated within the photogrammetry software, creating separate processing chunks for each lithofacies. This facies-based segmentation allows for targeted 3D reconstruction and classification, focusing exclusively on geologically relevant areas delineated by the lithofacies masks.

Dense point clouds are subsequently generated facies by facies using a depth-map-based MVS algorithm, which estimates depth information from multiple overlapping images and integrates this data to produce detailed, lithofacies-specific dense 3D point clouds. A manual editing step follows to refine the final point clouds, during which points characterized by low confidence (often due to insufficient image overlap) or points not corresponding to the

interpreted facies are removed. This quality control ensures that the resulting lithofacies point clouds are both spatially accurate and geologically coherent.

### 5.3.4. Strategy testing for parameter optimization

This section presents a series of experiments designed to systematically evaluate the impact of different training strategies and parameter settings on the performance of the CNN model, which forms the central contribution of this paper. Table 5.1 summarizes the main test configurations applied to the Assado and Vapumas datasets. The model performance was compared using the evaluation metrics described in Section 5.3.2, ensuring consistent and objective assessment across all tested configurations. Only the most relevant and conclusive results from these experiments are presented and discussed in the following subsections.

#### 5.3.4.1. Image resolution and epoch numbers

A series of tests were conducted on two key parameters, the image resolution and the number of training epochs, to optimize model performance while controlling computational cost. The goal was to find the best balance between training time and image detail that maximizes accuracy without excessive processing.

Regarding image resolution, training was initially conducted using a downscaled reference resolution of 192 × 128 pixels, approximately 42 times smaller than the original (8192 × 5460 pixels). To assess whether increasing resolution could improve model accuracy, additional tests were performed using doubled (384 × 256) and tripled (576 × 384) this reference resolution. Higher image resolutions may capture finer geological features and textures but also increase computational demands and training time.

An epoch is defined as one complete pass through the entire training dataset (Goodfellow et al., 2016), during which the model iteratively adjusts its parameters by learning from the data to improve performance. As the number of epochs increases, the model refines its internal representations and prediction capabilities: too few epochs may lead to underfitting, where the model fails to capture underlying patterns, while too many may cause overfitting, where the model memorizes the training data and performs poorly on unseen samples. To identify an appropriate balance, training was performed with 25, 50, and 100 epochs, and results were evaluated accordingly.

#### 5.3.4.2. Comparison of labeled image proportions

To evaluate the impact of training dataset size on model performance, experiments were conducted using different proportions of manually labeled images from the Assado and Vapumas sites. For the Assado outcrop, approximately 10% of the total image dataset was labeled and used for model training, corresponding to 49 images. This proportion results from the prior application of the method on this outcrop, as detailed in Roemers-Oliveira et al. (2025). For the Vapumas outcrop, about 7% of the dataset was labeled, with 31 images manually annotated.

**Table 5.1.** Summary of experimental test configurations for CNN training and evaluation. Each test is coded according to the parameter and dataset used: resolution (R), epochs (E), labeled image proportion (P), interpretation review (I), and data augmentation (EQ for equalized images only, RQ for raw plus equalized images). The outcrop associated with each test is indicated as Assado (A) or Vapumas (V).

| Test Code | Parameter/Type | Resolution | Epochs | Nº of labeled images | Geological Interpretation | Dataset | Outcrop |
|---|---|---|---|---|---|---|---|
| R1-A | Resolution | 192 × 128 pixels | 100 | 49 | Hybrid layer as SND | Equalized images | Assado |
| R2-A | Resolution | 384 × 256 pixels | 100 | 49 | Hybrid layer as SND | Equalized images | Assado |
| R3-A | Resolution | 576 × 384 pixels | 100 | 49 | Hybrid layer as SND | Equalized images | Assado |
| E1-A | Epochs | 384 × 256 pixels | 25 | 49 | Hybrid layer as SND | Equalized images | Assado |
| E2-A | Epochs | 384 × 256 pixels | 50 | 49 | Hybrid layer as SND | Equalized images | Assado |
| E3-A | Epochs | 384 × 256 pixels | 100 | 49 | Hybrid layer as SND | Equalized images | Assado |
| P1-A | Labeled image proportion | 384 × 256 pixels | 100 | 49 | Hybrid layer as SND | Equalized images | Assado |
| P1-V | Labeled image proportion | 384 × 256 pixels | 100 | 31 | Hybrid layer as SND | Equalized images | Vapumas |
| IG-A | Interpretation review | 384 × 256 pixels | 100 | 49 | Hybrid layer as GST | Equalized images | Assado |
| IS-A | Interpretation review | 384 × 256 pixels | 100 | 49 | Hybrid layer as SND | Equalized images | Assado |
| IG-V | Interpretation review | 384 × 256 pixels | 100 | 31 | Hybrid layer as GST | Equalized images | Vapumas |
| IS-V | Interpretation review | 384 × 256 pixels | 100 | 31 | Hybrid layer as SND | Equalized images | Vapumas |
| EQ-A | Data augmentation | 384 × 256 pixels | 100 | 49 | Hybrid layer as SND | Equalized images | Assado |
| RQ-A | Data augmentation | 384 × 256 pixels | 100 | 49 | Hybrid layer as SND | Raw + Equalized images | Assado |
| EQ-V | Data augmentation | 384 × 256 pixels | 100 | 31 | Hybrid layer as SND | Equalized images | Vapumas |
| RQ-V | Data augmentation | 384 × 256 pixels | 100 | 31 | Hybrid layer as SND | Raw + Equalized images | Vapumas |
| VA-V | Cross-outcrop test | 384 × 256 pixels | 100 | 49 / 31 | Hybrid layer as SND | Raw + Equalized images | Assado (train) / Vapumas (test) |

#### 5.3.4.3. Geological interpretation review

In the study area, a hybrid lithofacies layer occurs at the transition between the basal siliciclastic-dominated interval and the overlying carbonate-dominated deposits. In a previous interpretation (Roemers-Oliveira et al., 2025), the uppermost layer of the littoral open-lake facies association was labeled as grainstone (GST), based on its significant carbonate content observed in thin sections. However, as discussed by these authors, CNN-based classification frequently misclassified this layer as sandstone (SND), due to its visual similarity to sandstone in field photographs.

Since the CNN model relies solely on image-based features, the hybrid layer was re-evaluated to better reflect the model's input data. Accordingly, the label was revised from GST to SND in all relevant manually labeled images. Subsequent performance tests were conducted to assess the impact of this adjustment on classification accuracy.

#### 5.3.4.4. Data augmentation: raw and equalized images

This strategy investigates the use of both equalized and raw image sets to increase the variability of training data without requiring additional manual labeling. Since both datasets represent the same geological features, the same interpretation masks are applied to each version. By duplicating the input data in this manner, the model is exposed to a broader range of visual conditions, such as variations in lighting and contrast, which may enhance its generalization capability during training and improve robustness against illumination variability in field imagery.

## 5.4. Results

### 5.4.1. Impact of image resolution and epoch numbers

#### 5.4.1.1. Image resolution

Image resolution significantly affects the CNN model ability to segment lithofacies accurately, especially for thin or subtle geological features. To evaluate the influence of image resolution on model performance, three resolution levels were tested using the Assado dataset: the reference resolution (192 × 128 pixels), double (384 × 256 pixels), and triple (576 × 384 pixels) the reference resolution. Fig. 5.6 illustrates examples of image downscaling applied for CNN training, showing the original high-resolution image alongside progressively downscaled versions used to evaluate the balance between image detail and computational efficiency.

The computational cost increased exponentially with image size. On the Assado outcrop, processing a single epoch required approximately 20 seconds at base resolution, 85 seconds at double, and 198 seconds at triple resolution. Performance evaluation employed the F1-score metric for each lithofacies class, chosen because it jointly considers precision and recall, offering a balanced measure of classification effectiveness, as shown in Fig. 5.7, which displays the F1-scores per lithofacies for the three resolution tests.

The base resolution model achieved an overall accuracy of 78%. Doubling the resolution improved accuracy to 83%, with performance gains observed across all lithofacies classes. This increase was especially notable for thinner lithofacies such as crystalline carbonates (CLC) and rudstone (RUD), where F1-scores increased substantially (from 0.19 to 0.64 for CLC, and from 0.39 to 0.57 for RUD). In contrast, tripling the resolution provided only a modest increase in overall accuracy to 85%, just 2% higher than the double resolution model. Moreover, the per-class F1-scores showed subtle gains overall when comparing triple to double resolution, with

all classes improving slightly except for grainstone (GST), which remained unchanged, and mudstone (MUD) and heterolith (HET), which experienced slight decreases (with MUD decreasing from 0.72 to 0.71, and HET from 0.89 to 0.85).

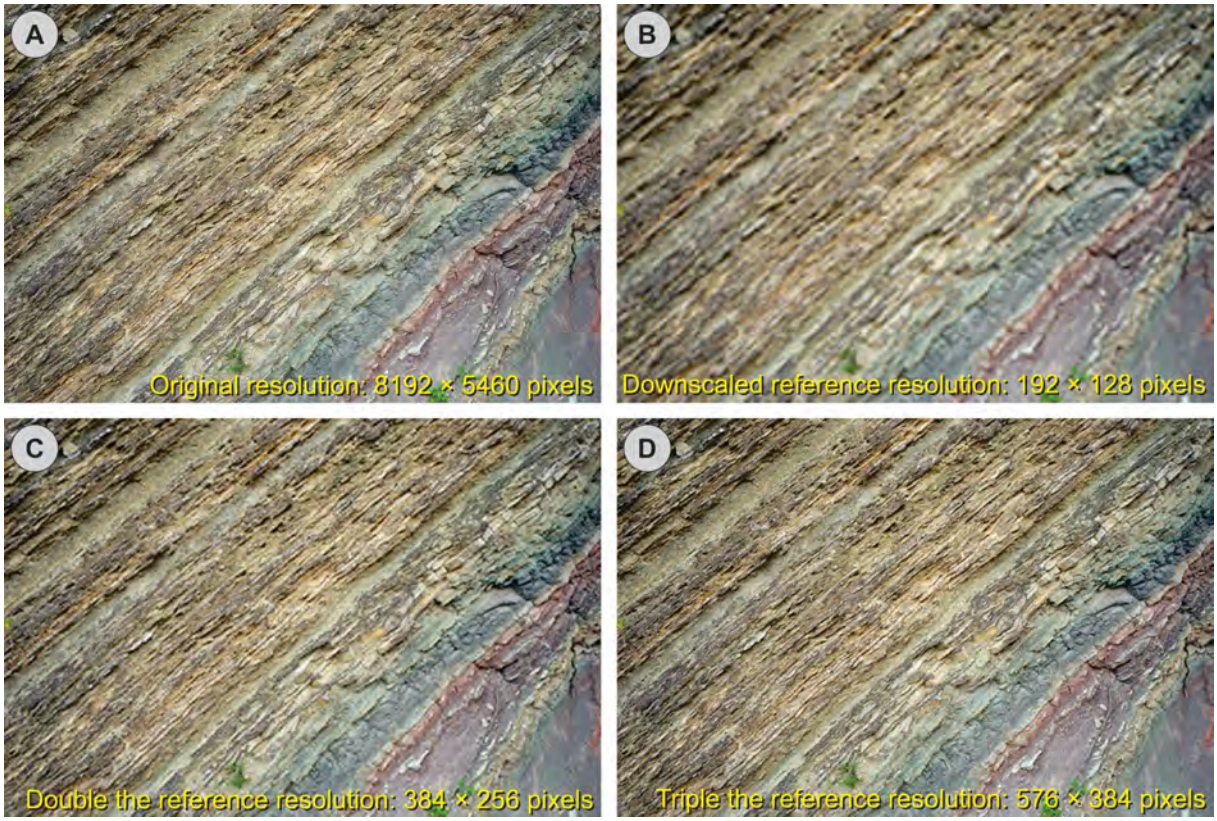


**Fig. 5.6.** Example of image downscaling applied for CNN training, showing the original resolution (A) and progressively higher downscaled resolutions used to test the balance between detail and computational cost (B–D).

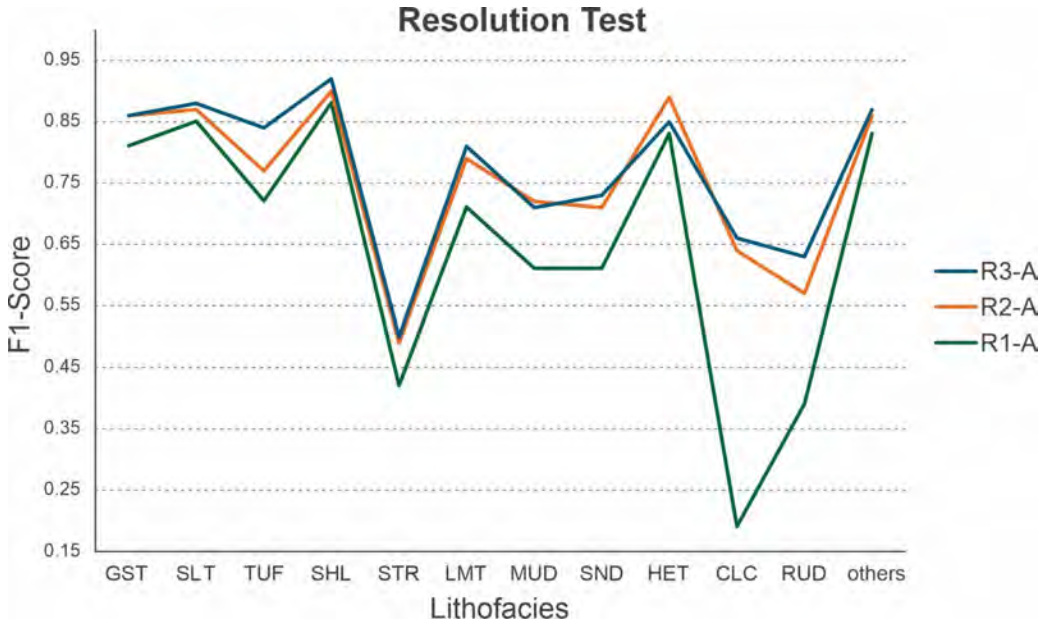


**Fig. 5.7.** F1-score performance for each lithofacies class across three image resolution tests on the Assado dataset: base, double, and triple resolution (R1-A, R2-A, R3-A, accuracies 78%, 83%, and 85%, respectively).

An accuracy-to-time ratio analysis indicated that the double resolution test offered the most efficient trade-off between performance improvement and computational cost. Consequently, this resolution was adopted as the standard setting for subsequent CNN training and testing in the remaining experiments.

### 5.4.1.2. Epoch numbers

The number of epochs plays a critical role in CNN model convergence and generalization. Training was performed for 25, 50, and 100 epochs to identify an appropriate balance between underfitting and overfitting. From 50% of the dataset reserved for training, 90% of the images were used for training and 10% for validation, which was used to monitor the model's convergence and detect overfitting through accuracy and loss metrics computed on both subsets. Training loss and accuracy were calculated on the training portion (displayed as blue curves), while validation loss and accuracy were computed on the validation subset (orange curves), as shown in Fig. 5.8.

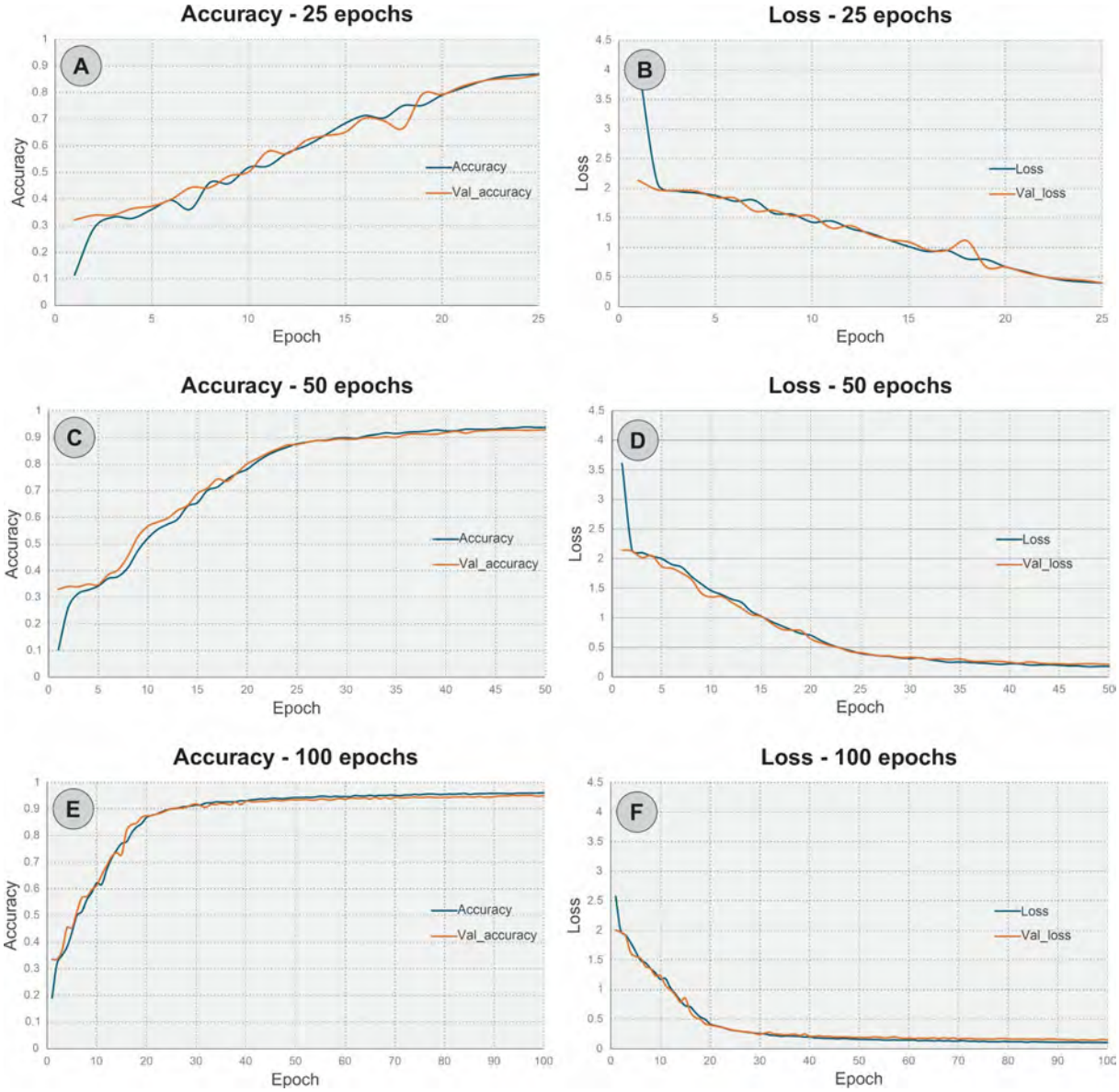


**Fig. 5.8**. Training and validation accuracy (top row) and loss (bottom row) curves for CNN models trained with 25 (E1-A), 50 (E2-A), and 100 (E3-A) epochs using double resolution images. Training metrics (blue curves) were computed on 90% of the training dataset, while validation metrics (orange curves) correspond to the remaining 10%. These plots illustrate the model's convergence behavior and stability across epochs, with improved performance and more stable convergence observed as the number of epochs increases, with no evident signs of overfitting in any of the models.

At 25 epochs, both accuracy and loss curves (Fig. 5.8A–B) were unstable and diverged, indicating underfitting and insufficient learning. At 50 epochs (Fig. 5.8C–D), the curves approached convergence, with stabilization beginning around 35 to 40 epochs, where the loss

and accuracy curves plateaued, forming a ‘floor’ for loss and a ‘ceiling’ for accuracy. However, full stabilization could not yet be confirmed. The model trained for 100 epochs demonstrated clear convergence, with well-defined accuracy ceilings (Fig. 5.8E) and loss floors (Fig. 5.8F) for both training and validation sets, indicating robust learning without overfitting. Overfitting is identified when a significant gap emerges between the training and validation curves, reflecting poor generalization; this suggests that the model memorizes training data rather than learning underlying patterns. The observed performance improvements justify selecting 100 epochs as the standard for subsequent experiments, balancing model accuracy and training time.

### 5.4.2. Effect of labeled image proportions

Following the precedent established in Roemers-Oliveira et al. (2025), a labeled image proportion of approximately 10% was used for the Assado outcrop (49 images). For the Vapumas outcrop, 7% of the image dataset was labeled (31 images). The experiments presented here were conducted using only the equalized images for both outcrops. Performance metrics including precision, recall, and F1-score were evaluated per lithofacies class, and overall accuracy was calculated to assess model generalization.

Fig. 5.9 presents the comparative results between the two outcrops, illustrating the impact of labeled image proportion on model classification performance. The overall accuracies achieved were 83% for Assado (P1-A) and 85% for Vapumas (P1-V), showing that comparable area coverage led to similar performance, with precision, recall, and F1-scores generally consistent across both outcrops. Notable strengths were observed in classes such as shale (SHL), siltstone (SLT), heterolith (HET), and grainstone (GST), all exhibiting F1-scores above 0.8 in both outcrops. Lower F1-scores were observed in less frequent or more challenging lithofacies, such as stromatolite (STR) and crystalline carbonate (CLC), with STR reflecting its complex geometries and CLC corresponding to a thin layer, even thinner at the Vapumas outcrop.

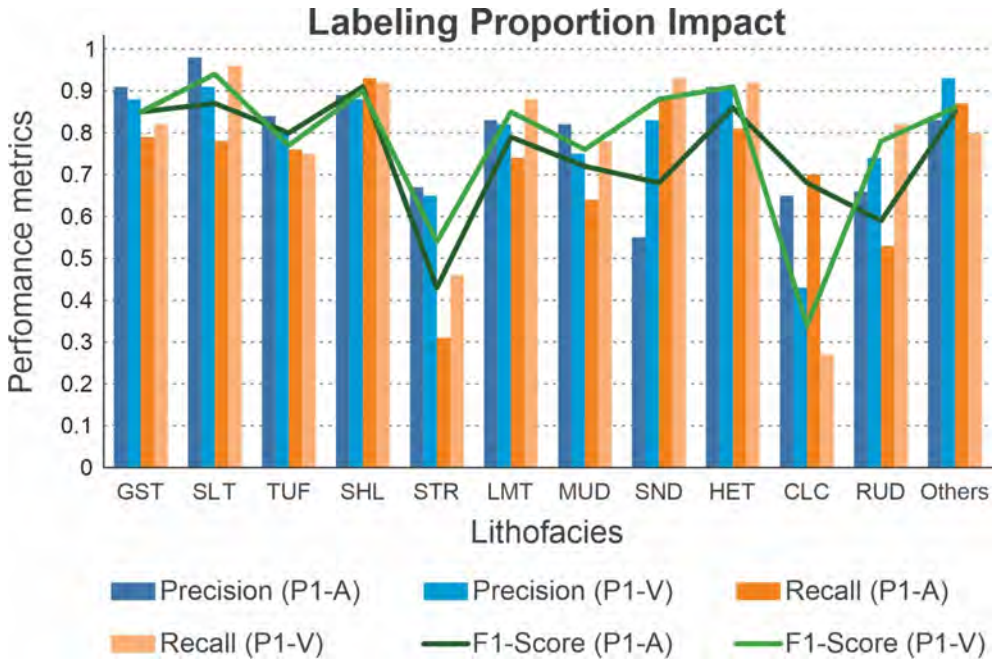


**Fig. 5.9.** Classification performance by lithofacies for Assado (P1-A) and Vapumas (P1-V) using labeled image proportions of 10% and 7%, respectively. Precision, recall (bars), and F1-score (lines) are shown for each class.

Although it may seem that a smaller proportion of labeled data at Vapumas was sufficient to achieve similar performance compared to Assado, the results indicate that the key factor is the

effective coverage of training images relative to the outcrop area. Considering only the images used for CNN training (half of the labeled dataset), these correspond to 0.51 of the total Assado outcrop area and 0.45 of the Vapumas outcrop area. This shows that, rather than an ideal percentage of the total dataset, it is more consistent to define the training set based on the number of images required to cover between 45–50% of the outcrop area, since the Vapumas outcrop has a smaller surface area and therefore required a lower proportion of images, as both outcrops were surveyed following similar acquisition protocols.

### 5.4.3. Influence of geological interpretation review

This section evaluates the impact of revising the geological interpretation of the hybrid lithofacies layer on the performance of CNN-based lithofacies classification. In previous work (Roemers-Oliveira et al., 2025), this hybrid layer was labeled as grainstone (GST) due to its carbonate-rich composition observed in thin sections. However, its visual similarity to sandstone (SND) in field images often led to misclassification by the CNN model.

Fig. 5.10A–F illustrate examples of the hybrid layer interpretation in the Assado and Vapumas outcrops, showing the original images and the labels before (GST) and after (SND) the reinterpretation. Subsequent classification tests were performed to assess how this reinterpretation influences model accuracy.

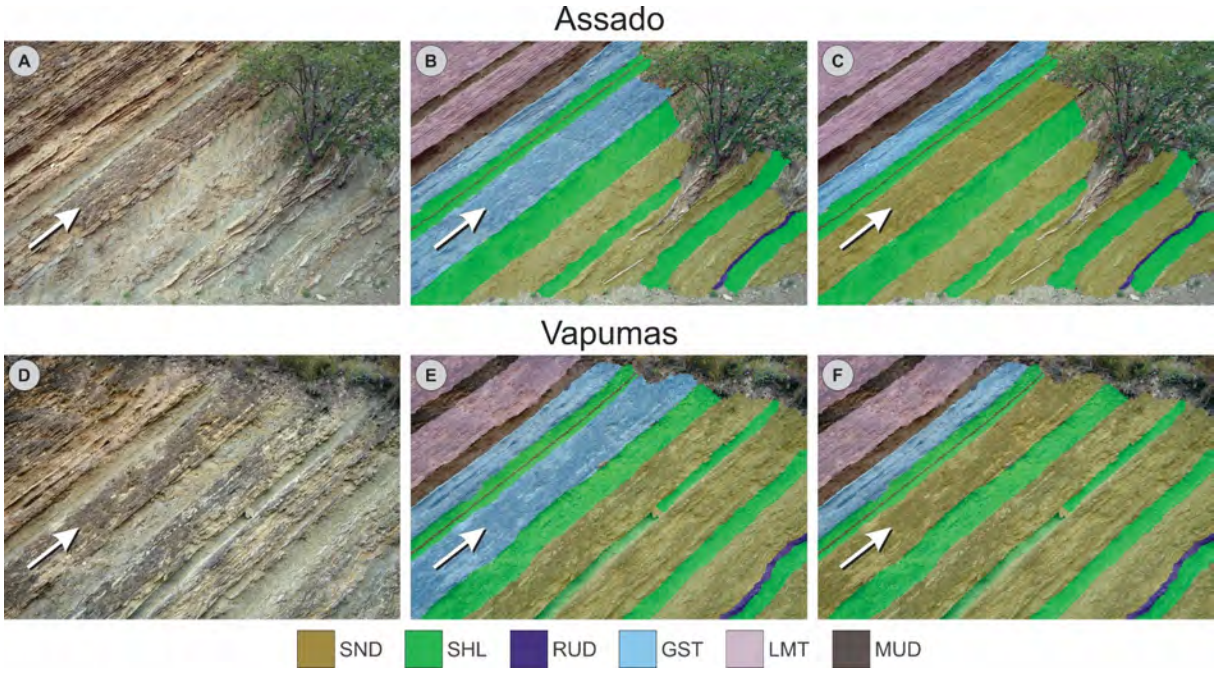


**Fig. 5.10.** Example of geological interpretation review at the Assado (A–C) and Vapumas (D–F) outcrops. Panels A and D show the original RGB images highlighting the hybrid lithofacies layer (white arrow). Panels B and E depict the initial interpretation labeling this layer as grainstone (GST). Panels C and F show the revised interpretation, with the hybrid layer relabeled as sandstone (SND).

The comparative performance metrics presented in Fig. 5.11 indicate minimal differences between the two interpretations. For Assado, overall accuracy was 82% with the hybrid layer labeled as GST and 83% when relabeled as SND. Similarly, Vapumas showed accuracies of 84% and 85%, respectively. The F1-score lines for each lithofacies class in both outcrops almost completely overlap, reflecting consistent classification performance regardless of interpretation. Although minor metric variations occur across classes, no significant changes attributable to the reinterpretation were observed.

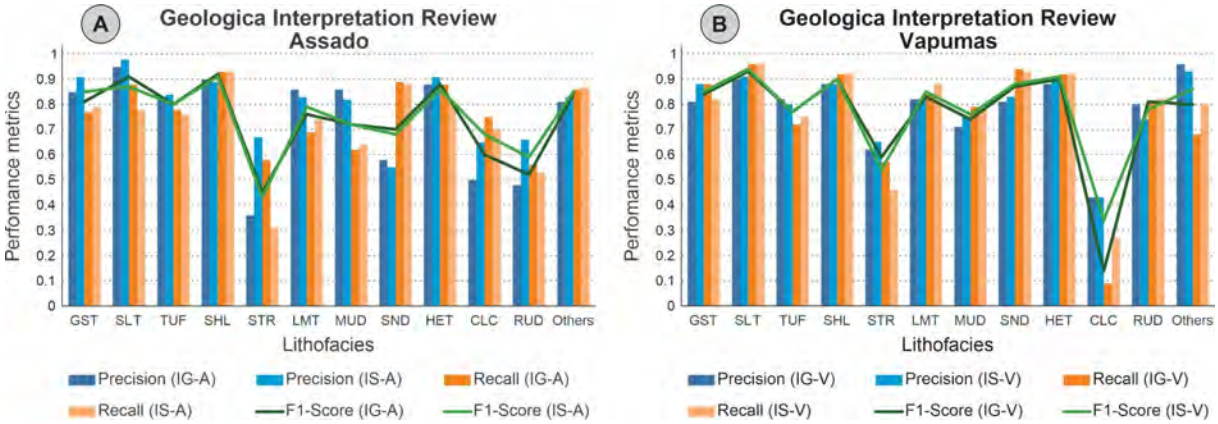


**Fig. 5.11.** Comparative classification performance metrics for the Assado (A) and Vapumas (B) outcrops, showing precision and recall (bars) and F1-score (lines) per lithofacies class. Results compare the initial geological interpretation (IG) with the revised interpretation (IS), where the hybrid layer is relabeled from GST to SND.

Given the similarity in model outcomes, the revised interpretation labeling the hybrid layer as sandstone (SND) was adopted for subsequent analyses. This decision aligns with the layer's stratigraphic position as the uppermost unit within the siliciclastic-dominated open-lake interval (see Fig. 5.2), providing a more coherent geological context for model training and classification.

### 5.4.4. Data augmentation: Effects of raw and equalized images

This section evaluates the impact of data augmentation by combining equalized and raw images on the classification performance of the CNN model for both the Assado and Vapumas outcrops. For the Assado outcrop, the model trained solely on equalized images (EQ-A) achieved an overall accuracy of 83%, which improved significantly to 90% when trained on the augmented dataset combining raw and equalized images (RQ-A). Most lithofacies exhibited increases in precision, recall, and F1-score with data augmentation, reflecting enhanced model robustness to visual variability. Notable improvements were observed in classes such as stromatolite (STR), sandstone (SND), rudstone (RUD), laminite (LMT), and mudstone (MUD). The only exception was the crystalline carbonate (CLC) class, which showed declines in all metrics, suggesting that this lithofacies is difficult to identify using the tested data augmentation approach (Fig. 5.12A).

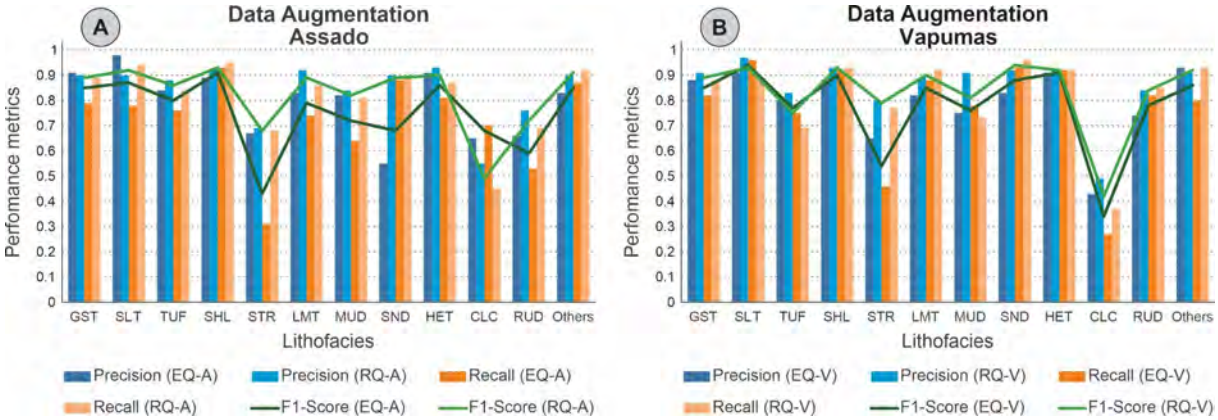


**Fig. 5.12.** Classification performance metrics for Assado (A) and Vapumas (B) outcrops comparing models trained with equalized images only (EQ) and with both raw and equalized images (RQ). Bars represent precision and recall, while lines indicate F1-scores for each lithofacies class.

Similarly, for the Vapumas outcrop, the model trained on equalized images alone (EQ-V) reached an overall accuracy of 85%, which increased to 91% with the addition of raw images

in the training set (RQ-V). The augmented dataset led to improvements in most lithofacies, including significant gains in grainstone (GST), shale (SHL), sandstone (SND), laminite (LMT), mudstone (MUD), rudstone (RUD), and stromatolite (STR), which showed the largest increase. Performance metrics remained practically unchanged for heterolith (HET), siltstone (SLT), and tuff (TUF), with slight, non-significant decreases in F1-score for SLT and TUF. Unlike Assado, the crystalline carbonate (CLC) class exhibited improvements in precision, recall and F1-score with data augmentation, with the latter rising from 0.34 to 0.42, though the values remained relatively low (Fig. 5.12B).

Overall, this data augmentation strategy demonstrates clear benefits for lithofacies classification accuracy in both outcrops, primarily by increasing the model robustness to varying visual conditions. However, it approximately doubles the computational time required for model training, which should be considered in practical applications.

### 5.4.5. 3D Point Cloud Modeling and Cross-Outcrop Test

#### 5.4.5.1. Point Cloud Generation with CNN Output

The final 3D point cloud models for the Assado and Vapumas outcrops, shown in Fig. 5.13, were generated by integrating the outputs of the optimized CNN models discussed in previous sections. These models employ classifications based on double resolution images, 100 training epochs, and labeled image proportions of approximately 10% for Assado and 7% for Vapumas. For geological consistency, the hybrid lithofacies layer was interpreted as sandstone (SND) in both outcrops. The CNN models were trained using a combination of raw and equalized images, which demonstrated the best classification performance according to the metrics evaluated.

The Assado point cloud model corresponds to the results of the RQ-A model (Fig. 5.12A), while the Vapumas model is based on the RQ-V data (Fig. 5.12B). Both dense point clouds were generated through the Multi-View Stereo (MVS) algorithm applied to the CNN classification masks, using the medium resolution setting available in Metashape (Agisoft Metashape, 2023). Subsequently, expert manual editing was performed to remove erroneously classified points (false positives); however, it is not possible to add points in areas where classifications are absent. The gaps observed in the classified point clouds correspond mainly to zones covered by vegetation, which were labeled as the ‘others’ class and excluded from the lithofacies classification.

This study focused on the Balbuena III Sequence and, although lower (Balbuena II) and upper (Balbuena IV) sequence intervals were occasionally interpreted and appear in some photographs, their classified point cloud portions were manually removed, as they fall outside this study’s scope.

As illustrated in Fig. 5.2, the Assado and Vapumas outcrops are separated by only 225 meters, supporting the expectation of strong stratigraphic correlation between them. In general, the stacking patterns in both outcrops are well preserved and correlatable. While the overall lithofacies distribution shows good lateral continuity and agreement between the two outcrop models, some expected variations are present, especially in thinner, less extensive layers such as rudstone (RUD) and stromatolite (STR). For example, five distinct RUD layers are visible in Assado compared to four in Vapumas. Vapumas displays two STR layers, whereas Assado shows only one. These observations align with prior manual geological interpretations.

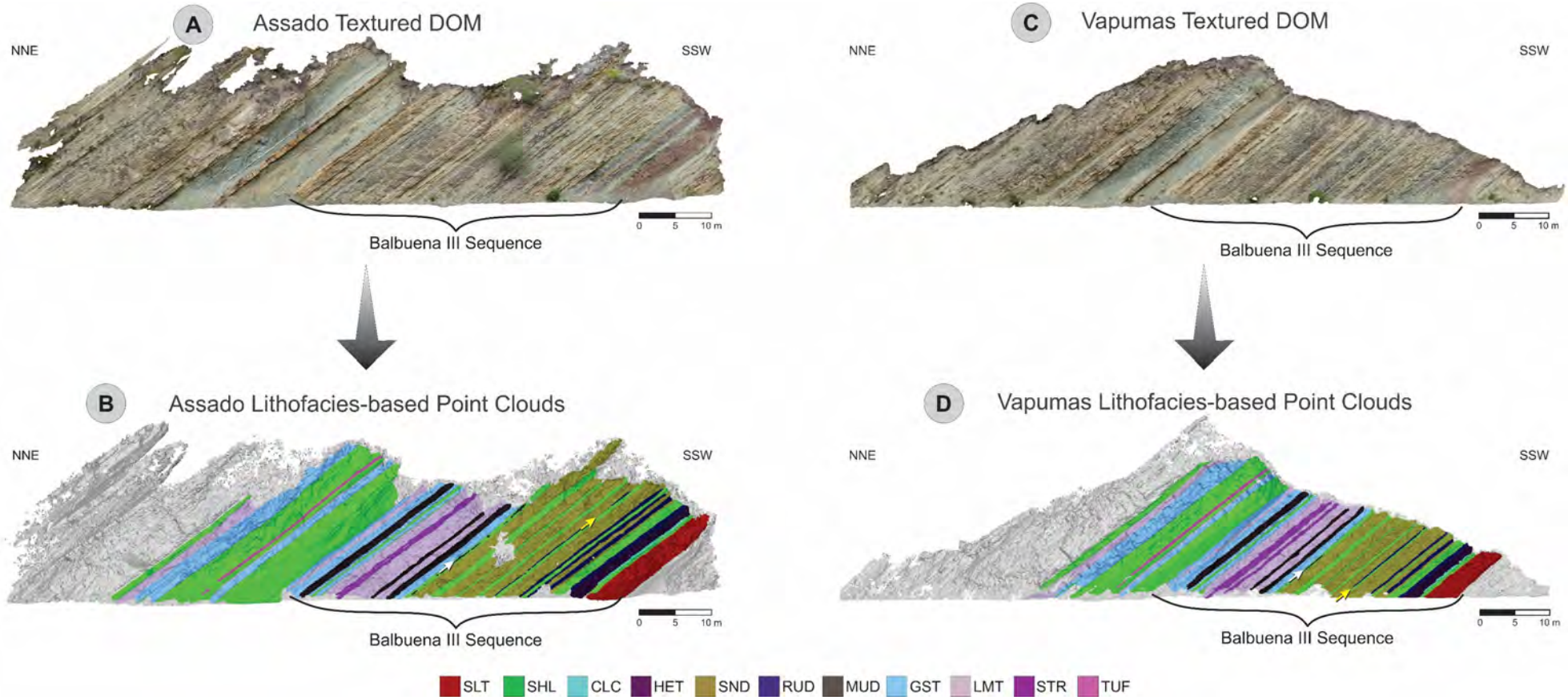


**Fig. 5.13.** Final 3D point cloud models of the Assado (panels A and B) and Vapumas (panels C and D) outcrops. Panels A and C show the textured DOMs, while panels B and D display the full classified point clouds. The white arrows mark a thin mudstone (MUD) layer within shale (SHL) that appears discontinuous in the models. The yellow arrows indicate a bioclastic rudstone (RUD) layer that also appears discontinuous in the models. Both layers are continuous in the field.

The thinner (<20 cm thick), less frequent layers posed greater challenges in accurate representation, particularly in demonstrating lateral continuity. A notable example is a thin mudstone (MUD) layer embedded within a shale (SHL) interval, marked by a white arrow in Fig. 5.13 on both models. Similarly, a bioclastic rudstone (RUD) layer, indicated by yellow arrows in the same figure, also appears discontinuous in the models, although it is continuous in the field. The crystalline carbonate (CLC) layer, despite its thinness and inherent complexity, was successfully reconstructed in both point cloud models.

### 5.4.5.2. Generalization Test Across Outcrops

The cross-outcrop generalization test evaluated the performance of the CNN model trained exclusively on the Assado dataset (RQ-A) when applied to classify the Vapumas dataset images (VA-V). This approach ensures the elimination of data leakage and bias, as the model had no prior exposure to any Vapumas images during training. The 31 manually labeled images from Vapumas were used solely for independent evaluation of the model's predictive accuracy.

Fig. 5.14 presents precision, recall, and F1-score metrics per lithofacies class for this test. The model achieved a global accuracy of 74%, with individual lithofacies performance categorized as follows: strong performance (F1 > 0.7) for grainstone (GST), shale (SHL), laminite (LMT), and sandstone (SND); moderate performance (F1 between 0.5 and 0.7) for siltstone (SLT), tuff (TUF), mudstone (MUD), and heterolith (HET); and lower performance (F1 < 0.5) for stromatolite (STR), rudstone (RUD), and crystalline carbonate (CLC).

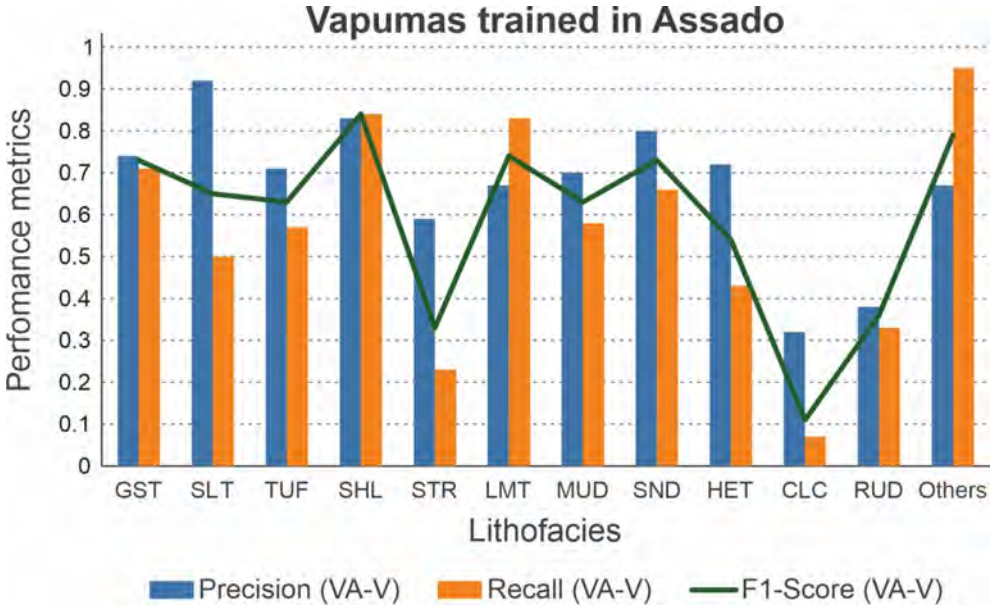


**Fig. 5.14.** Performance metrics (precision, recall, and F1-score) of the cross-outcrop test (VA-V) where the CNN model trained on Assado (RQ-A) was applied to classify Vapumas images. The overall accuracy was 74%.

While optimal lithofacies classification is achieved by training on the same outcrop, this cross-outcrop test demonstrates the method's robustness and validates that the CNN learns geological features rather than simply memorizing training data. It provides crucial evidence of the model's generalization capacity and reliability across spatially separated but geologically related datasets.

Visually comparing the final edited 3D point cloud model generated by the VA-V predictions (Fig. 5.15) with the Vapumas model trained on its own dataset (RQ-V, Fig. 5.13D), both models exhibit strong similarity in spatial distribution and recognition of major lithofacies. Some challenges persist, notably in the continuity and representation of thinner or more

complex lithofacies, such as the crystalline carbonate (CLC), which appears more fragmented in the VA-V model when examined in three dimensions.

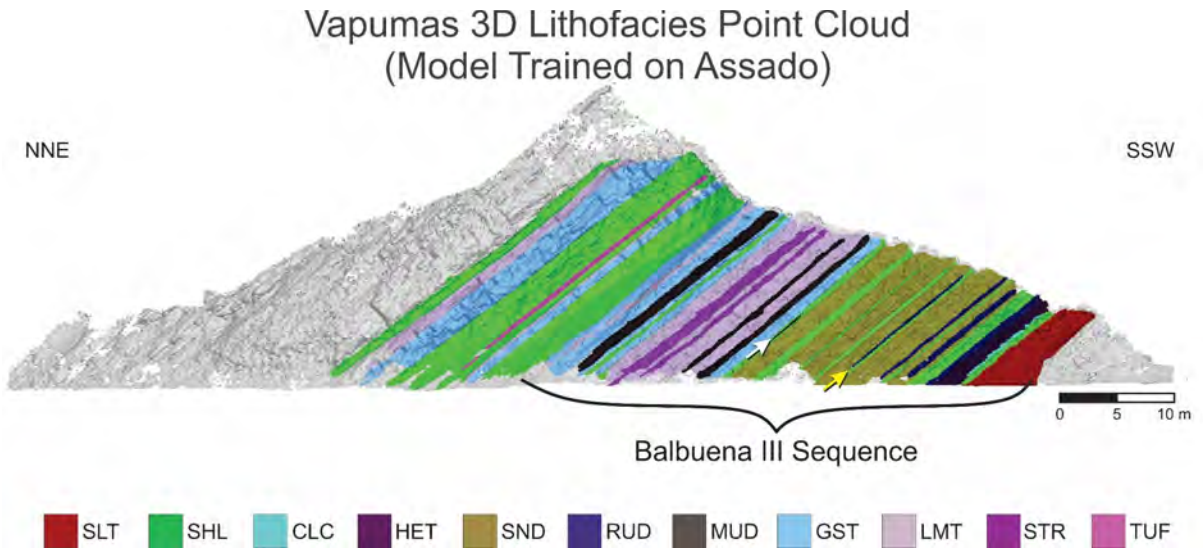


**Fig. 5.15.** Final edited 3D lithofacies point cloud model for Vapumas generated from VA-V cross-outcrop predictions. Despite some fragmentation in thin lithofacies such as crystalline carbonate (CLC), major lithofacies are well recognized compared to the Vapumas model trained on its own dataset (RQ-V, Fig. 13D). The arrows show lithofacies that appear discontinuous in the model: white indicates a thin mudstone (MUD) layer within shale (SHL); yellow indicates a bioclastic rudstone (RUD) that becomes discontinuous at both ends of the layer. Both are continuous in the field.

## 5.5. Discussion

### 5.5.1. Performance evaluation

The primary objective of this study was to define guidelines that balance model performance with computational efficiency, making CNN-based lithofacies classification feasible on standard personal computing resources. While advanced solutions such as clusters or high-performance computers (HPC) can alleviate computational demands, these resources are not always available. This work therefore establishes a practical trade-off between classification accuracy and processing time, adapted to the specific geological setting, as highlighted by Bergen et al. (2019) and Han et al. (2023).

The discussion that follows is organized into four main points: (i) the identification of optimal training parameters, (ii) the benefits of data augmentation through the integration of raw and equalized images, (iii) the cross-outcrop test as evidence of genuine model learning and generalization, and (iv) the role and limitations of different performance metrics, complemented by expert visual assessment. Together, these elements provide practical guidelines for the application of CNN-based lithofacies classification in outcrop analog studies.

The experiments conducted identified optimal parameters tailored to the requirements of this study. The combination of a double-resolution reference input (384 × 256 pixels), 100 training epochs, labeling enough images to ensure the training set covers approximately 50% of the outcrop area, and the integration of raw and equalized images proved to be an efficient and effective configuration, with no evidence of underfitting or overfitting. Importantly, the results show that rather than an ideal percentage of labeled images, the most consistent criterion is the effective coverage of training images relative to the outcrop area. In practice, this means that the number of images to be annotated must be adjusted according to outcrop size and acquisition conditions, such as the degree of image overlap.

The strategy of combining raw and equalized images yielded considerable gains in classification accuracy, increasing it by approximately 7 to 8%, without requiring additional annotation. This effectively augmented data diversity, enhancing model learning capabilities while only increasing computational runtime during execution, without additional investment in expert labor.

The cross-validation test, in which the model trained on the Assado outcrop was applied to Vapumas, confirmed that the CNN was genuinely learning discriminative patterns rather than merely memorizing training data (no data leakage occurred). This generalization capacity underscores the robustness of the method. Although pixel-level metrics decreased in this transfer scenario relative to training and testing on the same outcrop (Fig. 5.14), the final 3D lithofacies-classified point clouds (Fig. 5.13 and Fig. 5.15) exhibited remarkable similarity.

Regarding evaluation, pixel-based metrics such as accuracy, recall, and F1-score provide a quantitative measure of performance, but they only partially capture geological complexity. For example, the continuity of strata, which is a key element in geological interpretation, is not measured by these metrics and should be incorporated into future work. In this context, visual accuracy assessed by an expert becomes a valuable criterion. While subjective, this type of evaluation reflects practical geological use cases, where maintaining stratigraphic organization and enabling correlation across strata is more relevant than achieving 100% pixel-level accuracy. The results demonstrated that even when some classes presented lower F1-scores, the overall stratigraphic organization was preserved and interpretable. Manual refinement of the classified 3D point clouds also becomes a practical advantage of expert validation, since in this study approximately four hours were sufficient to refine an entire outcrop, whereas labeling a single image with the lithofacies complexity of SBIII required at least the same amount of time. This highlights the advantage of minimizing labeled data, as point cloud corrections provide a faster and more effective way to ensure reliable model performance than expanding image-level annotation.

### 5.5.2. Geological implications

Beyond defining parameter guidelines, the results also provide insights into how CNN-based classification handles different lithofacies characteristics within the Balbuena III Sequence. Even though F1-scores above 0.7 were obtained for most lithofacies in both outcrops (Fig. 5.12), some lithofacies, such as crystalline carbonate (CLC), bioclastic rudstones (RUD), and stromatolites (STR), showed lower performance. These aspects are addressed here in relation to two key challenges: (i) thin lithofacies layers and (ii) complex geometries. A third point of discussion highlights (iii) variations in facies patterns. Together, these elements underscore the geological implications of the proposed workflow for sedimentological and stratigraphic interpretation in DOMs.

Thin lithofacies layers, particularly those thinner than 20 cm, represent one of the most critical challenges. RUD, CLC, and volcanic tuff (TUF) correspond to thin units, and their recognition is directly affected by the image downscaling applied in this study. With an effective resolution of about 3.4 cm/pixel, strata thinner than 15–30 cm (5–10 pixels) are less reliably represented, constraining the detection of fine layers. Within this context, CLC was the lithofacies with the lowest performance metrics, particularly in the Vapumas outcrop. This layer has special importance as it marks the Cretaceous–Paleogene (K/Pg) boundary. Precisely for this reason, CLC was deliberately maintained in the labeling despite its reduced thickness. The results show that it was more effectively identified in the Assado outcrop, where it is slightly thicker, but even in the cross-outcrop validation model (Fig. 5.15) it was successfully reconstructed, enabling recognition of the K/Pg boundary event within the classified 3D point

clouds. Similarly, RUD layers were recognized in the point clouds where they occur, although their continuity was not always preserved (e.g., white and yellow arrows in Fig. 5.13B, D and Fig. 5.15). In contrast, TUF exhibited different behavior: although thin, it was consistently detected, likely due to its distinctive whitish color contrasting with the surrounding dark shale (SHL).

Complex geometries also represent a challenge for CNN classification. STR exemplifies this difficulty, as it may occur as laterally continuous biostromes or as isolated bioherms interbedded with or laterally transitioning into laminite (LMT) (Roemers-Oliveira et al., 2015). This variability in geometry, size, and distribution, combined with limited color contrast, complicates its representation both in CNN-based classification and in photogrammetric reconstructions. The observed variability in STR detection suggests that further methodological refinements may be required to fully capture its spatial complexity.

Finally, facies with transitional patterns highlight the interpretative dimension of lithofacies classification. The hybrid sandstone layer initially labeled as grainstone (GST) illustrates this case. Geological data inherently involve interpretational choices, and revisiting these interpretations is often necessary to ensure methodological consistency and geological coherence (Bergen et al., 2019; Karpatne et al., 2019). Initially labeled as GST, the hybrid layer exhibited ambiguous predictions in the CNN outputs, as reported by Roemers-Oliveira et al. (2025), sometimes appearing as GST, sometimes as sandstone (SND), including lateral transitions between these facies. A subsequent reinterpretation aligned the classification with SND, consistent with its stratigraphic position within the siliciclastic-dominated open-lake interval. Performance tests showed only minor differences between the two labeling strategies, indicating that geological knowledge should guide such decisions rather than small variations in quantitative metrics. This underlines the importance of integrating CNN-based classifications with field and laboratory observations.

Taken together, these results demonstrate that CNN-based workflows, while methodologically optimized, also yield relevant geological implications. Strategies can be adapted depending on the main objectives of the study. In the case of SBIII, the applied workflow enabled the generation of lithofacies-classified 3D point clouds that preserve key stratigraphic markers while also revealing challenges in representing thin and complex lithofacies.

## 5.6. Conclusions

This study established guidelines that optimize the balance between classification accuracy and computational efficiency in CNN-based lithofacies classification from outcrop imagery. Systematic testing of image resolution, training duration, labeling proportions, geological interpretation strategies, and data augmentation showed that a supervised CNN workflow can be applied on standard computing resources while still producing geologically coherent and spatially consistent 3D lithofacies-classified point clouds. The optimized configuration, which combined images at double the reference resolution, 100 training epochs, training images covering about half of the outcrop area, and the integration of raw and equalized images, proved to be a robust strategy that enhances performance and reduces annotation effort.

Beyond methodological advances, the results highlighted key geological implications. The workflow preserved the lateral continuity of major lithofacies and revealed the limitations posed by thin and complex geometries. It also reinforced the interpretative dimension of lithofacies labeling, showing that geological reasoning remains essential when addressing ambiguous cases, as exemplified by the reinterpretation of the hybrid layer.

Although the framework proved effective for the Balbuena III Sequence, broader applicability to other depositional systems or more heterogeneous stratigraphic contexts remains to be tested. Potential improvements for future work include more systematic strategies for image selection to ensure that labeled datasets capture the full range of facies and their textural and color variations, and the development of new performance metrics that better reflect geological coherence. Alternative machine learning strategies such as semi-supervised and active learning also represent promising directions. Semi-supervised learning combines a small set of labeled data with a larger pool of unlabeled samples to improve model performance, while active learning directs expert annotation toward the most informative images selected by the algorithm, optimizing the use of limited ground-truth data.

In summary, this work provides a practical guideline for applying CNN-based classification in 3D DOMs, demonstrating how optimized configurations enhance performance while minimizing annotation requirements. While challenges remain, the approach contributes to scalable digital workflows that complement traditional fieldwork and support both academic and applied studies of outcrop analogs.

## Acknowledgments

The authors gratefully acknowledge Petrobras (Brazil) for sponsoring the PhD research of the first author, and CEREGE/Aix-Marseille Université (France) for providing the M.Sc. scholarship of the second author. The acquisition of the imagery used in this study was funded through a cooperation agreement between Petrobras and Unipampa, supported by the Brazilian National Agency of Petroleum, Natural Gas and Biofuels (ANP), No. 0050.0121770.22.9 (SIGITEC 2022/00056–5). Special thanks to GEOMAP (Argentina) for supporting the fieldwork activities.

## References

Adobe Inc, 2024. Adobe Photoshop v25.1.0 (Version 25.1.0) [software]. https://photoshop.adobe.com

Agisoft Metashape, 2023. Agisoft Metashape Professional v2.0.1 (Version 2.0.1) [software]. https://www.agisoft.com

Bergen, K.J., Johnson, P.A., de Hoop, M. V., Beroza, G.C., 2019. Machine learning for data-driven discovery in solid Earth geoscience. Science 363. https://doi.org/10.1126/science.aau0323

Bianucci, H., Acevedo, O., Cerdán, J., 1981. Evolución tectono-sedimentaria del Grupo Salta en la subcuenca de Lomas de Olmedo (Provincias de Salta y Formosa), in: VIII Congreso Geológico Argentino. Servicio Geológico Nacional, San Luis, pp. 159–172.

Bistacchi, A., Mittempergher, S., Martinelli, M., 2022. Digital Outcrop Model Reconstruction and Interpretation, in: Bistacchi, A., Massironi, M., Viseur, S. (Eds.), 3D Digital Geological Models: From Terrestrial Outcrops to Planetary Surfaces. Wiley, pp. 11–32. https://doi.org/https://doi.org/10.1002/9781119313922.ch2

Cheng, G., Guo, W., 2017. Rock images classification by using deep convolution neural network, in: Journal of Physics: Conference Series. Institute of Physics Publishing, p. 012089. https://doi.org/10.1088/1742-6596/887/1/012089

Falivene, O., Auchter, N.C., de Lima, R.P., Kleipool, L., Solum, J.G., Zarian, P., Clark, R.W., Espejo, I., 2022. Lithofacies identification in cores using deep learning segmentation and

the role of geoscientists: Turbidite deposits (Gulf of Mexico and North Sea). AAPG Bulletin 106, 1357–1372. https://doi.org/10.1306/03112221015

Fan, G., Chen, F., Chen, D., Dong, Y., 2020. Recognizing multiple types of rocks quickly and accurately based on lightweight CNNs model. IEEE Access 8, 55269–55278. https://doi.org/10.1109/ACCESS.2020.2982017

Furukawa, Y., Hernández, C., 2015. Multi-View Stereo: A Tutorial. Foundations and Trends® in Computer Graphics and Vision 9, 1–148. https://doi.org/10.1561/0600000052

Gómez Omil, R.J., Boll, A., 1999. Sistema petrolero de la cuenca cretácica del noroeste argentino, in: IV Congreso de Exploración y desarrollo de hidrocarburos. IAPG, Mar del Plata, pp. 101–112.

Goodfellow, I., Bengio, Y., Courville, A., 2016. Deep Learning. MIT Press, Cambridge, MA.

Guadagnin, F., Gonçalves, Í.G., Roemers-Oliveira, E., Guedes, P.L., de Souza, E.G., Silveira, M. de M.L., Raja Gabaglia, G.P., Arienti Gonçalves, L., Oliveira, L.F.R. de, Selk, R., 2025. Building of classified 3D point clouds of outcrop with automatically segmented images. Geodata and AI 4, 100024. https://doi.org/10.1016/j.geoai.2025.100024

Han, W., Zhang, Xiaohan, Wang, Yi, Wang, L., Huang, X., Li, J., Wang, S., Chen, W., Li, X., Feng, R., Fan, R., Zhang, Xinyu, Wang, Yuewei, 2023. A survey of machine learning and deep learning in remote sensing of geological environment: Challenges, advances, and opportunities. ISPRS Journal of Photogrammetry and Remote Sensing 202, 87–113. https://doi.org/10.1016/j.isprsjprs.2023.05.032

Hernández, R., Echavarria, L., 2009. Faja Plegada y Corrida Subandina del Noroeste Argentino: Estratigrafía, Geometría y Cronología de la Deformación. Revista de la Asociación Geológica Argentina 65, 68–80.

Hernández, R.M., Disalvo, A., Boll, A., Gómez Omil, R., Gallli, C., 1999. Estratigrafia secuencial del Grupo Salta, con enfasis en las subcuencas de Metan-Alemania, noroeste Argentino, in: Bonorino, G.G., Omarini, R., Viramonte, J. (Eds.), Geología del Noroeste Argentino, Relatorio del XIV Congreso Geológico Argentino. pp. 263–283.

Hernández, R.M., Omil, G.R., Boll, A., 2008. Estratigrafía, Tectónica y Potencial petrolero del rift cretácico em la Provincia de Jujuy, in: XVII Congreso Geológico Argentino. Asociación Geológica Argentina, Jujuy, pp. 207–232.

Hubel, D.H., Wiesel, T.N., 1968. Receptive fields and functional architecture of monkey striate cortex. The Journal of Physiology 195, 215–243. https://doi.org/10.1113/jphysiol.1968.sp008455

Karpatne, A., Ebert-Uphoff, I., Ravela, S., Babaie, H.A., Kumar, V., 2019. Machine Learning for the Geosciences: Challenges and Opportunities. IEEE Transactions on Knowledge and Data Engineering 31, 1544–1554. https://doi.org/10.1109/TKDE.2018.2861006

Keidel, J., 1921. Sobre la distribución de los depósitos glaciares del Permico conocidos en la Argentina y su significación para la estratigrafia de la serie del Gondwana y la paleogeografia del Hemisferio Austral. Boletim da Academia Nacional de Ciencias 25, 239–368.

Koeshidayatullah, A., Morsilli, M., Lehrmann, D.J., Al-Ramadan, K., Payne, J.L., 2020. Fully automated carbonate petrography using deep convolutional neural networks. Marine and Petroleum Geology 122, 104687. https://doi.org/10.1016/j.marpetgeo.2020.104687

Krizhevsky, A., Sutskever, I., Hinton, G.E., 2012. ImageNet classification with deep convolutional neural networks, in: Advances in Neural Information Processing Systems (NeurIPS 25). pp. 1097–1105. https://doi.org/10.1145/3065386

LeCun, Y., Boser, B.E., Denker, J.S., Henderson, D., Howard, R.E., Hubbard, W.E., Jackel, L.D., 1989. Handwritten Digit Recognition with a Back-Propagation Network, in: Touretzky, D. (Ed.), Advances in Neural Information Processing Systems 2. Denver, pp. 396–404.

LeCun, Y., Bottou, L., Bengio, Y., Haffner, P., 1998. Gradient-based learning applied to document recognition. Proceedings of the IEEE 86, 2278–2324. https://doi.org/10.1109/5.726791

Lowe, D.G., 2004. Distinctive Image Features from Scale-Invariant Keypoints. International Journal of Computer Vision 60, 91–110. https://doi.org/https://doi.org/10.1023/B:VISI.0000029664.99615.94

Malik, O.A., Puasa, I., Lai, D.T.C., 2022. Segmentation for Multi-Rock Types on Digital Outcrop Photographs Using Deep Learning Techniques. Sensors 22, 8086. https://doi.org/10.3390/s22218086

Manning, C.D., Raghavan, P., Schütze, H., 2009. Introduction to Information Retrieval, 2nd ed. Cambridge University Press, Cambridge, UK.

Marquillas, R., Del Papa, C., Sabino, I., Heredia, J., 2003. Prospección del límite K/T en la cuenca del Noroeste, Argentina. Revista de la Asociación Geológica Argentina 58, 271–274.

Marquillas, R.A., Del Papa, C., Sabino, I.F., 2005. Sedimentary aspects and paleoenvironmental evolution of a rift basin: Salta Group (Cretaceous-Paleogene), northwestern Argentina. International Journal of Earth Sciences 94, 94–113. https://doi.org/10.1007/s00531-004-0443-2

Marquillas, R.A., Salfity, J.A., Matthews, S.J., Matteini, M., Dantas, E., 2011. U-Pb zircon age of the Yacoraite Formation and its significance to the Cretaceous-Tertiary boundary in the Salta Basin, Argentina. Cenozoic Geology of the Central Andes of Argentina 227–246.

Powers, D.M.W., 2011. Evaluation: From precision, recall and F-measure to ROC, informedness, markedness & correlation. Article in Journal of Machine Learning Technologies 2, 37–63. https://doi.org/10.9735/2229-3981

Python, 2023. Python v3.11.4 (Version 3.11.4) [software]. https://www.python.org/

Ramos, V.A., 1988. The tectonics of the Central Andes: 30o to 33o latitude, in: Clark, S., Burchfiel, D. (Eds.), Processes In Continental Litospheric Deformation. The Geological Society of America, pp. 31–54.

Roemers-Oliveira, E., Fernandes, L.A., Bento Freire, E., Amarante Simões, L.S., 2015. Microbial filaments in stromatolites and laminites of Balbuena III Sequence (Maastrichtian/Danian) of Yacoraite Formation in Metán-Alemania Sub-basin, Salta region, Argentina, and its palaeoenvironmental significance. Brazilian Journal of Geology 45, 399–413. https://doi.org/10.1590/2317-488920150030255

Roemers-Oliveira, E., Viseur, S., Fournier, F., Gonçalves, Í.G., Guadagnin, F., Raja Gabaglia, G.P., Bento Freire, E., Fragoso, D.G.C., Hernández, J., Freccia, A.C., de Godoy Rangel, G., 2025. Advanced digital techniques applied to outcrop models: Integrating Local Binary Pattern (LBP) and Convolutional Neural Network (CNN) to support stratigraphic and

sedimentological interpretation of reservoir analogs in the Salta Basin, Argentina. Marine and Petroleum Geology. https://doi.org/10.1016/

Ronneberger, O., Fischer, P., Brox, T., 2015. U-Net: Convolutional Networks for Biomedical Image Segmentation, in: Navab, N., Hornegger, J., Wells, W.M., Frangi, A.F. (Eds.), 18th International Conference on Medical Image Computing and Computer-Assisted Intervenction - MICCAI. Springer International Publishing, Switzerland, pp. 234–241. https://doi.org/10.1007/978-3-319-24574-4_28

Sato, R., Kikuchi, K., Naruse, H., 2025. Automatic facies classification using convolutional neural network for three-dimensional outcrop data: Application to the outcrop of the mass-transport deposit. AAPG Bulletin 109, 271–286. https://doi.org/10.1306/12162423082

Shorten, C., Khoshgoftaar, T.M., 2019. A survey on Image Data Augmentation for Deep Learning. Journal of Big Data 6, 60. https://doi.org/10.1186/s40537-019-0197-0

Souza, J.F.L., Santana, G.L., Batista, L. V., Oliveira, G.P., Roemers-Oliveira, E., Santos, M.D., 2020. CNN Prediction Enhancement by Post-Processing for Hydrocarbon Detection in Seismic Images. IEEE Access 8, 120447–120455. https://doi.org/10.1109/ACCESS.2020.3005916

TensorFlow, 2024. TensorFlow v2.18.0 (Version 2.18.0) [software]. https://www.tensorflow.org

Turner, J.C.M., 1958. Estratigrafía del Cordón de Escaya y de la Sierra de Rinconada (Jujuy). Revista De La Asociación Geológica Argentina 13, 15–41.

Villafañe, P.G., Frías-Saba, R. del C., Della-Vedova, M., Citton, P., Díaz-Martínez, I., de Valais, S., Aceñolaza, F.G., Marquillas, R.A., Cónsole-Gonella, C., 2022. Microbialitic deposits of the Yacoraite Formation, NW Argentina: distribution, environments, paleoecology, and economic implications. Brazilian Journal of Geology 52. https://doi.org/10.1590/2317-4889202220210088

Westoby, M.J., Brasington, J., Glasser, N.F., Hambrey, M.J., Reynolds, J.M., 2012. “Structure-from-Motion” photogrammetry: A low-cost, effective tool for geoscience applications. Geomorphology 179, 300–314. https://doi.org/10.1016/j.geomorph.2012.08.021

*La Route –Le Mur d'enceinte, Paul Cézanne, c. 1875-1876, via Wikimedia Commons.*

*« L'invisible est réel. »*

*Alfred de Vigny, La Maison du berger (1844)*

# Chapter 6
# Hyperspectral

This chapter is based on an article in preparation, for which the target journal will soon be defined.

# Outcrop-based hyperspectral data for lithofacies discrimination in lacustrine deposits in the Salta Basin, Argentina

Eduardo Roemers-Oliveira[1,2*], Sophie Viseur[1], Marcos Rafael Nanni[3], Felipe Guadagnin[4], Ítalo Gomes Gonçalves[4], Guilherme de Godoy Rangel[4], Caio Almeida[3], Lorenzo D'Angelo[1], François Fournier[1], Anderson de Lima Gonçalves[3], Guilherme Pederneiras Raja Gabaglia[2], Juan Hernández[5]

[1]Aix Marseille Université, CNRS, IRD, INRAE, CEREGE, Aix-en-Provence, France
[2]Petrobras – Petróleo Brasileiro S.A, Rio de Janeiro, Brazil
[3]Universidade Estadual de Maringá, GALeS, Maringá, Brazil
[4]Universidade Federal do PAMPA, Caçapava do Sul, Brazil
[5]Geomap, Salta, Argentina

## Abstract

Hyperspectral imaging (HSI) is increasingly used for lithological mapping, yet most outcrop applications assume full visible to shortwave infrared (VNIR–SWIR) coverage (450–2500 nm), while cases restricted to partial wavelength intervals remain underexplored. This study evaluates whether near-infrared imagery restricted to 900–1700 nm can discriminate and map lacustrine lithofacies in the Balbuena III Sequence (SBIII), Salta Basin, Argentina, based on two outcrops (Vapumas and Assado). Full-range field spectroradiometer measurements (450–2500 nm) defined lithofacies spectral behavior, and Linear Discriminant Analysis (LDA) successfully discriminated the ten SBIII lithofacies under ideal spectral coverage. For the restricted imagery, spectra from regions of interest in Vapumas were used to train supervised models, LDA and a Multilayer Perceptron (MLP), which were subsequently applied to Vapumas and Assado, with k-means serving as an unsupervised baseline. Hierarchical Agglomerative Clustering (HAC) identified distinct patterns within the limited range and guided the definition of three lithological groups. Classified 2D maps generated on four hyperspectral cubes reproduced stratified architecture, revealed within-facies heterogeneity, and showed that Vapumas-trained models successfully generalized to Assado. The study provides a practical workflow for partial-coverage HSI by establishing spectral references, using unsupervised analysis to define distinct groups, and applying models to classify hyperspectral cubes. Although restricted-range HSI omits key bands (~2150–2260 nm for clays and ~2315–2350 nm for carbonates) and cannot fully resolve fine mineralogical variability, it still yields geologically coherent facies divisions after lithotype regrouping, providing a scalable basis for future 3D, facies-based modeling.

**Keywords:** Digital outcrop models; Hyperspectral imaging; Lithofacies discrimination; Lacustrine facies; Salta Basin.

## 6.1. Introduction

Spectroscopy is the study of the interaction between matter and electromagnetic radiation, where materials can be identified by their unique spectral absorption features (Krupnik and Khan, 2019). This principle underpins its growing role in mineralogical identification and mapping, for which the visible to shortwave infrared (VNIR–SWIR, 0.4–2.5 μm) range has proven crucial for capturing diagnostic bands of several minerals (van der Meer et al., 2012; Ghamisi et al., 2017; Peyghambari and Zhang, 2021). Within this range, the visible and near-

infrared (VNIR, 400–1000 nm) domains are governed by absorption features that are particularly diagnostic for iron oxides and hydroxides such as hematite and goethite. In contrast, the shortwave infrared (SWIR, 1000–2500 nm) allows the detection of water, metal–OH bend combinations, clay minerals, and carbonate varieties (Ghamisi et al., 2017; Krupnik and Khan, 2019; Koerting et al., 2024). While VNIR–SWIR spectroscopy remains the most widely applied for mineral and lithological characterization, recent studies have also explored the mid-wave and long-wave infrared (MWIR and LWIR) ranges (e.g., Gairola et al., 2024; Thiele et al., 2025).

Hyperspectral imaging (HSI) builds on these principles by acquiring data in hundreds of continuous spectral bands, generating a spectral curve for each pixel (Krupnik and Khan, 2019). While experimental developments date back to the 1970s, the launch of NASA's Hyperion EO-1 in 2000, with 242 spectral bands, marked a turning point by making hyperspectral remote sensing broadly accessible (van der Meer et al., 2012; Peyghambari and Zhang, 2021). Since then, applications have diversified across scientific and applied domains, with geoscience studies in particular showing a marked increase over the past decade (Krupnik and Khan, 2019).

Within geosciences, HSI has been increasingly applied to mineralogical characterization, with growing but more limited applications to lithological studies. Key areas of focus include mineral exploration (e.g., Bedini, 2011; Kurz et al., 2012; Salehi et al., 2018; Galdames et al., 2019; Krupnik and Khan, 2019; Sun et al., 2019), clay mineral discrimination (e.g., Murphy et al., 2015; Attallah et al., 2024), and the distinction of carbonate phases such as calcite, dolomite, and diagenetic varieties (e.g., Buckley et al., 2013; McCormick et al., 2021; Kurz et al., 2022; Camargo et al., 2023; Gairola et al., 2024). Within this context, hyperspectral applications involve both non-imaging spectroradiometers (e.g., Souza et al., 2018; Camargo et al., 2023), imaging sensors that provide spatial and spectral information (e.g., Kurz et al., 2013; Galdames et al., 2019; Jacq et al., 2022; Thiele et al., 2021; Thiele et al., 2022a), and workflows combining both approaches (e.g., Kurz et al., 2022).

HSI is increasingly regarded as a valuable tool in field-based geological studies, particularly for mapping mineral and chemical variations in inaccessible, high, or near-vertical outcrops extending over kilometers (Kurz et al., 2013). Nevertheless, significant challenges remain, including data quality (spatial resolution and signal-to-noise ratio), the complexity of calibration and processing, and redundancy among bands, all of which continue to drive ongoing research and technological development (van der Meer et al., 2012; Ghamisi et al., 2017; Peyghambari and Zhang, 2021). In addition to these well-recognized technical challenges, the spectral coverage of the data itself can represent a critical limitation. Most hyperspectral applications in geosciences have relied on the full VNIR–SWIR range (400–2500 nm), where the majority of diagnostic mineral absorption features occur. By contrast, the potential to discriminate and map lithofacies using restricted spectral intervals has received little attention, considering that in many practical contexts only partial wavelength coverage can be available. This is particularly relevant when using lighter and less expensive sensors, which may represent the only feasible option in certain applications, such as Remotely Piloted Aircraft Systems (RPAS)-based surveys.

This study focuses on the Balbuena III Sequence (SBIII) of the Salta Basin, in the Metán–Alemanía sector (NW Argentina), an interval comprising a diverse set of lacustrine lithofacies, including siliciclastic, carbonate, hybrid, and volcaniclastic types. Two reference outcrops, Vapumas and Assado (Fig. 6.1), were selected, where SBIII is well exposed and has been previously characterized in detail sedimentologically and stratigraphically by Roemers-Oliveira et al. (2025). Point-based field spectroscopy (portable spectroradiometer, 450–2500 nm) was acquired to characterize the hyperspectral behavior of lithologies. Building on this reference

dataset, the study evaluates the potential of hyperspectral imaging for lithofacies identification and mapping under constrained spectral conditions, since the available imagery spans only the 900–1700 nm range. Although this interval excludes many diagnostic features commonly exploited in VNIR–SWIR spectroscopy, it retains absorption characteristics and reflectance intensity variations that can be leveraged for lithological discrimination. Within this framework, supervised discriminant methods, including Linear Discriminant Analysis (LDA) and Multilayer Perceptron (MLP), together with unsupervised K-means clustering, were applied alongside 2D mapping of hyperspectral cubes to assess classification performance across these two outcrops.

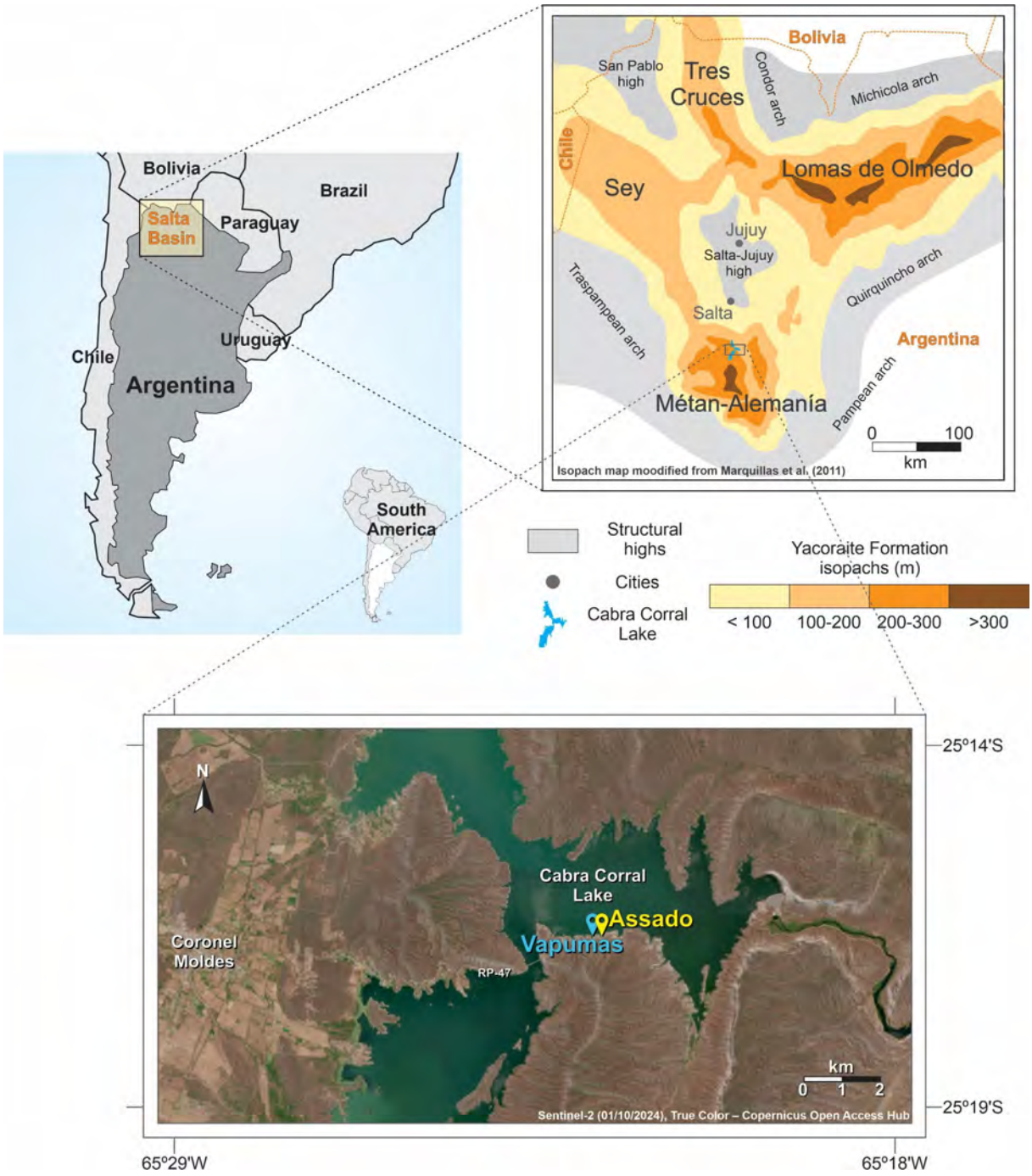


**Fig. 6.1.** Location of the Vapumas (25°16′39″S, 65°22′34″W) and Assado (25°16′38″S, 65°22′26″W) outcrops near Cabra Corral Lake, Salta Province, Argentina. Main panel: Sentinel-2 True Color image showing outcrops along RP-47. Upper right: isopach map of the Yacoraite Formation, highlighting carbonate thickness variations after Marquillas et al. (2011).

## 6.2. Geological setting

Located primarily in northwestern Argentina and extending into parts of Bolivia and Paraguay, the Salta Basin (Turner, 1958; Marquillas et al., 2005) spans approximately 150,000 km² and contains a sedimentary succession exceeding 5,000 m in thickness (Del Papa and Salfity, 1999). Its evolution reflects Cretaceous rifting linked to the Gondwana breakup, followed by a transition to compressional tectonics during the Eocene Andean orogeny (Hernández and Echavarria, 2009).

The basin's architecture includes several sub-basins (Marquillas et al., 2005), with the Metán–Alemanía Sub-basin, the southernmost sector of the basin, serving as the study area. The sedimentary infill is traditionally divided into syn-rift and post-rift phases. The former comprises fault-controlled depocenters developed during the Cretaceous, while the latter, beginning in the Maastrichtian, is associated with thermal subsidence and widespread tabular deposition (Del Papa and Salfity, 1999; Salfity and Marquillas, 1999; Hernández et al., 1999). A central uplift, the Salta–Jujuy Arch, remained exposed until the late Danian (Gómez Omil and Boll, 1999, 2005). Interpretations diverge regarding the continuity of the post-rift phase into the Paleocene, with some authors proposing a renewed extensional episode termed the Pre-Olmec Phase (e.g., Gómez Omil et al., 1989; Gómez Omil and Boll, 1999), while others consider it part of a prolonged sag phase (e.g., Reyes and Salfity, 1973; Marquillas et al., 2005).

Stratigraphically, the Salta Group encompasses Cretaceous to Paleogene units and includes the Pirgua, Balbuena, and Santa Bárbara subgroups (Moreno, 1970; Reyes and Salfity, 1973). These units can be grouped into supersequences within a sequence stratigraphic framework (Bianucci et al., 1981; Hernández et al., 1999). The Balbuena Supersequence, deposited during the post-rift phase, comprises four sequences, Balbuena I, II, III, and IV (Boll, 1991; Hernández et al., 1999, 2008), and is characterized by lacustrine strata exhibiting a cyclic pattern and strong lateral continuity, with depositional sequences traceable over tens of kilometers (e.g., Hernández et al., 1999; Bento Freire, 2012; Pedrinha et al., 2015; Roemers-Oliveira et al., 2025).

The Balbuena III Sequence (SBIII) ranges from 28 to 33 m in thickness and comprises carbonate, siliciclastic, and hybrid deposits accumulated in a lacustrine setting, where climate exerted a primary influence on sedimentation. Its lithofacies include carbonate facies such as oolitic and bioclastic grainstones and packstones, rudstones, floatstones, carbonate mudstones, laminites, and stromatolites; siliciclastic facies consisting of very fine-grained wavy sandstones, siltstones, and clay-rich mudstones; and hybrid facies represented by hybrid sandstones and marls. These lithofacies are grouped into four facies associations that reflect distinct hydrodynamic conditions and paleogeographic settings. Associations linked to open lake systems include both marginal and profundal settings, characterized mainly by mixed and siliciclastic deposits. In contrast, closed lake associations are dominated by carbonate facies, deposited under more evaporative and hydrologically restricted environments (Roemers-Oliveira et al., 2025).

Vertically, the lithofacies show the recurrence of two elementary sequences, expressed as transgressive–regressive (T–R) successions. This stratigraphic organization exhibits high-, medium-, and low-frequency cyclicity, with individual sequences traceable laterally for several tens of kilometers across the basin (Roemers-Oliveira et al., 2025). This stratigraphic arrangement is synthesized in Fig. 6.2, which illustrates how climatic-driven base-level variations controlled the alternation between siliciclastic- and carbonate-dominated successions within the SBIII.

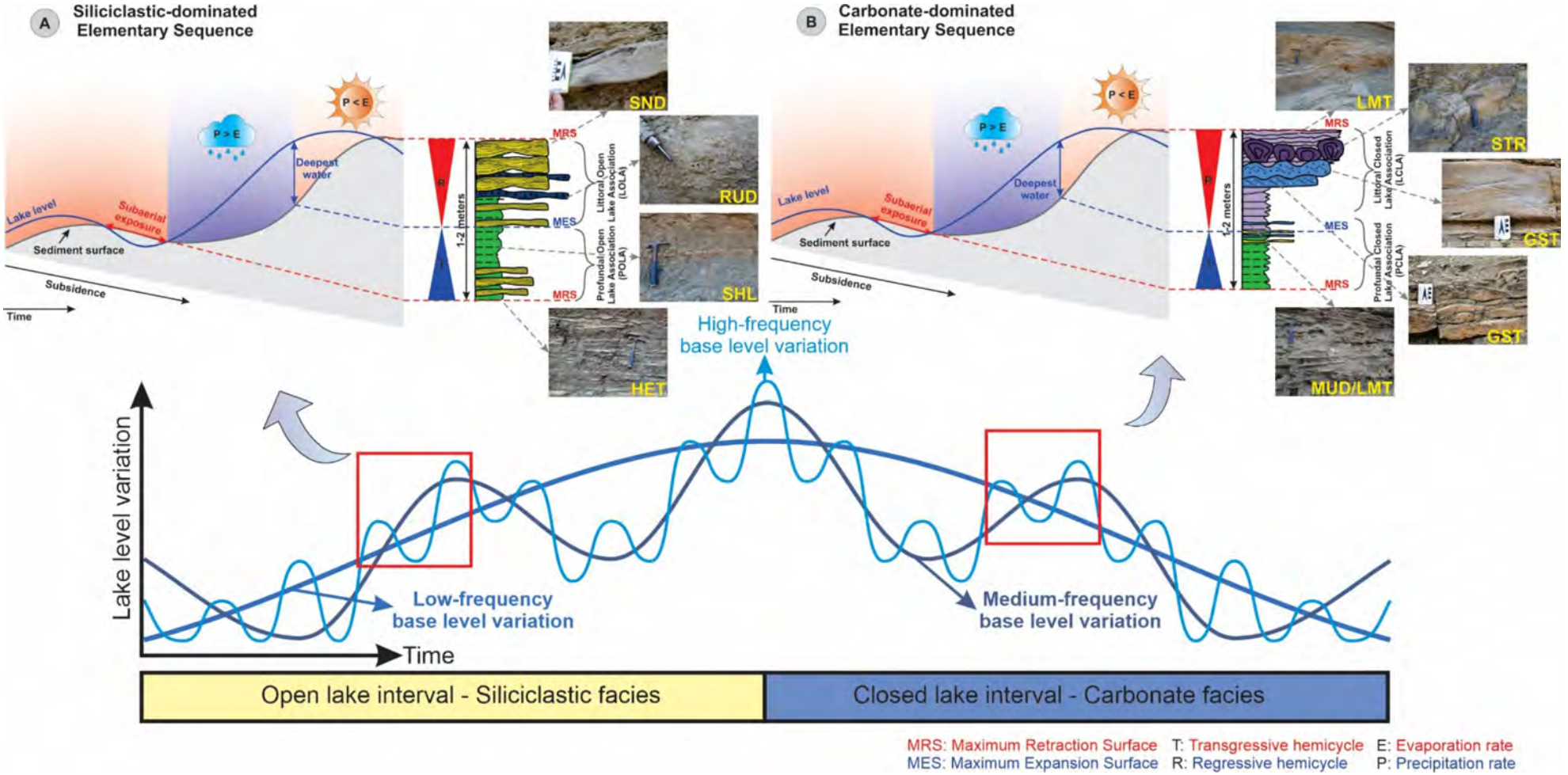


**Fig. 6.2.** Schematic representation of the stratigraphic organization and cyclicity of the Balbuena III Sequence (SBIII) in the study area. SBIII consists of recurrent transgressive–regressive (T–R) elementary sequences, reflecting climatically driven base-level variations. The lower interval (A) is dominated by siliciclastic facies linked to open lake conditions, whereas the upper portion (B) is characterized by carbonate-rich facies related to closed lake settings. This stacking pattern expresses high-, medium-, and low-frequency cyclicity through systematic vertical changes in facies proportions and depositional conditions. Facies codes: SND = sandstone, RUD = rudstone, SHL = shale, HET = heterolithic facies (sandstone–siltstone interbeds), LMT = laminite, STR = stromatolite, GST = grainstone, MUD = carbonate mudstone.

The absence of coarser siliciclastic sediments in the Cabra Corral reservoir area may be explained by the presence of the Guachipas High, which separates the Metán and Alemanía sub-basins. Although distinct in geometry, these sub-basins are commonly treated together in the literature due to their closely linked sedimentary evolution. The Guachipas High likely acted as a barrier to sediment transport, restricting coarse clastic input and influencing lateral facies transitions (Hernández et al., 1999; Bento Freire, 2012; Magalhães et al., 2020; Roemers-Oliveira et al., 2025). A detailed representation of the stratigraphic column for the Vapumas outcrop, considered as a reference section of the SBIII, is provided in the Database and Methods Section (see Fig. 6.3), where the distribution of sampling points is also illustrated.

## 6.3. Database and methods

### 6.3.1. Field data acquisition

Field data were acquired from two outcrops, Vapumas and Assado, located near Cabra Corral Lake in the Salta Basin (Fig. 6.1). These outcrops have previously been investigated for detailed sedimentological and vertical stratigraphic characterization (Roemers-Oliveira et al., 2025). A series of photographs was acquired using a Remotely Piloted Aircraft System (RPAS) to generate Digital Outcrop Models (DOMs), as detailed in Section 6.3.1.1. In addition, point-based hyperspectral measurements were acquired with an ASD FieldSpec portable spectroradiometer, and hyperspectral images were collected with a tripod-mounted camera, as described in Sections 6.3.1.2.1 and 6.3.1.2.2, respectively.

Complementary to the imaging datasets, 61 rock samples were collected from the Vapumas outcrop (sample locations are shown as yellow circles in Fig. 6.3 and Fig. 6.4) to support geochemical analyses. These sampling points correspond to the same positions where field hyperspectral spectroscopy measurements were conducted.

#### 6.3.1.1. Photogrammetry

High-resolution DOMs were generated for the Assado and Vapumas outcrops using a DJI Remotely Piloted Aircraft System model Matrice 300 RTK equipped with a Zenmuse P1 camera with a 35 mm lens and a real-time kinematic (RTK) Global Navigation Satellite System (GNSS) for centimeter-scale positioning accuracy. Image acquisition was carried out with the camera lens facing the outcrop surface. Flights were conducted at a minimum distance of 8 m from the outcrop faces, with an average of 12.9 m at both Assado and Vapumas. A total of 497 images were collected at Assado and 450 at Vapumas in stationary-flight mode, operated manually by two pilots: one controlling the RPAS and the other positioning the camera, ensuring the required image overlap (≥80% forward and ≥70% side). While effective for geometric accuracy, this method resulted in variations in lighting conditions due to extended acquisition time. To mitigate this, histogram matching was applied using a Python-based script to standardize brightness and contrast across the image set.

Photogrammetric processing followed a Structure-from-Motion (SfM) and Multi-View Stereo (MVS) workflow (Lowe, 2004; Bistacchi et al., 2022), implemented in Agisoft Metashape (Agisoft, 2023). The output consisted of 3D dense point clouds and textured meshes that reconstruct photorealistic outcrop models, with a final spatial resolution of approximately 1.57 mm per texture element at Assado and 1.68 mm at Vapumas.

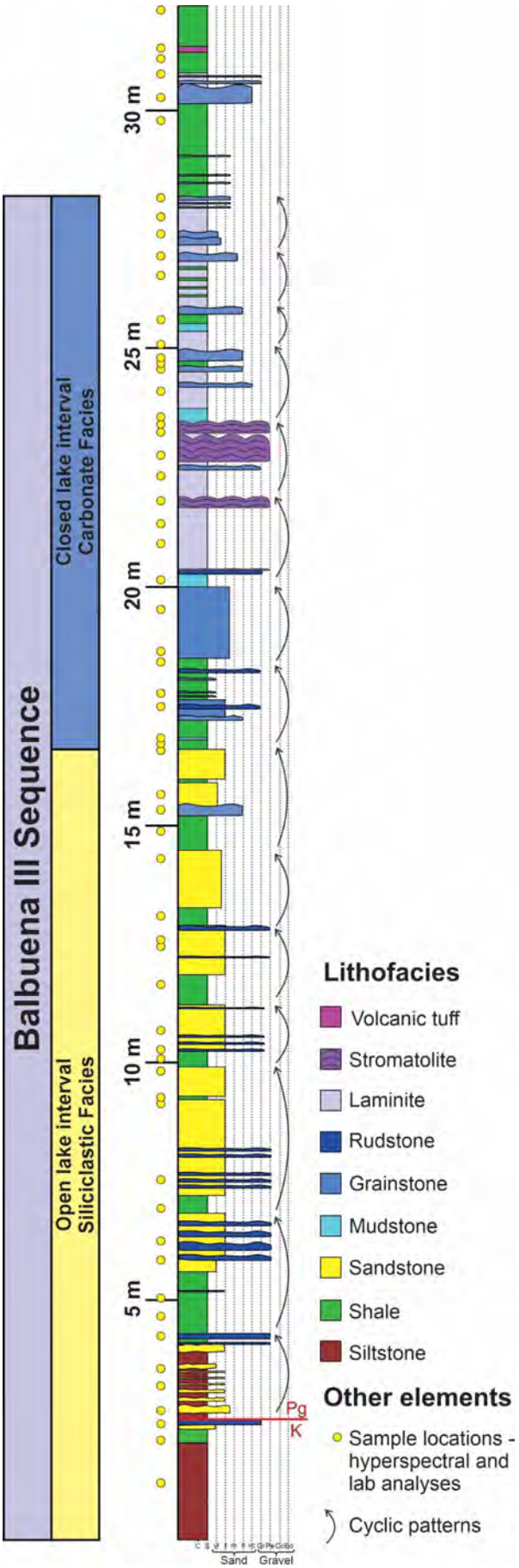


**Fig. 6.3.** Simplified vertical stratigraphic section of the Vapumas outcrop (modified from Roemers-Oliveira et al., 2025) indicating the sampling positions and the locations where spectral measurements were acquired using a portable spectroradiometer.

### 6.3.1.2. Hyperspectral data acquisition

#### 6.3.1.2.1. Field hyperspectral spectroscopy

Point-based hyperspectral data were acquired using a portable ASD FieldSpec FS3 350–2500 JR spectroradiometer, coupled with a contact probe equipped with an internal halogen light source, which provides stable and controlled illumination during measurements. The system collects reflectance spectra over the 350 to 2500 nm spectral range, using three detectors: a silicon array for 350–1000 nm, and two InGaAs arrays covering 1000–1800 nm and 1800–2500 nm, respectively. The spectral sampling interval is 1.4 nm in the visible to near-infrared (VNIR, 350–1000 nm) and 2 nm in the shortwave infrared (SWIR, 1000–2500 nm), resulting in spectra composed of over 2000 spectral bands. The measurement footprint was approximately 10 mm in diameter, corresponding to the field of view of the probe.

Radiometric calibration was performed using a Spectralon white reference panel **(**Labsphere Inc., North Sutton, NH, USA**)**, which was measured regularly during the acquisition process to ensure consistency across measurements. The contact probe setup eliminates the influence of ambient light and ensures standardized acquisition by maintaining a fixed illumination geometry and distance between the sensor and the rock surface. Spectral measurements were performed directly on the outcrop surface (Fig. 6.4A), targeting preferentially flat, clean, and fresh areas to maximize the signal-to-noise ratio and minimize the effects of surface roughness. For each lithofacies identified, a set of seven individual spectra were acquired at each representative position to capture the inherent variability in the spectral response.

A systematic acquisition strategy was applied along the entire stratigraphic profile, from base to top, ensuring full capture of the vertical variability in lithofacies. At each lithofacies change, a new set of spectra was recorded following the same acquisition protocol. This procedure provided a continuous and representative characterization of the spectral variability associated with each lithofacies.

#### 6.3.1.2.2. Field hyperspectral imaging

Hyperspectral images were acquired using a Specim AFX-17 hyperspectral camera, which operates with a pushbroom scanning system based on an InGaAs (Indium Gallium Arsenide) detector. The system covers the near-infrared (NIR) to shortwave infrared (SWIR) range from 900 to 1700 nm, divided into 224 spectral bands with a spectral resolution of approximately 3–4 nm. The sensor has a fixed focal length of 18 mm and records 640 pixels per line with a physical pixel size of 15 µm. The average camera-to-target distance during acquisition was about 10 m, resulting in a ground sampling distance (GSD) of ~1 cm per pixel per side.

For image acquisition, the camera was mounted on a tripod equipped with a rotational stage, positioned on the cargo bed of a pickup truck parked on the opposite side of the road, directly facing the outcrop (Fig. 6.4B). Each image was captured with the sensor in a stationary position using the rotational scan mode. Successive images were acquired by moving the tripod setup along the front of each outcrop at 3 m intervals, ensuring sufficient overlap and continuous coverage of the exposed stratigraphic sections. A calibration panel coated with barium sulfate ($BaSO_4$), due to its high reflectance and near-lambertian behavior, was placed within the field of view during each acquisition to support the conversion to reflectance. All images were collected under stable daylight conditions to minimize shadow effects and illumination variability along the scanning direction.

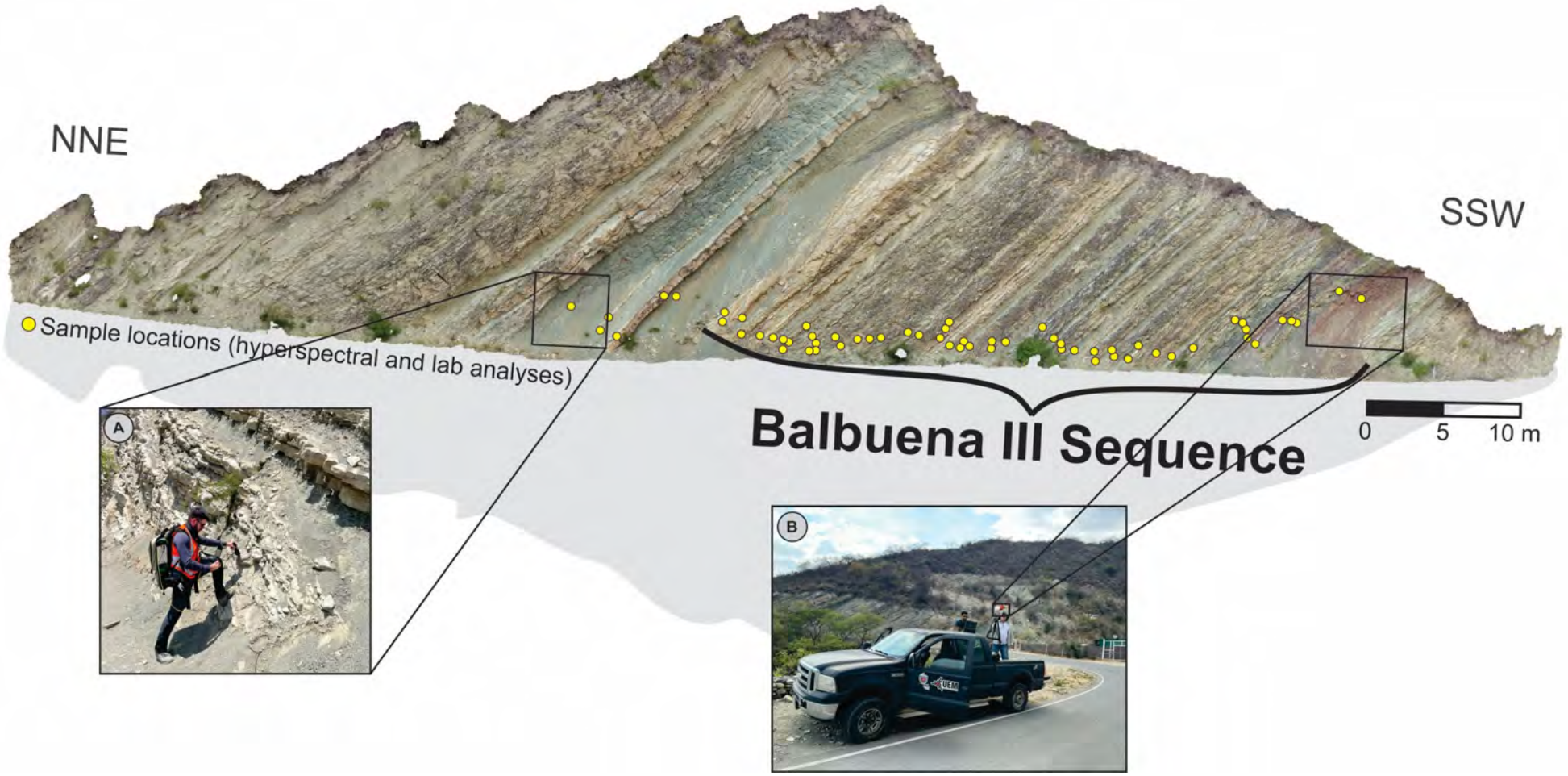


**Fig. 6.4.** Perspective view of the Vapumas DOM (Balbuena III Sequence, Salta Basin) showing sample locations (yellow circles) for hyperspectral and laboratory analyses. Detail photographs illustrate field data acquisition: (A) portable hyperspectral spectrometer measurements using lithofacies-based sampling, and (B) hyperspectral imaging using a vehicle-mounted system.

## 6.3.2. Data processing and analytical methods

### 6.3.2.1. Hyperspectral data processing

#### 6.3.2.1.1. Field hyperspectral spectroscopy processing

The raw spectral measurements were initially handled using the ViewSpec software (Analytical Spectral Devices, n.d.). Since the calibration with the standard white reference panel is stored in the software, each measurement is directly displayed in reflectance, with values between 0 and 1 (e.g., de Oliveira et al., 2023).

#### 6.3.2.1.2. Field hyperspectral imaging processing

The raw hyperspectral images were converted from digital numbers to reflectance, thereby reducing the influence of electronic noise and variable illumination conditions (e.g., Kurz et al., 2013; Lorenz et al., 2018; Thiele et al., 2022b). This procedure included subtraction of the dark image, captured with the shutter closed, followed by the use of a barium sulfate ($BaSO_4$) reference panel (e.g., Henriksen et al., 2022; Granemann et al., 2025). The workflow was implemented in ENVI (Exelis Visual Information Solutions, 2015) with the Scan Normalization tool, where a region of interest (ROI) was defined on the panel in each image to guide the conversion to reflectance.

The processing steps involved dark current subtraction and normalization of spectral values based on the ROI. After normalization, images were rotated to achieve horizontal alignment, and spectral bands strongly affected by atmospheric absorption, particularly between 1340–1463 nm, were excluded. The corrected hyperspectral cubes were exported in ENVI format (.hdr) to retain the full spectral information, while additional false-color composites in JPG format were generated from selected bands for visualization purposes.

### 6.3.2.2. Geochemical analyses (XRF)

Bulk geochemical analyses were carried out on the 61 rock samples collected from the Vapumas outcrop to quantify the proportions of major oxides and mineral phases potentially influencing the hyperspectral response. These data supported the definition of spectral signatures for the samples and, consequently, for the lithofacies analyzed.

Major element compositions were determined by X-ray fluorescence (XRF) at SGS Geosol Lab, Brazil, following industry-standard procedures based on fused glass disc preparation with lithium tetraborate flux. The analytical workflow included drying the samples at approximately 105 °C, pulverizing them to 95% passing 150 mesh using a steel mill, and producing fused beads to ensure total decomposition of the samples. This enabled accurate determination of major oxides, including $SiO_2$, $Al_2O_3$, $Fe_2O_3$, CaO, MgO, $TiO_2$, $P_2O_5$, $Na_2O$, $K_2O$, MnO, and loss on ignition (LOI). The LOI was determined separately by gravimetric analysis at 1000 °C. Quality control protocols were applied throughout all stages of sample preparation and analysis.

### 6.3.2.3. Discriminant methods

Three complementary approaches were applied for lithofacies discrimination: Linear Discriminant Analysis (LDA), Multilayer Perceptron (MLP), and K-means clustering. These methods were selected to encompass both supervised strategies (LDA and MLP) and an unsupervised approach (K-means), enabling comparison between traditional statistical classification and deep learning workflows. One of the main objectives was to apply discriminant analyses both to field spectroscopy data and to hyperspectral cubes, to generate

2D lithofacies maps of the outcrops. LDA of field spectroscopy was performed in RStudio (Posit, 2023) using the MASS package (Ripley and Venables, 2009). LDA of hyperspectral cubes was performed in Python (2023) using scikit-learn (Pedregosa et al., 2011), the MLP was implemented with the TensorFlow deep learning library (TensorFlow, 2024), and K-means clustering was carried out with scikit-learn (Pedregosa et al., 2011). In addition, Principal Component Analysis (PCA) and Hierarchical Agglomerative Clustering (HAC) were applied for dimensionality reduction and exploratory grouping of lithofacies, using scikit-learn (Pedregosa et al., 2011) in Python (2023).

To evaluate the performance of the discrimination methods, when applicable, standard classification metrics were calculated, including accuracy, precision, recall, and F1-score (Manning et al., 2009; Powers, 2011; Goodfellow et al., 2016). Accuracy expresses the proportion of correctly classified instances among all predictions. Precision quantifies the ratio of correctly predicted positive cases relative to all predicted positives, whereas recall (or sensitivity) measures the proportion of correctly identified positives relative to all actual positives. The F1-score corresponds to the harmonic mean of precision and recall, providing a balanced assessment of performance even under class imbalance. Stacked bar plots derived from the aggregated confusion matrix were also employed as a comprehensive visualization tool, illustrating the cumulative distribution of predicted versus actual classes across all executions.

Finally, to assess the performance of the discrimination analyses, the predicted maps from LDA, MLP, and K-means were quantitatively compared to the ground truth, considering only pixels within the interpreted regions. The ground truth was derived from expert-driven manual interpretation of lithofacies boundaries directly on the outcrops, supported by detailed geological knowledge of the study area. The complete workflow integrating all stages of hyperspectral data processing, classification, and evaluation is summarized in Fig. 6.5. Further details on each of the discriminant methods used are presented below.

#### 6.3.2.3.1. Linear Discriminant Analysis (LDA)

Linear Discriminant Analysis (LDA) is a supervised statistical technique introduced by Fisher (1936) to classify observations into predefined groups. It relies on estimating the conditional probability that an observation belongs to a given class based on its predictor variables, as expressed in Eq. (1) (Rakotomalala, 2020):

$$P(Y = y_k \mid X) \quad (1)$$

where $Y$ denotes the assigned class, $y_k$ represents one of the possible classes, and $X = (x_1, x_2, \dots, x_p)$ is the vector of predictor variables. LDA assumes that the predictor variables follow a multivariate normal distribution within each class, with identical variance–covariance matrices (homoscedasticity) (Ghojogh and Crowley, 2019; Tharwat et al., 2017).

Under these assumptions, the method defines a linear discriminant function for each class, as shown in Eq. (2) (Saporta, 2011; Rakotomalala, 2020):

$$d(y_k, X) = a_{k0} + a_{k1}x_1 + \cdots + a_{kp}x_p \quad (2)$$

where the coefficients $a_{kj}$ are estimated from the training data. Classification is achieved by assigning each observation to the class associated with the highest discriminant function value.

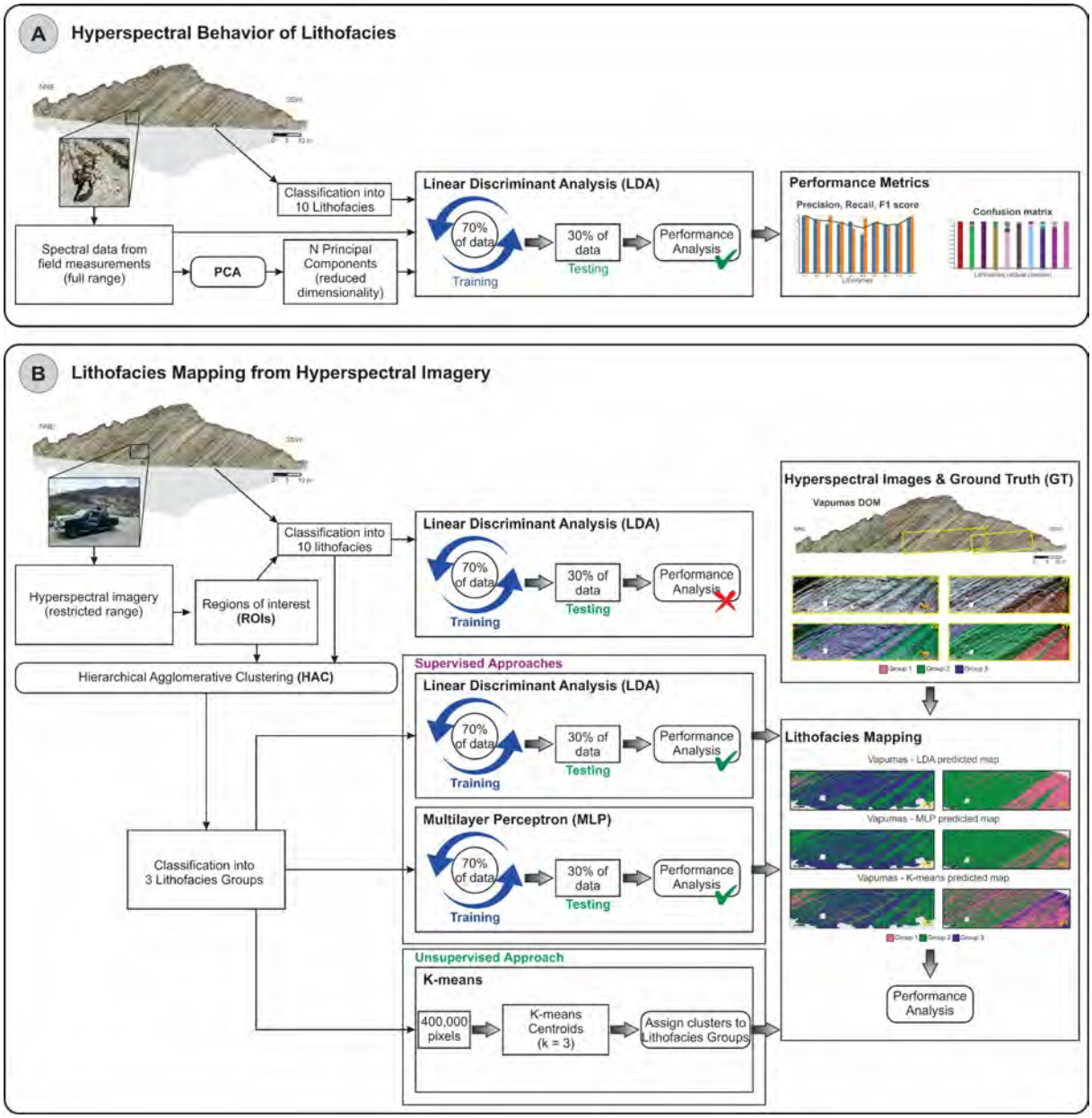


**Fig. 6.5.** Integrated workflow applied for hyperspectral lithofacies discrimination and mapping. (A) Definition of hyperspectral behavior of lithofacies based on field spectroscopy. (B) Application of supervised and unsupervised approaches to hyperspectral imagery for lithofacies mapping and performance evaluation.

LDA was applied in two complementary ways. First, it was used exclusively for evaluating classification performance on spectral datasets, namely (i) field spectra acquired with the portable spectroradiometer, and (ii) spectra extracted from hyperspectral image ROIs. In this case, each dataset was split into 70% training and 30% testing with a stratified procedure that ensured representation of every lithofacies in both subsets. After enforcing this per-class minimum, the remaining samples were randomly allocated to preserve the overall 70/30 proportion. Each experiment used a randomly selected seed, and the pipeline was executed for 10 independent seeds. Performance was summarized using mean accuracy, precision, recall, and F1-score across the 10 runs, as well as stacked bar plots.

Second, LDA was applied with the objective of generating 2D lithofacies maps from hyperspectral images. Here, models trained on spectra extracted from ROIs were applied to hyperspectral cubes to classify lithofacies directly at the pixel scale. Model robustness was initially evaluated using stratified cross-validation with multiple folds, providing estimates of average accuracy and variance. However, the model actually used for image classification was

trained with a 70/30 train–test split, where the 30% test partition was reserved exclusively for independent accuracy assessment. For image application, hyperspectral cubes were processed block-wise to optimize memory usage while ignoring invalid pixels. Post-processing involved spatial smoothing to reduce noise and isolated misclassifications. The final outputs included classified lithofacies maps, delivering continuous spatial representations of lithofacies across the outcrops.

#### 6.3.2.3.2. Multilayer Perceptron (MLP)

A Multilayer Perceptron (MLP) is a class of feedforward artificial neural networks composed of an input layer, one or more hidden layers with nonlinear activation functions, and an output layer that provides class probabilities (Haykin, 1999). Each neuron applies a nonlinear transformation that enables the network to learn complex mappings beyond linear decision boundaries. Conceptually, an MLP can also be viewed as a mathematical function obtained by composing simpler functions, where each layer provides a new representation of the input (Goodfellow et al., 2016). Training is typically performed using the backpropagation algorithm to compute gradients (Rumelhart et al., 1986), combined with optimization methods such as Adam (Kingma and Ba, 2015) to update weights iteratively and minimize prediction error.

The MLP was trained on spectral data extracted from ROIs of the hyperspectral images, labeled according to lithofacies classes. For evaluation purposes, its performance was first assessed on spectral data through repeated stratified hold-out validation (20 iterations with a 70/30 partition), ensuring balanced representation of all lithofacies across training and test subsets. After this evaluation, a version intended for image application was trained on the complete dataset, reserving 20% of the samples for internal validation during training. The adopted architecture comprised three fully connected layers of 50 neurons each with ReLU activation, interleaved with dropout layers (rate = 0.1), followed by a softmax output layer. Training was performed for 100 epochs using the Adam optimizer (learning rate = $3\times10^{-3}$) and a batch size of 100. The trained model was subsequently applied to hyperspectral cubes, with predictions carried out block-wise (10,000 pixels per block) to optimize memory usage, and outputs reconstructed into 2D classified maps.

#### 6.3.2.3.3. K-means clustering

K-means is an unsupervised algorithm that groups data into k clusters by minimizing the variance within clusters and maximizing separation between them. The method iteratively assigns each observation to the nearest cluster centroid and updates centroids until convergence (MacQueen, 1967; Hartigan and Wong, 1979; Goodfellow et al., 2016). K-means has been widely adopted because its simple design allows for efficient computation and effective handling of large datasets (MacQueen, 1967; Jain, 2010). This study used the k-means++ initialization method (Arthur and Vassilvitskii, 2007), set to automatically run several initializations and retain the best result. The random seed was fixed at 0 to ensure reproducibility

K-means clustering was applied directly to the hyperspectral cubes, with the sole objective of generating 2D maps for unsupervised lithofacies separation. Before clustering, invalid pixels were excluded, and preprocessing included destriping and dimensionality reduction through Principal Component Analysis (PCA). The K-means model was fitted on a representative random subset of up to 400,000 valid pixels and then applied block-wise (≈250,000 pixels per pass) to the full cube to optimize memory usage. The resulting cluster assignments were reconstructed into 2D maps. These unsupervised maps were subsequently compared with the

ground truth, and each cluster was assigned the label (and color) of the lithofacies class with the highest correspondence. This step enabled direct comparison with the reference data.

#### 6.3.2.3.4. Auxiliary multivariate tools

##### 6.3.2.3.4.1. Principal Component Analysis (PCA)

Principal Component Analysis (PCA) is an unsupervised dimensionality reduction technique that transforms correlated variables into a new set of orthogonal components ranked by decreasing explained variance (Jolliffe, 2002; Abdi and Williams, 2010). The main objectives of PCA are to extract the most relevant information from the dataset, to reduce its dimensionality by retaining only the essential variables, to simplify data representation, and to analyze the relationships among variables and observations (Abdi and Williams, 2010).

PCA was employed in specific cases to reduce thousands of spectral bands into a smaller set of variables, minimizing redundancy and simplifying the data structure. It was applied to compare results obtained from LDA when applied directly to spectroradiometer data versus after dimensionality reduction, and as a preprocessing step before K-means clustering of hyperspectral cubes, improving the stability of unsupervised classification and reducing noise effects.

##### 6.3.2.3.4.2. Hierarchical Agglomerative Clustering (HAC)

Hierarchical Agglomerative Clustering (HAC) is an unsupervised technique that organizes the data into nested partitions represented as a dendrogram (Gordon, 1987; Everitt et al., 2011; Murtagh and Legendre, 2014). In this study, the agglomerative approach was adopted, using the Euclidean distance and Ward's linkage criterion to build the hierarchy. HAC is particularly useful for exploratory analysis, as it does not require the *a priori* definition of the number of clusters.

HAC was employed to explore spectral grouping from hyperspectral images, which cover a more limited spectral range compared to field spectroradiometer measurements. The method was used to investigate how lithofacies classes group together based on their spectral similarity, guiding the selection of the number of clusters prior to supervised classification of hyperspectral cubes.

## 6.4. Results

### 6.4.1. Lithofacies classification and geochemical composition

Previous studies in the Balbuena III Sequence described 19 lithofacies in detail, encompassing siliciclastic, carbonate, hybrid, and volcaniclastic deposits (Roemers-Oliveira et al., 2025). For the present study, the focus was placed on evaluating the spectral response of lithofacies to hyperspectral data. To ensure both analytical robustness and stratigraphic representativity, these lithofacies were grouped into 10 classes (Fig. 6.6), which served as the actual classes (ground truth) for supervised analyses. These groups preserve the key sedimentological and stratigraphic variability of the SBIII, maintaining their correlation with the elementary transgressive–regressive sequences already defined for the study area (Fig. 6.2A–B. Bulk-rock geochemical compositions for the same classes are presented in Fig. 6.7, providing complementary information for lithofacies characterization.

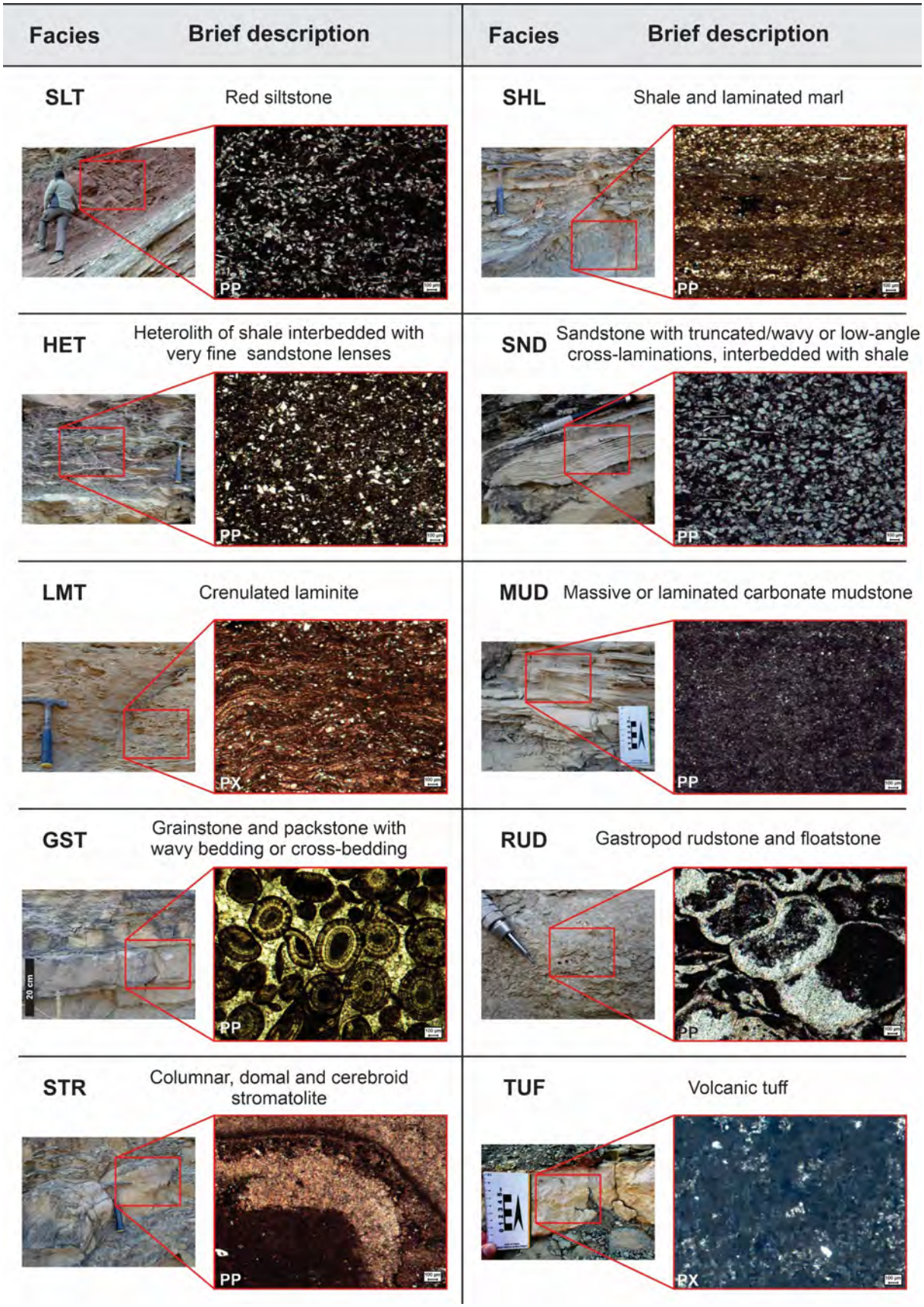


**Fig. 6.6.** Lithofacies identified in the Balbuena III Sequence and used as actual classes for supervised analyses (ground truth) in this study. Each facies is illustrated with representative outcrop photographs (left) and thin-section micrographs (right), accompanied by a brief description. Abbreviations: SLT – siltstone; SHL – shale; HET – heterolith; SND – sandstone; LMT – laminite; MUD – carbonate mudstone; GST – grainstone/packstone; RUD – gastropod rudstone/floatstone; STR – stromatolite; TUF – volcanic tuff.

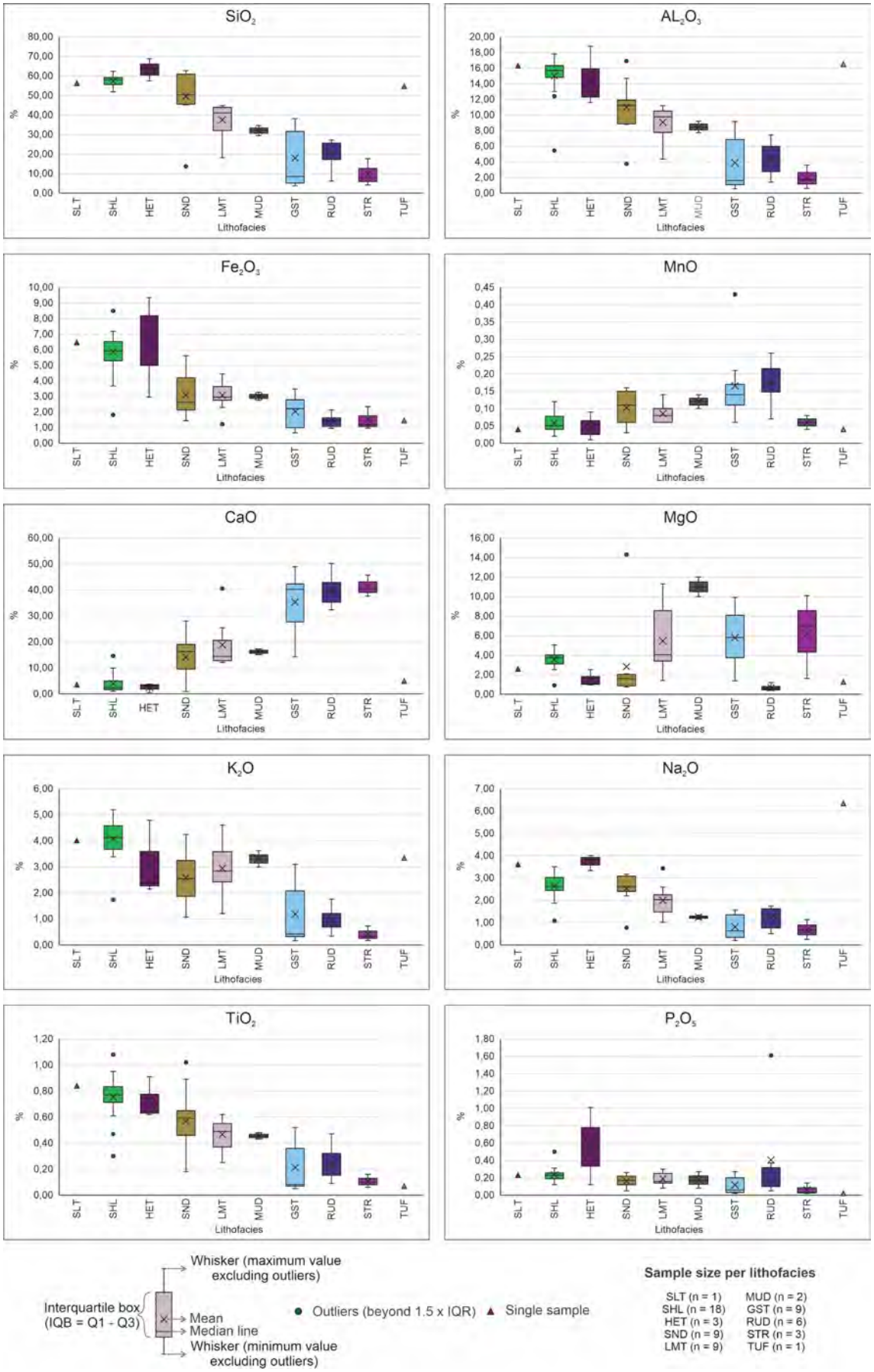


**Fig. 6.7.** Bulk-rock geochemical compositions of the lithofacies classes (ground truth) in the Balbuena III Sequence. Boxplots show the distribution of major oxides ($SiO_2$, $Al_2O_3$, $Fe_2O_3$, MgO, CaO, $K_2O$, $Na_2O$, $TiO_2$, $P_2O_5$, MnO). Lithofacies codes as defined in Fig. 6.6.

The combination of bulk-rock geochemistry and petrographic observations supports the interpretation of lithofacies composition, even though no quantified mineralogical data are available. Siliciclastic facies (SLT, SHL, HET, SND) are characterized by high $SiO_2$ contents, reflecting quartz, and by $Al_2O_3$ enrichment in SHL and SLT, indicating the presence of clay minerals; sericite (muscovite) and other mica traces are also observed in thin section. Moderate $K_2O$, $Na_2O$, and $TiO_2$ suggest K-bearing clays, feldspars, and heavy mineral contributions, whereas elevated $Fe_2O_3$ in SLT and HET reflects iron oxides related to oxidation processes, consistent with the reddish hue of these facies. Laminite (LMT) represents a hybrid facies: thin sections reveal quartz grains and micas interbedded with lamellar calcite crystals, corresponding to intermediate concentrations of $SiO_2$, $Al_2O_3$, and $K_2O$, together with slightly elevated MgO and $P_2O_5$. The $P_2O_5$ is likely derived from phosphatic fossil fragments, such as fish bones, whereas MgO is consistent with dolomite occurrence. The volcaniclastic tuff (TUF) displays a distinctive signature with high $SiO_2$ along with significant CaO, MgO, $Na_2O$, and $K_2O$, consistent with altered volcanic glass, feldspars, pyroxenes, and secondary clays. Carbonate facies (MUD, GST, RUD, STR) are dominated by very high CaO contents, especially in GST and RUD, reflecting calcite-rich matrices and bioclasts (particularly ostracods and gastropods), although gastropod shells are partially silicified in the RUD facies, as illustrated in Fig. 6.6. MgO enrichment in STR and MUD suggests the occurrence of microbial dolomite, while discrete $P_2O_5$ peaks in RUD and STR are likely related to phosphatic fossil material.

In summary, the geochemical signatures align with petrographic observations and typical lacustrine patterns: quartz- and clay-rich siliciclastic deposits, mixed carbonate–siliciclastic lithotypes, volcaniclastic material with altered mineralogy, and carbonate facies strongly influenced by microbial processes. The specific mineralogical combinations suggested in each facies are expected to govern their spectral signatures, which are examined in the following section.

### 6.4.2. Hyperspectral behavior of lithofacies

Field-acquired spectra for each lithofacies are presented in this section. Fig. 6.8 shows the mean curves for each class, whereas Fig. 6.9 illustrates the full variability, including $\pm 1\sigma$ envelopes, which allow the evaluation of both inter-group trends and intra-facies dispersion. The variability range provides a more accurate representation of the spectral signatures of lithofacies, since they are composed of mineral mixtures rather than pure components. As a result, their signatures are better represented as intervals than as discrete curves. In the graphs of Fig. 6.9, this variability is directly influenced by mineralogical heterogeneity and by the number of spectra acquired (each sample corresponds to seven measurements performed in closely spaced areas).

Siliciclastic facies (SLT, SHL, HET, SND) display low to moderate reflectance levels and discrete clay-related features, with minima around 2200–2220 nm. SLT exhibits the darkest curves, nearly flat across the VNIR–SWIR, with stronger absorption in the visible region, consistent with its reddish color and high Fe oxide contents. SHL and HET show a gentle increase toward the SWIR, with more pronounced clay-related features. SND displays intermediate reflectance and smoother curves, with less distinct spectral structure, consistent with its quartz-rich composition and lower abundance of strong absorbers, although clay- and carbonate-related concavities are still evident. Variability envelopes indicate greater intra-facies dispersion in SHL (Fig. 6.9B) and HET (Fig. 6.9C), whereas SND (Fig. 6.9D) is more homogeneous. SLT presents a narrower envelope (Fig. 6.9A), likely reflecting the limited number of samples rather than true homogeneity.

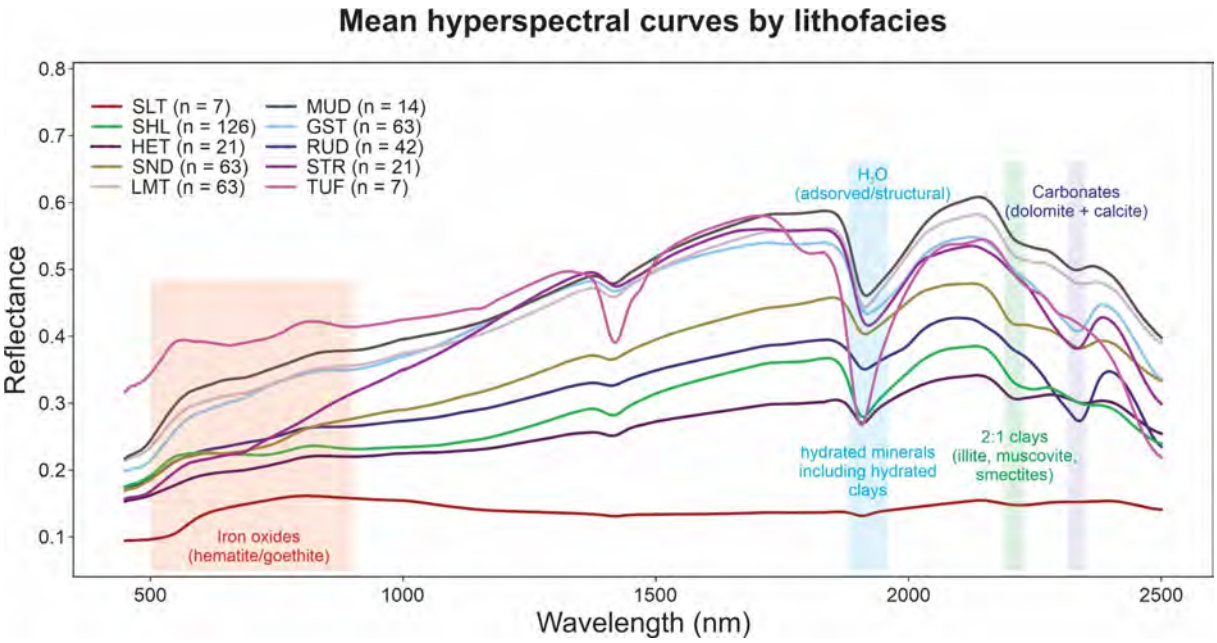


**Fig. 6.8.** Mean hyperspectral reflectance curves of lithofacies in the Balbuena III Sequence, measured with a field spectroradiometer. Diagnostic absorption features are highlighted: Fe-oxides (hematite/goethite), $H_2O$ (adsorbed/structural, hydrated minerals including clays), 2:1 clays (illite, muscovite, smectites), and carbonates (calcite + dolomite; band centers at ~2325 nm for dolomite and ~2345 nm for calcite), based on Kokaly (2017). n = total number of measurements.

Carbonate facies (MUD, GST, RUD, STR) plot at higher reflectance levels and display the diagnostic carbonate absorption between ~2330–2350 nm. MUD (Fig. 6.9F) and GST (Fig. 6.9G) exhibit bright and uniform curves with a well-defined carbonate band. STR (Fig. 6.9I) also shows bright, high-contrast curves with the same diagnostic feature. RUD (Fig. 6.9H), in contrast, tends to show comparatively lower reflectance among the carbonate facies but still preserves the diagnostic carbonate absorption, while presenting a wider envelope that reflects its more heterogeneous nature and its occurrence in thin layers frequently interbedded with siliciclastic facies (SND and SHL).

LMT curves, although with mean reflectance values as high as those of the carbonate facies, show less prominent features in the clay-related (~2200–2220 nm) and carbonate (~2330–2350 nm) intervals. Its envelope reveals wide internal variability (Fig. 6.9E), likely associated with its hybrid composition. The volcaniclastic facies (TUF) displays relatively high reflectance and is distinguished by a clear concavity around 1450–1490 nm. Fig. 6.9J shows its envelope as very narrow, most likely due to the small number of measurements.

The spectral patterns emphasize the consistent differences between siliciclastic and carbonate facies, while also revealing the distinctive behavior of hybrid and volcaniclastic lithofacies. The variability observed within and between classes provides a solid basis for evaluating their separability through subsequent supervised classification. To this end, Linear Discriminant Analysis (LDA) was first applied to the full-range spectroradiometer data.

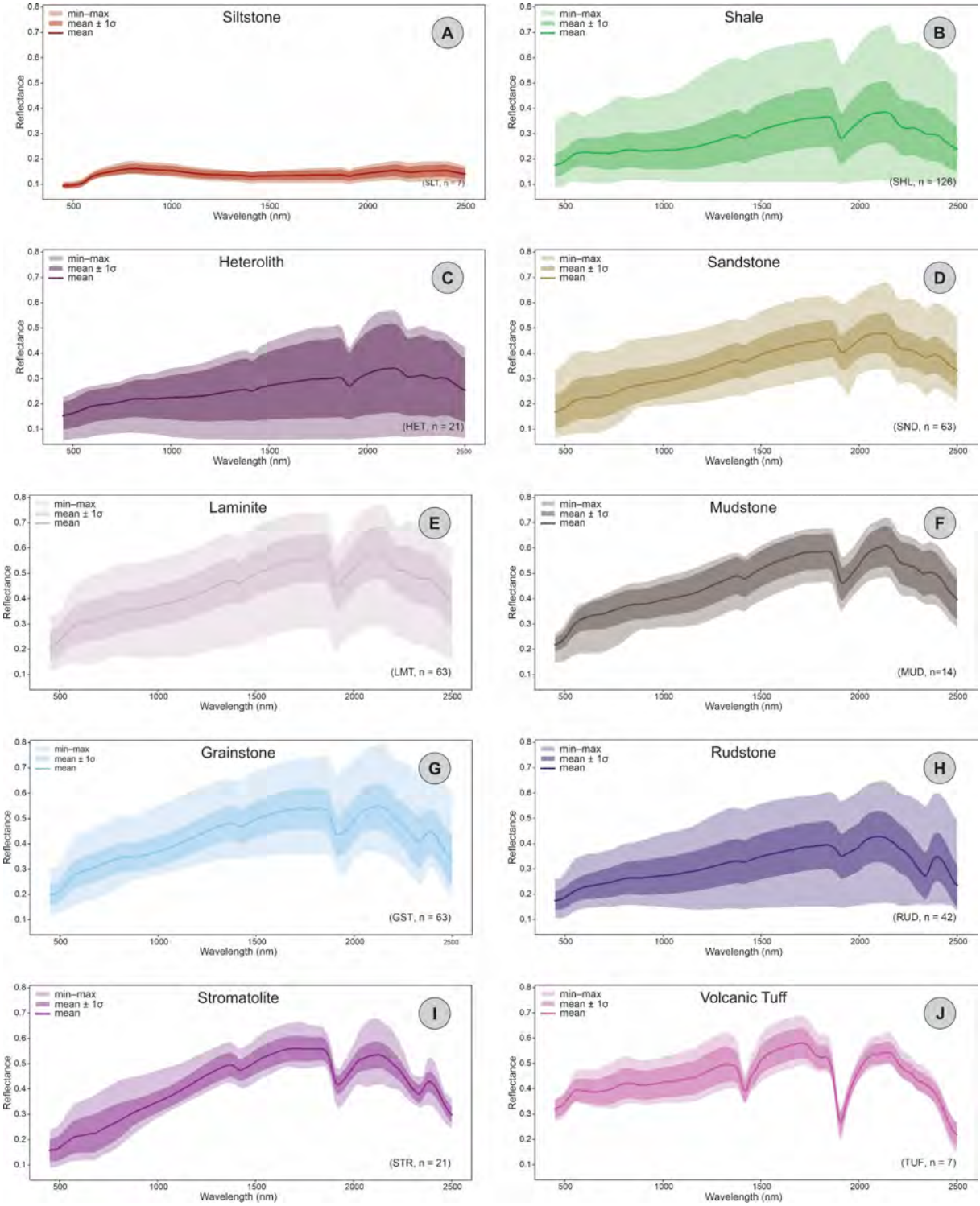


**Fig. 6.9.** Hyperspectral signatures of the lithofacies: (A) siltstone, (B) shale, (C) heterolith, (D) sandstone, (E) laminite, (F) mudstone, (G) grainstone, (H) rudstone, (I) stromatolite, and (J) volcanic tuff. Solid line = mean reflectance; darker band = ±1σ around the mean; lighter band = min–max range; n = number of spectra per class.

### 6.4.3. Linear Discriminant Analysis (LDA) of hyperspectral data

This section evaluates whether the lithofacies classes defined from sedimentological and geochemical criteria can be discriminated through Linear Discriminant Analysis (LDA). LDA was selected as a simple and computationally efficient statistical method, suitable for an initial assessment of class separability. The first approach consisted of directly applying LDA to the hyperspectral dataset across the full spectral range (450–2500 nm). Data were acquired with a portable spectrometer, yielding spectra with more than 2000 bands. Each sample was measured

seven times in the field, resulting in a total of 427 spectra. It is widely recognized that in many modern applications, including hyperspectral data analysis, the number of descriptors may reach hundreds or even thousands, whereas the number of samples often remains relatively small. This imbalance, known as the small sample size (SSS) problem, increases the risk of overfitting when discriminant methods are applied without prior dimensionality reduction (Ghojogh and Crowley, 2019; Tharwat et al., 2017; Rakotomalala, 2020).

To address this issue, LDA was also applied after dimensionality reduction through Principal Component Analysis (PCA). The relationship between the number of retained principal components (PCs) and classification accuracy was analyzed to identify both the elbow point and the configuration that maximized predictive performance. The elbow point was identified at approximately 11 PCs, corresponding to an accuracy of about 68%. Accuracy continued to increase gradually beyond this value, reaching 72.5% with the retention of 17 PCs, which together explain 99.99% of the total variance. Therefore, the final selection of 17 PCs represented a balance between preserving spectral variability and mitigating the risk of overfitting, while ensuring that virtually all spectral information was retained.

LDA without dimensionality reduction consistently outperformed the PCA-based approach. Overall accuracy ranged between 85 and 93%, averaging 88% across the ten runs. In contrast, PCA-LDA achieved lower performance, ranging from 70 to 80%, with an average of 74%. The analysis of precision, recall, and F1-scores (Fig. 6.10A and Fig. 6.10C) highlights marked differences among lithofacies. In the direct LDA application, SLT was consistently identified, with an F1-score of 1.0. SHL and HET also achieved strong results, both with F1-scores above 0.9, while SND reached 0.87. Among the carbonates, GST, STR, and RUD recorded F1-scores between 0.84 and 0.88. MUD showed the lowest performance across all classes (0.78), whereas TUF, with its distinctive spectral signature, reached values close to 1.0. In the PCA-LDA approach, an overall decrease in performance was observed, although this strategy reduces the risk of overfitting. Among siliciclastic facies, SLT and SHL retained F1-scores above 0.8, while SND reached 0.79. In contrast, HET showed the lowest performance, with an F1-score of 0.5. Carbonate facies displayed intermediate results, ranging from 0.6 (MUD) to 0.75 (RUD). As in the first approach, TUF remained clearly distinguishable, with an F1-score of 0.9.

Aggregated confusion matrices (Fig. 6.10B and Fig. 6.10D) reinforce these trends. In the direct LDA, most lithofacies were predominantly classified into their correct classes, with error rates below 20% in most cases (only LMT exhibited higher confusion, with 22%). In the PCA-LDA model, average accuracy remained above 60%, but with larger variability. Accuracies above 80% were restricted to SHL, SND, and TUF, with TUF being the only facies classified without errors. Accuracies between 60 and 80% occurred in SLT, LMT, MUD, GST, RUD, and STR, while HET showed the lowest accuracy, slightly above 40%.

The comparison between approaches shows that, despite lower accuracy, PCA-LDA reduces the risk of overfitting and underscores the inherent complexity of lithofacies classification, where mineral mixtures naturally produce overlapping and variable spectral signatures.

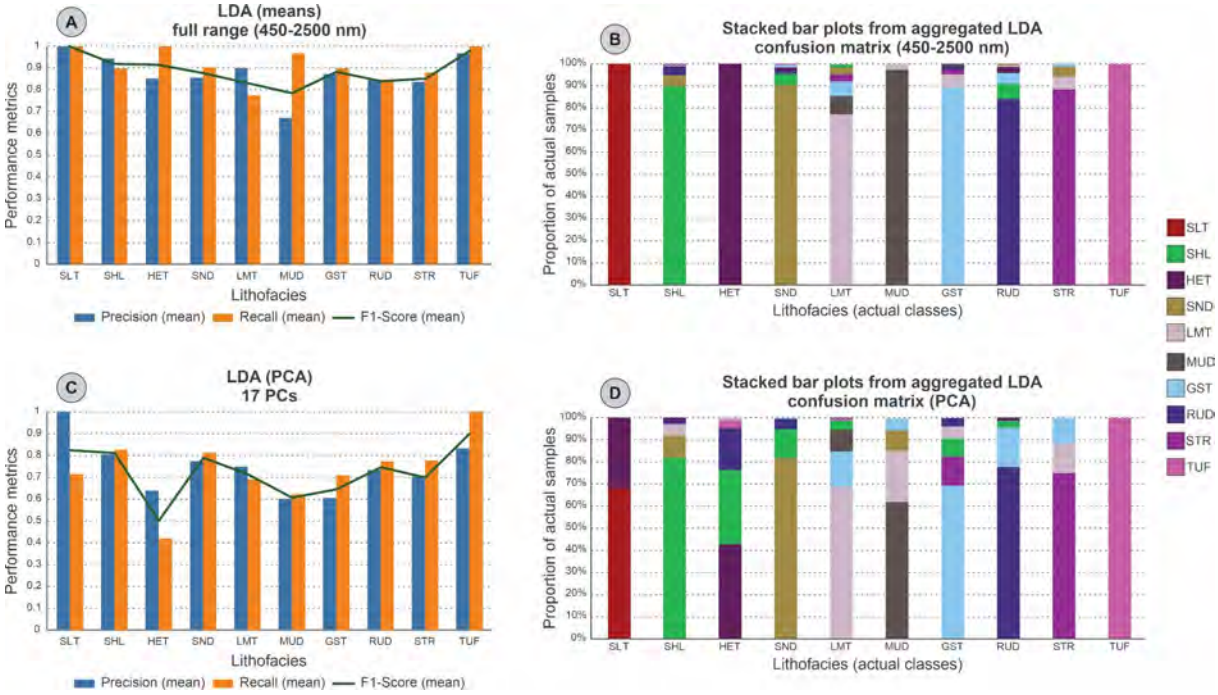


**Fig. 6.10**. Results of Linear Discriminant Analysis (LDA) applied to full-range hyperspectral data (450–2500 nm), based on ten runs with different seeds. (A) Precision, recall, and F1-scores by lithofacies, averages across runs. (B) Stacked bar plots from the aggregated LDA confusion matrix, showing prediction distribution per lithofacies. (C) LDA results after Principal Component Analysis (PCA) dimensionality reduction (17 PCs, averages across runs). (D) Stacked bar plots from the aggregated PCA-LDA confusion matrix.

### 6.4.4. Lithofacies classification from hyperspectral image ROIs

The application of LDA to the full-range field spectrometer dataset (450–2500 nm) primarily served to evaluate the discriminability of lithofacies under conditions where all major diagnostic absorption features were available. However, since the ultimate goal was to apply the discriminant model directly to hyperspectral cubes, the training data also needed to be derived from the images themselves, ensuring consistency between origin and spectral information. Spectra were therefore collected from regions of interest (ROIs) in the Vapumas outcrop, selected whenever possible to correspond to the same stratigraphic layers sampled in the field spectrometer dataset. To minimize the impact of underrepresented classes, a minimum of 30 spectra per lithofacies was required. The final dataset comprised more than 500 spectra, each described by 190 bands. Given this balanced relationship between the number of descriptors and samples, dimensionality reduction through PCA was not necessary, and LDA was applied directly to the spectral matrix.

Inspection of Fig. 6.11, which shows the mean spectra of lithofacies extracted from hyperspectral images, reveals that the curve shapes lose considerable detail compared to those in Fig. 6.8, derived from the field spectrometer dataset. Hyperspectral imagery, with its restricted coverage of 900–1700 nm, poses additional challenges for lithofacies discrimination, as this interval excludes key diagnostic absorption features, particularly those of clay minerals and carbonates beyond 2000 nm.

The application of LDA to hyperspectral image spectra (Fig. 6.12A) across the ten original lithofacies resulted in substantially lower performance compared to field-based data. Overall accuracy ranged from 56 to 68% across ten runs, averaging 61%. Precision, recall, and F1-scores highlight marked differences among lithofacies: while SLT and TUF achieved relatively high values, MUD, RUD, and LMT performed poorly. On average, only SLT, SHL, and TUF

reached F1-scores above 0.7. The confusion matrix (Fig. 6.12B) confirms this scenario, with extensive misclassification and widespread overlap between classes. These results reflect both the limited spectral range of the camera (900–1700 nm) and the inherent mineralogical heterogeneity of lithologies composed of complex mixtures.

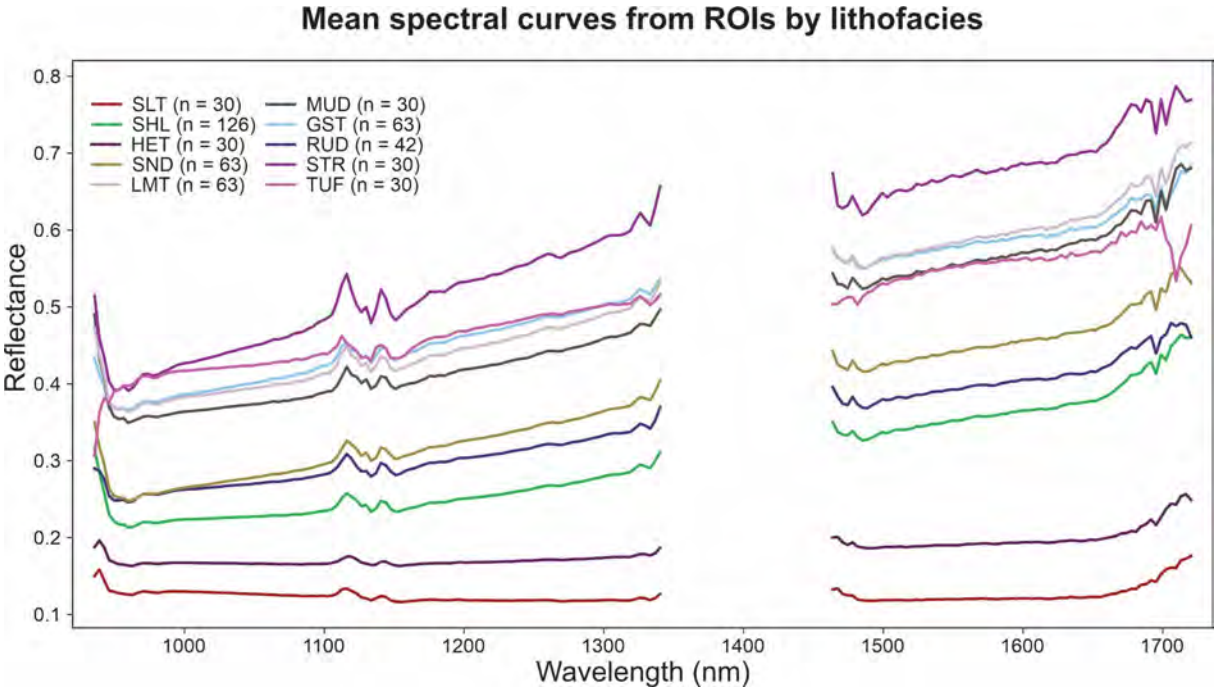


**Fig. 6.11.** Mean hyperspectral reflectance spectra of lithofacies from the Balbuena III Sequence, extracted from regions of interest (ROIs) in hyperspectral images.

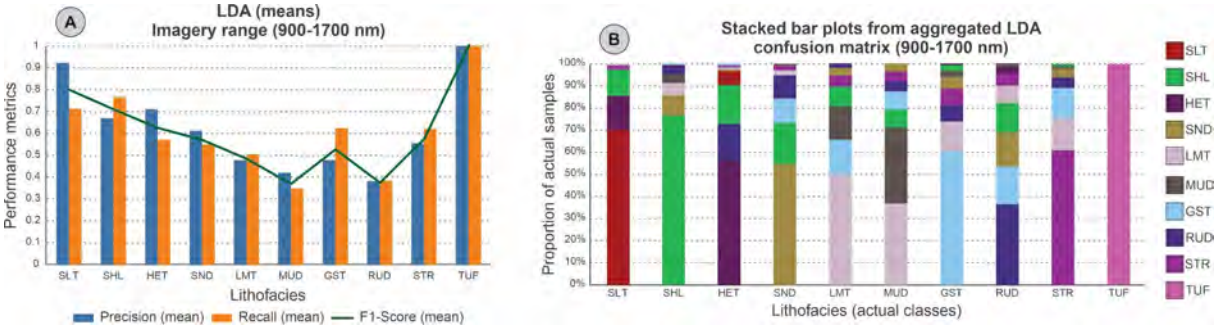


**Fig. 6.12.** Results of Linear Discriminant Analysis (LDA) applied to hyperspectral image data (900–1700 nm), based on ten runs with different seeds. (A) Precision, recall, and F1-scores by lithofacies (averages across runs). (B) Stacked bar plots from the aggregated LDA confusion matrix, showing prediction distribution per lithofacies.

To address this limitation, HAC was applied to determine an appropriate grouping of lithofacies. The analysis used the mean reflectance curve of each lithofacies as input and revealed a clear subdivision of the lithofacies into three main groups when applying a cut-off at a linkage distance of ~4 (Fig. 6.13A). This limited separability indicates that, although sedimentologically distinct, many lithofacies do not exhibit sufficiently contrasting spectral signatures in this interval, which justifies their regrouping for classification purposes. Group 1 (pink) includes SLT and HET, which cluster at relatively short distances, reflecting their strong spectral similarity. Group 2 (green) comprises SHL, SND, and RUD, which display moderate internal variability but form a consistent association. Group 3 (blue) incorporates GST, LMT, MUD, TUF, and STR. In general, Groups 1 and 2 encompass siliciclastic facies, with the exception of RUD, which, although carbonate, is commonly associated with sandstones and shales and may be difficult to isolate given the spectral resolution of the images. Group 3 includes the remaining carbonate facies together with the volcanic tuff, which, despite typically

exhibiting a distinct spectral signature, clustered with this group under the restricted spectral interval.

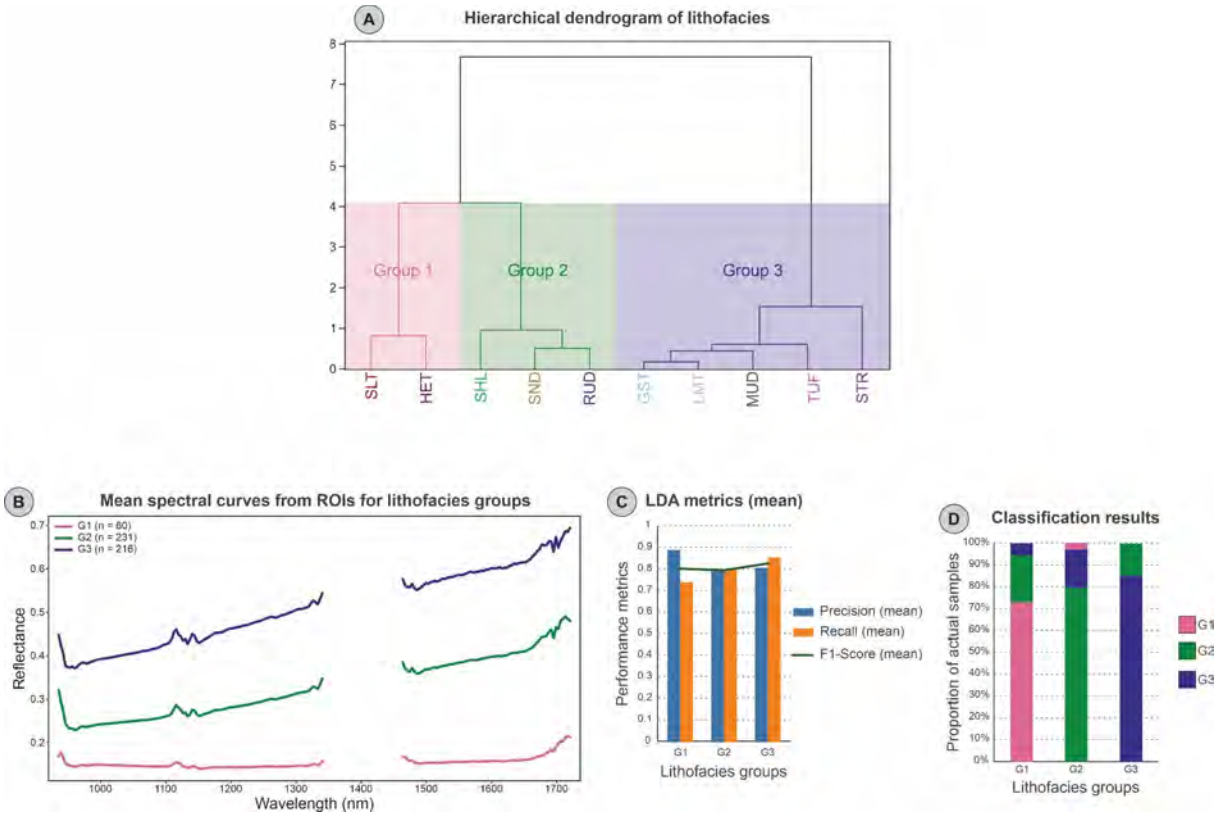


**Fig. 6.13**. Hierarchical clustering and classification results. (A) Hierarchical dendrogram of lithofacies using Ward's method and Euclidean distance. The cut-off at a linkage distance of ~4 defines three main lithofacies groups (pink, green, and blue). (B) Mean reflectance spectra from imagery ROIs for the three lithofacies groups. (C) Mean LDA performance metrics (precision, recall, and F1-score) for the 900–1700 nm imagery range. (D) Stacked bar plots derived from the aggregated LDA confusion matrix, showing proportions of correctly and incorrectly classified samples for each lithofacies group.

The mean spectra of these three groups display clearer separations than those of the individual lithofacies (Fig. 6.13B). After regrouping, LDA performance improved substantially: overall accuracy ranged from 79 to 85%, with a mean of 81%, and F1-scores averaged close to 0.8 for all three groups (Fig. 6.13C**)**. Furthermore, the confusion matrices indicate more consistent classifications and markedly reduced error rates (Fig. 6.13D), demonstrating that even under restricted spectral conditions, meaningful lithological discrimination can be achieved when data are treated at the level of broader groups.

Considering that the objective is to apply the discriminant model directly to the hyperspectral cubes restricted to the available 900–1700 nm range, subsequent classifications were carried out using the three-group configuration.

### 6.4.5. Discriminant methods applied to the hyperspectral imagery

To evaluate the performance of discriminant methods directly on hyperspectral cubes, four images were selected (V1 and V2 from Vapumas and A1 and A2 from Assado). For each outcrop, the pair of images spans the full thickness of the Balbuena III Sequence. Fig. 6.14 shows the location of the analyzed areas within each DOM, together with the manual interpretations provided by an expert. These interpretations, used as ground truth (GT), were derived from visual inspection of hyperspectral images converted into RGB for visualization

purposes. They provide a reference for evaluation, although they do not share the same spectral origin as the data used for model training and classification**.**

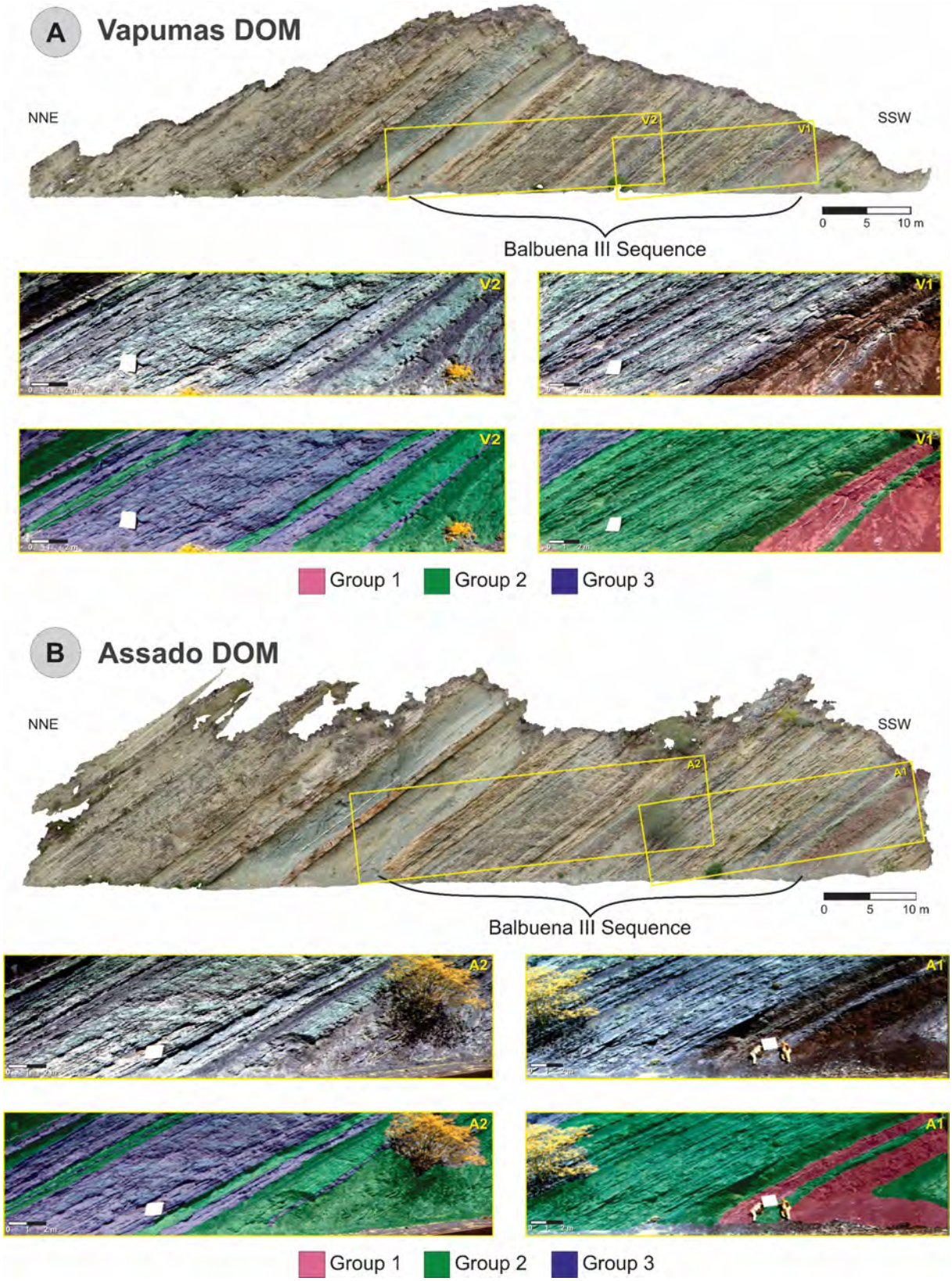


**Fig. 6.14.** Location of hyperspectral cubes used for classification. (A) Vapumas outcrop with selected cubes V1 and V2. (B) Assado outcrop with selected cubes A1 and A2. For each cube, the upper panel shows the hyperspectral image converted into RGB, and the lower panel shows the expert-derived ground truth (GT) maps with three lithofacies groups (G1–G3).

Based on spectra obtained exclusively from ROIs of the Vapumas outcrop, two supervised methods were tested: Linear Discriminant Analysis (LDA) and Multilayer Perceptron (MLP). Model performance was first evaluated on the Vapumas dataset itself, where ROI data were split into 70% for training and 30% for testing, ensuring independent validation for both methods. The resulting metrics, presented in Table 6.1 correspond to this internal evaluation based on Vapumas data. During training, both LDA and MLP achieved comparable overall accuracies (0.85 and 0.86, respectively). Evaluation metrics were satisfactory for both methods, with F1-scores above 0.83 across all three groups, indicating that they can be reliably spectrally discriminated.

**Table 6.1.** Class-level performance metrics for LDA and MLP based on spectral training datasets (ROIs) from the Vapumas outcrop. LDA results correspond to a single 70/30 train–test split, while MLP metrics are averaged over 20 stratified hold-out iterations with the same partition ratio. Metrics are reported per class (G1–G3) prior to model application to hyperspectral cubes.

| Group | LDA | | | MLP | | |
|---|---|---|---|---|---|---|
| | Precision | Recall | F1-score | Precision | Recall | F1-score |
| G1 | 0.71 | 1.00 | 0.83 | 0.88 | 0.96 | 0.92 |
| G2 | 0.85 | 0.81 | 0.83 | 0.85 | 0.86 | 0.85 |
| G3 | 0.90 | 0.85 | 0.88 | 0.89 | 0.85 | 0.86 |

Subsequently, the models were applied to the hyperspectral cubes, generating 2D prediction maps for the three lithofacies groups. In addition to these supervised models, an unsupervised K-means clustering approach was also applied, with the number of clusters set to three. After classification, clusters were relabeled as G1, G2, and G3 based on maximum correspondence with the GT maps, enabling direct comparison with the supervised methods. To assess model generalization, the classifiers trained on Vapumas data were also applied to the Assado outcrop cubes using the same spectral preprocessing and classification parameters. The products generated for the Vapumas outcrop are presented in Fig. 6.15, while the corresponding results for the Assado outcrop are shown in Fig. 6.16. To enable a more detailed comparison of classification performance, four areas of interest were selected in each outcrop (V1a–V2b in Vapumas; A1a–A2b in Assado) (Fig. 6.15 and Fig. 6.16). These windows highlight representative contrasts between lithofacies groups and provide a direct evaluation of the supervised (LDA and MLP) and unsupervised (K-means) approaches relative to the GT.

In the Vapumas outcrop (Fig. 6.15), the selected windows (V1a–V2b) illustrate distinct behaviors of the classification methods relative to the GT. In V1a, both LDA and MLP reproduced the overall stratified distribution of Groups 1 and 2, although LDA produced slightly sharper contacts and introduced a greater proportion of G1 interbedded with G2. The MLP outputs, by contrast, displayed more internal heterogeneity, with a reduced proportion of G1 compared to the GT, where it appears intercalated with both G2 and G3, as well as additional thin interbeds of G3 near the top. K-means displayed the highest proportion of G1 of all methods and, in this sector, interbedded G1 more with G3 than with G2. In the adjacent window (V1b), the GT shows only G2. The LDA classification introduced G1 at the top, while MLP added minor intercalations of G3, though in low proportion. K-means produced a more balanced mixture of the three groups, with G1, G2, and G3 interbedded in a more homogeneous manner, albeit with G2 slightly more abundant. Moving to V2a, the GT shows alternations between G2 and G3, which were reasonably well captured by both supervised methods. In both LDA and MLP, however, G3 was slightly overrepresented compared to the GT, and in LDA a few thin levels of G1 were also inserted. K-means produced a broadly similar distribution but with a greater insertion of G1 across the section. Finally, in V2b, the GT once again shows only intercalations of G2 and G3. The LDA classification introduced intervals of G1, particularly in

the upper part, whereas MLP reproduced only the alternation of G2 and G3, although with thinner interbeds compared to the GT. K-means produced the most heterogeneous result, with the three groups intercalated and a slight predominance of G1 in the upper portion.

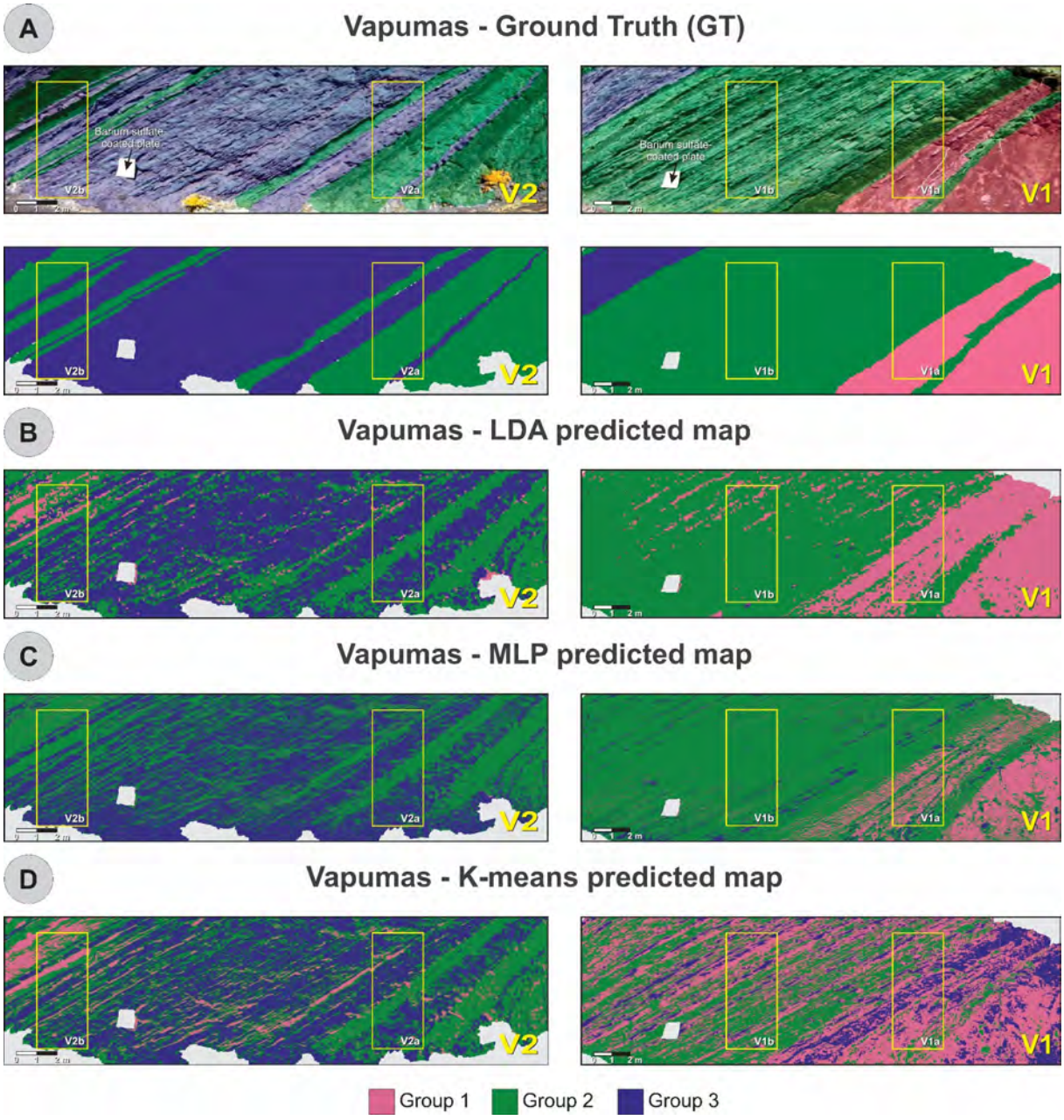


**Fig. 6.15.** Classification results for Vapumas hyperspectral cubes (V1 and V2). (A) GT maps, (B) LDA predictions, (C) MLP predictions, and (D) K-means clustering with three clusters, relabeled as G1–G3 according to maximum correspondence with GT. Windows V1a, V1b, V2a, and V2b indicate areas selected for detailed comparison between methods and GT.

In the Assado outcrop (Fig. 6.16), the selected windows (A1a–A2b) further illustrate the contrasts between the classification methods and the GT. In A1a, where the GT shows intercalations of G1 and G2, this pattern was relatively well reproduced by the supervised approaches. However, LDA increased the proportion of G1, while MLP introduced additional intercalations of G3. K-means, in contrast, produced a markedly different distribution, with G1 as the dominant group, followed by G3 and only thin, isolated layers of G2. In A1b, where the GT characterizes the section exclusively as G2, the LDA classification introduced G1 in the upper part of the section, while MLP generated a stronger intercalation of G2 with G3. K-means again produced three groups, with G3 occurring sparsely and G1 progressively increasing in abundance toward the top. In the upper interval, A2a corresponds to an alternation of G2 and

G3 in the GT, with G2 prevailing. LDA accentuated the proportion of G2 and inserted some thin levels of G1. MLP also reproduced the alternation of G2 and G3, but with a greater proportion of G3 than observed in the GT. K-means produced a thicker layering of the three groups, with G1 being the least frequent. Finally, in A2b, where the GT records alternations of G2 and G3 with a predominance of G3, the LDA classification reduced the abundance of G3, introduced intervals of G1, and shifted the predominance toward G2. MLP also emphasized G2 over G3, though it did not introduce G1. K-means generated the most homogeneous distribution, with all three groups occurring more evenly throughout the section.

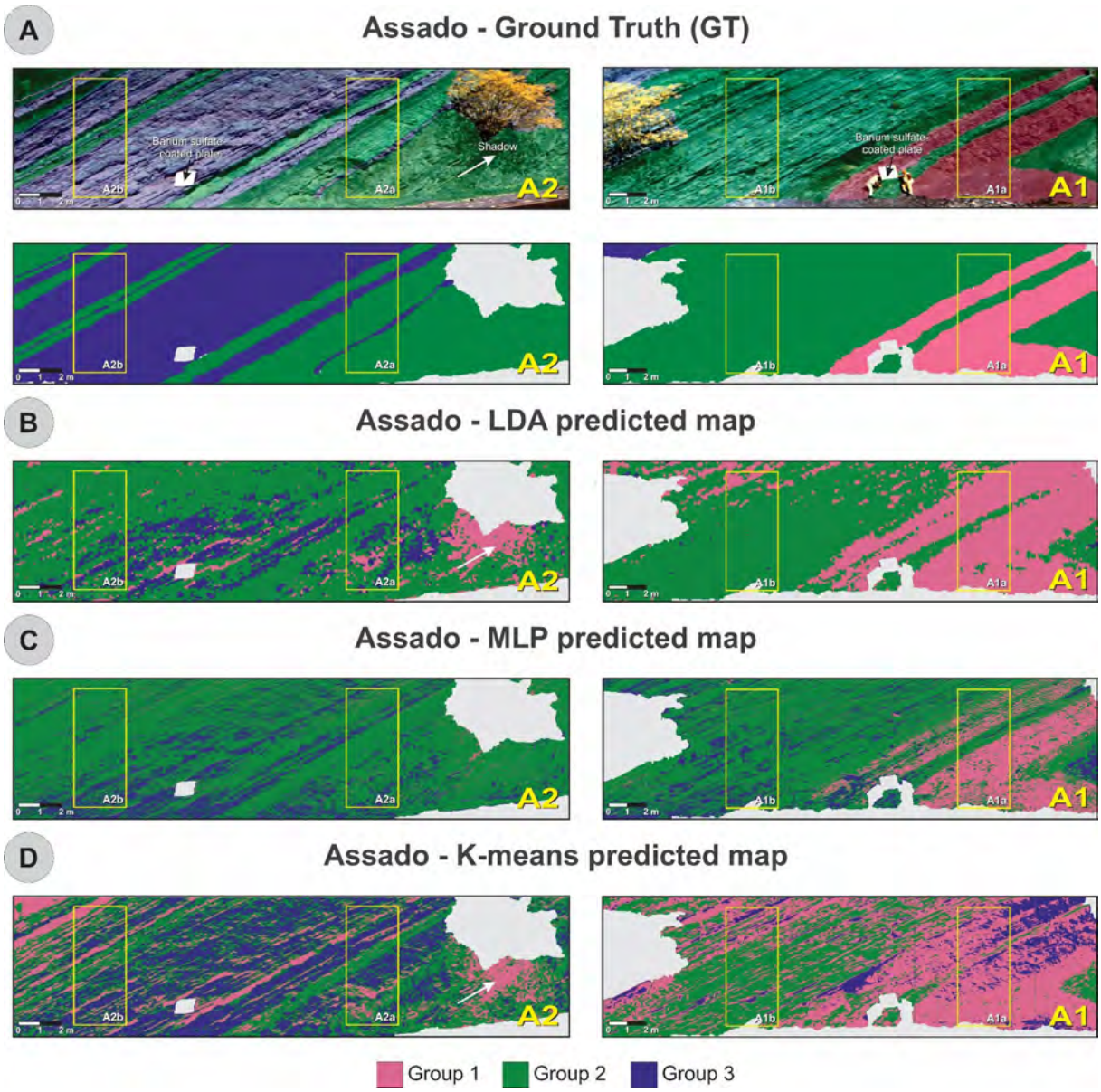


**Fig. 6.16.** Classification results for Assado hyperspectral cubes (A1 and A2). (A) GT maps, (B) LDA predictions, (C) MLP predictions, and (D) K-means clustering with three clusters, relabeled as G1–G3 according to maximum correspondence with the GT. Windows A1a–A2b highlight representative areas used for detailed comparison between methods and the GT. White arrows show the impact of shadows onto the LDA and K-means results.

The performance of the three approaches (LDA, MLP, and K-means) was quantitatively assessed by comparison with the GT maps, restricted to the expert-interpreted areas. Metrics of precision, recall, F1-score, and overall accuracy were computed for each lithofacies group (Table 6.2). When compared to the GT, the supervised methods consistently outperformed the unsupervised K-means clustering. The best correspondences with the GT occurred in the lower sections of both outcrops (V1 and A1), where LDA achieved the highest accuracies (0.79 and

0.80, respectively), while MLP yielded slightly lower but comparable results (0.76 and 0.73, respectively). In contrast, K-means showed consistently poorer correspondence with the GT, with accuracies not exceeding 0.51.

For the upper sections (V2 and A2), the comparisons revealed larger discrepancies relative to the GT. LDA accuracies were 0.58 in V2 and 0.40 in A2, while MLP yielded 0.56 and 0.48, respectively. K-means accuracies remained constant at 0.48 in both cubes, similar to those obtained in the lower sections. Analysis of group-level metrics and visual inspection of the classified maps (Fig. 6.15 and Fig. 6.16) indicate that supervised models tend to overpredict underrepresented groups in the GT, such as G3 in V1 and A1 or G1 in V2 and A2, leading to apparent mismatches in the evaluation.

A key observation is that both supervised methods displayed consistent behavior, with stronger agreement with the GT in the lower sections and weaker performance in the upper ones. Results from the Assado outcrop were broadly similar to those from Vapumas, with A2 performing worse than V2 but still demonstrating the generalization capacity of models trained exclusively on Vapumas. This consistency indicates that the spectral responses captured by the models are indeed associated with lithological groupings rather than outcrop-specific features. By contrast, the unsupervised K-means approach performed poorly overall, as expected, since it captures intrinsic spectral relationships without considering class labels.

While GT comparisons provide a useful benchmark, it should be noted that they reflect an expert-based interpretative model constrained by outcrop visibility and field observations, rather than an absolute reference. Consequently, hyperspectral-based classified maps often appear more heterogeneous than the GT, capturing spectral variations beyond the limits of visual interpretation.

## 6.5. Discussion

Field-based spectroscopy covering the VNIR–SWIR range (450–2500 nm) provided the spectral reference framework for this study, allowing the identification of diagnostic absorption features that distinguish the ten lithofacies considered in SBIII. Discriminant analysis (Fig. 6.6) applied to this full-range dataset confirmed that all lithofacies could be reliably separated when the complete spectrum was available. This demonstrates that, under ideal spectral coverage, hyperspectral imaging has the capacity to resolve the full lithological variability of the sequence. However, when restricted to the 900–1700 nm interval, analyses required grouping individual lithotypes into broader facies categories, emphasizing that the main limitation arises from spectral coverage rather than from the classification methods themselves.

Within this restricted range, lithofacies discrimination relies less on diagnostic absorption features, which are smoother, and more on reflectance amplitude and spectral slopes (Fig. 6.13B). This guided the decision to avoid normalization procedures such as continuum removal or spectral rescaling, which were tested but did not improve classification results, as they tend to attenuate amplitude differences (Clark, 1999) that, in this case, represent the main discriminant signal. By preserving absolute reflectance values (between 0 and 1), amplitude contrasts between groups remained the key factor enabling separation.

HAC played a central role in this workflow by objectively assessing the natural separability of the spectral data and guiding the decision on the number of groups that could be meaningfully distinguished. The three clusters defined through HAC (Fig. 6.13) correspond to the main lithological contrasts: Groups 1 and 2 comprise predominantly siliciclastic facies, whereas Group 3 encompasses carbonate ones. Among the siliciclastic types, Group 1 is distinguished by more oxidized, reddish facies with lower reflectance, while Group 2 includes non-oxidized facies with comparatively higher reflectance.

**Table 6.2.** Performance metrics of LDA, MLP, and K-means when compared against the ground truth (GT) maps of the Vapumas (V1, V2) and Assado (A1, A2) outcrops. Values above 0.70 are highlighted in gray.

| Outcrop cube | Group | LDA Precision | LDA Recall | LDA F1-score | MLP Precision | MLP Recall | MLP F1-score | K-means Precision | K-means Recall | K-means F1-score |
|---|---|---|---|---|---|---|---|---|---|---|
| Vapumas (V1) | G1 | 0.62 | 0.85 | 0.72 | 0.73 | 0.58 | 0.64 | 0.30 | 0.63 | 0.41 |
| | G2 | 0.87 | 0.84 | 0.85 | 0.82 | 0.88 | 0.85 | 0.86 | 0.40 | 0.55 |
| | G3 | 0.02 | 0.00 | 0.00 | 0.10 | 0.09 | 0.10 | 0.02 | 0.06 | 0.03 |
| | **Overall accuracy** | | **0.79** | | | **0.76** | | | **0.43** | |
| Vapumas (V2) | G1 | - | - | - | - | - | - | - | - | - |
| | G2 | 0.50 | 0.43 | 0.46 | 0.44 | 0.56 | 0.50 | 0.40 | 0.40 | 0.40 |
| | G3 | 0.68 | 0.67 | 0.68 | 0.68 | 0.55 | 0.61 | 0.66 | 0.52 | 0.58 |
| | **Overall accuracy** | | **0.58** | | | **0.56** | | | **0.48** | |
| Assado (A1) | G1 | 0.57 | 0.95 | 0.71 | 0.78 | 0.68 | 0.73 | 0.34 | 0.73 | 0.46 |
| | G2 | 0.97 | 0.76 | 0.85 | 0.88 | 0.76 | 0.81 | 0.95 | 0.44 | 0.60 |
| | G3 | 0.25 | 0.06 | 0.10 | 0.04 | 0.38 | 0.07 | 0.00 | 0.04 | 0.01 |
| | **Overall accuracy** | | **0.80** | | | **0.73** | | | **0.51** | |
| Assado (A2) | G1 | - | - | - | - | - | - | - | - | - |
| | G2 | 0.43 | 0.62 | 0.51 | 0.48 | 0.77 | 0.59 | 0.56 | 0.48 | 0.52 |
| | G3 | 0.53 | 0.18 | 0.27 | 0.52 | 0.20 | 0.29 | 0.66 | 0.49 | 0.56 |
| | **Overall accuracy** | | **0.40** | | | **0.48** | | | **0.48** | |

It is particularly noteworthy that reliance on reflectance amplitude made the models sensitive to external lighting effects. For instance, in some areas, tree shadows reduced pixel brightness, causing zones that actually belonged to Group 2 to be misclassified as Group 1 (white arrows in Fig. 6.16A, B, and D) by the LDA and K-means models. This misclassification does not reflect lithological similarity but rather the impact of diminished illumination, demonstrating the influence of acquisition conditions on reflectance-based discrimination.

The spatial resolution of the hyperspectral imagery (each pixel ~1 cm) introduced additional challenges, as each ROI encompassed multiple pixels. In thin geological layers, such as the rudstone facies (RUD), pixel mixing likely generated blended signals that hindered accurate separation. This effect was further compounded by the local replacement of gastropod shells with silica (Fig. 6.6), as observed in thin sections, which caused this carbonate facies to be grouped with siliciclastic facies by the classification models. These outcomes demonstrate how both spectral mixing and diagenetic overprints can compromise the robustness of discrimination.

An important observation is that the supervised models (Fig. 6.15B, C; Fig. 6.16B, C) consistently revealed heterogeneities within lithofacies that were not apparent to the naked eye or in field-based interpretation. For example, laminites appeared visually uniform to the interpreter, but the models highlighted internal spectral variability in the near-infrared domain, likely associated with subtle changes in clay content which are not easily detectable in the visible range. Similarly, other carbonate facies exhibited variations that may reflect both compositional differences and diagenetic overprints.

A further consideration is that the ground truth used in this study does not represent an absolute reference, but rather an expert-driven interpretative model constrained by outcrop visibility and field observations. Even when petrographic thin sections are available, the information remains point-based and cannot fully capture lateral or vertical heterogeneity within geological bodies. In contrast, hyperspectral data provide a different layer of information, capable of detecting spectral variations that are not visually discernible yet some of these variations may be influenced by illumination or surface conditions rather than purely compositional changes. For instance, subtle increases in clay content within a carbonate package initially classified as G3 by the interpreter were revealed by the hyperspectral response as internal variability more closely resembling portions of G2. Such effects contribute to the apparent reduction in model performance when compared to the ground truth, but in practice they reflect complementary perspectives. Consequently, hyperspectral-based classified maps often appear more heterogeneous than the ground truth, capturing spectral signatures that extend beyond the limits of visual interpretation.

Supervised models yielded broadly comparable results when evaluated against the ground truth, but with some notable differences. In the Assado outcrop, for instance, the MLP model proved more robust to external lighting effects, mitigating the impact of tree shadows that caused misclassification in the LDA outputs. When the Vapumas-trained models were applied to Assado, overall performance metrics remained comparable to those obtained for Vapumas itself, although correspondence with the ground truth was stronger in the lower interval (A1) than in the upper (A2). Visual inspection further showed that, in Assado, both LDA and MLP tended to classify more G2 in areas actually dominated by G3. The MLP also displayed slightly greater heterogeneity than LDA, reflecting its ability to capture non-linear relationships in the spectral data, which may enhance the detection of subtle within-facies variability while increasing interpretative complexity. Although cross-application was not the main objective of this work, with Assado serving here as a blind test, future efforts could explore training models on both outcrops to improve transferability.

The K-means clustering provided an unsupervised baseline, offering an independent view of latent spectral structures within the hyperspectral cubes. While its clusters could be matched to facies through post-hoc comparison with supervised models or the ground truth, discrepancies highlighted its sensitivity to initialization and the absence of geological constraints. Beyond serving as a baseline, K-means also enables exploration of latent spectral patterns that may not be captured by supervised classifications. In this sense, it can reveal unexpected subdivisions or subtle differences within apparently homogeneous facies, potentially indicating geologically relevant variations. Even with only three clusters, K-means reproduced the stratified character of SBIII while revealing greater internal heterogeneity than the supervised models in certain intervals.

Importantly, across all methods, supervised and unsupervised, the stratified character of SBIII was consistently reproduced, underscoring that the hyperspectral signal reflects depositional processes such as climatic variations that modulated siliciclastic influx and controlled carbonate accumulation in the lacustrine system. Looking forward, future work could benefit from integrating hyperspectral cubes with photogrammetric datasets to achieve geometric correction and reduce distortions inherent to 2D imagery, such as perspective effects and scale inconsistencies. By transferring spectral information onto point clouds, hyperclouds can be generated following procedures described by Lorenz et al. (2018), Krupnik and Khan (2019), and Thiele et al. (2021). Notably, Thiele et al. (2021) introduced the open-source Python library *hylite*, which provides a workflow for creating hyperclouds by fusing geometric information with hyperspectral imaging data, among other functionalities.

## 6.6. Conclusions

Despite the absence of the >2000 nm diagnostic bands for clays and carbonates, hyperspectral imaging restricted to 900–1700 nm, supported by field spectroscopy and expert interpretation, proved to be effective for lithofacies discrimination and mapping in the Balbuena III Sequence (SBIII), Salta Basin, when classes were treated at the level of broader facies groups. Key findings show that full-range field spectroscopy (450–2500 nm) separated the ten lithofacies with high accuracy using LDA, confirming the spectral distinctiveness of SBIII under ideal coverage. For the imagery range (900–1700 nm), HAC revealed three robust lithological groups that capture the main siliciclastic–carbonate contrasts. Trained on spectra extracted from image ROIs, LDA and MLP produced consistent group-level classifications and 2D facies maps, showing closer agreement with the ground truth than K-means, as expected from their methodological framework. Models trained on Vapumas generalized to Assado, indicating that the learned spectral patterns reflect lithological properties rather than site-specific effects. Comparisons against expert ground truth demonstrated the stratified architecture of SBIII and highlighted within-facies heterogeneity that is not always visible in the field.

The study contributes a practical workflow for outcrop-scale facies mapping when only partial spectral intervals are available: (i) establish spectral references with field measurements, (ii) use unsupervised analysis to determine separable groupings appropriate to the available bands, and (iii) apply supervised classification directly to hyperspectral cubes to generate consistent, interpretable maps. In lacustrine successions such as SBIII, this approach provides spatially continuous, objective information that complements sedimentological logging and petrography.

Limitations arise primarily from (i) the constrained spectral range, which shifts separability toward reflectance amplitude and slopes, making results sensitive to illumination; (ii) pixel mixing in thin beds and along irregular contacts; and (iii) the interpretative nature of the ground

truth, which cannot fully capture lateral and vertical heterogeneity. These constraints may yield apparent mismatches when hyperspectral data resolve variability beyond visual criteria.

Future studies would benefit from quantitative mineralogical data, such as X-ray diffraction (XRD), to refine spectral signatures by linking specific absorption bands to clay and carbonate phases, allowing a more precise identification of diagnostic features. If the goal is to achieve finer facies separation, full spectral coverage remains essential. In addition, integrating hyperspectral cubes with photogrammetric DOMs to reduce geometric distortions and project spectra onto 3D point clouds would enable more rigorous spatial evaluation. Expanding training data across outcrops and acquisition conditions, while exploring illumination-invariant preprocessing tailored to amplitude-driven separability, would likely enhance robustness and transferability. Taken together, the results demonstrate that even under restricted wavelength coverage, outcrop-based hyperspectral imaging can deliver geologically meaningful facies maps that preserve the stratified character of SBIII and expose compositional variability. Such capability supports lithofacies mapping applicable to reservoir analog studies, mineral exploration, and broader geoscientific investigations.

## Acknowledgements

The authors thank Petrobras for supporting this research. The imagery and field data acquisitions used in this study were conducted under the Petrobras–Unipampa cooperation agreement, with financial support from the Brazilian National Agency of Petroleum, Natural Gas and Biofuels (ANP), project No. 0050.0121770.22.9 (SIGITEC 2022/00056–5). We are also grateful to Roberto Hernández, CEO of Geomap (Argentina), for his kind assistance and invaluable logistical support during fieldwork. Special thanks are extended to Brenda Schreiner, Ezequiel Galvão, Luiz Felipe de Oliveira, and Samuel Araújo for their contributions to data acquisition.

## References

Abdi, H., Williams, L.J., 2010. Principal component analysis. WIREs Computational Statistics 2, 433–459. https://doi.org/10.1002/wics.101

Agisoft, 2023. Agisoft Metashape Professional v2.0.1 (Version 2.0.1) [software]. https://www.agisoft.com

Analytical Spectral Devices, n.d. ViewSpec PRO v6.2 (Version 6.2) [Software].

Arthur, D., Vassilvitskii, S., 2007. k-means++: The Advantages of Careful Seeding, in: Eighteenth Annual ACM-SIAM Symposium on Discrete Algorithms, SODA. SODA, Louisiana, pp. 1027–1035.

Attallah, Y., Zigh, E., Adda, A.P., 2024. Optimized 3D-2D CNN for automatic mineral classification in hyperspectral images. Reports on Geodesy and Geoinformatics 118. https://doi.org/10.2478/rgg-2024-0017

Bedini, E., 2011. Mineral mapping in the Kap Simpson complex, central East Greenland, using HyMap and ASTER remote sensing data. Advances in Space Research 47, 60–73. https://doi.org/10.1016/j.asr.2010.08.021

Bento Freire, E., 2012. Caracterização Estratigráfica em Alta Resolução das Sequências Calcárias de Origem Microbiana do Intervalo Paleocênico da Formação Yacoraite (Sequência Balbuena IV) Na Região de Salta-Argentina (MSc thesis). Universidade Federal do Rio de Janeiro, Rio de Janeiro.

Bianucci, H., Acevedo, O., Cerdán, J., 1981. Evolución tectono-sedimentaria del Grupo Salta en la subcuenca de Lomas de Olmedo (Provincias de Salta y Formosa), in: VIII Congreso Geológico Argentino. Servicio Geológico Nacional, San Luis, pp. 159–172.

Bistacchi, A., Mittempergher, S., Martinelli, M., 2022. Digital Outcrop Model Reconstruction and Interpretation, in: Bistacchi, A., Massironi, M., Viseur, S. (Eds.), 3D Digital Geological Models: From Terrestrial Outcrops to Planetary Surfaces. Wiley, pp. 11–32. https://doi.org/https://doi.org/10.1002/9781119313922.ch2

Boll, A., 1991. Identificación y correlación de secuencias somerizantes del Miembro Las Avispas (Formación Yacoraite). Noroeste Argentino., in: X Congreso Geológico Argentino. Asociación Geológica Argentina, San Miguel de Tucumán, pp. 153–156.

Buckley, S.J., Kurz, T.H., Howell, J.A., Schneider, D., 2013. Terrestrial lidar and hyperspectral data fusion products for geological outcrop analysis. Computers and Geosciences 54, 249–258. https://doi.org/10.1016/j.cageo.2013.01.018

Camargo, M.H.T., Ferreira, A.D., Pinto-Coelho, C.V., Oliveira, S.P., Guimarães, T.T., Cavallari, M.L., Veronez, M.R., de Filippis Alfaro, L., 2023. Hyperspectral analysis (VNIR-SWIR) applied to the characterization of a dolomitization context: a case study in Rio Bonito Quarry, Brazil. Carbonates and Evaporites 38. https://doi.org/10.1007/s13146-023-00846-0

Clark, R.N., 1999. Spectroscopy of Rocks and Minerals, and Principles of Spectroscopy, in: Rencz, A.N. (Ed.), Manual of Remote Sensing, Volume 3: Remote Sensing for the Earth Sciences. John Wiley & Sons, New York, pp. 3–58.

de Oliveira, K.M., Falcioni, R., Gonçalves, J.V.F., de Oliveira, C.A., Mendonça, W.A., Crusiol, L.G.T., de Oliveira, R.B., Furlanetto, R.H., Reis, A.S., Nanni, M.R., 2023. Rapid Determination of Soil Horizons and Suborders Based on VIS-NIR-SWIR Spectroscopy and Machine Learning Models. Remote Sensing 15. https://doi.org/10.3390/rs15194859

Del Papa, C.E., Salfity, J.A., 1999. View of Non-marine Paleogene sequences, Salta Group, Northwest Argentina. Acta Geologica Hispanica 34, 105–121.

Everitt, B.S., Landau, S., Leese, M., Stahl, D., 2011. Cluster Analysis, 5th ed.

Exelis Visual Information Solutions, 2015. ENVI v.5.3 (Version 5.3) [software].

Fisher, R.A., 1936. The use of multiple measurements in taxonomic problems. Annals of Eugenics 7, 179–188. https://doi.org/10.1111/j.1469-1809.1936.tb02137.x

Gairola, G.S., Thiele, S.T., Khanna, P., Ramdani, A., Gloaguen, R., Vahrenkamp, V., 2024. A data-driven hyperspectral method for sampling of diagenetic carbonate fabrics – A case study using an outcrop analogue of Jurassic Arab-D reservoirs, Saudi Arabia. Marine and Petroleum Geology 161. https://doi.org/10.1016/j.marpetgeo.2024.106691

Galdames, F.J., Perez, C.A., Estévez, P.A., Adams, M., 2019. Rock lithological classification by hyperspectral, range 3D and color images. Chemometrics and Intelligent Laboratory Systems 189, 138–148. https://doi.org/10.1016/j.chemolab.2019.04.006

Ghamisi, P., Yokoya, N., Li, J., Liao, W., Liu, S., Plaza, J., Rasti, B., Plaza, A., 2017. Advances in Hyperspectral Image and Signal Processing: A Comprehensive Overview of the State of the Art. IEEE Geoscience and Remote Sensing Magazine 5, 37–78. https://doi.org/10.1109/MGRS.2017.2762087

Ghojogh, B., Crowley, M., 2019. Linear and Quadratic Discriminant Analysis: Tutorial.

Gómez Omil, R.J., Boll, A., 2005. Cuenca Cretácica del Noroeste Argentino, in: VI Congreso de Exploración y Desarrollo de Hidrocarburos: Ampliando las Fronteras. IAPG, Mar del Plata, pp. 63–73.

Gómez Omil, R.J., Boll, A., 1999. Sistema petrolero de la cuenca cretácica del noroeste argentino, in: IV Congreso de Exploración y desarrollo de hidrocarburos. IAPG, Mar del Plata, pp. 101–112.

Gómez Omil, R.J., Boll, A., Hernández, R.M., 1989. Cuenca cretácico-terciaria del Noroeste argentino (Grupo Salta), in: Chebli, G.A., Spalletti, L.A. (Eds.), Cuencas Sedimentarias Argentinas. Tucumán, pp. 43–64.

Goodfellow, I., Bengio, Y., Courville, A., 2016. Deep Learning. MIT Press, Cambridge, MA.

Gordon, A.D., 1987. A Review of Hierarchical Classification. Journal of the Royal Statistical Society. Series A (General) 150, 119–137.

Granemann, D.C., Elias, A.R., Felipetto, H. dos S., Yoshino Watanabe, F.S., Piroli, E.L., 2025. Production and Calibration of a Lambertian Surface Based on Barium Sulfate (BaSO4) for the Calibration of Multispectral Cameras. Drones and Autonomous Vehicles 2, 10012–10012. https://doi.org/10.70322/dav.2025.10012

Hartigan, J.A., Wong, M.A., 1979. Algorithm AS 136: A K-Means Clustering Algorithm. Journal of the Royal Statistical Society. Series C (Applied Statistics) 28, 100–108.

Haykin, S., 1999. Neural Networks: A Comprehensive Foundation, 2nd ed. ed. Prentice Hall.

Henriksen, M.L., Pedersen, W.N., Klarskov, P., Hinge, M., 2022. One step calibration of industrial hyperspectral cameras. Chemometrics and Intelligent Laboratory Systems 227, 104609. https://doi.org/10.1016/j.chemolab.2022.104609

Hernández, R., Echavarria, L., 2009. Faja Plegada y Corrida Subandina del Noroeste Argentino: Estratigrafía, Geometría y Cronología de la Deformación. Revista de la Asociación Geológica Argentina 65, 68–80.

Hernández, R.M., Disalvo, A., Boll, A., Gómez Omil, R., Gallli, C., 1999. Estratigrafia secuencial del Grupo Salta, con enfasis en las subcuencas de Metan-Alemania, noroeste Argentino, in: Bonorino, G.G., Omarini, R., Viramonte, J. (Eds.), Geología del Noroeste Argentino, Relatorio del XIV Congreso Geológico Argentino. pp. 263–283.

Hernández, R.M., Omil, G.R., Boll, A., 2008. Estratigrafía, Tectónica y Potencial petrolero del rift cretácico em la Provincia de Jujuy, in: XVII Congreso Geológico Argentino. Asociación Geológica Argentina, Jujuy, pp. 207–232.

Jacq, K., Debret, M., Fanget, B., Coquin, D., Sabatier, P., Pignol, C., Arnaud, F., Perrette, Y., 2022. Theoretical Principles and Perspectives of Hyperspectral Imaging Applied to Sediment Core Analysis. Quaternary. https://doi.org/10.3390/quat5020028

Jain, A.K., 2010. Data clustering: 50 years beyond K-means. Pattern Recognition Letters 31, 651–666. https://doi.org/10.1016/j.patrec.2009.09.011

Jolliffe, I.T., 2002. Principal Component Analysis, 2nd ed. ed. Springer.

Kingma, D.P., Ba, J., 2015. Adam: A Method for Stochastic Optimization, in: 3rd International Conference on Learning Representations (ICLR).

Koerting, F., Asadzadeh, S., Hildebrand, J.C., Savinova, E., Kouzeli, E., Nikolakopoulos, K., Lindblom, D., Koellner, N., Buckley, S.J., Lehman, M., Schläpfer, D., Micklethwaite, S.,

2024. VNIR-SWIR Imaging Spectroscopy for Mining: Insights for Hyperspectral Drone Applications. Mining. https://doi.org/10.3390/mining4040057

Kokaly, R.F., C.R.N., S.G.A., L.K.E., H.T.M., P.N.C., W.R.A., B.W.M., L.H.A., D.R.L., and K.A.J., 2017. USGS Spectral Library Version 7 Data: U.S. Geological Survey data release. https://doi.org/https://doi.org/10.5066/F7RR1WDJ

Krupnik, D., Khan, S., 2019. Close-range, ground-based hyperspectral imaging for mining applications at various scales: Review and case studies. Earth-Science Reviews. https://doi.org/10.1016/j.earscirev.2019.102952

Kurz, T.H., Buckley, S.J., Howell, J.A., 2013. Close-range hyperspectral imaging for geological field studies: Workflow and methods. International Journal of Remote Sensing 34, 1798–1822. https://doi.org/10.1080/01431161.2012.727039

Kurz, T.H., Dewit, J., Buckley, S.J., Thurmond, J.B., Hunt, D.W., Swennen, R., 2012. Hyperspectral image analysis of different carbonate lithologies (limestone, karst and hydrothermal dolomites): The Pozalagua Quarry case study (Cantabria, North-west Spain). Sedimentology 59, 623–645. https://doi.org/10.1111/j.1365-3091.2011.01269.x

Kurz, T.H., Miguel, G.S., Dubucq, D., Kenter, J., Miegebielle, V., Buckley, S.J., 2022. Quantitative mapping of dolomitization using close-range hyperspectral imaging: Kimmeridgian carbonate ramp, Alacón, NE Spain. Geosphere 18, 780–799. https://doi.org/10.1130/GES02312.1

Lorenz, S., Salehi, S., Kirsch, M., Zimmermann, R., Unger, G., Vest Sørensen, E., Gloaguen, R., 2018. Radiometric Correction and 3D Integration of Long-Range Ground-Based Hyperspectral Imagery for Mineral Exploration of Vertical Outcrops. Remote Sensing 10, 176. https://doi.org/10.3390/rs10020176

Lowe, D.G., 2004. Distinctive Image Features from Scale-Invariant Keypoints. International Journal of Computer Vision 60, 91–110. https://doi.org/https://doi.org/10.1023/B:VISI.0000029664.99615.94

MacQueen, J., 1967. Some methods for classification and analysis of multivariate observations, in: Fifth Berkeley Symposium on Mathematical Statistics and Probability. pp. 281–297.

Magalhães, A.J.C., Raja Gabaglia, G.P., Fragoso, D.G.C., Bento Freire, E., Lykawka, R., Arregui, C.D., Silveira, M.M.L., Carpio, K.M.T., De Gasperi, A., Pedrinha, S., Artagão, V.M., Terra, G.J.S., Bunevich, R.B., Roemers-Oliveira, E., Gomes, J.P., Hernández, J.I., Hernández, R.M., Bruhn, C.H.L., 2020. High-resolution sequence stratigraphy applied to reservoir zonation and characterisation, and its impact on production performance - shallow marine, fluvial downstream, and lacustrine carbonate settings. Earth-Science Reviews 210. https://doi.org/10.1016/j.earscirev.2020.103325

Manning, C.D., Raghavan, P., Schütze, H., 2009. Introduction to Information Retrieval, 2nd ed. Cambridge University Press, Cambridge, UK.

Marquillas, R.A., Del Papa, C., Sabino, I.F., 2005. Sedimentary aspects and paleoenvironmental evolution of a rift basin: Salta Group (Cretaceous-Paleogene), northwestern Argentina. International Journal of Earth Sciences 94, 94–113. https://doi.org/10.1007/s00531-004-0443-2

Marquillas, R.A., Salfity, J.A., Matthews, S.J., Matteini, M., Dantas, E., 2011. U-Pb zircon age of the Yacoraite Formation and its significance to the Cretaceous-Tertiary boundary in the Salta Basin, Argentina. Cenozoic Geology of the Central Andes of Argentina 227–246.

McCormick, C.A., Corlett, H., Stacey, J., Hollis, C., Feng, J., Rivard, B., Omma, J.E., 2021. Shortwave infrared hyperspectral imaging as a novel method to elucidate multi-phase dolomitization, recrystallization, and cementation in carbonate sedimentary rocks. Scientific Reports 11. https://doi.org/10.1038/s41598-021-01118-4

Moreno, J.A., 1970. Estratigrafía y paleogeografía del Cretácico Superior en la Cuenca del Noroeste Argentino, con especial mención de los Subgrupos Balbuena y Santa Bárbara. Revista de la Asociación Geológica Argentina 25, 9–44.

Murphy, R.J., Taylor, Z., Schneider, S., Nieto, J., 2015. Mapping clay minerals in an open-pit mine using hyperspectral and LiDAR data. European Journal of Remote Sensing 48, 511–526. https://doi.org/10.5721/EuJRS20154829

Murtagh, F., Legendre, P., 2014. Ward's Hierarchical Agglomerative Clustering Method: Which Algorithms Implement Ward's Criterion? Journal of Classification 31, 274–295. https://doi.org/10.1007/s00357-014-9161-z

Pedregosa, F., Varoquaux, G., Gramfort, A., Michel, V., Thirion, B., Grisel, O., Blondel, M., Prettenhofer, P., Weiss, R., Dubourg, V., Vanderplas, J., Passos, A., Cournapeau, D., Brucher, M., Perrot, M., Duchesnay, E., 2011. Scikit-learn: Machine Learning in Python. Journal of Machine Learning Research 12, 2825–2830.

Pedrinha, S., Raja Gabaglia, G.P., Lykawka, R., Dias-Brito, D., 2015. High-resolution sequence tracking in Metán-Alemania Sub-basin (Salta Basin Maastrichtian – Argentina): detailed stratigraphic anatomy of a lacustrine system under the influence of microbial processes. Boletim de Geociências da Petrobras 23.

Peyghambari, S., Zhang, Y., 2021. Hyperspectral remote sensing in lithological mapping, mineral exploration, and environmental geology: an updated review. Journal of Applied Remote Sensing 15. https://doi.org/10.1117/1.jrs.15.031501

Posit, 2023. RStudio v2023.06.1 (Version 2023.06.1) [software]. https://posit.co/download/rstudio-desktop/

Powers, D.M.W., 2011. Evaluation: From precision, recall and F-measure to ROC, informedness, markedness & correlation. Article in Journal of Machine Learning Technologies 2, 37–63. https://doi.org/10.9735/2229-3981

Python, 2023. Python v3.11.4 (Version 3.11.4) [software]. https://www.python.org/

Rakotomalala, R., 2020. Pratique de l'Analyse Discriminante Linéaire. Lyon.

Reyes, F.C., Salfity, J.A., 1973. Consideraciones sobre la estratigrafia del Cretacico (Subgrupo Pirgua) del noroeste argentino, in: V Congreso Geológico Argentino. Asociación Geológica Argentina, Córdoba, pp. 335–385.

Ripley, B., Venables, B., 2009. MASS: Support Functions and Datasets for Venables and Ripley's MASS. https://doi.org/10.32614/CRAN.package.MASS

Roemers-Oliveira, E., Viseur, S., Fournier, F., Gonçalves, Í.G., Guadagnin, F., Raja Gabaglia, G.P., Bento Freire, E., Fragoso, D.G.C., Hernández, J., Freccia, A.C., de Godoy Rangel, G., 2025. Advanced digital techniques applied to outcrop models: Integrating Local Binary Pattern (LBP) and Convolutional Neural Network (CNN) to support stratigraphic and sedimentological interpretation of reservoir analogs in the Salta Basin, Argentina. Marine and Petroleum Geology. https://doi.org/10.1016/

Rumelhart, D.E., Hinton, G.E., Williams, R.J., 1986. Learning representations by back-propagating errors. Nature 323, 533–536. https://doi.org/10.1038/323533a0

Salehi, S., Lorenz, S., Sørensen, E.V., Zimmermann, R., Fensholt, R., Heincke, B.H., Kirsch, M., Gloaguen, R., 2018. Integration of vessel-based hyperspectral scanning and 3D-photogrammetry for mobile mapping of steep coastal cliffs in the Arctic. Remote Sensing 10. https://doi.org/10.3390/rs10020175

Salfity, J.A., Marquillas, R.A., 1999. La cuenca cretácico-terciaria del norte argentino, in: Caminos, R. (Ed.), Geología Argentina. Instituto de Geología y Recursos Minerales, Buenos Aires, pp. 613–626.

Saporta, G., 2011. Probabilités, analyse des données et statistique, 3e éd. ed. Editions Technip, Paris.

Souza, M.K. de, Tognoli, F.M.W., Veronez, M.R., de Oliveira, L.P.L., Gonzaga, L., Cagliari, J., Scaioni, M., 2018. High-resolution spectroscopy for detecting stratigraphic surfaces and stacking patterns in sedimentary basins. Journal of South American Earth Sciences 88, 287–293. https://doi.org/10.1016/j.jsames.2018.08.022

Sun, L., Khan, S., Shabestari, P., 2019. Integrated hyperspectral and geochemical study of sediment-hosted disseminated gold at the Goldstrike District, Utah. Remote Sensing 11. https://doi.org/10.3390/rs11171987

TensorFlow, 2024. TensorFlow v2.18.0 (Version 2.18.0) [software]. https://www.tensorflow.org

Tharwat, A., Gaber, T., Ibrahim, A., Hassanien, A.E., 2017. Linear discriminant analysis: A detailed tutorial. AI Communications 30, 169–190. https://doi.org/10.3233/AIC-170729

Thiele, S.T., Bnoulkacem, Z., Lorenz, S., Bordenave, A., Menegoni, N., Madriz, Y., Dujoncquoy, E., Gloaguen, R., Kenter, J., 2022a. Mineralogical mapping with accurately corrected shortwave infrared hyperspectral data acquired obliquely from UAVs. Remote Sensing 14. https://doi.org/10.3390/rs14010005

Thiele, S.T., Kereszturi, G., Heap, M.J., Ribeiro, A. de L., Kamath, A., Kidd, M., Tramontini, M., Rosas-Carbajal, M., Gloaguen, R., 2025. Hyperspectral mapping of density, porosity, stiffness, and strength in hydrothermally altered volcanic rocks. Solid Earth. https://doi.org/10.5194/egusphere-2025-1904

Thiele, S.T., Lorenz, S., Kirsch, M., Cecilia Contreras Acosta, I., Tusa, L., Herrmann, E., Möckel, R., Gloaguen, R., 2021. Multi-scale, multi-sensor data integration for automated 3-D geological mapping. Ore Geology Reviews 136. https://doi.org/10.1016/j.oregeorev.2021.104252

Thiele, S.T., Lorenz, S., Kirsch, M., Gloaguen, R., 2022b. A Novel and Open-Source Illumination Correction for Hyperspectral Digital Outcrop Models. IEEE Transactions on Geoscience and Remote Sensing 60, 1–12. https://doi.org/10.1109/TGRS.2021.3098725

Turner, J.C.M., 1958. Estratigrafía del Cordón de Escaya y de la Sierra de Rinconada (Jujuy). Revista De La Asociación Geológica Argentina 13, 15–41.

van der Meer, F.D., van der Werff, H.M.A., van Ruitenbeek, F.J.A., Hecker, C.A., Bakker, W.H., Noomen, M.F., van der Meijde, M., Carranza, E.J.M., de Smeth, J.B., Woldai, T., 2012. Multi- and hyperspectral geologic remote sensing: A review. International Journal of Applied Earth Observation and Geoinformation. https://doi.org/10.1016/j.jag.2011.08.002

*Les Joueurs de cartes, Paul Cézanne, 1890, via Wikimedia Commons.*

*« Tu deviens responsable pour toujours de ce que tu as apprivoisé. »*
*Antoine de Saint-Exupéry, Le Petit Prince (1943)*

# Chapter 7
# Transversal Discussion, Conclusions, and Perspectives

## 7.1. Transversal Discussion

The transversal discussion seeks to integrate the main findings of the thesis by combining results obtained from different datasets, scales, and methodological approaches. Building on individual outcomes, the emphasis is on how these complementary approaches, grounded in both the scientific and philosophical questions that frame this work, interact to advance the understanding of lacustrine depositional systems, their facies architecture, and their potential as reservoir analogs. The discussion is organized into four parts: first, the integrative character of the work is examined, showing how multi-method and multi-scale strategies provide a broader understanding while also revealing strengths and limitations. Second, the stratigraphic models derived from the Barre du Cengle and Salta Basin are compared, with attention to correlation patterns and distances across lacustrine and lacustrine/palustrine settings. Third, the conceptual and applied role of outcrop analogs is addressed, emphasizing their transferability to petroleum reservoir studies. Finally, the discussion turns to Pre-salt reservoirs, highlighting their challenges and the insights that can be drawn from the analogs studied.

### 7.1.1. Integration of Multi-Method and Multi-Scale Approaches

In petroleum geoscience, professional practice is commonly divided between exploration and production. Exploration geologists focus on locating hydrocarbon accumulations at regional scales, developing models and predictive criteria to identify depositional architectures with reservoir potential. In contrast, production geoscientists operate at much finer scales, aiming to understand and model reservoir heterogeneity to support efficient development strategies.

The research developed in this thesis is positioned at the reservoir scale, where data from outcrops play a fundamental role in defining conceptual reservoir models. The study focused on depositional successions of approximately 30 m in thickness, subdivided into smaller stratigraphic intervals for detailed facies and heterogeneity characterization. This approach reflects the perspective of production geology, where the core task is to study reservoir characteristics and understand how heterogeneities influence fluid flow (Weber and van Geuns, 2005). Production geoscientists rely on multidisciplinary collaborations that integrate sedimentology, diagenesis, structural geology, seismology, petrophysics, geomodelling, and geostatistics to construct predictive models (Weber and van Geuns, 2005; Branets et al., 2009; Li et al., 2017). Reservoir modeling is inherently multiscale, requiring the reconciliation of data ranging from core plugs and well logs to seismic surveys within unified three-dimensional frameworks (Branets et al., 2009; Li et al., 2017). Like a puzzle, this process integrates pieces from different datasets and disciplines into a coherent framework supporting reservoir characterization and development (Bruhn et al., 2017).

This integrative role is particularly challenging in carbonate systems, where porosity and permeability are governed not only by depositional facies but also by diagenetic processes such as dissolution, cementation, and dolomitization, as well as by fracture networks and karstification (Weber and van Geuns, 2005; Follows, 2025; Mehrabi et al., 2025). Wireline log data often fail to distinguish between different carbonate lithofacies, making it necessary to combine sedimentological, diagenetic, and structural information for robust flow characterization (Follows, 2025). In this context, outcrop analogs play a critical role, providing well-constrained spatial information on facies distribution and reservoir body geometries that support well-to-well correlations and predictive modeling (Weber and van Geuns, 2005).

This work follows the reservoir-oriented perspective by adopting a multiscale strategy that integrates datasets from the microscopic scale to mesoscale DOMs. Through the application of

multiple methods, the research aims to capture heterogeneity and generate parameters that contribute to more realistic reservoir-scale frameworks. This perspective is complemented by the discussion in Section 4.7.3 of Chapter 4, which addresses the use of outcrop analogs for reservoir modeling.

The HRSS model developed for La Barre du Cengle was progressively constructed through the integration of datasets acquired across multiple scales and methods (Fig. 7.1). The work began in the field, where vertical stratigraphic sections were logged and samples collected. Since the succession is predominantly composed of mud-supported carbonate facies, petrographic analysis was fundamental in recognizing microstructural features that refined the identification of eight distinct lithofacies. These were grouped into three facies associations representing lacustrine, palustrine, and pedogenic domains, and also supported the definition of an exposure index. A consistent transition was recognized, from lacustrine → palustrine → pedogenic, from west to east. The integration of petrography with field observations allowed the identification of five elementary sequences, which were then stacked into small-scale sequences. The maximum retraction surfaces (MRSs), which define the boundaries of the small-scale sequences, could be traced laterally across the cliff thanks to the photogrammetric DOM covering the entire Cengle Plateau, enabling the subdivision of the area into four stratigraphic intervals (Cengle I to Cengle IV). Geochemical analyses, including carbon and oxygen isotopes, together with U–Pb dating, provided chronological and environmental constraints, which were further refined through integration with petrographic observations.

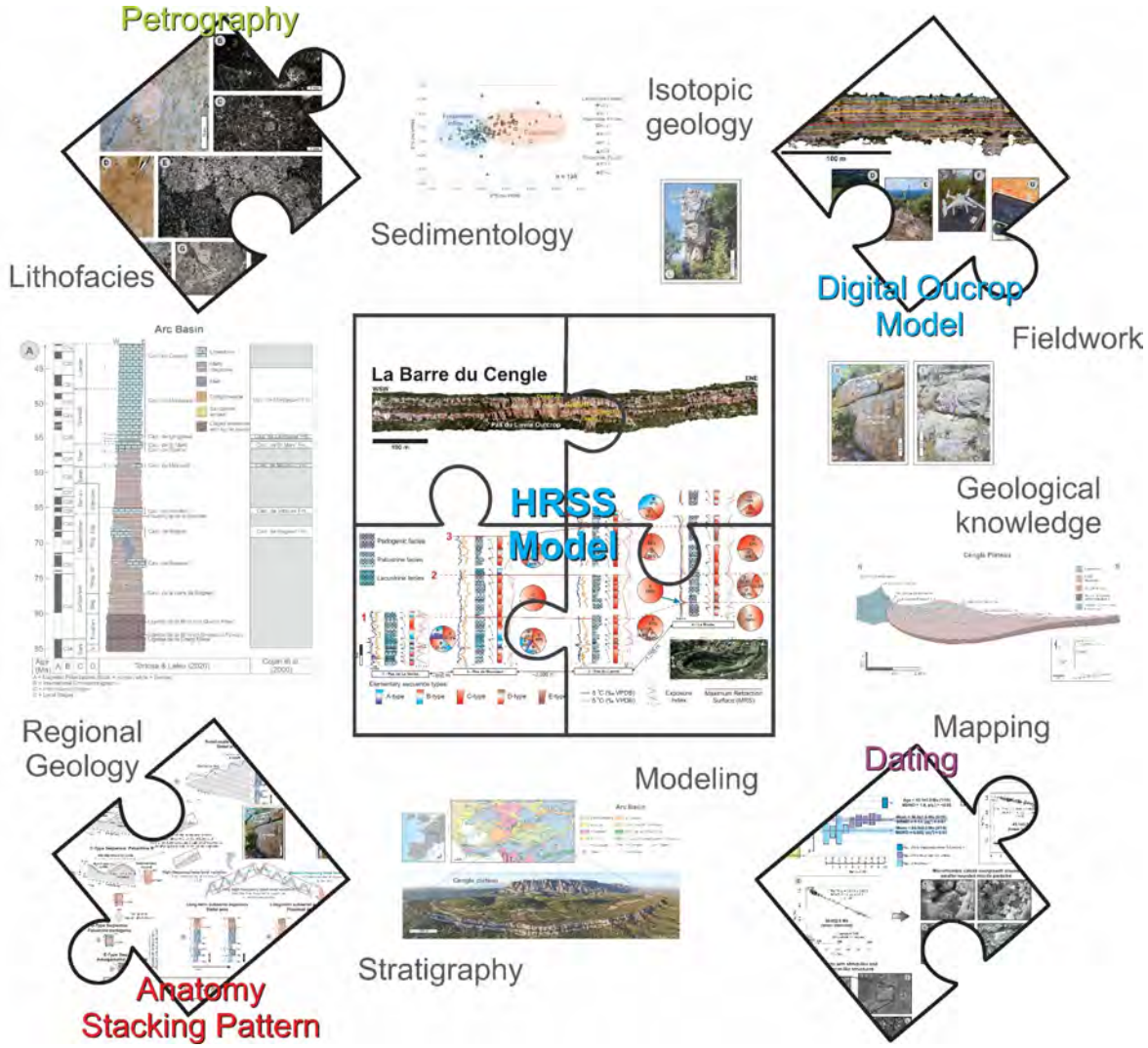


**Fig. 7.1.** Multi-scale integration of datasets applied to build the High-Resolution Sequence Stratigraphy (HRSS) model of La Barre du Cengle.

The integration of U–Pb dating on micrite with petrographic observations marked a key step forward in interpreting the succession. The new ages indicate deposition earlier than previously assumed, within the Danian–early Selandian stages, while petrographic analyses revealed the occurrence of benthic foraminifera in the uppermost stratigraphic interval (Cengle IV) of the Pas du Lièvre section, pointing to increased salinity during this interval. Together, these datasets not only support a revision of the chronostratigraphic framework of the Arc Basin but also suggest a potential link with marine transgression events documented in the Bas-Languedoc Basin during the Danian–Selandian. Importantly, Cengle IV is the only stratigraphic interval in which lacustrine facies were identified in the Pas du Lièvre section, the second easternmost profile studied. This indicates a phase of greater expansion of Lake Cengle.

In the Salta Basin, since sedimentological and stratigraphic aspects of this interval have been studied for more than a decade, although they remain subject to continuous updates, the present work could advance further by applying digital techniques. In particular, these methods were used to generate DOMs in which stratigraphic and facies products were highlighted (Fig. 7.2), while remaining firmly oriented by the high-resolution stratigraphic framework of the Balbuena III Sequence. This digital emphasis was anchored in field logging, petrography, and lithofacies analysis, which provided the essential basis for interpretation. In this case, 19 lithofacies were described and grouped into four facies associations, which at low frequency record the transition from an open-lake system dominated by siliciclastic facies at the base to a closed-lake system with predominantly carbonate facies at the top. This evolution allowed the definition of two elementary sequences, each corresponding to one of the dominant facies intervals, which recur and stack into four small-scale sequences, bounded by maximum retraction surfaces. Because the elementary sequences of the Balbuena III Sequence are predominantly of transgressive–regressive ($T{-}R$) type and exhibit strong facies contrasts, they offered favorable conditions for testing innovative workflows. DOMs not only enabled detailed mapping of stacking patterns and facies distribution but also served as the spatial reference for integrating complementary approaches such as LBP, CNN, and HSI.

The integration of these approaches provided new insights into the stratigraphic architecture and facies organization of the Balbuena III Sequence. LBP analysis highlighted cyclicity patterns and stratigraphic surfaces, supporting the recognition of elementary to medium-scale sequence boundaries. CNN workflows enabled the isolation of lithofacies as 3D geobodies within point clouds, directly linking facies distribution to depositional geometries. Hyperspectral imaging, though limited in spectral range, successfully discriminated lithological groups and produced consistent facies maps. Together, these results underscore the potential of digital methods to strengthen the HRSS approach by providing scalable, reproducible, and quantitative parameters for reservoir analog studies in lacustrine systems. They also demonstrate the ability of machine learning techniques to reduce the manual workload of specialized tasks.

By integrating traditional field and laboratory methods such as stratigraphic logging, petrography, geochemistry, and geochronology with digital approaches such as DOMs, LBP, CNN, and HSI, the workflows developed for La Barre du Cengle and the Salta Basin, anchored in a high-resolution stratigraphic framework, demonstrate how complementary strategies can refine the understanding of sedimentary processes and facies organization in lacustrine–palustrine systems. Beyond their local significance, these approaches provide predictive insights and transferable methodologies that can be applied to other basins with similar depositional settings, strengthening their role as reservoir analogs. While primarily developed in the context of petroleum systems, with appropriate adaptations these workflows are also

applicable to aquifer studies and carbon capture and storage (CCS), where limited subsurface data make reservoir analogs key elements for reducing uncertainty.

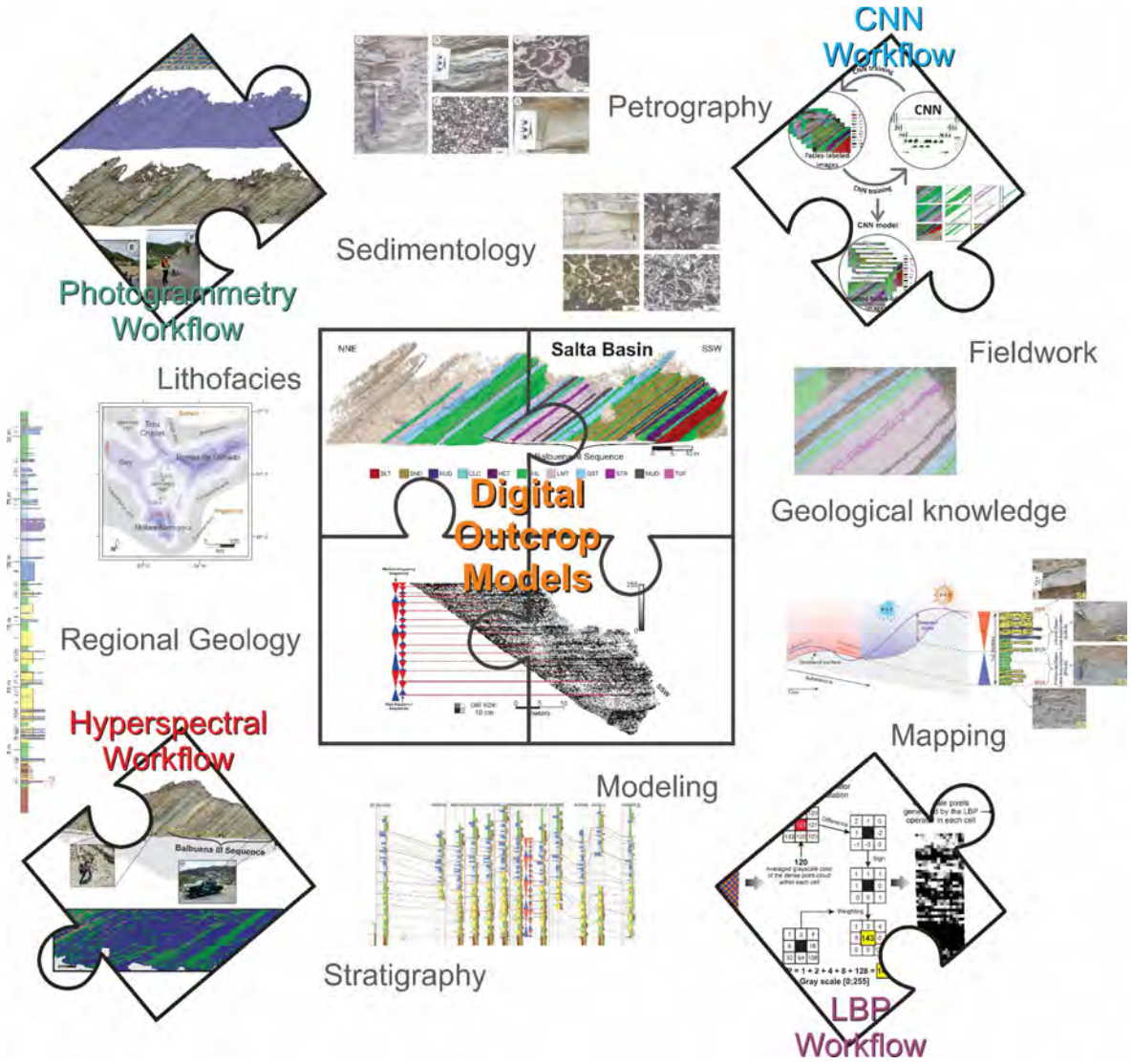


**Fig. 7.2.** Digital techniques applied to the Balbuena III Sequence (Salta Basin), with DOMs as the central framework to highlight stratigraphic and facies products, integrated with photogrammetry, LBP, CNN, and HIS.

### 7.1.2. Stratigraphic Models: Barre du Cengle versus Salta Basin

The stratigraphic models developed for La Barre du Cengle and the Salta Basin reveal contrasting architectures that reflect their dominant depositional domains. At La Barre du Cengle, the low-frequency framework corresponds to the entire carbonate bar that forms the cliff. This body extends for about 7 km in length and 2 km in width, although exposures are restricted to the southern margin. Thickness decreases from nearly 35 m in the west to around 20 m in the east. Medium-frequency architecture is expressed by four small-scale sequences (Cengle I to IV), each 6.5 to 11.5 m thick depending on whether the section lies in a more lacustrine, palustrine, or pedogenic domain. These sequences are bounded by maximum retraction surfaces (MRS) formed during long-term subaerial exposure, and their correlation can be traced along the entire 7 km-long cliff with the support of the photogrammetric DOM. High-frequency architecture is defined by three main types of elementary sequences, increasing to five if the long-term overprint of pedogenesis is considered. They are mostly regressive (*R*) type, with transgressive–regressive (*T* – *R*) sequences occurring more commonly in the western part of the cliff. Their thickness ranges from 0.5 to 1.5 m, and their lateral correlation potential

is limited to a few hundred meters. This restriction results from the overall low facies contrast of this muddy carbonate, low-energy deposit, which hampers high-resolution correlation. It is further accentuated by amalgamation and pedogenetic overprinting, including that associated with very high-frequency base-level variations responsible for the development of palustrine facies. The effect becomes more pronounced toward the east, where palustrine and pedogenic facies dominate due to the stronger influence of both short- and long-term subaerial exposures.

In contrast, the SBIII in the Salta Basin records a more continuous lacustrine succession, with stratigraphic organization well preserved at multiple frequencies. At low frequency, SBIII corresponds to a succession averaging 30 m in thickness, with minor variations from 25 to 30 m related to paleotopographic relief, such as local structural highs within the basin floor. This interval records the transition from an open-lake setting with dominant siliciclastic facies at the base to a closed-lake system with dominant carbonate facies at the top. Medium-frequency architecture is represented by four small-scale sequences, two in the siliciclastic interval and two in the carbonate part, with thicknesses of 6 to 9 m. Although the studied outcrops are discontinuous and correspond to isolated exposures, these sequences were correlated across all sections using key stratigraphic markers for reference. At high frequency, fifteen elementary sequences were identified, consisting of two recurring types: the Siliciclastic-dominated Elementary Sequence in the basal interval and the Carbonate-dominated Elementary Sequence at the top. They are predominantly transgressive–regressive (*T* – *R*) type, although regressive (*R*) ones also occur in the upper part. These elementary sequences can be correlated across the studied outcrops and traced for distances of about 45 km, which would correspond to nearly 70 km in the depositional context once Andean shortening is restored. Their strong correlation potential reflects both the clear facies contrasts and the dominantly lacustrine character of the succession. Subaerial exposure surfaces marked by shrinkage cracks occur at the top of some sequences but are superficial, rarely extending beyond a few centimeters, indicating that exposure events were relatively short.

The comparison between the two stratigraphic models of La Barre du Cengle and the Salta Basin (Fig. 7.3) can be understood through the *accordion effect* analogy proposed by Fragoso et al. (2021). In this framework, accommodation (A) is defined as the measurable thickness of space, at a specific location and time, that becomes filled with sediments during a given interval. This definition, introduced by Muto and Steel (2000), emphasizes its objective, rate-based nature and represents a refinement of earlier concepts, such as Jervey's definition (Jervey, 1988) of space below base level. In parallel, sediment supply (S) refers to the input of particles and solutes into the basin, derived from extrabasinal sources such as tectonic and climatic controls, or from intrabasinal processes including chemical, biochemical, and biogenic production (Reading and Levell, 1996; Fragoso et al., 2021). Thus, the preserved stratigraphic record reflects the balance between accommodation (A) and sediment supply (S), with variations in the A/S ratio directly controlling stacking patterns, preservation potential, and the resolution of stratigraphic analysis. However, it is important to note that the stratigraphic record corresponds to only a fraction of total geological time, with significant gaps where no deposition occurred or where previously deposited sediments were eroded (Barrell, 1917; Catuneanu, 2019; Fragoso et al., 2021).

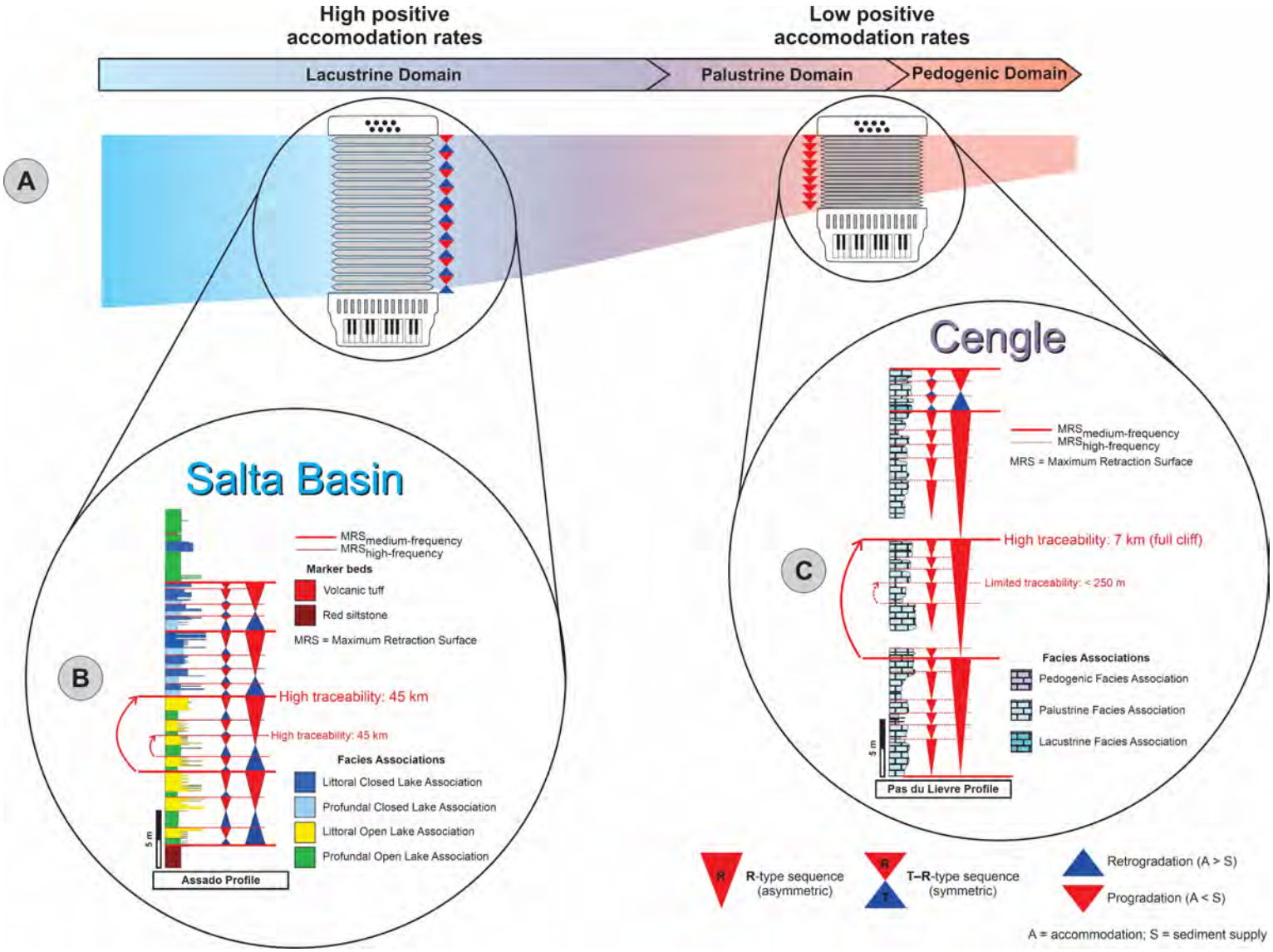


**Fig. 7.3.** Accordion effect analogy (A), adapted from Fragoso et al. (2021), applied to the stratigraphic models of the Balbuena III Sequence in the Salta Basin, Argentina (B) and La Barre du Cengle in the Arc Basin, France (C).

In the hypothetical scenario illustrated in Fig. 7.3A, the same stratigraphic time is represented along a transect showing the transition from lacustrine to palustrine and ultimately to pedogenic domains. For analogy, two positions are highlighted: a more distal lacustrine area and a more proximal palustrine position. Nine high-frequency sequences are represented in both schematic columns, yet their anatomy differs markedly. In distal conditions, sequences are thicker and display symmetric T–R stacking, whereas in proximal settings they become thinner, amalgamated, and develop asymmetric R-type patterns. Fig. 7.3B and Fig. 7.3C illustrate how the studied successions relate to this spectrum, with the Balbuena III Sequence in Salta exemplifying a distal lacustrine position and La Barre du Cengle representing a proximal palustrine domain.

In distal areas, where accommodation rates are higher and positive, the “accordion folds” expand, favoring the preservation of high-frequency depositional sequences. Under these conditions, the available space allows a clear distinction between transgressive and regressive hemicycles, enhancing correlation potential. This is exemplified by the lacustrine succession of the SBIII in Salta (Fig. 7.3B), illustrated through the Assado section, selected as the representative type section of the SBIII. Both high- and medium-frequency sequences can be traced laterally for at least 45 km. Conversely, when A < S, corresponding to low positive accommodation rates, progradational stacking dominates and resolution is progressively lost. In this scenario, the same folds exist but appear amalgamated, making them harder to distinguish, as seen in the palustrine succession of La Barre du Cengle (Fig. 7.3C). The Pas du Lièvre section illustrates this setting, representing a typically palustrine succession, although pedogenetic facies occur at the top of some sequences and lacustrine facies are present in the upper part of the succession. In this context, the correlation potential for high-frequency sequences is limited to a few hundred meters (< 250 m), whereas medium-frequency sequences can still be traced along the entire cliff. In such cases, depositional sequences may be eroded by subaerial exposure or masked by pedogenetic overprinting, removing the evidence of short-term fluctuations in the accommodation-to-sediment supply (A/S) ratio from the stratigraphic record. This process, known as signal shredding (Jerolmack and Paola, 2010), results in the creation of "missing beats" in the sedimentary record.

From an analog perspective, the two models, SBIII in the Salta Basin and La Barre du Cengle in the Arc Basin, provide complementary insights: together, they demonstrate how stratigraphic organization, correlation potential, and preservation are fundamentally governed by the prevailing depositional domain, underscoring the importance of selecting appropriate analogs when applying stratigraphic models to reservoir-scale studies.

### 7.1.3. Conceptual and Applied Perspectives on Outcrop Analogs

As outlined in the Introduction and in Chapter 4 of this manuscript, outcrop analogs are widely used to support petroleum reservoir characterization and modeling (Grammer et al., 2004; Hodgetts, 2013). By supplying mesoscale continuity typically absent from subsurface datasets, they elucidate facies distributions, depositional architectures, stacking trends, and internal reservoir heterogeneity. This is especially useful during the early phases of field development, when data availability is limited. Accordingly, outcrops provide a practical link between regional seismic interpretations and localized borehole observations (Pringle et al., 2004; Jones et al., 2011; Howell et al., 2014; Yeste et al., 2021). The use of outcrops as reservoir analogs for different objectives and methods, whether aimed at characterization or modeling, is well documented in the literature. Examples span multiple depositional systems, including fluvio-deltaic (e.g., Henares et al., 2016; Colombera et al., 2017; Roisenberg et al., 2022; Islam et al., 2025), shallow-marine siliciclastic (e.g., Noad, 2004; Sech et al., 2009; Mulhern et al.,

2019), deep-marine siliciclastic (e.g., Falivene et al., 2006; Mayall et al., 2006; Zhang and Li, 2020), marine carbonates (e.g., Grammer et al., 2004; Adams et al., 2005; Amour et al., 2013; Borgomano et al., 2020), and lacustrine carbonates (e.g., Seard et al., 2013; Thompson et al., 2015; Varejão et al., 2022; Mutti et al., 2023; Cupertino et al., 2024). Against this practical backdrop, the discussion that follows addresses the inherent limits of analogs and clarifies what is meaningfully transferable from outcrop to reservoir. These limits include representativeness, scale and continuity mismatches, diagenetic divergence, petrophysical dispersion, and seismic-resolution pitfalls (Grammer et al., 2004), as well as the need for careful analog selection, multiscale data integration, and explicit uncertainty analysis supported by digital methods and standardized databases (Howell et al., 2014).

No outcrop analog reproduces all characteristics of a subsurface reservoir. Even when the analog and the target belong to the same formation, differences are expected. The exposed portion has undergone telodiagenesis and other near-surface processes that did not affect the interval at depth. Fig. 7.4 illustrates this point with a playful poster created for the thirtieth anniversary of CEREGE, where a geologist appears as a “Ghostbuster” in search of the perfect analog. The underlying message is straightforward: “the perfect analog does not exist” (Howell et al., 2014), and the value lies in how we work this “imperfection”.

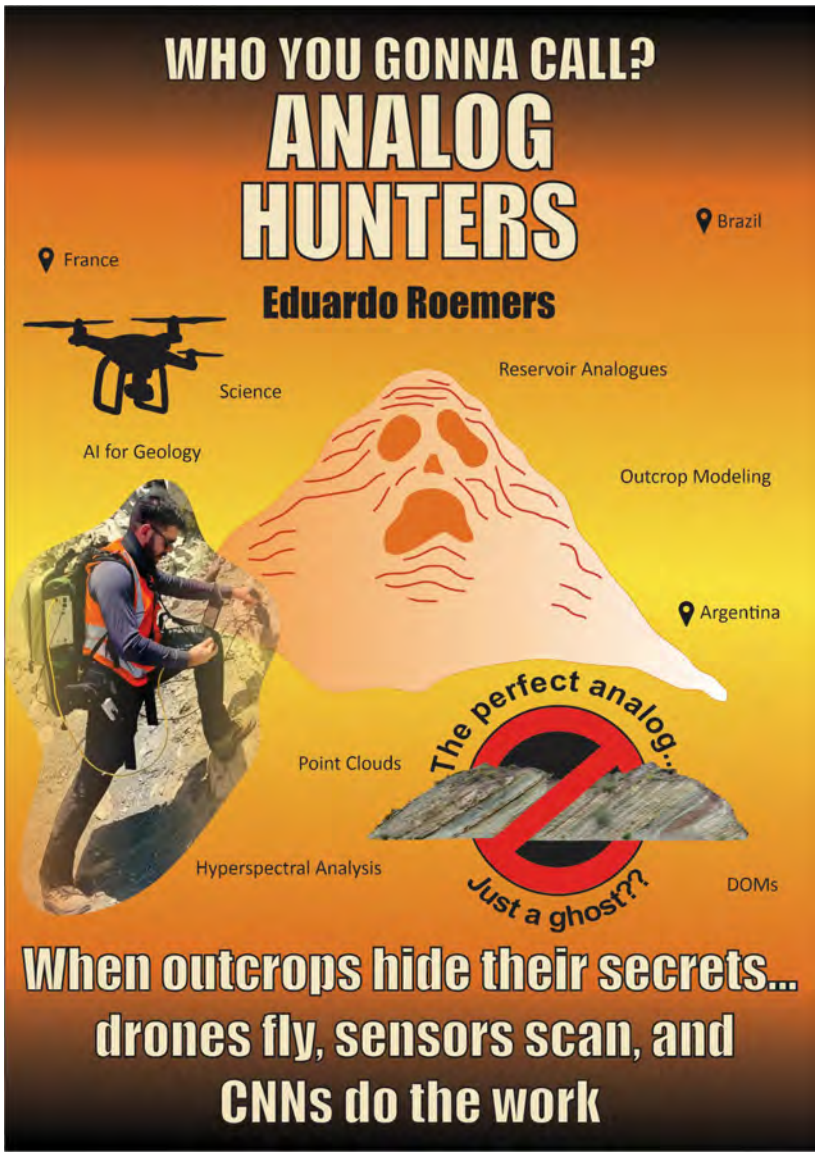


**Fig. 7.4.** In search of the perfect analog. CEREGE 30th-anniversary poster depicting the author as a "Ghostbuster" geologist, underscoring that no perfect analog exists and that value lies in developing conceptual models, selecting portable elements, and combining multiple analogs.

In this context, scientists work with conceptual models in the broad sense, not mirrors of reality. One of the main risks in this process is the creation of a Frankenstein model (sensu Fragoso et al., 2021), an unrealistic composite produced by assembling fragmentary observations from disparate contexts. The value of a conceptual model lies less in its polished final version and more in the investigator's logic and effort during construction. Geological sections, sets of genetically related outcrops, or even entire basins are not reproducible in a different spatial or temporal context. What can be transferred are the portable elements of the model, namely the constructive mechanisms and specific steps that can be applied, in part, to another geological reality.

Operationally, analogs ground the abstractions that define a useful conceptual model of the reservoir, while direct parameterization and transfer from outcrops to reservoirs should proceed with care. Direct transposition of geostatistical metrics from a single outcrop is not recommended because each outcrop and reservoir is unique; the role of outcrops is to illuminate parameter variability and geological controls, which requires comparative use of multiple exposures and support from curated databases (Hodgetts, 2013). The reservoir team determines what is and is not transferable based on the specific similarities and differences between analog and reservoir. Portable elements typically include geometries of architectural elements to represent geobodies more faithfully and stacking pattern rules within comparable depositional contexts.

Within the stratigraphic framework, HRSS enables zonation, improves correlation potential, and supports predictions of high-permeability zones, sealing intervals, and the distribution of heterogeneity at the metric scale (Grammer et al., 2004; Magalhães et al., 2020; Fragoso et al., 2021). The definition of stratigraphic cyclicity across scales, derived from stacking, vertical alternations, and trends in facies associations, follows universal methodological criteria (e.g., Magalhães et al., 2020; Fragoso et al., 2021, 2022). In practice, stacking patterns delineate where permeability tends to increase (commonly near maximum regression or maximum retraction surfaces) and where it tends to decrease (commonly near maximum flooding or maximum expansion surfaces), and they highlight intervals where facies contrasts are most pronounced. In comparable depositional settings, coastal to nearshore facies generally show better reservoir quality than pelitic-dominated intervals; therefore, even when sequence boundaries are subtle or only weakly correlatable, this paleogeographic position can host more permeable geobodies, enhancing connectivity across successive units and increasing net pay (the thickness of reservoir rock meeting saturation, porosity, and permeability cutoffs such that hydrocarbons can flow). Its application to petroleum reservoirs (e.g., Liechoscki de Paula Faria et al., 2017; Melo et al., 2021; Fragoso et al., 2023; Vital et al., 2023; Pedrinha and Artagão, 2024; Andrade et al., 2025) is typically supported by analogy with similar cases.

Avoiding a Frankenstein model is a direct consequence of this mindset. Such constructions conflict with actualism and overlook the ephemeral and transformative nature of sedimentary environments. A more realistic approach incorporates high-frequency paleogeographic evolution, recognizes that both gaps and preserved records follow predictable stratigraphic patterns across timescales, and accepts the incompleteness and dynamism of the geological record.

In this scenario, digital techniques and DOMs help unpack outcrop information with greater efficiency. DOMs enable quantitative, georeferenced analyses that can help populate geocellular reservoir models and support integrated outcrop workflows by combining classic field data with subsurface information to control heterogeneity more realistically (Yeste et al., 2021). Beyond enabling access to remote areas, they accelerate and standardize the derivation of parameters that support understanding, parameterization, and quantification. For reservoir

modeling, object-based approaches and multipoint statistics can be used together to capture geobody shapes, heterogeneities, and nonstationary trends at the reservoir scale, including azimuthal tendencies where appropriate (Yeste et al., 2021).

Along a given stratigraphic section, it becomes feasible to document stacking patterns and key surfaces, delineate facies tracts, parameterize architectural elements, and track mineralogical and diagenetic variations across beds of differing thicknesses and frequencies. The strategy of integrating data from different databases and different datasets complements single outcrop data acquisition. This provides a robust path to parameter ranges rather than single-value transpositions (Hodgetts, 2013; Howell et al., 2014). As such, information and data from DOMs are becoming increasingly essential in predictive workflows that support exploration and development decisions in reservoir management.

### 7.1.4. Pre-salt Reservoirs: Challenges and Insights from Outcrop Analogs

Although an overview of the Pre-salt was already presented in Section 4.7.2 in the context of the Salta Basin as a stratigraphic analog, it is important to revisit here the main characteristics of these reservoirs. The goal is to emphasize their significance, outline the challenges associated with their characterization and modeling, and underscore the relevance of using multiple outcrop analogs, since no single analog can be considered perfect (Section 7.1.3).

The term Pre-salt refers to sedimentary and igneous deposits underlying a thick Aptian evaporitic sequence offshore the Santos and Campos basins, along the southeastern and eastern Brazilian margins. These reservoirs extend from Espírito Santo to Santa Catarina states (Fig. 7.5A), in water depths of 1,500 to 3,000 m and burial depths of 3,000 to 4,000 m (Bueno de Moraes et al., 2024). They include rocks deposited during the rift and sag phases of these basins, later overlain by an extensive evaporite layer and followed by marine passive margin deposits related to the opening of the South Atlantic Ocean (Fig. 7.5B).

Exploratory activities in Pre-salt began in 2005 with the Parati and in 2006 with Tupi prospects. Parati was key in demonstrating that the multilayered seismic reflector corresponded to a thick stratified salt layer and confirmed the presence of hydrocarbons in the Pre-salt area, although the result was not considered economic. In contrast, the Tupi prospect marked the first commercial Pre-salt discovery in the Barra Velha Formation (Santos Basin), with the declaration of commerciality of Tupi field in 2010. Tupi became Brazil's first supergiant field, with 19.4 billion barrels of oil and 695 billion cubic meters of gas in place (Bueno de Moraes et al., 2024; De Paula et al., 2024). This success initiated a new exploratory phase, driven by the high quality of the oil (27-30 °API) hosted by the Pre-salt reservoir (Bruhn et al., 2017). It led to multiple discoveries between 2007 and 2014, including the Iara complex (Berbigão, Sururu, and Atapu fields), as well as Carcará, Sapinhoá, Itapu, Sépia, Mero, and Búzios fields (De Paula et al., 2024). Among these, Búzios, discovered in 2010, stands out as the largest commercial oil discovery in ultra-deep waters worldwide, with 29 billion barrels of oil and 816 billion cubic meters of gas in place (De Paula et al., 2024; Guerrero et al., 2024). This accumulation also highlighted the presence of rift-related reservoirs, such as bivalve coquina-rich deposits of the Itapema Formation in the Santos Basin. Correlations with equivalent intervals in the ultra-deepwater areas of the Campos Basin revealed additional reservoirs in the Coqueiros (rift) and Macabu (sag) formations (De Paula et al., 2024).

Beyond their great areal extent, thickness, and depth, Pre-salt reservoirs pose additional challenges due to their stratified architectures and atypical carbonate facies, such as spherulites interbedded with magnesian clays (Fig. 7.5C–D) and fascicular calcite shrubs (Fig. 7.5E–F). These facies are frequently reworked or resedimented (Fig. 7.5G–H) and exhibit strong

heterogeneity due to diagenetic processes, including dolomitization, silicification, dissolution, recrystallization, and structural compartmentalization influenced by faults and fractures. The occurrence of such atypical facies complicates the search for ideal analogs and sustains the ongoing debate on the origin of Pre-salt rocks.

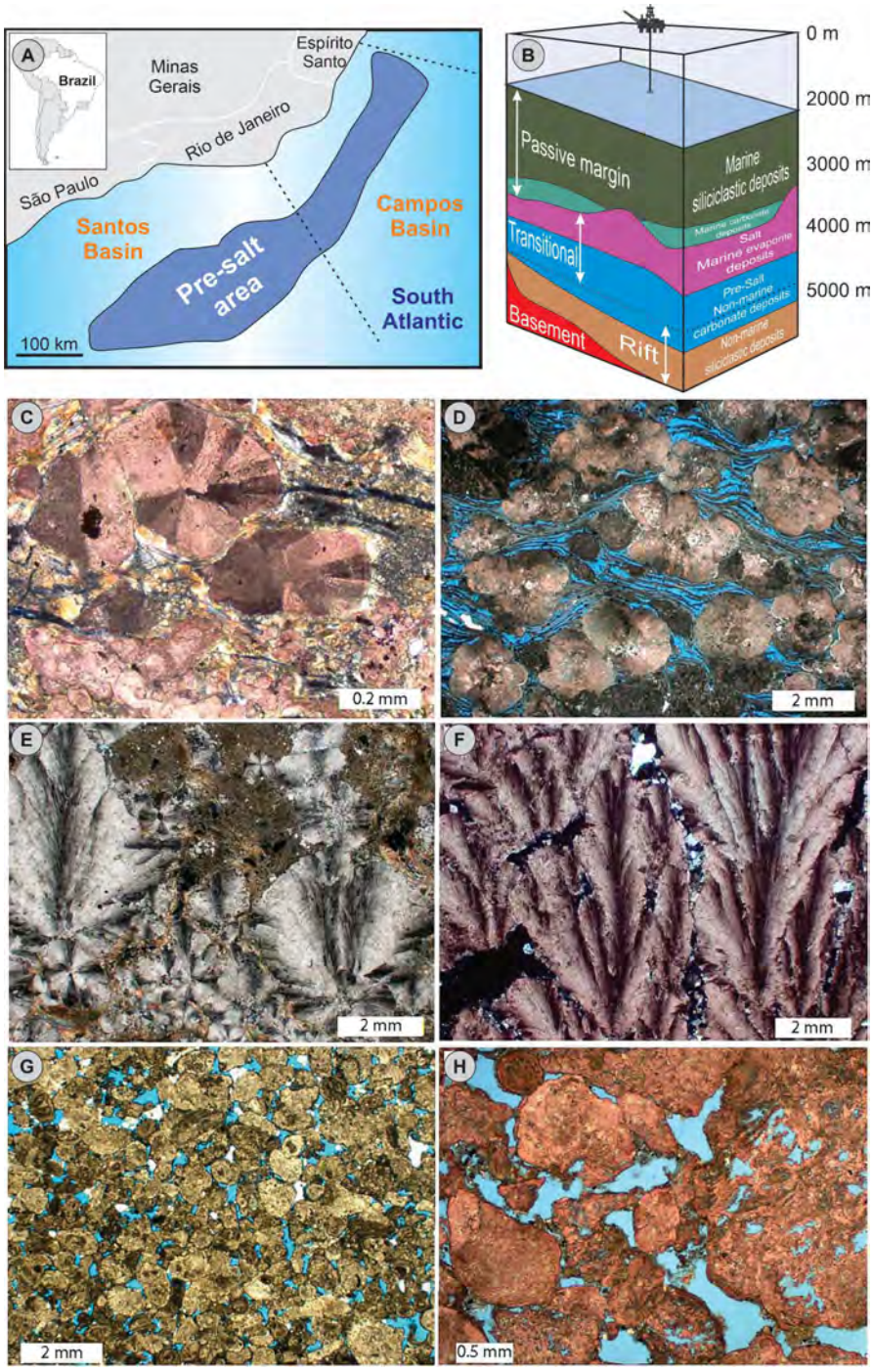


**Fig. 7.5.** Overview of Pre-salt reservoirs. (A) Location of the Pre-salt area in the Santos and Campos basins, southeastern Brazil, modified from Fragoso et al. (2023) and Bueno de Moraes et al. (2024). (B) Schematic block diagram illustrating the general stratigraphic architecture of the basins, including rift, transitional, and post-salt stages, adapted from Fragoso et al. (2023). (C–H) Petrographic thin-section images of Pre-salt lithotypes from De Ros and Oliveira (2023), showing representative textural and compositional features: (C) calcite spherulites replacing and displacing the Mg-silicate matrix; (D) porous spherulitic rock; (E) transitional forms between fascicular shrubs and spherulites; (F) fascicular calcite aggregates with growth-framework (inter-aggregate) porosity; (G) calcirudite of fascicular and microcrystalline intraclasts; (H) porous calcarenite of fascicular and spherulitic intraclasts. Photomicrographs C, G, and H under plane-polarized light; A, D, and E under cross-polarized light.

In 2010, Petrobras (Terra et al., 2010) released the first public images of these facies and attempted to establish a classification adapted to the lithotypes encountered. While consensus now exists that Pre-salt lithotypes formed in highly alkaline lacustrine environments, their origin remains debated, whether biotic, abiotic, or mixed. Early studies emphasized microbial processes and extensively used the term stromatolite or microbialite to describe the main reservoir rocks (e.g., Carminatti et al., 2008, 2009; Nakano et al., 2009; Terra et al., 2010). More recent works, however, argue that this term is inadequate, leading to efforts to establish new classifications specifically suited to Pre-salt lithotypes (e.g., Wright and Barnett, 2017, 2020; Gomes et al., 2020; Borghi et al., 2022; De Ros and Oliveira, 2023). Although different terminologies have been proposed, the terms shrubstone and spherulstone (also referred to as spherulitestone) have become increasingly common since 2020, reflecting a growing body of research on these reservoirs.

The abiotic model was first advanced by Wright and Barnett (2015), suggesting that evaporation and chemical precipitation controlled by lake geochemistry were the main processes responsible for Pre-salt formation. This interpretation has been supported by several authors (e.g., Wright and Tosca, 2016; Herlinger et al., 2017; Lima and De Ros, 2019; Carramal et al., 2022; Netto et al., 2022; Wright, 2022; Rossoni et al., 2024), who acknowledge, however, that microbialites may occur locally with only minor microbial influence. Others emphasize that biotic processes were fundamental for the development of *in situ* lithofacies (e.g., Muniz and Bosence, 2015; Tonietto et al., 2023; Gomes et al., 2024). Additional studies highlight hydrothermal influence, particularly in the Iara complex (e.g., Vital et al., 2023; Terra et al., 2023) and in fault-related areas of the Campos (e.g., Lima and De Ros, 2019; Strugale et al., 2024) and Santos (e.g., Tanaka et al., 2018) basins, associated with significant diagenetic transformations.

The diversity of interpretations underscores the difficulty of finding a truly compatible analog for the Pre-salt, since both depositional conditions and scale may be unique. The closest lithological analogs are in the Kwanza Basin, offshore Angola (e.g., Saller et al., 2016; Poros et al., 2017; Teboul et al., 2017, 2019), which represent the African counterpart of the Pre-salt, formed prior to the separation of South America and Africa. As both successions originated from the same depositional system, they share not only similarities but also the same challenges.

Recognizing these difficulties, this thesis did not aim to identify depositional analogs for Pre-salt lithofacies but instead focused on stratigraphic analogs that can improve understanding of vertical and lateral organization. Several studies have shown that variations in base level driven by climate controls provide a robust framework for interpreting stratigraphic stacking patterns in the Pre-salt (e.g., Muniz and Bosence, 2015; Fragoso et al., 2023; Tonietto et al., 2023; Guerrero et al., 2024; Pedrinha and Artagão, 2024). These concepts have been successfully applied in forward modeling (e.g., Liechoscki de Paula Faria et al., 2017; Pozzi et al., 2024) and reactive transport modeling (e.g., Carvalho et al., 2024), producing architectures consistent with those observed in hydrocarbon fields.

Because Pre-salt deposits are lacustrine, with base-level variations controlled by climate and extending for tens of kilometers, the Yacoraite Formation of the Salta Basin provides an excellent stratigraphic analog. At the same time, palustrine features such as breccias, pseudomicrokarsts, and shrinkage cracks described by Muniz and Bosence (2015) in Pre-salt reservoirs of the Campos Basin highlight parallels with the Barre du Cengle, where palustrine conditions dominate. Additional similarities include charophyte gyrogonites reported by Azerêdo et al. (2021) in the Pre-salt of Santos Basin, interpreted as evidence of a shallow, low-gradient, alkaline, and variably saline lake, again comparable to Cengle deposits.

These elements demonstrate that both Salta and Cengle, as described in detail in Section 7.1.2, provide valuable stratigraphic analogs for the Pre-salt, contributing to conceptual reservoir models and guiding strategies for characterization and modeling. While not direct lithological matches, they offer complementary insights: Salta reflects large-scale lacustrine organization, whereas Cengle represents more palustrine conditions. As highlighted in Section 4.7.2, studies such as Fragoso et al. (2023) and Pedrinha and Artagão (2024) indicate that medium-frequency sequences are most consistent with production data. In both Salta and Cengle, these sequences can be correlated across distances exceeding typical Pre-salt well spacing (about 2 km), supporting the delineation of stratigraphic surfaces for zonation and the identification of architectures that control compartmentalization and fluid flow.

## 7.2. Conclusions and Perspectives

This thesis aimed to contribute to the generation and extraction of quantitative geological data from outcrops to support reservoir characterization and modeling in carbonate-dominated lacustrine settings, with emphasis on analogs relevant to the Brazilian Pre-salt. The central research question was whether outcrop-derived methods could enhance the extraction of stratigraphic elements and the detection of geological bodies. The results demonstrate that this objective was achieved: the integrated use of multiscale and multidisciplinary approaches, combining field data, laboratory analyses, and advanced digital techniques, significantly improved the identification, organization, and quantification of sedimentological and stratigraphic elements in both lacustrine and palustrine contexts. These advances provide a robust basis for generating conceptual reservoir models and extracting quantitative parameters that, with appropriate precautions, hold substantial value for reservoir characterization and modeling workflows.

To further consolidate the contributions of this thesis, the following section revisits the specific objectives defined in Chapter 1 (Section 1.2). Each objective is examined considering the results obtained, highlighting how it was addressed throughout the different chapters and whether it was successfully achieved. This step ensures a direct connection between the research questions posed at the outset and the outcomes delivered.

**1. To acquire high-resolution field data and generate Digital Outcrop Models (DOMs) from key lacustrine and palustrine carbonate outcrops.**

In both study areas, high-resolution DOMs were successfully generated, providing the essential digital foundation for subsequent analyses. At La Barre du Cengle, a photogrammetric DOM covering the entire exposed portion of the cliff was produced at a resolution of approximately 2 cm/pixel, enabling the correlation of medium-frequency sequences along the whole escarpment. In addition, higher-resolution DOMs (~0.5 cm/pixel) were created at three of the four logged sections, ensuring precise positioning of stratigraphic logs and collected samples within the digital framework. In the Salta Basin, ultra–high-resolution DOMs (~2 mm/pixel) were generated for the Assado and Vapumas outcrops, which provide the best exposures of the Balbuena III Sequence in the study area. These models served as the basis for detailed facies mapping and 3D classification experiments within a high-resolution stratigraphic framework built from fourteen outcrops.

Despite the logistical complexities inherent to this workflow, such as field preparation, obtaining airspace and access permits, transporting equipment, and maintaining power supply for extended operations, the acquisition of RPAS-based photogrammetric data proved to be a relatively cost-effective and time-efficient method. Its long-term benefits are reinforced by the

availability of high-resolution models that can be revisited indefinitely, extending outcrop analysis beyond the field into the laboratory and enabling continuous refinement of data acquisition and interpretation.

**2. To integrate DOM-based analyses with traditional geological observations from the field and laboratory, ensuring consistent geological interpretation.**

The entire workflow developed in this thesis was conceived as an integrative and multidisciplinary effort, where diverse datasets were assembled like pieces of a puzzle to construct sedimentological and stratigraphic models anchored in HRSS. At La Barre du Cengle, eight lithofacies were grouped into three facies associations based on the integration of field logs and petrographic thin sections. These interpretations were further constrained by isotopic and U–Pb geochronology, refining the chronological and environmental framework of this predominantly palustrine system. In the Salta Basin, the case study focused on a lacustrine setting, where fieldwork and petrography supported the definition of 19 lithofacies grouped into four facies associations. These observations, when integrated with laboratory analyses, including geochemistry and spectroscopy, together with digital techniques, anchored digital interpretations and supported sedimentological and stratigraphic correlations. This systematic integration ensured that digital outputs such as DOMs, CNN, and HSI, remained geologically grounded and strengthened the understanding of depositional systems and their evolutionary trajectories.

**3. To establish correlation patterns and distances between lacustrine and lacustrine/palustrine settings across different study areas.**

In Salta, the dominance of a lacustrine setting enabled high- and medium-frequency sequences to be correlated over distances of more than 45 km, corresponding to a restored depositional length of nearly 70 km. At Cengle, correlation potential was shorter (<250 m for high-frequency, cliff-scale for medium-frequency), reflecting the limited accommodation space and the predominance of palustrine conditions. The juxtaposition of both sites highlights complementary positions along the accommodation/supply spectrum: distal lacustrine (Salta) versus proximal palustrine (Cengle). Importantly, in both settings, medium-frequency sequences extend well beyond typical Pre-salt well spacing (~2 km), directly supporting their use in reservoir zonation and in understanding heterogeneities that impact fluid flow.

**4. To apply and evaluate multiple methods (HRSS, LBP, CNN, HSI) for the classification and extraction of lithofacies and depositional sequences within an integrated stratigraphic framework.**

HRSS, a central method in this thesis, is more than just a methodology; it represents a predictive approach to reconstruct past depositional and preservation processes at high resolution. In this context, deposition is understood as a dynamic process, where each interval bounded by two stratigraphic surfaces represents a new paleogeographic scenario. Consequently, depositional systems should not be represented by a single 3D block but rather by a succession of scenarios that illustrate their evolution through time. HRSS integrates stacking patterns and stratigraphic surfaces into the interpretation of high-frequency sedimentary patterns, considering sedimentation, erosion, and depositional gaps.

Within the stratigraphic framework established by HRSS, additional digital methods were applied to complement its interpretations and to test their potential for enhancing sedimentological and stratigraphic analysis. At La Barre du Cengle, HRSS highlighted

elementary- to medium-frequency cyclicity and exposure surfaces, supporting the development of a conceptual depositional model verified by vertical anatomies at multiple hierarchies and through lateral facies variations. In the Salta Basin, HRSS provided the framework for applying LBP to detect repetitive stacking patterns directly from DOM imagery of SBIII. CNNs classified 11 facies into labeled point clouds, enabling the extraction of 3D geobodies, while HSI, even under restricted 900–1700 nm coverage, discriminated three main facies groups and produced coherent 2D maps after lithotype regrouping. Together, these methods demonstrate that digital techniques can significantly enhance and complement classical sedimentology and stratigraphy, delivering quantitative and reproducible products that strengthen both facies analysis and stratigraphic interpretation.

Regarding hyperspectral imagery, which can be very valuable in carbonate settings where color contrasts and compositional variations are generally imperceptible to the human eye, traditional DOMs, even with high spatial and geometric accuracy, do not provide sufficient spectral resolution to detect subtle lithological variations (Salehi et al., 2018), and several challenges remain. Hyperspectral cameras are still relatively scarce due to their high cost, and when available, they are not always optimized for carbonate mapping. This was the case in the Salta Basin, where the available camera operated within a restricted spectral range (900–1700 nm), excluding key diagnostic absorption features for carbonates and many clay minerals. At La Barre du Cengle, hyperspectral data were also acquired with a broader range suitable for carbonate mapping (HySpex VS-620 sensor: 400–2500 nm); however, as the outcrop is a vertical cliff, the only feasible option was RPAS-based acquisition. This configuration introduced significant noise, and the geometric correction of the dataset is still in progress.

These challenges illustrate the current limitations of hyperspectral imaging for geological applications. Ground-based systems, typically mounted on tripods (as used in the Salta Basin), are not suitable for cliffs or inaccessible outcrops (such as La Barre du Cengle), while RPAS-based systems are primarily designed for scanning sub-horizontal topographies in nadir configuration (Kim et al., 2022). Although part of the acquired data could not be processed within this thesis, it remains available, and efforts are ongoing to complete its post-processing, with the aim of continuing the analysis of hyperspectral data on the studied outcrops in future work.

**5. To contribute to the geological knowledge of each study area by improving the understanding of depositional architecture and stratigraphic organization.**

The study of La Barre du Cengle advanced the understanding of vertical facies evolution and lateral variation in a palustrine-dominated system. U–Pb dating indicated an older depositional age (Danian–early Selandian) than previously assumed, suggesting a potential revision of the Arc Basin chronostratigraphic framework. In the Salta Basin, the Balbuena III Sequence was subdivided into sequences of different hierarchies, documenting a transition from siliciclastic- to carbonate-dominated lacustrine systems correlatable over tens of kilometers. These findings refine regional stratigraphic frameworks and strengthen analog-based interpretations.

**6. To contribute to the advancement of digital techniques applied to outcrop analogs, highlighting their potential for generating conceptual geological models to support reservoir characterization.**

This thesis demonstrates practical workflows for digital geoscience: DOM-guided HRSS, LBP-based cyclicity detection, CNN-based point cloud classification, and HSI-based facies

mapping. These methods, when integrated with field- and laboratory-based data, not only accelerate data extraction but also reveal heterogeneities not always easily visible in the field, thereby expanding geological knowledge and contributing to more realistic conceptual geological models. By bridging quantitative outcrop observations with subsurface challenges, these digital techniques enhance the transferability of analogs and help reduce uncertainties in complex Pre-salt reservoirs.

## Limitations and Future Directions

Despite the positive results achieved by the workflow developed in this thesis, bridging classical sedimentology and stratigraphy with digital geoscience and providing reproducible methodologies that go beyond qualitative description, many challenges remain. These do not invalidate the results but instead highlight the need for careful calibration and integration with multiple data sources.

Although DOMs have revolutionized field studies in geosciences, they generate large volumes of data that require significant storage capacity and high-performance computing resources. In addition, the absence of well-structured and consistently labeled ground-truth datasets remains a major limitation for training deep learning models. Generating interpreted and labeled data to serve as training sets for deep learning techniques is time-consuming and further complicated by the interpretative nature of geological data.

Validation metrics also need to be improved. At present, there are no quantitative methods to assess the results of LBP applied to cyclicity. Similarly, CNN-based classifications still lack dedicated metrics capable of evaluating the reproduction of facies continuity, topological relationships, and stratigraphic positioning. The metrics used in image-based methods are mainly based on pixel-level accuracy, but other approaches should be developed to better adapt to geological purposes. Photogrammetry and HSI are also highly sensitive to acquisition conditions, requiring preprocessing steps.

Not all of the methods applied here are suitable for every depositional context. The application of CNNs in the Salta Basin proved highly effective, but this approach cannot be easily transferred to deposits with more subtle lithofacies variations, such as La Barre du Cengle. In Cengle, lithofacies are mainly matrix-supported, making the visual definition of geological bodies more difficult and complicating the generation of labeled data to be used as ground truth.

The hyperspectral acquisition at La Barre du Cengle, at the Pas du Lièvre outcrop (Fig. 7.6), aimed to collect hyperspectral imagery using the HySpex VS-620 sensor mounted on a Freefly Alta X platform (Fig. 7.6E), equipped with a Movi Pro gimbal. The objective was to capture high-resolution (1 cm/pixel) vertical imagery of the cliff, which presents a complex geometry combining planar, curved, and stepped surfaces. The acquisition was planned in UgCS (Universal Ground Control Software) using the Vertical Scan function, with flight lines programmed successively downward to cover the entire target. However, the need to rotate the camera by 90° in both tilt and roll to align the scan lines with the outcrop caused the loss of one gimbal axis, resulting in variable roll distortions in the images, classified as low, moderate, and high (Fig. 7.6A–C). A radiometric reference panel coated with barium sulfate (Fig. 7.6F) was installed on the cliff for radiometric calibration.

Despite successful acquisition, geometric correction remains the main challenge. The first correction step using Trimble's POSPac UAV, required to process GNSS (Global Navigation Satellite System) and IMU (Inertial Measurement Unit) data and generate the smoothed best estimate trajectory (SBET), could not be completed, preventing the final geometric correction

in the open-source *Hylite* toolbox (Thiele et al., 2022). At present, the research team is in contact with HySpex technical specialists, who have offered support for the post–POSPac UAV stage to facilitate completion of the geometric correction.

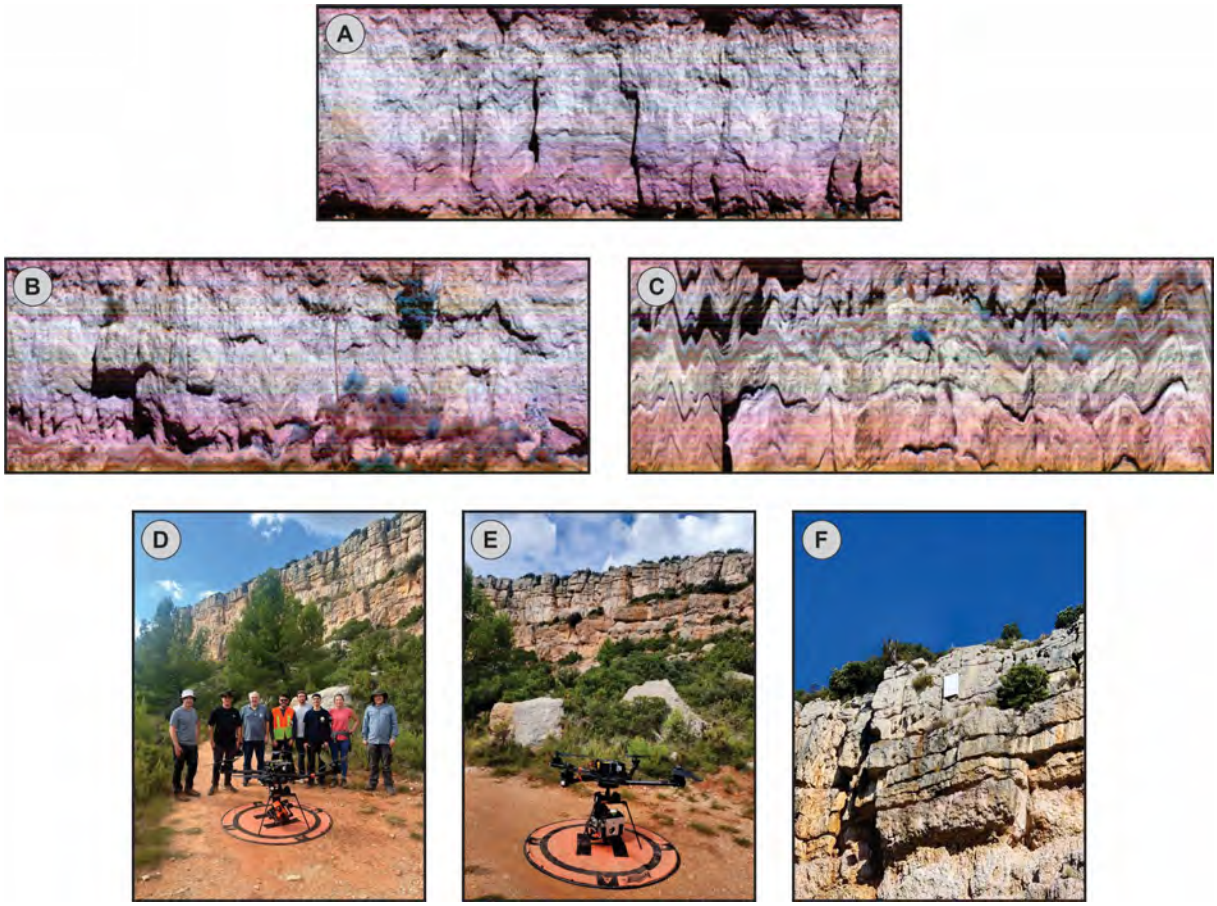


**Fig. 7.6.** Hyperspectral acquisition at La Barre du Cengle (Pas du Lièvre outcrop). (A–C) Examples of hyperspectral images showing low, moderate, and high levels of image distortion, respectively. (D) Field team during data acquisition. (E) Freefly Alta X platform equipped with HySpex VS-620 hyperspectral sensor and Movi Pro gimbal. (F) Radiometric reference panel coated with barium sulfate, installed on the cliff for radiometric calibration.

Looking ahead, several research avenues emerge. In the short term in the Salta Basin, hyperspectral datasets should be expanded using sensors that cover the most suitable spectral ranges for characterizing clay minerals and carbonates, thereby improving lithofacies discrimination and highlighting variations not visible to the naked eye. At La Barre du Cengle, completing the geometric correction of the existing dataset will be a priority, after which hyperspectral imaging could also be used to emphasize different intensities of pedogenesis, supporting the reconstruction of sequence evolution and improving the understanding of the geological history of the area. More broadly, future research should focus on expanding training datasets across a wider variety of outcrops and acquisition conditions, integrating DOMs with full-range hyperspectral imagery and quantitative mineralogical datasets (e.g., XRD), and ultimately generating 3D hyperclouds that combine geometric and spectral data.

## Final Remark

By uniting classical and digital approaches, this work demonstrated that outcrops can serve as both a memory of past environments and a laboratory for future reservoir models.

## References


Adams, E.W., Grotzinger, J.P., Watters, W.A., Schröder, S., McCormick, D.S., Al-Siyabi, H.A., 2005. Digital characterization of thrombolite-stromatolite reef distribution in a carbonate ramp system (terminal proterozoic, Nama Group, Namibia). American Association of Petroleum Geologists Bulletin 89, 1293–1318. https://doi.org/10.1306/06160505005

Amour, F., Mutti, M., Christ, N., Immenhauser, A., Benson, G.S., Agar, S.M., Tomás, S., Kabiri, L., 2013. Outcrop analog for an oolitic carbonate ramp reservoir: A scale-dependent geologic modeling approach based on stratigraphic hierarchy. AAPG Bulletin 97, 845–871. https://doi.org/10.1306/10231212039

Andrade, P.R. de O., Alves, T.M., Cavalcanti de Araújo, M.N., da Silva Schmitt, R., Carnier Fragoso, D.G., Henrique de Melo, A., 2025. Spatiotemporal hierarchy of fault systems and associated syn-rift stratigraphic sequences across the Santos Basin, offshore SE Brazil. Marine and Petroleum Geology 107384. https://doi.org/10.1016/j.marpetgeo.2025.107384

Azerêdo, A.C., Duarte, L. V., Silva, A.P., 2021. The challenging carbonates from the Pre-Salt reservoirs offshore Brazil: facies, palaeoenvironment and diagenesis. Journal of South American Earth Sciences 108, 103202. https://doi.org/10.1016/j.jsames.2021.103202

Barrell, J., 1917. Rhythms and the measurements of geologic time. Geological Society of America Bulletin 28, 745–904. https://doi.org/10.1130/GSAB-28-745

Borghi, L., Da Silva, M.C.A.S., Favoreto, J., Santos, J., 2022. Defining a new common language: a multi-scale descriptive classification for the pre-salt carbonates of the Barra Velha Formation, in: Rio Oil and Gas Expo and Conference. IBP - Instituto Brasileiro de Petroleo e Gás, pp. 26–27. https://doi.org/10.48072/2525-7579.rog.2022.026

Borgomano, J., Massonnat, G., Lanteaume, C., Danquigny, C., Samson, P., Rolando, J.-P., Rebelle, M., 2020. Application of Stratigraphic Forward Modelling to Carbonate Reservoir Characterization – A New Paradigm from the Albion R&D Project, in: Abu Dhabi International Petroleum Exhibition & Conference. SPE. https://doi.org/10.2118/202775-MS

Branets, L. V, Ghai, S.S., Lyons, S.L., Wu, X.-H., 2009. Challenges and Technologies in Reservoir Modeling. COMMUNICATIONS IN COMPUTATIONAL PHYSICS 6, 1–23.

Bruhn, C.H.L., Pinto, A.C.C., Johann, P.R.S., Branco, C.C.M., Salomão, M.C., Freire, E.B., 2017. Campos and Santos Basins: 40 Years of Reservoir Characterization and Management of Shallow- to Ultra-Deep Water, Post- and Pre-Salt Reservoirs - Historical Overview and Future Challenges, in: Offshore Technology Conference Brazil. OTC. https://doi.org/10.4043/28159-MS

Bueno de Moraes, M.F., Viana, A.R., Jahnert, R.J., Machado, M.A.P., Chagas, A.A.P., 2024. O Pré-sal nas Bacias de Campos e Santos: como tudo começou, in: Chagas, A.A.P., Araújo, C.C. de, Santos, L.A. (Eds.), As grandes descobertas do pré-sal no Atlântico Sul. Rio de Janeiro, pp. 21–69.

Carminatti, M., Dias, J.L., Wolff, B., 2009. From turbidites to carbonates: breaking paradigms in deep waters., in: Offshore Technology Conference. Houston.

Carminatti, M., Wolff, B., Gamboa, L., 2008. New exploratory frontiers in Brazil, in: 19th World Petroleum Congress. Madrid.

Carramal, N.G., Oliveira, D.M., Cacela, A.S.M., Cuglieri, M.A.A., Rocha, N.P., Viana, S.M., Toledo, S.L.V., Pedrinha, S., De Ros, L.F., 2022. Paleoenvironmental insights from the deposition and diagenesis of aptian Pre-salt magnesium silicates from the Lula Field, Santos Basin, Brazil. Journal of Sedimentary Research 92, 12–31. https://doi.org/10.2110/jsr.2020.139

Carvalho, A.M.A., Collard, N., Hamon, Y., Meiller, C., 2024. Assessing the role of local versus regional fluid circulation in the pre-salt sag section of Santos Basin (Brazil): Insights from reactive transport modeling. Marine and Petroleum Geology 162, 106711. https://doi.org/10.1016/j.marpetgeo.2024.106711

Catuneanu, O., 2019. Model-independent sequence stratigraphy. Earth-Science Reviews. https://doi.org/10.1016/j.earscirev.2018.09.017

Colombera, L., Mountney, N.P., Russell, C.E., Shiers, M.N., McCaffrey, W.D., 2017. Geometry and compartmentalization of fluvial meander-belt reservoirs at the bar-form scale: Quantitative insight from outcrop, modern and subsurface analogues. Marine and Petroleum Geology. https://doi.org/10.1016/j.marpetgeo.2017.01.024

Cupertino, D.F., Ramnani, C.W., Vanden Berg, M.D., Awramik, S.M., 2024. Formation of magnesium-clay in a lacustrine microbialite-bearing carbonate deposit, Eocene Green River Formation, Sanpete County, Utah. Sedimentology 71, 263–292. https://doi.org/10.1111/sed.13136

De Paula, L., Caldas, M.F., Costa, F. de O., Carlotto, M.A., Chagas, Anderson Antonio Pinheiro, 2024. Os gigantes, o risco geológico e o processo de delimitação na Bacia de Santos, in: Chagas, Anderson A. Pinheiro, Araújo, C.C. de, Santos, L.A. (Eds.), As Grandes Descobertas Do Pré-Sal No Atlântico Sul. pp. 70–134.

De Ros, L.F., Oliveira, D.M., 2023. An operational classification system for the south atlantic Pre-salt rocks. Journal of Sedimentary Research 93, 693–704. https://doi.org/10.2110/jsr.2022.103

Falivene, O., Arbués, P., Howell, J., Muñoz, J.A., Fernández, O., Marzo, M., 2006. Hierarchical geocellular facies modelling of a turbidite reservoir analogue from the Eocene of the Ainsa basin, NE Spain. Marine and Petroleum Geology 23, 679–701. https://doi.org/10.1016/j.marpetgeo.2006.05.004

Follows, E.J., 2025. The role of the production geologist in carbonate reservoir development. Geological Society, London, Special Publications 548. https://doi.org/10.1144/SP548-2023-154

Fragoso, D.G.C., Gabaglia, G.P.R., Magalhães, A.J.C., Scherer, C.M.D.S., 2021. Cyclicity and hierarchy in sequence stratigraphy: An integrated approach. Brazilian Journal of Geology 51, e20200106. https://doi.org/10.1590/2317-4889202120200106

Fragoso, D.G.C., Kuchenbecker, M., Magalhães, A.J.C., Scherer, C.M.D.S., Gabaglia, G.P.R., Strasser, A., 2022. Cyclicity in Earth sciences, quo vadis? Essay on cycle concepts in geological thinking and their historical influence on stratigraphic practices. History of Geo- and Space Sciences 13, 39–69. https://doi.org/10.5194/hgss-13-39-2022

Fragoso, D.G.C., Melo, A.H. de, Gonçalves, L.A., Bunevich, R.B., Araujo, J. de A.M., Costa, T.C. da, Pedrosa, C.A., Scherer, C.M.D.S., 2023. High-resolution sequence stratigraphy applied to reservoir characterization of the Brazilian Cretaceous pre-salt section, Campos Basin: Guidelines for geological modeling and reservoir management. Marine and Petroleum Geology 151, 106203. https://doi.org/10.1016/j.marpetgeo.2023.106203

Gomes, J.P., Bunevich, R.B., Tedeschi, L.R., Tucker, M.E., Whitaker, F.F., 2020. Facies classification and patterns of lacustrine carbonate deposition of the Barra Velha Formation, Santos Basin, Brazilian Pre-salt. Marine and Petroleum Geology 113. https://doi.org/10.1016/j.marpetgeo.2019.104176

Gomes, J.P.B., Bunevich, R.B., Sartorato, A.C.L., Tedeschi, L.R., Tonietto, S.N., Tucker, M.E., Whitaker, F., 2024. Early diagenetic evolution based on petrography and stable isotope analysis in the Barra Velha Formation of the Brazilian Pre-salt. The Depositional Record. https://doi.org/10.1002/dep2.288

Grammer, G.M., Harris, P.M., Eberli, G.P., 2004. Integration of Outcrop and Modern Analogs in Reservoir Modeling: Overview with Examples from the Bahamas, in: Grammer, G.M., Harris, P.M., Eberli, G.P. (Eds.), Integration of Outcrop and Modern Analogs in Reservoir Modeling: AAPG Memoir 80. pp. 1–22.

Guerrero, J.C., Brazil, F.A. de F., Carvalho, R.K., Silva, C.M. de A., Moliterno, A.M.C., Araújo, C.H.V., Barbosa, G.F., Yamato, A.A., Cacela, A.S.M., Leite, C. de O.N., Rocha, N.P., Oliveira, V.C.B. de, Campos, M.T.R., Silva, V.G.M. da R. e, Natori, H.O.H., Lima, F.P., Oliveira, D.L. de, Queiroz, L.E.S., Souza, L.B. de, Cruz, E.M.A., 2024. Campo de Búzios: a jornada desde a caracterização dos reservatórios ao início do desenvolvimento da produção AUTORES, in: Chagas, A.A.P., Araújo, C.C. de, Santos, L.A. (Eds.), As grandes descobertas do Pré-sal no Atlântico Sul. Rio de Janeiro, pp. 946–1037.

Henares, S., Caracciolo, L., Viseras, C., Fernández, J., Yeste, L.M., 2016. Diagenetic constraints on heterogeneous reservoir quality assessment: A Triassic outcrop analog of meandering fluvial reservoirs. AAPG Bulletin 100, 1377–1398. https://doi.org/10.1306/04041615103

Herlinger, R., Zambonato, E.E., De Ros, L.F., 2017. Influence of diagenesis on the quality of lower cretaceous pre-salt lacustrine carbonate reservoirs from northern Campos Basin, Offshore Brazil. Journal of Sedimentary Research 87, 1285–1313. https://doi.org/10.2110/jsr.2017.70

Hodgetts, D., 2013. Laser scanning and digital outcrop geology in the petroleum industry: A review. Marine and Petroleum Geology. https://doi.org/10.1016/j.marpetgeo.2013.02.014

Howell, J.A., Martinius, A.W., Good, T.R., 2014. The application of outcrop analogues in geological modelling: a review, present status and future outlook. Geological Society, London, Special Publications 387, 1–25. https://doi.org/10.1144/sp387.12

Islam, S., Rahman, M.M., Hossain, S., Shaikh, P.K., 2025. Reservoir heterogeneity in the fluvio-deltaic outcrop analogue: A case study from the Surma Group, Bengal Basin, Bangladesh. Heliyon 11. https://doi.org/10.1016/j.heliyon.2025.e42757

Jerolmack, D.J., Paola, C., 2010. Shredding of environmental signals by sediment transport. Geophysical Research Letters 37. https://doi.org/10.1029/2010GL044638

Jervey, M.T., 1988. Quantitative geological modeling of siliciclastic rock sequences and their seismic expression, in: Sea-Level Changes. SEPM (Society for Sedimentary Geology), pp. 47–69. https://doi.org/10.2110/pec.88.01.0047

Jones, R.R., Pringle, J.K., McCaffrey, K.J.W., Imber, J., Wightman, R.H., Guo, J., Long, J.J., 2011. Extending Digital Outcrop Geology into the Subsurface, in: Outcrops Revitalized. SEPM (Society for Sedimentary Geology), pp. 31–50. https://doi.org/10.2110/sepmcsp.10.031

Kim, J.I., Chi, J., Masjedi, A., Flatt, J.E., Crawford, M.M., Habib, A.F., Lee, J., Kim, H.C., 2022. High-resolution hyperspectral imagery from pushbroom scanners on unmanned aerial systems. Geoscience Data Journal 9, 221–234. https://doi.org/10.1002/gdj3.133

Li, Y., Wu, S., Hou, J., Liu, J., 2017. Progress and prospects of reservoir development geology. Petroleum Exploration and Development 44, 603–614. https://doi.org/10.1016/S1876-3804(17)30069-1

Liechoscki de Paula Faria, D., Tadeu dos Reis, A., Gomes de Souza, O., 2017. Three-dimensional stratigraphic-sedimentological forward modeling of an Aptian carbonate reservoir deposited during the sag stage in the Santos basin, Brazil. Marine and Petroleum Geology 88, 676–695. https://doi.org/10.1016/j.marpetgeo.2017.09.013

Lima, B.E.M., De Ros, L.F., 2019. Deposition, diagenetic and hydrothermal processes in the Aptian Pre-Salt lacustrine carbonate reservoirs of the northern Campos Basin, offshore Brazil. Sedimentary Geology 383, 55–81. https://doi.org/10.1016/j.sedgeo.2019.01.006

Magalhães, A.J.C., Raja Gabaglia, G.P., Fragoso, D.G.C., Bento Freire, E., Lykawka, R., Arregui, C.D., Silveira, M.M.L., Carpio, K.M.T., De Gasperi, A., Pedrinha, S., Artagão, V.M., Terra, G.J.S., Bunevich, R.B., Roemers-Oliveira, E., Gomes, J.P., Hernández, J.I., Hernández, R.M., Bruhn, C.H.L., 2020. High-resolution sequence stratigraphy applied to reservoir zonation and characterisation, and its impact on production performance - shallow marine, fluvial downstream, and lacustrine carbonate settings. Earth-Science Reviews 210. https://doi.org/10.1016/j.earscirev.2020.103325

Mayall, M., Jones, E., Casey, M., 2006. Turbidite channel reservoirs-Key elements in facies prediction and effective development. Marine and Petroleum Geology 23, 821–841. https://doi.org/10.1016/j.marpetgeo.2006.08.001

Mehrabi, M., Fatemi Aghda, S.M., Sarkheil, H., Teshnehlab, M., Salehi, E., Kamrani, K., Yamini, A., 2025. A systematic review to identify carbonate rock exploration paradigms and examine current and future research directions: a case study at one of the southwest oil fields of Iran. Journal of Petroleum Exploration and Production Technology 15, 34. https://doi.org/10.1007/s13202-024-01899-0

Melo, A.H., Magalhães, A.J.C., Menegazzo, M.C., Fragoso, D.G.C., Florencio, C.P., Lima-Filho, F.P., 2021. High-resolution sequence stratigraphy applied for the improvement of hydrocarbon production and reserves: A case study in Cretaceous fluvial deposits of the Potiguar basin, northeast Brazil. Marine and Petroleum Geology 130. https://doi.org/10.1016/j.marpetgeo.2021.105124

Mulhern, J.S., Johnson, C.L., Martin, J.M., 2019. Modern to Ancient Barrier Island Dimensional Comparisons: Implications for Analog Selection and Paleomorphodynamics. Frontiers in Earth Science 7. https://doi.org/10.3389/feart.2019.00109

Muniz, M.C., Bosence, D.W.J., 2015. Pre-salt microbialites from the Campos Basin (offshore Brazil): Image log facies, facies model and cyclicity in lacustrine carbonates. Geological Society Special Publication 418, 221–242. https://doi.org/10.1144/SP418.10

Muto, T., Steel, R.J., 2000. The accommodation concept in sequence stratigraphy: some dimensional problems and possible redefinition, Sedimentary Geology.

Mutti, M., Vallati, M., Tomás, S., Galli, C., Bahniuk Rumbelsperger, A.M., Maerz, S., Coira, B., 2023. Constraining depositional evolution and reservoir compartmentalization in a mixed carbonate-siliciclastic lacustrine system: The Yacoraite formation, Salta Group,

NW Argentina. Marine and Petroleum Geology 149. https://doi.org/10.1016/j.marpetgeo.2022.106049

Nakano, C.M.F., Pinto, A.C.C., Marcusso, J.L., Minami, K., 2009. Pre-Salt Santos Basin – extended well test and production pilot in the Tupi area – the planning phase, in: Offshore Technology Conference, Houston. OTC, Houston.

Netto, P.R.A., Pozo, M., da Silva, M.D., Gomes, M.E.B., Mexias, A., Ramnani, C.W., Parizek-Silva, Y., Borghi, L., Rios-Netto, A. de M., 2022. Paleoenvironmental Implications of Authigenic Magnesian Clay Formation Sequences in the Barra Velha Formation (Santos Basin, Brazil). Minerals 12. https://doi.org/10.3390/min12020200

Noad, J., 2004. The use of field analogues in the correlation and static reservoir methodology used in the Tern Field, Northern North Sea, UK. Marine and Petroleum Geology 21, 485–497. https://doi.org/10.1016/j.marpetgeo.2004.03.006

Pedrinha, S., Artagão, V. de M., 2024. High-resolution stratigraphy and characterization of reservoir-critical heterogeneities in the giant Tupi Field, pre-salt Santos Basin, Brazil. Geological Society, London, Special Publications 548. https://doi.org/10.1144/SP548-2023-91

Poros, Z., Jagniecki, E., Luczaj, J., Kenter, J., Gal, B., Correa, T.S., Ferreira, E., McFadden, K.A., Elifritz, A., Heumann, M., Johnston, M., Matt, V., 2017. Origin of Silica in Pre-Salt Carbonates, Kwanza Basin, Angola, in: AAPG Annual Convention and Exhibition. AAPG, Texas.

Pozzi, R.P.C., Fernandes, R.A.R., Silva, R.C.B. da, Oliveira, L.C. de, Sartorato, A.C.L., Figuiredo Jr, F.P., Penatti, A.P.R., Rancan, C.C., Cruz, F.E.G. da, Carlotto, M.A., Mizuno, T.A., Oliveira, V.C. de, 2024. Campo de Mero: caracterização dos reservatórios e desenvolvimento da produção, in: Chagas, A.A.P., Araújo, C.C. de, Santos, L.A. (Eds.), As Grandes Descobertas Do Pré-Sal No Atlântico Sul. pp. 884–945.

Pringle, J.K., Westerman, A.R., Clark, J.D., Drinkwater, N.J., Gardiner, A.R., 2004. 3D high-resolution digital models of outcrop analogue study sites to constrain reservoir model uncertainty: an example from Alport Castles, Derbyshire, UK. Petroleum Geoscience 10, 343–352.

Reading, H.G., Levell, B.K., 1996. Controls on the sedimentary rock record, in: Reading, H.G. (Ed.), Sedimentary Environments: Processes, Facies and Stratigraphy. Wiley-Blackwell., Oxford, pp. 5–36.

Roisenberg, H.B., Bállico, M.B., Guadagnin, F., Manna, M.O., de Souza, E.G., 2022. Digital Outcrop Models applied to high-resolution stratigraphy in braided fluvial systems: A study case at Jaicós formation in Parnaíba Basin, NE Brazil. Journal of South American Earth Sciences 119, 104006. https://doi.org/10.1016/j.jsames.2022.104006

Rossoni, R.B., Porcher, C.C., Koester, E., Sobiesiak, J.S., da Silva, L.A.C., Mexias, A.S., Gomes, M.E.B., Ramnani, C.W., De Ros, L.F., 2024. The role of compaction in the diagenetic evolution of Pre-Salt Aptian deposits of Santos Basin, Brazil. Sedimentary Geology 466, 106650. https://doi.org/10.1016/j.sedgeo.2024.106650

Salehi, S., Lorenz, S., Sørensen, E.V., Zimmermann, R., Fensholt, R., Heincke, B.H., Kirsch, M., Gloaguen, R., 2018. Integration of vessel-based hyperspectral scanning and 3D-photogrammetry for mobile mapping of steep coastal cliffs in the Arctic. Remote Sensing 10. https://doi.org/10.3390/rs10020175

Saller, A., Rushton, S., Buambua, L., Inman, K., McNeil, R., Dickson, J.A.D.T., 2016. Presalt stratigraphy and depositional systems in the Kwanza Basin, offshore Angola. AAPG Bulletin 100, 1135–1164. https://doi.org/10.1306/02111615216

Seard, C., Camoin, G., Rouchy, J.M., Virgone, A., 2013. Composition, structure and evolution of a lacustrine carbonate margin dominated by microbialites: Case study from the Green River formation (Eocene; Wyoming, USA). Palaeogeography, Palaeoclimatology, Palaeoecology 381–382, 128–144. https://doi.org/10.1016/j.palaeo.2013.04.023

Sech, R.P., Jackson, M.D., Hampson, G.J., 2009. Three-dimensional modeling of a shoreface-shelf parasequence reservoir analog: Part 1. Surface-based modeling to capture high-resolution facies architecture. AAPG Bulletin 93, 1155–1181. https://doi.org/10.1306/05110908144

Strugale, M., Lima, B.E.M., Day, C., Omma, J., Rushton, J., Olivito, J.P.R., Bouch, J., Robb, L., Roberts, N., Cartwright, J., 2024. Diagenetic Products, Settings and Evolution of the Presalt Succession in the Northern Campos Basin, Brazil. Geological Society, London, Special Publications 548. https://doi.org/10.1144/sp548-2023-93

Tanaka, A.P., Gomes, J.P., Liechoscki de Paula Faria, D., Gomes de Souza, O., 2018. Geological characterization and modeling of an Aptian carbonate reservoir in the Santos Basin, Brazil, in: AAPG Annual Convention and Exhibition. AAPG, Salt Lake City.

Teboul, P.-A., Durlet, C., Girard, J.-P., Dubois, L., San Miguel, G., Virgone, A., Gaucher, E.C., Camoin, G., 2019. Diversity and origin of quartz cements in continental carbonates: Example from the Lower Cretaceous rift deposits of the South Atlantic margin. Applied Geochemistry 100, 22–41. https://doi.org/10.1016/j.apgeochem.2018.10.019

Teboul, P.A., Kluska, J.M., Marty, N.C.M., Debure, M., Durlet, C., Virgone, A., Gaucher, E.C., 2017. Volcanic rock alterations of the Kwanza Basin, offshore Angola - Insights from an integrated petrological, geochemical and numerical approach. Marine and Petroleum Geology 80, 394–411. https://doi.org/10.1016/j.marpetgeo.2016.12.020

Terra, G.J.S., Spadini, A.R., França, A.B., Sombra, C.L., Zambonato, E.E., Juschaks, L.C. da S., Arienti, L.M., Erthal, M.M., Blauth, M., Franco, M.P., Matsuda, N.S., Silva, N.G.C. da, Moretti Jr, P.A., D'Avila, R.S.F., Souza, R.S. de, Tonietto, S.N., Anjos, S.M.C. dos, Campinho, V.S., Winter, W.R., 2010. Classificação de rochas carbonáticas aplicável às bacias sedimentares brasileiras. Boletim de Geociências da Petrobras 18, 9–29.

Terra, S.A., Lima da Silva, D.R., Ribeiro, A., Borghi, L., 2023. The lower Barra Velha formation (Aptian) in the Atapu field, Santos basin: Geological model for a pre-salt succession. Journal of South American Earth Sciences 131, 104589. https://doi.org/10.1016/j.jsames.2023.104589

Thiele, S.T., Bnoulkacem, Z., Lorenz, S., Bordenave, A., Menegoni, N., Madriz, Y., Dujoncquoy, E., Gloaguen, R., Kenter, J., 2022. Mineralogical mapping with accurately corrected shortwave infrared hyperspectral data acquired obliquely from UAVs. Remote Sensing 14. https://doi.org/10.3390/rs14010005

Thompson, D.L., Stilwell, J.D., Hall, M., 2015. Lacustrine carbonate reservoirs from Early Cretaceous rift lakes of Western Gondwana: Pre-Salt coquinas of Brazil and West Africa. Gondwana Research. https://doi.org/10.1016/j.gr.2014.12.005

Tonietto, S.N., Gomes, J.P.B., Bunevich, R.B., Erthal, M.M., 2023. Spherulitestone as a transitional facies responding to lake level variation – diagenetic or depositional?, in: SEG/AAPG Image. AAPG, Houston.

Varejão, F.G., Warren, L. V., Simões, M.G., Cerri, R.I., Alessandretti, L., Santos, M.G.M., Assine, M.L., 2022. Evaluation of distinct soft-sediment deformation triggers in mixed carbonate-siliciclastic systems: Lessons from the Brazilian Pre-Salt analogue Crato Formation (Araripe Basin, NE Brazil). Marine and Petroleum Geology 140. https://doi.org/10.1016/j.marpetgeo.2022.105673

Vital, J.C. dos S., Ade, M.V.B., Morelatto, R., Lupinacci, W.M., 2023. Compartmentalization and stratigraphic-structural trapping in pre-salt carbonate reservoirs of the Santos Basin: A case study in the Iara complex. Marine and Petroleum Geology. https://doi.org/10.1016/j.marpetgeo.2023.106163

Weber, K.J., van Geuns, L.C., 2005. PETROLEUM GEOLOGY | Production, in: Encyclopedia of Geology. Elsevier, Delft, pp. 308–330. https://doi.org/https://doi.org/10.1016/B0-12-369396-9/00249-5

Wright, V.P., 2022. The mantle, CO2 and the giant Aptian chemogenic lacustrine carbonate factory of the South Atlantic: Some carbonates are made, not born. Sedimentology 69, 47–73. https://doi.org/10.1111/sed.12835

Wright, V.P., Barnett, 2017. Classifying reservoir carbonates when the status quo simply does not work: a case study from the Cretaceous of the South Atlantic, in: AAPG Annual Convention and Exhibition. AAPG, Texas, pp. 51419–51419.

Wright, V.P., Barnett, A.J., 2020. The textural evolution and ghost matrices of the Cretaceous Barra Velha Formation carbonates from the Santos Basin, offshore Brazil. Facies 66, 7. https://doi.org/10.1007/s10347-019-0591-2

Wright, V.P., Barnett, A.J., 2015. An abiotic model for the development of textures in some South Atlantic early Cretaceous lacustrine carbonates. Geological Society Special Publication 418, 209–219. https://doi.org/10.1144/SP418.3

Wright, V.P., Tosca, N., 2016. A Geochemical Model for the Formation of the Pre-Salt Reservoirs, Santos Basin, Brazil: Implications for Understanding Reservoir Distribution, in: American Association of Petroleum Geologists Annual Convention and Exhibition. AAPG, Calgary.

Yeste, L.M., Palomino, R., Varela, A.N., McDougall, N.D., Viseras, C., 2021. Integrating outcrop and subsurface data to improve the predictability of geobodies distribution using a 3D training image: A case study of a Triassic Channel – Crevasse-splay complex. Marine and Petroleum Geology 129, 105081. https://doi.org/10.1016/j.marpetgeo.2021.105081

Zhang, L., Li, Y., 2020. Architecture of deepwater turbidite lobes: A case study of Carboniferous turbidite outcrop in the Clare Basin, Ireland. Petroleum Exploration and Development 47, 990–1000. https://doi.org/10.1016/S1876-3804(20)60111-2

## Chapter 1: General Introduction



## Chapter 2: Geological and Methodological Frameworks

### Chapter 3: La Barre du Cengle

### Chapter 4: Salta Basin

## Chapter 5: CNN Optimization

### Chapter 6: Hyperspectral

### Chapter 7: Transversal Discussion, Conclusions, and Perspectives

### Chapter 1: General Introduction



### Chapter 3: La Barre du Cengle



### Chapter 4: Salta Basin



### Chapter 5: CNN Optimization



### Chapter 6: Hyperspectral

# Appendices

Theme 1. Continental carbonates, karst and cave deposits

General Session

Poster presentation

# Anatomy and stacking pattern of palustrine-dominated carbonate parasequences (Thanetian–Ypresian, SE France): insights from carbonate petrography associated with aerial photogrammetry

Eduardo Roemers-Oliveira[1,2], François Fournier[1], Sophie Viseur[1], Guilherme Pederneiras Raja Gabaglia[2]

[1]Aix-Marseille University, CEREGE – European Center for Research and Education of Environmental Geosciences, Marseille, France
[2]Petrobras, Rio de Janeiro, Brazil
eduardoroemers@gmail.com

The Arc Basin is an E–W oriented depression, located in southeastern France, in which marine, lagoon, lacustrine, fluvial, palustrine and pedogenic sedimentary deposits were formed from the Upper Cretaceous (Santonian) to the Middle Eocene (Lutetian). This research covers the sedimentological and stratigraphical analyses of the outcrops of "La Barre du Cengle" cliff in which Thanetian/Ypresian limestones (Saint-Marc limestone) are exposed with thicknesses ranging from 20 to 35 m. The Cengle plateau is located south of the Sainte-Victoire Mountain, about 15 km east of the city of Aix-en-Provence. It is elliptical in shape and is 7 km long, east to west, and 3 km transversely. Its average altitude is around 500 m. With the aim of lithofaciological characterization of the studied area, samples were collected in four vertical stratigraphic logs measured at 1:40 scale. "La Barre du Cengle" consists of greyish, beige, and pinkish limestones which have been deposited in a lacustrine/palustrine environment. Deposits from this sedimentary interval were repeatedly subjected to subaerial exposure and are organized into decimeter to meter-scale parasequences. The facies comprise densely packed dark micrite mudstone and bioclastic wackestone/packstone with massive, brecciated, nodular or granular textures. The main bioclast observed correspond to reworked fragments of prismatic calcitic crystals from microcodium aggregates. Well-preserved rosettes and lamellar aggregates of microcodium have been identified in fractures/cracks. Fragments of charophytes and shells of ostracods, gastropods and bivalves complete the fossil assemblage seen in the thin sections. Subaerial exposure features like cracking, brecciation, root traces, nodulation, coated grains, pseudomicrokarst and grainification are present at different intensities. These features indicate different stages in the pedogenetic evolution and allowed the elaboration of an exposure index. The exposure index allowed the understanding of vertical and horizontal lithofaciological variation in the studied sedimentary succession. The main exposure surfaces as well as the lateral changes in lithofacies could be traced on the cliff in virtual models of outcrops generated by aerial photogrammetry acquired by UAV (unmanned aerial vehicle).

# Depositional context of the Balbuena III Sequence (Maastrichtian/Danian) in the Salta Basin, Argentina: integrated approach from sedimentological, stratigraphical and digital outcrop models

**Eduardo Roemers-Oliveira[1,2], Sophie Viseur[1], François Fournier[1], Guilherme Pederneiras Raja Gabaglia[2] & Ednilson Bento-Freire[2]**

*[1] Aix-Marseille Université, Marseille, France*
*[2] Petrobras, Rio de Janeiro, Brazil*

The Salta Basin, located in northwest Argentina, was associated with the breakup of Gondwana during the Cretaceous period. It is subdivided into four sub-basins (Lomas de Olmedo - east; Sey - west; Tres Cruces - north; and Metán-Alemania - south) that were filled with sediments from Pirgua (synrift phase) and Balbuena (sag phase) supersequences. The sag phase is divided into four sequences: Balbuena I, II, III, and IV, from bottom to top. This research presents an integrated approach combining traditional and digital methods to characterize the sedimentology and stratigraphy of the Balbuena III Sequence (Maastrichtian/Danian) of the Yacoraite Formation in the Metán-Alemania sub-basin, Cabra Corral dam region, Coronel Moldes district, Argentina. Field data, including samples for petrographic and sedimentological analyses, were collected from vertical stratigraphic profiles, along which gamma-ray spectral records were also acquired. Finally, digital models of three outcrops were generated using aerial photogrammetry obtained by an unmanned aerial vehicle (UAV). They served as support for automatic processing of their geometry (roughness) and texture to interpret the observed facies and cycles on different scales. In the studied outcrops, the Balbuena III Sequence ranges from 28 to 33 m in thickness and consists of carbonate, siliciclastic, and mixed facies deposited in a lacustrine environment, whose climate was the main depositional controller. The carbonate facies include oolitic/bioclastic grainstones, oolitic/bioclastic packstones, bioclastic rudstones and floatstones, carbonate mudstones, laminites, and stromatolites. The siliciclastic facies comprise very fine wavy sandstones, siltstones, and siliciclastic mudstones. Mixed lithofacies deposition consist of hybrid sandstones and marls. The lithofacies have been grouped into four facies associations and two vertical successions of facies (elementary cycles). The observed cycles have been ranked into sequences of high, middle, and low frequencies and could be traced for tens of kilometres in the basin. These cycles have been also highlighted by numerical outcrop processing. First, the LBP (Local Binary Pattern) operator computed from the grey scale of the outcrop texture proved to be robust in identifying changes in lithofacies. Second, the fractal dimension was estimated from local variogram fitting and used as a tool for analysing the surface roughness. It allowed the identification of different lithological types, as they present distinct granulometries and responses to weathering. The combined analysis of field data and digital outcrop models makes it possible, in addition to understand the stratigraphic framework of the Basin, to map the cyclicity in areas of difficult or impossible access, such as cliffs and escarpments.

# ANATOMY AND STACKING PATTERN OF PALUSTRINE-DOMINATED CARBONATES FROM 'LA BARRE DU CENGLE', PALEOCENE, SE FRANCE

#Oral

Eduardo Roemers de Oliveira [1, 2*], François Fournier [1], Sophie Viseur [1], Guilherme Raja Gabaglia [2], Jules Fleury [1], Véronique Rinalducci [1], Abel Guihou [1], Lionel Marié [1], Felipe Guadagnin [3], Pierre Deschamps [1], Alain Tonetto [4]

*(1) Aix Marseille Univ, CNRS, IRD, INRAE, CEREGE, Technopôle de l'arbois,13545 Aix en Provence, France*

*(2) Petrobras – Petróleo Brasileiro S.A, 20031-170 Rio de Janeiro, Brazil*

*(3) Universidade Federal do Pampa, 96570-000 Caçapava do Sul, Brazil*

*(4) Aix Marseille Université, CNRS, FSCM, PRATIM, 13003 Marseille, France*

*eduardoroemers@gmail.com

The Arc Basin, located in southeastern France, is an east-west-oriented depression where marine, lagoon, fluvial, lacustrine, palustrine, and pedogenetic deposits were formed from Upper Cretaceous to the Middle Eocene [1]. Among the Early Paleogene deposits in this basin lies the cliff of the Cengle Plateau, locally known as "La Barre du Cengle." This cliff exposes carbonates dominated by palustrine deposits, which integrate the "Calcaire de Saint-Marc" Formation [1, 2, 3].

The elliptical plateau of Cengle is situated 15 km east of Aix-en-Provence, France, extending 7 kilometers east-west and 2 kilometers transversely. The thicknesses of its cliffs range from 20 to 35 meters. These cliffs are characterized by the occurrence of grayish, beige, and pinkish limestones deposited in a lacustrine/palustrine environment that has been constantly altered by pedogenesis [4].

An interdisciplinary approach, integrating petrography, photogrammetry, geochronology, SEM, and geochemical analyses, was employed to analyze lithofacies, stacking patterns, lateral facies variations, and interpret the environmental dynamics during the deposition of the carbonates of "La Barre du Cengle".

Generating digital outcrop models through aerial photogrammetry not only enabled the mapping of surfaces subdividing the studied area into four stratigraphic intervals but also facilitated understanding of vertical and lateral facies variations along "La Barre du Cengle".

The facies consist of densely compacted dark micritic mudstone and bioclastic wackestone/packstone with massive, brecciated, nodular, or granular textures. Facies analysis allowed the construction of an exposure index serving as a relative indicator of subaerial exposure time.

Deposits of the Cengle Plateau cliff are organized into elementary sequences at decimeter to meter scales, which, in turn, accumulate into small-scale sequences at decameter orders.

The sedimentary succession reflects the cyclical nature of the climatic variations that control the deposition.

Subaerial exposures mirror variations in lake level at different frequencies. At least four base-level variation frequencies were identified: i) very high and seasonal frequency, generating very short-term subaerial exposures and transforming lacustrine facies into palustrine ones; ii) high frequency resulting in short-term subaerial exposures and generating surfaces that bound elementary sequences; iii) medium frequency leading to long-term subaerial exposures, resulting in the formation of pedogenic facies and features; and iv) low frequency corresponding to the deposition of the entire set of limestones forming the Cengle Plateau cliff.

U-Pb data on carbonates revealed three age groups: i) 64.3 ± 2.5 Ma (Danian to early Selandian), interpreted as the age of deposition of the Cengle limestones; ii) 56 ± 1.6 Ma, characterized by a neomorphic phase; and iii) 43.07 ± 3.87 Ma, represented by a late cementation phase.

In the depositional context, the transition between lacustrine, palustrine, and pedogenic environments consistently occurs from west to east over time. In the more distal regions, the proportion of lacustrine facies tends to increase, and the thickness of preserved sedimentary record is greater. Conversely, in the closer areas, palustrine and pedogenic facies predominate, typically resulting in lesser thickness.

***Acknowledgements***

Thanks to the landowners along the Cengle Plateau for granting access to their areas, which facilitated fieldwork and data collection. Special thanks to Petrobras for funding and supporting this research.

***References***

**[1]** M. Floquet. S. Leleu, T. Tortosa, *Du bassin marin aux bassins continentaux sud-provençaux durant le Crétacé supérieur et au Paléogène, de -100 à -43 Ma*, in *La Géologie des Bouches-du-Rhône : Roches et Paysages Remarquables*, BRGM, 2020.

**[2]** J.P. Durand, *Paléocène et Éocène*, in *Synthèse Géologique du Sud-est de la France. Mémoire du Bureau de Recherches Géologiques et Minières*, S. Debrand-Passard (Ed.), BRGM, 1984.

**[3]** I. Cojan, M.G. Moreau, L.E. Stott, *Stable carbon isotope stratigraphy of the Paleogene pedogenic series of southern France as a basis for continental-marine correlation*, *Geology*, 28 (2000).

**[4]** J.P. Durand, *Les formations fluvio-lacustres Éocènes du Plateau du Cengle près d'Aix-en-Provence, Annales de la faculté des sciences de Marseille 34 (1963).*

# Reading Rock Record through Digital Outcrop Models: An Integrative Workflow for Decoding Stratigraphy and Facies in the Salta Basin, Argentina

E. Roemers-Oliveira[1,3], S. Viseur[1*], I. Gomes-Goncalves[2], F. Guadagnin[2], J. Marchini[1], A. C. Freccia[2], G. Rangel[2], G. Pederneiras Raja Gabaglia[3], F. Fournier[1]

[1] *Aix-Marseille University, CNRS, IRD, Collège de France, INRAE, CEREGE, UMR7330, Avenue Louis Philibert, 13545, Aix-en-Provence, France, viseur@cerege.fr*

[2] *Universidade Federal do PAMPA, Caçapava do Sul, Brazil*

[3] *Petrobras – Petróleo Brasileiro S.A, Rio de Janeiro, Brazil*

***Key words:*** *Digital Outcrop Model, Reservoir analogues, Sedimentology, Roughness, texture, Machine Learning*

For several decades, Digital Outcrop Models (DOMs) have facilitated the geological study of outcrops, allowing detailed interpretations of sedimentary or tectonic structures. However, processing all this data still remains tedious despite the implementation of automatic detection techniques, such as recently developed neural networks. Moreover, when using these outcrops as reservoir analogues, the big question is what level of information to include in 3D models, especially since the studied outcrops are carbonate cliffs several kilometres long, for two reasons: i) carbonates are difficult to differentiate from a distance; ii) cliffs involve large amounts of data to process. On the one hand, large-scale analyses miss fine levels of facies that are crucial for flow or dating, and on the other hand, detailed analyses are time-consuming and provide information that is not easily integrated or useful in models. The present work aims to propose a multi-approach workflow to optimise the information extraction from outcrops for reservoir modelling.

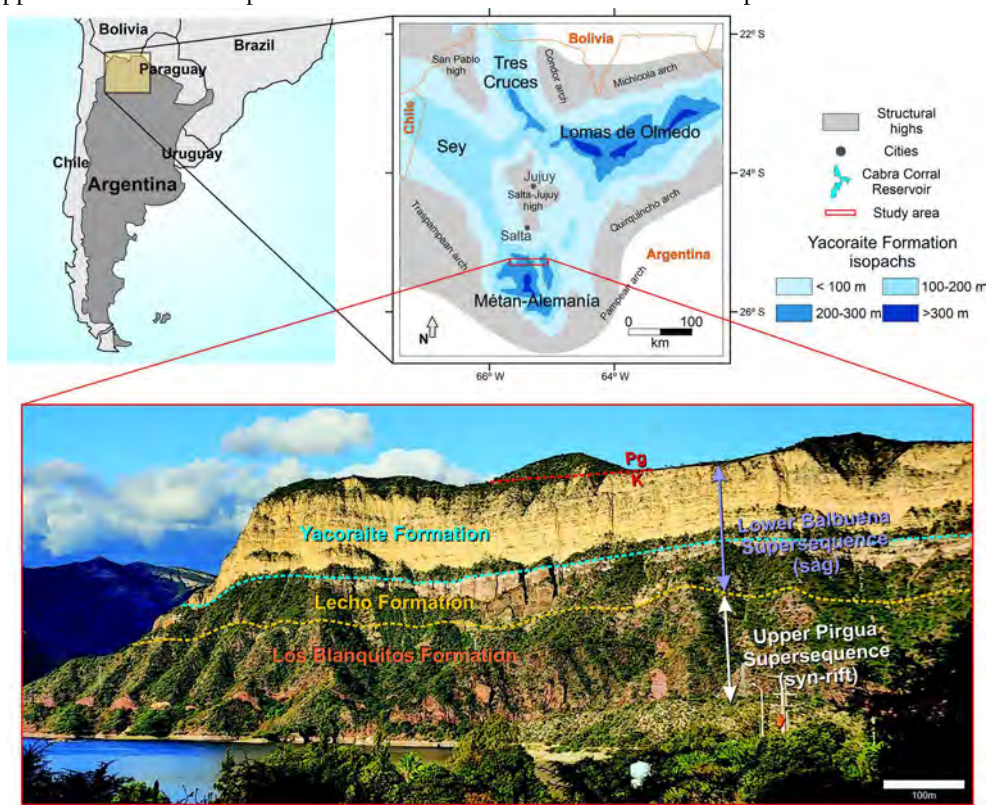


*Figure 1: Case study: top) Location map of the Salta Basin and its sub-basins; bottom) photo of an outcrop near the Cabra Corral reservoir with the stratigraphic nomenclature of the units.*

The Balbuena III Sequence of the Salta Basin, Argentina, is a well-known basin analogue for Brazilian pre-salt carbonate reservoirs (RAJA GABAGLIA *et al.*, 2011). The lacustrine successions, observable at several outcrops, consist of carbonate, siliciclastic, mixed, and volcanic facies, arranged in stacking patterns that can be correlated over tens of kilometres, and are interpreted to reflect climatically driven base-level changes (Fig. 1). Outcrops are located in the southern part of the Salta Basin, close to the Cabra Corral reservoir. We have developed a multi-approach workflow (Fig. 2) to improve the understanding of depositional environments, facies architecture and cyclic stacking patterns within the Balbuena III Sequence

but also to extract quantitative key information for nourishing further 3D surbsurface reservoir models. It combines high-resolution sequence stratigraphy (HRSS), supported by traditional field-based methods, with digital techniques: texture (Local Binary Pattern, LBP) and roughness analyses (VISEUR et al., 2022), and Convolutional Neural Networks (CNNs) applied onto the photogrammetric data.

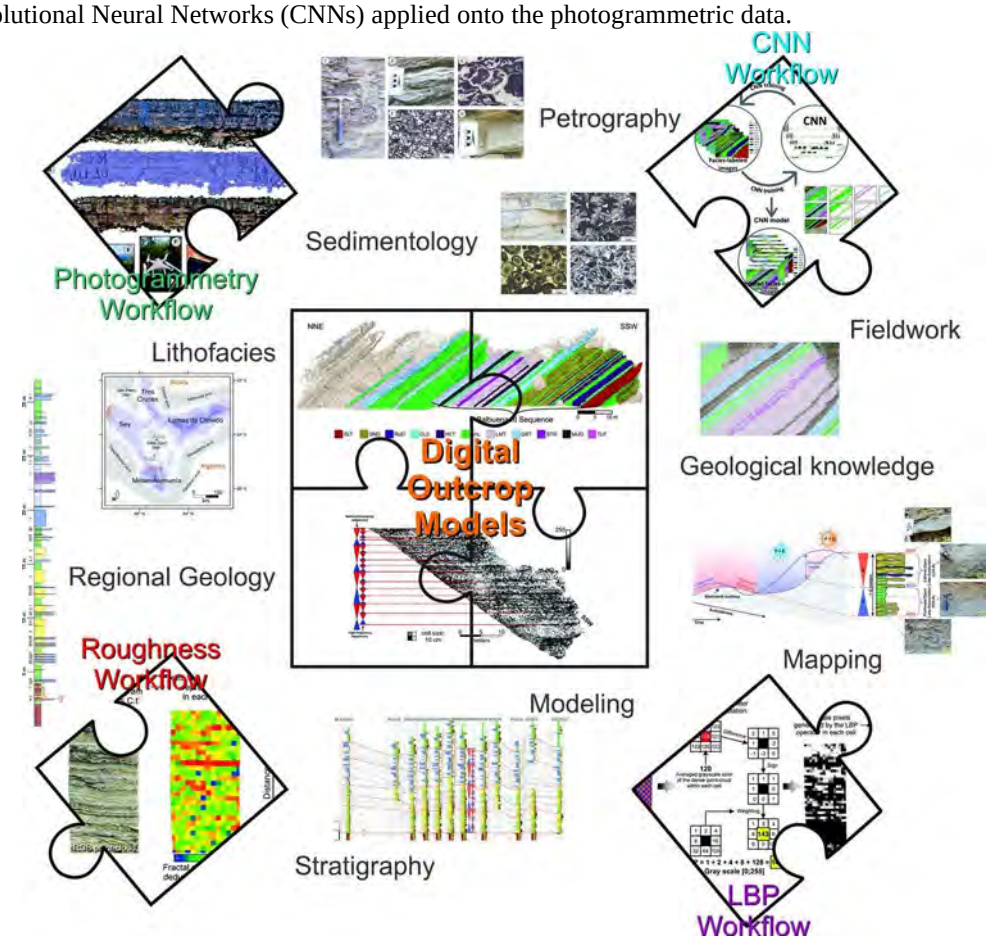


*Figure 2. Imbricated and multi-approach workflow for extracting essential information from data.*

The LBP and roughness analyses defined proxies for stratigraphic interpretation: LBP seems more efficient in exhibiting high-frequency cycles and roughness analyses in highlighting medium-frequency stratigraphic sequences. A CNN-based segmentation combined with photogrammetric algorithms (GUADAGNIN *et al.*, under review) provided facies maps directly on outcrops, allowing 11 lithofacies to be identified, including carbonate, siliciclastic, mixed, and volcanic facies. The combined numerical approaches allow for a more in-depth analysis by increasing efficiency, and thus capacity to analyse large datasets. Combining these techniques with traditional methods improves the analysis of outcrop analogues and thus contributes to a more adequate geological modelling of oil fields and hydrocarbon recovery.

**Acknowledgements**: The authors would like to thank Petrobras (Brazil) for funding and supporting this research. We also extend our gratitude to Geomap (Argentina) and its CEO**.**

## References

GUADAGNIN, F., GONÇALVES, I.G., ROEMERS-OLIVEIRA, E., GUEDES, P.L., SOUZA, E.G., SILVEIRA, M.M.L., RAJA GABAGLIA, G.P., GONÇALVES, L.A., OLIVEIRA, L.F.R., SELK, R., UNDER REVIEW. BUILDING OF CLASSIFIED 3D POINT CLOUDS OF OUTCROP WITH AUTOMATICALLY SEGMENTED IMAGES. GEODATA AND AI.

RAJA GABAGLIA, G.P., BENTO FREIRE, E., TERRA, G.J.S., RODRIGUES, E.B., LYKAWKA, R., HERNÁNDEZ, R.M., 2011. Cyclostratigraphy and climatic control on microbiol influenced sedimentation (Balbuena Supersequence, Yacoraite Formation, Paleocene, Salta–Argentina, in: 28th Internatinal Association of Sedimentology Meeting. Zaragosa.

VISEUR, S., LAMARA, T., PAREL, G., BENEDETTI, L., 2022. Automatic tools for quantitative analysis of multi-scale spatial slip variabilities from DEM and DOM, in: 21 Annual Conference of the International Association for Mathematical Geosciences. IAMG

# Optimising Facies Interpretation Using Neural Networks on Images and Photogrammetric Data: A Case Study from Salta (Argentina)

J. Marchini[1*], E. Roemers-Oliveira[1,3], S. Viseur[1], I. Gomes-Goncalves[2], F. Guadagnin[2], A. C. Freccia[2], G. Rangel[2], G. Pederneiras Raja Gabaglia[3], F. Fournier[1]

[1] *Aix-Marseille University, CNRS, IRD, Collège de France, INRAE, CEREGE, UMR7330, Avenue Louis Philibert, 13545, Aix-en-Provence, France, viseur@cerege.fr*

[2] *Universidade Federal do PAMPA, Caçapava do Sul, Brazil*

[3] *Petrobras – Petróleo Brasileiro S.A, Rio de Janeiro, Brazil*

***Key words:*** *CNN, Photogrammetry, Labelling, optimisation, time-efficiency, evaluation*

The interpretation of sedimentary facies in outcrop analogues provides valuable insights for characterising subsurface reservoirs, particularly when integrated with high-resolution imaging and deep learning methods. This study aims to evaluate the application of Convolutional Neural Networks (CNNs), specifically a U-Net architecture, for pixel-wise lithofacies classification from photogrammetric images of two well-exposed outcrops, Assado and Vapumas, located in the Salta Basin (Argentina). This work relies on a workflow whose effectiveness has already been demonstrated in (Guadagnin et al., 2025; Roemers-Oliveira et al., under review) and which combines acquisition of images, manual interpretation, CNN-based automatic labelling, and 3D lithofacies point cloud generation.

A series of tests were conducted to evaluate the performance of this CNN-based workflow while trying to reduce the most time-consuming steps and minimise the reliance on expert manual labelling. The testing strategies included modifications to input image resolution, number of epochs, expansion of the training dataset, changes in the geological interpretation, and data augmentation. The limited reproducibility of the CNN algorithm was mitigated by fixing the seeds of the random number generators, enabling comparative analysis of performance metrics across the same set of training images under multiple test configurations.

To apply the CNN algorithm, photo labelling was required. A small subset of the total image dataset (~500 per outcrop) was manually interpreted by generating one image mask per facies within each photo (Fig. 1). The labelled dataset comprises 49 images for Assado and 31 for Vapumas, with lithofacies classes defined based on *prior* sedimentological and stratigraphic studies.

Good results were achieved, with 83% overall accuracy for Assado using a training set comprising 10% of the full image dataset, and 84% for Vapumas using just 7% of the total dataset.

As a result, optimal resolution and number of epochs versus running time have been determined in this work. Moreover, it was first demonstrated that a CNN model using a dataset with raw images combined with brightness, contrast, and colour equalised across the entire training dataset enhances results without requiring new labelling. This highlights the importance of the developed approaches, as manual interpretation is the most time-consuming expert task associated with the workflow presented in this study. Secondly, the facies classification may also have an impact on results. Facies can vary gradually, and it is not always easy to group hybrid facies into coherent sets. In this work, several facies association groupings were tested to determine which produced the most effective results, while being consistent with the reservoir application of this study.

Finally, point clouds coloured by predicted lithofacies enabled the visualisation and parametrisation of geological bodies in 3D Digital Outcrop Models (DOMs), confirming the consistency of spatial patterns with known stratigraphy (Fig. 2). Figure 2 shows the first 3D facies mapping of the Vapumas outcrop.

Despite positive results, challenges remain, including sensitivity to class imbalance. Future works includes cross-outcrop model transfer, i.e., applying a CNN trained on one outcrop to another with similar facies.

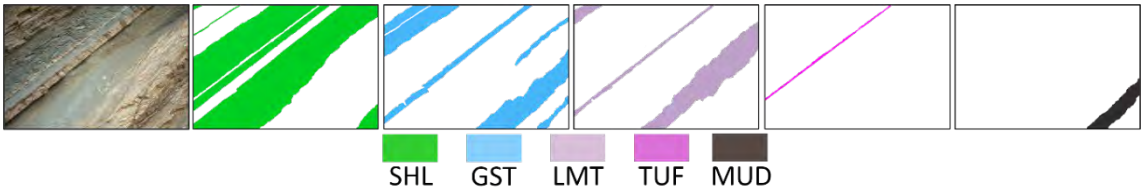


Fig. 1. Example of mask export for CNN training. Each lithofacies present in the outcrop image is exported as a separate binary mask, corresponding to a specific label class used in the supervised learning workflow.

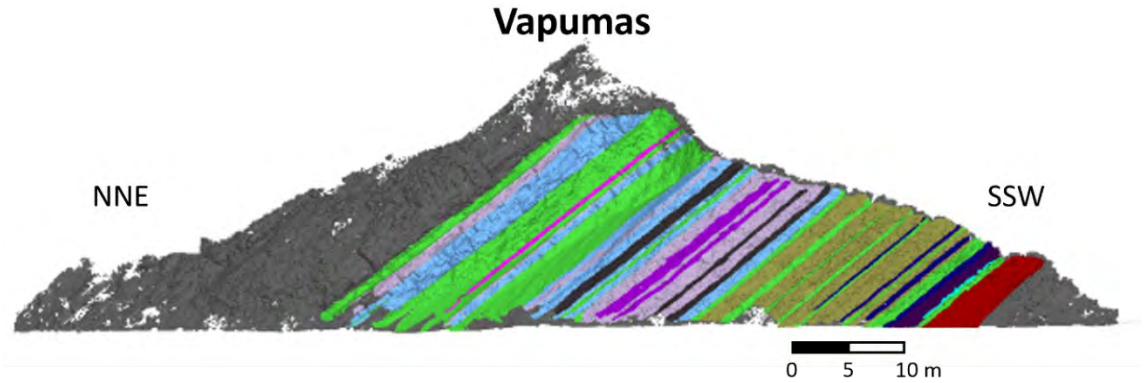


*Fig. 2. 3D point cloud generated for the Vapumas outcrop. Lithofacies were grouped and coloured in CloudCompare, using the same colour code applied in the CNN. The point cloud was also manually edited.*

## References

Guadagnin, F., Gonçalves, I.G., Roemers-Oliveira, E., Guedes, P.L., Souza, E.G., Silveira, M.M.L., Raja Gabaglia, G.R., Gonçalves, L.A., Oliveira, L.F.R., Selk, R., 2025. Building of classified 3D point clouds of outcrop with automatically segmented images. Geodata and AI.

Roemers-Oliveira, E., Viseur, S., Fournier, F., Gonçalves, I.G., Guadagnin, F., Raja Gabaglia, G.R., Bento Freire, E., Fragoso, D.G.C., Freccia. A. C., Rangel. G. G., n.d. Advanced digital techniques applied to outcrop models: Integrating LBP and CNN to support stratigraphic and sedimentological interpretation of reservoir analogs in the Salta Basin, Argentina. Mar Pet Geol.

Geodata and AI 4 (2025) 100024

Contents lists available at ScienceDirect

Geodata and AI

journal homepage: www.elsevier.com/locate/geoai

# Building of classified 3D point clouds of outcrop with automatically segmented images

Felipe Guadagnin[a,*], Ítalo Gomes Gonçalves[a], Eduardo Roemers-Oliveira[b,c], Pablo Losano Guedes[a], Ezequiel Galvão de Souza[a], Miguel de Morais Lima Silveira[b], Guilherme Pederneiras Raja Gabaglia[b], Lucas Arienti Gonçalves[b], Luiz Felipe Ribeiro de Oliveira[a], Ronaldo Selk[a]

[a] Universidade Federal do Pampa, Campus de Caçapava do Sul, Caçapava do Sul, 96570-000, Brazil
[b] PETROBRAS, Rio de Janeiro, 20231-030, Brazil
[c] Aix-Marseille Université, CNRS, IRD, INRAE, CEREGE, Aix-en-Provence, 13545, France

ARTICLE INFO

*Keywords:*
U-net segmentation
Turbidite depositional system
Convolutional neural network
Photogrammetry
3D Point Clouds

ABSTRACT

3D point clouds of outcrops are digital representations of rock exposures used for geological surveying. These datasets often have high spatial density, up to a thousand points per square meter. By integrating georeferenced data into the 3D point cloud and applying remote sensing interpretation techniques, geoscientists can extract geological features and build 3D models. However, interpreting 3D point clouds remains labor-intensive, non-reproducible, and prone to human bias. Convolutional neural networks have been applied to segment the images used to build the 3D models, based on a few labeled training and testing subsets, to reduce the amount of human labour. This work used a U-Net encoder-decoder network architecture to segment images of turbidite architectural elements in the La Jardinera Region, Neuquén Basin, Argentina. Approximately 10 % of the images were labeled by an expert interpreter, with half used for training and half for testing the model, yielding % overall accuracy of 82 %. The model was then retrained on the full labeled set and applied to the remaining unlabeled images. The final segmented outputs were processed through a photogrammetry pipeline to generate classified 3D point clouds, capturing the spatial distribution of architectural elements within the outcrop.

## 1. Introduction

The use of 3D point clouds of rock exposures (outcrops) for facies analysis is now standard in both academic and industry investigations (e.g., Pringle et al., 2006; Keogh et al., 2014; Bilmes et al., 2019; Marques et al., 2020; Roisenberg et al., 2022; Gross et al., 2023; Kamaruzaman et al., 2024). Facies analysis is central in any geological survey, as it defines a rock's texture, composition, structure, and external geometry (e.g., Catuneanu, 2022). Georeferenced 3D point clouds offer key advantages for a geological survey, as they provide 3D photorealistic outcrop models with a high density of data, capturing up to thousands of points per square meter, with a high-resolution representation of outcrop surfaces. These models enable the integration of various types of georeferenced datasets, such as compositional, mineralogical, petrographic, structural, multi- and hyperspectral, geophysical, and petrophysical, across 1D, 2D, or 3D formats. Geological remote sensing techniques are then used to extract digital objects (points, lines, surfaces, or volumes) from the outcrop models, to which geological attributes can be assigned. Ultimately, all this information feeds into constructing 3D geological models tailored to project-specific objectives (e.g., Howell et al., 2014; Burnham & Hodgetts, 2019).

3D point clouds can be generated using LiDAR or photogrammetry techniques, with data acquisition conducted via ground-based or aerial surveys (e.g., Cawood et al., 2017). Photogrammetry is based on the parallax effect—the apparent displacement of objects viewed from different locations (e.g., Sherman & Craig, 2018)—and is often favored over LiDAR due to shorter processing time, lower equipment and computational cost, and flexibility in spatial resolution. The latter depends on camera specifications and the distance to the target. Photogrammetry products typically yield higher spatial resolution when using digital single-lens reflex or mirrorless cameras (e.g., Carrivick et al., 2016; Cawood et al., 2017; Diara & Roggero, 2022).

Facies analysis has traditionally relied on manual classification by human interpreters—a time-consuming process that lacks error estimation, reproducibility, and scalability (e.g., Pires de Lima et al., 2020; Falivene et al., 2022; Malik et al., 2022; Dawson et al., 2023).

* Corresponding author.
*E-mail address:* felipeguadagnin@unipampa.edu.br (F. Guadagnin).

https://doi.org/10.1016/j.geoai.2025.100024
Received 31 January 2025; Received in revised form 17 May 2025; Accepted 19 May 2025

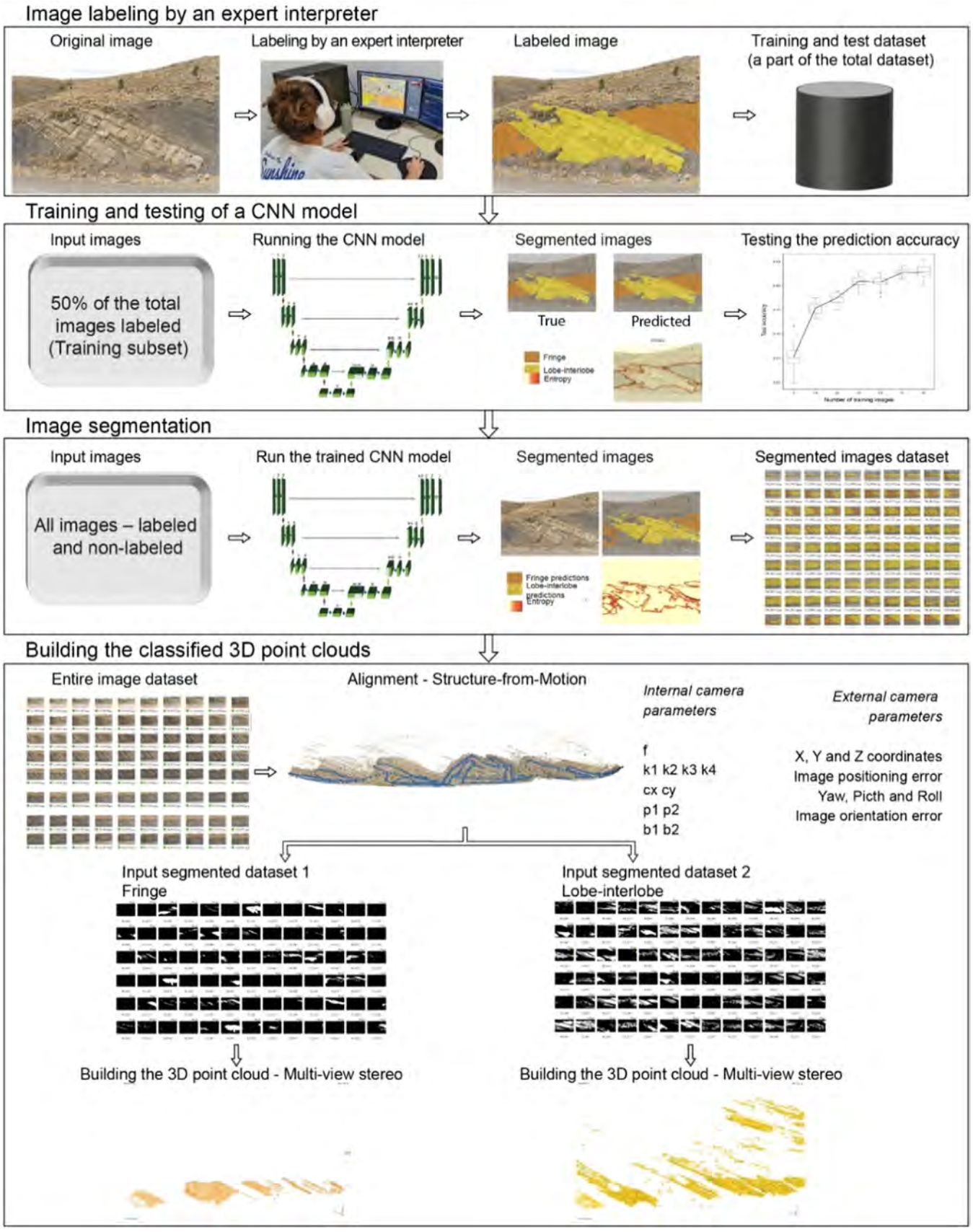


**Fig. 1.** Workflow for generating classified 3D point clouds of outcrop for rock facies analysis.

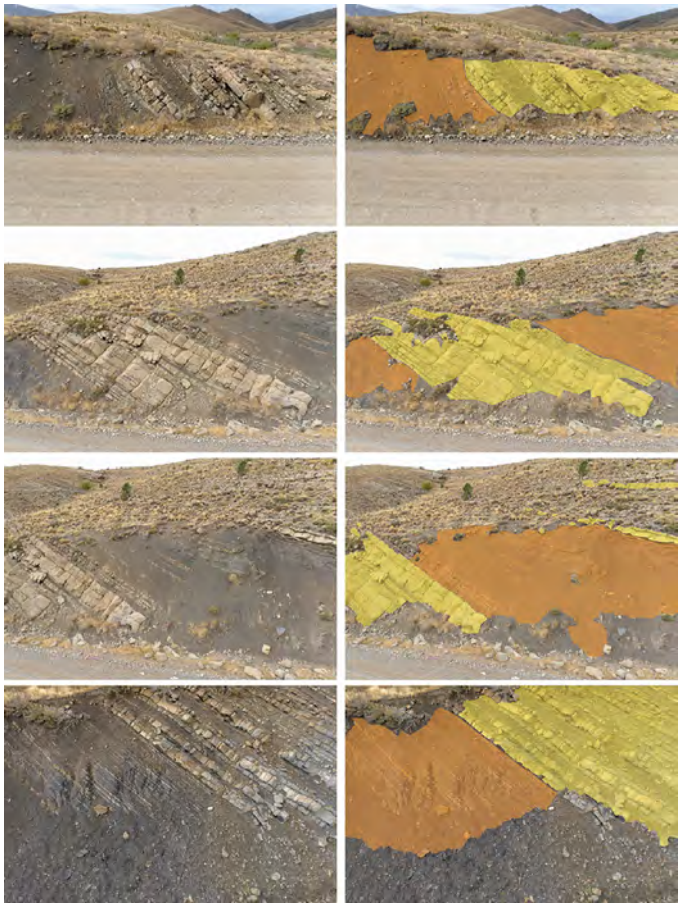

**Fig. 2.** Examples of labeled images from the La Jardinera outcrop used in this study. Turbidite lobes-interlobes are shown in yellow, and fringe facies are marked in orange.

Furthermore, the volume of data produced during a typical outcrop survey far exceeds what a human can realistically process. Despite these limitations, facies analysis of 3D point clouds is often performed manually (e.g., Buckley et al., 2019; Horota et al., 2023). The increasing availability of image classification techniques based on convolutional neural networks (CNNs) has led to a growing number of applications of these methods to geological problems across various scales and settings. These approaches offer improved interpretation accuracy, greater scalability, and reduced subjectivity and interpretation time. CNNs learn to recognize patterns of RGB color, edges, and texture by segmenting images according to their characteristic features. For example, Cheng and Guo (2017) analyzed rock granularity, Koeshidayatullah et al. (2020), Liu and Song (2020), Pires de Lima et al. (2020), Pires de Lima and Duarte (2021), Xu et al. (2022), Dawson et al. (2023), and Liu et al. (2023) classified rock specimens in thin-section images; Souza et al. (2020) enhanced hydrocarbon lead mapping in seismic images; Falivene et al. (2022) identified common lithofacies using core images; and Malik et al. (2022) segmented sandstone from mudstone classes using outcrop images.

Image segmentation using CNNs is a supervised deep learning technique in which human interpreters label a portion of the dataset. These labeled images are used to train a CNN model, which minimizes discrepancies between predicted and true labels with the training set (e.g., Dawson et al., 2023). Once trained with high accuracy (i.e., the fraction of correct predictions), the model can be applied to segment the remaining unlabeled dataset. The segmented images can then be processed through the photogrammetry pipeline to generate the 3D classified point clouds. Similar procedures have been used in fields like building façades classification in complex urban settings (e.g., Lotte et al., 2018; Bacharidis et al., 2020) and coral reefs mapping and classification (e.g., Hopkinson et al., 2020; Yuval et al., 2021; Sauder et al., 2023; Marlow et al., 2024).

This work presents a workflow for generating 3D point clouds classified by facies from outcrop images using CNN-based image segmentation combined with photogrammetry. The main objective is to reduce human bias in the interpretation process while enhancing reproducibility and efficiency. The workflow is applied to a case study at the La Jardinera outcrop in the Neuquén Basin, Argentina, an internationally recognized exposure of a turbidite depositional system. The

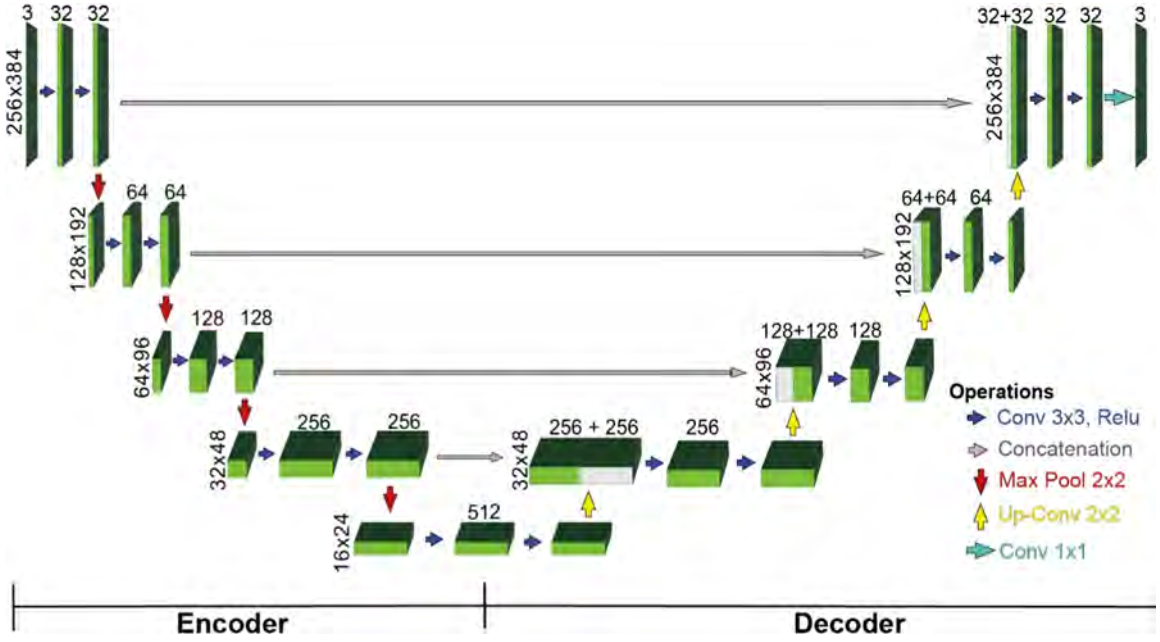


**Fig. 3.** U-net architecture, divided into the encoder and decoder components (e.g., Ronneberger et al., 2015).

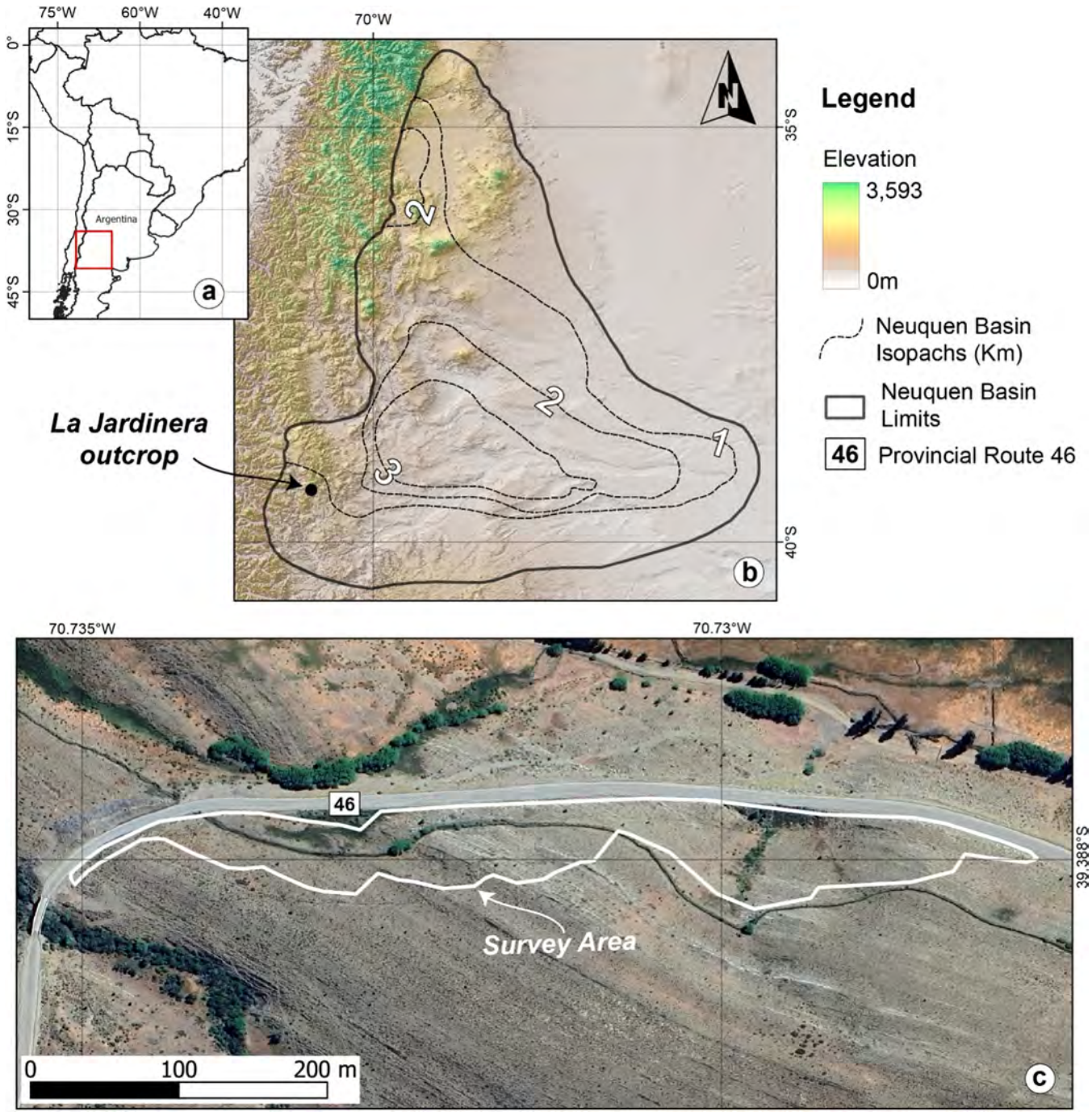


**Fig. 4.** Location of the survey area at the La Jardinera outcrop. (a) Regional geographic context, with the red polygon showing the map's extent in (b). (b) Map showing the Neuquén Basin limits (adapted from Howell et al., 2005) and isopachs (Cordani et al., 2016) over a digital elevation model (SRTM 90 m), indicating the La Jardinera outcrop location. (c) Detailed view of the survey area over a Google satellite image. The central coordinates of the survey area are 39.387705° W latitude and 70.731289° S longitude (WGS 84 datum).

results demonstrate high accuracy in classifying two different architectural elements within the system. The code used in the case study is available on GitHub (https://github.com/italo-goncalves/unet_tools), and the dataset is available upon request.

## 2. Workflow

The workflow for generating a classified 3D point cloud of outcrops for rock facies consists of four main steps: (i) image labeling by an expert interpreter, (ii) CNN model training and testing, (iii) image segmentation, and (iv) construction of the classified 3D point clouds (Fig. 1).

### 2.1. Image labeling by an expert interpreter

To train the CNN model, a portion of the outcrop images must first be labeled for use in training and testing. Labeling involves an expert interpreter classifying image sections by facies or facies associations (Fig. 2). It can be done manually or with tools such as a polygonal lasso, magic wand, paint bucket, mask manager, available in open-source and commercial software like GIMP or Adobe Photoshop. Features in the images that do not represent outcrop rock, such as sky, vegetation, loose sediments, and human-made objects, are not labeled. Image segmentation automatically assigns these features to the "other" category.

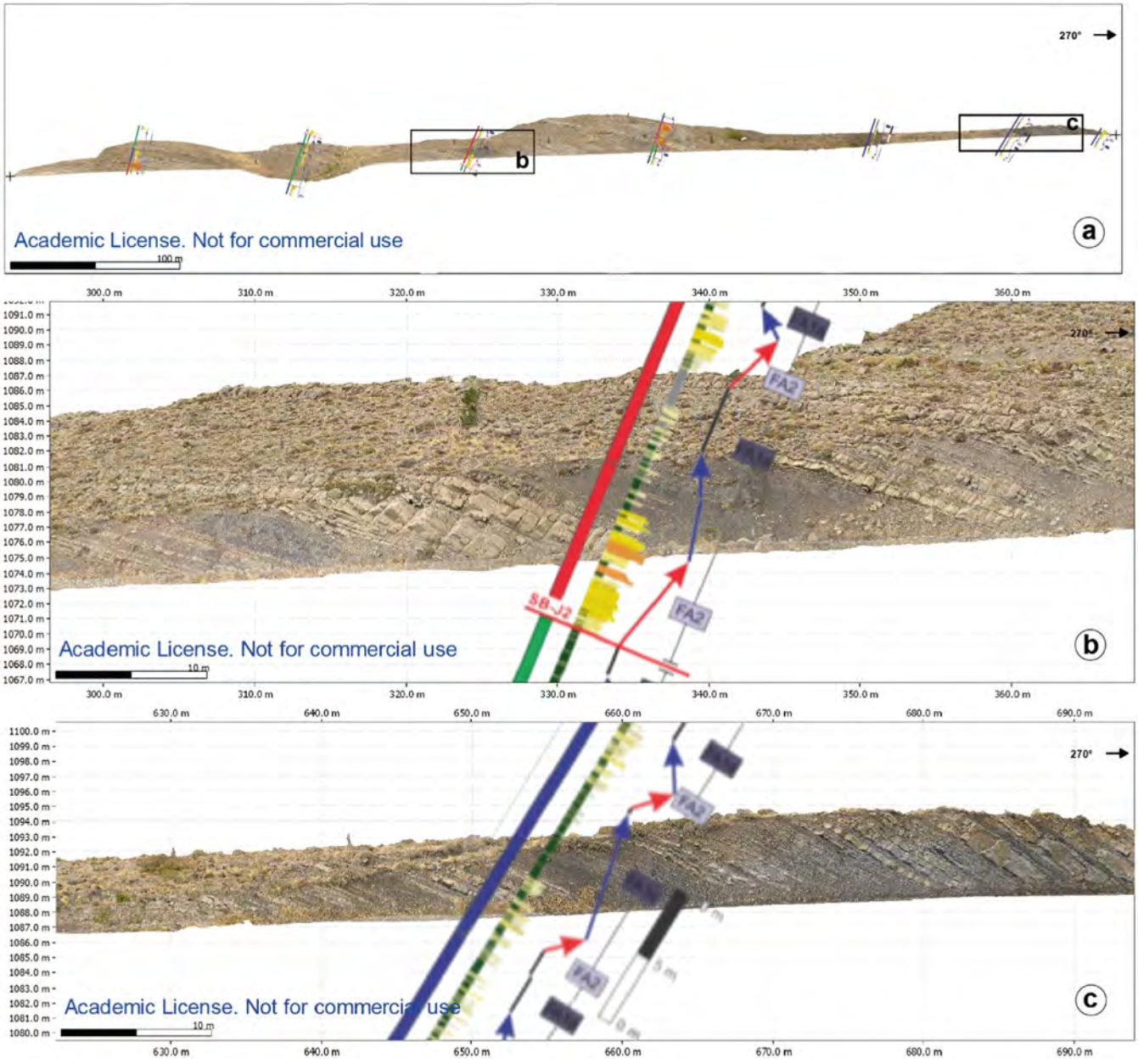


**Fig. 5.** Measured facies and facies associations log (Gonçalves et al., 2022) tied to the orthophoto mosaic of the La Jardinera outcrop in an east-west-oriented vertical section (a). Panels (b) and (c) show detailed view of the section. Facies code FA1 corresponds to fringe, and FA2 to lobe–interlobe deposits.

### *2.2. Training and testing a CNN model*

Since the workflow aims to label only images available at training time, it follows a transductive learning approach, rather than the more common inductive learning, which aims to generalize to unseen data points. With this in mind, the number of labeled images required to achieve sufficient accuracy must be carefully assessed. A balance between model accuracy and the manual labor required must be found. A small fraction of the images (typically around 5 %) is labeled as a starting point. The labeled dataset is split into training and testing subsets, with a small proportion of training data. The CNN model is trained on the training subset, and its accuracy is evaluated on the testing subset. The train/test split is repeated 20 times to obtain a range of accuracy values to ensure robust results. Additional labeled images are progressively added to the training set, which is repeated until the test accuracy stabilizes.

### *2.3. Image segmentation*

Before running the segmentation model, the following preprocessing steps are applied to speed up and optimize the process:

- Image resolution reduction to 256 × 384 pixels.
- Data Augmentation (Shorten & Khoshgoftaar, 2019), which encompasses techniques that increase the size of training data sets, such as mirroring and transposing the images.

The CNN architecture employed in this work is the U-net (Ronneberger et al., 2015), initially developed for segmentation and pattern recognition in biomedical slide data. U-net consists of the encoder and the decoder (Fig. 3). The encoder progressively applies convolutional layers to extract low-level features, followed by an activation function that introduces non-linearity to the system. Subsequently, the image size is halved using a max pooling function, and the process

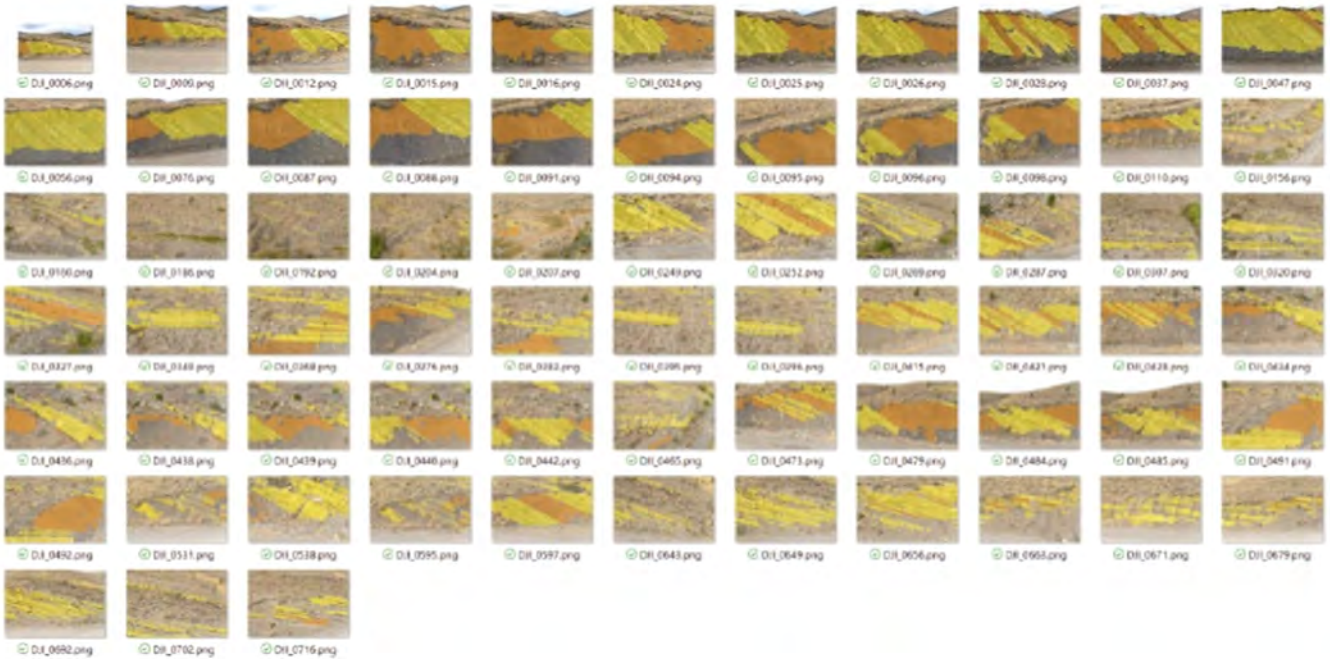

**Fig. 6.** 69 randomly selected labeled images as lobe-interlobe (yellow) and fringe (orange).

**Table 1**
Validation results for a 50/50 train/test split.

| | Precision | Recall | F1-score |
|---|---|---|---|
| Lobe-interlobe | 0.71 | 0.71 | 0.71 |
| Fringe | 0.70 | 0.65 | 0.68 |
| Other | 0.88 | 0.89 | 0.88 |

continues to the next convolutional level. The decoder reconstructs the segmented image to its original size, incorporating feature information extracted in the previous step. This is accomplished through transposed convolutional layers (up-convolutions) and concatenation with the corresponding features in the contraction path.

In this work, the U-net contains two convolutional layers with 32 channels. Four max-pooling operations are performed, and after each, the data passes through another two convolutional layers with twice the number of channels. The decoder mirrors this process, concatenating each encoder tensor with the corresponding decoded tensor after the up-convolution step. The ReLU activation is used in all layers except the final one, which employs the softmax activation (Fig. 3).

The predictions' entropy is used to visually assess model uncertainty, particularly for unlabeled images. Entropy quantifies the average level of uncertainty associated with a variable's potential states (e.g., Shannon, 1948). Given the model's output as a probability distribution $p$ over each pixel's facies or association label, obtained with the softmax activation, the entropy is computed as:

$$H = -p * [Log\ p]$$

The entropy will be low when the model assigns a high probability to a specific facies, indicating high confidence in its prediction. In contrast, the entropy will be high when the model assigns similar probabilities across two or more facies, reflecting greater uncertainty in the prediction.

### 2.4. Building the classified 3D point clouds

The Structure-from-Motion–Multi-view Stereo (SfM-MVS) pipeline generates the classified 3D point clouds. In this workflow, the entire dataset is first used to align all images, after which each segmented subset is processed to create individual classified 3D point clouds.

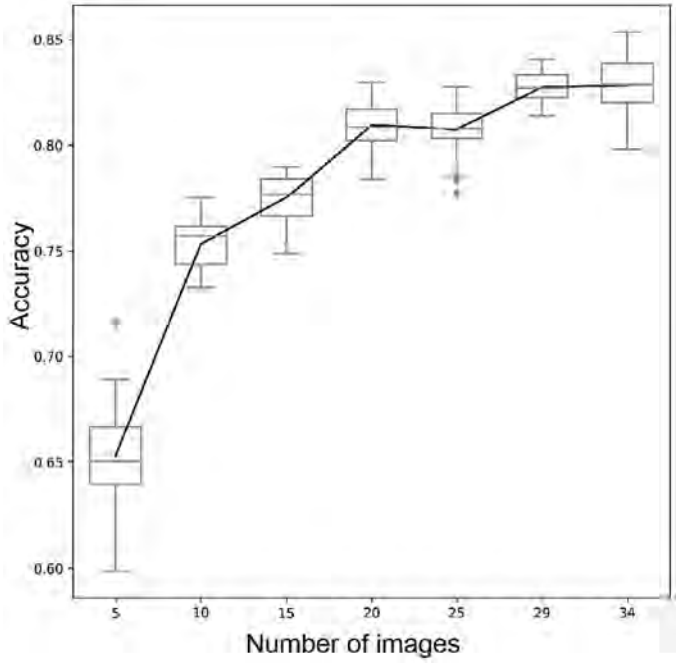


**Fig. 7.** Test accuracy as a function of dataset size.

The alignment procedure is the first step of the SfM-MVS pipeline (e.g., Westoby et al., 2012; Carrivick et al., 2016; Toffanin, 2023). It involves several key algorithms for: (a) feature detection in individual images (e.g., Scale-Invariant Feature Transform; Lowe, 2004), (b) features matching across different images (e.g., Approximate Nearest Neighbor; Lowe, 2004), (c) elimination of geometrically inconsistent correspondences (e.g., Random Sample Consensus; Fischler & Bolles, 1981), and (d) Bundle Adjustment to refine the 3D scene geometry, calculate image positions and orientations, and solve internal camera parameters (e.g., Tavani et al., 2024). This process can be performed using commercial or open-source software, or through libraries available for Python or

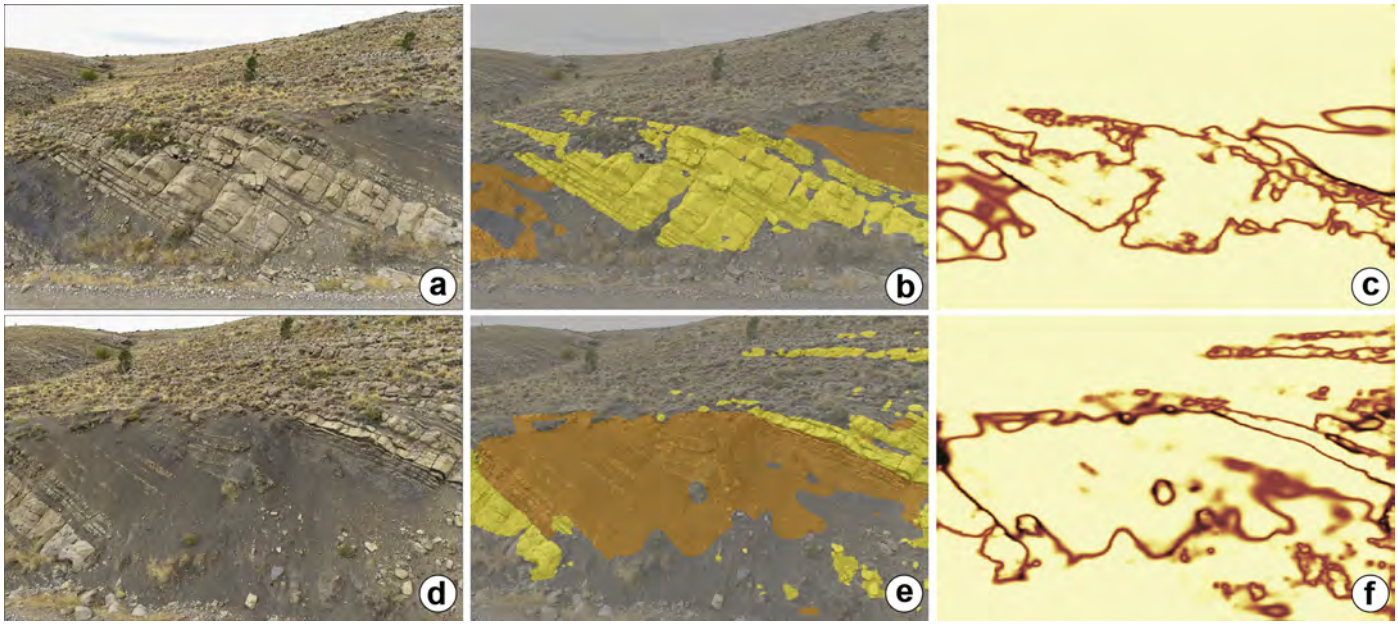


**Fig. 8.** Example of the model´s prediction ('b' and 'e') for lobe-interlobe (in yellow) and fringe (in orange) over two originally unlabeled images ('a' and 'd'), along with the corresponding entropy map ('c' and 'f').

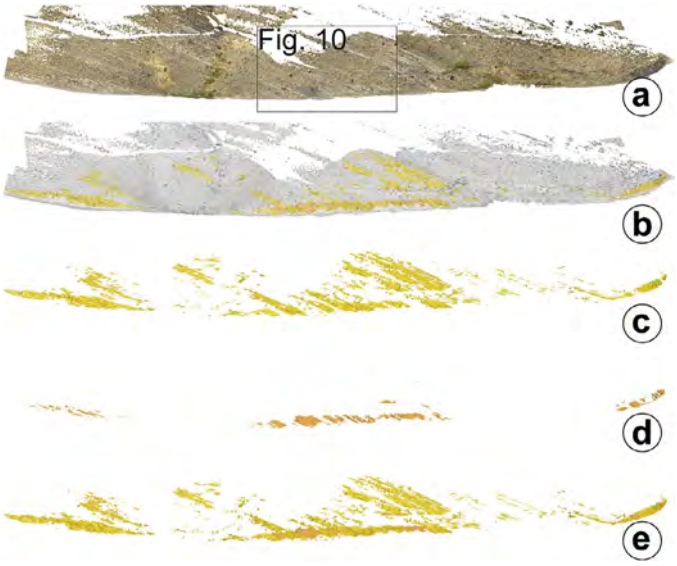


**Fig. 9.** Oblique perspective view of the 3D point clouds of the La Jardinera outcrop. (a) RGB-colored 3D point cloud of the entire dataset, with the area detailed in Fig. 10 highlighted. (b) Classified points showing lobe–interlobe (yellow), fringe (orange), and unclassified points (gray). (c) Lobe–interlobe points only. (d) Fringe points only. (e) Combined lobe–interlobe and fringe points.

other languages, such as OpenSfM. It is important to note that different software or code may apply different strategies for the alignment procedure.

Building the 3D point clouds is the second stage of the SfM-MVS pipeline. Multi-view stereo (MVS) algorithms increase the point cloud density obtained from the alignment procedure (e.g., Furukawa & Hernández, 2015). MVS method can be based on voxel, surface evolution, depth map merging, or patch methods (e.g., Tavani et al., 2024). The MVS procedure is run separately for each segmented subset in this workflow. The segmented images are used as masks, ensuring the MVS algorithm densifies the point cloud only within the segmented areas. This produces a distinct 3D point cloud for each subgroup. The steps include: (i) import and align all images; (ii) duplicate the processing group; (iii) import the segmented images as masks into the corresponding processing group; and (iv) run the MVS separately on each processing group.

## 3. Case study - La Jardinera outcrop

The dataset used in this work was acquired from the La Jardinera outcrop, covering a survey area of approximately 32,350 $m^2$ (Fig. 4). It consists of 721 images captured using a DJI Remotely Piloted Aerial System model Phantom 4 Pro, equipped with a 1″ CMOS sensor that produces georeferenced images at a resolution of 5.472 × 3.648-pixel (20-megapixel).

The La Jardinera outcrop exposes sedimentary rocks deposited in Upper and Middle Jurassic in turbidite systems, formed in slope-rise and basin-plain settings (Paim et al., 2008; Giacomone et al., 2020; Olariu et al., 2020; Gonçalves et al., 2022; Silveira et al., 2024). These strata belong to the Los Molles Formation of the Cuyo Group. Using a sequence stratigraphy approach (*sensu* Catuneanu, 2019), Gonçalves et al. (2022) defined four 4th-order sequences mainly composed of lobes, interlobes, and wide channels interlayered with fringe sediments, which are distinguished by facies and facies associations (architectural elements).

In the studied interval, two architectural elements are visually distinct: turbiditic lobes-interlobes and fringes (Fig. 2; Paim et al., 2008; Gonçalves et al., 2022). The lobes and interlobes consist of tabular beds of medium- to fine-grained sandstones, either amalgamated or interlayered with thin beds of dark shales. In contrast, fringes are characterized by dark and light grey shale beds with flat bases, interbedded with thin tabular beds of fine-grained sandstones and convoluted sandstones and shale layers (Gonçalves et al., 2022).

The measured facies and facies associations log from Gonçalves et al. (2022) was tied to the 3D point cloud built from the entire dataset using the SfM-MVS pipeline. The tying process used the Move software with a 2D section view. An orthophotomosaic was constructed from the 3D outcrop model, projected onto an east-west-oriented vertical plane. This orthophotomosaic was then imported into Move as a georeferenced section. The facies and facies associations log was also imported into the same section, then scaled and rotated to fit

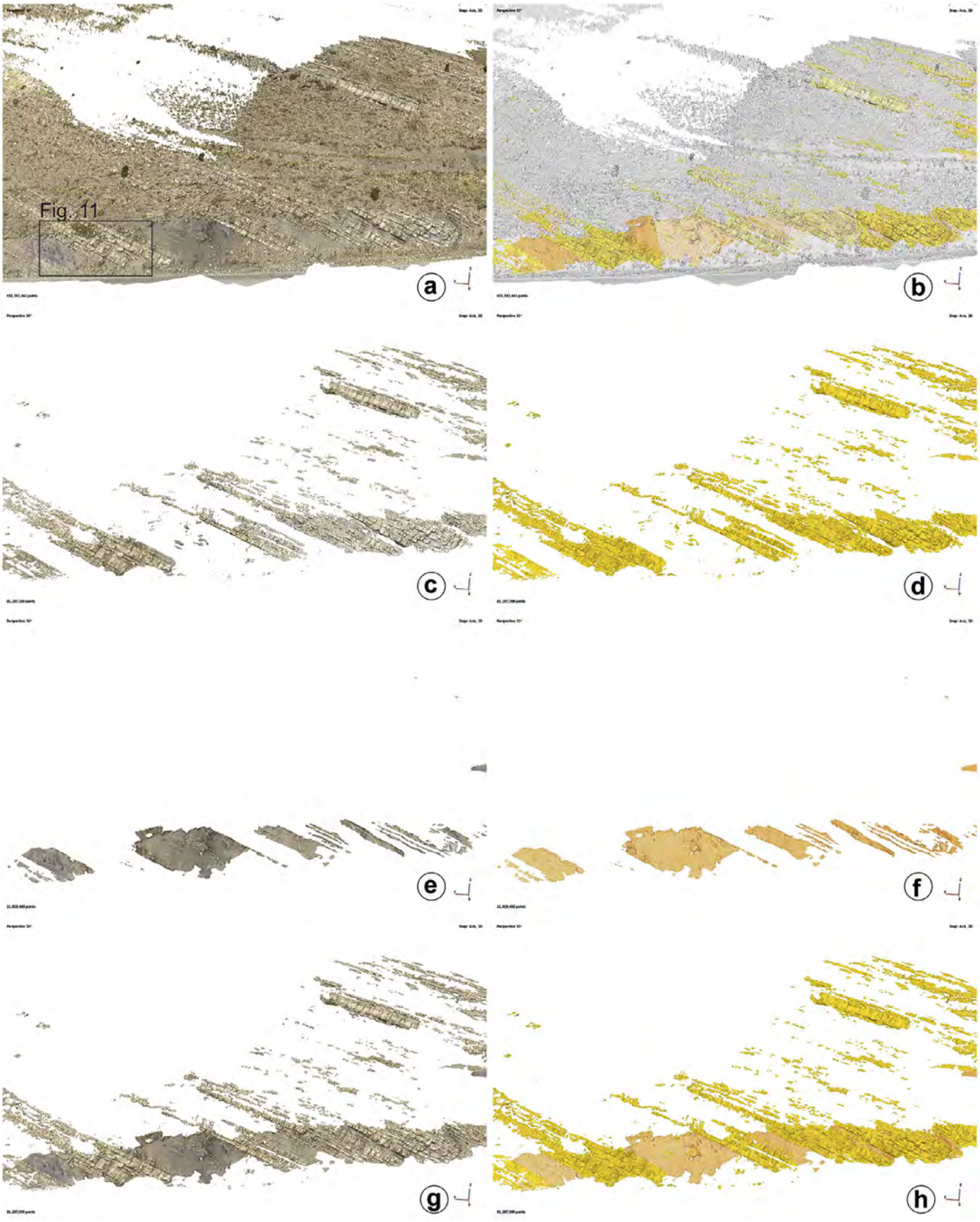


**Fig. 10.** Closer view of the 3D point clouds in the same oblique perspective as Fig. 9. (a) RGB-colored 3D point cloud of the entire dataset, with the area detailed in Fig. 11 highlighted. (b) Classified and unclassified points. (c) Lobe–interlobe architectural elements shown as RGB-colored points. (d) Lobe–interlobe elements shown in yellow. (e, f) Fringe elements. (g, h) Combined lobe–interlobe and fringe points.

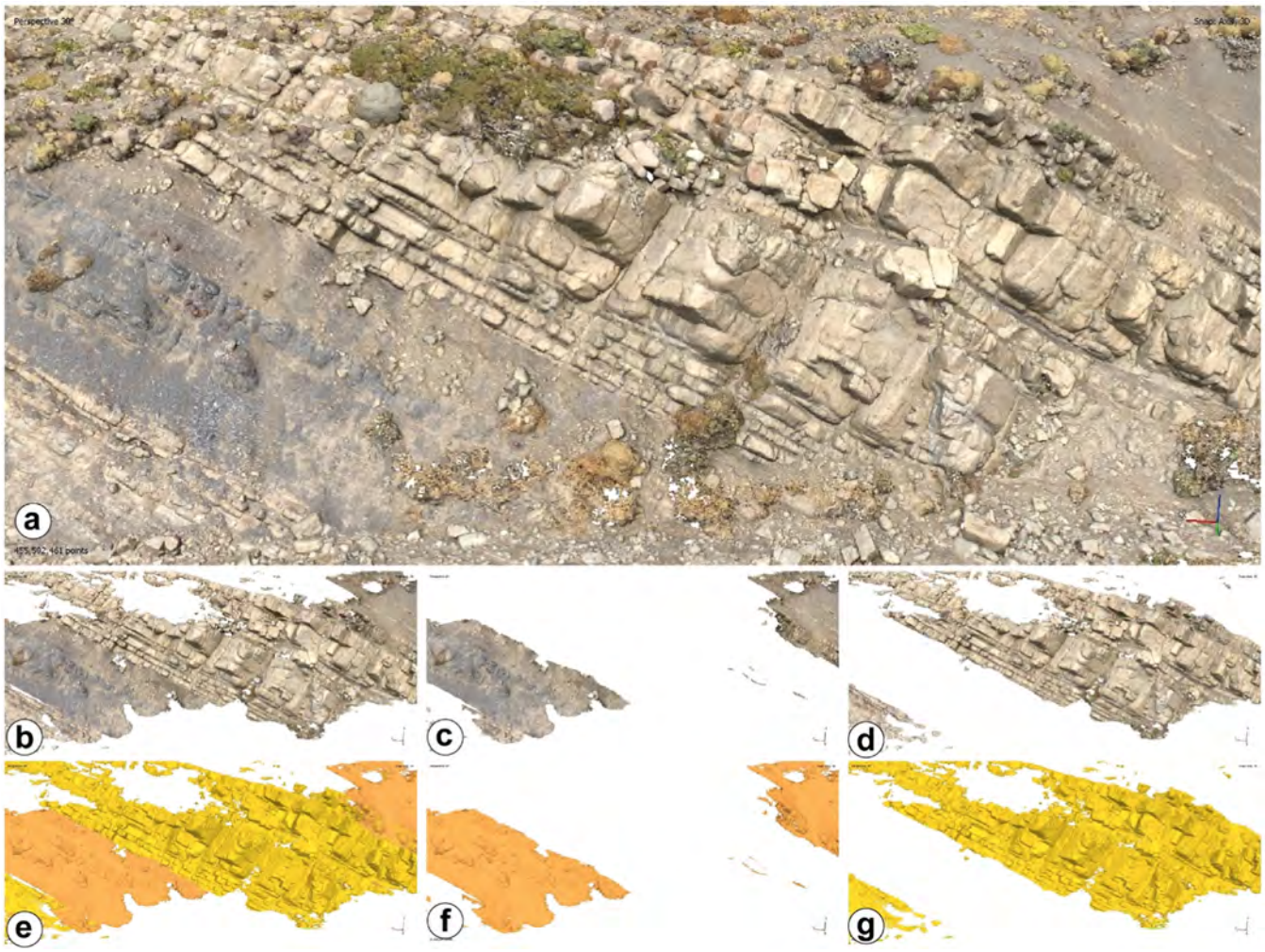


**Fig. 11.** Detailed view of the point clouds in the same oblique perspective as Figs. 9 and 10. (a) RGB-colored 3D point cloud of the entire dataset. (b–d) Fringe and lobe–interlobe points. (e–g) Fringe and lobe–interlobe classes are shown in orange and yellow, respectively.

the stratigraphic framework with the orthophotomosaic, as shown in Fig. 5.

### 3.1. Image labeling

The images were labeled in Adobe Photoshop through the following steps: (i) creating two new layers for lobe-interlobe and fringe labels; (ii) using the quick selection tool, either using a computer mouse or a pen tablet, to select the portion of the image corresponding to each label; (iii) applying the paint bucket tool to fill the label to the corresponding layer using a pre-defined colour; and (iv) exporting each layer as a separate PNG image for each label.

Of the 721 images captured in the field, 69 were randomly selected and labeled using this approach (Fig. 6), with an average labeling time of 9 min and 18 s. Labeling the entire dataset required approximately 10 h of human work.

### 3.2. CNN results

The CNN model's accuracy assessment (Section 2.2) was performed in increments of five images. As shown in Fig. 7, after 30 labeled images, the model stabilized at an average accuracy of 82 %. Table 1 shows the validation results for a 50/50 train/test split. The final model was then trained on all 69 labeled images and applied to segment the full dataset.

The model was implemented in Python using the specialized TensorFlow library and run on a machine equipped with an Intel Core I7 (12th generation) processor and an NVIDIA GeForce RTX A5500 graphics card with 24 GB of dedicated memory and 32 GB of shared memory. The output produced 721 labels for the lobe-interlobe and 721 for the fringe.

Fig. 8 illustrates the retrained model's final predictive capability. Analyzing the entropy maps allows it to identify regions where the model was more confident in its predictions and areas where it struggled to predict the actual architectural elements.

### 3.3. SfM-MVS

The SfM-MVS pipeline was implemented using the Agisoft Metashape software. The entire dataset was imported into a single processing group (chunk), and the original image size and generic preselection were set to run the alignment procedure, resulting in 711,000 tie points. The MVS procedure has been applied to the entire dataset, producing 455 million points in the cloud (Fig. 9a).

The processing group was duplicated twice, and each label set was imported into the software. The MVS procedure was then run by calculating depth maps for each image only in the labeled image region. This generated two separate classified 3D point clouds: one for the lobe-interlobe architectural element, containing 85 million points, and one for the fringe element, containing 21 million points (Fig. 9c and d).

Even though the U-net's accuracy might not be perfect, the SfM-MVS pipeline reconstructs the 3D point clouds based on two or more overlap-

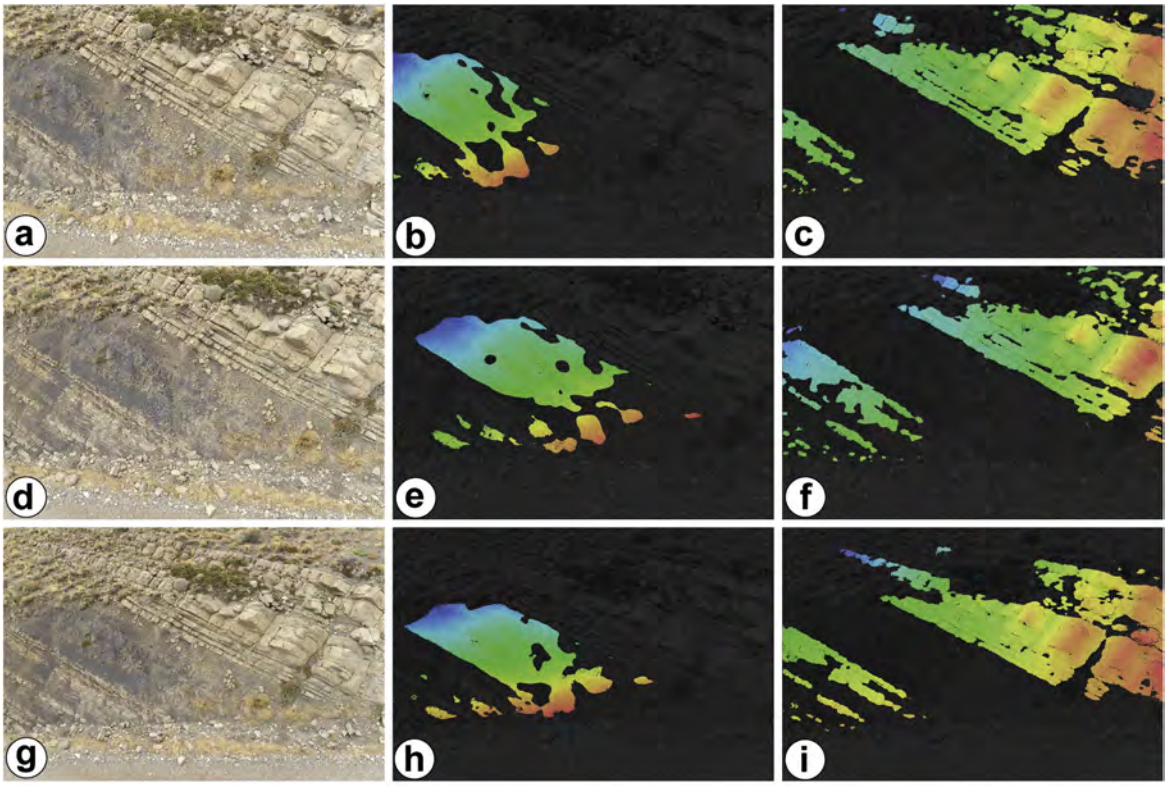


**Fig. 12.** Three images from the dataset to exemplify the segmentation results of the points shown in Fig. 11. The original image (a, b, and g), the depth maps for the fringe architectural element (b, e, and h), and for the lobe-interlobe (c, f, and i) are shown.

ping segmented images; eventual segmentation errors are automatically filtered out from the cloud. As the model's output is used to mask the images for the photogrammetry step, only points in space covered by multiple masks will be present in the 3D point cloud. Additionally, the workflow classifies architectural elements, removes noisy points, and effectively filters out points that do not correspond to outcropping rocks, such as vegetation and surface sediments. As shown in Figs. 9, 10, and 11, the resulting classified 3D point clouds contain minimal classification errors or noisy points, primarily containing points related to the segmented architectural elements.

## 4. Discussions

The proposed workflow for generating classified 3D point clouds for facies based on CNN-segmented images offers several advantages over traditional manual classification, though it also has some limitations, which are discussed here. Manual classification of 3D point clouds from rock outcrops, open-pit mines, road cuts, or tunnels is generally impractical (e.g., Weidner & Kromer, 2019). The main reasons are: (i) the high volume of data in a typical survey, which can cover hundreds to several thousand square meters and contain hundreds of millions or even billions of points in the cloud; (ii) the process is excessively time-consuming, requiring intense human labor usually carried out by a team of expert geoscientists; (iii) manual classification is prone to errors, such as misidentifying or misclassifying points due to fatigue, subjectivity, or differing interpretations of rock features; (iv) inconsistent results, as different experts might classify the same point cloud differently based on their experience or perspective, reducing the reliability and reproducibility; and (v) limited scalability, as it is nearly impossible to manually interpret large areas or multiple sites (e.g., Waldhauser et al., 2014; Kong et al., 2020; Daghigh et al., 2022; Mirzaei et al., 2022).

In contrast, the proposed workflow reduces human labor and interpretation time, increases reproducibility, and allows uncertainty estimation. One key benefit is the removal of noisy points and non-geological elements such as vegetation, soil, the sky, or man-made objects. Furthermore, the approach potentially applies to various geological scenarios, as discussed below.

In the La Jardinera case study, labeling the two visible architectural elements, lobe-interlobe and fringe, took about 10 min per image, totaling approximately 10 h of human labor. This time may vary depending on the geological complexity and heterogeneity of the exposure and the interpreter's experience. Manual point-by-point labeling of the 3D point cloud is unfeasible, as it contains 45 million points. In contrast, manually labeling groups of points is feasible and could be completed in the same 10-hour timeframe. However, this would still be subject to the same limitations of manual interpretation, including misclassification and lack of reproducibility. The proposed workflow can be rerun anytime by simply executing the code. Users can identify misclassifications, and the corresponding images can be labeled and added to the dataset. This interactivity helps to reduce the widespread manual work by focusing it only where necessary.

Noisy points and non-geological elements are removed from the segmented point clouds because the SfM-MVS pipeline requires at least two images of the same feature, captured from distinct perspectives, to generate the 3D point cloud. As a result, when CNN identifies a geological feature in only one image, the pipeline does not generate points for it, effectively filtering it out. The same applies to non-geological features not segmented in the CNN model (Figs. 11 and 12). As a result, the final 3D models are more robust against misclassification.

The labels used in the case study can be applied to classify 3D point clouds in similar geological records – turbidite deposits in proximal environments, where lobe-interlobe and fringe architectural elements are present. Beyond that, the workflow has the potential to be applied in different geological scenarios, as it has already been used to segment 3D point clouds of coral reefs by Hopkinson et al. (2020), Yuval et al. (2021), Sauder et al. (2023), and Marlow et al. (2024); and

to segment building façades (e.g., Lotte et al., 2018; Bacharidis et al., 2020), achieving satisfactory results.

Considering the results presented here and those published in the literature, the workflow shows promise for a broader application in geological settings where visually distinct geological features occur. In the future, continued research in CNN-based segmentation of geological outcrop images could lead to developing a large labeled dataset, similar to those used in medical imaging applications (e.g., Armato III et al., 2015), ultimately enabling broader applicability across various geological contexts.

A key limitation of this workflow is the need to reduce the image resolution to improve computational performance, which can hinder the model's ability to classify thin layers accurately. Another limitation is the model's tendency to confuse fresh rock with segregated material due to similar color and texture. Both issues can be mitigated through improved pre-processing and data augmentation strategies.

## 5. Conclusions

The workflow presented in this study has been successfully applied to segment the 3D point cloud of the La Jardinera outcrop and classify the architectural elements within the turbidite depositional system. Notably, only a small fraction (~10 %) of the images required manual labeling, which took approximately 10 h of human effort. The workflow efficiently reduces human interference and interpretation time while improving reproducibility. The resulting classified 3D point clouds contain very few noisy points and focus on accurately reconstructing the exposed rocks, minimizing the need to filter out vegetation, sediments, and sky.

Additionally, future workflow applications in different geological settings will be essential to demonstrate their versatility and validate their broader applicability. Generating large, interpreted datasets may also provide a foundation for training models in unexplored areas, thereby contributing to the advancement of deep learning techniques in geological research.

## Declaration of competing interest

The authors declare the following financial interests/personal relationships which may be considered as potential competing interests:

Felipe Guadagnin reports that Petrobras provided financial support to purchase equipment, cover expenses, and travel costs. Eduardo Roemers-Oliveira, Miguel de Morais Lima Silveira, Guilherme Pederneiras Raja Gabaglia, Lucas Arienti Goncalves reports a relationship with Petrobras that includes: employment. If there are other authors, they declare that they have no known competing financial interests or personal relationships that could have appeared to influence the work reported in this paper.

## CRediT authorship contribution statement

**Felipe Guadagnin:** Writing – original draft, Visualization, Validation, Supervision, Methodology, Investigation, Formal analysis, Conceptualization. **Ítalo Gomes Gonçalves:** Writing – review & editing, Writing – original draft, Validation, Methodology, Investigation, Formal analysis, Conceptualization. **Eduardo Roemers-Oliveira:** Writing – review & editing, Writing – original draft, Validation, Methodology, Conceptualization. **Pablo Losano Guedes:** Writing – original draft, Methodology, Investigation. **Ezequiel Galvão de Souza:** Writing – review & editing, Writing – original draft, Validation, Investigation, Formal analysis. **Miguel de Morais Lima Silveira:** Writing – review & editing, Visualization, Methodology, Formal analysis, Conceptualization. **Guilherme Pederneiras Raja Gabaglia:** Writing – review & editing, Visualization, Investigation, Conceptualization. **Lucas Arienti Gonçalves:** Writing – review & editing, Validation, Investigation. **Luiz Felipe Ribeiro de Oliveira:** Writing – review & editing, Visualization, Methodology, Formal analysis. **Ronaldo Selk:** Writing – review & editing, Validation, Methodology, Investigation, Formal analysis.

## Data availability

Data will be made available on request.

## Acknowledgements

The authors would like to acknowledge the funding support provided by the Brazilian National Agency of Petroleum, Natural Gas and Biofuels (ANP) through cooperation agreement No. 0050.0121770.22.9 (SIGITEC 2022/00056–5) with Petrobras. PE Limited (Petex) is acknowledged for providing access to the MOVE software available through academic licenses. We are also grateful to the editor and reviewers for their constructive comments, which significantly improved the manuscript. Thanks to Gustavo Zvirtes for his valuable assistance with editing the English language.

## References

Armato III, S. G., McLennan, G., Bidaut, L., McNitt-Gray, M. F., Meyer, C. R., Reeves, A. P., Zhao, B., Aberle, D. R., Henschke, C. I., Hoffman, E. A., Kazerooni, E. A., MacMahon, H., Van Beek, E. J. R., Yankelevitz, D., Biancardi, A. M., Bland, P. H., Brown, M. S., Engelmann, R. M., Laderach, G. E., Max, D., Pais, R. C., Qing, D. P. Y., Roberts, R. Y., Smith, A. R., Starkey, A., Batra, P., Caligiuri, P., Farooqi, A., Gladish, G. W., Jude, C. M., Munden, R. F., Petkovska, I., Quint, L. E., Schwartz, L. H., Sundaram, B., Dodd, L. E., Fenimore, C., Gur, D., Petrick, N., Freymann, J., Kirby, J., Hughes, B., Casteele, A. V., Gupte, S., Sallam, M., Heath, M. D., Kuhn, M. H., Dharaiya, E., Burns, R., Fryd, D. S., Salganicoff, M., Anand, V., Shreter, U., Vastagh, S., Croft, B. Y., & Clarke, L. P. (2015). Data from LIDC-IDRI [Data set]. *The Cancer Imaging Archive*. 10.7937/K9/TCIA.2015.LO9QL9SX.

Bacharidis, K., Sarri, F., & Ragia, L. (2020). 3D Building façade reconstruction using Deep learning. *International Journal of Geo-Information, 9*. 10.3390/ijgi9050322.

Bilmes, A., D'Elia, L., Lopez, L., Richiano, S., Varela, A., Alvarez, M. P., Bucher, J., Eymard, I., Muravchik, M., Franzese, J., & Ariztegui, D. (2019). Digital outcrop modelling using "structure-from- motion" photogrammetry: Acquisition strategies, validation and interpretations to different sedimentary environments. *Journal of South American Earth Sciences, 96*, Article 102325. 10.1016/j.jsames.2019.102325.

Buckley, S. J., Ringdal, K., Naumann, N., Dolva, B., Kurz, T. H., Howell, J. A., & Dewez, T. J. B. (2019). LIME: Software for 3-D visualization, interpretation, and communication of virtual geoscience models. *Geosphere, 15*, 222–235. 10.1130/GES02002.1.

Burnham, B. S., & Hodgetts, D. (2019). Quantifying spatial and architectural relationships from fluvial outcrops. *Geosphere, 15*, 236–253. 10.1130/GES01574.1.

Carrivick, J. L., Smith, M. W., & Quincey, D. J. (2016). *Structure from motion in geoscience*. John Wiley & Sons, Ltd. ISBN 9781118895818.

Catuneanu, O. (2022). *Principles of sequence stratigraphy*. Elsevier Science.

Catuneanu, O. (2019). Model-independent sequence stratigraphy. *Earth-Science Reviews, 188*. 10.1016/j.earscirev.2018.09.017.

Cawood, A. J., Bond, C. E., Howell, J. A., Butler, R. W. H., & Totake, Y. (2017). LiDAR, UAV or compass-clinometer? Accuracy, coverage and the effects on structural models. *Journal of Structural Geology, 98*, 67–82. 10.1016/j.jsg.2017.04.004.

Cheng, G., & Guo, W. (2017). Rock images classification by using deep convolution neural network. *Journal of Physics: Conference Series, 887*, Article 012089. 10.1088/1742-6596/887/1/012089.

Cordani, U.G., Ramos, V.A., Fraga, L.M., Cegarra, M., Delgado, I., Souza, K.G., Gomes, F.E.M., & Schobbenhaus, C. (2016). *Tectonic map of South America, 2nd. Ed*. Paris: CGMW-CPRM-SEGEMAR. 1 map. Scale 1:5.000.000.

Daghigh, H., Tannant, D. D., Daghigh, V., Lichti, D. D., & Lindenbergh, R. (2022). A critical review of discontinuity plane extraction from 3D point cloud data of rock mass surfaces. *Computers & Geosciences, 169*, Article 105241. 10.1016/j.cageo.2022.105241.

Dawson, H. L., Dubrule, O., & John, C. M. (2023). Impact of dataset size and convolutional neural network architecture on transfer learning for carbonate rock classification. *Computers and Geosciences, 171*, Article 105284. 10.1016/j.cageo.2022.105284.

Diara, F., & Roggero, M. (2022). Quality assessment of DJI Zenmuse L1 and P1 LiDAR and photogrammetric systems: Metric and statistics analysis with the integration of Trimble SX10 data. *Geomatics, 2*, 254–281. 10.3390/geomatics2030015.

Falivene, O., Auchter, N. C., Pires de Lima, R., Kleipool, L., Solum, J. G., Zarian, P., & Espejo, I. (2022). Lithofacies identification in cores using deep learning segmentation and the role of geoscientists: Turbidite deposits (Gulf of Mexico and North Sea). *American Association of Petroleum Geologists Bulletin, 106*, 1357–1372. 10.1306/03112221015.

Fischler, M. A., & Bolles, R. C. (1981). Random sample consensus: A paradigm for model fitting with applications to image analysis and automated cartography. *Communications of the ACM, 24*(6), 381–395. 10.1145/358669.358692.

Furukawa, Y., & Hernández, C. (2015). Multi-view stereo: A tutorial. *Foundations and Trends® in Computer Graphics and Vision, 9*. 10.1561/0600000052.

Giacomone, G., Olariu, C., Steel, R., & Shin, M. (2020). A coarse-grained basin floor turbidite system – the Jurassic Los Molles Formation, Neuquen Basin, Argentina. *Sedimentology*, 67. 10.1111/sed.12771.

Gonçalves, L. A., Arienti, L. M., D'Ávila, R. F. S., Carbone, O. C., & Ribeiro, A. (2022). High-resolution sequence stratigraphy applied to turbidites: The case study of jurassic los molles formation, Neuquén basin, Argentina. *Journal of South American Earth Sciences, 120*. 10.1016/j.jsames.2022.104078.

Gross, E. C., Carr, M., & Jobe, Z. R. (2023). Three-dimensional bounding surface architecture and lateral facies heterogeneity of a wet aeolian system: Entrada Sandstone, Utah. *Sedimentology*, 70. 10.1111/sed.13035.

Hopkinson, B. M., King, A. C., Owen, D. P., Johnson-Roberson, M., Long, M. H., & Bhandarkar, S. M. (2020). Automated classification of three-dimensional reconstructions of coral reefs using convolutional neural networks. *Plos One*. 10.1371/journal.pone.0230671.

Horota, R. K., Rossa, P., Marques, A., Jr., Gonzaga, L., Jr., Senger, K., Cazarin, C. L., Spigolon, A., & Veronez, M. R (2023). An immersive virtual field experience structuring method for geoscience education. *IEEE Transactions on Learning Technologies, 16*, 121–132. 10.1109/TLT.2022.3207089.

From Howell, J. A., Schwarz, E., Spalletti, L. A., & Veiga, G. D. (2005). The Neuquén Basin: An overview. In G. D. Veiga, L. A. Spalletti, J. A. Howell, & E. Schwarz (Eds.), *The neuquén basin, argentina: A case study in sequence stratigraphy and basin dynamics*. *The neuquén basin, argentina: A case study in sequence stratigraphy and basin dynamics*: 252 Geological Society, London, Special Publications. 10.1144/GSL.SP.2005.252.01.01.

Howell, J. A., Martinius, A. W., & Good, T. R. (2014). The application of outcrop analogues in geological modelling: A review, present status and future outlook. *Geological Society Special Publications, 387*. 10.1144/SP387.12.

Kamaruzaman, E. H., La Croix, A. D., & Kamp, P. J. J (2024). Interpreting environments of deposition from facies analysis of outcrop versus seismic reflection data: A cautionary tale from the Mount Messenger Formation, Taranaki Basin (New Zealand). *Marine and Petroleum Geology, 167*. 10.1016/j.marpetgeo.2024.106934.

Keogh, K. J., Leary, S., Martinius, A. W., Scott, A. S. J., Riordan, S., Viste, I., Gowland, S., Taylor, A. M., & Howell, J. (2014). Data capture for multiscale modelling of the Lourinhã Formation, Lusitanian Basin, Portugal: An outcrop analogue for the Statfjord Group, Norwegian North Sea. *Geological Society Special Publications, 387*. 10.1144/SP387.1.

Koeshidayatullah, A., Morsilli, M., Lehrmann, D. J., Al-Ramadan, K., & Payne, J. L. (2020). Fully automated carbonate petrography using deep convolutional neural networks. *Marine and Petroleum Geology, 122*, Article 104687. 10.1016/j.marpetgeo.2020.104687.

Kong, D., Wu, F., & Saroglou, C. (2020). Automatic identification and characterization of discontinuities in rock masses from 3D point clouds. *Engineering Geology, 265*, Article 105442. 10.1016/j.enggeo.2019.105442.

Liu, X., & Song, H. (2020). Automatic identification of fossils and abiotic grains during carbonate microfacies analysis using deep convolutional neural networks. *Sedimentary Geology, 410*, Article 105790. 10.1016/j.sedgeo.2020.105790.

Liu, X., Chandra, V., Ramdani, A. I., Zuhlke, R., & Vahrenkamp, V. (2023). Using Deep-Learning to predict Dunham textures and depositional facies of carbonate rocks from thin sections. *Geoenergy Science and Engineering, 227*, Article 211906. 10.1016/j.geoen.2023.211906.

Lotte, R. G., Haala, N., Karpina, M., Aragão, L. E. O. C., & Shimabukuro, Y. E. (2018). 3D Façade labeling over complex scenarios: A case study using convolutional neural network and structure-from-motion. *Remote Sensing, 10*. 10.3390/rs10091435.

Lowe, D. G. (2004). Distinctive image features from scale-invariant keypoints. *International Journal of Computer Vision, 60*, 91–110. 10.1023/B:VISI.0000029664.99615.94.

Malik, O. A., Puasa, I., & Lai, D. T. C. (2022). Segmentation for multi-rock types on digital outcrop photographs using deep learning techniques. *Sensors, 22*, 8086. 10.3390/s22218086.

Marques, A., Horota, R. K., Souza, E. M., Kupssinskü, L., Rossa, P., Aires, A. S., Bachi, L., Veronez, M. R., Gonzaga, L., & Cazarin, C. L. (2020). Virtual and digital outcrops in the petroleum industry: A systematic review. *Earth-Science Reviews, 208*, Article 103260. 10.1016/j.earscirev.2020.103260.

Marlow, J., Halpin, J. E., & Wilding, T. A. (2024). 3D photogrammetry and deep learning deliver accurate estimates of epibenthic biomass. *Methods in Ecology and Evolution*. 10.1111/2041-210X.14313.

Mirzaei, K., Arashpour, M., Asadi, E., Masoumi, H., Bai, Y., & Behnood, A. (2022). 3D point cloud data processing with machine learning for construction and infrastructure applications: A comprehensive review. *Advanced Engineering Informatics, 51*. 10.1016/j.aei.2021.101501.

Olariu, O., Steel, R. J., Vann, N. K., Tudor, E. P., Shin, M., Winter, R. R., Gan, Y. P., Jung, E., Almeida, F. N., Giacomone, G., Minisini, D., Brinkworth, W., Loss, M. L., Iñigo, J., & Gutierrez, R. (2020). Criteria for recognizing shelf-slope clinoforms in outcrop; Jurassic Lajas and Los Molles formations, S. Neuquén Basin, Argentina. *Basin Research, 32*, 279–292. 10.1111/bre.12395.

Paim, P. S., Silveira, A. S., Lavina, E. L., Faccini, U. F., Leanza, H. A., Teixeira de Oliveira, J. M. M., & D'Avila, R. S (2008). High resolution stratigraphy and gravity flow deposits in the Los Molles Formation (Cuyo Group, Jurassic) at La Jardinera region, Neuquén basin. *Revista de la Asociación Geológica Argentina, 63*(4), 728–753.

Pires de Lima, R., Nicholson, D., Slatt, C., & Marfurt, K. J. (2020). Petrographic microfacies classification with deep convolutional neural networks. *Computers & Geosciences, 142*, Article 104481. 10.1016/j.cageo.2020.104481.

Pires de Lima, R., & Duarte, D. (2021). Pretraining convolutional neural networks for mudstone petrographic thin-section image classification. *Geosciences, 11*(336). 10.3390/geosciences11080336.

Pringle, J. K., Howell, J. A., Hodgetts, D., Westerman, A. R., & Hodgson, D. M. (2006). Virtual outcrop models of petroleum reservoir analogues: A review of the current state-of-the-art. *First Break, 24*. 10.3997/1365-2397.2006005.

Roisenberg, H. B., Bállico, M. B., Guadagnin, F., Manna, M. O., & de Souza, E. G. (2022). Digital Outcrop Models applied to high-resolution stratigraphy in braided fluvial systems: A study case at Jaicós formation in Parnaíba Basin, NE Brazil. *Journal of South American Earth Sciences, 119*, Article 104006. 10.1016/j.jsames.2022.104006.

edited by Ronneberger, O., Fischer, P., & Brox, T. (2015). U-net: Convolutional networks for biomedical image segmentation. In N. Navab, J. Hornegger, W. M. Wells, & A. F. Frangi (Eds.), *Proceedings of the 18th International Conference on Medical Image Computing and Computer-Assisted Intervention* (pp. 234–241) Springer Link. edited byISBN 9783319245744.

Sauder, J., Banc-Prandi, G., Meibom, A., & Tuia, D. (2023). Scalable semantic 3D mapping of coral reefs with deep learning. *Methods in Ecology and Evolution*. 10.1111/2041-210X.14307.

Shannon, C. E. (1948). A mathematical theory of communication. *The Bell System Technical Journal*, 27. 10.1002/j.1538-7305.1948.tb01338.x.

chap. 3, 108–188 pp., authored by Sherman, W. R., & Craig, A. B. (2018). In W. R. Sherman, & A. B. Craig (Eds.), *The human in the loop* Morgan Kaufmann Publishers. chap. 3, 108–188 pp., authored byISBN 9780128009659.

Shorten, C., & Khoshgoftaar, T. M. (2019). A survey on image data augmentation for deep learning. *Journal of Big Data, 6*, 1–48. 10.1186/s40537-019-0197-0.

Silveira, A. S., Cardoso, M., Jr., Paim, P. S. G., Faccion, J. E., D'Ávila, R. S. F., & Leanza, H. (2024). 3D stochastic simulation of a deep-water turbidite system: An example from the Los Molles Formation, southern region of the Neuquén Basin, Argentina. *Journal of South American Earth Sciences*, 149. 10.1016/j.jsames.2024.105229.

Souza, J. F., Santana, G. L., Batista, L. V., Oliveira, G. P., Roemers-Oliveira, E., & Santos, M. D. (2020). CNN prediction enhancement by post-processing for hydrocarbon detection in seismic images. *IEEE access : Practical innovations, open solutions*. 10.1109/ACCESS.2020.3005916.

Tavani, S., Corradetti, A., Mercuri, M., & Seers, T. (2024). Virtual outcrop models of geological structures - from the construction of photogrammetric 3D models to their application towards the analysis of geological structures. *Società Geologica Italiana* ISSN: 9788894484465.

Toffanin, P. (2023). *OpenDroneMap: The missing guide*, UAV4GEO.

Yuval, M., Alonso, I., Eyal, G., Tchernov, D., Loya, Y., Murillo, A. C., & Treibitz, T. (2021). Repeatable semantic reef-mapping through photogrammetry and label-augmentation. *Remote Sensing, 13*. 10.3390/rs13040659.

Waldhauser, C., Hochreiter, R., Otepka, J., Pfeifer, N., Ghuffar, S., Korzeniowska, K., & Wagner, G. (2014). Automated classification of airborne laser scanning point clouds. In *Solving Computationally Expensive Engineering Problems. Springer Proceedings in Mathematics & Statistics: 97*. 10.48550/arXiv.1404.4304.

Weidner, L., & Kromer, W. R. (2019). Classification methods for point clouds in rock slope monitoring: A novel machine learning approach and comparative analysis. *Engineering Geology, 263*, Article 105326. 10.1016/j.enggeo.2019.105326.

Westoby, M. J., Brasington, J., Glasser, N. F., Hambrey, M. J., & Reynolds, J. M. (2012). Structure-from-motion' photogrammetry: A low-cost, effective tool for geoscience applications. *Geomorphology (Amsterdam, Netherlands), 179*, 300–314. 10.1016/j.geomorph.2012.08.021.

Xu, Z., Ma, W., Lin, P., & Hua, Y. (2022). Deep learning of rock microscopic images for intelligent lithology identification: Neural network comparison and selection. *Journal of Rock Mechanics and Geotechnical Engineering, 14*(4), 1140–1152. 10.1016/j.jrmge.2022.05.009.